Femtosecond Optical Frequency Comb: Principle, Operation, and Applications

Kluwer Academic Publishers / Springer
Norwell, MA

Jun Ye and Steven T. Cundiff
Editors

PREFACE

Over the last few years, there has been a convergence between the fields of ultrafast science, nonlinear optics, optical frequency metrology, and precision laser spectroscopy. These fields have been developing largely independently since the birth of the laser, reaching remarkable levels of performance. On the ultrafast frontier, pulses of only a few cycles long have been produced, while in optical spectroscopy, the precision and resolution have reached one part in 10^{14}. Although these two achievements appear to be completely disconnected, advances in nonlinear optics provided the essential link between them. The resulting convergence has enabled unprecedented advances in the control of the electric field of the pulses produced by femtosecond mode-locked lasers. The corresponding spectrum consists of a comb of sharp spectral lines with well-defined frequencies. These new techniques and capabilities are generally known as "femtosecond comb technology." They have had dramatic impact on the diverse fields of precision measurement and extreme nonlinear optical physics.

The historical background for these developments is provided in the Foreword by two of the pioneers of laser spectroscopy, John Hall and Theodor Hänsch. Indeed the developments described in this book were foreshadowed by Hänsch's early work in the 1970s when he used picosecond pulses to demonstrate the connection between the time and frequency domains in laser spectroscopy. This work complemented the advances in precision laser stabilization developed by Hall. The parallel efforts on mode-locked lasers by Charles Shank, Erich Ippen, and others laid the groundwork for the development in the 1990s by Wilson Sibbett of Kerr-lens mode locking, the instantaneous nature of which yields sub-10 fs pulses directly from laser oscillators that correspond to strong phase-locking of the comb components across a broad optical spectrum. The synergy between precision spectroscopy and ultrafast lasers was catalyzed by the development of novel optical fiber with high nonlinearity and controlled dispersion.

In Chapter 1 we provide an introductory description of mode-locked lasers, the connection between time and frequency descriptions of their

output, the physical origins of the electric field dynamics, and an overview of applications of femtosecond comb technology. Chapter 2 by Ippen, Kärtner and Cundiff discusses the development of ultrashort lasers, particularly focusing on how to achieve an octave-spanning spectrum and pulse dynamics that are relevant to the stability and control of the comb. Chapter 3 by Bartels describes in detail high-repetition-rate ring oscillators for precision frequency metrology. Chapter 4 by Gaeta and Windeler provides in-depth discussions relating to the physics of bandwidth generation and the underlying noise process during pulse propagation through microstructure fibers. Certain aspects of comb dynamics and stability are presented in Chapters 5 by Steinmeyer and Keller. An attractive approach presented in Chapter 6 by Kobayashi makes use of optical parametric generation to produce high-peak-power, femtosecond pulses in the IR spectral domain. A detailed review of the traditional harmonic-based frequency chain is provided in Chapter 8 by Schnatz, Stenger, Lipphardt, Haverkamp, and Weiss, while the new epoch of absolute optical frequency measurement using femtosecond comb technology is reviewed in Chapter 7 by Udem, Zimmermann, Holzwarth, Fischer, Kolachevsky, and Hänsch. Chapter 9 by Diddams, Ye, and Hollberg provides an account of the current state-of-the-art performance and characterization of femtosecond comb systems used for optical frequency measurement, synthesis, and optical atomic clocks. Chapter 10 by Baltuška, Paulus, Lindner, Kienberger, and Krausz provides a thorough discussion of the generation of the high-intensity pulses needed to access the regime of extreme nonlinear optics and a review of the results obtained for above-threshold ionization. Control of high-harmonic generation is addressed in Chapter 11 by Gibson, Christov, Murnane and Kapteyn. Stabilization of mode-locked lasers and their applications to ultrasensitive sensors are discussed in Chapter 12 by Diels, Jones, and Arissian.

The rapid progress during the last 5–6 years has been breathtaking and has made a tremendous impact on both science and technology. We foresee an undiminished potential for similar advances in the near future. We hope that the readers of this book will share our enthusiasm and benefit from the material presented in this book.

The editors thank all of the chapter authors for their contributions. The efforts of Julie Phillips and Lynn Hogan in the JILA Scientific Reports Office are also gratefully acknowledged.

Boulder
September, 2004 Jun Ye and Steven T. Cundiff

CONTENTS

Foreword

HISTORY OF OPTICAL COMB DEVELOPMENT

John L. Hall,[1] and Theodor W. Hänsch,[2]
[1] *JILA, National Institute of Standards and Technology and University of Colorado*

[2] *Max-Planck-Institut für Quantenoptik*

In the past five years, progress in laser stabilization, optical frequency measurement, femtosecond laser development and stabilization, nonlinear optics, and related topics has been stunning and unexpected. The excitement surrounding the rapid evolution in these fields since 1999 gives us a hint of what it must have been like after 1927 when the first ideas of quantum mechanics were being introduced. With laser optics, however, the explosion of knowledge is based upon years of detailed, painstaking research in the independent fields of laser stabilization, ultrafast laser development, and highly nonlinear optics [1]. The coalescence of these fields has provided five years of almost unprecedented discovery while, at the same time, a new millennium in metrology has generated advances of fundamental value in the contributing fields and in their spin-offs. To give just two examples: (1) the precise synchronization of picosecond and femtosecond lasers [2] allows nonlinear surface probing at the single-molecule level using coherent anti-Stokes Raman microscopy and spectroscopy [3] and (2) the use of stabilized comb pulses allows time and frequency dissemination [4] over extended distances via fiber optics. The latter offers a new capability to metrologists and researchers interested in developing new accelerators and large-array radio telescopes.

Here we offer our perspective on how we got started on this incredible journey of discovery and why it is occurring at this time. The rest of this timely book highlights key technical advances from the perspective of the researchers who made them. Consequently, this book should be of interest to students, practitioners in this rapidly evolving field, and physicists, chemists, and biologists whose research will be enhanced by the insights and discoveries recounted here.

The historical development of pulsed and continuous wave (cw) lasers diverged right from the beginning. The solid-state ruby laser of Ted Maiman involved kilojoule discharges into flash lamps and repetition rates from zero up to once per minute. (The laser's high ion density implied that a serious power level would be involved.) In contrast, the gas laser of Ali Javan had much lower gain margins and required temporal stability to allow its incremental approach to the laser threshold. From the early 1960s until about 1990, the pulse and cw laser communities continued to diverge. The cw laser folks liked to enhance the stability of their lasers, because stability was the main good feature they had. Certainly it wasn't the ability to burn holes through Gillette razor blades, a popular specification for pulsed lasers of the day. Over the years, the cw-laser teams learned to frequency stabilize their milliwatt-scale lasers, eventually reaching into the subhertz domain. Some members of the pulse-laser community escalated to kilojoule pulse energies delivered in nanoseconds for fusion target compression and even larger discharges to be delivered to potentially hostile moving targets.

On the other hand, the university research community wanted pulse lasers with high repetition rates that would enhance nonlinear responses, enable signal averaging over many pulses, and reduce the destructive impact of the probing radiation on the probed system. Thus began the search for laser media that were quiet and calm enough to lead to repeatable pulses, even at high repetition rate. First came the mode-locked He-Ne laser followed by actively mode-locked Argon lasers, which were developed commercially to give nanosecond pulses at 100 MHz rates. By the time synchronously pumped mode-locked picosecond dye lasers were introduced in the mid-1970s, the comb approach to frequency measurement was probably already inevitable, albeit more than 20 years in the future.

A driving force in the development of laser (and optical comb) technologies was the desire to learn more about the physical world. For instance, Professor Hänsch's group at Stanford (and later in Garching) focused on learning about the hydrogen spectrum, comparing hydrogen with deuterium to see the isotope shifts, accurately determining energies associated with various principal quantum numbers, and so forth. From the beginning, they realized that certain physical parameters, such as the Lamb shift or proton-size changes, could be isolated by using their quantum-number-scaling dependence and thus probed in the optical regime.

At Stanford, Hänsch's team demonstrated one of the first mode-locked "femtosecond" dye lasers (with a pulse length of less than one picosecond) in 1977 [5]. Their progress in laser research was closely connected to the invention of spectroscopic techniques in the sub-Doppler regime as part of their work on precision spectroscopy of the simplest atomic system, hydrogen. The group's new tunable dye-laser pulses were soon used in a

landmark experiment to demonstrate Fourier's reality to us: stable pulse trains — evenly-spaced in time — represented as stable combs of frequency components. We note that in the late 1970s, Veniamin Chebotayev in Novosibirsk had also begun thinking about stable, repetitive laser pulse trains. Even though the early experiments could not yet verify the precisely equal spacing of the comb frequencies, Eckstein, Ferguson, and Hänsch [6] used a comb structure to measure some fine and hyperfine frequency intervals in atomic sodium in 1978. This classic paper would help define the future impact of ultrafast lasers on precision measurement. Then, as the work at Garching progressed over the years, one dream became clear and insistent: if *only* we could measure optical frequencies directly and accurately!

This vision led the Garching team to flirt with extended chains of synchronized frequency sources. In the late 1980s, their new idea [7] was to deal with a series of increasing frequency *differences* between tunable diode laser sources. In this way, they hoped to avoid one of the major headaches of traditional chains — the step-wise increase of *absolute* frequencies throughout the chain that obliges one to develop a different laser technology at many points to cover the 10^5 frequency ratio from the microwave regime to the visible. A number of laser-diode frequency-interval-divider stages were built. A four-stage system was used for one of the hydrogen frequency measurements.

The comb idea jumped ahead with the demonstration of intracavity modulator-based spectral comb generators by Kourogi et al. [8]. In these experiments, pulses were modulated onto stable cw laser beams. Researchers in both Garching [9] and Boulder [10] recognized the utility of these devices and launched frequency-measurement programs using their few terahertz width modulator-based optical combs to bridge the awkward frequency gaps.

In the meantime, the ultrafast laser community continued to work toward improved pulse train stability and shorter pulses. Researchers developed several solid-state lasers, such as the cw-pumped mode-locked Nd:YAG, that were attractive for their stability. However, pulse durations below 30 ps were difficult to obtain because of the gain-bandwidth limitation of the laser material itself. Eventually the "intelligent and beautiful princess" — the titanium-doped sapphire laser system — was introduced and developed, along with the important discovery of Kerr-lens mode locking by Wilson Sibbett in St. Andrews [11]. These inventions changed femtosecond lasers from delicate contraptions to simple and reliable devices. Soon afterwards, commercial Ti:sapphire femtosecond lasers became readily available and they offered sub-100 fs pulses by the early 1990s. By 1994, the Garching group had acquired a Coherent Mira* laser for frequency metrology experiments. This laser and other similar devices opened the door to solving an array of challenging problems.

The factors that limit the shortness of the generated laser pulses arise from two issues: (1) finite gain-bandwidth product (which is not a problem for Ti:sapphire) and (2) intracavity dispersion. A short pulse can be viewed as the superposition of many cw phase-locked modes, all of which oscillate at their own cavity-defined frequencies. For the pulse train to be stable in time, the modes must have a common frequency separation. Because of dispersion in the sapphire, intracavity air, and mirror coatings, these cavity frequencies are generally not exactly evenly spaced. This is particularly true as the spectral bandwidth dramatically increases. So even with the ~30% bandwidth of Ti:sapphire, further shortening of sub-100 fs pulses proved difficult until Asaki et al. [12] employed a sufficiently general analysis of the pulse laser cavity. This model included the index of refraction characteristics of the intracavity dispersion-compensating prisms, the resulting color influence on the refraction direction, associated cavity path lengths, and some modeling of the air and laser crystal dispersion. Space-time focusing of the light bullet in the laser crystal was another important consideration.

In the early 1990s, when most of researchers were working feverishly to shorten pulse widths, some dreamers began to think of pulses so short that their Fourier representation would span from radio frequencies up into the visible domain. This idea seemed like science fiction to one of the authors (JLH) and a likely possibility to the other (TWH). Of course, spectral self-broadening was well known. By focusing powerful amplified pulses into water or some solids, one could basically generate a white-light continuum. At elevated pulse energy levels, one expected serious disruption of the calmness of the intermolecular bonds; consequently, one would not expect to find a phase-stable repetition of the generated white light. Perhaps a glass sample *could* melt and recrystallize at a 100 MHz rate, emitting a similar thermal spectrum on every heating cycle. However, to form a coherent optical comb in the forward direction, the timing would need to be stable to ~1 radian — at the visible frequency! Few believed that this thermal process would be stable at the 0.3 fs level needed. Rather, it seemed clear that a more gentle process would be required, in which somewhat less-powerful laser pulses would strongly distort some atomic wave functions but not disrupt chemical bonds. Atomic frequencies are so high that when the pulse is gone, calmness can return; the next pulse would be able to generate just the same effect on the system. In this case, the phase-coherence of the source pulses could insure that the nonlinearly generated frequencies would be mutually coherent pulse-to-pulse.

Researchers in both Garching and Boulder set out to learn about this subject. In Europe, an amplified pulse was split into two parts and focused onto two separate spots in a CaF_2 crystal. The white light produced in each spot in the CaF_2 plate interfered with each other in a geometry that allowed

the time delays to be equalized. Miraculously, stable white interference fringes could be seen by eye [13]. In this way, the Garching group realized that the phase of the nonlinearly generated light was stable enough to form an optical comb! This experiment led to Hänsch's detailed six-page proposal, dated March 30, 1997, for an octave-spanning self-referenced universal optical-frequency comb synthesizer. Following this proposal, developments in the art of femtosecond-laser frequency comb generation began to appear quickly.

The next year (1998) saw the first crucial test of a Kerr-lens mode-locked Ti:sapphire laser in Garching [14]. This experiment clearly proved the viability of femtosecond-laser frequency comb synthesizers. Before this experiment, some researchers had argued that the laser comb spectrum would be completely washed out by phase noise. Although some publications were held back due to the restrictions of German patent law, by 2000 the Garching team reported its first absolute frequency measurement with a comb (made in 1999) [15]. In a direct comparison with the transportable cesium fountain clock of the Bureau National de Métrologie – Systèmes de Référence Temps Espace, they measured the frequency of the hydrogen 1S–2S two-photon resonance with an uncertainty of 1.9×10^{-14}, which is more than an order of magnitude more accurate than any previous optical frequency measurement. This experiment firmly established the viability of optical frequency metrology with femtosecond laser frequency combs. It also electrified the frequency metrology community. The convenience and simplicity of octave-spanning frequency combs added to the attraction of this new approach.

In the meantime, researchers in Boulder were studying the spectral expansion associated with pulse propagation in an optical fiber as a possible replacement for their modulator-based comb generator. They showed that a cw test beam in the fiber developed a comb structure on it because of the co-propagating femtosecond pulses. However, the new comb only contained information about the repetition rate of the pulses, not about their optical frequency [16]. Of course, in retrospect, it is clear that this "cross-modulation" result (as opposed to "four-wave mixing") was preordained because of the huge difference in the phase velocities of the two colors. The interesting frequency-coupled wavelets never got a chance to coherently build up along the fiber's length. This experiment also showed that spectrally narrow features would be generated across a broad spectral range even when "pounding" on a fiber with powerful femtosecond pulses.

A classic 1999 paper [17] offered a complete description of issues and techniques for comb-based optical frequency measurement, including the famous carrier-envelope phase-slipping issue [18]. The Garching team made their first self-contained rf-to-optical frequency comparison [19] using a

comb configuration that had a stabilized carrier-envelope-offset frequency. Since the comb spectrum did not yet span an octave, some interval-divider stages with auxiliary lasers had to be used for self-referencing.

Soon afterwards, the world was turned upside down by Jinendra Ranka, Robert Windeler, and Andrew Stentz. During the 1999 CLEO postdeadline session, they announced that they had demonstrated that *white light* could be produced in a revolutionary way by using an internally structured fiber incorporating a number of air holes [20]. They showed pictures in which the input dark red pulse gradually transformed itself into green and blue, with expansion into the IR direction occurring as well. Soon it was discovered that supercontinuum could also be obtained in tapered fibers [21].

The central rod in the fiber preform had been surrounded by a number of hollow tubes. When drawn down to fiber scale, the inner "core" was surrounded by air that presented a vastly larger index contrast than found in normal fiber (where the contrast may be ~0.01). Consequently, a single-mode microstructure fiber would have a much smaller diameter for a given wavelength, for example 1.7 instead of 5 micrometers for 800 nm light. This meant that a laser beam focused into this fiber would have a ~tenfold higher intensity and generate ~tenfold larger self-induced phase shifts during the pulse because of the Kerr effect, which is analogous to the quadratic Stark effect in atoms. Suddenly, researchers learned that white light could be generated by normal femtosecond oscillators without expensive and low-repetition-rate amplifiers!

Researchers also realized that the special fiber could help with the phase matching needed for a big coupling to accrue. In the "holey" fiber, a number of fiber parameters could be designer variables: the basic glass and its dispersion, the core size, the fractional angular coverage of supporting web, the size, and number of surrounding air holes. By design, it proved possible to make a strong cancellation between dispersion of the fiber core material and the dispersion associated with the geometric structure. In this way an input pulse could propagate vastly longer distances — millimeters rather than micrometers — before its peak intensity was diminished by the different propagation speeds of its spectral components.

Knowing that the pulses were so gentle the fiber was not damaged and that all the frequency components would be cross-coupled together by the nearly constant propagation speed, we predicted the output of the fiber would be a *spectral comb of coherent frequencies*. Of course, for precision metrology, this idea would have to be tested.

The first question was: how can we get some "Magic Rainbow Fiber?" Our combined approaches to friends, colleagues, and administrators at Bell Labs all came to nothing, apparently because of the lawyers there. Luckily for the JILA team, its most recently recruited colleague, Steve Cundiff, had

been in a nearby group in the same part of Bell Labs. By some unknown means, the JILA team came up with a sample of "Magic Fiber" to test by November 1999. The Garching group teamed up with the powerful fiber group of P. St. J. Russell at the University of Bath (UK), which had been working with both microstructure and tapered fibers. New results began immediately rolling in [21, 22], and the publication competition began in earnest! (Since then, many alternatives to the Magic Fiber approach have emerged, including supercontinuum generation in tapered fibers [21], octave-spanning laser oscillators without the use of external fibers, mode-locked fiber lasers with some highly nonlinear ordinary fiber for spectral broadening, and schemes incorporating difference-frequency generation to determine the carrier-envelope-offset frequency with combs spanning less than an octave.)

At this point, the Boulder team had a significant advantage. They had already worked on laser stabilization and optical frequency standards for many years because of JILA's affiliation with the Boulder campus of the National Institute of Standards and Technology (NIST). Indeed, the authors of this foreword first met in Novosibirsk in 1969 at a conference organized by the late Veniamin Chebotayev on the topic of stabilized lasers. There, JLH presented his progress with a methane-stabilized He-Ne laser.

While other researchers were busy improving cw and pulsed lasers, national metrology and standards laboratories around the world had been trying to verify the frequencies of their "as-maintained" national wavelength standards. The first such measurements occurred in Boulder and led, in 1972, to the measurement of the frequency and wavelength of the methane standard. This measurement, in turn, led to a new and definitive value for the speed of light. Other national laboratories joined in, and a long discussion ensued about the philosophical and practical issues associated with calculating meters from the frequency of light rather than simply adopting new wavelength standards as they became available. Within 10 years, national laboratories in Canada, the United Kingdom, Japan, Germany, and Gaithersburg, Maryland, had confirmed parts of the Boulder work and the frequency of the He-Ne iodine-stabilized red laser had been determined. In 1983, the meter was redefined based on the speed of light.

The reproducibility of most of the reference lasers developed during this era was so good that their imperfections had little practical consequence for length metrology. Still, the optical frequency standards business continued to develop as researchers sought better designs and new reference transitions. More importantly, each nation wanted to confirm its own standards at the highest level.

Both NIST and PTB built very good systems to measure the calcium intercombination transition at 657 nm, for example. In addition, the PTB

team built up one of the best rf-to-optical harmonic frequency "chains," which took advantage of several decades of work on system components. While PTB's "traditional" frequency chain worked well, its sheer complexity was daunting. The German laboratory's state-of-the-art measurement [23] of the Ca frequency was published in 1996 and had a frequency uncertainty of ~ 430 hertz, arising from both the Ca standard and the measurement scheme. (By 2003 using femtosecond comb techniques, both NIST and PTB were reporting uncertainties for this frequency in the ~10 hertz range, limited mostly by interesting spectroscopic issues with the optical Ca standard.)

Its experience with optical frequency standards allowed the Boulder team at JILA to take Ranka et al.'s groundbreaking discovery of the properties of Magic Fiber and run with it. The Boulder team was the first to measure (and control) the carrier-envelope-offset frequency with a ν-to-2ν self-referenced comb [24]. With this method, they determined the frequency offset of the comb lines from the positions of harmonics of the repetition rate. Some known optical frequencies were confirmed. Within a few months, the group was also attempting to generate femtosecond pulses of controlled shape, in which the pulse-to-pulse carrier-envelope-offset phase was under the experimenter's control.

The absolute frequency measurements in the pre-comb epoch (prior to 1999) were suddenly such a bother! The simplicity and efficiency of the new comb-based measurements attracted wide interest and provided a huge boost to the optical frequency metrology and standards field. Some parts of a total optical frequency metrology system even became available commercially (see, for example, http://www.menlosystems.com/*). Five years into the optical frequency comb epoch, the once-independent laser research subcommunities are now extremely interdependent, at least as viewed from the perspective of results. Of course, each advance has been primarily an independent step, attractive in its own context. Which market planner could have organized this beauty?

One question remains, however: how can we be sure of the frequency comb results? The accuracy of comb techniques has been the subject of a number of tests, but no problems have turned up so far. JILA has used the comb technique to measure "known" optical standards. Rather than discovering limitations of the comb technique, we have typically found that these measurements refine our knowledge of the "known" standard [25]. Thus the obvious method of testing the comb by measuring a physical standard by both methods *is not successful because of limitations of the standards themselves*.

Using another approach, the Garching team compared an octave-spanning frequency-comb synthesizer [26] with the more complex frequency synthesizer used in their 1999 hydrogen-frequency measurement. By starting with a

common 10 MHz rf reference and comparing comb lines near 350 THz, they verified agreement within a few parts in 10^{16}; the precision of the experiment was probably limited by Doppler shifts due to air pressure changes or thermal expansion of the optical tables.

The Garching group also made additional accuracy tests on the comb-spacing uniformity using one stage of a frequency-interval divider [14]. The interval between comb lines near the edges of the "white" spectrum could be divided to find the "center" by two methods. Or, an edge line could be combined with one near the middle to seek a dispersive effect. No problems could be found. To really press to the testing limits, comb vs comb tests — using different comb frequencies, materials, or whatever we think could be important — are probably necessary. By late 2004, tests still had discovered no problems, and the accuracy in the context of frequency combs had reached 10^{-21} [27].

As we begin the next era in optical comb research, with each group measuring specific frequencies with femtosecond comb techniques, the realization of the cesium standard frequency is likely to be the first weak point. With a day's averaging, the GPS system can help us know our local frequency standard's average performance, but it takes about a day to deliver an accuracy ~1×10^{-14}; achieving this accuracy requires us to know the timing comparisons separately with each of the satellites used in the test. To test optical frequency combs against the highest traditional standard, modern fountain cesium clocks are usually available either by fiber link [4] or by physical transport.

Femtosecond combs are now ready to accurately measure any desired frequency such as those of some isolated hydrogen atoms at rest in a field-free vacuum, single Hg^+ or Yb^+ ions in an ion trap, or a million cold Sr atoms trapped in an optical lattice/trap. In addition, frequency comb techniques are having an impact on ultrafast physics. By making it possible to produce few-cycle pulses with a stabilized carrier-envelope phase, these tools are leading to the discovery of novel phenomena in nonlinear light-matter interactions. For example, by 2004 amplified phase-stabilized pulses had been used to produce controlled bursts of soft x-rays with time durations in the attosecond range [28].

So where do we go from here?

In contrast to the digital security of frequency measurement, in the final accuracy-defining step, it usually comes out that spectroscopic line-shape issues are what limit our results. How well do we know the connection between the center of the observed resonance line and the desired physical quantity? Resonance frequencies can be shifted by fields, laser intensity, Doppler shifts, and ... Careful treatment of such issues is part of what makes our field so fun. And, of course, many interesting measurements can be

designed so they measure *differences* or *temporal changes* and hence are better isolated from such limitations. But as our experiments improve, the line-center question will continue to reappear, ideally at an increasingly reduced sensitivity.

In summary, optical frequency combs have given us some comfortable metrological headroom for pushing ideas for new optical frequency standards and for measuring interesting physical constants. And, we feel confident that the new metrology based on integer arithmetic and femtosecond combs will be sufficient to reveal shortcomings in our spectroscopy ideas and implementations.

*Use of product name for technical information only and does not constitute an endorsement by NIST.

REFERENCES

[1] J. L. Hall, IEEE J. Sel. Top. Quantum Electron. **6**, 1136-1144 (2000).
[2] R. K. Shelton, L. S. Ma, H. C. Kapteyn, M. M. Murnane, J. L. Hall, and J. Ye, Science **293**, 1286-1289 (2001).
[3] E. O. Potma, D. J. Jones, J. X. Cheng, X. S. Xie, and J. Ye, Opt. Lett. **27**, 1168-1170 (2002).
[4] J. Ye, J. L. Peng, R. J. Jones, K. W. Holman, J. L. Hall, D. J. Jones, S. A. Diddams, J. Kitching, S. Bize, J. C. Bergquist, L. W. Hollberg, L. Robertsson, and L. S. Ma, J. Opt. Soc. Am. B **20**, 1459-1467 (2003).
[5] A. I. Ferguson, J. N. Eckstein, and T. W. Hänsch, Appl. Phys. Lett. **49**, 5389-5391 (1978).
[6] J. N. Eckstein, A. I. Ferguson, and T. W. Hänsch, Phys. Rev. Lett. **40**, 847-850 (1978).
[7] H. R. Telle, D. Meschede, and T. W. Hansch, Opt. Lett. **15**, 532-534 (1990).
[8] M. Kourogi, K. Nakagawa, and M. Ohtsu, IEEE J. Quantum Electron. **29**, 2693-2701 (1993).
[9] A. Huber, T. Udem, B. Gross, J. Reichert, M. Kourogi, K. Pachucki, M. Weitz, and T. W. Hänsch, Phys. Rev. Lett. **80**, 468-471 (1998).
[10] J. L. Hall, L. S. Ma, M. Taubman, B. Tiemann, F. L. Hong, O. Pfister, and J. Ye, IEEE Trans. Instrum. Meas. **48**, 583-586 (1999).
[11] D. E. Spence, P. N. Kean, and W. Sibbett, Opt. Lett. **16**, 42-44 (1991).
[12] M. T. Asaki, C. P. Huang, D. Garvey, J. P. Zhou, H. C. Kapteyn, and M. M. Murnane, Opt. Lett. **18**, 977-979 (1993).
[13] M. Bellini and T. W. Hänsch, Opt. Lett. **25**, 1049-1151 (2000).
[14] T. Udem, J. Reichert, R. Holzwarth, and T. W. Hänsch, Opt. Lett. **24**, 881-883 (1999).
[15] M. Niering, R. Holzwarth, J. Reichert, P. Pokasov, T. Udem, M. Weitz, T. W. Hänsch, P. Lemonde, G. Santarelli, M. Abgrall, P. Laurent, C. Salomon, and A. Clairon, Phys. Rev. Lett. **84**, 5496-5499 (2000).

[16] D. J. Jones, S. A. Diddams, M. S. Taubman, S. T. Cundiff, L. S. Ma, and J. L. Hall, Opt. Lett. **25**, 308-310 (2000).
[17] J. Reichert, R. Holzwarth, T. Udem, and T. W. Hänsch, Opt. Commun. **172**, 59-68 (1999).
[18] J. Eckstein, Ph.D Thesis, Stanford University (1978).
[19] J. Reichert, M. Niering, R. Holzwarth, M. Weitz, T. Udem, and T. W. Hänsch, Phys. Rev. Lett. **84**, 3232-3235 (2000).
[20] J. K. Ranka, R. S. Windeler, and A. J. Stentz, Opt. Lett. **25**, 25-27 (2000).
[21] T. A. Birks, W. J. Wadsworth, and P. S. Russell, Opt. Lett. **25**, 1415-1417 (2000).
[22] J. K. Ranka and R. S. Windeler, in *Opt. Photonics News*, 2000), Vol. 11, p. 20-25; J. K. Ranka, R. S. Windeler, and A. J. Stentz, Opt. Lett. **25**, 796-798 (2000).
[23] H. Schnatz, B. Lipphardt, J. Helmcke, F. Riehle, and G. Zinner, Phys. Rev. Lett. **76**, 18-21 (1996).
[24] D. J. Jones, S. A. Diddams, J. K. Ranka, A. Stentz, R. S. Windeler, J. L. Hall, and S. T. Cundiff, Science **288**, 635-639 (2000); S. A. Diddams, D. J. Jones, J. Ye, S. T. Cundiff, J. L. Hall, J. K. Ranka, R. S. Windeler, R. Holzwarth, T. Udem, and T. W. Hänsch, Phys. Rev. Lett. **84**, 5102-5105 (2000).
[25] J. Ye, T. H. Yoon, J. L. Hall, A. A. Madej, J. E. Bernard, K. J. Siemsen, L. Marmet, J.-M. Chartier, and A. Chartier, Phys. Rev. Lett. **85**, 3797 (2000).
[26] R. Holzwarth, T. Udem, T. W. Hänsch, J. C. Knight, W. J. Wadsworth, and P. S. J. Russell, Phys. Rev. Lett. **85**, 2264-2267 (2000).
[27] M. Zimmermann, C. Gohle, R. Holzwarth, T. Udem, and T. W. Hänsch, Opt. Lett. **29**, 310-312 (2004).
[28] R. Kienberger, E. Goulielmakis, M. Uiberacker, A. Baltuska, V. Yakovlev, F. Bammer, A. Scrinzi, Th.Westerwalbesloh, U. Kleineberg, U. Heinzmann, M. Drescher, and K. F., Nature **427**, 817-821 (2004).

Chapter 1

INTRODUCTION

Optical Frequency Combs and their Applications

Jun Ye and Steven T. Cundiff
JILA, National Institute of Standards and Technology and the University of Colorado

Abstract: Recently there has been a remarkable synergy between the technology of precision laser stabilization and mode-locked ultrafast lasers. This has resulted in control of the frequency spectrum, which consists of a regular "comb" of sharp lines, produced by mode-locked lasers. Such a controlled mode-locked laser is a "femtosecond optical frequency comb generator." For a sufficiently broad comb, it is possible to determine the absolute frequencies of all of the comb lines. This ability has revolutionized optical frequency metrology and synthesis. It has also served as the basis for the recent demonstrations of atomic clocks that utilize an optical frequency transition. In addition, it is having an impact on time-domain applications, including phase-sensitive extreme nonlinear optics and pulse manipulation and control. In this chapter, we first review the frequency-domain description of a mode-locked laser and the connection between the pulse phase and the frequency spectrum to provide a basis for understanding how the absolute frequencies can be determined and controlled. Using this understanding, applications in optical frequency metrology, optical atomic clocks, and precision spectroscopy are discussed. Next, we discuss applications of the carrier-envelope phase coherence in time-domain experiments. This chapter serves as a broad introduction and summary for all subsequent chapters that present detailed discussions of specific topics.

Key words: frequency comb, carrier-envelope phase, spectroscopy, optical frequency metrology, optical atomic clock, quantum coherence

Mode-locked lasers generate "ultrashort" optical pulses by establishing a fixed phase relationship across a broad spectrum of frequencies. Progress in the technology of mode-locked lasers has resulted in the generation of optical pulses that are only 5 femtoseconds (fs) in duration [1], which corresponds to less than 2 cycles of the laser light. Although "mode locking"

is a frequency-domain concept, mode-locked lasers and their applications are typically discussed in the time domain. Recently, a paradigm shift in the field of ultrafast optics has been brought about by switching to a frequency-domain treatment of the lasers and the pulse trains that they generate. Understanding mode-locked lasers in the frequency domain has allowed the extensive tools of frequency-domain laser stabilization to be employed with dramatic results.

The central concept of these advances is that the pulse train generated by a mode-locked laser has a frequency spectrum that consists of a discrete, regularly spaced series of sharp lines, known as an optical frequency comb. As described below, if the comb spectrum is sufficiently broad, it is possible to directly measure the two radio frequencies (rf) that describe the comb. This fact has had an immediate impact in the field of optical frequency metrology/synthesis [2-5] and has enabled the recent demonstration of optical atomic clocks [6]. Because the comb spectrum can be related to phase evolution in the pulse train [2, 7], these results also promise important advances in ultrafast science, specifically in extreme nonlinear optics [8] and coherent control. In addition, the union of time- and frequency-domain techniques has yielded remarkable results in pulse synthesis [9].

The idea that a regularly spaced train of pulses corresponds to a comb in the frequency domain and can thereby excite narrow resonances was realized more than 20 years ago [10]. Teets et al. [11] used a train of pulses generated externally to the laser. However, it was quickly realized that mode-locked lasers were superior as demonstrated in a measurement of the sodium hyperfine splitting using a picosecond laser [12]. Some of the concepts being developed today were described in these early papers, but the technology was insufficient to demonstrate them at the time. Advances in mode-locked laser technology, specifically the Kerr-lens–mode-locked Ti:sapphire laser, renewed interest in this area [13-15]. The observation of supercontinuum generation from nanojoule pulses in microstructure fiber [16] led to the recent, sudden explosion in activity.

In this chapter, we first discuss the time- and frequency-domain pictures of mode-locked lasers and the intrinsic connections between the evolution of the optical phase of the pulses and the frequency shift in the comb spectrum. This discussion provides the background for understanding how the absolute frequencies of the comb lines are determined and how the frequency-domain-based control techniques are used to exert time-domain effects. The ease and precision with which different parts of the electromagnetic spectrum can be connected has led to wide-ranging applications in precision optical frequency metrology including rf-based absolute optical frequency measurement, optical frequency synthesis and distribution, and rf-clock signal generation from a precisely stabilized optical clock oscillator. These

new capabilities have brought novel approaches to precision atomic and molecular spectroscopy and sensitive measurement instrumentation. For time-domain applications, precise control of comb frequency and phase has resulted in tight synchronization and phase lock among independent mode-locked laser sources, connecting various parts of optical spectra and synthesizing optical waveforms. The precise control of the carrier-envelope phase has led to new experimental capabilities in ultrafast science, including extreme nonlinear optical phenomena and coherent control. For example, interference among multiple photon-order excitation pathways can now be manipulated and controlled via a single mode-locked laser. The intrinsic ultrafast time scale associated with the sub-optical-cycle phase control has enabled ultrafast science to advance into the attosecond domain with a remarkable level of experimental command and precision.

1. TIME- AND FREQUENCY-DOMAIN PICTURES OF A MODE-LOCKED LASER

Understanding the connection between the time-domain and frequency-domain descriptions of a mode-locked laser and the pulse train that it emits is crucial. In this section, we first briefly introduce mode-locked lasers to provide the necessary background. Then we discuss how, given a spectrum that spans an octave, to determine the frequency spectrum of the pulse train emitted by a mode-locked laser and how the absolute frequencies of the comb spectrum can be determined. Finally, we present a prototype femtosecond comb generator along with some relevant characterization techniques.

A key concept in this discussion will be the carrier-envelope phase. This phase is based on the decomposition of an ultrashort pulse into an envelope function, $\hat{E}(t)$, that is superimposed on a continuous carrier wave with frequency ω_c, so that the electric field of the pulse is written $E(t) = \hat{E}(t)e^{i\omega_c t}$. The carrier-envelope phase, ϕ_{ce}, is the phase shift between the peak of the envelope and the closest peak of the carrier wave. In any dispersive material, the difference between group and phase velocities will cause ϕ_{ce} to evolve as the pulse propagates.

1.1 Introduction to mode-locked lasers

Mode-locked lasers generate short optical pulses by establishing a fixed-phase relationship between all of the lasing longitudinal modes (for a textbook level discussion, see [17]). Mode locking requires a mechanism

that results in a higher net gain for short pulses as compared to continuous wave (cw) operation. This mechanism can be either an active element or implemented passively with saturable absorption (real or effective). Passive mode locking yields the shortest pulses because, up to a limit, the self-adjusting mechanism becomes more effective as the pulse shortens [18]. Real saturable absorption occurs in a material with a finite number of absorbers, for example, a dye or semiconductor. The shortness of the pulses is limited by the finite lifetime of the excited state. Effective saturable absorption typically uses the nonlinear index of refraction of some material together with spatial effects or interference to produce higher net gain for shorter pulses. The ultimate limit on minimum pulse duration in such a mode-locked laser is due to the interplay between the mode-locking mechanism, group-velocity dispersion (GVD), and net gain bandwidth [18]. Chapter 2 discusses the development of ultrashort lasers, particularly focusing on how to achieve an octave-spanning spectrum and pulse dynamics that are relevant to the stability and control of the comb. Further aspects of the comb dynamics and stability are presented in Chapters 5, 7, 9, 10, and 12.

Currently, the generation of ultrashort optical pulses is dominated by the Kerr-lens–mode-locked Ti:sapphire (KLM Ti:sapphire) laser because of its excellent performance and relative simplicity. Kerr-lens mode locking is based on a combination of self-focusing in the Ti:sapphire crystal and an aperture that selects the spatial mode corresponding to the presence of self-focusing. The Ti:sapphire crystal is pumped by green light from either an Ar^+-ion laser or a diode-pumped–solid-state (DPSS) laser, which provides far superior performance in terms of laser stability and noise. The Ti:sapphire crystal provides gain and serves as the nonlinear material for mode locking. Prisms or dispersion-compensating mirrors compensate the GVD in the gain crystal [19]. Chapter 3 describes in detail a high repetition-rate ring oscillator system. Since the discovery of KLM [20], the pulse width obtained directly from mode-locked lasers has been shortened by approximately an order of magnitude by first optimizing the intracavity dispersion [21] and then using dispersion-compensating mirrors [1], yielding pulses that are less than 6 fs in duration, i.e., less than two optical cycles. Recently, output spectra that span an octave (factor of two in frequency) have been obtained directly from a mode-locked laser [22], which is an important accomplishment for phase stabilization.

1.2 Frequency spectrum of a mode-locked laser

To understand how frequency-domain techniques can be used to control mode-locked lasers, we must first connect the time- and frequency-domain

descriptions [23]. To start, we ignore the carrier-envelope phase and assume identical pulses, i.e., ϕ_{ce} is a constant. If we just consider a single pulse, it will have a power spectrum that is the Fourier transform of its envelope function and is centered at the optical frequency of its carrier. Generally, for any pulse shape, the frequency width of the spectrum will be inversely proportional to the temporal width of the envelope. For a train of identical pulses, separated by a fixed interval, the spectrum can easily be obtained by a Fourier series expansion, yielding a comb of regularly spaced frequencies, where the comb spacing is inversely proportional to the time between pulses, i.e., it is the repetition rate (f_r) of the laser that is producing the pulses. The Fourier relationship between time and frequency resolution guarantees that any spectrometer with sufficient spectral resolution to distinguish the individual comb lines cannot have enough temporal resolution to separate successive pulses. Therefore, the successive pulses interfere with each other inside the spectrometer and the comb spectrum occurs because there are certain discrete frequencies at which the interference is constructive. Using the result from Fourier analysis that a shift in time corresponds to a linear phase change with frequency, we can readily see that the constructive interference occurs at $n f_r$, where n is an integer.

When ϕ_{ce} is evolving with time, such that from pulse to pulse (at a time separation of $T = 1/ f_r$) there is a phase increment of $\Delta\phi_{ce}$, then in the spectral domain, a rigid shift will occur for the frequencies at which the pulses add constructively. This shift is easily determined to be $(1/2\pi)\ \Delta\phi_{ce}\ /T$. Thus the optical frequencies, ν_n, of the comb lines are $\nu_n = nf_r + f_0$, where n is a large integer of the order of 10^6 that indexes the comb line, and f_0 is the comb offset due to the pulse-to-pulse phase shift. The comb offset is connected to the pulse-to-pulse phase shift by $f_0 = (1/2\pi) f_r \Delta\phi_{ce}$. The relationship between time- and frequency-domain pictures is summarized in Figure 1-1. The pulse-to-pulse change in the phase for the train of pulses emitted by a mode-locked laser occurs because the phase and group velocities inside the cavity are different. The pulse-to-pulse change in the phase for the train of pulses emitted by a mode-locked laser can be expressed in terms of the average phase (v_p) and group (v_g) velocities inside the cavity. Specifically, $\Delta\phi_{ce} = (1/v_g - 1/v_p)\, l_c \omega_c$, where l_c is the round-trip length of the laser cavity and ω_c is the "carrier" frequency.

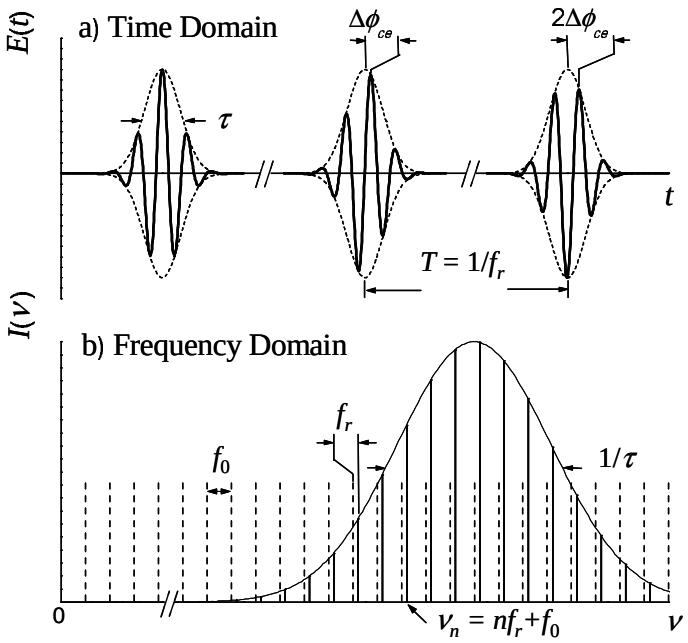

Figure 1-1. Summary of the time-frequency correspondence for a pulse train with evolving carrier-envelope phase.

1.3 Determining absolute optical frequencies with octave-spanning spectra

Armed with the understanding of the frequency spectrum of a mode-locked laser, we now turn to the question of measuring the absolute frequencies of comb lines. For a frequency measurement to be absolute, it must be referenced to the hyperfine transition of ^{133}Cs that defines the second. From the relations listed above, we see that determining the absolute optical frequencies of the femtosecond comb requires two rf measurements, that of f_r and f_0. Measurement of f_r is straightforward: we simply detect the pulse train's repetition rate (from tens of megahertz to several gigahertz) with a fast photodiode. On the other hand, measurement of f_0 is more involved as the pulse-to-pulse–carrier-envelope phase shift requires interferometric measurement, whether it is carried out in the time domain or in the frequency domain. When the optical spectrum spans an octave in frequency, i.e., the highest frequencies are a factor of two larger than the lowest frequencies, measurement of f_0 is greatly simplified. If we use a second harmonic crystal to frequency double a comb line, with index n, from the low-frequency portion of the spectrum, it will have approximately the same

frequency as the comb line on the high-frequency side of the spectrum with index $2n$. Measuring the heterodyne beat between these two families of optical comb lines yields a difference, $2\nu_n - \nu_{2n} = 2(nf_r + f_0) - (2nf_r + f_0) = f_0$, which is just the offset frequency. Thus an octave-spanning spectrum enables a direct measurement of f_0. However, an octave-spanning spectrum is not required; it just represents the simplest approach. We designate this scheme, shown in Figure 1-2(a), as "self-referencing" since it uses only the output of the mode-locked laser.

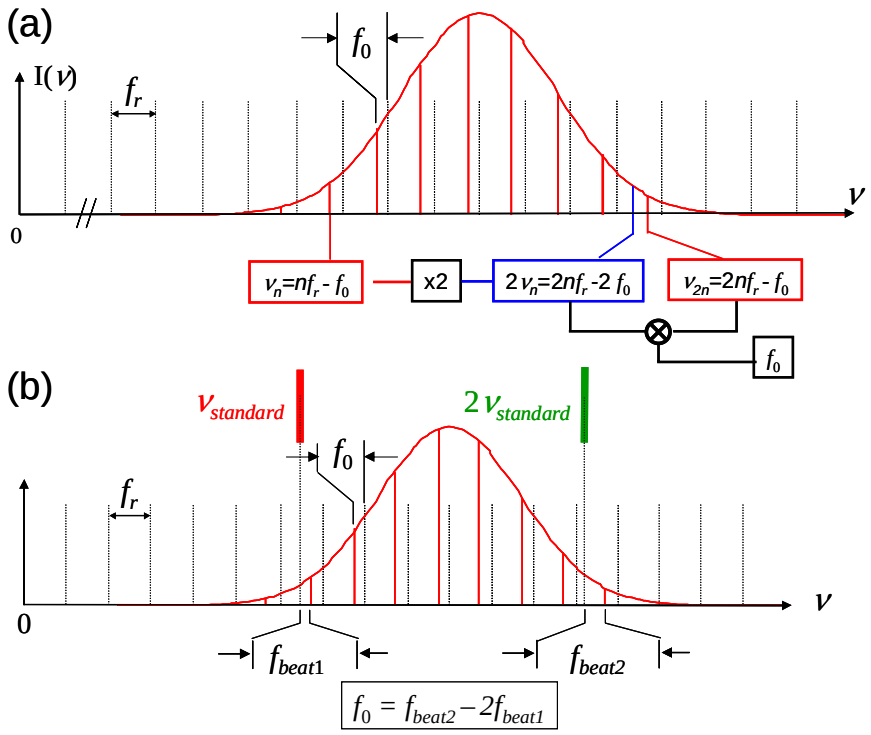

Figure 1-2. Two equivalent schemes for the measurement of f_0 using an octave-spanning optical frequency comb. In the self-referencing approach, shown in (a), frequency doubling and comparison are accomplished with the comb itself. In the second approach shown in (b), the fundamental frequency ($\nu_{standard}$) and its second harmonic of a cw optical standard are used to determine f_0. These two basic schemes are employed for absolute optical frequency measurement and implementation of optical atomic clocks.

Self-referencing is not the only means of determining the absolute optical frequencies given an octave-spanning spectrum. For example, the absolute optical frequency of a cw laser can be determined if its frequency lies close to comb line n in the low-frequency portion of the femtosecond comb

spectrum. Then the second harmonic of the cw laser will be positioned close to the comb line 2*n*. Measurement of the heterodyne beat between the cw-laser frequency, ν_s, and the comb line *n* gives $f_{beat1} = \nu_s - (nf_r + f_0)$ and between the second harmonic of the cw laser and comb line 2*n* gives $f_{beat2} = 2\nu_s - (2nf_r + f_0)$. Mixing the beats with appropriate weighting factors gives $f_{beat2} - 2f_{beat1} = 2\nu_s - (2nf_r + f_0) - (2\nu_s - 2(nf_r + f_0)) = f_0$, which represents the second detection scheme shown in Figure 1-2(b). Another interesting fact is that by mixing the two beat signals, one establishes a direct link between the optical and rf frequencies (ν_s and f_r) as in $f_{beat2} - f_{beat1} = 2\nu_s - (2nf_r + f_0) - \nu_s + (nf_r + f_0) = \nu_s - nf_r$.

1.4 Femtosecond optical-frequency comb generator

A frequency comb generator produces a spectrum that consists of a series of equally spaced sharp lines with known frequencies. Microwave comb generators are commercially available. Optical-frequency comb generators have been constructed by injecting a single-frequency cw laser into a high-quality optical cavity that contains an electro-optic modulator [24]. Typically, comb bandwidths of a few terahertz have been achieved using this method [25]. If the absolute optical frequency of the cw laser is known, then the resulting comb can be used to directly measure nearby frequencies [26]. Alternatively, without needing to know the absolute frequency of the cw laser, a comb generator can be used to span a frequency gap in a more complex frequency-measurement chain [27, 28].

Based on our discussion above, it is clear that a mode-locked laser also generates an optical frequency comb. However, there is no equivalent to the cw laser, which can provide *a priori* knowledge about the absolute frequencies of the comb. Thus, the first applications of mode-locked lasers were based on the use of precisely determined spanning intervals in more complex chains [14] or between a known and unknown frequency [15].

The discussion in Section 1.3 shows that knowledge of the absolute frequencies of the comb generated by a mode-locked laser is easily obtained if it generates a spectrum that spans an octave. A Fourier-transform-limited pulse with a full-width–half-maximum (FWHM) bandwidth of an octave centered at 800 nm would only be a single optical cycle in duration. Such short pulses have not been achieved; the shortest pulses generated by a mode-locked oscillator (i.e., not including external amplification and broadening) are just under two cycles in duration [1, 22]. Fortunately, neither a transform-limited pulse nor a FWHM of an octave is needed to implement the methods for obtaining the absolute frequencies. The pulse width is unimportant as the methods are purely frequency-domain

techniques. Experimentally, it has been found that even if the power at the octave-spanning points is 40 dB below the peak, it is still possible to observe strong ν-to-2ν heterodyne beats.

Since Ti:sapphire, which has the broadest gain bandwidth of all known laser media, does not support an octave-spanning spectrum, additional spectral content must be generated. This is accomplished by using self-phase modulation, which is based on a temporal variation in the index of refraction because of a combination of a short optical pulse and an intensity-dependent index of refraction [29]. The broadening can be achieved outside the laser cavity by using optical fiber or internally by creating coincident secondary time and space foci [22]. The latter technique requires carefully designed mirrors [30] and is challenging to implement; therefore the former is significantly more common. (For more detailed discussions, see Chapter 2.) Recent results have shown that additional spectral bandwidth can be obtained by minor changes in the cavity configuration of a high-repetition-rate laser, although this technique has not yet yielded sufficient intensity at the octave points for observation of ν-to-2ν beats. (See Reference [31] and related discussions in Chapter 3.)

The amount of spectral broadening that can be obtained in ordinary optical fiber is limited, primarily because temporal spreading of the pulse, due to GVD in the fiber, reduces the peak intensity. Using a low-repetition-rate laser (to raise the pulse energy) an octave-spanning spectrum has been obtained with ordinary fiber [7]. The discovery [16] that microstructure fiber can have zero group-velocity dispersion within the emission spectrum of a Ti:sapphire laser eliminated this difficulty and led to rapid progress in the field of femtosecond-optical-frequency combs by allowing broadband-continuum generation with only nanojoule-pulse energies.

Microstructure fiber uses air holes surrounding a fused silica core to obtain the index-of-refraction contrast needed for waveguiding. This method results in a much larger index contrast than can be obtained using doping. The large index contrast has two consequences: (1) the ability to generate a zero in the GVD at visible or near-infrared wavelengths and (2) the possibility of using a much smaller core size. The first consequence means that the pulse does not spread temporally and hence maintains its high peak power. In addition, it results in phase matching between the generated spectral components. The second outcome greatly increases the light intensity in the core, thereby enhancing nonlinear effects. Chapter 4 provides in-depth discussions relating to the physics of bandwidth generation and the underlying noise process during pulse propagation through these relatively novel microstructure fibers.

We have now introduced all of the concepts and components needed to construct a femtosecond-optical-frequency comb generator that produces

known absolute frequencies. There are several possible implementations, one of which we present in Figure 1-3.

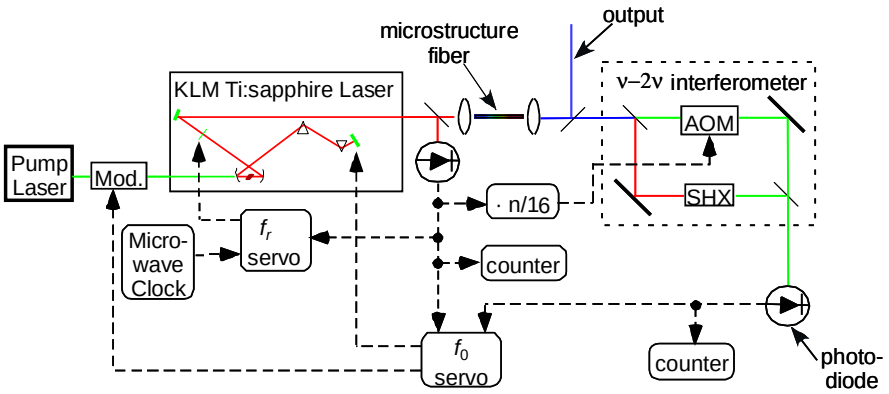

Figure 1-3. Schematic of a femtosecond comb generator. AOM: acousto-optic modulator; SHX: second-harmonic-generation crystal.

The heart of the comb generator is a KLM Ti:sapphire laser. A small portion of the output is detected using a high-speed photodiode to measure the repetition rate. Greater precision is obtained by measuring a large harmonic of the repetition rate rather than the fundamental. Ultimately, in implementing an optical clockwork with a frequency comb (cf. Chapter 9), the relevant information regarding the repetition frequency is collected in the optical domain with a gain factor of nearly a million for enhanced measurement precision. A servo loop controls the repetition rate of the laser by comparing this signal to a microwave clock or an optical-frequency standard.

The output of the KLM Ti:sapphire laser is launched into a length of microstructure fiber. Using the minimum possible amount of spectral broadening in the microstructure fiber works best. For this reason, all metrology experiments start with KLM Ti:sapphire lasers that produce pulse widths of 30 fs or less. This strategy generally results in an octave-spanning spectrum for modest pulse energies and short lengths of microstructure fiber. The output of the microstructure fiber is split into two parts. One part serves as the useful output of the comb generator, while the other part is used in an ν-to-2ν interferometer to measure f_0.

The input to the ν-to-2ν interferometer is divided into long and short wavelength portions by a dichroic beam splitter. The long wavelength portion is frequency doubled by a second-harmonic crystal. The beams in the two arms of the interferometer, which now have the same spectral components, are recombined and detected with a photodiode. The lengths of

the two arms must be matched in order to achieve temporal overlap, including compensation for GVD in the microstructure fiber.

The detected signal from the ν-to-2ν interferometer contains a forest of signals including multiples of f_r and ν-to-2ν beat-note signals spaced above and below each repetition-rate signal by f_0. One of the beat notes must be chosen and isolated for counting and stabilizing the laser. If the signal-to-noise ratio is sufficiently large, an appropriate rf-bandpass filter is usually sufficient to process the signal without cycle slips, otherwise regeneration with a tracking oscillator can be employed.

The final step is to close the loop to stabilize f_0. This requires a "knob" on the laser that can be used to adjust f_0, which is determined by the difference between the intracavity group and phase velocities. One common method for adjusting f_0 is to swivel the end mirror in the arm of the laser cavity that contains the prism sequence [32]. Since the spectrum is spatially dispersed on this mirror, a small swivel produces a linear phase delay with frequency, which is equivalent to a group delay. An alternative method of controlling f_0 is to modulate the pump power [7, 33]. Empirically, this clearly causes a change in f_0 [34]. However, the details are somewhat unclear, as there are likely contributions from the nonlinear phase, spectral shifts, and intensity dependence in the group velocity [35]. Each method has advantages and disadvantages with respect to servo speed and impact on amplitude noise.

1.5 Time- and frequency-domain characterizations of f_0

Carrier-envelope phase coherence is critical for all of the time-domain processes discussed in the remainder of this section. Physically, the carrier-envelope phase coherence simply reflects how well we can tell what the carrier-envelope phase is of a given pulse in the train if we know the phase of an earlier pulse. Knowing the carrier-envelope phase of a given pulse is important, however, for coherent pulse synthesis because we need to maintain carrier-envelope coherence between the two lasers. For experiments sensitive to ϕ_{ce}, it is difficult to determine how ϕ_{ce} affects the outcome if ϕ_{ce} is varying wildly during the measurement.

The connection between time and frequency can be illustrated by measuring the cross-correlation between successive pulses emitted by the comb generator. A cross-correlator is based on the interferometric autocorrelator commonly used to measure ultrashort pulses [17], with the modification that one arm of the interferometer is longer than the other by a multiple of the cavity round-trip time [34]. The asymmetric arm lengths allow appropriate delays to be introduced so that the pulse-to-pulse phase shift $\Delta\phi_{ce}$ can be measured. An autocorrelation curve is always symmetric. However, in an interferometric cross-correlation only the envelope is

symmetric, and the shift of the fringes from the peak of the envelope is due to the pulse-to-pulse phase shift $\Delta\phi_{ce}$. By stabilizing f_0 at different frequency offsets, differing values of $\Delta\phi_{ce}$ are obtained, as discussed in Section 1.2. Another technique, known as spectral interferometry, can also be employed to determine the values of $\Delta\phi_{ce}$ and the related f_0 if the interfering pulses are separated by at least one cavity round-trip time. This technique also yields additional spectral-phase information. For single-shot experiments, a variation of the spectral-interferometry technique that involves interference between the fundamental and its second harmonic spectra, which overlap if the fundamental optical bandwidth exceeds one octave, becomes the most effective approach to measuring $\Delta\phi_{ce}$ [36].

Although cross-correlation measurements can demonstrate some degree of phase coherence, they are actually quite insensitive to phase fluctuation because they measure the change between pulses that are separated by only a few round-trip times because of the practical size limitation of the interferometer. Instead, frequency-domain measurements of the frequency-noise spectrum of f_0 are much more sensitive since they can monitor the frequency/phase evolution of f_0 over much longer time intervals. Typically, f_0 is determined from the self-referencing technique discussed earlier, from which one can make a close examination of the frequency- and phase-noise power spectral density associated with f_0.

Given a measurement of the frequency-noise power spectral density of f_0, $s_\nu^{f_0}$, the accumulated root-mean-square fluctuations of ϕ_{ce} are given by $\Delta\phi_{ce}^{rms}\Big|_{\tau_{obs}} = \sqrt{2\int_{1/2\pi\tau_{obs}}^{\infty}\frac{1}{f^2}s_\nu^{f_0}(f)df}$ for an observation time τ_{obs} [37]. Once a femtosecond laser has been properly phase stabilized, experimental results have indicated that the linewidth of f_0 is actually limited by the measurement time of a few thousand seconds [38]. The standard definition for coherence time is the τ_{obs} at which 1 radian of phase fluctuations have accumulated. Performing such an integration reveals that the coherence time can reach beyond 1000 s.

We would like to emphasize that carrier-envelope phase coherence is not the same as optical coherence. A process that shifts the position the pulse without changing the ϕ_{ce} of the pulse destroys the optical coherence but does not affect the carrier-envelope phase coherence.

2. PRECISION OPTICAL FREQUENCY METROLOGY USING FEMTOSECOND-OPTICAL-FREQUENCY COMBS

It is useful to review the historical development of optical frequency metrology and its perspectives in precision spectroscopy, clock-signal generation, and frequency synthesis. The outstanding spectral properties of optical frequency standards offer unprecedented resolution and precision and potentially the highest accuracy for physical measurements [39]. Even at the cost of extraordinary complexity and remarkable resources, researchers have explored and constructed optical-frequency synthesis chains that span the vast frequency gap between the optical and microwave spectral regions (see for example References [40, 41]). Previous efforts concentrated on measurement of a few discrete optical lines that are chosen to be optical frequency standards. Even limited frequency-measurement capabilities brought a number of significant advances in fundamental physics including: (1) the determination of the speed of light [40, 42] and the linkage between the fundamental physical units of length and time; (2) the refinement of the Rydberg constant and the Lamb shift [43] predicted by quantum electrodynamics; (3) the competitive measurement of various fundamental constants such as the fine structure constant [14, 44] and the ratio of proton-to-electron mass [45]; and (4) a test of relativity theory [46]. However, until recently it was deemed an overwhelming challenge to synthesize arbitrary, absolute optical frequencies. The significance of the wide-bandwidth optical comb lies in the fact that it has substantially reduced this challenge. A detailed review of the traditional harmonic-based frequency chain is provided in Chapter 8, while the new epoch of absolute optical frequency measurement using femtosecond comb technology is reviewed in Chapter 7.

2.1 Measurement of absolute optical frequency

The dramatic simplification of a complex optical frequency chain to a single mode-locked laser has facilitated optical frequency measurement. An important aspect of this new technology is its high degree of reliability and precision together with a lack of systematic errors. For example, recent tests have shown that the repetition rate of a mode-locked laser equals the mode spacing to within the measurement uncertainty of 10^{-16} [13]. The uniformity of the comb's mode spacing has also been verified to a level below 10^{-17} [13], even after spectral broadening in fiber. Comparison between two separate femtosecond comb systems, both linked to a common reference source (microwave or optical), allows one to examine the intrinsic accuracy

of a femtosecond comb-based–frequency-measurement system at a level of a few parts in 10^{16}, with no measurable systematic effects [47]. Chapter 9 provides an account of the current state-of-the-art performance and characterization of femtosecond comb systems used for optical frequency measurement and synthesis.

Another confirmation of femtosecond comb accuracy was provided by comparison of the measured frequency of a He-Ne laser frequency stabilized on a molecular iodine transition. Using an elaborate scheme of transfer standards and crosschecks, we were able to reliably compare the absolute frequency of the laser measured with a femtosecond comb in JILA and that measured by a traditional harmonic-optical-frequency synthesis chain located at the National Research Council Canada [48]. The difference between the two measurements is below 1.6×10^{-12}. While the accuracy of this test has fewer digits, it is comforting to find such agreement in a direct comparison of the two synthesis methods at two national laboratories.

As mentioned in Sections 1.3 and 1.4, one simple use of a femtosecond comb is to stabilize one degree of freedom, namely f_r, and use the comb to span a frequency difference between two cw optical frequencies to be measured. A typical approach is to stabilize f_r directly to a known microwave standard. Experimental observation has clearly confirmed that the actual limitation in precision with femtosecond comb-based measurements is the quality of the rf-reference sources [49]. For example, commercial cesium clocks have a stability $\sim 5 \times 10^{-12}/\tau^{1/2}$ and can be calibrated to an accuracy ~1 x 10^{-14}. For absolute measurement of a single optical frequency, one also needs to measure f_0 in addition to f_r , and then count the heterodyne beat between one of the comb lines and the cw optical frequency. The comb mode order can be determined by varying f_r, for example. Telle et al. have also introduced a clever method of using the comb from a mode-locked laser to measure the ratio of two optical frequencies [50]. By a judicious choice of mixing frequencies, they show it is possible to transfer the frequency stability of one optical source to a different optical frequency without additional noise from the comb. The advantage of this frequency-transfer method is that the frequency noise introduced by the mode-locked laser is taken out of the measurement process. Thus it is possible to compare two narrow optical atomic lines without requiring the optical frequency comb to be highly stabilized. In a demonstration experiment, Telle et al. obtained narrow optical beat signals in the terahertz range that were actually the transferred beat notes between three optical frequency standards [50]. This frequency-transfer method and the use of a free-running frequency comb have limitations but can be useful tools for measuring frequency ratios from rf to the visible.

There has been an explosion of absolute frequency measurements using femtosecond comb methods since 2000. Not surprisingly, the most accurate results come from optical standards that are based on transitions with extraordinary quality factors. One of the most precise measurements is the determination of the Hydrogen 1*S*–2*S* transition frequency at the Max-Planck Institute for Quantum Optics (MPQ) in Garching [51], as discussed in Chapter 7. The MPQ team took advantage of the high stability of a transportable cesium fountain clock as the reference for their femtosecond comb. Their result was quoted at the 1.8×10^{-14} accuracy level. Some national laboratories have both trapped-ion teams and primary frequency-standard teams that form a powerful collaboration. After investing many years of effort on the Hg^+ trap [52], a team at the National Institute of Standards and Technology (NIST) in Boulder, Colorado, can now determine the frequency of an electric quadrupole transition of the Hg^+ ion to $<1 \times 10^{-14}$ [5]. Yb^+ was measured with similar accuracy at the Physikalish-Technische Bundesanstalt (PTB) in Braunschweig [53]. Excellent results are also obtained for frequency determination of a spin-forbidden intercombination line in cold calcium atoms at both NIST and PTB [4, 5]. Indeed, with this new increase in measurement precision, testing fundamental physical postulates or determining constants at the next decimal place are again attracting great interest [54].

Another direction to explore is the "everyman's frequency measurement system" where one can consider tradeoffs such as a ~tenfold lower accuracy for a $\sim 10^3$ scale reduction for the apparatus. Femtosecond combs based on compact and energy efficient mode-locked lasers (such as fiber lasers) and super-continuum generation fibers can offer portable versions of a frequency-measurement device. Cell-based optical frequency standards, such as a solid-state laser stabilized on sub-Doppler transitions of molecular iodine, already offer a competitive stability near or below 1×10^{-14} when averaged over 10 to 1000 s [55, 56]. The long-term reproducibility of such a molecular standard over a period of more than three years was limited to about 3×10^{-13}. Better stability and reproducibility are expected from an improved iodine spectrometer [57, 58].

Cell-based optical standards play an essential role in length metrology [59]. For different national laboratories to establish a common basis for a length standard, an assortment of wavelength-reference lasers realized separately at each laboratory need to be regularly intercompared. The traditional practice has been to hold regular conventions, organized by the Bureau International des Poids et Mesures (BIPM), where stabilized lasers from different national laboratories were gathered at the same physical location and directly compared. A more economic and precise approach to carry out this task can now be accomplished by local calibrations of the

length-standard lasers with GPS systems to an accuracy ~1×10^{-14}. Another rather pleasant outcome of the absolute frequency-calibration process is the associated capability of unambiguous testing of the manufacturing process of reference cells and their long-term variations [56].

2.2 Optical atomic clocks

With the advent of wide-bandwidth–optical-comb technology, it is now possible to transfer the stability of the highest-quality optical frequency standards across vast frequency gaps to other optical spectral regions. Furthermore, the comb technology has also established a straightforward possibility to transfer the optical stability down to the rf domain and vice versa. One can now realize a network of microwave and optical frequencies at a level of stability and reproducibility that surpasses the properties of basically all commercially available frequency sources — and at a reasonable cost. Easy access to the resolution and stability offered by optical standards will greatly facilitate the application of frequency metrology both to precision experiments for fundamental physics and to practical devices.

As elaborated in Chapter 9, recent experimental demonstrations support the concept that, in the future, the most stable and accurate frequency standards will be based on optical transitions. The advantage of an optical frequency standard over a traditional microwave standard is apparent if we examine the frequency stability of an atomic clock. Resonance natural widths, $\Delta\nu$, in the few kilohertz to the subhertz domain are available by selection of an atomic transition with a natural decay time, τ_0, in the 100 μs to 1 s domain. In principle, one could obtain ~$1/(2\tau_0)$ interactions per second with approximately twofold broadening of the resonance linewidth by the interrogation process. So, if we collect all the available information-bearing photons for a single measurement, a signal-to-noise ratio (*SNR*) of $\sim\sqrt{N}$ should be available, where N is the number of participating particles. Normalizing to a standard 1 s measurement time produces $SNR \sim \sqrt{N} \times \sqrt{1/(2\tau_0)}$. An optimum-frequency control system could find the center of the resonance with a precision of ~$1/SNR$ in 1 s. Taking the resonance linewidth into account leads to a frequency uncertainty $\delta\nu$ (at 1 s) ~$\Delta\nu/SNR = (2/N\tau_0)^{1/2}$. Assuming the Ramsey separated-field method and in the case where the interrogation time, T_R, is shorter than the actual lifetime of the transition under study, the fractional frequency (in-)stability is $\sigma_y(\tau) = \frac{\delta\nu}{\nu_0} = \frac{1}{\omega_0\sqrt{NT_R\tau}}$. In this expression, ω_0 (=$2\pi\nu_0$) is the clock transition frequency and τ ($\tau > T_R$) is the total averaging time. Clearly, higher

stability is most easily attained if we can increase ω_0 by changing ω_0 from a microwave to an optical frequency.

To create an optical atomic clock, one uses an optical frequency standard (ν_{cw}) to stabilize f_r of a femtosecond comb, thus transferring the optical-phase information to the microwave domain. Since the comb system has two degrees of freedom, f_r and f_0, one has to ensure that a direct and unambiguous phase relation between ν_{cw} and f_r is established. This implies that either f_0 is strictly known, for example, via tight phase stabilization to a known reference, or the variable f_0 is somehow eliminated from the optical heterodyne beat that connects a comb component to that of ν_{cw}, such as in the example shown at the end of Section 1.3.

Figure 1-2 and the related discussions presented in Section 1.3 provide basic guidelines for implementation of these schemes. The first approach, as shown in Figure 1-2 (a), uses the self-referencing technique to recover f_0, which is then stabilized with respect to either f_r or an auxiliary stable rf source. Stabilization of f_0 to a few millihertz is more than adequate, as it yields a fractional frequency noise of $< 10^{-17}$ for an optical carrier. A heterodyne beat between one of the comb components and the cw laser (ν_{cw}), which acts as the optical frequency standard, reveals fluctuations in f_r. After appropriate processing, this error signal is used to stabilize the phase of f_r coherently to ν_{cw}, thereby producing a clock signal output in the rf domain derived from ν_{cw}. The second approach, as shown in Figure 1-2(b), uses two beat signals between a stabilized cw laser (ν_{cw}) and its second harmonic ($2\nu_{cw}$) against two respective comb components in the corresponding spectral domains. One immediately sees that we are taking the same advantage of the octave bandwidth of the femtosecond comb. Through appropriate electronic mixing of the two beats, one can derive two servo-control error signals associated with f_0 and f_r, respectively, or one can simply eliminate the variable f_0 from the equation.

One of the JILA optical frequency standards is a diode-pumped solid state Nd:YAG laser (ν_{cw}) with its second harmonic ($2\nu_{cw}$) locked on a hyperfine component of an iodine transition (R(56) 32-0, a_{10}) near 532 nm; this system offers an (in-)stability of 4×10^{-14} at 1 s [27, 55]. This optical frequency standard presents an ideal case for the scheme shown in Figure 1-2(b), since both ν_{cw} and $2\nu_{cw}$ are located within the spectrum of a Ti:sapphire-based femtosecond comb.

With the tracking of the comb system exceeding the stability of the current optical frequency standards, we expect the stability of the derived clock signal to be basically that of the optical standard. To characterize the system, the optical clock signal is compared against other well-established microwave/rf frequency standards such as cesium atomic clocks or hydrogen masers. The comparison typically involves a heterodyne-beat experiment

between the two signal sources with a frequency counter recording the resultant beat-frequency fluctuations over a period of time. There has been good progress in the process of extracting high-stability rf-output signals from an optical clock at a level that approaches the optical stability. Further work along this line is continuing. We also still face some technical challenges in making an optical clock a reliable scientific device. Technical developments necessary for an advanced optical atomic clock include: (1) highly accurate, cold-atom optical frequency standards and portable, high-stability optical frequency standards (see Chapters 8, 9); (2) development of ultrastable optical local oscillators suitable for the most demanding spectroscopic tasks (see Chapter 9); (3) stabilization and control of wide-bandwidth optical combs, including exploration of novel generation and detection techniques and approaches to reduce noise (see Chapters 5, 7, 9); (4) reliable, stable, and compact ultrafast laser technology for practical implementation of optical clocks (see Chapters 2, 3, 4, 6); (5) development and use of femtosecond combs for intercomparison of optical frequency standards and the cesium primary standard (see Chapters 7, 8, 9); and (6) development of frequency- and time-transfer methods over extended fiber optic links that can support the next generation of atomic frequency standards (see Chapter 9).

2.3 Optical frequency synthesizer

As will be discussed in Section 4, a future goal of ultrafast technology is to demonstrate arbitrary pulse synthesis in the time domain, including the capability of phase-coherent stitching of distinct optical bandwidths. This time-domain capability would complement the goal of constructing an optical frequency synthesizer that allows access in the frequency domain to any optical-spectral feature with a well-defined optical carrier wave. Such a capability would greatly simplify precision-laser spectroscopy.

With the development of an optical comb, we have now established an optical frequency grid with lines repeating every repetition frequency (100 MHz–1 GHz) over an octave optical bandwidth and with every line stable at or below the 1-hertz level. This capability creates the basic infrastructure to construct a highly stable frequency synthesizer for both rf and optical spectral domains and, in principle, anything in between. An rf (optical) reference signal can be used to derive a phase-coherent secondary signal in any part of either the rf or the optical domains. Chapter 9 presents a more detailed discussion about transfer noise and accuracy relevant to this frequency distribution and synthesis process. In a traditional rf synthesizer, the output is a single-frequency rf-“delta” function (of reasonable power) that can be tuned to any desired frequency on demand. Realization of such a

frequency synthesizer in the optical domain requires a wide-tunable cw laser or an array of them that would collectively cover most of the visible spectrum. The frequency of the cw lasers would be controlled by the underlying optical frequency comb and therefore be directly related to the absolute time/frequency standard in a phase-coherent fashion. Setting of the optical frequency will be accomplished via computer control. Such a system (with continuous, precise frequency tuning and arbitrary frequency setting on demand) has indeed already been demonstrated [60].

3. ATOMIC AND MOLECULAR SPECTROSCOPY

The advent of precision femtosecond optical combs brings a new set of tools for precision atomic and molecular spectroscopy and allows us to explore spectroscopy in a broader sense. For example, ultrafast lasers are now being used not only for time-resolved spectroscopy on fast dynamics, but also for precision spectroscopy on structural information. Indeed, coherent control of dynamics and precision measurement are merging into a joint venture.

The ability to make absolute optical frequency measurements in both visible and infrared (IR) spectral regions adds a new meaning to the term "precision molecular spectroscopy." The understanding of molecular structure and dynamics often involves detailed spectral analysis over a broad wavelength range. Such a task can now be accomplished accurately and uniformly across all relevant spectral windows, allowing precise investigations of minute changes in the molecular structure over a large dynamic range. For example, absolute frequency measurement of vibration-overtone transitions and other related resonances (such as hyperfine splitting) can reveal precise information about the molecular potential-energy surface and relevant perturbation effects. We have pursued such a study with iodine molecules, as we discuss in Section 3.2.

3.1 Precise, simultaneous determination of global atomic structure and transition dynamics

The investigation of two-photon transitions in laser-cooled ^{87}Rb atoms using a precisely stabilized femtosecond comb represents the first example of direct femtosecond comb spectroscopy. Phase coherence among the successive pulses interacting with a cold atomic sample is similar to the approach of Ramsey interference for precision atomic spectroscopy. However, the difference here is that the bandwidth associated with the

femtosecond pulse is so broad that one is able to explore the structure of a large number of atomic states simultaneously, while at the same time, one could study coherent and incoherent population transfer in a multilevel system. In short, one can simultaneously explore the global structure and dynamics of an atomic system. The multipulse interference in the time domain gives an interesting variation and generalization of the two-pulse-based, temporal coherent control of the excited state wave packet.

From the frequency domain perspective, spectroscopic resolution and precision will not be compromised by the use of ultrafast pulses, since they are associated with a phase-stabilized, wide-bandwidth femtosecond comb. Phase coherence among various transition pathways through different intermediate states produces multipath quantum-interference effects on the resonantly enhanced two-photon-transition probability in cold ^{87}Rb atoms. The two-photon-transition spectrum can be analyzed in terms of the pulse repetition rate (f_r) and the carrier-envelope-offset frequency (f_0). Both can be stabilized to high precision. With a set of measurements taken at a few different combinations of f_r and f_0, one can essentially derive all relevant atomic-energy-level positions in absolute terms.

Doppler-free–two-photon spectroscopy is usually carried out with two equal-frequency cw laser beams propagating in opposite directions. The two-photon-transition rate can be resonantly enhanced via the intermediate states with two different laser frequencies [61] or accelerated atomic beams [62]. High-resolution–two-photon spectroscopy using pulsed picosecond light has also been demonstrated [12], with the recent extension to cold atoms [63]. A unique feature of the wide-bandwidth optical comb allows all relevant intermediate states to resonantly participate in the two-photon excitation process. This participation, in turn, permits phase coherence among different comb components to induce a stronger transition rate through quantum interference. The resonant interaction with the intermediate states also makes it possible to explore population-transfer dynamics and the mechanical consequences of light-atom interactions. Following the initial proposal [64] and the subsequent theoretical investigations, we are exploring this novel, high-resolution spectroscopy using a femtosecond laser.

Figure 1-4 shows the relevant ^{87}Rb energy levels involved in the two-photon transition from the ground state $5S_{1/2}$ to the excited state $5D_{3/2}$. The dipole-allowed intermediate states, $5P_{3/2}$ and $5P_{1/2}$, are located ~2 and 17 nm below the virtual level, respectively. Also shown is a regularly spaced comb of optical frequencies around 800 nm. The experimental bandwidth of the comb (emitted from a 10 fs, 100 MHz repetition-rate, mode-locked Ti:sapphire laser) is ~50 nm. Adjustment of f_r and f_0 allows the comb components to line up with the corresponding hyperfine states of $5P_{3/2}$ and $5P_{1/2}$ to resonantly enhance the two-photon transition. The frequency-domain

analysis is complemented by the time-domain-multipulse Ramsey interference picture, also illustrated in Figure 1-4, where the relevant quantities for interaction are $\tau = 1/f_r$ and $\Delta\phi_{ce}$. Both the frequency-domain and the time-domain analyses produce the same result on the two-photon-transition spectra when one assumes a static distribution among the relevant atomic states. However, to follow the time evolution of the system, it is necessary to explore the interaction dynamics from one pulse to the next, taking into account both the atomic coherence and the optical coherence. The general Liouville equation for the density-matrix components of the atomic states, along with phenomenological decay terms, are used to derive a set of Bloch equations describing the evolution of all relevant levels associated with the ground, excited, and intermediate states.

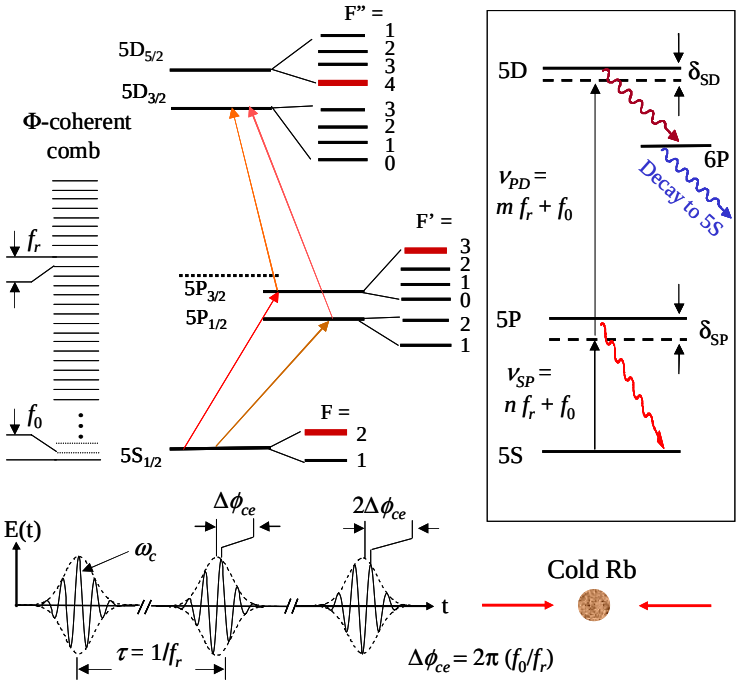

Figure 1-4. Top: Schematic of the relevant energy levels of the ^{87}Rb atom and the frequency-domain perspective of the atom-light interaction. Bottom: Time-domain picture showing a sequence of mode-locked pulses, with the relevant interaction parameters in f_r and $\Delta\phi_{ce}$. The inset at right shows the relevant "three-level" model used for construction of the Bloch equations to solve for population-transfer dynamics. An example for the on-resonance, stepwise transition is shown with relevant detunings at δ_{SP} and δ_{SD} for the pair of comb modes that make the dominant contribution to the transition probability amplitude.

Experimental two-photon spectra resonantly enhanced by the intermediate states confirm the theoretical model where the effect of population transfer becomes non-negligible as the number of interacting pulses increases. Not surprisingly, the most dominant transition pathway when a large number of pulses is involved is $5S_{1/2}$ (F=2) → $5P_{3/2}$ (F=3) → $5D_{5/2}$ (F=4), which represents a closed transition. If necessary, an appropriate repumping scheme, sometimes involving the probing femtosecond laser itself, can be employed to allow investigation of various transition pathways at longer time scales. This incoherent population-redistribution process is complemented by coherent-accumulation effects observed at shorter time scales. The relatively long lifetime associated with the atomic D-state allows phase-coherent accumulation of the transition amplitudes stimulated from successive pulses, resulting in a significant enhancement of the desired D-state population. Only a few comb components are primarily responsible for the on-resonance, stepwise excitation since the linewidth (~6 MHz) of the intermediate $P_{3/2}$ and $P_{1/2}$ states and their hyperfine sublevels is much smaller than the comb-frequency spacing (f_r = 100 MHz). Another interesting fact is that mechanical effects of the light on the cold atomic sample are clearly visible and can be controlled via various settings of f_r and f_0, which control the detuning δ_{5P} of the corresponding comb modes from the intermediate states. Although the laser spectrum spans about 50 nm, the resultant spectroscopy resolution approaches the limit of the atomic natural linewidth of 660 kHz associated with the D-state lifetime. This level of resolution is a result of careful control of the comb parameters, the use of ultracold atoms, and a good understanding of the light's mechanical effects. The work on simple two-photon-transition dynamics provides a solid link between the time-domain picture of the carrier-envelope phase and the frequency-domain picture of f_r and f_0. One practical consequence of these results is that we can now directly control both degrees of freedom for the femtosecond comb by a transition in cold atoms. In future experiments, the exquisite control in the time-domain phase coherence will be complemented by spectral-domain amplitude and phase manipulations, leading to even greater control and spectroscopic investigative power.

3.2 I_2 hyperfine interactions, optical frequency standards, and clocks

With the development of an optical frequency synthesizer, namely a tunable, cw Ti:sapphire laser guided by and referenced to an accurate femtosecond comb [Figure 1-5(a)], we have performed high-resolution and high-precision measurement of hyperfine interactions of the first excited electronic state (B) of I_2 over an extensive range of vibrational and rotational

quantum numbers towards the dissociation limit [65]. Experimental data demonstrate systematic variations in the hyperfine parameters that confirm calculations based on *ab initio* molecular potential-energy curves and electronic wave functions derived from a separated-atomic-basis set. We have accurately determined the state-dependent quantitative changes of hyperfine interactions caused by perturbations from other electronic states and identified the respective perturbing states. Our work on I_2 near the dissociation limit is also motivated by the desire to improve cell-based, portable optical frequency standards. Indeed, I_2-stabilized lasers have already demonstrated high stability ($< 5 \times 10^{-14}$ at 1 s averaging time) and have served well for optical atomic clocks.

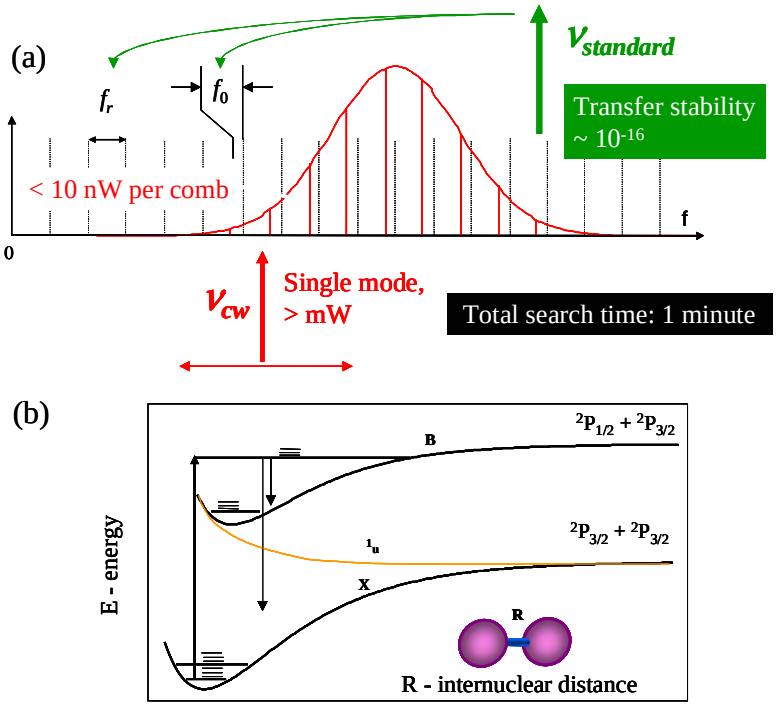

Figure 1-5. (a) Random access and precise stabilization of a cw laser (ν_{cw}) using the frequency reference grid provided by the femtosecond comb stabilized by optical ($\nu_{standard}$) and rf standards. (b) The ground state and the first excited state of I_2 with their associated dissociation limits. The transition linewidth narrows when the excited state approaches the dissociation limit.

The hyperfine structure of I_2 rovibrational levels includes four contributions: (1) nuclear electric quadrupole (eqQ), (2) spin-rotation (C), (3) tensorial spin-spin (d), and (4) scalar spin-spin (δ) interactions.

Agreement between experiment and theory using the four-term effective hyperfine Hamiltonian is at the kilohertz level for a few selected transitions. For the first excited electronic state B with the $^2P_{3/2} + {}^2P_{1/2}$ dissociation limit, our goal is to perform a systematic, high-precision investigation of hyperfine interactions over an extensive range of rovibrational quantum numbers coupled with a large range of internuclear separations. Such a study has allowed us to understand the rovibrational dependence of the hyperfine interactions (and the dependence on internuclear distance) based on *ab initio* molecular potential-energy curves and the associated electronic wave functions. Analysis of various perturbation effects leads to precise determination of molecular structure over a large dynamic range [66].

Prior studies have concentrated on a few, isolated rovibrational levels for the high vibrational levels $v' = 40–82$ in the B state. For vibrational levels below $v' = 43$, only functional forms of the state-dependent variations of the hyperfine interactions have been investigated from empirical data. Combining absolute optical frequency metrology with high-resolution and broad-wavelength-coverage laser spectroscopy, we have measured ~80 rovibrational transitions with the upper vibrational levels (from $v' = 42$ up to $v' = 70$) stretching from a closely bonded molecular basis to a separated-atomic basis appropriate for the $^2P_{3/2} + {}^2P_{1/2}$ dissociation limit and providing kilohertz-level line accuracies for most hyperfine components. The study is performed in the wavelength region of 530–498 nm. Measurements performed on a large set of rovibrational quantum numbers provide systematic information on state-dependent variations in the hyperfine interactions caused by perturbation from other nearby states. Figure 1-5(b) shows a simple schematic of the ground and the first excited electronic states of I_2 and their relevant dissociation limits. There is a clear trend of linewidth narrowing with decreasing transition wavelength [57]. However, this tendency is complicated by variations in linewidths among different rotational or hyperfine components when the transitions approach the predissociation region. The initial linewidth narrowing at shorter wavelength may indicate, among other interesting effects, that the Franck-Condon factor in the transition probability is reduced when the excited state reaches a higher vibration level. As the excited state approaches the dissociation threshold, the limit on lifetime imposed by predissociation and other effects will need to be taken into consideration.

Figure 1-6 illustrates the systematic rovibrational dependences for all four hyperfine parameters. Each solid line is a fit of the experimental data for rotational dependence belonging to a single vibrational level (v'). In general, all hyperfine parameters have a monotonic dependence on both rotational and vibrational quantum numbers except for the levels in the vicinity of $v' = 57–59$. However, the v-dependence of eqQ_B reverses its trend

after $v' = 60$. For the sake of figure clarity, the eqQ_B data for $v' > 60$ are not shown. Another important observation is that for levels of $v' = 57–59$, all hyperfine parameters except for C_B bear abnormal J-dependences due to perturbations from a 1_g state through accidental rotational resonances.

Combining data from this work and the literature [67], investigations of the hyperfine spectra now cover the majority of the vibrational levels ($3 \leq v' \leq 82$) in the B state. Therefore, it is now possible and useful to explore the global trend of these hyperfine parameters in the B state. Suppressing the rotational dependence, hyperfine parameters as functions of pure vibrational energy $E(v')$ are found to increase rapidly when molecules approach the dissociation limit, which is a result of the increasingly strong perturbations from other high-lying electronic states sharing the same dissociation limit with the B state. While the variation of C_B is smooth over the whole range, eqQ_B, d_B, and δ_B all have local irregularities at three positions: (1) $v' = 5$ where the $B''{:}1_u$ state crosses nearby, (2) around $v' = 57–59$ (see discussions above), and from $v' = 76–78$, because of the same 1_g state.

To examine these hyperfine parameters in terms of the internuclear separation R, the vibrational average of the hyperfine parameters is removed by inverting the expression $O(v', J') = \langle v'_{J'} | O(R) | v'_{J'} \rangle$, where $O(v',J')$ denotes one of the four hyperfine parameters. eqQ_B, C_B, d_B, and δ_B against R-centroid are evaluated from $\langle v'_{J'} | R | v'_{J'} \rangle$ (with $|v'_{J'}\rangle$ properly normalized). Consistent with C_B's smooth variation, the interpolation function $C_B(R)$ has small residual errors (within ±0.03, relative) for the entire range from $v' = 3–70$. In contrast, the large residual errors in the interpolation of eqQ_B, d_B, and δ_B for $v' \geq 56$ reflect abnormal variations observed around $v' = 57$ and 59, restricting a reliable interpolation only to levels of $v' < 56$. In the region of $R < 5$ Å, valuable information can be readily extracted from eqQ_B to assist the investigation of I_2's electronic structure. Unlike the other three hyperfine parameters whose major parts originate from perturbations at nearly all possible values of R, a significant part of eqQ_B is due to the interaction between the nuclear quadrupole moment Q and the local electric-field gradient $q(R)$ generated by the surrounding charge distribution of a largely B-state character. Thus, for $R < 5$ Å, where perturbations from other electronic states are negligible, the vibration-removed interpolation function $eqQ_B(R)$, coupled with *a priori* information on $q(R)$, can be used to determine the I_2 nuclear quadrupole moment or serve as a benchmark for molecular *ab initio* calculations of the electronic structure at various values of R.

Precision measurements on $B–X$ hyperfine spectra provide an alternative, and yet effective, way to investigate the potential energy curves (*PEC*s) sharing the same dissociation limit with the B state and the associated

electronic wave functions. To demonstrate this method, we perform calculations of eqQ_B, C_B, d_B, and δ_B based on the available *PEC*s and electronic wave functions derived from a separated atomic-basis set. For both vibrational and rotational dependences, the *ab initio* calculation results agree very well with the experimental data for $v' \geq 42$ (R centroid ≥ 3.9 Å). In short, we have extended the range of separated atomic-basis calculations from levels near the dissociation limit to low vibrational levels ($v' = 5$) and have found very good agreement with the experimental data on both vibrational and rotational dependences.

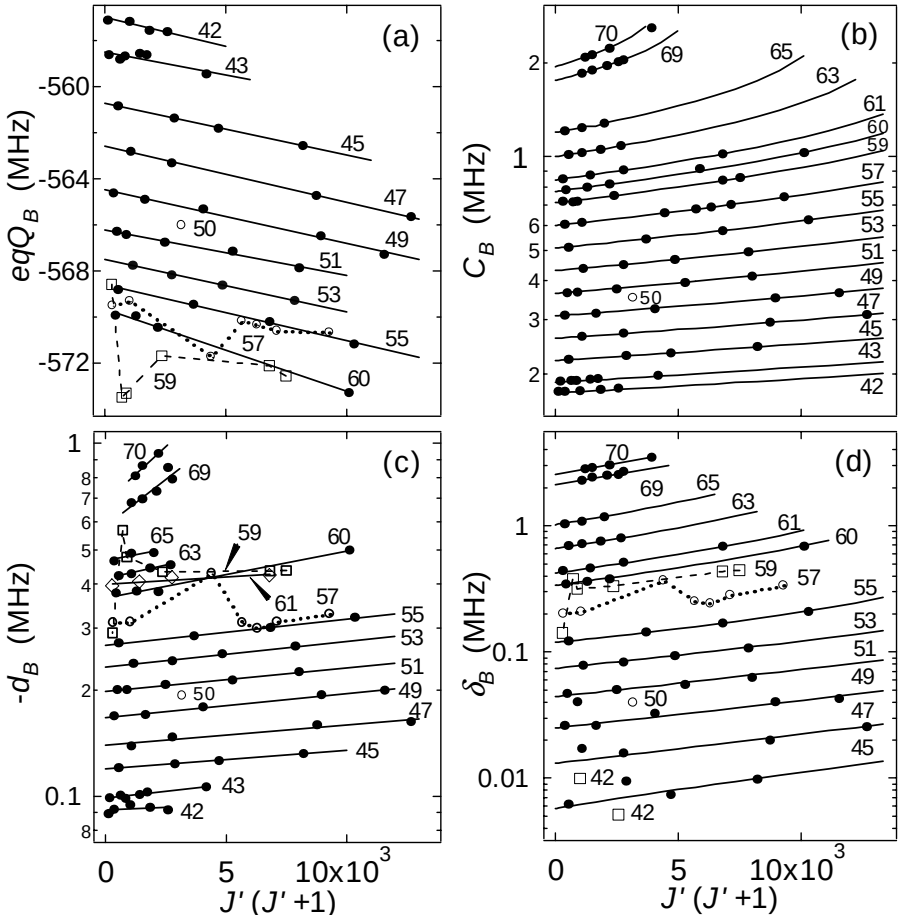

Figure 1-6. Rovibrational dependence of the B-state hyperfine parameters: (a) eqQ_B, (b) C_B, (c) d_B, and (d) δ_B. Graphs (b), (c), and (d) are semilog plots and the vertical scale of (c) has been inverted. Each solid line is a fit for J-dependence for each vibrational level (v' indicated in the figure). Experimental data in squares and open circles show abnormal variations of eqQ_B, d_B, and δ_B around $v' = 57$ and 59.

4. CARRIER-ENVELOPE PHASE COHERENCE AND TIME-DOMAIN APPLICATIONS

Prior to the development of femtosecond comb technology, mode-locked lasers were used almost exclusively for time-domain experiments. Although femtosecond comb technology has primarily impacted the frequency-domain applications described earlier, it is having an effect on time-domain experiments and promises to bring about just as dramatic advances in the time domain as it has in optical frequency metrology and optical clocks. Indeed, it is fascinating to blur the boundary between traditional cw precision spectroscopy and ultrafast phenomena. The time-domain applications put stringent requirements on carrier-envelope phase coherence. Stabilization of the "absolute" carrier-envelope phase at a level of tens of milliradians has been demonstrated. This phase coherence is maintained over an experimental period exceeding many minutes, laying the groundwork for synthesizing electric fields with known amplitude and phase at optical frequencies. Working with two independent femtosecond lasers operating at different wavelength regions, we can synchronize the two pulse trains at the femtosecond level and also phase lock the carrier frequencies. This procedure establishes phase coherence between the two lasers. By coherently stitching optical bandwidths together, a "synthesized" pulse has been generated. With the same pair of Ti:sapphire mode-locked lasers, we can generate widely tunable femtosecond pulses in the mid and far IR using difference-frequency generation. The flexibility of this new experimental approach is evidenced by the capability for rapid and programmable switching and modulation of the wavelength and amplitude of the generated IR pulses. A fully developed capability for producing phase-coherent visible and IR pulses over a broad spectral bandwidth, coupled with arbitrary control of amplitude and pulse shape, represent the ultimate instrumentation for coherent control of molecular systems. A pulse train with good carrier-envelope-phase coherence is also very promising for experiments that are sensitive to ϕ_{ce}, i.e., the "absolute" pulse phase. This sensitivity can be manifested in "extreme" nonlinear optics experiments or coherent control.

The capability of precisely controlling pulse timing and the carrier-envelope phase allows one to manipulate pulses using novel techniques and achieve unprecedented levels of flexibility and precision. For example, the simultaneous control of timing jitter and carrier-envelope phase can be used to phase coherently superpose a collection of successive pulses from a mode-locked laser. By stabilizing the two degrees of freedom of a pulse train to an optical cavity acting as a coherent delay, constructive interference of sequential pulses will be built up until a cavity dumper switches out the "amplified" pulse [68]. Such a passive-pulse 'amplifier," along with the

synchronization technique we developed for pulse synthesis, have made a strong impact on the field of nonlinear optical spectroscopy and imaging of biomolecular systems, offering significant improvements in experimental sensitivity and spatial resolution [69]. With enhanced detection sensitivity comes the capability of tracking real-time biological dynamics. An ultrafast laser locked to a high-stability cavity is also expected to demonstrate extremely low pulse jitter and carrier-envelope-phase noise, features that will be particularly attractive for time-domain experiments. In addition, we are exploring the use of pulse-cavity interactions to obtain a high sensitivity in intracavity spectroscopy (linear and nonlinear) with wide spectral coverage and to enhance nonlinear interaction strengths for high-efficiency, nonlinear optical experiments.

The carrier-envelope phase can also be used for deterministic control in the low-field regime because of interference between reaction channels in chemical systems and population transfer between quantum states [70, 71]. This interference had been demonstrated using separate phase-related pulses in atoms [72, 73], molecules [74], and in direct-gap semiconductors [75, 76]. Recently, it was demonstrated in a direct-gap semiconductor using ϕ_{ce} stabilized pulses [77].

4.1 Timing synchronization of mode-locked lasers

To establish phase coherence among independent ultrafast lasers, it is necessary to first achieve a level of synchronization among these lasers so that the remaining timing jitter is less than the oscillation period of the optical carrier, namely 2.7 fs for lasers centered around 800 nm. In the push for greater stability and precision of femtosecond optical combs, a number of effective techniques for ultralow-jitter timing synchronization have emerged. They include an all-electronic approach for active stabilization of repetition rates [78], cross-phase modulation to passively synchronize two mode-locked lasers that share the same intracavity gain medium [79], the linkage of lasers' repetition rates to the same optical standard [80], and optical cross-correlation between the pulse trains to be synchronized [81].

Detecting timing jitter should be carried out at a high harmonic of f_r to attain much-enhanced detection sensitivity. The harmonic order can range from 100 to 10^6. This approach has enabled tight synchronization between two independent mode-locked Ti:sapphire lasers with a residual-rms timing jitter on the order of 1 fs or less, integrated over a bandwidth of a few megahertz. Of course the enhanced detection sensitivity comes with a price of reduced dynamic range for the change in the nominal value of f_r. This problem can be alleviated by invoking another control loop that works with lower harmonics of f_r. The low-frequency control loop can be used to

achieve a desired timing offset between the two pulse trains. The high stability loop can then be activated to achieve the ultimate level of synchronization at the preset value of timing offset. For example, in the all-electronic implementation of laser synchronization, we use two phase-locked loops (PLLs). The low-resolution PLL compares and locks the fundamental repetition frequencies (100 MHz) of the lasers. The second, high-resolution, PLL compares the phase of the 140^{th} harmonic of the two repetition frequencies at 14 GHz. A transition of control from the first PLL to the second PLL is sufficiently smooth to allow synchronization at the femtosecond level for any timing offsets within the entire dynamic range, e.g., one pulse period of 10 ns [82]. The synchronization lock can be maintained for several hours.

The ability to synchronize a passively mode-locked laser to an external reference or to a second laser has many applications. Previous work in electronic synchronization of two mode-locked Ti:sapphire lasers demonstrated timing jitter of, at best, a few hundred femtoseconds. Therefore the present level of synchronization would make it possible to take full advantage of this time resolution for applications such as high-power sum- and difference-frequency mixing [83], novel pulse generation and shaping [9], new generations of laser/accelerator-based light sources, or experiments requiring synchronized laser light and x-rays or electron beams from synchrotrons [84]. Indeed, accurate timing of high-intensity fields is essential for several important schemes in quantum coherent control and extreme nonlinear optics such as efficient x-ray generation. Two recent applications that have been developed in our laboratories include tunable, subpicosecond pulse generation in the IR [85] and coherent anti–Stokes-Raman scattering (CARS) microscopy with two tightly synchronized picosecond lasers [69]. The flexibility and general applicability of the two-laser-synchronization approach are clearly demonstrated in the straightforward generation of programmable light sources for these applications.

4.2 Phase lock between separate mode-locked lasers

Phase locking of separate femtosecond lasers requires a step beyond synchronization of the two pulse trains. One needs effective detection and stabilization of the phase difference between the two optical carrier waves underlying the pulse envelopes [86]. After synchronization matches the repetition rates ($f_{r\,1} = f_{r\,2}$), phase locking requires that the spectral combs of the individual lasers are maintained exactly coincident in the region of spectral overlap so that the two sets of optical frequency combs form a continuous and phase-coherent entity. We detect a coherent heterodyne-beat

signal between the corresponding comb components of the two mode-locked lasers. Such heterodyne detection yields information related to the difference in the offset frequencies of the two lasers, $\delta f_0 = f_{01} - f_{02}$, which can then be controlled. By phase locking δf_0 to a frequency of a mean zero value, we effectively achieve $(\Delta\phi_{ce1} - \Delta\phi_{ce2}) = 0$, leading to two pulse trains that have nearly identical phase evolution. When stabilized, fluctuations associated with the recorded beat-frequency signal (δf_0) can be suppressed to just a few millihertz with an averaging time of 1 s.

The established phase coherence between the two mode-locked lasers can also be revealed via a direct time-domain analysis. For example, spectral interferometry analysis of the joint spectra of the two pulses produces interference fringes that correspond to phase coherence between the two pulse trains persisting over the measurement time period. A cross-correlation measurement between the two pulse trains also manifests phase coherence in the display of persistent fringe patterns. A more powerful and straightforward demonstration of the "coherently synthesized" aspect of the combined pulse is through a second-order autocorrelation measurement of the combined pulse. For this measurement, the two pulse trains are maximally overlapped in the time domain before the autocorrelator. When the two femtosecond lasers are phase locked, autocorrelation reveals a clean pulse that is often shorter in apparent duration and larger in amplitude than the individual original pulses. A successful implementation of coherent light synthesis has therefore become reality: the coherent combination of output from more than one laser where the combined output can be viewed as a coherent femtosecond pulse being emitted from a single source [9].

4.3 Extending phase-coherent femtosecond combs to the mid-IR spectral region

Being able to combine the characteristics of two or more pulsed lasers working at different wavelengths provides a more flexible approach to coherent control. The capability of synchronizing the repetition rates and phase locking the carrier frequencies of two mode-locked lasers opens up many applications. This capability may be particularly important in the generation of tunable femtosecond sources in other previously unreachable spectral regions. For example, two stabilized mode-locked Ti:sapphire lasers can be employed to enable both sum- (SFG) and difference-frequency generation (DFG). The DFG signal produced by a GaSe crystal can be tuned from 6 microns to any longer wavelength region with a high repetition rate (the same as the original laser's) and a reasonable average power (tens of microwatts). Arbitrary amplitude-waveform generation and rapid wavelength switching in these nonlinear signals are simple to implement.

The ultimate goal of this work is to make an optical-waveform synthesizer that can create an arbitrary optical pulse on demand and use the novel source to study and control molecular motion. For frequency metrology and precision molecular spectroscopy in the IR region, the DFG approach produces an absolute frequency-calibrated-IR comb when the two Ti:sapphire lasers are synchronized and share a common offset frequency f_0. Another attractive approach presented in Chapter 6 makes use of optical parametric generation to produce high-peak-power femtosecond pulses in the IR spectral domain. This scheme presents an attractive property of automatic cancellation of the carrier-envelope-phase shift in IR pulses.

One of the important spectral regions is 1.5 μm, where compact, reliable, and efficient mode-locked lasers exist. Here there is rich information on molecular spectra. Frequency reference grids in this spectral window could find applications in dense-wavelength–division-multiplexed (DWDM) communications systems, photonic samplers in high-speed–analog-to-digital conversion, and distribution of optical frequency standards over optical fiber networks. The synchronization and phase-locking approach for Ti:sapphire lasers can be extended to cover mode-locked lasers at 1.5 μm [87]. We have indeed achieved tight synchronization and coherent phase locking between the repetition rates and the optical carriers, respectively, for the 1.5 μm mode-locked laser sources and a Ti:sapphire-based femtosecond frequency comb, which is used as the clockwork for an optical atomic clock [88].

To achieve phase locking between the optical carriers of the Ti:sapphire and the 1.5 μm mode-locked lasers, one requires spectral overlap between the two combs. The wide-bandwidth optical frequency comb generated by the mode-locked femtosecond Ti:sapphire laser is phase locked to a highly stable, visible optical frequency standard. The optical comb of the 1.5 μm source is frequency doubled and compared against the Ti:sapphire comb at a mutually accessible spectral region to generate a heterodyne beat between the two combs. Under simultaneous control of synchronization and phase locking, the 1.5 μm laser faithfully duplicates both the repetition frequency and the carrier phase of the Ti:sapphire laser. Therefore the optical clock information has now been transferred onto the 1.5 μm mode-locked laser, which can be used in a fiber network to transfer highly stable clock signals to remote ends [89]. This topic is discussed in Chapter 9.

4.4 Femtosecond lasers and external optical cavities

The combination of ultrashort pulse trains and optical cavities will open doors for a variety of exciting experiments. Such experiments will require an understanding of intricate pulse-cavity interactions and the development of techniques to efficiently couple ultrashort pulses into a high-finesse optical

cavity and coherently store them in it. An immediate impact will be on the precision stabilization of ultrafast lasers (see more detailed discussions in Chapter 12). Similar to the state-of-the-art stabilization of cw lasers, a cavity-stabilized ultrafast laser is expected to demonstrate superior short-term stability of both the pulse-repetition frequency and the carrier-envelope phase [90]. The improved stability is beneficial in particular for time-domain applications where the signal-processing bandwidth is necessarily large. Another attractive application lies in broadband and ultrasensitive spectroscopy. The use of high-finesse cavities has played a decisive role in enhancing sensitivity and precision in atomic and molecular spectroscopy. We expect a dramatic advancement in the efficiency of intracavity spectroscopy by exploiting the application of ultrashort pulses. In other words, high detection sensitivity is achievable uniformly across the broad spectrum of the pulse. Applying cavity-stabilization techniques to femtosecond lasers, the comb structure of the probe laser can be precisely matched to the resonance modes of an empty cavity, allowing an efficient energy coupling for a spectroscopic probe. Molecular samples located inside the high-finesse cavity will have a strong impact on the dispersive properties of the cavity. In fact, it is this dispersion-related–cavity-pulling effect that will aid our sensitive detection process when we analyze the light transmitted through the cavity. Preliminary data on spectrally resolved, time-domain–ring-down measurement for intracavity loss over the entire femtosecond-laser bandwidth are already quite promising.

To develop sources for ultrafast nonlinear spectroscopy, a properly designed, dispersion-compensated cavity housing a nonlinear crystal will provide efficient nonlinear optical frequency conversion of ultrashort optical pulses at spectral regions where no active gain medium exists. Furthermore, by simultaneously locking two independent mode-locked lasers to the same optical cavity, efficient SFG and/or DFG can be produced over a large range of wavelengths. Similarly, a passive cavity can be used to explore coherent superposition of ultrashort pulses, with cavity stabilization providing the means to phase coherently superpose a collection of successive pulses from a mode-locked laser. The coherently enhanced pulse stored in the cavity can be switched out using a cavity-dumping element (such as a Bragg cell), resulting in a single phase-coherent, amplified pulse. The use of a passive cavity also offers the unique ability to effectively amplify pulses in spectral regions where no suitable gain medium exists such as for IR pulses from difference-frequency mixing or the ultraviolet light from harmonic generation. Unlike actively dumped laser systems, the pulse energy is not limited by the saturation of a gain medium or the requirement for a saturable absorber for mode locking. Instead, the linear response of the passive cavity allows the pulse energy to build up inside the cavity until limited by cavity

loss and/or dispersive pulse spreading. Therefore storage and amplification of ultrashort pulses in the femtosecond regime require precise control of the reflected spectral phase of the resonator mirrors and the optical loss of the resonator. While the reflected group delay of the mirrors only changes the effective length of the resonator, the group-delay dispersion (GDD) and higher-order derivatives of the group delay with respect to frequency affect the pulse shape. The net cavity GDD over the bandwidth of the pulse needs to be minimized to maintain the shape of the resonant pulse and allow for the coherent addition of energy from subsequent pulses.

We have applied the coherent pulse-stacking technique to both picosecond [91] and femtosecond pulses [92]. Initial studies have already demonstrated amplification of picosecond pulses of more than thirtyfold at repetition rates of 253 kHz, yielding pulse energies greater than 150 nJ. With significant room left for optimization of the cavity finesse (current value of ~350, limited by the cavity input-coupling mirror), we expect that amplifications greater than a hundredfold are feasible, which would bring pulse energies into the μJ range. While the use of picosecond pulses allows us to separate out complications arising from intracavity dispersion, for sub-100 fs pulses, dispersive phase shifts in the cavity mirrors become an important topic. Preliminary results in enhancing low individual pulse energies for sub-50 fs pulses illustrate the importance of GDD control. The external enhancement cavity incorporated specially designed negative GDD low-loss mirrors to simultaneously compensate for the Bragg cell's 3 mm of fused silica and provide a high finesse. The input-coupling mirror transmission is ~0.8%, with a measured cavity finesse of 440. An intracavity energy build-up ratio of ~130 is expected, leading to single pulse amplifications of approximately 52 for the current setup, given the 40% dumping efficiency of our Bragg cell. The negative GDD mirrors are designed to only partially compensate for the total cavity dispersion. The remaining cavity GDD is estimated at +20 to +30 fs^2. Controlling the intracavity pressure allows fine tuning of the net cavity GDD to zero. Experimental results are in good agreement with independent numerical calculations. The input pulses of 47 fs duration are experimentally enhanced by a factor of ~120 inside the passive cavity, with the output pulses broadened only to ~49 fs. These results are shown in Figure 1-7.

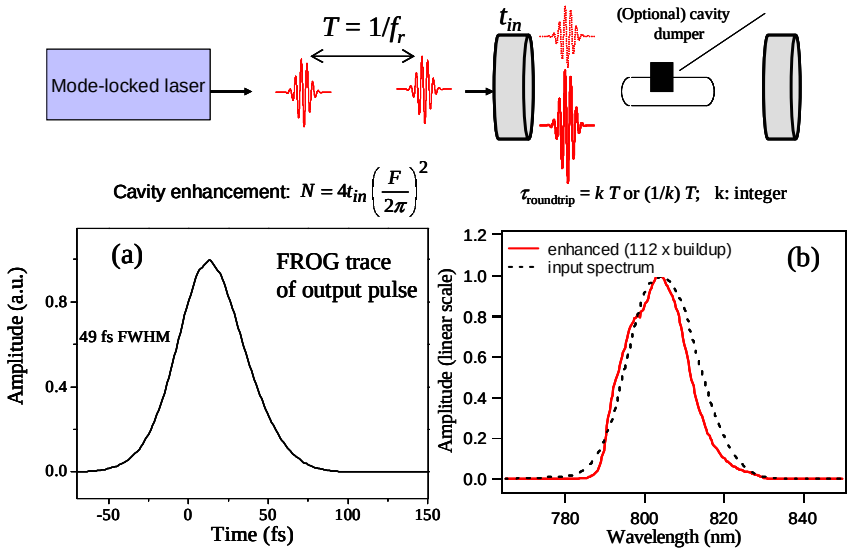

Figure 1-7. Top: Illustration of the principle of coherent-pulse amplification with the aid of an optical cavity, showing the matching of the pulse-repetition period with the cavity round-trip time. The intracavity pulse is switched out when sufficient energy is built up in the cavity. The build-up factor is given ideally by the cavity finesse, with appropriate intracavity dispersion compensation. Bottom: Coherent evolution of a 50 fs pulse inside the cavity. The left panel displays a FROG measurement of the amplified pulse switched out of the passive cavity shown at FWHM of 49 fs, slightly wider than the input pulse width of 47 fs. The right panel presents a comparison of the input and output pulse spectra, showing no significant distortion to the input pulse spectrum after the intracavity power is built up by a factor of 112.

An important application of these advanced pulse-control technologies is in the field of nonlinear optical spectroscopy and nanoscale imaging. For example, using two tightly synchronized picosecond lasers, one can achieve significant improvements in experimental sensitivity and spatial resolutions for CARS microscopy. Vibrational imaging based on CARS spectroscopy is a powerful method for acquisition of chemically selective maps of biological samples. In CARS microscopy, pulsed-pump and Stokes beams are focused tightly to a single focal spot in the sample to achieve a high spatial resolution. The third-order nonlinear interaction produces a signal photon that is blue-shifted (anti-Stokes signal) with respect to the incident beams. Strong CARS signals are obtained whenever the frequency difference between the pump and Stokes coincides with a Raman-active vibrational mode, which gives rise to the molecule-specific vibrational contrast in the image. Recent studies and technological improvements have demonstrated the capability of CARS microscopy to attain high-resolution vibrational images of unstained living cells [93]. Practical applications of the CARS

microscopy technique require pulsed light sources, because optimized peak powers help boost the nonlinear signal. Pulses with temporal widths of 1–2 picoseconds (ps) are used to match to the vibration bandwidths to optimize the CARS signal with minimized nonresonant background and compromising spectral resolution [94]. An important technical challenge is to achieve tight synchronization between two mode-locked lasers that produce the frequency difference that matches the vibrational resonance [95]. Another important consideration is that while the repetition rate of the pulse train needs to be low enough to avoid thermal damage to the cell due to a high average power, the peak power of the pulses needs to be reasonably high to improve the nonlinear signal strength. The technologies of pulse synchronization and coherent pulse stacking therefore become ideal tools for carrying out this task of combining spectroscopy with microscopy.

4.5 Coherent control via quantum interference between one- and two-photon absorption

Control of molecular reactions is a central goal of chemistry. The development of the laser led to the proposal that light fields could be used to control reaction pathways; for recent reviews, see [70] and [96]. Many techniques are sensitive to the phase of the applied fields and thus dubbed "coherent control." To date, only the relative phase between two laser fields, or the relative internal phase of a femtosecond pulse (i.e., its chirp) has been demonstrated to have physical impacts. Some new schemes explore interference between pathways involving *n*-photons and *m*-photons. When *n* and *m* have opposite parity, a dependence on ϕ_{ce} will occur for excitation by single ultrashort pulse. Early studies demonstrated the interference phenomenon by using a pair of phase-controlled pulses to ionize rubidium [72] and control electrical currents in bulk semiconductors [75]. In both cases, there is a connection between spatial direction and the relative phase. The latter system has recently been shown to be sensitive to ϕ_{ce} [77].

In a semiconductor, the phase sensitivity can be understood by considering the **k** dependence of the transition amplitudes. In GaAs, when the phase is such to produce constructive interference between one- and two-photon absorption at –**k**, it produces, to good approximation, destructive interference at **k**. This effect is schematically shown in Figure 1-8. For an octave-spanning pulse, the frequency components for one-photon absorption come from the high-energy tail of the spectrum, while for the two-photon absorption, they come from the low-frequency tail. Thus ϕ_{ce} determines their relative phase in a manner analogous to the beat signal that occurs in a standard ν-to-2ν interferometer. The noninterfering carrier populations do not contribute to the signal, which makes it intrinsically balanced and thus

insensitive to amplitude fluctuations. This insensitivity provides an advantage over the standard ν-to-2ν interferometer, which relies on an ordinary photodiode for conversion of the light to an electrical signal.

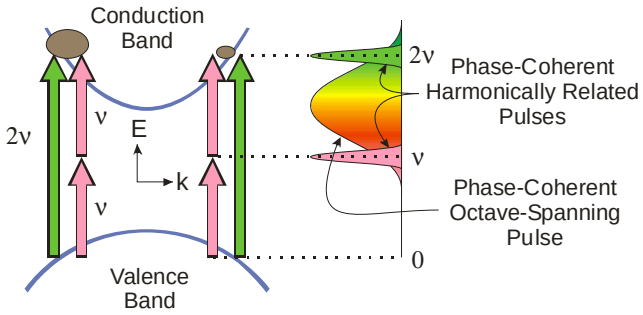

Figure 1-8. Conceptual diagram of quantum interference between one- and two-photon absorption in a direct-gap semiconductor. The two interfering absorption pathways are driven by the spectral wings of a single octave-spanning pulse. An imbalance in the otherwise symmetric carrier-population distribution in momentum space (represented by ovals) occurs due to interference and results in a net current. The resulting photocurrent is sensitive to ϕ_{ce}.

The experimental demonstration of quantum interference control of the injected photocurrent in a semiconductor is shown in Figure 1-9 [77]. The carrier-envelope evolution of the laser was stabilized so that f_0 = 2400 Hz using a standard ν-to-2ν interferometer in a servo loop. A portion of the resulting phase-stabilized pulse train was then used to illuminate a low-temperature grown GaAs sample with gold electrodes. The electrodes are used to collect the resulting photocurrent, which also oscillates at f_0.

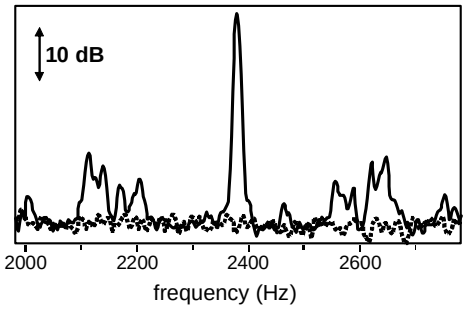

Figure 1-9. Spectrum of the measured quantum interference signal in a semiconductor. The dotted line is the background (no light on the sample).

These results provide an interesting route to a simple, solid-state detector of the carrier-envelope phase. The first step is to use it simply to stabilize f_0.

However this requires a significant improvement in signal-to-noise ratio and bandwidth. This technique does not suffer from the arbitrary offsets that plague detection using a standard ν-to-2ν interferometer and thus may allow measurement of the "absolute" ϕ_{ce} [97]. However, shifts due to dispersion in the GaAs detector still need to be considered.

4.6 Extreme nonlinear optics

The expression "extreme nonlinear optics" refers to experiments where the optical pulses are so intense that the electric field of the pulse is more relevant than the intensity profile, as is the case in the "perturbative" regime [8]. In this regime, the electric field can be strong enough to distort the potential energy well for an electron bound to an atom so much that ionization occurs via tunneling. Such tunneling ionization, also known as "above-threshold ionization," typically displays a threshold with respect to the electric field of the pulse. This effect causes tunneling ionization to depend both on the phase of sufficiently short pulses and whether the threshold is close to the maximum field in the pulse. Indirect evidence for such a phase dependence has been observed in high-harmonic generation [98], which occurs when the ionized electrons slam back into the ion. More recently, measurements of the photoelectron yield in opposite directions have provided evidence for a phase dependence in above-threshold ionization [99]. Chapter 10 provides a thorough discussion of the generation of the high-intensity pulses needed to access the regime of extreme nonlinear optics together with a review of the results obtained for above-threshold ionization. Control of high-harmonic generation is addressed in Chapter 11.

5. SUMMARY

Recent developments in femtosecond comb generators have enabled breakthroughs in optical frequency metrology, optical frequency synthesis, and optical atomic clocks. Femtosecond combs have been built, or are being built, for these applications around the world. Although not large on an absolute scale, the number is a large multiple of the total number of frequency multiplication chains ever built. Indeed, here in Boulder, Colorado, between NIST and JILA, there are more femtosecond comb-based frequency chains than were operating in the world prior to 1999! Thus, we are confident that precision, absolute optical frequency metrology and synthesis are becoming common laboratory tools.

The time-domain applications engendered by femtosecond combs are just being realized. They also promise very exciting results in the near future.

ACKNOWLEDGEMENTS

The authors would like to acknowledge the many contributors to the work on femtosecond combs at JILA. Special acknowledgement goes to Jan Hall for building the foundation for precision-laser stabilization at JILA over the last 40 years. Others include D. J. Jones, R. J. Jones, T. M. Fortier, K. Holman, S. Foreman, L. Chen, M. Stowe, A. Marian, P. A. Roos, K. Moll, M. Thorpe, S. A. Diddams, L.-S. Ma, D. Hudson, R. Shelton, L. Hollberg, H. C. Kapteyn, M. M. Murnane, T. W. Hänsch, and T. Udem. Our research is funded by NIST, NSF, ONR, NASA, AFOSR, and DARPA. Both authors are staff members of the NIST Quantum Physics Division. Ye's email is ye@jila.colorado.edu and Cundiff's email is cundiffs@jila.colorado.edu.

REFERENCES

[1] U. Morgner, F. X. Kärtner, S. H. Cho, Y. Chen, H. A. Haus, J. G. Fujimoto, E. P. Ippen, V. Scheuer, G. Angelow, and T. Tschudi, Opt. Lett. **24**, 411-413 (1999)**;** D. H. Sutter, G. Steinmeyer, L. Gallmann, N. Matuschek, F. Morier-Genoud, U. Keller, V. Scheuer, G. Angelow, and T. Tschudi, Opt. Lett. **24**, 631-633 (1999)**.**

[2] D. J. Jones, S. A. Diddams, J. K. Ranka, A. Stentz, R. S. Windeler, J. L. Hall, and S. T. Cundiff, Science **288**, 635-639 (2000)**.**

[3] S. A. Diddams, D. J. Jones, J. Ye, S. T. Cundiff, J. L. Hall, J. K. Ranka, R. S. Windeler, R. Holzwarth, T. Udem, and T. W. Hänsch, Phys. Rev. Lett. **84**, 5102-5105 (2000)**;** R. Holzwarth, T. Udem, T. W. Hänsch, J. C. Knight, W. J. Wadsworth, and P. S. J. Russell, Phys. Rev. Lett. **85**, 2264-2267 (2000)**;** S. T. Cundiff, J. Ye, and J. L. Hall, Rev. Sci. Instrum. **72**, 3746-3771 (2001)**.**

[4] J. Stenger, T. Binnewies, G. Wilpers, F. Riehle, H. R. Telle, J. K. Ranka, R. S. Windeler, and A. J. Stentz, Phys. Rev. A **63**, 021802 (2001)**.**

[5] T. Udem, S. A. Diddams, K. R. Vogel, C. W. Oates, E. A. Curtis, W. D. Lee, W. M. Itano, R. E. Drullinger, J. C. Bergquist, and L. Hollberg, Phys. Rev. Lett. **86**, 4996-4999 (2001)**.**

[6] S. A. Diddams, T. Udem, J. C. Bergquist, E. A. Curtis, R. E. Drullinger, L. Hollberg, W. M. Itano, W. D. Lee, C. W. Oates, K. R. Vogel, and D. J. Wineland, Science **293**, 825-828 (2001)**;** J. Ye, L. S. Ma, and J. L. Hall, Phys. Rev. Lett. **87**, 270801 (2001)**.**

[7] A. Apolonski, A. Poppe, G. Tempea, C. Spielmann, T. Udem, R. Holzwarth, T. W. Hänsch, and F. Krausz, Phys. Rev. Lett. **85**, 740-743 (2000)**.**

[8] T. Brabec and F. Krausz, Rev. Mod. Phys. **72**, 545-591 (2000)**.**

[9] R. K. Shelton, L. S. Ma, H. C. Kapteyn, M. M. Murnane, J. L. Hall, and J. Ye, Science **293**, 1286-1289 (2001)**.**

[10] T. W. Hänsch, in *Tunable Lasers and Applications*, edited by A. Mooradain, T. Jaeger and P. Stokseth (Springer-Verlag, Berlin, 1976); E. V. Baklanov and V. P. Chebotaev, Sov. J. Quantum Electr. **7**, 1252-1255 (1977).

[11] R. Teets, J. Eckstein, and T. W. Hänsch, Phys. Rev. Lett. **38**, 760-764 (1977).

[12] J. N. Eckstein, A. I. Ferguson, and T. W. Hänsch, Phys. Rev. Lett. **40**, 847-850 (1978).

[13] T. Udem, J. Reichert, R. Holzwarth, and T. W. Hänsch, Opt. Lett. **24**, 881-883 (1999).

[14] T. Udem, J. Reichert, R. Holzwarth, and T. W. Hänsch, Phys. Rev. Lett. **82**, 3568-3571 (1999).

[15] S. A. Diddams, D. J. Jones, L. S. Ma, S. T. Cundiff, and J. L. Hall, Opt. Lett. **25**, 186-188 (2000).

[16] J. K. Ranka, R. S. Windeler, and A. J. Stentz, Opt. Lett. **25**, 25-27 (2000).

[17] J.-C. Diels and W. Rudolph, *Ultrashort Laser Pulse Phenomena : Fundamentals, Techniques, and Applications on a Femtosecond Timescale* (Academic Press, San Diego, 1996).

[18] E. P. Ippen, Appl. Phys. B **58**, 159-170 (1994).

[19] R. L. Fork, O. E. Martinez, and J. P. Gordon, Opt. Lett. **9**, 150-152 (1984).

[20] D. E. Spence, P. N. Kean, and W. Sibbett, Opt. Lett. **16**, 42-44 (1991); D. K. Negus, L. Spinelli, N. Goldblatt, and G. Feugnet, in *Advanced Solid-State Lasers* (OSA, 1991), Vol. 10.

[21] M. T. Asaki, C. P. Huang, D. Garvey, J. P. Zhou, H. C. Kapteyn, and M. M. Murnane, Opt. Lett. **18**, 977-979 (1993).

[22] R. Ell, U. Morgner, F. X. Kärtner, J. G. Fujimoto, E. P. Ippen, V. Scheuer, G. Angelow, T. Tschudi, M. J. Lederer, A. Boiko, and B. Luther-Davies, Opt. Lett. **26**, 373-375 (2001).

[23] S. T. Cundiff, J. Phys. D. **35**, R43 (2002).

[24] M. Kourogi, K. Nakagawa, and M. Ohtsu, IEEE J. Quantum Electron. **29**, 2693-2701 (1993).

[25] J. Ye, L. S. Ma, T. Day, and J. L. Hall, Opt. Lett. **22**, 301-303 (1997).

[26] K. Nakagawa, M. deLabachelerie, Y. Awaji, and M. Kourogi, J. Opt. Soc. Am. B **13**, 2708-2714 (1996).

[27] J. L. Hall, L. S. Ma, M. Taubman, B. Tiemann, F. L. Hong, O. Pfister, and J. Ye, IEEE Trans. Instrum. Meas. **48**, 583-586 (1999).

[28] T. Udem, J. Reichert, T. W. Hänsch, and M. Kourogi, Phys. Rev. A **62**, 1801-1804 (2000).

[29] G. P. Agrawal, *Nonlinear Fiber Optics* (Academic Press, San Diego, 1995).

[30] F. X. Kärtner, U. Morgner, R. Ell, T. Schibli, J. G. Fujimoto, E. P. Ippen, V. Scheuer, G. Angelow, and T. Tschudi, J. Opt. Soc. Am. B **18**, 882-885 (2001).

[31] A. Bartels and H. Kurz, in *XIII International Conference on Ultrafast Phenomena*, edited by M. M. Murnane, N. F. Scherer, D. J. D. Miller and A. M. Weiner (OSA, Vancouver, BC, 2002), Vol. 72, p. 173-174.

[32] J. Reichert, R. Holzwarth, T. Udem, and T. W. Hänsch, Opt. Commun. **172**, 59-68 (1999).
[33] A. Poppe, R. Holzwarth, A. Apolonski, G. Tempea, C. Spielmann, T. W. Hänsch, and F. Krausz, Appl. Phys. B **72**, 977-977 (2001).
[34] L. Xu, C. Spielmann, A. Poppe, T. Brabec, F. Krausz, and T. W. Hänsch, Opt. Lett. **21**, 2008-2010 (1996).
[35] H. A. Haus and E. P. Ippen, Opt. Lett. **26**, 1654-1656 (2001).
[36] P. Dietrich, F. Krausz, and P. B. Corkum, Opt. Lett. **25**, 16-18 (2000).
[37] J. Ye, S. T. Cundiff, S. Foreman, T. M. Fortier, J. L. Hall, K. W. Holman, D. J. Jones, J. D. Jost, H. C. Kapteyn, K. Leeuwen, L. S. Ma, M. M. Murnane, J. L. Peng, and R. K. Shelton, Appl. Phys. B **74**, S27-S34 (2002).
[38] T. M. Fortier, D. J. Jones, J. Ye, S. T. Cundiff, and R. S. Windeler, Opt. Lett. **27**, 1436-1438 (2002).
[39] J. C. Bergquist ed., *Proceedings of the Fifth Symposium on Frequency Standards and Metrology* (Singapore, Woods Hole, Massachusetts, 1996).
[40] K. M. Evenson, J. S. Wells, F. R. Petersen, B. L. Danielson, and G. W. Day, Appl. Phys. Lett. **22**, 192 (1973).
[41] A. Clairon, B. Dahmani, A. Filimon, and J. Rutman, IEEE Trans. Instrum. Meas. **34**, 265-268 (1985).
[42] D. A. Jennings, K. M. Evenson, and D. J. E. Knight, Proc. IEEE **74**, 168-179 (1986); R. L. Barger and J. L. Hall, Appl. Phys. Lett. **22**, 196-199 (1973).
[43] T. Udem, A. Huber, B. Gross, J. Reichert, M. Prevedelli, M. Weitz, and T. W. Hänsch, Phys. Rev. Lett. **79**, 2646-2649 (1997); C. Schwob, L. Jozefowski, B. de Beauvoir, L. Hilico, F. Nez, L. Julien, F. Biraben, O. Acef, and A. Clairon, Phys. Rev. Lett. **82**, 4960-4963 (1999).
[44] A. Peters, K. Y. Chung, B. Young, J. Hensley, and S. Chu, Philos. Trans. R. Soc. Lond. Ser. A **355**, 2223-2233 (1997).
[45] B. de Beauvoir, C. Schwob, O. Acef, L. Jozefowski, L. Hilico, F. Nez, L. Julien, A. Clairon, and F. Biraben, Euro. Phys. J. D **12**, 61-93 (2000).
[46] D. Hils and J. L. Hall, Phys. Rev. Lett. **64**, 1697-1700 (1990).
[47] S. A. Diddams, L. Hollberg, L. S. Ma, and L. Robertsson, Opt. Lett. **27**, 58-60 (2002).
[48] J. Ye, T. H. Yoon, J. L. Hall, A. A. Madej, J. E. Bernard, K. J. Siemsen, L. Marmet, J.-M. Chartier, and A. Chartier, Phys. Rev. Lett. **85**, 3797 (2000).
[49] J. Ye, J. L. Hall, and S. A. Diddams, Opt. Lett. **25**, 1675 (2000).
[50] J. Stenger, H. Schnatz, C. Tamm, and H. R. Telle, Phys. Rev. Lett. **88**, 073601 (2002).
[51] M. Niering, R. Holzwarth, J. Reichert, P. Pokasov, T. Udem, M. Weitz, T. W. Hänsch, P. Lemonde, G. Santarelli, M. Abgrall, P. Laurent, C. Salomon, and A. Clairon, Phys. Rev. Lett. **84**, 5496-5499 (2000).
[52] B. C. Young, F. C. Cruz, W. M. Itano, and J. C. Bergquist, Phys. Rev. Lett. **82**, 3799-3802 (1999).
[53] J. Stenger, C. Tamm, N. Haverkamp, S. Weyers, and H. R. Telle, Opt. Lett. **26**, 1589-1591 (2001).

[54] S. G. Karshenboim, Laser Physics **11**, 1083-1087 (2001).
[55] J. Ye, L. Robertsson, S. Picard, L. S. Ma, and J. L. Hall, IEEE Trans. Instrum. Meas. **48**, 544-549 (1999).
[56] R. J. Jones, W. Y. Cheng, K. W. Holman, L.-S. Chen, J. L. Hall, and J. Ye, Appl. Phys. B **74**, 597 (2002).
[57] W. Y. Cheng, L. S. Chen, T. H. Yoon, J. L. Hall, and J. Ye, Opt. Lett. **27**, 571-573 (2002).
[58] C. Ishibashi, J. Ye, and J. L. Hall, in *SPIE - Methods for ultrasensitive detection II*, edited by C. W. Wilkerson (SPIE, San Jose, 2002), Vol. SPIE 4634, p. 58.
[59] T. J. Quinn, Metrologia **36**, 211-244 (1999).
[60] J. D. Jost, J. L. Hall, and J. Ye, Opt. Expr. **10**, 515 (2002).
[61] J. E. Bjorkholm and P. F. Liao, Phys. Rev. Lett. **33**, 128-131 (1974).
[62] O. Poulsen and N. I. Winstrup, Phys. Rev. Lett. **47**, 1522-1525 (1981).
[63] M. J. Snadden, A. S. Bell, E. Riis, and A. I. Ferguson, Opt. Commun. **125**, 70-76 (1996).
[64] T. H. Yoon, A. Marian, J. L. Hall, and J. Ye, Phys. Rev. A **63**, 011402 (2000).
[65] L. S. Chen and J. Ye, Chem. Phys. Lett. **381**, 777-783 (2003).
[66] L. S. Chen, W. Y. Cheng, and J. Ye, J. Opt. Soc. Am. B **21**, 820-832 (2004).
[67] B. Bodermann, H. Knockel, and E. Tiemann, Eur. Phys. J. D **19**, 31 (2002).
[68] R. J. Jones and J. Ye, Opt. Lett. **27**, 1848-1850 (2002).
[69] E. O. Potma, D. J. Jones, J. X. Cheng, X. S. Xie, and J. Ye, Opt. Lett. **27**, 1168-1170 (2002).
[70] P. Brumer and M. Shapiro, Chem. Phys. Lett. **126**, 541-546 (1986).
[71] M. Shapiro and P. Brumer, Advances in Atomic Molecular, and Optical Physics, Vol. 42 **42**, 287-345 (2000).
[72] Y.-Y. Yin, C. Chen, D. S. Elliot, and A. V. Smith, Phys. Rev. Lett. **69**, 2353 (1992).
[73] D. Z. Anderson, N. B. Baranova, C. Green, and B. Y. Zeldovich, Zhurnal Eksperimentalnoi I Teoreticheskoi Fiziki **102**, 397-405 (1992).
[74] B. Sheehy, B. Walker, and L. F. Dimauro, Phys. Rev. Lett. **74**, 4799-4802 (1995).
[75] A. Haché, Y. Kostoulas, R. Atanasov, J. L. P. Hughes, J. E. Sipe, and H. M. van Driel, Phys. Rev. Lett. **78**, 306-309 (1997).
[76] A. Haché, J. E. Sipe, and H. M. van Driel, IEEE Journal of Quantum Electronics **34**, 1144-1154 (1998).
[77] T. M. Fortier, P. A. Roos, D. J. Jones, S. T. Cundiff, R. D. R. Bhat, and J. E. Sipe, Phys. Rev. Lett. **92**, 147403 (2004).
[78] L.-S. Ma, R. K. Shelton, H. C. Kapteyn, M. M. Murnane, and J. Ye, Phys. Rev. A **64**, 021802 (2001).
[79] A. Leitenstorfer, C. Furst, and A. Laubereau, Opt. Lett. **20**, 916-918 (1995); Z. Y. Wei, Y. Kobayashi, Z. G. Zhang, and K. Torizuka, Opt. Lett. **26**, 1806-1808 (2001).

[80] A. Bartels, S. A. Diddams, T. M. Ramond, and L. Hollberg, Opt. Lett. **28**, 663-665 (2003).

[81] T. R. Schibli, J. Kim, O. Kuzucu, J. T. Gopinath, S. N. Tandon, G. S. Petrich, L. A. Kolodziejski, J. G. Fujimoto, E. P. Ippen, and F. X. Kaertner, Opt. Lett. **28**, 947-949 (2003).

[82] R. K. Shelton, S. M. Foreman, L. S. Ma, J. L. Hall, H. C. Kapteyn, M. M. Murnane, M. Notcutt, and J. Ye, Opt. Lett. **27**, 312-314 (2002).

[83] R. A. Kaindl, M. Wurm, K. Reimann, P. Hamm, A. M. Weiner, and M. Woerner, J. Opt. Soc. Am. B **17**, 2086-2094 (2000).

[84] R. W. Schoenlein, W. P. Leemans, A. H. Chin, P. Volfbeyn, T. E. Glover, P. Balling, M. Zolotorev, K. J. Kim, S. Chattopadhyay, and C. V. Shank, Science **274**, 236-238 (1996).

[85] S. M. Foreman, D. J. Jones, and J. Ye, Opt. Lett. **28**, 370-372 (2003).

[86] R. K. Shelton, L. S. Ma, H. C. Kapteyn, M. M. Murnane, J. L. Hall, and J. Ye, J. Mod. Opt. **49**, 401-409 (2002).

[87] J. Rauschenberger, T. M. Fortier, D. J. Jones, J. Ye, and S. T. Cundiff, Opt. Expr. **10**, 1404-1410 (2002); D. J. Jones, K. W. Holman, M. Notcutt, J. Ye, J. Chandalia, L. A. Jiang, E. P. Ippen, and H. Yokoyama, Opt. Lett. **28**, 813-815 (2003).

[88] K. W. Holman, D. J. Jones, J. Ye, and E. P. Ippen, Opt. Lett. **28**, 2405-2407 (2003).

[89] K. W. Holman, D. J. Jones, D. D. Hudson, and J. Ye, Opt. Lett. **29**, 1554-1556 (2004).

[90] R. J. Jones, I. Thomann, and J. Ye, Phys. Rev. A **69** (2004).

[91] E. O. Potma, C. Evans, X. S. Xie, R. J. Jones, and J. Ye, Opt. Lett. **28**, 1835-1837 (2003).

[92] R. J. Jones and J. Ye, Opt. Lett., in press (2004).

[93] A. Volkmer, J. X. Cheng, and X. S. Xie, Phys. Rev. Lett. **87**, 023901 (2001).

[94] L. D. Book, J. X. Cheng, A. Volkmer, and X. S. Xie, Biophys. J. **80**, 171A-171A (2001).

[95] D. J. Jones, E. O. Potma, J. X. Cheng, B. Burfeindt, Y. Pang, J. Ye, and X. S. Xie, Rev. Sci. Instrum. **73**, 2843-2848 (2002).

[96] H. Rabitz, R. de Vivie-Riedle, M. Motzkus, and K. Kompa, Science **288**, 824-828 (2000).

[97] E. O. Potma, X. S. Xie, L. Muntean, J. Preusser, D. Jones, J. Ye, S. R. Leone, W. D. Hinsberg, and W. Schade, J. Phys. Chem. B **108**, 1296-1301 (2004).

[98] C. G. Durfee, A. R. Rundquist, S. Backus, C. Herne, M. M. Murnane, and H. C. Kapteyn, Phys. Rev. Lett. **83**, 2187-2190 (1999); C. Spielmann, N. H. Burnett, S. Sartania, R. Koppitsch, M. Schnurer, C. Kan, M. Lenzner, P. Wobrauschek, and F. Krausz, Science **278**, 661-664 (1997).

[99] G. G. Paulus, F. Grasbon, H. Walther, P. Villoresi, M. Nisoli, S. Stagira, E. Priori, and S. De Silvestri, Nature **414**, 182-184 (2001).

Chapter 2

FEMTOSECOND LASER DEVELOPMENT

Franz X. Kärtner[1], Erich P. Ippen[1] and Steven T. Cundiff[2]
[1]*Research Laboratory of Electronics, Massachusetts Institue of Technology*

[2]*JILA, National Institute of Standards and Technology and University of Colorado*

Abstract: Advances in ultrashort-pulse laser technology have led to few-cycle-duration optical pulses, with octave-spanning spectra, generated directly from laser oscillators at high repetition rates. These new laser systems promise to be reliable sources of carrier-envelope–phase-stabilized femtosecond pulse trains and highly stable laser frequency combs. In this chapter, we review the pulse and carrier-envelope phase dynamics of these laser sources and discuss different laser designs based on prismless cavities and cavities including prism pairs for dispersion compensation.

Key words: mode-locked lasers, carrier-envelope phase, frequency comb

1. INTRODUCTION

Remarkable progress in the generation of femtosecond pulses with solid-state lasers has followed from the discovery of self-mode-locking in a Ti:sapphire laser by the Sibbett group in 1991 [1]. Explained as a consequence of self-focusing inside the laser [2], this self-mode-locking behavior has become known as Kerr-lens mode locking (KLM). It is now the basis for femtosecond pulse generation in a wide variety of other solid-state laser systems as well. As shown in Figure 2-1, KLM has resulted in the shortest pulses, superceding previous marks set using dye lasers, amplification, and spectral broadening.

Self-focusing in the KLM laser in the presence of aperturing due either to the size of the gain spot or some other physically introduced aperture can cause pulse shortening in precisely the manner described by "fast saturable absorber" mode-locking theory [3]. In addition, simultaneously occurring self-phase modulation (SPM), in the presence of group-velocity dispersion (GVD) in the resonator, provides a strong soliton like shaping to the pulses. This latter process can, in fact, be the dominant pulse-shaping effect;

however, the KLM remains necessary to suppress the growth of noise between the pulses, thereby stabilizing the mode locking. An important variant of soliton shaping occurs when the GVD alternates between positive and negative values as the pulse propagates. The result can be the formation of "dispersion-managed solitons" even when the average GVD in the resonator is zero or net normal [4]. Such dispersion management has found important application in "stretched-pulse" fiber lasers [5] and may also play a role in very short pulse Ti:sapphire lasers [6].

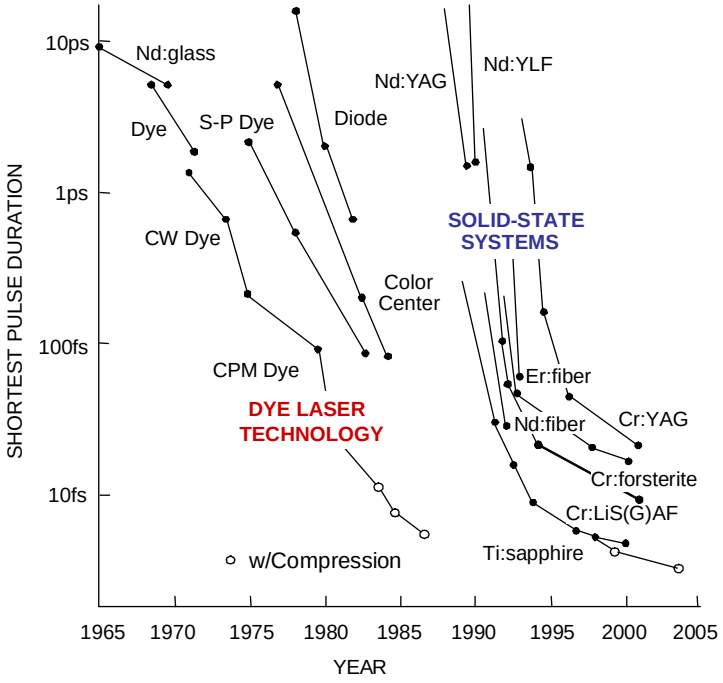

Figure 2-1. History of ultrashort pulse duration.

Ultrashort pulse durations have been reduced to well below 10 fs by a variety of researchers including the university groups at Washington State University [7], the Technical Universiy of Vienna [8], ETH-Zurich [9], the Massachusetts Institute of Technology (MIT) [10], and the University of Karlsruhe [11]. The Washington State group, responsible for a number of successful early cavity designs, first documented the limitations to pulse shortening by higher-order dispersion. The TU-Vienna group introduced chirped mirrors for dispersion compensation, an approach that was further refined at ETH-Zurich with the concept of a double-chirped mirror design. Dispersion compensation over one octave, ultimately achieved by the use of double-chirped mirror pairs at MIT and the University of Karlsruhe, finally

led to the generation of 5 fs pulses containing less than two optical cycles. The wings of the spectrum of these pulses extend over more than one octave, an achievement that has important implications for the control of the electric field waveform of the pulse. It had been recognized earlier by Xu et al.[12] that for few-cycle pulses, the maximum electric field in a pulse quantitatively depends on the phase relationship between the carrier wave and the maximum of the envelope (see Figure 2-1).

Nonlinear optical processes, which depend on powers of the electric field amplitude, must therefore also depend on the carrier-envelope phase for very short pulses. This dependence is visualized in Figure 2-2, which shows sketches of spectra resulting from instantaneous $\chi^{(2)}$ and $\chi^{(3)}$ processes produced by a chirp-free pulse with a rectangular-shaped spectrum spanning an octave. For a one-octave pulse, the spectra of the second-harmonic and optical-rectification terms overlap with the fundamental spectrum. Interference in the overlap regions will be constructive or destructive depending on the carrier-envelope phase. Use of this interference for carrier-envelope phase control is called the ν-to-2ν self-heterodyne technique. If higher-order processes are employed, such as a $\chi^{(3)}$ nonlinearity, there are similar interference terms between the $\chi^{(2)}$ and $\chi^{(3)}$ terms. Thus a phase-dependent interference is already possible even if the pulse spans only 2/3 of an octave. All of these interferences have been used to detect and control the carrier-envelope phase.

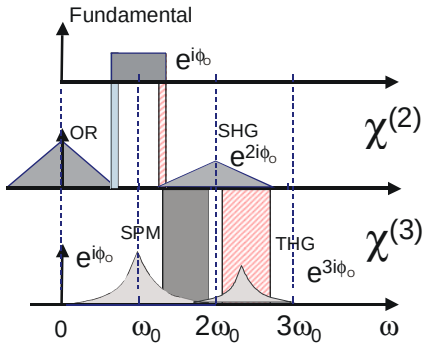

Figure 2-2. Top: Fundamental spectrum of an octave-spanning pulse centered at ω_0; Below: Spectra generated by instantaneous second- and third-order nonlinearities due to optical rectification (OR), second-harmonic generation (SHG), self-phase modulation (SPM), and third-harmonic generation (THG).

A special case, pointed out by Baltuška et al. [13], is that optical rectification or difference-frequency mixing of an optical pulse directly produces a phase-independent IR pulse. Currently, control of the carrier-

envelope phase for a variety of applications is one of the strongest motivations for the development of ultrabroadband lasers.

This chapter reviews progress made in phase-stabilized–octave-spanning lasers, starting with a discussion of the dispersion-managed pulse dynamics in sub-10 fs Ti:sapphire lasers in Section 2. In Section 3, the experimental realization of systems using combinations of prism pairs and chirped mirrors for dispersion compensation and prismless systems are described. Section 4 discusses the carrier-envelope phase dynamics of some sources. The results achieved are summarized in Section 5.

2. PULSE DYNAMICS

The generation of ultrashort pulses from Ti:sapphire lasers has progressed rapidly over the past decade and led to the generation of pulses as short as 5 fs directly from the laser. The spectra generated by these lasers are not of simple shape [7, 11, 14], and various models to explain this complexity have been presented. Christov et al. [15] have shown by numerical simulations that, when the second-order group-velocity dispersion is balanced, fourth-order dispersion with gain bandwidth filtering and KLM action can lead to steady-state pulse generation. Extensive three-dimensional simulations have been carried out [15-17]. However, so far, a fully three-dimensional numerical simulation of a KLM laser is still too time consuming for computation of the steady-state solution. Also, the solution is known from experimental observation to be very sensitive to changes in the self-focusing dynamics caused by slight parameter variations. This sensitivity adds to the difficulty of obtaining meaningful information from steady-state simulations that require many hours of computer time.

A schematic setup of current 5 fs Ti:sapphire lasers using only chirped mirrors for dispersion compensation is shown in Figure 2-3(a). For insight into the dynamics of this laser, we start by considering only the temporal dynamics, which are modeled by the nonlinear Schrödinger equation

$$\frac{\partial}{\partial z}a = -iD(z)\frac{\partial^2}{\partial t^2}a + i\delta(z)|a|^2 a\,, \tag{1}$$

describing propagation of the envelope function a in a medium with distributed dispersion, $D(z)$, and self-phase modulation, $\delta(z)$. The distribution of dispersion and nonlinearity in the laser is sketched in Figure 2-3(b). It was first pointed out by Spielmann et al. that for very-short-pulse Ti:sapphire lasers, large changes in the pulse occur within one round trip and

that the ordering of the pulse-shaping elements within the cavity has a major effect on the pulse formation [18]. The discrete action of linear dispersion in the arms of the laser resonator and the discrete, but simultaneous, action of positive SPM and positive GDD in the laser crystal cannot be neglected any longer. The importance of the strong variations in dispersion was first discovered in a fiber laser and called stretched-pulse mode locking [19]. The positive dispersion in the Er-doped fiber section of a fiber ring laser was balanced by a negative-dispersion passive fiber. The pulse circulating in the ring was stretched and compressed by as much as a factor of 20 in one round trip. One consequence of this behavior was a dramatic decrease of the nonlinearity and thus increased stability against the SPM-induced instabilities. Also, the formation of Kelly sidebands [20] occurring for large nonlinear phase shifts per round trip in conventional soliton lasers was greatly suppressed. The energy of the output pulses could be increased a hundredfold [21]. These important consequences can explain the high power densities that can be achieved in sub-10 fs KLM lasers without undergoing catastrophic self-focusing in the laser crystal.

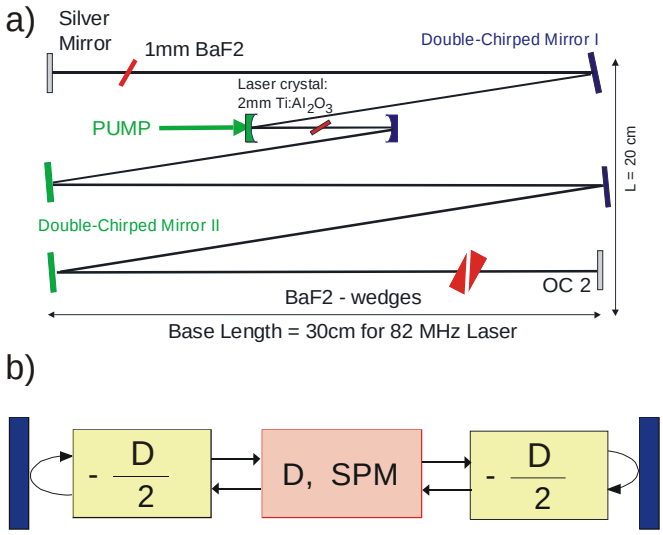

Figure 2-3. (a) Schematic of a Kerr-lens–mode-locked Ti:sapphire laser using double-chirped mirrors and BaF_2 for dispersion compensation. (b) Distribution of dispersion and nonlinearity inside the laser cavity.

Here, we consider the impact of the discrete action of dispersion and nonlinearity, which become important in the sub-10 fs range, in Ti:sapphire

lasers on the spectral shape of the laser pulses. The dispersion distribution shown in Figure 2-3(b) suggests an analogy with pulse propagation along a dispersion-managed fiber transmission link [4]. A system with sufficient variation of dispersion can support waves that have been called nonlinear Bloch waves [22]. One can show that the Kerr nonlinearity produces a self-consistent nonlinear scattering potential that permits formation of a periodic solution with a simple phase factor in a system with zero net dispersion. It has been shown further that nonlinear propagation along dispersion-managed fiber near zero net GDD possesses a narrower spectrum in the segment of positive dispersion than in the segment of negative dispersion [4, 22]. Thus, the effect of negative dispersion is greater than that of the positive dispersion, and the pulse sees an effective net negative dispersion. This effective negative dispersion can balance the Kerr-induced phase, leading to steady-state pulses at zero net dispersion. This is true even when there is no nonlinearity in the negative dispersion segment. The pulses are analogous to solitons in that they are self-consistent solutions of the Hamiltonian (lossless) problem as are conventional solitons. But, they are not secant hyperbolic in shape. Figure 2-4 shows a numerical simulation of a self-consistent solution of the Hamiltonian pulse-propagation problem in a linear medium of negative dispersion and subsequent propagation in a nonlinear medium of positive dispersion with positive self-phase modulation following Equation (1).

The dispersion map $D(z)$ is shown as an inset in Figure 2-5. The dispersion coefficient $D(z)$ and the nonlinear coefficient $\delta(z)$ are defined per unit length. In Figure 2-4, the steady-state intensity profiles are shown at the center of the negative dispersion segment over 1000 round trips. In addition, we can include in the model the saturable gain, Lorentzian gain filtering, and KLM modeled by a fast saturable absorber. Figure 2-5 shows the behavior in one period (one round trip through the resonator) including these effects. The response of the absorber is $q(a) = q_0 \Big/ \left(1 + |a|^2 / P_A\right)$, with $q_0 = 0.01$/mm and P_A = 1 MW. The bandwidth-limited gain is modeled by a Lorentzian gain profile with bandwidth $\Omega_g = 2\pi \times 43\,\text{THz}$. The filtering and saturable absorber reduce the spectral and temporal side lobes of the Hamiltonian problem, respectively, as can be inferred from Figures 2-4 and 2-5. The steady-state pulse formation can be understood in the following way: By symmetry, the pulses are chirp free in the middle of the dispersion cells. A chirp-free pulse starting in the center of the gain crystal, i.e., nonlinear segment, is spectrally broadened by the SPM and disperses in time because of the GVD, which generates a mostly linear chirp over the pulse.

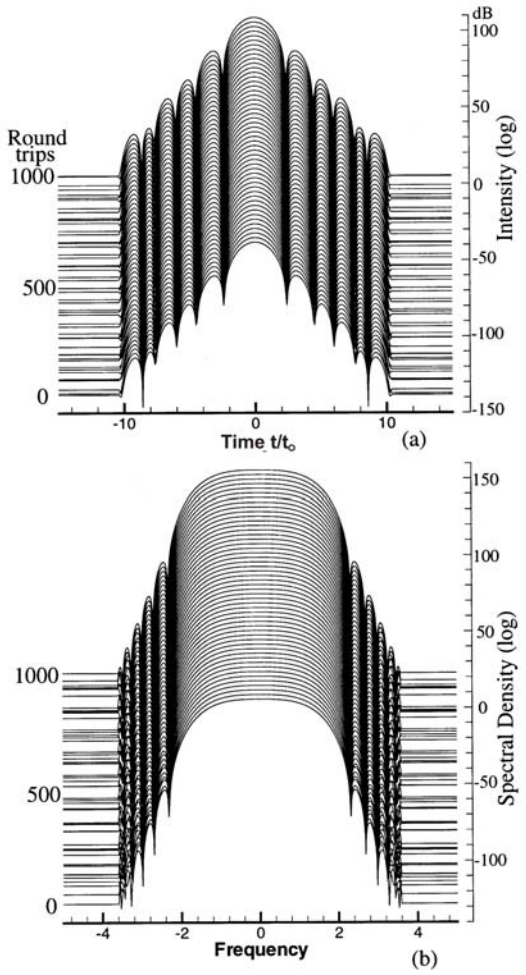

Figure 2-4. Simulation of the Hamiltonian problem. Temporal (a) and spectral (b) intensity profiles at the center of the negatively dispersive segment are shown for successive round trips. The total extent in 1000 round trips. $D = D^{(\pm)} = \pm 60$ fs/mm for the segment of crystal length $L = 2$ mm, $\tau_{FWHM} = 5.5$ fs, $\delta = 0$ for $D < 0$, $\delta = 1$ (MW-mm) for $D > 0$.

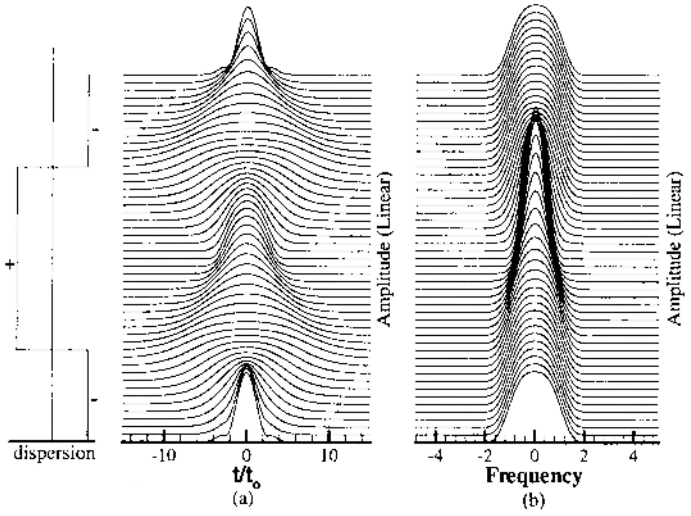

Figure 2-5. Pulse shaping in one round trip. The negative segment has no nonlinearity.

After the pulse leaves the crystal, it experiences GVD in the arms of the laser resonator. The positively chirped pulse is compressed to its transform limit at the end of each arm, where output couplers can be placed. Propagation back towards the crystal imposes a negative chirp, generating the time-reversed solution of the nonlinear Schrödinger Equation (1). Therefore, subsequent propagation in the nonlinear crystal compresses the pulse spectrally and temporally to its initial shape in the center of the crystal. The spectrum is narrower in the crystal than in the negative-dispersion sections, because it is negatively prechirped before it enters the SPM section. Spectral spreading occurs again only after the pulse has been compressed. This result further explains that in a laser with a linear cavity, for which the negative dispersion is located in only one arm of the laser resonator (i.e., in the prism pair and no use of chirped mirrors), the spectrum is widest in the arm that contains the negative dispersion [18]. In a laser with a linear cavity, for which the negative dispersion is equally distributed in both arms of the cavity, the pulse runs through the dispersion map twice per round trip. The pulse is short at each end of the cavity, and, most importantly, the pulses are identical in all passes through the crystal; thus they can exploit the full KLM action twice per round trip [23]. For this reason, a symmetric dispersion distribution may lead to an effective saturable absorption that is twice as strong as an asymmetric dispersion distribution and that can produce substantially shorter pulses. Furthermore, the dispersion swing between the negative and positive dispersion sections is only half as large, which allows

for shorter dispersion-managed solitons operating at the same average power level.

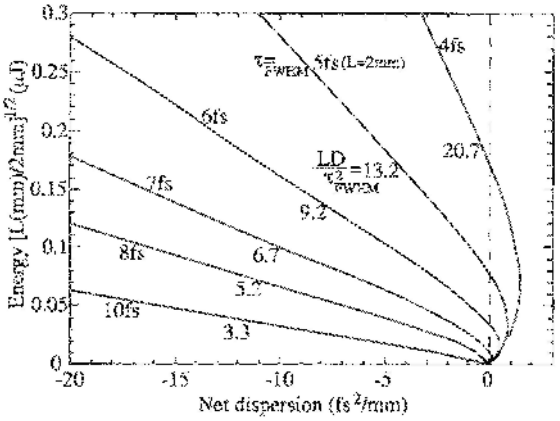

Figure 2-6. Energy of the pulse in the lossless dispersion-managed system with stretching $S = LD/\tau_{FWHM}^2$ or, for a fixed crystal length L and pulse width as parameters; $D = 60$ fs^2/mm for Ti:sapphire at 800 mm.

A major difference from conventional soliton formation is illustrated in Figure 2-6. The figure shows the parameter ranges for a dispersion-managed Hamiltonian system (no gain, no loss, no filtering) that is unbalanced by the net dispersion that serves as the abscissa of the figure. Each curve gives the locus of energy vs net cavity dispersion for a stretching ratio $S = LD/\tau_{FWHM}^2$ (or pulse width with fixed crystal length L). One can see that for a pulse width longer than 8 fs with crystal length L = 2 mm, no solution of finite energy exists in the dispersion-managed system for zero or positive net dispersion. Pulses of durations longer than 8 fs require net negative dispersion. Hence, one can reach the ultrashort operation at zero net dispersion only by first providing the system with negative dispersion. At the same energy, one can form a shorter pulse by reducing the net dispersion, provided that the 8 fs threshold has been passed. For a fixed-dispersion swing ± D, the stretching increases quadratically with the spectral width or the inverse pulse width. Long pulses with no stretching have a sech shape. For stretching ratios of 3–10, the pulses are Gaussian shaped. For even larger stretching ratios, the pulse spectra become increasingly more flat topped, as shown in Figure 2-4.

These dynamics explain why there are steady-state pulses even at zero and slightly positive linear intracavity dispersion as confirmed in the experiment. These pulses would, of course, be unstable in the presence of

gain filtering due to the finite gain bandwidth of Ti:sapphire and, therefore, there is a need for strong-saturable-absorber action to keep the pulse stable against continuum radiation exploiting the peak of the gain. This saturable-absorber action is due to the Kerr-lens effect and can be optimized by various techniques [23, 24], which shall not be repeated here. Also, the spectral shape of the output pulses is greatly distorted because of the finite bandwidth of the output coupler, which can greatly enhance the wings of the laser spectrum, as we will see in the next section.

3. OCTAVE-SPANNING LASERS

Although an octave of spectrum can be generated by spectral broadening in microstructure fiber, there are advantages to using a laser that generates an octave directly. Since there is no medium with a gain spectrum that spans an octave (for Ti:sapphire, it approaches a half-octave), an octave-spanning laser clearly must rely on nonlinear broadening inside the laser cavity. The first demonstration of an octave-spanning laser used a second time-and-space focus in a separate glass element to enhance the nonlinearity [11]. More recently, there have been several demonstrations of Kerr-lens–mode-locked Ti:sapphire lasers that use the Ti:sapphire alone as the nonlinear medium. In this section, we discuss an implementation that uses intracavity prisms for dispersion compensation [25] and one that only uses dispersion-compensating mirrors [26].

The primary advantage of using an octave-spanning laser is that, by eliminating the microstructure fiber [27], issues of coupling and damage are also eliminated. Since the microstructure fiber has a very small core, the coupling is very alignment sensitive and tends to degrade with time. This poses a limit of approximately 10 hours on the duration of experiments. Although long enough for many applications, a proper clock needs to be able to run for days or longer. Damage to the microstructure fiber also limits the durations of experiments. However, there is significant variability as to how long it takes for damage to occur. Under some conditions, the fiber only lasts for hours, while under others it seems to last for weeks.

For time-domain experiments that are affected by carrier-envelope phase, it is important to maintain a short (transform-limited) pulse. The large higher-order dispersion in the fiber coupled with high nonlinearity essentially makes this impossible, whereas with an octave-spanning laser, it is possible.

With these advantages also come some disadvantages. The very high intracavity peak powers needed to obtain sufficient nonlinear spectral broadening makes these lasers susceptible to damaging the Ti:sapphire

crystal. This damage takes some time to occur but can limit the duration of experiments. In addition, the output spatial mode exhibits strong frequency dependence, which can also impact experiments.

Intracavity continuum generation has been demonstrated in a Ti:sapphire laser that was operated in the self-Q-switching regime [28]. However, in this regime, the spectrum is unstable and therefore not useful for femtosecond comb applications. As described in Chapter 3, intracavity continuum generation has also been observed in high-repetition-rate lasers [29], but there was insufficient power at the octave points to implement ν-to-2ν stabilization. A 2ν-to-3ν scheme had to be used [30].

Finally, we would like to comment on the definition of "octave spanning." The span of a spectrum is often taken as the width at some power below the peak (often full-width at half-maximum or perhaps even at the 10 dB points). However, for femtosecond comb applications, there is a good operational definition of octave spanning, namely that it is possible to obtain ν-to-2ν beats. A slightly stronger version of this is that the beats are sufficiently strong to be used to stabilize the offset frequency of the laser. This criterion can be met even when the intensity at the octave points is as much as 40 dB below the peak.

3.1 Octave-spanning laser using prisms

The early designs for broadband Kerr-lens–mode-locked Ti:sapphire lasers [31] used a two-prism sequence for dispersion compensation [32]. Some mechanism for generating anomalous dispersion is needed to correct for the chirp acquired by the pulse as it passes through the normal dispersion Ti:sapphire crystal (and air for extreme bandwidth). The development of dispersion-compensating mirrors (also called "chirped mirrors") [33], which have anomalous dispersion, meant that broadband mode locking could be achieved without prisms [34]. Dispersion-compensating mirrors not only provide anomalous dispersion, but they also have a much larger reflection bandwidth than standard dielectric mirrors. Incorporating both prisms and dispersion-compensating mirrors added additional flexibility in the design and enabled the production of sub-two-cycle pulses [10]. In this section, an octave-spanning laser that incorporates both prisms and dispersion-compensating mirrors is presented. To meet the operational definition of "octave spanning," we show that clean ν-to-2ν beats can be obtained and used to lock the offset frequency of the laser comb.

3.1.1 Design

The prism-based–octave-spanning Ti:sapphire laser is an x-folded cavity that uses commercially available negatively chirped mirrors and intracavity CaF_2 prisms for dispersion compensation, as shown in Figure 2-7. M1 and M2 (10 cm radius of curvature) are both double-chirped mirrors (DCM) designed to be used with CaF_2 prisms [10]. M3 and EM are both negatively chirped Layertec™ mirrors,* part numbers 100466 and 101515, respectively. The output coupler (OC) is G034-007 from Spectra Physics* and the prism separation between the two CaF_2 prisms is ~82 cm. The laser crystal is 2.3 mm long and the pump focusing lens has a focal length of 10 cm. When the laser is pumped with 5.5 W of 532 nm light, the spectrum, at its broadest, extends from ~570 to ~1280 nm (-35 dB from the 800 nm portion of the spectrum). The average ML power is > 400 mW (100 mW cw) at an 88 MHz repetition rate. Mode locking is easily initiated by quickly changing the insertion of the prism furthest from EM.

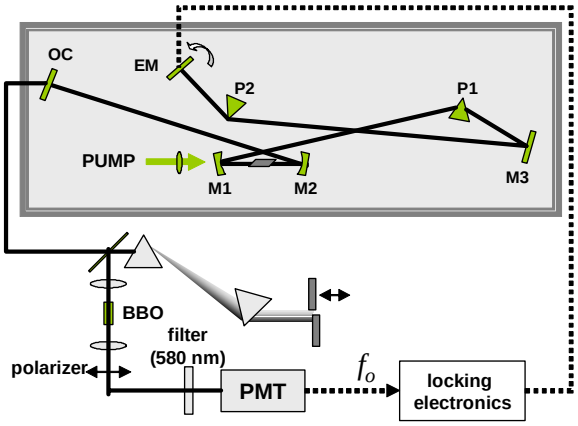

Figure 2-7. Schematic of laser and ν-to-2ν detection of f_0.

The continuum generated by the laser relies on the interplay between an enhancement of SPM and dispersion compensation, where the latter allows for the existence of the former. The exact choice of chirped mirrors, the prism separation, and the prism insertion appear not to be very important. Different combinations of mirrors for M1 and M2 (Layertec 101568), M3 (DCM, Layertec 100466 and 101515) and EM (Layertec 100466 and

* This information is given for technical purposes only and does not represent an endorsement on the part of the National Institute of Standards and Technology.

101515), and a protected silver mirror were tested and yielded octave-spanning spectra. Also, two OC's (Spectra Physics G034-007 and CVI Laser PR2 — 2% transmission @ 800nm) resulted in an octave of bandwidth. We have not been able to reproduce the octave spectrum using fused silica prisms. Apparently, in this case, the continuum generation does not result from meticulous dispersion compensation. This is not surprising since the continuum is created on a single pass through the crystal. As a result, careful dispersion compensation may only be necessary over the bandwidth indicated by the OC reflectivity and not the entire spectrum.

The position of the curved mirrors is critical for producing an octave-spanning spectrum. Typically, KLM is obtained by displacing one curved mirror away from the optimum mirror position for cw operation. Here, the mirror furthest from the pump is translated inward to the point that the laser is on the edge of stability for cw operation. This arrangement increases the discrimination between mode-locked and cw operation and requires the formation of a strong Kerr-lens to correct for the misalignment with respect to the pump. To optimize the bandwidth, both curved mirrors are then translated in the same direction away from the pump, just before the point where the laser begins Q-switching.

3.1.2 Carrier-envelope phase stabilization

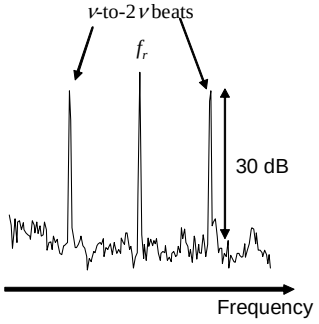

Figure 2-8. Rf spectrum showing a repetition rate peak and ν-to-2ν heterodyne beats.

To measure and stabilize the carrier-envelope phase in this laser, we implement the simplest self-referencing scheme, which compares the second harmonic on the low frequency extreme of the laser spectrum with the fundamental on the extreme high end of the spectrum (see Chapter 2). A ν-to-2ν interferometer is used to measure f_0. Specifically, f_0 is obtained via optical heterodyne between the fundamental light of the laser spectrum at ~580 nm and doubled light at ~1160 nm, see Figure 2-7. For the

measurements presented here, the signal-to-noise ratio of the offset-frequency beat note, using the octave spectrum (see Figure 2-8), is greater than 30 dB at 100 kHz resolution bandwidth. Once measured, f_0 is then stabilized by actively tilting the end mirror (EM) [35] with an in-loop-accumulated phase error of 0.18 rad (1.65 mHz–102kHz), as shown in Figure 2-8. Because this is an in-loop measurement of the phase noise, it therefore may not be used alone to characterize the noise on the output of the laser. However, using the octave spectrum from the laser directly, we have eliminated the out-of-loop phase noise generated by microstructure fiber [36]. Also, because the prism-based ν-to-2ν interferometer used in the measurement of f_0 minimizes non-common-mode mirrors, the dominant source of out-of-loop phase noise on the laser results from the feedback electronics.

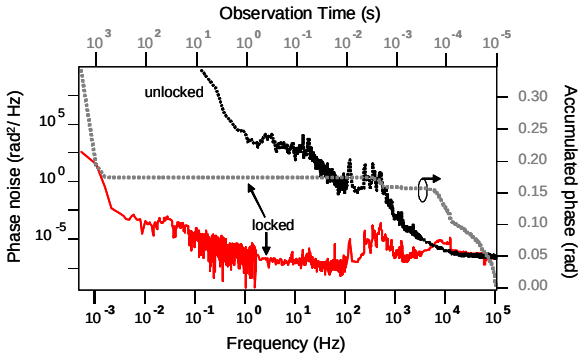

Figure 2-9. Power spectral density of phase noise (left axis) and accumulated rms phase fluctuations (right axis).

3.1.3 Frequency-dependent spatial mode

Since the light in the wings of the spectrum is generated by self-phase modulation and is outside the gain bandwidth, it is not truly lasing and does not have to obey resonance conditions in the cavity. This means the spatial mode in the wings can vary significantly. This variation is relevant to f_0 detection as it can degrade the spatial-mode matching and thus limit the signal-to-noise ratio of the f_0 beat note. It may also pose problems to pulse compression. This mismatch in mode profiles is depicted Figure 2-10. Figure 2-11 shows the result of a 90/10 knife-edge method that was used to perform a second moment measurement of the beam profiles to yield the beam spot sizes as a function of wavelength [37]. From this result, we see that the spectral extremes exhibit a significant increase in asymmetry and deviation

away from the resonant Gaussian TEM_{00} mode and its corresponding $1/\lambda$ diffraction limit.

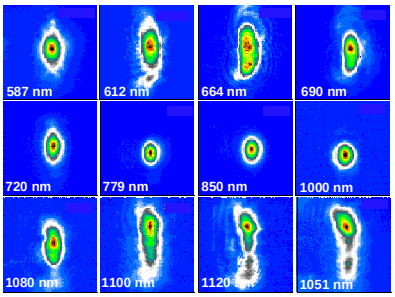

Figure 2-10. Beam profiles at various wavelengths.

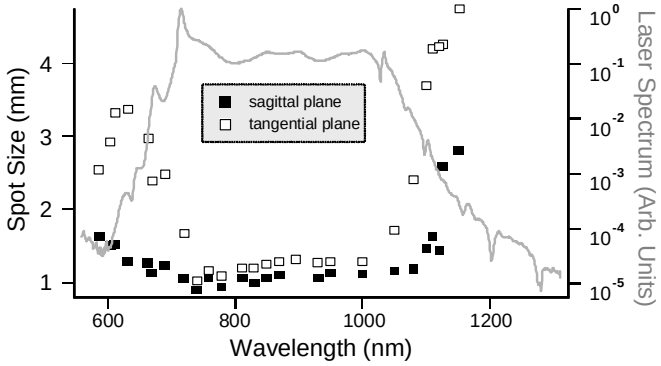

Figure 2-11. Measured sagittal and tangential spot sizes as a function of wavelength (squares, left axis). Line shows laser spectrum (right axis).

Measurement of the beam parameters at the output coupler, as shown in Figure 2-12, explains the increase in spot size in the wings of the spectrum. The beam waist shows a sudden decrease of the nonresonant as compared to the resonant modes. This decrease should cause a greater divergence in the wings of the laser spectrum, thereby leading to the larger spots sizes observed in the far field (see Figure 2-10). Figure 2-13 compares the measured beam divergence to that which would result from the propagation of a Gaussian TEM_{00} mode given the respective measured beam waists in Figure 2-12. The ratio of the former to the latter gives the M^2 value as a function of wavelength, indicating the strength of the non-TEM_{00}-Gaussian beam propagation (non-Gaussian modes and/or higher modes).

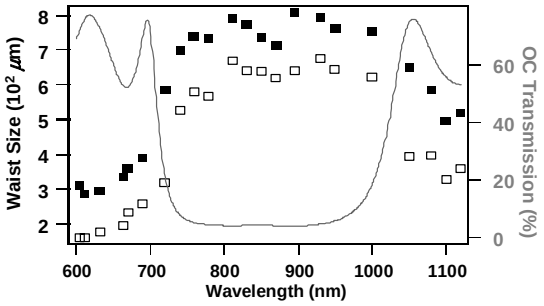

Figure 2-12. Waist size at output coupler as a function of wavelength for sagittal and tangential planes (squares, left axis). Output coupler transmission is line (right axis).

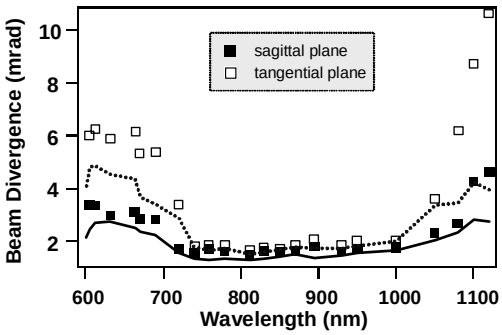

Figure 2-13. Measurement of beam divergence (squares) and predicted divergence based on waist size (lines).

The mode profiles and the sudden decrease in waist in the extremes of the spectrum still need to be explained. For resonant modes, the cavity geometry determines the waist size and divergence. The beam characteristics of the nonresonant modes, however, can be directly influenced by the Kerr lens in the crystal and by diffraction and aperturing of optics without the self-correcting effects of the cavity. The Kerr lensing is considerable since intracavity continuum generation, for this laser, requires significant realignment away from ideal cw operation. This realignment results in a highly asymmetric cw beam (tangential waist/sagittal waist = 1.56) and a large discrimination in average output power between cw and mode-locked operation (4:1). The asymmetry implies that the nonlinear correction for the cw asymmetry may result in the formation of an asymmetric Kerr lens, which may explain the observed asymmetry in the wings of the spectrum. This mirror positioning also results in a different initial cw condition than for

"normal" KLM because it gives rise to a much more tightly focused cw beam than the pump beam (~ ratio of 4:1, calculated using ABCD cavity propagation based on the observed cw asymmetry). This leads us to the conclusion that the effect of the Kerr lens should be one that increases the waist of the mode-locked beam. The increased waist size improves the efficiency with which power is extracted from the pump beam and thus still acts as an effective saturable absorber. This is consistent with the observed beam waists (Figure 2-12), as the frequency at the very edges of the spectrum should be produced by a weaker Kerr lens than those of the resonant modes [37]. Complete modeling of the relationship between nonlinear effects in the crystal and pulse formation, however, is beyond the scope of this chapter but has been addressed elsewhere [16].

3.2 Prismless octave-spanning laser

We have also built octave-spanning lasers where dispersion compensation is completely achieved by double-chirped mirror pairs [38] and thin BaF_2 wedges for fine adjustment of the dispersion [26, 39]. Prismless lasers do have the advantage of being scalable to GHz repetition rates because of the compact dispersion compensation via chirped mirrors. Higher repetition rates mean higher power per mode at the same average output power, which is advantageous for frequency metrology. Also, the compactness of the cavity makes it less sensitive to temperature variations and environmental perturbations.

3.2.1 Design

The lasers consist of astigmatically compensated x- or z- folded cavities. The x-folded version is shown in Figure 2-14(a). The lasers have a 2 mm long Ti:sapphire crystal with an absorption of α=7 cm^{-1} at 532 nm. They are pumped by a diode-pumped, frequency-doubled Nd:vanadate laser. The radius of curvature (ROC) of the folding mirrors is 10 cm, and the pump lens has a 60 mm focal length. All mirrors in the cavity, with the exception of the end mirrors, are type I (gray) and type II (black) double-chirped mirrors (DCM) that generate smooth group-delay dispersion when used together in pairs [38]. Figure 2-9(b) shows the reflectivity and group delay of the DCM pairs. The total group delay is smooth from 600 to 1200 nm. The average reflectivity over the full octave can be as high as 99.9%. One cavity end mirror is a silver mirror and the other is a broadband output coupler, made of either $ZnSe/MgF_2$ (80 MHz repetition-rate laser) or TiO_2/SiO_2 (150 MHz repetition-rate laser) coatings with 1% transmission. The output power in cw operation is typically 40 mW with 4.4 W pump power. In mode-locked

operation, the average power is 90 mW. The output power is limited by low output coupling and scattering losses in the OC coating and the silver mirror. Presumably, further optimization of output coupling and elimination of the silver mirror would increase laser efficiency.

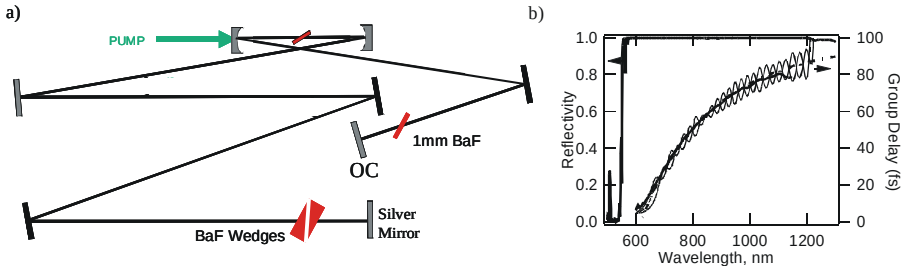

Figure 2-14. (a) Schematic diagram of octave-spanning prismless laser. Gray and black mirrors are type I and II double-chirped mirrors (DCMs), respectively. The BaF_2 wedges are used for fine-tuning of the dispersion. (b) Reflectivity (left scale) of the type I DCMs with pump window shown as thick solid line. The group-delay design is given by the thick, dash-dotted line. The individual group delays (right scale) of type I and II DCMs are shown as thin lines and the average as a dashed line (almost identical to the design goal over the wavelength range of interest from 650–1200 nm). The measured group delay, using white-light interferometry, is shown as the thick solid line from 600–1100 nm. Beyond 1100 nm, the sensitivity of the Si detector limited the measurement.

In one round trip of the laser pulse through the cavity, the total number of bounces on DCMs (12 bounces) generates the precise negative dispersion required to compensate for positive second- and higher-order dispersion caused by the laser crystal, the air path in the cavity, and the BaF_2 wedge pairs used to fine-tune the intracavity dispersion.

We used BaF_2 for dispersion compensation because it has the lowest ratio of third- to second-order dispersion in the wavelength range from 600–1200 nm, and the slope of the dispersion of BaF_2 is nearly identical to that of air. These features make it possible to scale the cavity length and repetition rate without changing the overall intracavity dispersion. To achieve mode-locked operation, it is necessary to reduce the amount of BaF_2 inside the laser cavity (by withdrawing one of the wedges).

The broadest spectrum can be achieved by optimizing the insertion of the BaF_2 wedge, so that the laser operates very close to the zero average-dispersion point. In this case, the spectral width of the laser is critically dependent on the dispersion balance. With the prismless lasers, adjusting the dispersion does not significantly change the cavity alignment. Figures 2-15(a) and (b) show the spectrum under broadband operation of an 80 MHz and a 150 MHz laser, respectively. The octave is already reached at a

spectral density about 25 dB below the average power level. The same plots also show the corresponding OC transmission curves. The detailed shape of this transmission curve is a determining factor in the width of the output spectrum, since it significantly enhances the spectral wings. A roll-off of the output coupler matched to the intracavity spectrum is necessary to generate the octave-spanning spectrum.

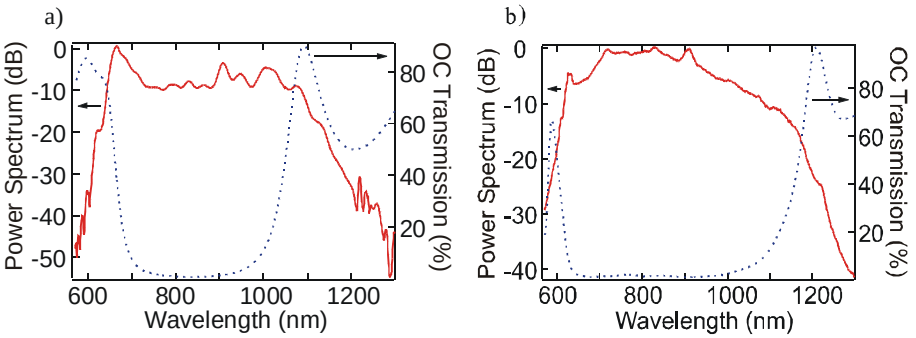

Figure 2-15. (a) Measured output spectra for lasers with 80 MHz repetition rate and (b) 150 MHz repetition rate. In both cases, the octave is reached at approximately 25 dB below the average power level. The average mode-locked power is 90 mW for both lasers. Also shown (dashed lines) are the respective output coupler (OC) transmission curves for the ZnSe/MgF_2 Bragg-stack (a) and a broadband SiO_2/TiO_2 stack (b). Both have about 1% transmission at 800 nm.

3.2.2 Carrier-envelope phase stabilization

We directly measure f_0 by the ν-to-2ν technique described earlier, as shown in Figure 2-16(a). Using a dichroic beamsplitter, we split the laser output into long- and short-wavelength components and recombine them after insertion of a proper time-delay stage. The delay stage is essential to compensate for the difference in group delay between the 580 and 1160 nm radiation in the optical components (splitters, OC and BBO crystal). The recombined beam is then focused into a 1 mm BBO crystal cut for type I second harmonic of 1160 nm. The resulting output is sent through a 10 nm wide spectral filter centered at 580 nm. After projecting the doubled 1160 nm light and the fundamental into the same polarization to enable interference, the beat signal is detected by a photomultiplier tube (PMT). Figure 2-16(b) shows the detected f_0 beat signals with 10 kHz and 100 kHz measurement bandwidths. The signal-to-noise ratios are 30 dB and 40 dB, respectively. The f_0 beat is very stable and the laser stays mode locked over many days. In the absence of active feedback and without any temperature control, the f_0 frequency stays within the bandwidth of the bandpass filter

following the PMT, which is 8MHz, for more than 10 hours. On the time scale of seconds, the beat can jitter by about 100 kHz. The f_0 lock only breaks because of a slow drift of the beat note out of the filter bandwidth of the 8 MHz filter, which is not yet controlled.

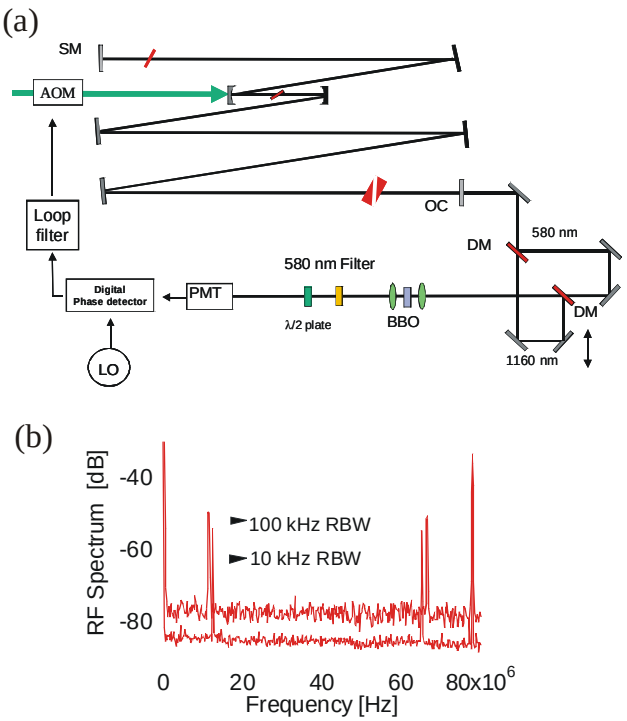

Figure 2-16. (a) Setup for f_0 detection and lock. (b) Measured carrier-envelope beat signal from the 80 MHz laser.

To demonstrate control over the comb, we filter the component $f_r + f_0$ at 130 MHz from the PMT signal and phase lock it to a stable rf synthesizer using a phase-locked loop. To increase the locking range, the 130 MHz component of the signal is properly filtered and amplified, sent to a thirty-two-fold frequency divider, and then compared with the synthesizer signal in a digital phase detector. The properly filtered and amplified phase-error signal controls the pump power via an acousto-optic modulator that directly controls the carrier-envelope frequency of the mode-locked laser.

Figure 2-17 shows the measured phase-error spectral densities of the f_0 beat with and without active stabilization. The integrated phase error for the in-loop measurement is 0.2 rad (from 1 Hz to 10 MHz). The major contribution to this phase-noise error comes from the yet unsuppressed pump noise. We expect further improvement in the residual carrier-envelope phase

fluctuations with an improved loop filter design for stronger noise suppression.

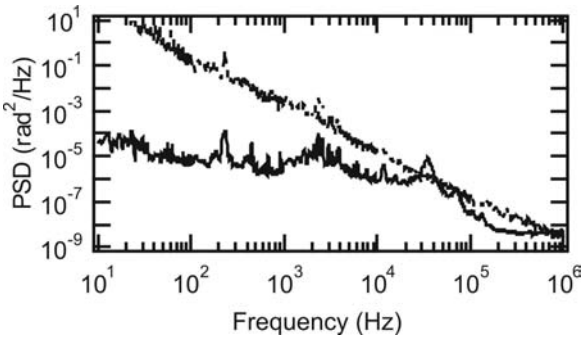

Figure 2-17. Spectral densities of the phase-error signal at the output of the digital phase detector for the f_0 lock (solid line) and free running f_0 (dashed line).

4. CARRIER-ENVELOPE PHASE DYNAMICS

The carrier-envelope phase evolution in a mode-locked laser depends on the pulse energy. This is not surprising as there is a nonlinear contribution to the phase shift of the intracavity pulse as it passes through the gain crystal. At the simplest level, this nonlinear phase shift happens because of the Kerr effect, i.e., the index of refraction depends on intensity and hence so does the optical path length. This is clearly an over simplification. Better insight is based on treating the pulse as a soliton. However, care is needed as classical soliton theory does not include the fact that the group velocity also depends on intensity (known as the "shock" term) or the fact that dispersion and nonlinearity in the laser are not constant as a function of position in the cavity. The intensity dependence of the carrier-envelope phase has both positive and negative aspects. On the positive side, it provides a parameter by which the carrier-envelope phase can be controlled. On the negative side, it means the amplitude noise will be converted to phase noise.

One of the first experiments to measure carrier-envelope phase evolution (using a cross-correlator) observed its intensity dependence [12]. However, the slope, $d\Delta\phi_{ce}/dI$, had the opposite sign from what was expected based on classical soliton theory. This result was explained as being caused by an intensity-dependent shift in the spectrum.

Subsequent theoretical work included the effect of the shock term [40]. It was found that the shock term causes the group velocity to change twice as fast with intensity as does the phase velocity. This fact results in an opposite sign of $d\Delta\phi_{ce}/dI$ from what it would be if the shock term were ignored.

Further experiments using self-referencing to detect $\Delta\phi_{ce}$ showed that $d\Delta\phi_{ce}/dI$ could actually change signs [41]. The results were consistent with the shifting of the spectrum with intensity also changing signs. These measurements also showed that for shorter pulses, $\Delta\phi_{ce}$ was much less sensitive to changes in the pulse intensity. This finding is consistent with theoretical work [40] but may also be simply due to clamping of the spectrum because of implicit spectral filtering in the laser.

Numerical simulations of nonlinear pulse propagation in sapphire also show a change in the sign of $d\Delta\phi_{ce}/dI$ that arises from warping of the envelope at high intensities [42]. There was no corresponding change in the direction of spectral shift, as was observed experimentally. However, this work only modeled propagation in sapphire and did not treat the rest of the laser cavity.

More recent theoretical treatment based on a multiple-scales treatment of dispersion-managed solitons included both managed dispersion and nonlinearity [43]. Both shock and third-order dispersion were considered as well. The results confirmed the earlier conclusions [40], although the details varied because of differences in the treatment of and inclusion of additional effects.

At this point, a number of phenomena have been identified in theory and experiment, although a clear connection between them remains elusive. A further understanding is important as these effects, which are used to control $\Delta\phi_{ce}$, can also corrupt its stability and hence that of the generated spectral comb.

5. SUMMARY

The recent explosion in work on carrier-envelope phase stabilization of ultrashort pulses and the resulting stable frequency comb has been built on a foundation of mode-locked laser technology. The culmination of this has been the development of lasers that directly generate an octave-spanning spectrum. At the same time, the need for stabilization has pushed mode-locked laser technology in new directions and forced the development of an improved understanding of the lasers.

ACKNOWLEDGEMENTS

S.T.C. acknowledges the contributions of T. M. Fortier, D. J. Jones, P. M. Goorgian, B. Ilan and M. Ablowitz to this work and support by NIST, ONR and NSF. E. P. I. and F. X. K. acknowledge contributions from T.

Schibli, L. Matos and O. Kuzucu. Work at MIT was supported by NSF-ECS-0322740, AFOSR-FA9550-04-1-0011and ONR-N00014-02-1-0717.

REFERENCES

[1] D. E. Spence, P. N. Kean, and W. Sibbett, Opt. Lett. **16**, 42-44 (1991).

[2] D. K. Negus, L. Spinelli, N. Goldblatt, and G. Feugnet, in *Advanced Solid-State Lasers* (OSA, 1991), Vol. 10; F. Salin, J. Squier, and M. Pichè, Opt. Lett. **16**, 1674-1676 (1991); M. Pichè, Opt. Commun. **86**, 156-160 (1991).

[3] H. A. Haus, IEEE J. Quantum Electron. **11**, 736-746 (1975).

[4] J. H. B. Nijhof, N. J. Doran, W. Forysiak, and F. M. Knox, Electron. Lett. **33**, 1726-1727 (1997).

[5] K. Tamura, H. A. Haus, and E. P. Ippen, Electron. Lett. **28**, 2226-2228 (1992).

[6] Y. Chen, F. X. Kärtner, U. Morgner, S. H. Cho, H. A. Haus, E. P. Ippen, and J. G. Fujimoto, J. Opt. Soc. Am. B **16**, 1999-2004 (1999).

[7] J. P. Zhou, G. Taft, C. P. Huang, M. M. Murnane, H. C. Kapteyn, and I. P. Christov, Opt. Lett. **19**, 1149-1151 (1994).

[8] A. Stingl, C. Spielmann, F. Krausz, and R. Szipocs, Opt. Lett. **19**, 204-206 (1994).

[9] D. H. Sutter, G. Steinmeyer, L. Gallmann, N. Matuschek, F. Morier-Genoud, U. Keller, V. Scheuer, G. Angelow, and T. Tschudi, Opt. Lett. **24**, 631-633 (1999).

[10] U. Morgner, F. X. Kärtner, S. H. Cho, Y. Chen, H. A. Haus, J. G. Fujimoto, E. P. Ippen, V. Scheuer, G. Angelow, and T. Tschudi, Opt. Lett. **24**, 411-413 (1999).

[11] R. Ell, U. Morgner, F. X. Kärtner, J. G. Fujimoto, E. P. Ippen, V. Scheuer, G. Angelow, T. Tschudi, M. J. Lederer, A. Boiko, and B. Luther-Davies, Opt. Lett. **26**, 373-375 (2001).

[12] L. Xu, C. Spielmann, A. Poppe, T. Brabec, F. Krausz, and T. W. Hänsch, Opt. Lett. **21**, 2008-2010 (1996).

[13] A. Baltuška, T. Fuji, and T. Kobayashi, Phys. Rev. Lett. **88**, art. no.-133901 (2002).

[14] L. Xu, C. Spielmann, F. Krausz, and R. Szipocs, Opt. Lett. **21**, 1259-1261 (1996).

[15] I. P. Christov, H. C. Kapteyn, M. M. Murnane, C. P. Huang, and J. P. Zhou, Opt. Lett. **20**, 309-311 (1995).

[16] I. P. Christov, V. D. Stoev, M. M. Murnane, and H. C. Kapteyn, Opt. Lett. **21**, 1493-1495 (1996).

[17] I. P. Christov and V. D. Stoev, J. Opt. Soc. Am. B **15**, 1960-1966 (1998).

[18] C. Spielmann, P. F. Curley, T. Brabec, and F. Krausz, IEEE J. Quantum Electron. **30**, 1100-1114 (1994).

[19] K. Tamura, E. P. Ippen, H. A. Haus, and L. E. Nelson, Opt. Lett. **18**, 1080-1082 (1993).

[20] S. M. J. Kelly, Electron. Lett. **28**, 806-807 (1992); J. P. Gordon, J. Opt. Soc. Am. B **9**, 91-97 (1992).
[21] K. Tamura, E. P. Ippen, and H. A. Haus, App. Phys. Lett. **67**, 158-160 (1995).
[22] Y. Chen and H. A. Haus, J. Opt. Soc. Am. B **16**, 24-30 (1999).
[23] R. Reinisch and G. Vitrant, Prog. Quantum Electron. **18**, 1-38 (1994).
[24] E. J. Grace, A. Ritsataki, P. M. W. French, and G. H. C. New, Opt. Commun. **183**, 249-264 (2000).
[25] T. M. Fortier, D. J. Jones, and S. T. Cundiff, Opt. Lett. **28**, 2198-2200 (2003).
[26] L. Matos, O. Kuzucu, T. R. Schibli, J. Kim, E. P. Ippen, D. Kleppner, and F. X. Kärtner, Opt. Lett. **29** (2004).
[27] J. K. Ranka, R. S. Windeler, and A. J. Stentz, Opt. Lett. **25**, 25-27 (2000).
[28] J. P. Likforman, A. Alexandrou, and M. Joffre, App. Phys. Lett. **73**, 2257-2259 (1998).
[29] A. Bartels and H. Kurz, Opt. Lett. **27**, 1839-1841 (2002).
[30] T. M. Ramond, S. A. Diddams, L. Hollberg, and A. Bartels, Opt. Lett. **27**, 1842-1844 (2002).
[31] M. T. Asaki, C. P. Huang, D. Garvey, J. P. Zhou, H. C. Kapteyn, and M. M. Murnane, Opt. Lett. **18**, 977-979 (1993).
[32] R. L. Fork, O. E. Martinez, and J. P. Gordon, Opt. Lett. **9**, 150-152 (1984).
[33] R. Szipocs, K. Ferencz, C. Spielmann, and F. Krausz, Opt. Lett. **19**, 201-203 (1994).
[34] A. Stingl, M. Lenzner, C. Spielmann, F. Krausz, and R. Szipocs, Opt. Lett. **20**, 602-604 (1995).
[35] S. T. Cundiff, J. Ye, and J. L. Hall, Rev. Sci. Instrum. **72**, 3746-3771 (2001).
[36] T. M. Fortier, J. Ye, S. T. Cundiff, and R. S. Windeler, Opt. Lett. **27**, 445-447 (2002).
[37] S. T. Cundiff, W. H. Knox, E. P. Ippen, and H. A. Haus, Opt. Lett. **21**, 662-664 (1996).
[38] F. X. Kärtner, U. Morgner, R. Ell, T. Schibli, J. G. Fujimoto, E. P. Ippen, V. Scheuer, G. Angelow, and T. Tschudi, J. Opt. Soc. Am. B **18**, 882-885 (2001).
[39] T. R. Schibli, O. Kuzucu, J. W. Kim, E. P. Ippen, J. G. Fujimoto, F. X. Kaertner, V. Scheuer, and G. Angelow, IEEE J. Sel. Top. Quantum Electron. **9**, 990-1001 (2003).
[40] H. A. Haus and E. P. Ippen, Opt. Lett. **26**, 1654-1656 (2001).
[41] K. W. Holman, R. J. Jones, A. Marian, S. T. Cundiff, and J. Ye, Opt. Lett. **28**, 851-853 (2003); K. W. Holman, R. J. Jones, A. Marian, S. T. Cundiff, and J. Ye, IEEE J. Sel. Top. Quantum Electron. **9**, 1018-1024 (2003).
[42] P. M. Goorjian and S. T. Cundiff, Opt. Lett. **29**, 1363 (2004).
[43] M. J. Ablowitz, B. Ilan, and S. T. Cundiff, Opt. Lett. **29**, 1808-1810 (2004).

Chapter 3

GIGAHERTZ FEMTOSECOND LASERS

The tools for precise optical frequency metrology

Albrecht Bartels
Time and Frequency Division, National Institute of Standards and Technology

Abstract: Femtosecond lasers with a repetition rate of approximately 1 GHz are commonly used frequency comb generators for precise optical frequency metrology. They are conveniently compact, yield unambiguous frequency readings with the help of a commercial wavemeter, and can yield greater heterodyne beat signals against a cw laser than systems with lower repetition rates. This chapter reviews the technology of oscillators based on Ti:sapphire and Cr:forsterite that operate at repetition rates of up to 3.5 GHz. Aside from a discussion of these "standard" lasers with a typical full-width-at-half-maximum (FWHM) bandwidth of 30 nm, one section is dedicated to the generation of a broadband continuum with a 1 GHz oscillator. This laser allows frequency measurements without additional spectral broadening and can be phase locked to a reference oscillator for uninterrupted periods exceeding one day.

Keywords: mode-locked lasers, optical atomic clocks, optical frequency metrology

1. INTRODUCTION

The first report of a femtosecond laser based on Ti:sapphire as the gain material was published in 1991 [1]. Since then a number of research groups have attempted to increase the repetition rate from 100 MHz to even higher values. In 1998, right before the dawn of optical frequency metrology with femtosecond laser combs, the oscillators by Ramaswamy et al. [2] and Stingl et al. [3] were conceptually the most intriguing for realizing higher repetition rates. Both researchers employed a new, more compact method for intracavity dispersion management, replacing the long prism sequences that had been part of every femtosecond laser until then. The prior configuration had prevented repetition rates higher than ≈300 MHz.

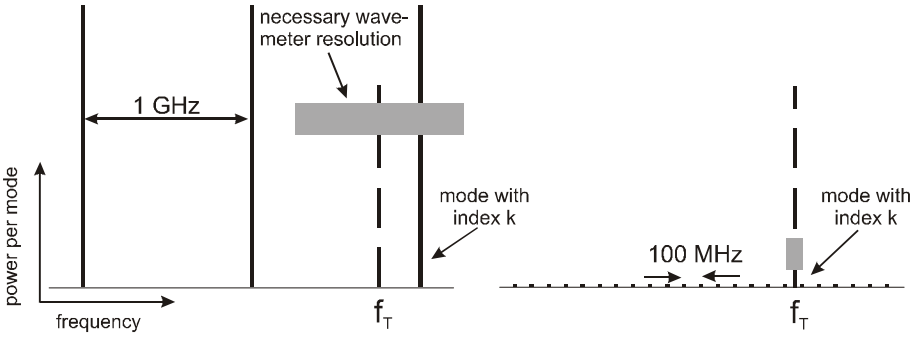

Figure 3-1. Illustration of the advantages for frequency metrology of the frequency comb emitted by a 1 GHz femtosecond laser (left) compared to that of a 100 MHz laser (right). The length of the two sets of comb teeth (solid vertical lines) scales with the power per mode. The lengths of the gray horizontal bars represent the necessary resolution for premeasurement of the frequency to be measured (f_T, indicated by the dashed line) to determine the index k of the mode against which f_T is beat.

In 1999 Udem et al. [4] demonstrated an optical frequency measurement with a femtosecond laser-based frequency comb for the first time. The comb was used to bridge the 18 THz wide gap between a calibrated reference frequency and the measured frequency f_T. Soon afterwards, Jones et al. [5] showed that a femtosecond laser can be "self-referenced." Self-referencing implies that both degrees of freedom of the optical frequency comb, the laser's repetition rate f_r and its carrier-envelope offset frequency f_0, are accessible and controllable. Because f_0 and f_r are electronically manageable microwave frequencies, the entire optical frequency comb with a multitude of components $\nu_n = f_0 + nf_r$ (where n is a large integer) in the hundreds of terahertz range can be directly linked to a cesium clock and subsequently used for absolute measurements of optical frequencies. Since then, many groups have successfully used femtosecond lasers for optical frequency measurements and to realize optical atomic clocks [6].

Even before these early experimental demonstrations of femtosecond laser-based optical frequency metrology, Reichert et al. [7] pointed out that repetition rates higher than the usually available 100 MHz would be greatly advantageous because they would yield a wider-spaced frequency comb. Typically in a frequency measurement, the result is given by $f_T = f_0 + kf_r + f_b$, where f_b is the frequency of the heterodyne beat between f_T and the neighboring frequency comb component with index k. While f_0, f_r, and f_b can easily be measured, an unambiguous result for f_T requires determination of k via a premeasurement of f_T with a resolution of better than $\pm f_r/2$. In contrast to a 100 MHz system with a 1 GHz laser, this task is easily solved using a commercial wavemeter. (The best available wavemeter resolution within the

wavelength range of Ti:sapphire-based frequency combs is ≈100 MHz.) Also, with a cavity length of 30 cm, a 1 GHz oscillator is conveniently compact (commercially available models come in a ≈32×20×10 cm box) as compared to a 3 m long 100 MHz resonator. See Figure 3-1 for a comparison of the two systems.

A femtosecond laser with a 1 GHz repetition rate yields ≈100 times more usable optical power per comb component (mode) than does a 100 MHz laser. This additional power increases the signal-to-noise ratio of a heterodyne beat signal against a continuous-wave (cw) laser, which is used as a local oscillator to realize f_T, by the same amount. The factor of 100 is caused by two features of the femtosecond laser: First, the average output power of a well-designed Ti:sapphire laser is usually on the order of 25% of the absorbed pump power, regardless of the repetition rate. At a repetition rate 10 times higher, the average output power is distributed to one-tenth the number of modes, increasing the power per mode by a factor of 10. Second, the spectrally narrow output of a typical laser (FWHM ≈30–60 nm) needs to be broadened to span at least one octave via self-phase modulation (SPM) in a microstructure fiber [8] to allow self-referencing. However, nonlinear amplification of shot noise present on the input light limits the pulse energy that can be launched into a microstructure fiber and still attain usefully quiet output light [9, 10]. Above a threshold of ≈300 pJ of pulse energy, the excess noise on the fiber output grows exponentially. This behavior implies that a maximum average power of 300 mW in a 1 GHz system can be launched into a microstructure fiber. In comparison, only 30 mW can be sent into microstructure fiber in a 100 MHz system.

Some problems remain, related mainly to the long-term reliability of frequency metrology systems and their ease of use. A great improvement was achieved in 2004 with a 1 GHz laser that readily spans a broadband continuum and can be self-referenced without the use of microstructure fiber for uninterrupted periods in excess of one day. This oscillator will be addressed in the last section.

2. HIGH-REPETITION-RATE RING OSCILLATORS

2.1 Design criteria and basic resonator layout

The repetition rate f_r of a passively mode-locked femtosecond laser is determined by the physical cavity length L and the round-trip-averaged group velocity $\bar{v}_g$:

$$f_r = \frac{\bar{v}_g}{L}. \tag{1}$$

Thus, increasing the repetition rate means shrinking the cavity length. The realization of gigahertz repetition rates for Ti:sapphire femtosecond lasers has been straightforward. A few simple specific design criteria now exist. They can be discussed in the context of a steady-state duration τ of a pulse circulating in a cavity in which only SPM, provided by the nonlinear refractive index $n_2 \approx 3\times10^{-16}\text{m}^2/\text{W}$ of the Ti:sapphire gain crystal, and negative group-delay dispersion (GDD), designated as D_2, shape the pulse (see, for example, Reference [11]). This limit applies in good approximation to all Kerr-lens–mode-locked femtosecond lasers as long as higher-order dispersion is negligible:

$$\tau = 4\ln\left(1+\sqrt{2}\right)\frac{|D_2|\lambda w_0^2}{d\, n_2 E_P}, \tag{2}$$

where λ is the carrier wavelength, w_0 is the waist radius inside the laser crystal, d the length of the crystal, and E_P the pulse energy.

When shrinking a 100 MHz cavity to yield a 1 GHz repetition rate, the pulse energy E_P is reduced by a factor of 10 (assuming constant average power). This results in a steady-state pulse duration 10 times longer. The combination of lower pulse energy and greater pulse duration reduces the peak by a factor of 100. This alone does not present a fundamental problem for achieving higher repetition rates. However, in practice Kerr-lens mode locking (KLM) is required to maintain stable pulsed operation over cw operation. A Kerr lens is induced by a high-intensity Gaussian beam profile in the Ti:sapphire crystal via its nonlinear refractive index. To achieve KLM, the cavity is arranged in a way that the Kerr lens modulates the net gain or loss of the cavity for a pulsed beam. Either it reduces the net cavity losses by increasing the transmission through a hard aperture (e.g., a slit) at an appropriate position in the resonator (hard-aperture KLM), or it increases the net gain by increasing the overlap with the finite gain volume inside the crystal (soft-aperture KLM). KLM gets more efficient with higher peak intensity. (High pulse energies and short pulse widths in the cavity are essential.) Thus the reduction of peak power due to the increased repetition rate must be compensated for. This is accomplished by reducing the amount of output coupling with respect to a 100 MHz oscillator (from ≈10% to ≈1%) and shrinking the waist radius w_0 inside the gain crystal by tighter focusing.

The second major concern is the achievement of negative net-GDD in the cavity. The standard method of employing a four-prism sequence (or a

double-passed, two-prism sequence) fails for high repetition rates because even with highly dispersive materials, an apex distance of ≈30 cm per prism pair is required [12]. This requirement sets an upper limit of ≈300 MHz on the repetition rate. An elegant way to replace a prism sequence is by using negative dispersion mirrors that reflect light with longer wavelengths from a deeper region in the coating than light with shorter wavelengths. A variety of structures has been developed, of which only Gires-Tournois interferometer (GTI) mirrors and chirped mirrors are used here [13].

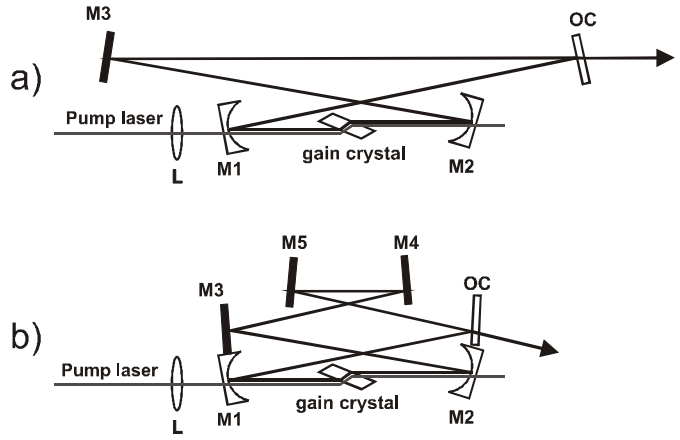

Figure 3-2. (a) Four-mirror cavity with the gain crystal enclosed by focusing mirrors M1 and M2. The flat mirror M3 and the output coupler (OC) form the collimated part of the cavity. The pump light enters the crystal through lens L and M1. (b) Equivalent to (a) but with extra folding using flat mirrors M4 and M5.

The ring oscillators shown in Figure 3-2 are the basis for all lasers presented here. A ring configuration has been chosen for geometrical reasons. With a given number of components, it allows a higher repetition rate than a linear cavity. Also, ring cavities are less sensitive to back-reflections. In the following sections, the cavities will be discussed in detail along with actually realized lasers.

As with all Kerr-lens–mode-locked femtosecond lasers, these oscillators need an initial perturbation, such as tapping a mirror mount, to generate an intracavity power fluctuation that builds up to a stable circulating femtosecond pulse. As opposed to cw operation, which is bidirectional, mode-locked operation is unidirectional and starts in a random direction [14].

2.2 Standard Ti:sapphire lasers for 0.3–3.5 GHz repetition rate

The four-mirror cavity, as shown in Figure 3-2(a), is usually employed to achieve the highest repetition rates because it can be made the most compact. The cavity contains a Ti:sapphire crystal of length d=1.5 mm (absorption coefficient α=5 cm^{-1}) that is pumped with a frequency-doubled Nd:YVO_4 laser at 532 nm through lens L with f_L = 30 mm. The crystal is placed at Brewster's angle between mirrors M1 and M2. The pump beam radius inside the crystal is ≈10 µm. Mirrors M1 and M2 have a focal length of 15 mm, leading to a calculated waist radius of the resonator mode inside the crystal between 8 and 20 µm for repetition rates ranging from 0.5 to 3.5 GHz. The angles at which the intracavity beam is reflected off M1 and M2 are set such that the cavity is astigmatically compensated [15]. The crystal introduces a GDD of ≈87 fs^2 at 800 nm wavelength. Chirped mirrors with a GDD of ≈ -45 fs^2 at 800 nm are used for M1–M3 to achieve a net GDD of ≈ -48 fs^2 (the GDD of the OC is negligible). The output coupler has a reflectance of 98%, and the cavity length is set to yield a repetition rate of 2 GHz.

This laser is operated at pump powers between 1.8 and 5.5 W. Figure 3-3 shows output power as a function of pump power with a rather low slope efficiency of 13.6%. The low efficiency is due to the short gain crystal, whose length is limited by the constraint to achieve a negative net GDD. However, if the absorbed pump power is considered, the slope efficiency rises to 25.8%.

Figure 3-4(a) shows a measured autocorrelation trace of the laser output when operating at 5.5 W pump power after compensation of extracavity dispersion by multiple reflections off a pair of chirped mirrors. The envelope of a 24 fs long pulse, assuming a $\mathrm{sech}^2(t)$ intensity profile, is fitted to the trace, showing good agreement. Figure 3-4(b) shows the corresponding output spectrum with a FWHM of 32 nm. The time-bandwidth product of 0.35 deviates slightly from the ideal of 0.315. The inset of Figure 3-4(a) shows the pulse duration of the same laser operated at different intracavity pulse energies. (Variation of the pulse energy was attained by changing the pump power.) The theoretical pulse durations as a function of pulse energy, as in Equation (2), are also plotted in the inset and agree well with the experiment. (w_0 was calculated using ABCD matrices to generate the theoretical curve.) The agreement between theory and experiment confirms that SPM and GDD dominantly shape the pulses in this laser; thus, pulse width and bandwidth can be easily and well controlled.

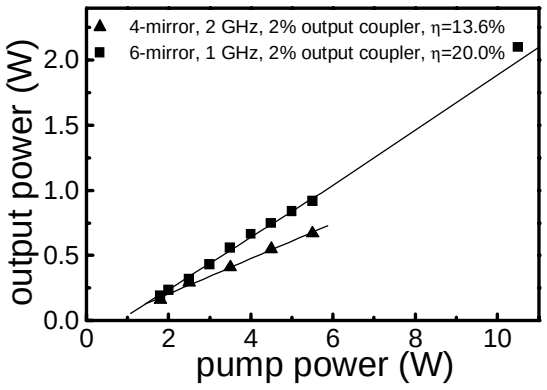

Figure 3-3. Laser output power as a function of incident pump power for the four-mirror (triangles) and six-mirror (squares) lasers described in the text. The solid lines are linear fits to the datasets.

Attempts to further shorten the pulse duration were undertaken by reducing $|D_2|$. We found a limit at 14 fs (at a spectral bandwidth of 70 nm FWHM) due to higher-order terms in the intracavity dispersion.

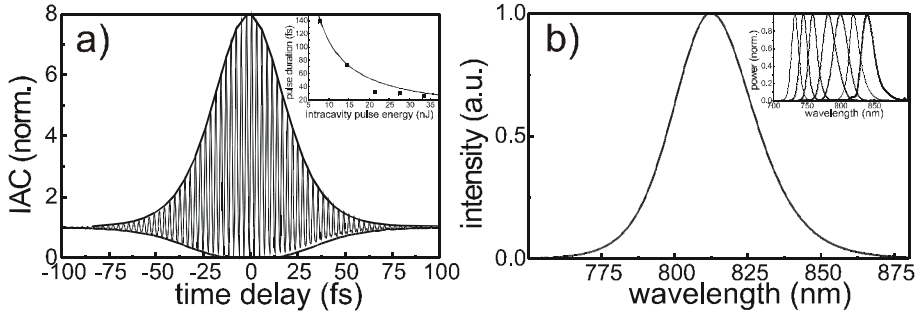

Figure 3-4. (a) Interferometric autocorrelation trace of the pulses from the four-mirror laser at 5.5 W pump power. Inset: Pulse duration as a function of intracavity pulse energy (squares) and theoretical values according to Equation (2). (b) Corresponding output spectrum. Inset: Series of output spectra of a continuously tunable version of the six-mirror cavity [16].

Often neglected in scientific papers, but important for real-world applications, is the beam quality of a femtosecond laser. Figure 3-5(a) shows a beam profile of the four-mirror cavity recorded at the focus after focusing the laser output with a lens of 200 mm focal length. It shows no noticeable deviation from circular symmetry. Figure 3-5(b) shows a cross section

through the beam profile with a fitted Gaussian, again with no noticeable deviation from ideal. A measurement of the M^2-factor has been performed, yielding values of 1.1 for both tangential and saggital planes. (See Reference [17] for a definition of M^2.) The excellent beam quality is attributed to the fact that spatially dispersive elements are absent in the cavity.

With the four-mirror cavity, repetition rates between 1 GHz and 3.5 GHz were attained. The upper limit was set by geometrical constraints, i.e., it has not been possible to move the components closer together. It is anticipated that even higher repetition rates of up to 10 GHz are feasible by minimizing mechanical components and further reducing the focal lengths of M1 and M2. The disadvantage of this cavity is that the short-gain crystal results in a relatively low output power.

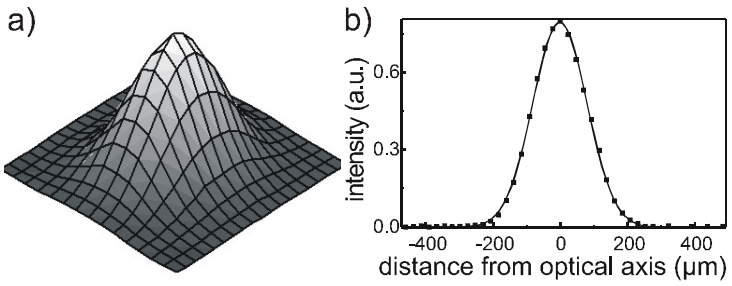

Figure 3-5. (a) Mode profile of a four-mirror laser at the focus of a 200 mm lens. (b) Cross section (squares) through the profile shown in (a) and fit with a Gaussian (solid line).

Folding with two additional negative dispersion mirrors in the cavity as in the six-mirror configuration shown in Figure 3-2(b) allows one to use a longer Ti:sapphire crystal, achieve more gain, and, at the same time, ensure a negative net GDD in the cavity. This approach is favored when higher output powers and moderate repetition rates are required. The oscillator depicted in Figure 3-2(b) has a crystal of length d = 2.5 mm and an absorption α = 5 cm^{-1}. It employs the same chirped mirrors that were used for the four-mirror cavity in positions of M1–M5 and has a repetition rate of 1 GHz. The net cavity GDD in this case is -80 fs^2. With a 2% output coupler, the output power as a function of incident pump power is shown in Figure 3-3. The slope efficiency is 20%; with respect to the absorbed pump power, it is 28%, comparable to that of the four-mirror laser. At the highest available pump power of 10.5 W, a remarkably high output power of 2.1 W is attained.

With respect to output spectra, pulse duration, and beam quality, the six-mirror cavity performs equivalently to the four-mirror cavity. It has been realized at repetition rates between 300 MHz and 2 GHz.

The two oscillators described in this section are widely used frequency comb generators for optical frequency metrology. They are commonly operated between 0.8 GHz and 1 GHz. This range has proven to be the best compromise between high-repetition rate and sufficient pulse energy to generate an octave-spanning spectrum in common microstructure fibers. (See e.g., Reference [18] for a typical octave-spanning spectrum from a 1 GHz four-mirror laser and a microstructure fiber.)

The six-mirror cavity has also been realized in a wavelength-tunable modification at a repetition rate of 1 GHz [16]. A half-Brewster prism was used to introduce spatial dispersion into the resonator with the effect that horizontally tilting a cavity mirror allowed continuous tunability from 733 to 850 nm with pulse durations of ≈40 fs. A series of output spectra is shown in the inset of Figure 3-4(b).

2.3 Cr:forsterite oscillator at 433 MHz — extension to telecommunication wavelengths

It is a logical step to extend the concept that has successfully been used with Ti:sapphire to gain media that operate at longer wavelengths. One reason is to obtain access to the telecommunication bands and thus be able to calibrate and characterize system components, such as wavelength references or wavelength-division multiplexing filters, in that region. A second goal is to generate a mode-locked spectrum that is adjacent to and that can be phase coherently combined with the output spectrum of a Ti:sapphire laser (specifically the one described in the next section) to generate an extraordinarily broad "superfrequency comb." The gain material that is best suited for both tasks is Cr:forsterite, which has a gain spectrum extending from wavelengths of ≈1150 to 1350 nm.

A femtosecond laser with Cr:forsterite was realized at a repetition rate of 433 MHz in the six-mirror configuration [see Figure 3-2(b)] [19]. The 10 mm gain crystal with an absorption coefficient of α=1.1 cm^{-1} at 1075 nm is significantly longer than in the Ti:sapphire lasers to allow for sufficient pump light absorption. The crystal is pumped with 10 W from an Yb:glass fiber laser emitting at 1075 nm through a lens with f_L = 40 mm. The crystal is cooled to 0° C to increase the gain and to reduce problems with thermal lensing. (Cr:forsterite has a thermal conductivity ≈5 times lower than Ti:sapphire.) The focal lengths of mirrors M1 and M2 are 25 mm; they are longer than what has been used for the Ti:sapphire lasers to better match the confocal length of the cavity mode to the length of the gain crystal. With chirped mirrors at positions M1–M3, a GTI mirror at M4, a low-dispersive high reflector at M5, and the GDD of the gain crystal of 185 fs^2 [20], the net GDD is ≈ -260 fs^2. A 1.5% transmission output coupler at 1280 nm is used.

The mode-locked output power of this laser is 620 mW. A spectrum of the output pulses is shown in Figure 3-6. The spectral bandwidth is 59 nm centered around 1280 nm. The pulse duration of 30 fs was determined with an intensity autocorrelation measurement.

Alignment of this laser for stable mode locking is more difficult than for Ti:sapphire lasers. Ti:sapphire lasers consistently mode lock at the inner edge of the cavity's stability range, as expected from modeling KLM. This systematic guideline for finding mode-locked operation does not work in Cr:forsterite because of thermal lensing. However, once a working point has been found, the laser's operation is reliable and reproducible. Mode-locked operation has been observed uninterrupted for up to seven days.

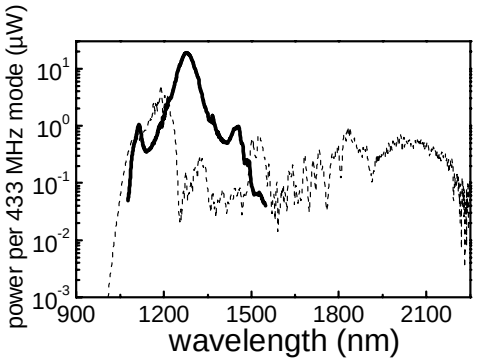

Figure 3-6. Output spectrum of the Cr:forsterite laser (solid line) and spectrum after broadening in a highly nonlinear Ge-doped silica fiber (HNLF) (dashed line).

The output from this laser was successfully broadened via SPM in highly nonlinear Ge-doped silica fiber (HNLF) to form a frequency comb that spans more than one octave [19, 21], as shown in Figure 3-6. This frequency comb has been referenced to the National Institute of Standards and Technology's (NIST's) Ca optical frequency standard and a cesium atomic clock. Its utility for optical frequency measurements was demonstrated by Corwin et al. [22] who used the broadened Cr:forsterite comb for the characterization of telecommunication-band frequency standards.

The creation of a phase-coherent superfrequency comb, ranging from wavelengths of 570 to 1450 nm, was demonstrated by actively linking the output of the Cr:forsterite laser, described above, and a broadband Ti:sapphire laser described in the next section [23].

3. BROADBAND TI:SAPPHIRE OSCILLATOR

A new type of extremely broadband femtosecond laser has been realized with a slight modification of the four-mirror cavity described earlier [see Figure 3-2(a)]. The modified cavity has a convex mirror with a radius of curvature of 1 m at the position of M3. M1, M2, and M3 are chirped mirrors. The output coupler has a transmission of 2% at 800 nm. The net intracavity dispersion of the resonator, including air and the Ti:sapphire crystal (d = 2.0 mm), and the mirror reflectivities are shown in Figure 3-7. The net GDD at 800 nm is ≈ -20 fs^2. When the cavity is operated close to the inner edge of its stability range, continuous translation of mirror M2 towards M1 results in bidirectional mode locking and stages of stable and chaotic multipulsing in two directions and in one direction until a state with a single stable pulse circulating unidirectionally in the cavity is reached. At a pump power of 10.5 W, the mode-locked output power is ≈1 W. The cavity length is adjusted to yield a 1 GHz repetition rate.

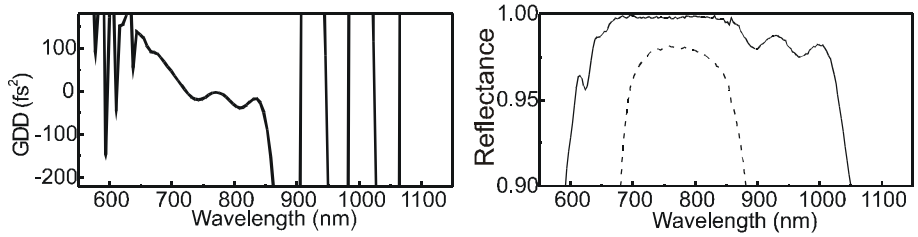

Figure 3-7. Left panel: Net cavity group-delay dispersion (GDD) of the broadband laser. Right panel: Reflectance of the chirped mirrors (solid line) and the output coupler (dashed line).

The output spectrum of the laser is shown in Figure 3-8. It spans from 570 to 1100 nm at a power level of 1 nW per 1 GHz frequency mode. (1 nW per mode is the power typically required to measure a beat note against a milliwatt-scale cw laser with sufficient signal-to-noise ratio for a frequency measurement.) The spectrum has pronounced maxima at 670 nm, 845 nm, 900 nm, and 927 nm. The peak around 670 nm can be isolated by a double reflection off a pair of 657 nm high reflectors, leading to the spectrum shown in the inset of Figure 3-8(b). It contains 450 mW of average power.

The duration of the output pulses has only been roughly characterized by using an intensity autocorrelation measurement. Assuming a temporal $sech^2$ shape, it is 11 fs when the nonlinear crystal is angle-tuned to optimally phase match the central part of the spectrum. The peak around 670 nm yields bandwidth-limited pulses of 33 fs after isolation from the longer-wavelength part of the spectrum.

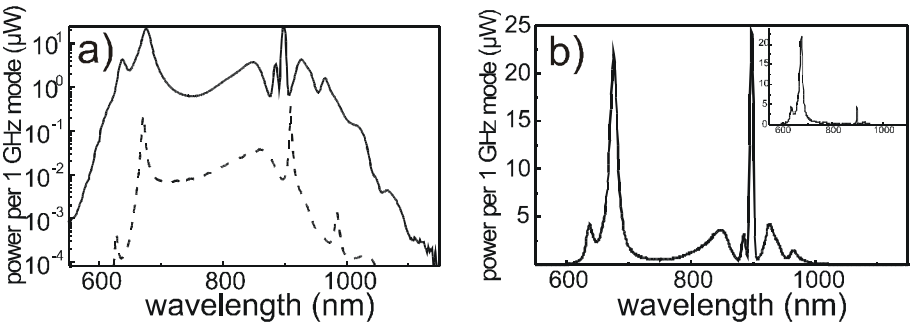

Figure 3-8. (a) Output spectrum of the broadband laser on a logarithmic scale (solid line). At a level of 1 nW per 1 GHz mode, it extends from 570 to 1100 nm. The dashed line shows a simulated spectrum, offset by 20 dB for clarity. (b) Output spectrum of the broadband laser on a linear scale. Inset: spectrum after reflection off a pair of 657 nm high reflectors.

3.1 How does it work?

The performance of this laser is extraordinary in a number of respects: First, when mode locking is stopped (e.g., by briefly intersecting the pump beam) and the laser falls back into cw operation, the output power drops by more than an order of magnitude to about 60 mW. Assuming that a Kerr-lens-based effective saturable absorber is responsible for this behavior, a simple rate equation model leads to the conclusion that ≈30% saturable absorption is required to explain this drop. This high saturable absorption contrasts with what is usually observed for standard Ti:sapphire femtosecond lasers, which have an effective saturable absorption of ≈1–2%. Second, considering the fact that Ti:sapphire has no gain below 690 nm, the 450 mW of power contained in the peak around 670 nm is very remarkable and indicates that this strong component is generated during only a few round trips through the cavity. Finally, assuming that SPM and GDD dominate pulse shaping, mode locking of the laser at such extreme bandwidth should not be possible. The strong GDD modulation and the positive values outside a band ranging from 700 to 850 nm should quickly spread the pulse and prevent mode locking (see Figure 3-7 for the net intracavity dispersion).

To get an idea of how this laser functions, it is helpful to review the two practical routes towards shorter pulses and broader spectra in a femtosecond laser. One approach is to engineer the dispersion inside the resonator in a way that short pulses with extremely broad spectra do not spread in time during a cavity round trip. This involves careful design of mirrors to have negative GDD over the desired large bandwidth and compensate for the positive-gain crystal dispersion with a low net-higher-order dispersion. This

approach has been taken with great success by Ell et al. [24]. Their carefully engineered intracavity dispersion is capable of generating spectra exceeding one octave with 5 fs pulses at a repetition rate of 64 MHz. In our case, however, because of the narrow bandwidth of the chirped mirrors, both with respect to their dispersive and reflective properties, this limit is inapplicable. Alternatively, one can allow higher-order dispersion in the resonator but, at the same time, ensure that the leading and trailing edges of the temporally spreading spectrum are sufficiently suppressed, such that only a short pulse remains stable in the cavity. This effect can be attained by employing an effective fast saturable absorber. In the case of our Ti:sapphire lasers, this effective saturable absorber is provided by a soft aperture KLM (see Section 2.1). While this effect is actually a self-gain modulation, it can theoretically be treated as an equivalent fast saturable absorber. These effects are more generally referred to as self-amplitude modulation (SAM).

There are strong indications that the broadband laser described above operates in the limit of an increased SAM. The strongest support for this idea is the experimental observation that the mode-locked output power and the continuous output power of the laser differ by more than an order of magnitude. This difference indicates that the Kerr-lens-induced effective saturable absorber has a saturable absorption of approximately 30%. Theoretical calculations of the change in beam waist diameter inside the gain medium (i.e., the soft-aperture Kerr-lens effect) show that replacing flat mirror M3 with a slightly convex mirror (in our case with a radius of curvature of 1 m) can increase the SAM of pulses circulating in the ring cavity [25]. While the theory applied to calculate this effect is valid only at power levels of about a factor of four below the power at which our oscillator operates, it still has provided a clue to understanding this new type of femtosecond oscillator.

A full theory explaining why the convex mirror leads to a stronger effective saturable absorber does not yet exist. However, modeling the resonator with a split-step Fourier simulation allows us to understand why this laser functions. The model includes the Ti:sapphire gain spectrum and dispersion, all reflective amplitude and phase properties of the cavity mirrors, SPM, and a fast saturable absorber (of the same type as used by Chen et al. [26]). The dashed curve in Figure 3-9 shows a simulation of a cavity with the same mirrors as the broadband laser cavity but with a shorter crystal (d = 1.5 mm) and a saturable absorption of $q_{sat.}$ = 2%. Its net GDD at 800 nm is -45 fs^2. It represents a standard laser with a relatively narrow spectrum of 45 nm bandwidth. An attempt to get shorter pulses from this laser by increasing the net cavity GDD to ≈ -20 fs^2 by using a longer crystal (d = 2.0 mm) fails because the simulation does not yield a stable solution anymore. Higher-order dispersion spreads the seed pulse and randomizes its

phase. However, when $q_{sat.}$ is increased to 30% for the d = 2 mm configuration, the model again delivers a stable solution, shown as the solid line in Figure 3-9. The solution corresponds to the new broadband laser where, despite dominant higher-order dispersion, a stable mode-locked solution is obtained because of the pulse-cleaning effect of the enhanced SAM. This simulation agrees very well with the experimental spectrum in its main features, which include the pronounced peaks at ≈670 nm and ≈900 nm, the asymmetric central contribution around 835 nm, and the spectrum's approximate width [see Figure 3-8(a)].

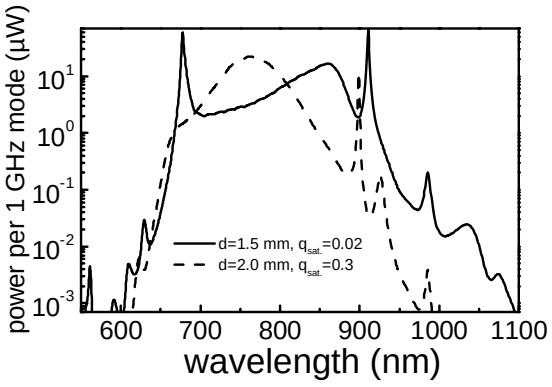

Figure 3-9. Modeled output spectra of a standard laser (d = 1.5 mm, $q_{sat.}$= 0.02) and a broadband laser (d = 2.0 mm, $q_{sat.}$ = 0.3) using a split-step Fourier simulation.

3.2 Application in frequency metrology and optical clocks

As previously explained, optical frequency metrology and optical-clock designs require measurements of both degrees of freedom of a femtosecond laser, its repetition rate f_r and its carrier envelope offset frequency f_0. This section briefly discusses how the broadband 1 GHz laser described in the last section is different from (and offers advantages over) the standard 1 GHz laser because of the way that the new laser's offset frequency is measured.

The standard ν-to-2ν-scheme for measuring f_0 is to frequency double a low-frequency portion of the laser spectrum (typically ≈1100 nm) and beat it against a spectral matching, high-frequency part of the fundamental spectrum (≈550 nm) [5]. This approach requires a spectrum covering at least one octave. For standard lasers, the only way to attain such a broad spectrum

has been SPM in microstructure fibers. However, coupling light into the core of fibers with a diameter less than 2 μm is a difficult task. As SPM is a third-order nonlinearity, slight changes in coupling efficiency can result in large changes of the attained spectrum and usually limit the time over which a measurement of f_0 can be maintained with sufficient signal-to-noise ratio. Apart from that, microstructure fibers also limit the amount of useful average power achievable for the continuum spectrum because the nonlinear broadening process inherently amplifies both technical and shot noise present on the input light. (References 10 and 27 provide an overview on noise amplification during supercontinuum generation in microstructure fibers.)

The broadband laser allows one to circumvent these problems with microstructure fiber because its broad spectral coverage allows for a direct measurement of its offset frequency. Although the output spectrum has wavelength components that are one octave apart, the power contained in them is too low to facilitate a measurement of f_0 using the standard ν-to-2ν method. Therefore, we employ a 2ν-to-3ν method: A portion around 930 nm is frequency tripled and beat against the second harmonic of a portion around 620 nm to yield a signal at f_0. Details of this setup can be found in Ramond et al. [28].

Although the 2ν-to-3ν method is more complicated than the standard method, the broadband laser has an unprecedented long-term stability as a frequency measurement tool. First, it routinely stays mode locked for periods of many days (>1 week demonstrated) without noticeable changes to its output power or spectrum. Second, the f_0 signal usually has a signal-to-noise ratio of 25–30 dB in the 300 kHz bandwidth and does not degrade over time because of the absence of microstructure fiber in the measurement apparatus.

In a test of its long-term stability, we have operated the laser in an optical clock configuration. Here, the repetition rate f_r of the broadband laser is phase locked to a cavity-stabilized single-frequency laser diode at frequency f_{LD} = 456 THz that represents the optical frequency standard that would be used in an optical clock. Specifically, a beat between the laser diode and the neighboring component of the frequency comb with frequency f_b has been phase locked to a synthesizer at 600 MHz by feedback to the femtosecond laser's cavity length via a mirror mounted onto a piezoelectric transducer. (All synthesizers were referenced to the NIST primary standard.) Additionally, f_0 was phase locked to a synthesizer at 100 MHz by feedback to the pump power via an acousto-optic modulator. It can be shown that f_r now derives its frequency and instability entirely from the laser diode or, in the case of an optical clock, from the optical frequency standard and is effectively the microwave output of the optical clock [23]. We then counted f_0, f_b and f_r simultaneously with frequency counters at 10 s gate time. The

offset of the counter readings from their preset values (f_0 = 100 MHz, f_b = 600 MHz, set by the synthesizers; f_r = 998,092,449.54 Hz, defined by f_{LD} and the choices of f_0 and f_b) over a period of 21 hours are displayed in Figure 3-10. The data set shows uninterrupted and hands-off operation of the f_0 phase lock for 21 hours with counter-resolution-limited deviations on the millihertz scale until the system was turned off. The phase lock on f_b operated similarly for ≈14 h with only one detected feedback-loop error (cycle slip) at ≈4 h, i.e., ≈10 h of continuously phase-locked data were obtained. The failure at ≈14 h was likely caused by the failure of the stabilization of f_{LD} to the Fabry-Perot cavity that prevented the feedback loop from tracking the diode laser frequency rather than failure of the femtosecond laser itself. As f_r represents a measurement of the laser diode frequency ($f_{LD} = f_0 + n_{LD} f_r + f_b$, where n_{LD} is the mode number of the frequency comb component against which f_{LD} is beat), the time record of the offset of f_r from 998,092,449.54 Hz can be multiplied with n_{LD} = 456,857 to give a record of the temporal drift of the Fabry-Perot cavity on the right axis of the graph in Figure 3-10. The cycle slip in the f_b feedback loop does not appear in the f_r record because the effect of the 120 mHz excursion in f_b results in an error of 260 nHz in f_r, which is below our measurement limit.

These results show that the broadband laser facilitates a phase-coherent, cycle-slip-free link between an optical oscillator at 456 THz and the 1 GHz laser repetition rate for 10 h. In other words, we have the ability to count 1.6×10^{19} optical cycles at 456 THz without ever losing track of the oscillation. It has also been shown that f_r and f_0 of the broadband laser can be continuously phase locked to a synthesizer for more than 48 hours.

4. CONCLUSION

Ti:sapphire ring oscillators at 1 GHz repetition rate are currently the best available frequency comb generators for optical frequency metrology. They are compact, have a conveniently large comb spacing, and yield 100 times more power per mode than conventional 100 MHz lasers. Their simple ring-laser architecture employing negative dispersion mirrors for GDD control allows repetition rates between 300 MHz and 3.5 GHz with Ti:sapphire. The concept is extendable to other gain media, as has been demonstrated with Cr:forsterite at 433 MHz repetition rate.

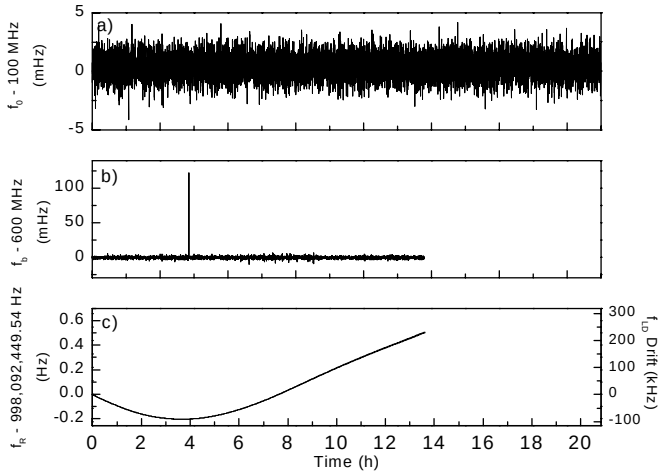

Figure 3-10. (a) A record of consecutive counter readings at 10 s gate time for the phase-locked f_0. The preset value of 100 MHz has been subtracted. (b) The simultaneously measured offset of f_b from 600 MHz. In this plot, one cycle slip of the phase-locked loop controlling f_b has occurred. (c) A time record of the offset of the laser repetition rate from 998,092,449.54 Hz (left scale) that can be translated into a drift of f_{LD} (right scale).

The most critical development has been the 1 GHz broadband Ti:sapphire laser that eliminates troublesome microstructure fibers from optical-frequency-measurement setups. This laser has enabled the construction of an optical clockwork with an unprecedented continuous operation time in excess of 48 hours. This laser might also become interesting in basic research as a source of femtosecond pulses in the range from 620 to 690 nm.

ACKNOWLEDGEMENTS

T. Dekorsy and H. Kurz (Institute of Semiconductor Electronics, RWTH Aachen) made invaluable contributions to the first stages of this work that are highly appreciated. I also thank Christof Janke (GigaOptics GmbH), Isabell Thomann, Tanya Ramond, Scott Diddams, Leo Hollberg, Brian Washburn, Nathan Newbury and Kristan Corwin (NIST) for their important contributions. Jeff Nicholson provided the fiber used for the data presented in Figure 3-6.

REFERENCES

[1] D. E. Spence, P. N. Kean, and W. Sibbett, Opt. Lett. **16**, 42-44 (1991).

[2] M. Ramaswamypaye and J. G. Fujimoto, Opt. Lett. **19**, 1756-1758 (1994).

[3] A. Stingl, C. Spielmann, R. Szipocs, and F. Krausz, in *Conference on Lasers and Electrooptics* (Opt. Soc. Am., 1996), p. 66

[4] T. Udem, J. Reichert, R. Holzwarth, and T. W. Hänsch, Phys. Rev. Lett. **82**, 3568-3571 (1999).

[5] D. J. Jones, S. A. Diddams, J. K. Ranka, A. Stentz, R. S. Windeler, J. L. Hall, and S. T. Cundiff, Science **288**, 635-639 (2000).

[6] S. A. Diddams, D. J. Jones, J. Ye, S. T. Cundiff, J. L. Hall, J. K. Ranka, R. S. Windeler, R. Holzwarth, T. Udem, and T. W. Hänsch, Phys. Rev. Lett. **84**, 5102-5105 (2000); M. Niering, R. Holzwarth, J. Reichert, P. Pokasov, T. Udem, M. Weitz, T. W. Hänsch, P. Lemonde, G. Santarelli, M. Abgrall, P. Laurent, C. Salomon, and A. Clairon, Phys. Rev. Lett. **84**, 5496-5499 (2000); S. A. Diddams, T. Udem, J. C. Bergquist, E. A. Curtis, R. E. Drullinger, L. Hollberg, W. M. Itano, W. D. Lee, C. W. Oates, K. R. Vogel, and D. J. Wineland, Science **293**, 825-828 (2001); J. Stenger, T. Binnewies, G. Wilpers, F. Riehle, H. R. Telle, J. K. Ranka, R. S. Windeler, and A. J. Stentz, Phys. Rev. A **63**, 021802 (2001); T. Udem, S. A. Diddams, K. R. Vogel, C. W. Oates, E. A. Curtis, W. D. Lee, W. M. Itano, R. E. Drullinger, J. C. Bergquist, and L. Hollberg, Phys. Rev. Lett. **86**, 4996-4999 (2001); G. D. Rovera, F. Ducos, J. J. Zondy, O. Acef, J. P. Wallerand, J. C. Knight, and P. S. Russell, Meas. Sci. Techn. **13**, 918-922 (2002).

[7] J. Reichert, R. Holzwarth, T. Udem, and T. W. Hänsch, Opt. Commun. **172**, 59-68 (1999).

[8] J. K. Ranka, R. S. Windeler, and A. J. Stentz, Opt. Lett. **25**, 25-27 (2000); J. C. Knight, T. A. Birks, P. S. Russell, and D. M. Atkin, Optics Letters **21**, 1547-1549 (1996).

[9] L. Hollberg, C. W. Oates, E. A. Curtis, E. N. Ivanov, S. A. Diddams, T. Udem, H. G. Robinson, J. C. Bergquist, R. J. Rafac, W. M. Itano, R. E. Drullinger, and D. J. Wineland, IEEE J. Quantum Electron. **37**, 1502-1513 (2001).

[10] K. L. Corwin, N. R. Newbury, J. M. Dudley, S. Coen, S. A. Diddams, K. Weber, and R. S. Windeler, Phys. Rev. Lett. **90**, 113904 (2003).

[11] T. Brabec, C. Spielmann, and F. Krausz, Opt. Lett. **17**, 748-750 (1992).

[12] R. L. Fork, O. E. Martinez, and J. P. Gordon, Opt. Lett. **9**, 150-152 (1984).

[13] F. Gires and C. R. Tournois, Science **258**, 6112 (1964); R. Szipocs, K. Ferencz, C. Spielmann, and F. Krausz, Opt. Lett. **19**, 201-203 (1994).

[14] A. Bartels, T. Dekorsy, and H. Kurz, Opt. Lett. **24**, 996-998 (1999).

[15] H. W. Kogelnik, C. V. Shank, A. Dienes, and E. P. Ippen, IEEE J. Quantum Electron. **8**, 373 (1972).

[16] A. Bartels, T. Dekorsy, and H. Kurz, in *Conference on Lasers and Electro-Optics* (OSA Technical Digest, 2000), p. CMF3

[17] A. E. Siegman, *Lasers* (University Science Books, Mill Valley, California, 1986).
[18] S. A. Diddams, T. Udem, K. R. Vogel, C. W. Oates, E. A. Curtis, R. S. Windeler, A. Bartels, J. C. Bergquist, and L. Hollberg, in *Laser Frequency Stabilization: Standards, Measurement and Applications*, edited by J. L. Hall and J. Ye (SPIE, San Jose, 2001), Vol. SPIE 4269, p. 77-83.
[19] I. Thomann, A. Bartels, K. L. Corwin, N. R. Newbury, L. Hollberg, S. A. Diddams, J. W. Nicholson, and M. F. Yan, Opt. Lett. **28**, 1368-1370 (2003).
[20] I. Thomann, L. Hollberg, S. A. Diddams, and R. Equall, Appl. Optics **42**, 1661-1666 (2003).
[21] J. W. Nicholson, M. F. Yan, P. Wisk, J. Fleming, F. DiMarcello, E. Monberg, A. Yablon, C. Jorgensen, and T. Veng, Opt. Lett. **28**, 643-645 (2003).
[22] K. L. Corwin, I. Thomann, T. Dennis, R. W. Fox, W. Swann, E. A. Curtis, C. W. Oates, G. Wilpers, A. Bartels, S. L. Gilbert, L. Hollberg, N. R. Newbury, S. A. Diddams, J. W. Nicholson, and M. F. Yan, Opt. Lett. **29**, 397-399 (2004).
[23] A. Bartels, N. R. Newbury, I. Thomann, L. Hollberg, and S. A. Diddams, Opt. Lett. **29**, 403-405 (2004).
[24] R. Ell, U. Morgner, F. X. Kärtner, J. G. Fujimoto, E. P. Ippen, V. Scheuer, G. Angelow, T. Tschudi, M. J. Lederer, A. Boiko, and B. Luther-Davies, Opt. Lett. **26**, 373-375 (2001).
[25] A. Bartels and H. Kurz, Opt. Lett. **27**, 1839-1841 (2002).
[26] Y. Chen and H. A. Haus, J. Opt. Soc. Am. B **16**, 24-30 (1999).
[27] N. R. Newbury, B. R. Washburn, K. L. Corwin, and R. S. Windeler, Opt. Lett. **28**, 944-946 (2003).
[28] T. M. Ramond, S. A. Diddams, L. Hollberg, and A. Bartels, Opt. Lett. **27**, 1842-1844 (2002).

Chapter 4

MICROSTRUCTURE FIBER AND WHITE-LIGHT GENERATION

Alexander L. Gaeta[1] and Robert S. Windeler[2]
[1] *School of Applied and Engineering Physics, Cornell University*

[2] *OFS Laboratories*

Abstract: Microstructure fibers have played a key role in the production of coherent frequency combs that span more than an octave of bandwidth. In this chapter, we review the fabrication process for such fibers and their linear and nonlinear optical properties. We also discuss the underlying physical processes that give rise to supercontinuum generation.

Key words: microstructure fiber, supercontinuum generation, ultrashort pulse propagation, fiber dispersion

1. INTRODUCTION

The unlikely merger of ultrafast optics, microstructure fibers, and nonlinear optics with frequency stabilization techniques has led to a revolution in frequency metrology. Development over the past decade of ultrafast solid-state laser systems, such as Ti:sapphire, has resulted in laser oscillators that can produce sub-100 fs, nanojoule-energy mode-locked pulses in the near infrared (IR). In parallel, novel single component fibers with cross sections consisting of regularly spaced air holes were created [1] that for large air holes allowed the creation of waveguides that strongly confine the light field to a small area and shift the zero dispersion point of the fiber close to the operating wavelength of the Ti:sapphire oscillators. The combination of the high peak intensities due to strong light confinement and the large effective interaction lengths in the fibers results in a highly intense, nonlinear interaction that can generate a remarkably broad-bandwidth spectrum spanning more than an octave of the central laser frequency [2].

This coherent white-light spectrum is precisely what is needed to stabilize the underlying frequency comb of the mode-locked laser oscillator. It has also led to other applications such as optical coherence tomography [3].

In this chapter, we review the basic properties of microstructure fibers, how they are fabricated, and the underlying physics of supercontinuum generation using ultrashort laser pulses in these fibers.

2. MICROSTRUCTURE FIBER FABRICATION

Microstructure fibers have unique properties and can deliver functionalities superior to many of the best transmission and specialty fibers. Their unique properties are obtained from an intricate cross section of high- and low-index regions that traverse the length of the fiber. The vast majority of these fibers consist of silica for the high-index region and air for the low-index region. These fibers are known by several different names including microstructure fiber, holey fiber, and photonic crystal fiber.

The index profiles that make these fibers unique can also lead to inherently high loss. Loss occurs at connections launching light in and out of the fiber and along the length of the fiber. Light is launched into these fibers by free-space optics, low-temperature fusion splicing, or butt coupling. For microstructure fibers with small cores, coupling with free-space optics produces the smallest insertion loss. Loss due to significant mode mismatch occurs when splicing or butt coupling standard fibers to small-core microstructure fibers. Attenuation along the fiber length can occur because of impurities, hole surface roughness, or poor confinement but is presently low enough that it is not important for most device applications.

Like traditional fibers, microstructure fibers are fabricated in a two-step process. First, a large-scale template of the fiber, called a preform, is fabricated. Second, the preform is drawn (stretched) into a fiber, typically kilometers in length. However, new preform fabrication and draw techniques had to be developed to incorporate air holes in the preform and have them remain through draw.

2.1 Preform fabrication

Preforms are long cylinders, typically less than a few centimeters in diameter, that closely match the structure of the desired fiber. Their large scale, compared to fiber, makes them easy to handle when assembling the desired microstructure pattern. They are typically composed of silica with air holes running uniformly along their length. Other amorphous materials are

also being explored such as polymers and highly nonlinear multicomponent glasses.

The basic parameters of the fiber are hole size, hole position, pitch (center-to-center hole spacing), core diameter, and number of layers. They are usually determined by the geometry of the holes in the preform. However, changes in the size and shape of the fiber's holes can be made purposely or accidentally during draw, causing deviations between the fiber and preform profiles.

The most common method used to fabricate microstructure fibers is to stack tubes, rods, and core rods (rods containing doped cores) in a closely packed arrangement such as a triangular or hexagonal lattice (Figure 4-1). This assembly is bound together by a large tube, called an overclad tube. Fibers can be made with complicated or asymmetric index profiles by strategically placing tubes with the same outer diameter (for good stacking) but with different inner diameters to change the index profile in that region. For example, a birefringent fiber can be produced by placing smaller holes on opposite sides of the core.

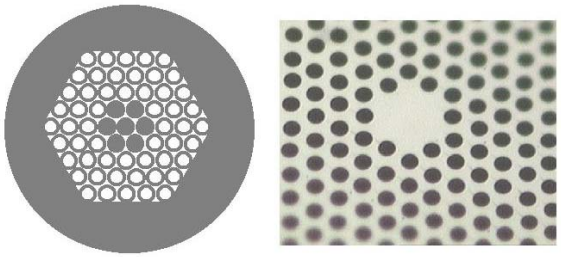

Figure 4-1. Left: Drawing of a preform fashioned from a close-pack arrangement of tubes and rods. Right: A scanning-electron-microscope (SEM) micrograph showing the fiber after the preform is drawn.

The main advantages of stacking are that no special equipment is needed for fabricating preforms and that doped cores can be easily added. However, there are several disadvantages: First, the stacking method is limited to simple geometries of the air holes because the tubes are stacked in a closely packed arrangement. Second, unless hexagonal tubes are used, interstitial areas are created between the tubes that may not be desired in the final fiber. Third, the method is labor intensive and requires significant glass handling, making it difficult to produce ultralow-loss fiber because of impurities.

Several alternative methods are being used to fabricate microstructure performs, including casting, extrusion, and drilling. Like stacking, each process has its advantages and disadvantages. The methods most likely to

replace or coexist with stacking are extrusion and casting. These processes have the advantage of not requiring precision tubing and are ideal for polymer, sol-gel slurry, or low melting-point glass. The main advantage of extrusion and casting is that complicated structures can be fabricated in which the position, size, and shape of the air regions are independent of one another. These methods may become more common as complex air structures are needed to make advanced microstructure fibers.

Another method consists of drilling holes in a traditional preform or rod. Drilling is well understood and is used for other specialty fibers. The advantage of this method is that it is easy to put variously sized holes in any position in a preform, including doped regions. The disadvantages are that the holes cannot be drilled very deep compared to a standard preform length; the distance between holes may be limited due to cracking; and the fiber may experience high loss due to surface roughness of the holes and impurities incorporated during drilling.

2.2 Fiber draw

Draw is the most difficult part of making a microstructure fiber. There are typically many holes in the preform that all have a propensity to shrink to decrease the surface tension of the preform. There are two techniques that can be use to minimize or stop hole collapse. The first is to draw the preform under very high tension by operating the draw furnace at a low temperature. Minimal hole collapse will occur if the draw tension is significantly larger than the surface tension. However, this method also results in a substantial increase in the number of breaks during draw. This is not important if only small lengths are needed, but it is not practical as a production method.

The second method is to pressurize the holes with an external source to counteract the surface tension. The holes can be made larger or smaller during draw by changing the pressure. However, the process can become unstable because a large hole needs a lower pressure to maintain its size than a small hole. If holes of different sizes exist, a larger hole will grow at the expense of a smaller one regardless of the pressure used. To minimize the instability, this method is typically performed in conjunction with relatively high-tension drawing.

3. MICROSTRUCTURE FIBER TYPES

The different types of microstructure fiber are achieved by varying the size, spacing, and pattern of the air holes within the fiber. Most microstructure fiber types guide light by total internal reflection. Large air

holes in the fiber create substantial refractive-index differences that result in large numerical apertures and optically isolated regions within the fiber. Fibers with large holes surrounding a small core create ideal nonlinear fibers at short wavelengths [Figure 4-2(a)]. As discussed in Section 5.2, these fibers can be designed to have zero-group-velocity dispersion in the near-visible regime, and their small core can result in very high intensities over extended interaction lengths.

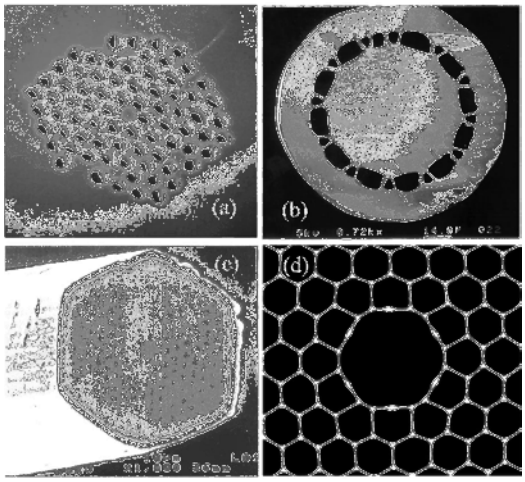

Figure 4-2. SEM photographs of several types of microstructure fiber. (a) High-nonlinearity fiber. (b) Air-clad fiber. (c) Endlessly single-mode fiber [4]. (d) Band-gap fiber [6].

Air-clad fibers consist of large air holes closely packed around an inner cladding containing a doped core [Figure 4-2(b)]. These fibers have inner claddings with very high numerical apertures and are ideal for generating efficient, high-power cladding pump amplifiers and lasers.

At the other extreme, fibers with small air holes have been designed [4] such that the cladding index changes with wavelength to create fibers that are endlessly single moded [Figure 4-2(c)]. These fibers can have very large core diameters and therefore can propagate high powers at low intensities.

Fibers with precise, periodically spaced index regions in the cladding can create band-gap guidance, allowing light to be guided in a core with an index lower than the cladding [Figure 4-2(d)]. Guidance in an air core has been demonstrated [5] and has the potential to have an attenuation over an order of magnitude lower than the best traditional transmission fiber [6].

4. LINEAR OPTICAL PROPERTIES OF MICROSTRUCTURE FIBER

The success of using small-core microstructure fibers with large core-cladding index contrast to produce frequency combs that extend for more than an octave at optical frequencies can be attributed to two properties that occur simultaneously when the core diameter is made small: (1) strong waveguide confinement that enhances the effective nonlinearity of the fiber, and (2) the shift of the zero-group-velocity dispersion point to a wavelength that coincides with that of Ti:sapphire femtosecond laser oscillators.

Microstructure fibers can be modeled reasonably well as a step-index fiber with a glass core and a surrounding cladding region with an effective refractive index governed by the air-filling fraction of the glass lattice. As such, the mechanism that effectively guides light in these fibers is total internal reflection. However, unlike conventional fibers where the contrast of the refractive indices of the core and cladding is small, the index contrast for microstructure fibers can vary over a much larger range and can be effectively as large as that for a glass rod in air. Many of the optical properties can be well approximated by the effective index model in which the effective index n_{eff} of refraction of the cladding region is given by

$$n_{eff}^2 = f + (1 - f) n_{glass}^2 , \tag{1}$$

where f is the air-filling fraction of the cladding region and n_{glass} is the index of the glass that comprises the structure. The solutions for the modes and the dispersion using this simple step-index model can be obtained analytically, and the dispersion for the fundamental mode agrees very well with the predictions of the full-vector model [7]. It is apparent by calculating the effective V-number [8] that even for small cores and reasonably large air-filling fractions ($f > 0.5$), the fiber is multimode (i.e., $V > 2.405$). Nevertheless, since the difference in the propagation constant between the fundamental mode and the higher-order modes is large, a strong perturbation is required to couple energy from the fundamental mode to the higher-order modes. Thus if the fundamental mode is initially excited, the energy does not easily couple to the higher-order modes [9]. In addition, the large index contrast also leads to a strong confinement of the fundamental mode with little energy lying outside the core. This results in a large effective nonlinearity that allows for strong nonlinear interactions with relatively modest pulse energies such as those from a femtosecond Ti:sapphire oscillator.

A key property for determining the propagation of ultrashort pulses in the fiber and for generation of a broad-band frequency comb is the group-velocity dispersion (GVD) $\beta_2 = d^2k/d\omega^2$ of the propagating mode, where $k(\omega) = n_{eff}(\omega)\ \omega/c$ is the wave number for the fundamental mode. The two sources of dispersion in the fiber are material dispersion and waveguide dispersion. For bulk fused-silica glass, the wavelength at which the GVD is zero is $\lambda = 1.27$ μm. In conventional step-index fibers with small index contrast, material dispersion dominates and is only slightly modified by the waveguide contribution. However, in small-core microstructure fibers with a large air-filling fraction, the waveguide dispersion dominates over most of the visible and near-IR regimes. Figure 4-3(a) is a plot using the simple step-index model of the predicted GVD parameter $D = (-2\pi c/\lambda^2)\beta_2$ for an air-filling fraction of unity for various values of the core diameter. For $D > 0$ (<0) the GVD is termed anomalous (normal). For comparison, the dispersion for bulk-fused-silica glass is also shown. As the core diameter is reduced, the zero-GVD point shifts to shorter wavelengths and the maximal value of the anomalous dispersion increases. For sufficiently small cores, the zero-GVD point can be shifted completely into the visible regime, allowing for the generation of solitons in the near IR [9] and potentially the visible regime. For a 2 μm diameter core, the zero-GVD point is close to the central operating wavelength of femtosecond Ti:sapphire laser oscillators. Figure 4-3(b) shows the dispersion for a fiber with a 2 μm core for various values of the cladding's air-filling fraction f. The primary effect of decreasing f is to decrease the maximal anomalous dispersion and change the slope of the GVD (i.e., the third-order dispersion) at the zero-GVD point. The shift in the zero-GVD wavelength is relatively small. Thus, a "rule of thumb" in designing these high air-filling fraction fibers for a particular application is that the location of the zero-GVD point is controlled by the size of the core and the third-order dispersion at this point is controlled by the air-filling fraction. Such a picture has been verified by experiments that have characterized the dispersion properties of the fibers with a range of core sizes [10] and provides insight for the creation of microstructure fibers with a relatively flat GVD over a large wavelength span.

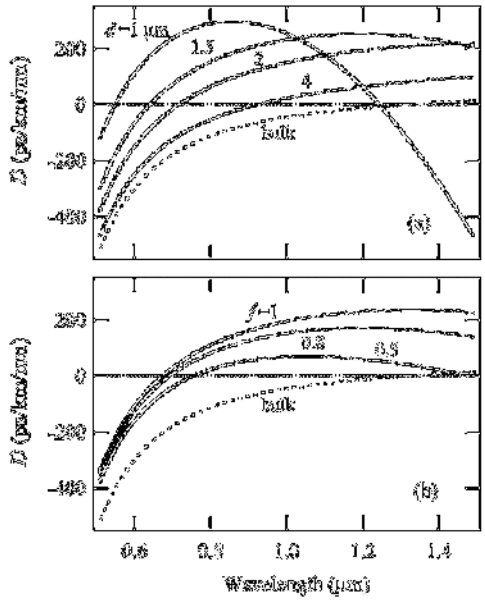

Figure 4-3. Plots of the group-velocity-dispersion parameter D for (a) various values of the diameters d and an air-filling fraction $f = 1$ and (b) various values of f for a core diameter $d = 1.7$. The dashed line represents the dispersion curve for bulk-fused-silica glass.

5. SUPERCONTINUUM GENERATION

5.1 Nonlinear envelope equation

For subpicosecond optical pulses propagating in optical fibers, the dominant optical nonlinearity is the intensity-dependent refractive index. This nonlinear-index change leads to self-phase modulation that results in a time-dependent phase that spectrally broadens the laser pulse. The addition of new frequency components significantly outside the bandwidth of the pulse can also occur via four-wave mixing. The efficiency of these nonlinear processes can be greatly altered by the linear dispersion of the fiber since it leads to a temporal broadening of the pulse and a corresponding decrease in the peak intensity. As a result of these nonlinear interactions, the spectral bandwidth of a pulse propagating within the fiber can increase substantially and, most importantly for frequency comb applications, become greater than the center input frequency ω_0 of the incident pulse. The broad spectral radiation that is produced under such conditions is termed supercontinuum generation, or white-light generation. A theoretical description of

propagation under these conditions becomes difficult since the concepts of a pulse-amplitude envelope and a carrier frequency break down. Nevertheless, much of the underlying physics describing supercontinuum generation can be described within the framework of the one-dimensional nonlinear envelope equation (NEE) [11] with the inclusion of the effects of stimulated Raman scattering.

In this model, the pulse is assumed to propagate along the *z*-axis with a wave vector amplitude $k_0 = n_0\omega_0/c$ where n_0 is the linear refractive index of the material at the central frequency ω_0 of the pulse. For an input pulse with a peak amplitude A_0 and a pulse duration τ_p, the equation for the normalized amplitude $u(z, t) = A(z, t)/ A_0$ can be expressed as

$$\frac{\partial u}{\partial \zeta} = -i\,\mathrm{sgn}(\beta_2)\sum_{n=2}\frac{L_{ds}}{L_{ds}^{(n)}} + i\left(1+\frac{i}{\omega_0\tau_p}\frac{\partial}{\partial\tau}\right)p_{nl}\,, \tag{2}$$

where $L_{ds} = \tau_p^2/|\beta_2|$ is the dispersion length, $\zeta = z/L_{ds}$ is the normalized propagation distance, β_2 is the group-velocity dispersion (GVD), $L_{ds}^{(n)} = \tau_p^n/\beta_n$ is the n^{th}-order dispersion length, $\tau = (t - z/v_g)/\tau_p$ is the normalized retarded time for the pulse traveling at the group velocity v_g, and p_{nl} is the normalized nonlinear polarization. Inclusion of both instantaneous (i.e., electronic) and noninstantaneous (i.e., nuclear) nonlinear refractive index changes in the nonlinear polarization yields

$$p_{nl} = \frac{L_{ds}}{L_{nl}}\left[(1-f)|u|^2 + f\int_{-\infty}^{\tau} d\tau g(\tau-\tau')|u|^2\right]u\,, \tag{3}$$

where $L_{nl} = (c/\omega_0\, n_2 I_0)$ is the nonlinear length, $I_0 = n_0 c|A_0|^2/2\pi$ is the peak input intensity, f is the fractional contribution of Raman scattering to the nonlinear refractive index, and $g(\tau)$ is the Raman-response function [12]. The presence of the operator $1+ i\partial/\omega_0\tau_p\partial\tau$ in the nonlinear polarization term accounts for self-steepening effects and allows for the modeling of the propagation of pulses with spectral widths comparable to the central frequency ω_0.

5.2 Spectral superbroadening

For a femtosecond pulse propagating in a fiber, the central wavelength of the pulse relative to the zero-GVD point strongly determines the nature of the spectral broadening and supercontinuum generation. For the case in which the bandwidth of the pulse overlaps the zero-GVD point, the

qualitative characteristics of the supercontinuum generation can be attributed to the combined action of self-phase modulation and third-order dispersion [13]. Figure 4-4 plots the supercontinuum spectrum and temporal profile at two distances within the medium under conditions similar to that of Reference [2] of an initially 100 fs, 10 kW pulse at 770 nm inside a fused-silica microstructure fiber with a core size of 1.7 μm in diameter. That is, L_{ds} = 500 cm, $\omega_0 \tau_p$ = 140, $L_{ds}/ L_{ds}^{(3)}$ = 0.5, $L_{ds}/ L_{ds}^{(4)}$ = –0.005, and f = 0.15. After only a 2 mm propagation distance [Figure 4-4(a)], the pulse spectrum has broadened to an octave. The temporal profile [Figure 4-4(b)] is highly complicated with no well-defined pulse structure. At longer distances [Figure 4-4(c)], the spectral "envelope" exhibits little change; however, a significant amount of substructure is seen. This substructure can be understood as arising from the formation of well-defined pulses [Figure 4-4(d)], known as soliton fission [14], that is accompanied by nonsolitonic radiation at the short-wavelength side. Although stimulated Raman scattering and self-steepening result in quantitative changes in the spectrum, in the limit where the GVD is small, the basic shape of the supercontinuum spectrum depends primarily on the amount of third-order dispersion and, to a lesser extent, the amount of fourth-order dispersion.

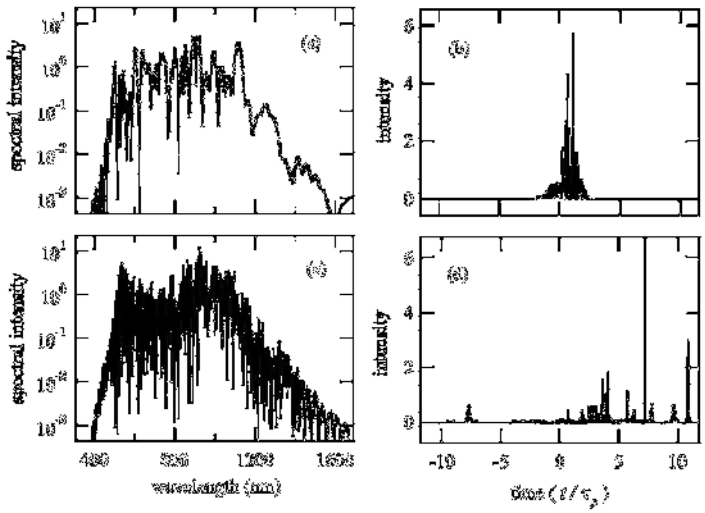

Figure 4-4. Theoretically predicted supercontinuum spectra and temporal profiles for z = 0.02 cm (a,b) and z = 1.2 cm (c,d).

For the case in which picosecond and nanosecond pulses are used, four-wave mixing and Raman scattering can produce a broadband supercontinuum in long fiber lengths [15]. Tailoring the dispersion of the

fiber can result in control of the continuum such that certain spectral parts of the continuum are suppressed and others are enhanced [16]. The generated supercontinuum has also been found to be highly dependent on polarization because of the birefringent nature of microstructure fibers [17].

5.3 Continuum instability and noise

Although at these powers, changes in the input pulse energy do not significantly alter the spectral envelope of the supercontinuum. However, numerical simulations show that the fine substructure is highly sensitive to the initial pulse energy. Figures 4-5(a) and (b) show spectra under identical conditions, except that the curve in (b) is for 0.1% higher input pulse energy, which corresponds to the fluctuations in a typical Ti:sapphire femtosecond oscillator. Although the gross spectral shape in both cases is nearly the same, the fine substructure for the two cases is completely different. This fine substructure and spectral instability were not observed in early supercontinuum-generation experiments either because of insufficient spectral resolution or as a result of the spectra consisting of an average over many laser pulses. Later experiments [18], in which single-pulse spectra were obtained, confirmed the existence of this fine substructure and its sensitivity to input pulse energy, as shown in Figure 4-6. The same wavelength subsection is shown for two different single-shot supercontinuum spectra, and the fine substructures are observed to be uncorrelated. Also shown is an average of four single-shot spectra. For certain applications, this sensitivity of the supercontinuum spectra to input fluctuations could impose limitations on its applicability.

Another important issue for frequency-locking applications is noise added as a result of the nonlinear interaction, even for the case in which the input pulse is perfectly stable. Stimulated Raman scattering and modulational instability arising from four-wave mixing both result in amplification of vacuum fluctuations and spontaneous Raman scattering. These processes lead to a reduction in the degree of coherence of the continuum spectrum [19] and to noise as much as 40 dB above the shot-noise limit in the frequency regions between the modes of the frequency comb [20]. The conclusion from these experiments and theoretical analysis is that for frequency metrology applications, it is desirable to use laser pulses with durations of less than 50 fs to minimize the effects of modulational instability and stimulated Raman scattering.

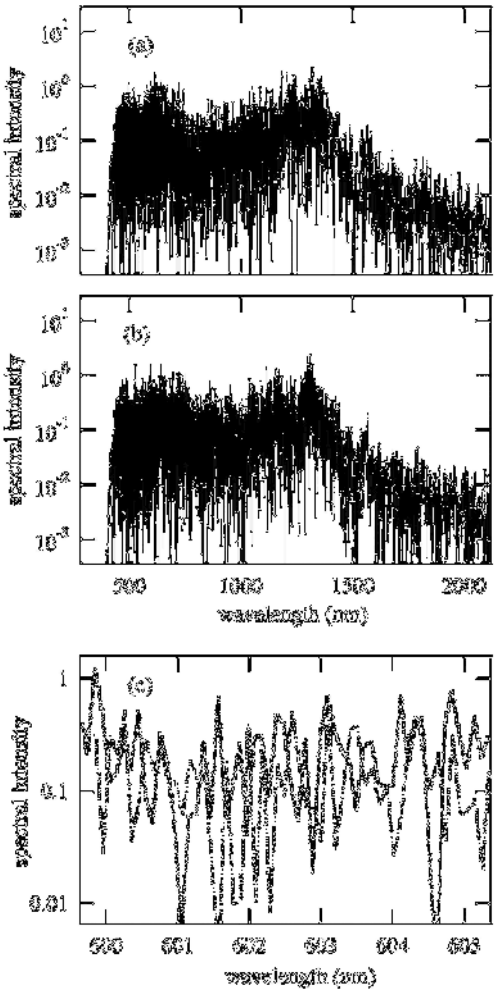

Figure 4-5. (a) Output spectrum for an input peak power P = 16 kW and the propagation distance 1.5 cm. (b) Same as (a), but with 0.1% higher peak power. (c) High resolution window of the spectra in (a) (solid line) and (b) (dotted line).

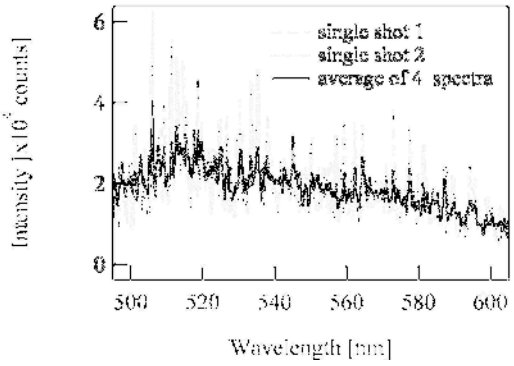

Figure 4-6. Experimental observation of spectral sensitivity to input pulse fluctuations, as described in Reference 21. The dashed and dotted curves are single-shot spectra taken seconds apart. The solid curve is the average of four spectra.

6. CONCLUSIONS

We expect that advances in supercontinuum generation in microstructure fibers will continue to be made and that applications, such as carrier-envelope phase control for attosecond pulse generation [21], will be developed for this coherent white-light source. Future advances could include designing both the transverse and longitudinal structure of the fiber to tailor the shape of the continuum for specific applications. For example, by using a combination of both anomalous and normal dispersion sections, the fine substructure and overall sensitivity of the continuum to input fluctuation could be minimized [22]. Other designs could be developed to lower the threshold power, which could help avoid long-term damage to the fiber endfaces that are crucial for frequency-stabilization techniques requiring extended time periods. Further developments of femtosecond fiber laser systems with nanojoule energies also promise to create highly compact, stable, and coherent white-light systems that can be used under environmentally challenging field conditions.

ACKNOWLEDGEMENTS

A.L.G. gratefully acknowledges discussions over the past few years on these topics with F. Ahmad, S. Cundiff, J. Dudley, M. Foster, K. Koch, K. Moll, D. Ouzounov, J. Ranka, R. Trebino, and J. Ye.

REFERENCES

[1] J. C. Knight, T. A. Birks, P. S. Russell, and D. M. Atkin, Opt. Lett. **21**, 1547-1549 (1997).

[2] J. K. Ranka, R. S. Windeler, and A. J. Stentz, Opt. Lett. **25**, 25-27 (2000).

[3] I. Hartl, X. D. Li, C. Chudoba, R. K. Ghanta, T. H. Ko, J. G. Fujimoto, J. K. Ranka, and R. S. Windeler, Opt. Lett. **26**, 608-610 (2001).

[4] T. A. Birks, J. C. Knight, and P. S. Russell, Opt. Lett. **22**, 961-963 (1997).

[5] J. C. Knight, J. Broeng, T. A. Birks, and P. S. J. Russel, Science **282**, 1476-1478 (1998).

[6] C. M. Smith, N. Venkataraman, M. T. Gallagher, D. Muller, J. A. West, N. F. Borrelli, D. C. Allan, and K. W. Koch, Nature **424**, 657-659 (2003).

[7] R. D. Meade, A. M. Rappe, K. D. Brommer, J. D. Joannopoulos, and O. L. Alerhand, Phys. Rev. B **48**, 8434-8437 (1993).

[8] G. P. Agrawal, *Nonlinear Optics* (Academic Press, San Diego, 2001).

[9] J. K. Ranka, R. S. Windeler, and A. J. Stentz, Opt. Lett. **25**, 796-798 (2000).

[10] J. C. Knight, J. Arriaga, T. A. Birks, A. Ortigosa-Blanch, W. J. Wadsworth, and P. S. Russell, IEEE Photonics Technol. Lett **12**, 807-809 (2000); D. Ouzounov, D. Homoelle, W. Zipfel, W. W. Webb, A. L. Gaeta, J. A. West, J. C. Fajardo, and K. W. Koch, Opt. Commun. **192**, 219-223 (2001).

[11] T. Brabec and F. Krausz, Phys. Rev. Lett. **78**, 3282-3285 (1997).

[12] R. H. Stolen, J. P. Gordon, W. J. Tomlinson, and H. A. Haus, J. Opt. Soc. Am. B **6**, 1159-1166 (1989).

[13] A. L. Gaeta, Opt. Lett. **27**, 924-926 (2002).

[14] A. V. Husakou and J. Herrmann, Phys. Rev. Lett. **8720**, art. no.-203901 (2001); J. Herrmann, U. Griebner, N. Zhavoronkov, A. Husakou, D. Nickel, J. C. Knight, W. J. Wadsworth, P. S. J. Russell, and G. Korn, Phys. Rev. Lett. **88**, art. no.-173901 (2002).

[15] J. M. Dudley, L. Provino, N. Grossard, H. Maillotte, R. S. Windeler, B. J. Eggleton, and S. Coen, J. Opt. Soc. Am. B **19**, 765-771 (2002); S. Coen, A. H. L. Chau, R. Leonhardt, J. D. Harvey, J. C. Knight, W. J. Wadsworth, and P. S. J. Russell, J. Opt. Soc. Am. B **19**, 753-764 (2002).

[16] K. M. Hilligsoe, T. V. Andersen, H. N. Paulsen, C. K. Nielsen, K. Molmer, S. Keiding, R. Kristiansen, K. P. Hansen, and J. J. Larsen, Opt. Expr. **12**, 1045-1054 (2004).

[17] Z. M. Zhu and T. G. Brown, Opt. Expr. **12**, 791-796 (2004).

[18] X. Gu, L. Xu, M. Kimmel, E. Zeek, P. O'Shea, A. P. Shreenath, R. Trebino, and R. S. Windeler, Opt. Lett. **27**, 1174-1176 (2002).

[19] J. M. Dudley and S. Coen, Opt. Lett. **27**, 1180-1182 (2002); X. Gu, M. Kimmel, A. P. Shreenath, R. Trebino, J. M. Dudley, S. Coen, and R. S. Windeler, Opt. Expr. **11**, 2697-2703 (2003).

[20] K. L. Corwin, N. R. Newbury, J. M. Dudley, S. Coen, S. A. Diddams, K. Weber, and R. S. Windeler, Phys. Rev. Lett. **90**, 113904 (2003); J. N.

Ames, S. Ghosh, R. S. Windeler, A. L. Gaeta, and S. T. Cundiff, Appl. Phys. B **77**, 279-284 (2003).

[21] A. Baltuska, T. Udem, M. Uiberacker, M. Hentschel, E. Goulielmakis, C. Gohle, R. Holzwarth, V. S. Yakoviev, A. Scrinzi, T. W. Hänsch, and F. Krausz, Nature **421**, 611-615 (2003).

[22] T. Hori, J. Takayanagi, N. Nishizawa, and T. Goto, Opt. Expr. **12**, 317-324 (2004).

Chapter 5

OPTICAL COMB DYNAMICS AND STABILIZATION

Günter Steinmeyer[1] and Ursula Keller[2]
[1]*Max-Born-Institut für Nichtlineare Optik und Kurzzeitspektroskopie*

[2]*Institut für Quantenelektronik, ETH Zürich*

Abstract: The spectrum of a mode-locked laser consists of a comb of equidistantly spaced frequencies. This comb has only two degrees of freedom, its offset frequency at zero and the spacing of the teeth of the comb. While the spacing of the frequencies is simply determined by the repetition rate of the laser and can be relatively easily controlled, the offset frequency is governed by phase differences between the carrier and the envelope of the pulses during one round trip through the laser cavity. This carrier-envelope offset (CEO) phase is measured via heterodyning different harmonics of the mode-locked laser spectrum. In an unstabilized laser, this CEO phase exhibits very strong noise and can fluctuate several thousand radians in only one second. We provide an analysis of CEO phase-noise contributions and track their origin. The passive stability with respect to CEO fluctuations can be greatly improved by suitable cavity design, which greatly simplifies the stabilization of the CEO phase. Recent efforts on carrier-envelope stabilization are reviewed and some limitations are outlined.

Key words: dispersion, carrier-envelope phase, phase noise, phase stabilization

1. INTRODUCTION

Ultrashort pulse generation reached pulse durations of a few femtoseconds around the turn of the century [1]. Some of the shortest pulses have a width of only two optical cycles [2-4]. When pulse durations approach this regime, the commonly used approach of the slowly varying envelope approximation (SVEA) starts to fail. Nonlinear optical effects are then expected to depend not only on the envelope structure of the pulses, but also on the structure of the electric field itself, including its relative phase to

the envelope, which has been referred to as the absolute phase. In 2001 and 2003, the first experimental evidence for the failure of the SVEA was reported [5].

In this chapter, we describe how to monitor the relative phase between the envelope and the carrier of an optical pulse train from a mode-locked optical oscillator. The chapter is organized as follows: First, we introduce the definition of the carrier-envelope-offset (CEO) phase and frequency. We show how both entities are connected with intracavity dispersion. Methods to measure the CEO frequency are discussed, with an emphasis on the most wide spread ν-to-2ν scheme. Careful characterizations of the CEO-phase-noise spectra are used to isolate the physical mechanisms behind the excessive fluctuations of the CEO phase of a free-running oscillator. This insight allows building femtosecond lasers with an increased passive stability of the CEO and forms the basis for subsequent stabilization of the CEO frequency. Finally, we discuss how to optimize control of the CEO phase and how to push residual phase jitter into the attosecond range.

2. COMB PARAMETERS AND THEIR CONNECTION TO INTRACAVITY DISPERSION

2.1 Carrier-envelope-offset phase and frequency in the time domain

Figure 5-1 shows the envelope and the carrier of two subsequent pulses from a mode-locked laser. The envelope travels at group velocity $v_g = c/n_g = c/(n + \omega dn/d\omega)$ and repeats itself after the cavity round-trip time T_R. The underlying carrier propagates at phase velocity $v_p = c/n$. Generally, $v_p \neq v_g$ in any dispersive medium. This means that the electric-field structure of the pulse will undergo a permanent change. The drift of the relative phase between carrier and envelope can be tracked down to the $\mathrm{d}n/\mathrm{d}\omega$ term in the definition of the group velocity.

When propagating through a dispersive material with an index of refraction $n(z)$ along the axis z, the pulse will accumulate a phase offset between the carrier and envelope of

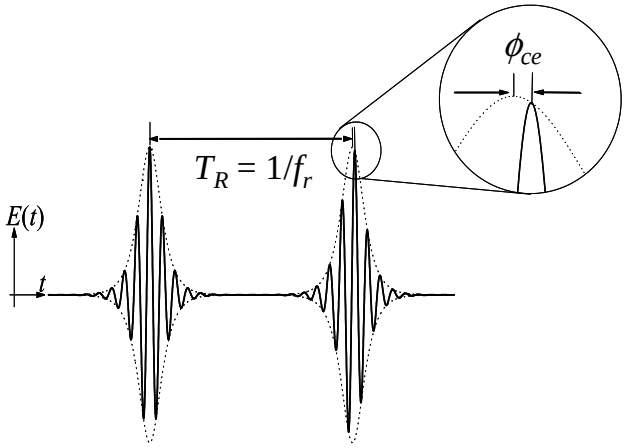

Figure 5-1. The electric field $E(t)$ of two subsequent pulses from a mode-locked laser (solid line). The envelope $\pm A(t)$ is shown as dashed lines. The electric-field patterns of the pulses experience a pulse-to-pulse phase shift $\Delta\phi_{ce}$ according to Equation (1).

$$\Delta\phi_{ce} = \left[\frac{2\pi}{\lambda} \int_0^L n_g(z) - n(z)\,\mathrm{d}z \right] \bmod 2\pi = \left[\frac{\omega^2}{c} \int_0^L \frac{dn(z)}{\mathrm{d}\omega}\,\mathrm{d}z \right] \bmod 2\pi. \qquad (1)$$

Here L is the length of the dispersive material. For the case of a linear cavity, L takes the role of twice the cavity length, and the carrier-envelope offset (CEO) phase $\Delta\phi_{ce}$ is the change of the phase ϕ_{ce} per round trip:

$$\Delta\phi_{ce}(t) = \phi_{ce}(t) - \phi_{ce}(t - T_R)\,. \qquad (2)$$

The CEO phase $\Delta\phi_{ce}$ must not be confused with the phase ϕ_{ce}, which is typically defined such that a pulse with $\phi_{ce} = 0$ has the largest possible value of the electric field [6]. Some authors have referred to ϕ_{ce} as the absolute phase. An example for such a pulse is shown as the left pulse in Figure 5-1. $\Delta\phi_{ce}$, however, is defined as the difference of the absolute phase of two subsequent pulses. It is useful to introduce the CEO frequency [7]

$$f_0 = \frac{\Delta\phi_{ce}}{2\pi} f_r\,, \qquad (3)$$

where f_r equals the inverse round-trip time $1/T_R$ of the cavity and f_0 is time dependent unless the intracavity dispersion and the cavity length are

absolutely constant with time. Changes of f_0 or $\Delta\phi_{ce}$ tend to be unnoticeably small on a pulse-to-pulse time scale but can reach significant magnitudes on millisecond time scales, rendering stabilization of these parameters a nontrivial task. For a detailed derivation of the fundamental comb parameters from periodic waveforms and their connection to intracavity dispersion, we refer the reader to Reference [8].

2.2 The frequency comb and its dynamics

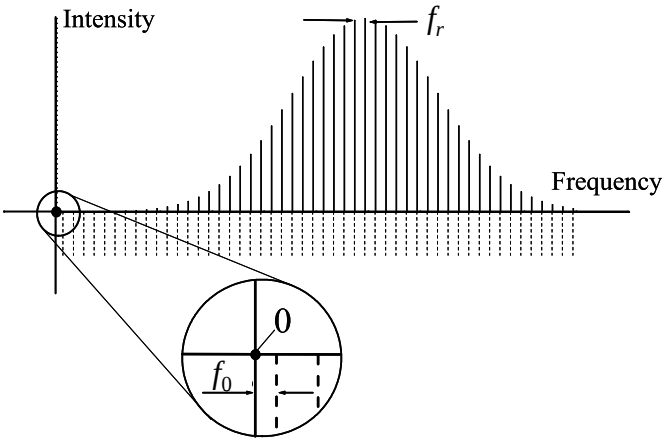

Figure 5-2. Equidistant frequency comb of a mode-locked laser. The comb lines are spaced by the repetition rate f_r and exhibit a nonvanishing offset frequency f_0 at zero frequency unless the electric-field pattern exactly reproduces from pulse to pulse (compare to the time domain picture in Figure 5-1).

For the following considerations, it is useful to revisit the scenario of Figure 5-1 in the Fourier domain. As the pulses follow each other at a constant delay T_R, their spectrum consists of a comb of equidistantly spaced frequencies with a separation $f_r = 1/T_R$. This frequency comb must not be confused with the modes of a linear cavity, which are only equidistant in the absence of intracavity dispersion. In contrast, if the spacing between the teeth in the mode-locked frequency comb were not constant, different Fourier components of the pulse in Figure 5-1 would travel at different repetition rates inside the cavity, and the pulse would slowly, but surely, drift apart. The fact that the separation of the frequencies is constant over the entire comb has been experimentally checked to better than 10^{-15} [9].

Differing phase and group velocity cause a translation of the entire frequency comb by the carrier-envelope-offset frequency f_0. The frequencies of the i^{th} comb component can therefore be written in the form:

$$\nu_i = f_0 + i f_r \,. \tag{4}$$

Tl
co
ki
in
C]

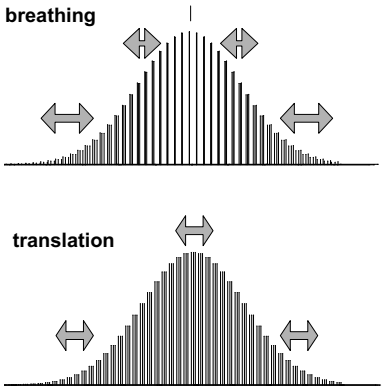

Figure 5-3. Comb dynamics [10]. The frequencies inside the comb structure are determined by two parameters, f_0 and f_r . This gives rise to a translational degree of freedom and a breathing mode. Noise contributions will induce a characteristic linear combination of both degrees of freedom.

However, there is always a fixed frequency f_x that remains unaffected by a distortion X [11].

$$f_x = f_0 + f_r \frac{\partial f_0}{\partial X}\left(\frac{\partial f_r}{\partial X}\right)^{-1}, \tag{5}$$

where X could be any physical parameter of the cavity, e.g., its length or the temperature of the laser crystal. Let us illustrate the concept of a fixed point by choosing X as the cavity length. Cavity length fluctuations only affect the repetition rate f_r of the laser but leave the per-round-trip phase shift $\Delta\phi_{ce}$ between envelope and carrier unchanged. Inserting Equation (3) into Equation (5) yields $f_x = 2 f_0$, i.e., a value very close to zero frequency. A complementary example would be an effect that causes only a change of the cavity group delay but leaves the phase delay unchanged. This could be achieved, e.g., by tilting a mirror in an intracavity prism sequence with the pivot point adjusted to the center frequency of the mode-locked spectrum

[12]. Retarding the group by one cycle relative to the phase changes f_0 by one free spectral range (i.e., the repetition rate), whereas the repetition rate itself only changes by a very small amount. In this case, one calculates that f_x equals the carrier frequency of the pulse. Most environmental contributions to comb dynamics, such as thermal or nonlinear changes of the intracavity refractive indices, have an f_x located between zero frequency and the carrier frequency [11]. This means that they neither add a pure contribution to the group delay nor do they only affect the phase delay of the group. Measuring the fixed frequency f_x can help to pinpoint the source of dominant frequency comb dynamics.

3. MEASUREMENT OF THE CEO FREQUENCY

An early approach for measurement of f_0 employed an interferometric method based on second-harmonic generation (SHG) cross-correlation between two subsequent laser pulses [13]. For vanishing $\Delta\phi_{ce}$, the cross-correlation signal is identical to the interferometric autocorrelation, with a symmetric fringe pattern. In all other cases, the fringe pattern appears shifted with the fringe maximum located at $\Delta\phi_{ce}/\omega_c$ and the cross-correlation is asymmetric. Even though this measurement in the time domain works in principle [14], it is very susceptible to offset errors. Any offset between group and phase delay in the long arm of the cross-correlator will induce a measurement error in determining f_0. Therefore, phase-coherent methods are indispensable for precise control of the CEO phase as was suggested in Reference [6].

3.1 Heterodyning different laser harmonics

Figure 5-4 provides the key to the measurement of f_0 by heterodyning harmonics from different parts of the mode-locked spectrum. The technique was first proposed by Telle et al. [6]. Taking the N^{th} harmonic of a comb line $N\nu_{m_1} = Nf_0 + Nm_1 f_r$ and beating it with the M^{th} harmonic of another comb line $M\nu_{m_2} = Mf_0 + Mm_2 f_r$ yields

$$N\nu_{m_1} - M\nu_{m_2} = (N-M) f_0, \tag{6}$$

which requires that $Nm_1 = Mm_2$. Equation (6) is the key to any measurement of the carrier-envelope offset and was used in the first experimental demonstrations by Jones et al. [14] and Apolonski et al. [15] for the case of

N = 1. The beat note of Equation (6) delivers the carrier-envelope-phase-slippage rate, either directly or as one of its harmonics. An example for a measurement of the CEO frequency, which is based on this scheme, is shown in Figure 5-5.

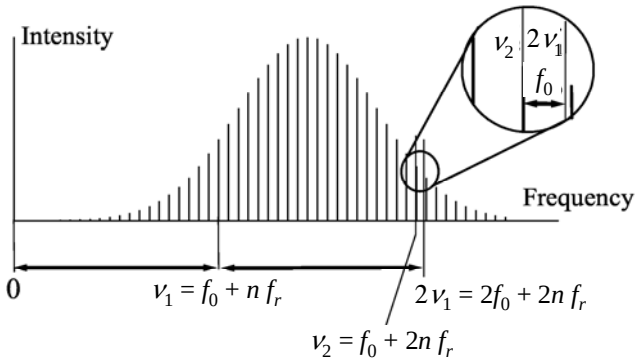

Figure 5-4. Scheme for measuring the CEO-frequency of a laser comb for the case of heterodyning the fundamental and the second harmonic, i.e., N = 1 and M = 2 in Equation (6). Graphically, this scheme mirrors the origin at $f = \nu_1$, transferring the f_0 beat from dc into a region with nonvanishing spectral content.

However, the scheme of Equation (6) requires a certain minimum spectral width of the comb $\Delta\nu/\nu = 2(N-M)/(N+M)$; e.g., beating of the fundamental and second harmonic requires an optical octave of bandwidth with $\Delta\nu/\nu = 0.67$. The situation of second-harmonic generation is illustrated in Figure 5-4. Often, an octave-spanning spectrum is not directly available from the oscillator. Alternatively, one can meet the bandwidth requirement by additional external broadening, as shown in the schematic setup in Figure 5-6, which is actually the most commonly used scheme to measure the CEO frequency of a laser.

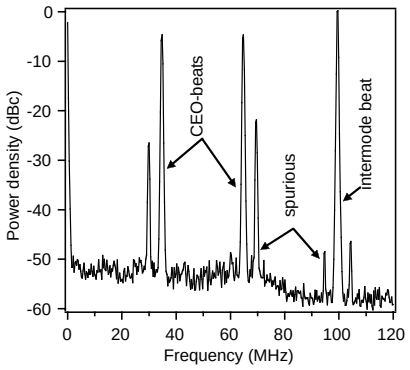

Figure 5-5. Typical rf spectrum of the CEO beat note signal. This signal was measured at a Ti:sapphire laser heterodyning the fundamental and the second-harmonic-generation (SHG) signal from a continuum generated in a microstructure fiber [16]. The CEO beat is located at 35 MHz with a signal-to-noise ratio of >45 dB in a 100 kHz bandwidth. Its mirror frequency is also visible at 65 MHz. The laser has a 100 MHz repetition rate. Some spurious contributions have been generated by nonlinear electronic mixing processes in the detector circuitry.

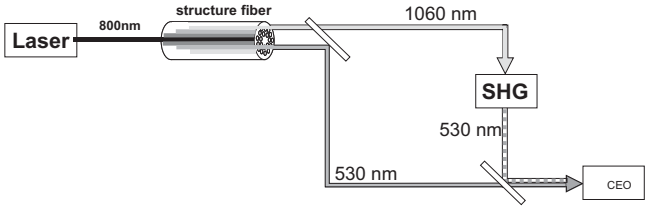

Figure 5-6. Schematic drawing of a practical implementation of Equation (6) and Figure 5-4. The laser is spectrally broadened to more than an optical octave using continuum generation in a microstructure fiber. Two wavelengths forming one octave are separated. The long-wavelength component is frequency doubled and heterodyned with the fundamental signal. The beat note contains an rf component at the CEO frequency. Specific wavelengths shown are meant as example values.

3.2 Transfer oscillators and interval bisection

Let us briefly mention other ways to circumvent the bandwidth bottleneck [6]. These alternative methods rely on transfer oscillators and interval bisection. A transfer oscillator is an additional single-frequency cw laser with frequency ν_{trans}. This frequency or one of its harmonics has to be locked to one of the comb frequencies. At the same time, the fundamental

transfer oscillator is used for sum-frequency generation from the low-frequency part of the comb to the high-frequency part. The beat notes of both then allow extraction of the CEO frequency. In particular, when the second or third harmonic of the transfer oscillator can be generated at sufficient power, this scheme can be operated with smaller bandwidth requirements. If the second harmonic of the transfer oscillator is locked to the comb, only 0.6 of an optical octave is required in the comb. For third-harmonic generation, only 0.4 optical-octave bandwidth is required.

Frequency-interval bisection [17] can be employed to divide the required comb width. The simplest scheme of this type uses a one-octave interval-divider stage that generates the frequency ν_a at the midpoint of ν_b and $2\nu_b$. This can be done by phase locking the second harmonic of ν_a to the sum frequency of ν_b and $2\nu_b$ to yield

$$\frac{\nu_a}{2\nu_b} = \frac{3\nu_b/2}{2\nu_b} = \frac{3}{4}. \tag{7}$$

This way, one now has available two phase-locked oscillators at only half-an-octave spectral separation. Locking one to the comb and phase comparison of the other allow extraction of the CEO frequency of the comb.

4. CEO PHASE NOISE

From the discussion so far, it should be clear that the carrier-envelope phase of a femtosecond oscillator is extremely sensitive to any kind of environmental influence and changes of the laser parameters such as pulse duration or power fluctuations. In this section, we discuss measurements of the carrier-envelope-phase noise of a laser oscillator. From these measurements, one can judge the severity of the noise problem. It is also helpful to reach an understanding of the mechanisms behind the carrier-envelope-phase noise before attempting to stabilize the CEO phase. For this reason, we discuss measurements of the CEO phase noise for different laser configurations. We restrict ourselves to measurements of Ti:sapphire lasers, as the CEO-phase noise in these lasers has been analyzed with great scrutiny. The general carrier-envelope-phase noise shows striking similarities with timing-jitter noise in mode-locked lasers [18, 19]. We therefore use a similar formalism to describe and analyze the dynamics of the carrier-envelope-offset frequency and phase.

4.1 Noise densities and rms phase jitter

The easiest way to characterize the CEO-noise properties consists of frequency-to-voltage conversion of the CEO beat noise and subsequent spectral analysis with a Fourier analyzer or a similar spectrum analyzer. Multiplying the measured voltage noise by the conversion factor of the frequency-to-voltage converter yields the single-sideband frequency noise density $\sigma_{f_0}(f)$ in units $\mathrm{Hz}/\sqrt{\mathrm{Hz}}$ vs Fourier frequency f [16]. Other ways to measure the frequency noise density have been described in [20]. However, the latter approach relied on constant amplitude-to-phase coupling over the entire measurement range. The frequency-noise density can be easily converted into a phase-noise density using the identity

$$\sigma_{\phi_{ce}} = \frac{\sigma_{f_0}}{f}. \tag{8}$$

For an interpretation of the noise data, it is sometimes more useful to integrate the noise densities according to

$$\delta f_0(f_{low}) = \sqrt{2\int_{f_{low}}^{f_r/2} \sigma_{f_0}^2 \, df}, \qquad \delta\phi_{ce}(f_{low}) = \sqrt{2\int_{f_{low}}^{f_r/2} \left(\frac{\sigma_{f_0}}{f}\right)^2 df}. \tag{9}$$

The integration spans from a lower frequency f_{low} given by the inverse measurement time to an upper bound that is ideally half the repetition rate itself. Typically, one can only carry the integration to a few tens or hundreds of kilohertz, which is normally considered sufficient as the noise rolls off very rapidly at high frequencies. The integrated noise densities $\delta\phi_{ce}(f_{low})$ and $\delta f_0(f_{low})$ can be interpreted as rms widths of the fluctuation range of phase or frequency, respectively.

4.2 CEO-phase noise of mode-locked oscillators

Examples of phase-noise measurements are shown in Figures 5-7 and 5-8 [16, 21]. From the data in Figure 5-7, one can see that the noise generally rolls off above 1 kHz. At the very end of the measurement range shown in Figure 5-7, there seems to be an increase of noise that may be explainable by relaxation oscillations, similar to observations of timing-jitter noise [19]. The major noise contributions, however, are located in the range of a few 100 Hz to 1 kHz. For an interpretation of the severity of the noise, it is useful to

inspect the integrated phase noise starting at high frequencies and locating the point where the $\delta\phi_{ce}$ approaches unity. In Figure 5-8, one can clearly see that the integrated phase noise already reaches one radian at several kHz Fourier frequency. Around 1 kHz, the noise grows dramatically, reaching values of several hundred to thousands of radians at 100 Hz offset frequency. In summary, this means that severe phase-noise contributions accumulate within approximately 1 ms of measurement time. For a successful phase lock of the CEO frequency, however, it is mandatory to keep residual jitters below $\delta\phi_{ce} \approx 0.3$ rad [22]. This requirement is only set by the cycle-slip-free functioning of the phase-locked loop, whereas applications may demand an even tighter locking to smaller jitter values. These considerations make it clear that for any meaningful stabilization of the CEO frequency, servo bandwidths of 10 kHz or more are required, which makes the use of acousto-optic or electro-optic controls preferable to a mechanical adjustment of intracavity dispersion.

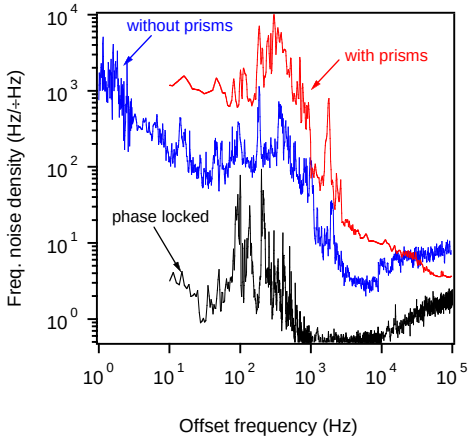

Figure 5-7. Frequency noise density of different Ti:sapphire lasers [16, 21]. The top trace shows a measurement for a laser with intracavity prisms; the middle trace is measured for a prismless variant of the same laser. The bottom trace shows how the measured frequency noise density drops farther when a phase lock to a reference oscillator is activated. This measurement has to be interpreted as a noise floor, as it is limited by the stability of the local oscillator in the measurement.

Moreover, Figures 5-7 and 5-8 contain measurements for both oscillators with and without prisms for intracavity dispersion compensation. In these measurements, an identical pump laser was used for the prismless and the prism setup. It becomes evident that prism-based femtosecond oscillators are about ten times as noisy as prismless lasers. This can only be explained by an additional physical mechanism present because of the intracavity prisms.

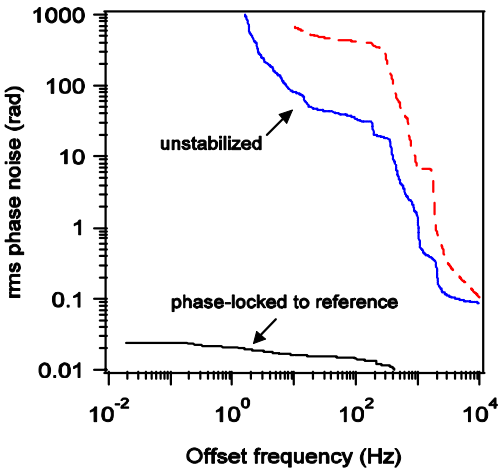

Figure 5-8. Integrated phase-noise density of different Ti:sapphire lasers [16, 21]. The top and middle traces have been computed from the data displayed in Figure 5-7 using Equations (8) and (9). The bottom trace is based on a direct phase comparison of a stabilized oscillator and an rf reference using an rf lock-in amplifier.

4.3 Physical mechanisms behind CEO fluctuations

The key to understanding the mechanisms forming the CEO noise is Equation (1). Any change of temperature, air pressure, or laser power may also affect $\Delta\phi_{ce}$. For simplicity, let us assume that we have a laser cavity of length L filled with a material of index n. We can then rewrite the dependence of Equation (1) on any laser or environmental parameter X as [13, 21, 23]:

$$\frac{\partial}{\partial X}\Delta\phi_{ce} = 2\omega_c \frac{\partial\omega_c}{\partial X}\frac{\partial n}{\partial\omega}L + \omega_c^2 \frac{\partial n}{\partial\omega}\frac{\partial L}{\partial X} + \omega_c^2 \frac{\partial^2 n}{\partial\omega\partial X}L\,. \qquad (10)$$

These three partial derivatives account for changes of the center frequency ω_c [13], changes of the cavity geometry [21], and changes of the first-order dispersion of the cavity [16, 23], respectively. Let us first consider environmental effects, which equal X for temperature or air pressure. Temperature changes of the laser crystal or intracavity prisms immediately translate into changes of the CEO frequency. Nevertheless, such variations are relatively slow and cannot fully explain the noise contributions at the high Fourier frequencies well above 1 kHz in Figures 5-7 and 5-8. A similar argument holds for pressure variations, which couple to the CEO frequency by refraction changes caused by the air in the cavity. Another coupling

mechanism is displacement of the cavity mirrors. The latter effect is much less of a concern than for stabilization of single-frequency lasers, because the fixed frequency of the comb dynamics lies close to zero frequency. Thus there is only a negligible effect on f_0. In summary, environmental contributions are an important input to the low-frequency part of the CEO noise spectrum. Nevertheless, they can be relatively easily reduced by enclosing the laser in a box, thereby avoiding air turbulence. Typically, environmental contributions can be suitably reduced by these passive measures. Therefore they rarely represent an obstacle to successful stabilization of the CEO frequency.

4.4 Amplitude-to-phase conversion effects

Amplitude-to-phase conversion (APC) is a special case of Equation (10). The case where X is the intensity deserves special attention, as the resulting fluctuations of $\Delta\phi_{ce}$ can be arbitrarily fast when electronic nonlinearities such as the all-optical Kerr effect are mediating between amplitude fluctuations and CEO-phase noise. APC effects are mainly taking place in the laser crystal, as this is the position of highest intracavity intensities.

Spectral shifting of the laser spectrum has been proposed as the first mechanism giving rise to APC effects [13]. The carrier frequency ω_c shifts with pump power or intracavity intensity, an effect that strongly depends on the operating conditions of the laser. Generally, both effects seem to be weaker when the laser bandwidth is wider. In a recent publication, spectral shifting was observed for a 750 MHz repetition-rate laser below 50 nm mode-locked bandwidth, whereas it did not appear to play a role in a 100 MHz repetition-rate laser with its stronger mode locking and higher pulse energy [23]. APC coefficients $\partial f_0 / \partial I$ on the order of 10^{-7} HzW/m^2 were observed when spectral shifting dominates the APC, resulting in the prevalent contribution to Equation (9). In contrast, the APC coefficient drops to a few 10^{-9} HzW/m^2 in the absence of spectral shifting [16, 21, 23].

A second contribution to CEO-phase noise arises from geometrical changes of the laser cavity affecting the total cavity length L. This contribution is typically negligible in prismless cavities but can play a role in cavities that use intracavity prism sequences for dispersion compensation [3, 21]. One potential mechanism behind such laser dynamics is beam-pointing variations inside the laser cavity together with the directional sensitivity of the dispersion of a prism compressor [21, 24]. If the beam direction inside the prism sequence changes, this will also affect the net first-order dispersion of the cavity via the second term in Equation (10). Beam-pointing variations can be induced by changes of the refractive index of the laser crystal. If the index of refraction of the laser crystal changes, Snell's law demands a change

of angles inside and outside the laser crystal [21]. Beam-pointing effects are held responsible for an approximately tenfold increase of CEO-phase noise of prism laser cavities as compared to prismless variants.

The third term in Equation (10) contains contributions to CEO-phase noise via intensity-induced changes of the refractive index [25]. Nonlinear refraction is well known as the all-optical Kerr effect [26], but according to Equation (10), only the dispersion of the Kerr effect affects changes of the CEO phase. The issue of dispersion of the Kerr effect has been addressed by [27, 28]. According to Sheik-Bahae et al. [27], the main contribution to the first-order dispersion of a dielectric medium well below half the band edge stems from a Kramers-Kronig term induced by two-photon absorption. As per their example, for sapphire at 800 nm, one calculates $\partial^2 n/\partial\omega\,\partial I \approx 10^{-36}$ s m^2/W rad. Inserting values for typical Ti:sapphire laser cavities [4], one computes a theoretical estimate of $\partial f_0/\partial I = 5\times10^{-9}$ HzW/m^2, which agrees well with the lowest experimentally observed values of $\partial f_0/\partial I$. Again, these low APC coefficients can only be reached in the absence of geometrical effects and spectral shifting.

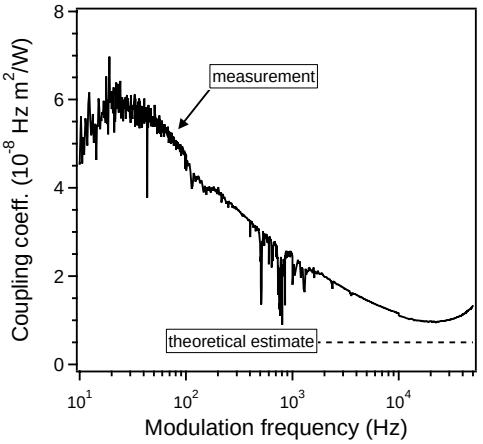

Figure 5-9. Transfer function of laser intensity noise into fluctuations of the CEO frequency [16]. These measurements were done in a prismless laser in the absence of spectral shifting. The measurements reflect Kerr contributions to the APC and thermally induced amplitude-to-phase conversion (APC) effects at low frequencies.

A measurement of the APC coefficient is shown in Figure 5-9. The theoretical estimate from Reference [27] is shown as a dashed line. The measurement was performed at different modulation frequencies. For frequencies below 1 kHz, an APC coefficient of a few times 10^{-8} HzW/m^2 is observed. At higher modulation frequencies, the APC levels off to about 10^{-8}

HzW/m^2. Spectral shifting does not seem to play a role in these experiments, and geometrical effects are also not a concern because of a prismless cavity. At lower frequencies, additional contributions from thermally induced changes of the refractive index increase the APC effect. For modulation frequencies of about 10 kHz or more, the coupling dynamics appear to be restricted to a purely electronic-refractive nonlinearity.

From the experimental observations, some guidelines can be given on how to keep APC effects to a minimum. The first recommendation is to use a prismless cavity, which is also strongly supported by the data in Figures 5-7 and 5-8. In prismless cavities, beam pointing does not translate into CEO-phase noise [21]. Spectral shifting is the other APC effect that can be avoided by suitable design of the laser. For a stable position of the laser spectrum, a broad mode-locked bandwidth of more than 50 nanometers and a high pulse energy appear to be favorable conditions [23]. If geometric effects and spectral shifting can be avoided, the APC effects are restricted to nonlinear refractive mechanisms, both Kerr-type and an additional thermally induced mechanism at low Fourier frequencies. Values on the order of $\partial f_0 / \partial I = 10^{-8}$ HzW/m^2 or less are indicative of a dominance of nonlinear refraction in the APC dynamics.

5. STABILIZATION OF THE CEO FREQUENCY

In previous sections, we have introduced methods to measure the CEO frequency. We have also analyzed sources of CEO-phase noise and given guidelines on how to increase the passive stability of the CEO phase. Even if such measures can be further improved, the residual noise of the free-running laser is still prohibitive for many applications in extreme nonlinear optics, which demand a stable CEO phase for seconds or minutes of integration times.

5.1 Controlling the CEO frequency of a laser oscillator

The only missing link to stabilization of the CEO frequency is now a mechanism for external control of the CEO frequency. Such a mechanism allows closing the servo loop, forcing the CEO frequency into a lock with an rf-reference oscillator. Ideally, a control mechanism should only act on the CEO frequency and leave other cavity parameters unchanged (orthogonality). If we leave this concern aside, all mechanisms causing APC are suited, in principle, for control of the CEO frequency. As was discussed previously, a servo bandwidth of more than 10 kHz is needed, which rules

out many slow mechanisms. Choice of the control mechanism is therefore a trade-off between orthogonality and bandwidth.

In lasers with intracavity prism sequences, an elegant way of controlling the CEO frequency of a laser without affecting other laser parameters is offered. Tilting the end mirror after the prism sequence affects only the difference between the group and phase delay in the cavity but leaves other laser parameters widely unchanged [12, 29]. The tilt of the end mirror has to be restricted to small excursions compared to the angular aperture of the beam at the end mirror. Only then can one be sure that the intracavity power is not also affected by the mirror tilt. Mirror excursion in the microradian range is sufficient to control the CEO frequency within one spectral range. This makes mirror tilting the method of choice for cavities with prisms. However, it is typically very difficult to reach a servo bandwidth of more than 1 kHz with mirror tilting because of mirror inertia. Reaching sufficient bandwidth requires an optimized setup of the tilt actuator. Bandwidths up to 25 kHz have been demonstrated using a mirror of low mass directly mounted on a split piezoelectric transducer (PZT) actuator [30].

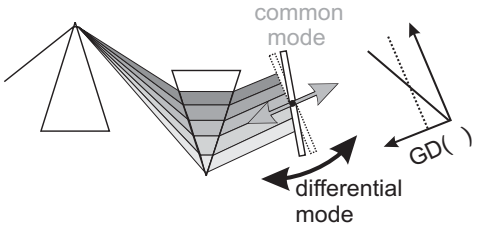

Figure 5-10. Control of intracavity first-order dispersion by tilting of an end mirror after a dispersive delay line. Translation of the mirror parallel to the optical axis acts on both group and phase delay; tilting changes the difference between them. Provided a choice of the correct pivot point has been made, tilting only affects the CEO-frequency.

Mirror tilting is not an option when a prismless setup is used. Then the method of choice is modulation of the pump power either with an acousto-optic modulator [16] or with an electro-optic device [20]. As the required pump-power modulation is on the order of 10^{-3}, it is typically very easy to reach bandwidths of several tens to hundreds of kHz. Pump-power modulation relies on the APC mechanisms discussed in the previous section and is currently the most widespread mechanism for CEO-frequency control.

5.2 Performance of CEO phase locks

Several detailed investigations on stabilization of the CEO frequency and the resultant residual CEO phase noise have been published [16, 20, 21, 30]. All these authors used microstructure fibers for additional external

broadening of the laser spectra. A first attempt to directly stabilize the CEO frequency of an octave-spanning laser was reported by Morgner et al. [3]. However, because this laser only spanned the octave at about -40 dBc, the authors achieved a CEO beat note that was considered minimum for a robust stabilization. The authors thus proposed a 2ν-to-3ν scheme. This scheme has been carried out recently with resulting small residual timing jitters and excellent long-term stability [31]. Still, a direct stabilization is more challenging than stabilization based on additional spectral broadening.

Another important issue is the setup of the locking electronics. For any meaningful application, a phase lock to an rf-reference source is required. A phase lock can be as simple as that depicted in Figure 5-11, which consists of a double-balanced mixer and some means to adjust the servo loop gain. The gain has to be optimized for a sufficient phase margin of the loop to prevent self-oscillation of the servo circuit.

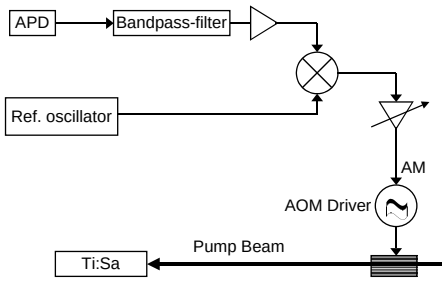

Figure 5-11. Simple phase-lock circuit used for stabilization of the CEO frequency [16]. The avalanche photo detector (APD) measures the beat note signal [Equation (6), Figure 5-5]. Suitable bandpass filtering isolates the beat note and suppresses mirror frequencies and spurious contributions. After mixing the signal with the reference oscillator, the mixing product is directly fed back via an acousto-optic modulator. The servo loop gain has to be adjusted for sufficient phase margin.

The simple circuit of Figure 5-11 has only a very limited capture range and may not be able to avoid cycle slips in the presence of strong CEO-phase noise. An alternative is usage of a phase detector with enhanced capture range [32]. Such a circuit is based on an electronic counter and can boost the phase capture range to tens or hundreds of π. This strategy comes at the price of decreased sensitivity that will ultimately limit the overall performance of the lock. The general recommendation is to reduce noise mechanisms as far as possible by enhancing the passive stability of the laser. Capture range enhancement should only be used as a last resort and then moderately; otherwise, extra noise of the stabilized laser will result.

Some of the best results in terms of residual phase noise were achieved with the simple double-balanced mixer (Reference [16], Figure 5-11). The measured data is also shown in Figures 5-7 and 5-8. From the data in Figure 5-8, one can conclude that the residual phase jitter in these measurements was only about 20 mrad in a 10 kHz to 0.01 Hz interval. This corresponds to residual timing jitters of only 10 as associated with the CEO phase.

5.3 Limitations of CEO control

Using additional external broadening in a piece of microstructure fiber is currently the most widespread method for measuring and stabilizing the CEO frequency. As APC effects play a strong role in intracavity CEO dynamics, it would be surprising if the strong Kerr nonlinearities involved in continuum generation would not also give rise to APC effects extracavity. There is an important difference that immediately explains why extracavity APC effects are a much lesser concern than the effects discussed in Section 4.4. If the same element with identical amplitude-to-phase coupling is moved from intracavity to extracavity, it generates CEO-phase noise via

$$\sigma_{\phi_{ce}}^{(extracavity)}(f) = \frac{1}{f_r}\sigma_{f_0}^{(intracavity)}(f). \tag{11}$$

The highest measured noise densities of the prismless oscillator of $\sigma_{f_0}^{(intracavity)} \approx 1\,\text{kHz}/\sqrt{\text{Hz}}$ would therefore translate into extracavity-phase noise densities of only $\sigma_{\phi_{ce}}^{(extracavity)} \approx 10^{-5}\,\text{rad}/\sqrt{\text{Hz}}$.

Several approaches to experimentally quantify the strength of extracavity APC have been reported. Fortier et al. measured a coupling coefficient of 3.8 rad/pJ for a 100 MHz laser [33]. These measurements relied on an out-of-loop characterization of the stabilized oscillator, employing a second totally independent microstructure fiber and a second ν-to-2ν interferometer. A differential CEO-phase measurement using two independent CEO-measurement schemes was reported in [8]. In this measurement, two independent CEO measurements on the same source were compared. A differential phase-noise spectrum is displayed in Figure 5-12. One can immediately see that the residual uncertainty of the CEO-phase measurement is several orders of magnitude smaller than the phase noise of the free-running oscillator. The phase noise shown in Figure 5-12 adds up to an rms value of about π in a 5 s integration time [compare Equation (9) and Figure 5-8]. The differential phase noise is mainly due to slow drifts that can corrupt measurements at long integration times.

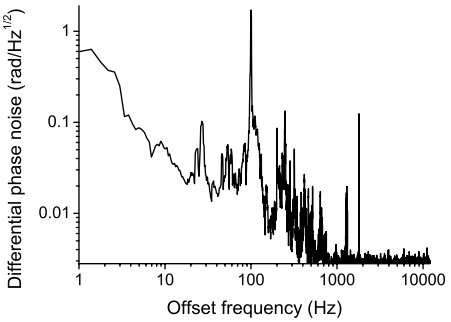

Figure 5-12. Differential phase-noise spectrum of two independent measurements of the CEO phase.

Several ways have been suggested for overcoming these residual effects. Rather than using the laser pulses directly, one can use the white-light continuum pulses for any kind of CEO-sensitive application. Using the spectrum directly from an octave-spanning oscillator would also rule out APC effects in the microstructure fiber. Still, both these solutions suffer from interferometer drift. One way to strongly reduce drift effects is a common-path interferometer, as suggested by Kakehata et al. [34] for single-shot CEO-phase measurements.

6. SUMMARY

We have discussed fluctuations of the CEO phase in oscillators and explained their origin. The CEO phase turns out to be a very sensitive parameter that is easily influenced by nearly all laser and environmental parameters. Many of these contributions either give rise to slow drift effects or can be easily shielded by enclosing the laser. From the perspective of stabilizing the CEO frequency of the laser, however, amplitude-to-phase noise conversion turns out to be a much more significant problem that cannot totally be avoided. Several mechanisms contribute to the conversion of laser amplitude noise into CEO frequency fluctuations. Again, some of these contributions, such as spectral shifting or beam pointing, can be avoided, or at least reduced, by construction and choice of favorable operating conditions. With all these measures in place, it is possible to provide a tight lock to an external rf reference, with resulting residual timing jitters between carrier and envelope of the laser of only a few attoseconds. Even with such superior performance, one has to be careful to avoid intrinsic sources of CEO phase noise in the measurement set-up itself. Amplitude-to-phase conversion also takes place in external continuum generation, which is often used to broaden the laser spectrum to an optical octave. The ν-to-2ν

interferometer is another weak point and can give rise to a small residual drift. These residual effects are relatively weak and do not appear to corrupt most applications of frequency combs demonstrated to date. Nevertheless, they can be avoided. An improved control of frequency comb parameters offers even higher precision in metrology applications and opens up novel applications in extreme nonlinear optics. Understanding the dynamics of the comb is the key to further progress in these areas.

REFERENCES

[1] G. Steinmeyer, D. H. Sutter, L. Gallmann, N. Matuschek, and U. Keller, Science **286**, 1507-1512 (1999); U. Keller, Nature **424**, 831-838 (2003).

[2] M. Nisoli, S. Desilvestri, O. Svelto, R. Szipocs, K. Ferencz, C. Spielmann, S. Sartania, and F. Krausz, Opt. Lett. **22**, 522-524 (1997); A. Baltuška, M. S. Pshenichnikov, and D. A. Wiersma, Opt. Lett. **23**, 1474-1476 (1998); A. Baltuška, T. Fuji, and T. Kobayashi, Opt. Lett. **27**, 1241-1243 (2002); R. Ell, U. Morgner, F. X. Kärtner, J. G. Fujimoto, E. P. Ippen, V. Scheuer, G. Angelow, T. Tschudi, M. J. Lederer, A. Boiko, and B. Luther-Davies, Opt. Lett. **26**, 373-375 (2001).

[3] U. Morgner, R. Ell, G. Metzler, T. R. Schibli, F. X. Kärtner, J. G. Fujimoto, H. A. Haus, and E. P. Ippen, Phys. Rev. Lett. **86**, 5462-5465 (2001).

[4] D. H. Sutter, G. Steinmeyer, L. Gallmann, N. Matuschek, F. Morier-Genoud, U. Keller, V. Scheuer, G. Angelow, and T. Tschudi, Opt. Lett. **24**, 631-633 (1999).

[5] G. G. Paulus, F. Grasbon, H. Walther, P. Villoresi, M. Nisoli, S. Stagira, E. Priori, and S. De Silvestri, Nature **414**, 182-184 (2001); G. G. Paulus, F. Lindner, H. Walther, A. Baltuška, E. Goulielmakis, M. Lezius, and F. Krausz, Phys. Rev. Lett. **91**, 253004 (2003).

[6] H. R. Telle, G. Steinmeyer, A. E. Dunlop, J. Stenger, D. H. Sutter, and U. Keller, Appl. Phys. B **69**, 327-332 (1999).

[7] T. Brabec and F. Krausz, Rev. Mod. Phys. **72**, 545-591 (2000).

[8] F. W. Helbing, G. Steinmeyer, and U. Keller, IEEE J. Sel. Top. Quantum Electron. **9**, 1030-1040 (2003).

[9] T. Udem, J. Reichert, R. Holzwarth, and T. W. Hänsch, Opt. Lett. **24**, 881-883 (1999).

[10] T. F. Albrecht, K. Bott, T. Meier, A. Schulze, M. Koch, S. T. Cundiff, J. Feldmann, W. Stolz, P. Thomas, S. W. Koch, and E. O. Göbel, Phys. Rev. B **54**, 4436-4439 (1996).

[11] N. Haverkamp, B. Lipphardt, J. Stenger, H. R. Telle, C. Fallnich, and H. Hundertmark, In *Conference On Ultrafast Phenomena*, Vancouver, BC, 2002), P. Me31-31.

[12] K. F. Kwong, D. Yankelevich, K. C. Chu, J. P. Heritage, and A. Dienes, Opt. Lett. **18**, 558-560 (1993).

[13] L. Xu, C. Spielmann, A. Poppe, T. Brabec, F. Krausz, and T. W. Hänsch, Opt. Lett. **21**, 2008-2010 (1996).

[14] D. J. Jones, S. A. Diddams, J. K. Ranka, A. Stentz, R. S. Windeler, J. L. Hall, and S. T. Cundiff, Science **288**, 635-639 (2000).

[15] A. Apolonski, A. Poppe, G. Tempea, C. Spielmann, T. Udem, R. Holzwarth, T. W. Hänsch, and F. Krausz, Phys. Rev. Lett. **85**, 740-743 (2000).
[16] F. W. Helbing, G. Steinmeyer, U. Keller, R. S. Windeler, J. Stenger, and H. R. Telle, Opt. Lett. **27**, 194-196 (2002).
[17] H. R. Telle, D. Meschede, and T. W. Hänsch, Opt. Lett. **15**, 532-534 (1990).
[18] U. Keller, K. D. Li, M. Rodwell, and D. M. Bloom, IEEE J. Quantum Electron. **25**, 280-288 (1989).
[19] R. P. Scott, C. Langrock, and B. H. Kolner, IEEE J. Sel. Top. Quantum Electron. **7**, 641-655 (2001).
[20] A. Poppe, R. Holzwarth, A. Apolonski, G. Tempea, C. Spielmann, T. W. Hansch, and F. Krausz, Appl. Phys. B **72**, 373-376 (2001).
[21] F. W. Helbing, G. Steinmeyer, J. Stenger, H. R. Telle, and U. Keller, Appl. Phys. B **74**, S35-S42 (2002).
[22] H. R. Telle, In *Frequency Control Of Semiconductor Lasers*, Edited By M. Ohtsu (John Wiley & Sons, New York, 1996), P. 137-167.
[23] K. W. Holman, R. J. Jones, A. Marian, S. T. Cundiff, and J. Ye, Opt. Lett. **28**, 851-853 (2003).
[24] R. L. Fork, O. E. Martinez, and J. P. Gordon, Opt. Lett. 9, 150-152 (1984); R. E. Sherriff, J. Opt. Soc. Am. B **15**, 1224-1230 (1998).
[25] J. Stenger and H. R. Telle, Opt. Lett. **25**, 1553-1555 (2000); H. A. Haus and E. P. Ippen, Opt. Lett. **26**, 1654-1656 (2001).
[26] G. P. Agrawal, *Nonlinear Optics* (Academic Press, San Diego, 2001).
[27] M. Sheikbahae, D. C. Hutchings, D. J. Hagan, and E. W. Van Stryland, IEEE J. Quantum Electron. **27**, 1296-1309 (1991).
[28] R. Desalvo, A. A. Said, D. J. Hagan, E. W. Van Stryland, and M. Sheik-Bahae, IEEE J. Quantum Electron. **32**, 1324-1333 (1996).
[29] J. Reichert, R. Holzwarth, T. Udem, and T. W. Hänsch, Opt. Commun. **172**, 59-68 (1999).
[30] T. M. Fortier, D. J. Jones, J. Ye, S. T. Cundiff, and R. S. Windeler, Opt. Lett. **27**, 1436-1438 (2002).
[31] A. Bartels, S. A. Diddams, T. M. Ramond, and L. Hollberg, Opt. Lett. **28**, 663-665 (2003).
[32] U. Tietze, C. Schenk, and E. Schmid, *Electronic Circuits: Design And Applications* (Springer, New York, 1991).
[33] T. M. Fortier, J. Ye, S. T. Cundiff, and R. S. Windeler, Opt. Lett. **27**, 445-447 (2002).
[34] M. Kakehata, Y. Fujihira, H. Takada, Y. Kobayashi, K. Torizuka, T. Homma, and H. Takahashi, Appl. Phys. B **74**, S43-S50 (2002).

Chapter 6

FEMTOSECOND NONCOLLINEAR PARAMETRIC AMPLIFICATION AND CARRIER-ENVELOPE PHASE CONTROL

Takayoshi Kobayashi
Department of Physics, Faculty of Science, University of Tokyo

Abstract: This chapter presents the basic principles for three parametric interactions that enhance bandwidth to obtain short pulses while maintaining phase matching. To extend the bandwidth, we introduced a noncollinear configuration between the pump and signal. The idea is used in three different parametric processes: optical parametric generation (OPG), optical parametric amplification (OPA), and optical parametric oscillation (OPO). Using noncollinear phase matching, we developed a noncollinear-optical-parametric amplifier (NOPA) that delivers 4 fs visible-near-infrared pulses. We designed geometrical and temporal configurations of the NOPA that broaden the gain bandwidth in excess of 250 THz. The main requirements for bandwidth enhancement include (1) phase matching, (2) group-velocity matching, (3) pulse-front matching, and (4) optimization of the angular dispersion of the pump. To achieve the extended-gain bandwidth, full phase adjustment is performed by several compensators, including a prism pair, a grating-mirror system equivalent to a grating pair, chirped mirrors, and a deformable mirror. By adding these devices to the NOPA system, we obtained pulse widths of 3.9 fs in the visible and NIR spectral range.

Key words: carrier-envelope phase, optical parametric amplification

1. INTRODUCTION

Femtosecond laser systems are experiencing explosive growth in both the number of users and variety of applications. In the process, pulse duration is continually being reduced. Optical pulses with a duration of only a few optical cycles have been achieved with the proliferation of diverse types of Ti:sapphire lasers. Sub-5 fs pulses have become available with 800 nm

Ti:sapphire lasers that employ self-phase modulation (SPM) and spectral broadening in both quartz [1-3] and hollow waveguides [4-6]. The broadband pulses are compressed to a nearly Fourier-transformed pulse with novel pulse compression techniques such as chirped mirrors [7].

Even though sub-5 fs pulse durations have been achieved [8], methods utilizing SPM for spectral broadening have two major drawbacks. First, they do not offer tunable pulses. Only limited tunability can be achieved (at the expense of reduced bandwidth) by filtering out various components of an SPM-broadened spectrum. Second, is the spectral modulation inherent in the SPM process. This limitation is perhaps the most fundamental. On the one hand, the interplay between material dispersion and SPM can substantially improve the smoothness of the broadened spectra [9]. On the other hand, pulse stretching due to dispersion lowers the peak intensity and makes it impossible to sustain strong SPM action over a long propagation distance. The result is limited spectral broadening.

However, the invention of microstructure fiber [10] led to the generation of extremely broadband white-light continua with spectra that could support 2-fs pulses. This remarkable feat is a consequence of the dramatic lowering of fiber dispersion. The same feature responsible for such unprecedented spectral broadening also yields substantial spectral modulation. The latter makes it nearly impossible to use these pulses in many demanding applications of nonlinear spectroscopy, which are sensitive to both the time and frequency distributions of the electric field. This feature also makes it difficult to use microstructure fiber in pump-probe experiments. Measurements of time-resolved spectra are subject to large errors induced by fluctuations (hugely enhanced by enormous nonlinearity) of the sharp (spiky) spectral structure.

Unlike these schemes, which involve cumbersome fiber-chirping stages, remarkable progress in the generation of record-breaking short pulses has been made directly with Ti:sapphire lasers [11]. Few-cycle pulses at the few nJ level have been reported by several research groups. Even though short-pulse generation directly from cavities is simpler than the elaborate extracavity compression [1, 6], the two methods share the same spectral range and the lack of wavelength tunability, except when the latter is implemented at the expense of shortness of pulse duration. In 2001-2002, a different approach to generating even shorter pulses directly from laser cavities was developed. Researchers demonstrated that it was possible to phase lock two independent Ti:sapphire oscillators [12] or two oscillators based on different gain media [13]. This approach could provide a straightforward way to generate an ultimately short, single-cycle optical pulse by coherently combining the output from several lasers employing different gain media [8]. Both the intracavity and extracavity methods of

pulse shortening should make it possible to generate broad laser spectra at the laser's fundamental frequency or around one of its harmonics; however, this makes continuous wavelength tuning impossible in the shortest pulse regime. This difficulty, however, can be readily overcome in parametric pulse generation and amplification.

In the 1990s, optical parametric oscillation (OPO) and optical parametric amplification (OPA) had become popular methods for tunable femtosecond pulse generation, especially since the appearance of femtosecond Ti:sapphire lasers [14-16]. The high power and excellent stability of a Ti:sapphire system make optical parametric conversion the most promising method for obtaining tunable ultrashort pulses. In addition, important progress was made during the 1980s in the growth of nonlinear optical crystals with large nonlinear coefficients and high damage thresholds. These advances opened the door to new and versatile applications of these crystals in the new century [17].

Beginning about 1994, with an OPA pumped by a Ti:sapphire amplifier, it became possible to create ultrashort pulses tunable outside the 800 nm region with a few-μJ pulse energy. An OPA pumped with a Ti:sapphire laser with peak wavelength around 800 nm generates near-infrared (NIR) pulses between 1 and 4 μm, whereas an OPA pumped at about 400 nm (the second harmonic of Ti:sapphire) can cover the shorter, visible–NIR optical frequency region between 450 nm and 3.5 μm [15, 16, 18-22]. Following the difference frequency generation (DFG) of the signal and idler, they can be used to cover the range from 200 nm to 12 μm, or almost the entire optical frequency region [15, 16]. However, the shortening of the output pulse from an OPA faces a problem with phase-matching bandwidth.

2. ADVANCES OF NONCOLLINEAR-PHASE-MATCHED OPTICAL PARAMETRIC CONVERSION

The idea of a noncollinear phase matching is not new for broadband interaction. Takeuchi et al. [23] reported broadband generation of idler pulses by focusing a white-light continuum with a large convergence angle into a crystal to be phase-matched noncollinearly among a wide range of the continuum. The bandwidth was increased to as broad as 1300 cm^{-1} in the NIR. They used an optical parametric generator in a noncollinear configuration to generate signal and idler beams just around the pump axis. In the present work, noncollinear phase matching is investigated where the

signal and idler are arranged with larger noncollinear angles, as shown in Figure 6-1.

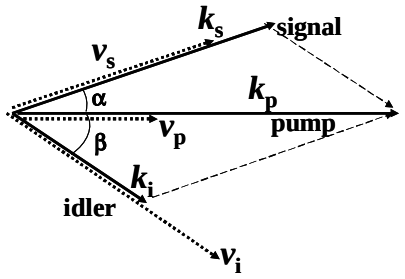

Figure 6-1. Geometric configuration of the wave vectors in an optical-parametric-amplification (OPA) nonlinear crystal. The wave vectors of the pump ($\mathbf{k}_p$), signal [$\mathbf{k}_s$ (λ_s)], and idler [$\mathbf{k}_i(\lambda_i)$] are shown in the gain crystal. The angles α and β are internal noncollinear angles between pump and signal beams and pump and idler beams, respectively. The group velocities of the pump (v_p), signal (v_s), and idler (v_i) are also shown by dashed lines.

Noncollinear phase matching has advantages over collinear phase matching. In an OPO, noncollinear phase matching is often adopted to compensate for spatial walk-off of the extraordinary ray in the crystal and to increase the gain [14, 24-26]. Temporal walk-off caused by the group-velocity mismatch can also be improved by noncollinear phase matching [27-29]. Trapani et al. demonstrated noncollinear phase matching in an OPA for satisfying the group-velocity matching between the pump pulse and signal or idler pulses in a β-BaB_2O_4 (BBO) crystal to obtain higher conversion efficiency with longer interaction length than for a collinear OPA [27-29].

The first use of noncollinear phase matching to eliminate temporal walk-off was reported by Gale et al. in 1995 [26]. They constructed a synchronously pumped OPO using a BBO crystal. The noncollinear configuration between the pump and oscillating signal beams resulted in broadband phase-matching and generated pulses as short as 13 fs in the visible. The generation of a broad spectrum of over 100 nm in a nanosecond OPO based on the same configuration was also reported [30]. We demonstrated a noncollinearly phase-matched OPA (NOPA) using a BBO and achieved tunable 14 fs pulse generation in the visible with 3–8 μJ pulse energies in 1997 [31, 32]. Although there are restrictions for synchronizing the pump and signal pulses and bandwidth limitations due to cavity mirrors in a synchronously pumped OPO [33], a femtosecond NOPA will likely generate shorter pulses with multi microjoule pulse energies and broad tunability. Extensive subsequent investigations have been performed [34-

38], and the NOPA continues to attract attention owing to its remarkable advantages.

We will now describe the development of a noncollinear parametric amplifier. First, we introduced a pulse-front-matching geometry [36] to achieve a sub-5 fs light source using methods other than the conventional continuum-compression scheme. In the nonlinear configuration, the group velocity of a faster-traveling wave (the idler) is projected at an angle onto a slower wave (the signal), thus improving the temporal overlap of the two and achieving broadband phase matching. The importance of parametric conversion in the visible and near infrared has been dramatically increased by the discovery of the unique phase-matching conditions in a type-I BBO crystal pumped by the second harmonic of the Ti:sapphire laser [36, 38]. As a result, widely tunable sub-20 fs NOPAs have become more or less routinely used [34, 39]. Tunable operation in a 10 fs regime in both the visible and infrared has also been demonstrated [32, 36, 37, 40]. The development of sophisticated pulse-compression schemes has made phase correction over the entire parametric-amplification bandwidth possible, resulting in the realization of sub-5 fs pulse generation in the visible–NIR region [38, 41-43].

The great potential of sub-10 fs NOPAs was proven by several spectacular applications of nonlinear spectroscopy such as time-domain studies of ultrafast molecular dynamics in the condensed phase [42, 44]. Although other methods of ultrashort pulse generation may, in some cases, be better than NOPAs for both pulse length and spectral width [45], parametric amplifiers produce noticeably smoother spectra with high stability. The smooth, stable spectra play a vital role in time- and frequency-resolved spectroscopy with high time resolution and with relatively high spectral resolution when the spectrometer is placed after the sample. The demand for continuing improvement of the NOPA pulse quality is evident.

The second step in obtaining short optical pulses is to control the phase of the field to be constant over the whole gain bandwidth. A constant field phase leads not only to improved pulse compression, but also to easier dispersion manipulation in phase-sensitive applications of nonlinear spectroscopy. Several dispersion-control techniques have been employed to obtain the shortest pulses from NOPAs. For instance, sub-5 fs pulses have been achieved both by using a combination of a 45°-angled-prism compressor and a set of ultrabroad-chirped mirrors (UBCM) [38] and by using custom-designed UBCMs alone [43]. While it is feasible to fabricate a set of “ideal” UBCMs, the fixed dispersion of such multilayer dielectric structures makes it impossible to introduce fine wavelength-selective control of group delay, which is required in the daily optimization of a pulse

compressor. Similarly, typical elements of tunable negative dispersion, such as the prism and grating pairs [46-48], are rendered virtually nonadjustable because of the large spectral bandwidth of a sub-5 fs pulse.

Thus, additional improvement of pulse quality cannot be achieved without implementing a flexible phase-correction method. The usefulness of a flexible phase method has been demonstrated in a computer-controlled shaping of tunable 16 fs pulses from a NOPA using a liquid crystal mask [49]. Micromachined flexible mirrors with electrostatic actuators, invented in the late 1990s, offer the possibility of adaptive pulse shaping. An inexpensive, commercially available membrane of this type was used to obtain nearly ideal spectrum-limited pulses of 15 fs duration from a Ti:sapphire laser [50] and subsequently employed for shaped-pulse optimization of the coherent emission of soft x-rays produced by high-harmonic generation [51]. By implementing this compression method for a NOPA signal wave, a visible 7 fs pulse was obtained [52]. A successful optimization of the compression in a similar 10 fs tunable NOPA has been reported by Baum et al. [53]. Previously, we have briefly described the use of this technique to compress the NOPA pulses [54] and discuss it here in detail. We demonstrate how computer-controlled optimization combined with second-harmonic frequency-resolved optica-gating [55] allows us to reduce the output pulse duration down to about 4 fs at the central wavelength near 600 nm.

3. PRINCIPLE OF PARAMETRIC AMPLIFICATION

We describe the principle of optical parametric interaction, in particular noncollinear interaction, in this section. The requirements for efficient spectral conversion in optical parametric interactions are given by the two conditions among wave vectors and frequencies,

$$\kappa_p = \kappa_s + \kappa_i , \tag{1}$$

$$\omega_p = \omega_s + \omega_i . \tag{2}$$

Here κ_j and ω_j are the wave vector and angular frequency with the suffixes $j = p, s,$ and i corresponding to the pump, signal, and idler, respectively. The first is a phase-matching condition corresponding to momentum conservation among the relevant three photons; the second is the requirement of energy conservation. Hereafter, we assume a plane-wave

interaction among them. This assumption is well satisfied in the case when the beam diameter (including the beam waist at the focal point) is much larger than the wavelength. By neglecting the pump depletion and spectral width, the well-known parametric gain G is [56, 57]

$$G = \left(\Gamma l_c \sinh\left(g l_c\right)/g l_c\right)^2 + 1$$

$$g = \left(\Gamma^2 - \left(\Delta k/2\right)^2\right)^{1/2}, \quad \Gamma = 2d_{eff}\sqrt{\frac{\omega_s \omega_i \Phi}{\varepsilon_0 n_s n_i n_p c^3}}, \tag{3}$$

where Γ is the coupling constant, d_{eff} is the effective second-order nonlinear coefficient of the nonlinear optical crystals, c is the vacuum light velocity, ε_0 is the vacuum dielectric constant, Φ is the pump intensity, l_c is the crystal length, and n_j is the refractive index of the corresponding wave. The phase mismatch $\Delta\kappa$ along the pump direction is

$$\Delta\kappa = \kappa_p - \kappa_s \cos\alpha - \kappa_i \cos\beta, \tag{4}$$

where α and β are the noncollinear angles between the wave vectors of the pump and signal and those between pump and idler, respectively. Figure 6-1 illustrates the arrangement of the general noncollinear configuration.

In the conventional collinear geometry (α = β = 0), the expression is simplified. By the Taylor expansion in powers of the angular frequencies around the central frequencies $\omega_{s0} - \omega_{i0}$, $\Delta\kappa$ is given by

$$\Delta\kappa = \left(\frac{1}{v_s} - \frac{1}{v_i}\right)\Delta\omega_s - \frac{1}{2}\left(\frac{\partial^2\kappa_s}{\delta\omega^2} + \frac{\delta^2\kappa_i}{\delta\omega_i^2}\right)\left(\Delta\omega_s\right)^2 + \ldots \tag{5}$$

where $\Delta\omega \equiv \omega_s - \omega_{s0}$ and $\Delta\omega \equiv \omega_{i0}$ and we use $\Delta\omega_i = -\Delta\omega_s$. Within the monochromatic pump approximation, as assumed above, $v_j = \left(\frac{\delta\kappa_j}{\delta\omega_j}\right)^{-1}$ is the group velocity of a j^{th} component at the central frequency. The first-order derivative includes the parametric bandwidth [57],

$$\Delta\nu_{parametric} = 0.53\sqrt{\Gamma/l_c}\,\Big/\left(c\left(1/v_s - 1/v_i\right)\right), \tag{6}$$

which is defined as the full width at half maximum (FWHM) of the gain spectrum $G(\omega_s)$. This represents the group-velocity mismatch (GVM) between the signal and idler in the nonlinear optical crystal that determines the bandwidth of an OPA. The GVM is an intrinsic effect for the ultrashort pulse interaction and determines the parametric bandwidth around 200–500 cm^{-1} in standard OPAs [57]. Previously reported femtosecond OPAs with collinear geometry suffered from this problem, and the shortest pulse durations were limited to 40 fs in the visible [20] and to 30 fs in the NlR [16, 21]. Broadening of the parametric bandwidth is essential for obtaining a tunable sub-10 fs light source. Sosnowski et al. [58] demonstrated a spectral broadening of the signal to about 800 cm^{-1} in the visible region by multistage amplification in which different spectral regions were amplified at each stage with slightly different crystal angles. However, this method has shortcomings, such as being rather complicated. In the late 1990s, novel NIR OPAs were reported [59, 60]. For example, Fournier et al. used the effectively cascading third-order process of second-harmonic generation of a signal and obtained self-compression to 20 fs signal pulses [59]. Nisoli et al. [60] demonstrated 14.5 fs signal pulse generation around 1.5 μm using an ultrashort 18 fs pump source from a Ti:sapphire amplifier followed by a hollow-fiber compressor. Both methods seem to be difficult and too sensitive to the pump energy. Third-order effects play an essential role in the characteristic pulse propagation in their schemes. Simpler and more robust methods are strongly desired for shorter pulse generation.

3.1 Noncollinear-optical-parametric amplification (NOPA)

In a noncollinear geometry, phase mismatch is expressed with more parameters than in the collinear geometry. Angles α and β are wavelength dependent and are expanded around the central frequency as

$$\cos\alpha = \cos\alpha_0 - \sin\alpha_0\left(\frac{\delta\alpha}{\delta\omega_s}\right)\Delta\omega_s - \frac{1}{2}\cos\alpha_0\left(\frac{\delta^2\alpha}{\delta\omega_s^2}\right)_0(\Delta\omega_s)^2 + \ldots \qquad (7a)$$

$$\cos\beta = \cos\beta_0 - \sin\beta_0\left(\frac{\delta\beta}{\delta\omega_s}\right)\Delta\omega_s - \frac{1}{2}\cos\beta_0\left(\frac{\delta^2\beta}{\delta\omega_s^2}\right)_0(\Delta\omega_s)^2 + \ldots, \qquad (7b)$$

where the subscript 0 denotes the central value. From the phase-matching condition of Equation (1) we obtain

$$\kappa_p = \kappa_{s0}\cos\alpha_0 + \kappa_{i0}\cos\beta_0\,, \tag{8a}$$

$$\kappa_{s0}\sin\alpha_0 = \kappa_{i0}\sin\beta_0\,. \tag{8b}$$

By substituting Equations (7) and (8) into (4) we can expand the phase mismatch as

$$\Delta\kappa = -\left[\frac{\cos\alpha_0}{v_s} - \frac{\cos\beta_0}{v_i} - \kappa_{s0}\sin\alpha_0\left(\frac{\partial\alpha}{\partial\omega_s}\right)_0 + \kappa_{i0}\sin\beta_0\left(\frac{\partial\beta}{\partial\omega_i}\right)_0\right]\Delta\omega_s + \ldots \tag{9}$$

Thus, the first-order coefficient can include the dispersion of the noncollinear angles. It means that the signal-idler–group-velocity mismatch in (6) can be modified by the wavelength-dependent noncollinear angles. If the condition

$$\frac{\cos\alpha_0}{v_s} - \frac{\cos\beta_0}{v_i} - \kappa_{s0}\sin\alpha_0\left(\frac{\partial\alpha}{\partial\omega_s}\right)_0 + \kappa_{i0}\sin\beta_0\left(\frac{\partial\beta}{\partial\omega_i}\right)_0 = 0 \tag{10a}$$

is satisfied, then the first-order phase mismatch is eliminated and extremely broadband phase matching is expected. The corresponding condition for the component perpendicular to the pump can be derived in the same way as

$$\frac{\sin\alpha_0}{v_s} + \frac{\sin\beta_0}{v_i} + \kappa_{s0}\cos\alpha_0\left(\frac{\partial\alpha}{\partial\omega_s}\right)_0 + \kappa_{i0}\cos\beta_0\left(\frac{\partial\beta}{\partial\omega_i}\right)_0 = 0\,. \tag{10b}$$

We can define the group-velocity matching in the noncollinear geometrical configuration by Equations (10a) and (10b). For a conventional collinear geometry ($\alpha = \beta = 0$), this condition is satisfied only when

$$v_s = v_i \tag{11}$$

is fulfilled. This condition is only satisfied for the case of the degeneracy $\left(\omega_s = \omega_i = \omega_p/2\right)$ in a type-I interaction ($e \rightarrow o + o$ or $o \rightarrow e + e$). In a type-II interaction ($e \rightarrow o + e$ or $o \rightarrow o + e$) the GVM is usually larger than that in a type-I interaction because of the large birefringence in the crystals [22, 57]

used in type II interactions. In a noncollinear geometry, the angular dispersion can eliminate the GVM and a broadband phase matching can be attained. The schematic of this configuration is shown in Figure 6-2.

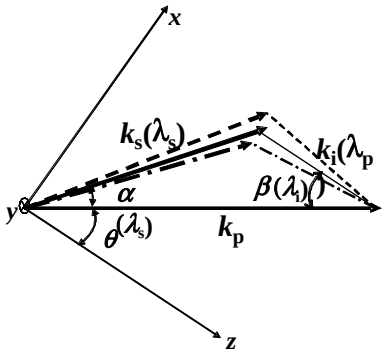

Figure 6-2. Signal-idler–group-velocity matching in an OPA nonlinear crystal with a general geometry. The wave vectors of the pump (k_p), signal ($k_s(\lambda)$), and idler ($k_i(\lambda_i)$) are shown in the gain crystal. The angles $\alpha(\lambda_s)$ and $\beta(\lambda_i)$ are internal noncollinear angles between pump and signal beams and between pump and idler beams, respectively. Coordinates *x*, *y*, and *z* and angle θ denote the crystal axes and angle between the optical axis of the crystal and a pump beam, respectively.

The angular dispersions satisfying this condition are calculated from (10) as

$$\left(\frac{\partial\alpha}{\partial\omega_s}\right)_0 = \frac{\nu_s^{-1}\cos(\alpha_0+\beta_0)-\nu_i^{-1}}{\kappa_{i0}\sin(\alpha_0+\beta_0)} \tag{12a}$$

$$\left(\frac{\partial\beta}{\partial\omega_i}\right)_0 = \frac{\nu_i^{-1}\cos(\alpha_0+\beta_0)-\nu_s^{-1}}{\kappa_{i0}\sin(\alpha_0+\beta_0)}\ . \tag{12b}$$

This kind of phase matching is well known as achromatic phase matching [58, 59] and has been used to obtain broadband wavelength conversion of ultrashort pulses [23, 60-62].

For practical applications of the amplified signal or generated idler, it is better to remove the angular dispersion. Thus we consider the case where the signal has no angular dispersion ($\alpha=\alpha_0$). The schematic is shown in (Figure 6-2). For $\alpha=\alpha_0$, (12) yields the simple group-velocity matching condition

$$\nu_s = \nu_i\cos(\alpha+\beta), \tag{13}$$

with

$$\frac{\partial\beta}{\partial\omega_i} = -\frac{1}{\kappa_i \cos\beta}\left(\frac{\sin\alpha}{v_s} + \frac{\sin\beta}{v_i}\right) = \frac{\tan(\alpha+\beta)}{\kappa_i v_i}, \tag{14}$$

where the subscript 0 is dropped for simplicity. The physical meaning of this condition can be stated as the projection of the idler group velocity on the signal direction is equal to the signal group velocity. The phase mismatch in Equation (9) can then be rewritten

$$\Delta\kappa = -\frac{\cos(\alpha+\beta)}{\cos\beta}\left(\frac{1}{v_s} - \frac{1}{v_i\cos(\alpha+\beta)}\right)\Delta\omega_s + \ldots. \tag{15}$$

Group-velocity matching is satisfied at the expense of the collimation of the idler beam. This means that the angular dispersion of the idler given by Equation (12) absorbs the group-velocity mismatch between the signal and idler. We use the term "signal-idler–group-velocity matching" in this special case. For simplicity, the generalized group-velocity matching is called "achromatic phase matching" hereafter.

Under the condition of a small noncollinear angle α, which is satisfied in many experimental situations, then $\frac{\cos(\alpha+\beta)}{\cos\beta} \approx 1$ can be used. It is convenient to use the general group-velocity mismatch defined as:

$$\mathrm{GVM}_{s-i} = \frac{1}{v_s} - \frac{1}{v_i\cos(\alpha+\beta)}. \tag{16}$$

The GVM between the pump and signal, which limits the interaction length in the crystal, is [27]

$$\mathrm{GVM}_{p-s} = \frac{1}{v_p} - \frac{1}{v_s\cos\alpha}. \tag{17}$$

As clearly seen from Equations (16) and (17), both GVMs are dependent on the noncollinear angle α. Each of the GVMs can be eliminated by selecting a geometrical arrangement satisfying Equation (16) or (17). Group-velocity matching between the pump and signal or between the signal and idler using noncollinear geometry in the case of $v_s > v_i$ has been reported; an order-of-

magnitude longer interaction length than in the collinear geometry was also obtained [27-29]. Our current interest is the signal-idler–group-velocity matching, which is possible if $\nu_s > \nu_i$. The bandwidth is broadened by more than tenfold and only limited by the group-velocity dispersion (GVD, as indicated in Equation (5) [57]; ultrashort pulse generation is thus expected.

4. SIGNAL-WAVELENGTH-INSENSITIVE PHASE MATCHING

In this section, we discuss signal-wavelength-insensitive phase matching or, in other words, broadband phase-matching. Recently, a simple expression for the phase-matching angle for different collinear and noncollinear type-I nonlinear-optical interactions in a negative uniaxial crystal was presented [63]. The phase matching and the energy-conservation conditions among the interacting beams are

$$k_1^e = k_2^0 + k_3^0, \tag{18}$$

$$\omega_1 = \omega_2 + \omega_3. \tag{19}$$

Here, k_i and ω_t (λ_i) are the wave vector and the frequency (wavelength), respectively, of i-th beam, and i = 1, 2, and 3. Solving Equations (18) and (19), we obtain the following expression for the phase-matching angle θ that is defined as the internal angle made by the extraordinary (e) polarized pump beam with the optic axis of the crystal:

$$\theta = \cos^{-1}\sqrt{\frac{\left(A^e/Y\right)^2 - 1}{\left(A^e/A^O\right)^2 - 1}}. \tag{20}$$

Here,

$$Y = \sqrt{\left[\left(k_2^o\right)^2 + \left(k_3^o\right)^2 + 2k_2^o k_3^o \cos\psi\right]}, \tag{21}$$

$$\psi = \alpha + \beta, \tag{22}$$

$$\beta = \sin^{-1}[(k_2^o k_3^o)\sin\alpha], \tag{23}$$

and $A^o = 2\pi(n_1^o/\lambda_1)$, $A^e = 2\pi(n_1^e/\lambda_1)$, $k_2^o = |\boldsymbol{k}_2^o| = 2\pi(n_2^o/\lambda_2)$, and $k_3^o = |\boldsymbol{k}_3^o| = 2\pi(n_3^o/\lambda_3)$; n_1, n_2, and n_3 are refractive indices of the three interacting radiations with wavelengths λ_1, λ_2, and λ_3. The superscripts *o* and *e* correspond to the ordinary and extraordinary polarizations, respectively, and α *(*β*)* is the noncollinear angle between the pump and the signal (idler) beams. Here k_2^o and k_3^o are the wave numbers corresponding to the signal and idler beams, respectively. *Y* is defined as the 'average' wave number of the signal and idler beams parallel to the pump beam. Considering the phase matching along the direction perpendicular to $\boldsymbol{k}_1$, Equation (23) is obtained. In the case of monochromatic pump, from Equation (20) we observe that the phase-matching angle θ will be independent (to first order) of the signal wavelength or signal frequency (ω_2) if $\partial\theta/\partial\omega_2 = 0$, for any value of ω_2. In Equation (20), all the parameters except *Y* are independent of ω_2. Therefore, the condition may be expressed as follows:

$$\partial Y/\partial\omega_2 = 0. \tag{24}$$

It can be shown easily that

$$Y = k_2^o \cos\alpha + k_3^o \cos\beta\,. \tag{25}$$

If the incident angle of the tunable seed beam has no frequency or, equivalently, wavelength dependency, the noncollinear angle α between the pump and tunable seed pulses will remain unchanged even with the change of the signal frequency, i.e., $\partial\alpha/\partial\omega_2 = 0$. From Equations (24) and (25)

$$(\cos\alpha/v_{g2} - \cos\beta/v_{g3}) - k_3^o\sin\beta(\partial\beta/\partial\omega_2) = 0, \tag{26}$$

where, $v_{gi} = \partial\omega_i/\partial k_i$, is the group velocity of the *i*-th beam (i = 2 and 3) with frequencies of ω_i. To obtain Equation (26), we have used $\partial\omega_2 = -\partial\omega_3$, since ω_1 = constant because the pump is monochromatic. From Equation (23)

$$k_3^o \sin\beta = k_2^o \sin\alpha\,. \tag{27}$$

Differentiating Equation (27) with respect to ω_2 and considering $\partial\alpha/\partial\omega_2 = 0$ and $\partial\omega_2 = -\partial\omega_3$, it can be shown that $\partial\beta/\partial\omega_2 = (\sin\alpha/v_{g2} + \sin\beta/v_{g3})/(k_3^o\cos\beta)$. Substituting $\partial\beta/\partial\omega_2$ in Equation (26) and after some algebraic simplification, we get $(\cos\psi/v_{g2} - 1/v_{g3})/\cos\beta = 0$, which is equivalent to

$$v_{g2} = v_{g3} \cos\psi. \tag{28}$$

Equation (28) can also be derived [31] by equating the first-order derivative of the phase mismatch with respect to ω_2 to zero, assuming a monochromatic pump and setting $\partial\alpha/\partial\omega_2 = 0$. Using this method, we found that for a NOPA, the effective inverse group-velocity mismatch between the signal and the idler pulses [31]

$$\mathrm{GVM}_{2-3} = [1/v_{g2} - 1/(v_{g3}\cos\psi)]. \tag{29}$$

We observe from Equation (29) that GVM_{2-3} can be eliminated if Equation (28) is satisfied. Thus the condition given by Equation (28) is considered to be the requirement for group-velocity matching in a NOPA [31]. Therefore, with earlier methods [31], it can be shown only implicitly that Equation (28) is the condition for the insensitivity of the phase-matching angle with respect to the variation of signal frequency or wavelength. However, the derivation above is straightforward and simple starting from the expression of the phase-matching angle θ. We show explicitly that to achieve the insensitivity of the phase-matching angle with respect to the variation of signal frequency or wavelength of the NOPA, Equation (28) must be satisfied, i.e., the components of the group velocities of the idler beams with a broad spectrum along the signal direction must be equal to that of the corresponding signal beam. We studied the optical parametric properties of a relatively recently developed NLO crystal LB4 and found that Equation (28) is also satisfied if this crystal is employed as a NLO amplifier crystal in a 395 nm pumped type-I NOPA with a particular value of the noncollinear angle α [63].

5. GROUP-VELOCITY MATCHING IN β-BAB_2O_4

This section describes achromatic phase matching in a BBO crystal, which is widely used as the gain crystal in an OPA. A BBO crystal has the advantages of broad tunability, a high damage threshold, and a large nonlinear coefficient [57]. A type-I ($e \rightarrow o + o$) OPA is more suited to ultrashort pulse generation than a type-II ($e \rightarrow o + e$) OPA because of the smaller GVM and larger effective nonlinear coefficient [22, 57, 60] in the former case. From Equation (8), the angle θ between the pump beam and the z axis (optic axis) and the idler noncollinear angle β satisfying the type-I phase matching are respectively

$$\vartheta(\lambda_{s,}\alpha)=\cos^{-1}\left\{\frac{1}{\sqrt{n_0^{-2}(\lambda_p)-n_e^{-2}(\lambda_p)}}\times\right.$$

$$\left.\sqrt{\frac{1}{\lambda_0^2\left(n_0(\lambda_s)\cos\alpha/\lambda_s+\sqrt{(n_0(\lambda_i)/\lambda_i)^2-(n_0(\lambda_s)\sin\beta/\lambda)^2}\right)^2}-\frac{1}{n_c^2(\lambda_p)}}\right. \quad (30a)$$

$$\beta(\lambda_s,\alpha)=\sin^{-1}\left(\frac{n_0(\lambda_0)}{n_0(\lambda_i)}\frac{\lambda_i}{\lambda_s}\sin\alpha\right). \quad (30b)$$

Here the three wavelengths (λ_j 's) satisfy the relation, $\lambda_i=\left(\lambda_p^{-1}-\lambda_s^{-1}\right)^{-1}$, and n_o and n_e are the refractive indices of the ordinary and extraordinary rays, respectively. The wavelength dependency of the refractive indices is obtained by the Sellmeier equations.

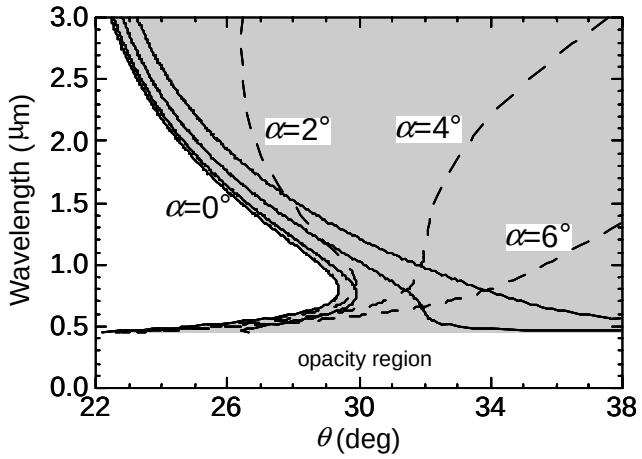

Figure 6-3. Theoretical phase-matching curves. Phase-matched probe wavelength dependence on the angle θ between the crystal axis Z and the pump beam in a type-I BBO OPA pumped at 395 nm with several different values of the signal noncollinear angle α. The signal branches (solid curves) and idler branches (dashed curves) are shown. The area in gray indicates the region where the achromatic phase matching is possible. The opacity region indicates that the OPA gain cannot be obtained because of the corresponding idler absorption.

The curves of $\theta(\lambda_s, \alpha)$ for various α with pump wavelength at 395 nm are shown in Figures 6-3 and 6-4. There are two branches corresponding to the signal and idler in the phase-matching curve for each non-zero α. These figures show that the most characteristic feature of the phase-matching curve is the broad spectral range. The region filled in gray in Figure 6-3 can satisfy the phase-matching condition by a noncollinear interaction. For a given θ, the signal and idler waves can be simultaneously emitted in a broad range of wavelength as shown in Figure 6-5. For a smaller angle between the pump beam and the crystal axis $\theta < 29.4°$, the range of the spectrum is partially limited, whereas for $\theta > 29.4°$, optical modes extending from 450 nm to 3 μm are excited. This limit is due to the absorption of the idler in the crystal. The broad bandwidth can be explained in terms of noncollinear configuration with an extended group-velocity matching condition.

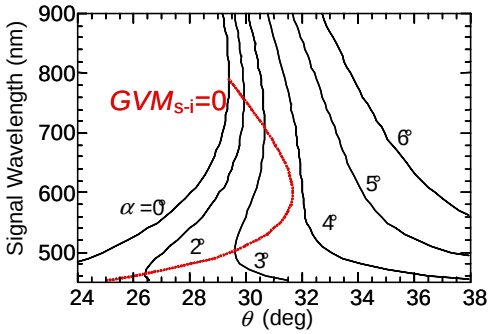

Figure 6-4. Signal branches of the theoretical phase-matching curves magnified in a wavelength region between 450 and 900 nm. The gray curve indicates the signal-idler–group-velocity matching points.

By utilizing a noncollinear geometry, group-velocity matching can take place for λ_s < 790 nm, as indicated by a dashed curve in Figure 6-4. The wavelength dependence of α that yields $\mathrm{GMV}_{s-i} = 0$ is calculated. It is found that over a spectral range broader than 100 nm, the noncollinear angle of α needed for phase matching varies from $3.7°$ only by less than $0.1°$. A broad plateau at $\theta = 31.5 \pm 0.1°$ between 520 to 710 nm appears in the phase-matching curve for $\alpha = 3.7°$, as presented in Figure 6-6.

Figure 6-7 shows parametric gain curve given by Equation (3) calculated for the configuration of $\theta = 31.5°$ with effective angular dependent nonlinear coefficient $d_{eff} = 1.6 \cos\theta$ pm/V [64] and with the pump intensity level of $\Phi = 50$ GW/cm^2. The gain extends the extremely broadband in the visible and NIR range from 520 to 750 nm with a small intensity variation and structure. The bandwidth reaches a breadth of 160 THz (5300 cm^{-1}), and

from the Fourier transform of the gain spectrum shortest possible pulse width is estimated to be 4.4 fs. Note again that the idler waves are also generated with the same broad bandwidth in the NIR with the angular dispersion to be phase-matched with the broad spectrum of the signal waves (see Figure 6-6).

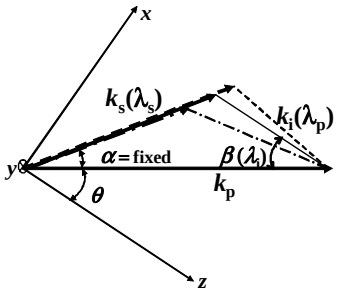

Figure 6-5. Signal-idler–group-velocity matching in an OPA with a special geometry of constant pump-signal angle (α = fixed). The wave vectors of the pump (k_p), signal [$k_s(\lambda_s)$], and idler [$k_i(\lambda_i)$] are shown in the gain crystal. The angles α and $\beta(\lambda_i)$ are internal noncollinear angles between pump and signal beams and pump and idler beams, respectively. Coordinates *x*, *y*, and *z* denote the crystal axes and *q* is the angle between the optical axis of the crystal and the pump beam.

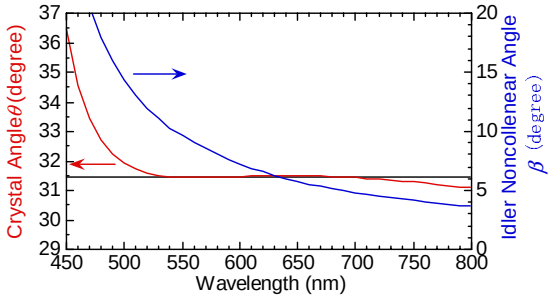

Figure 6-6. Noncollinear phase-matching curves. Wavelength dependence of pump incident angle θ and idler noncollinear angle β in the case of the pump-signal noncollinear angle of α = 3.7°.

These features indicate that a NOPA is a promising light source for generating ultrashort pulses over a wide visible and NIR range in a sub-10 fs regime. In the present work this characteristic signal-idler group-velocity matched interaction is focused on and the applicability to the ultrashort pulse generation is extensively investigated and explored.

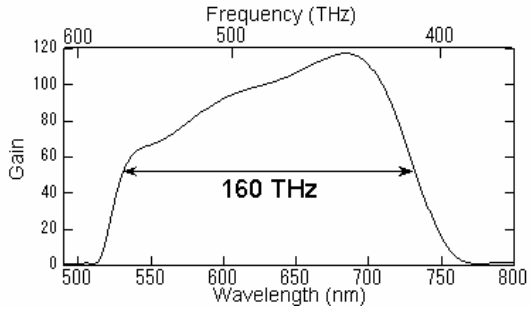

Figure 6-7. Wavelength dependence of the parametric gain [Equation (3)] in the type-I NCPM for the pump-signal noncollinear angle of $\alpha = 3.7°$. Here the experimental parameters $L_c = 1$ mm and $\Phi = 50$ GW/cm^2 are used.

6. FEMTOSECOND NOPA BASED ON β-BAB_2O_4

6.1 Broadband amplification of a single-filament continuum

Figure 6-8 shows the experimental setup for the noncollinear-phase-matched OPA (NOPA) developed in our group. The center wavelength, pulse energy, and duration of the regenerative amplifier pulse Ti:sapphire laser are about 790nm, 300 μJ, and 120 fs, respectively. The second harmonic at 395 nm is generated with a 1 mm thick BBO crystal by type-I phase matching with a cut angle of $\Phi = 29.4°$. The second harmonic generated with a 100 μJ pulse energy is used as a pump. The pulse width of the second harmonic is estimated to be 150 fs by the cross-correlation trace with the fundamental pulse. After passing through a delay line for synchronization, the pump beam is telescoped to obtain a peak intensity of ~300 GW cm^{-2} and pumps a 1 mm thick BBO crystal (type I, $\Phi = 30°$). The small beam diameter of 0.5 mm is used to suppress the effect of the pulse-front tilting [29]. The crystal is placed with the *xz*-plane lying in the plane of the page, and the polarization of the pump beam is in the plane as an *e*-ray. The thickness of the BBO crystal is determined so that the temporal walk-off due to GVM_{p-s} (~100 fs/mm) is well below the duration of the pump pulse.

A small fraction of the pulse energy (1–2 μJ at 790 nm) is focused onto a 2 mm thick sapphire plate and converted to a single-filament continuum to be used as the signal beam [19-21, 65]. The continuum is obtained by carefully adjusting the incident pulse energy to be only slightly higher than the threshold of continuum generation. The stabilities of the intensity and spectrum and the spatial coherence along the cross section are both excellent

and suited to be used as the seed of an OPA. The spectrum of the single-filament continuum covers a broad spectral range from 450 nm to longer than 1000 nm. There is a strong spike around 790 nm because of the fundamental. Outside this region, the spectrum is smooth and flat, i.e., well-suited for obtaining a smooth, short pulse without temporal structure because of the Fourier-transformation relation.

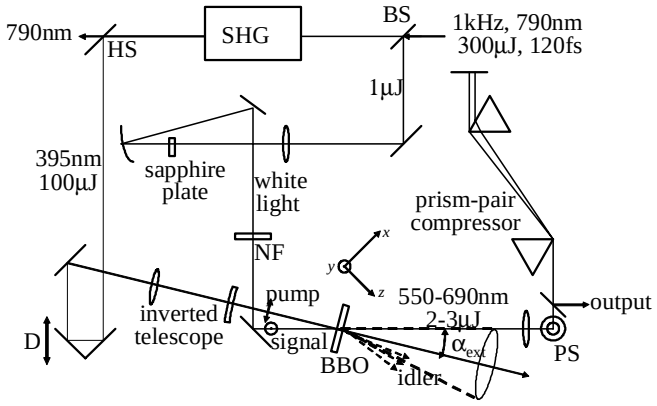

Figure 6-8. Experimental setup for the noncollinear-phase-matched OPA (NOPA). SHG: nonlinear crystal for second-harmonic generation; BS: beam splitter; HS: fundamental and second-harmonic separator; NF: notch filter centered at 800 nm; D: variable optical delay line; PS: periscope for rotating the polarization of the signal. The conelike parametric fluorescence with the minimized dispersion (see text) is illustrated with the external cone angle α_{ext}. Also illustrated are the crystal axes *x*, *y*, and *z*.

The sum-frequency pulse of the continuum at different wavelengths and 120 fs gate pulses at 790 nm are generated in a 0.5 mm thick BBO crystal (type I, $\Phi = 35°$) and probed to measure the group delay. The wavelength-dependent group delay is determined as the center-of-mass delay position in the corresponding cross-correlation trace [66]. The effect of dispersion in air is corrected using refractive index data in the literature [67]. Because of unsaturated self-phase modulation, the single-filament continuum does not posses a linear chirp across the whole range of the spectrum as is well known in optical fibers [1, 68]. The continuum beam is collimated and passes through a notch filter with a peak reflectance of -90% at 800 nm to reduce the fundamental pulse energy. It is then injected to propagate along the dispersion-minimized cone surface. The direction is in the *xz*-plane to be matched with the Poynting vector of the pump for the walk-off compensation [24]. A broad spectral range of the continuum is

noncollinearly amplified to a 2–3 μJ pulse energy with a short-term peak-to-peak fluctuation of about 10%.

6.2 Output properties

The center wavelength of the amplified signal depends sensitively on the delay of the pump pulse owing to the chirp of the continuum. By sweeping the delay line length by 50 μm, the signal is stably and continuously tuned from 550 to 690 nm, as shown in Figure 6-9. Each delay yields a broad spectrum with the bandwidth up to 2000 cm^{-1}. The small peaked structures around 530 nm and 760 μm are caused by the imperfect flatness of the phase-matching curve and the strong seed intensity near the fundamental, respectively. The notch filter suppresses the unexpected dual-wavelength amplification by decreasing the fundamental intensity and by separating temporally the two spectral components in the single beam.

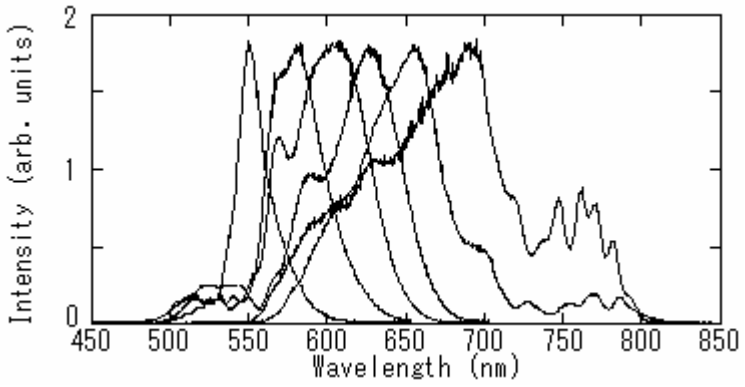

Figure 6-9. Spectra of the amplified signal. The center wavelength can be tuned only by scanning the delay line of the pump by 50 μm.

In this group-velocity-matched geometry, the idler is broadly generated and fan shaped with a spanning angle of about 7° in the *xz*-plane, which can be observed by the second harmonic of the idler generated from the same BBO crystal. Figure 6-10 shows the wavelength dependence of the external noncollinear angle with respect to the pump direction.

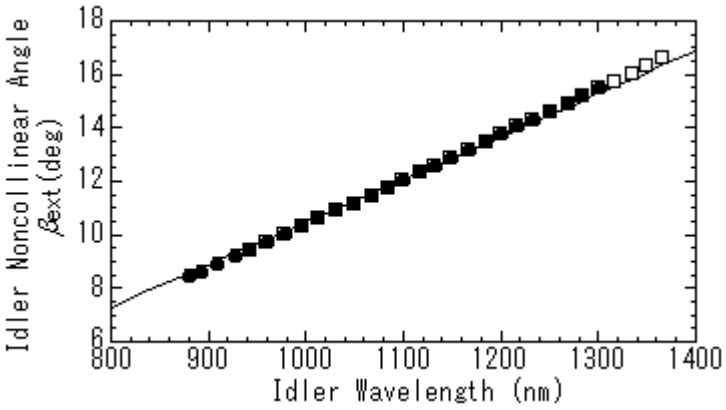

Figure 6-10. Angular-dispersion property of the idler. Measured external noncollinear angles β_{ext} with respect to the pump are shown (full circles at λ_s = 680 nm and open squares at λ_s = 600 nm). Also shown is the calculated phase-matching curve (solid curve).

Figure 6-11 shows the background-free intensity autocorrelation trace at 625 nm after the pulse compression. A 100 μm thick BBO (Type I, $\theta = 45°$) is used for the second-harmonic generation. The pulse compressor is a pair of BK7 Brewster prisms. It is optimized to a 37 cm slant length with a minimum insertion. By assuming that the envelope function is a sech^2 pulse, a least-squares best fit yields a pulse width of 14 fs. The spectral width of a 66 nm at FWHM corresponds to a temporal pulse width as short as 8 fs, indicating the pulse is far from transform-limited.

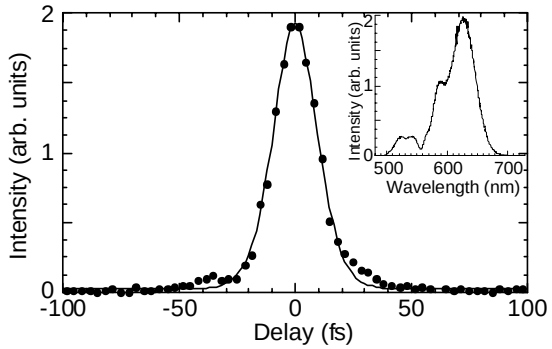

Figure 6-11. Intensity autocorrelation trace of the amplified signal after pulse compression (full circles). Autocorrelation measured with a second-harmonic generation crystal. The sech^2-fit (solid curve) pulse width is 14 fs (FWHM). The spectrum is shown in the inset.

The measured pulse width and time-bandwidth product over the pump-delay-tuning range are shown in Figure 6-12. The bandwidth is 700 cm^{-1} at a central wavelength of 550 nm. The bandwidth reaches up to 2000 cm^{-1} when the center wavelength is tuned to 690 nm. For both tunings, the pulse duration is sub-20-fs. The time-bandwidth product varies from 0.6 to 1.1, except at 550 nm where it is 0.4. In the long wavelength region, the spectrum spreads to beyond 800 nm with a non-negligible spike that degrades the time-bandwidth products to be larger than 1. The large time-bandwidth product is partly due to the pulse-width measuring apparatus that may overestimate the pulse width. The devices responsible could include the autocorrelator composed of a 100 μm thick BBO with a group-velocity mismatch of 40 fs at 600 nm and dispersive media, such as the lens and beam splitter. Using the 3.3 fs/step delay stage, the time resolution of the pulse stage used for the delay line also hinders accurate measurement of the pulse width. The wings on both sides observed in the autocorrelation traces also indicate higher-order dispersion. These problems have been eliminated as discussed below.

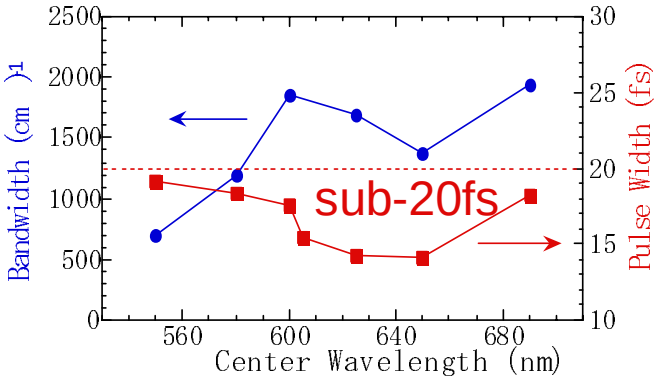

Figure 6-12. Wavelength dependence of the pulse width (full circles, $sech^2$-fit) and time-bandwidth product (full squares). The dotted line indicates the product of transform-limited pulse (0.315) in the case of a $sech^2$-pulse envelope.

The low conversion efficiency (-5%) can be improved by additional two-stage amplification, where both pump and signal beams are reflected back to the crystal twice by plane mirrors with small, vertical tilt angles. Even though the gain of the first stage is as high as 10^4, the gain in the succeeding stage is smaller than 3. The reason for this is not clear but may be caused by the degradation of the beam quality from higher-order nonlinear effects. The resultant pulse energy is up to about 8 μJ, resulting from a longer pulse duration (~18 fs) and an increased time-bandwidth product of larger than 1.

7. LIMITATION OF PULSE WIDTH BECAUSE OF PULSE-FRONT MISMATCH

The NOPA based on the signal-idler–group-velocity matching can generate sub-20 fs pulses with a wide tuning range in the visible regime. However, from the broad spectra with bandwidths exceeding 2000 cm^{-1}, much shorter pulses of less than 10 fs duration are expected. The unexpectedly large time-bandwidth products are partly due to the non-optimized autocorrelator and pulse compressor. However, it seems difficult to explain a broadening factor of 2–3 from the transform-limited duration.

The most probable reason for the broadening is pulse-front tilting, an intrinsic effect of the noncollinear interaction of ultrashort pulses [29]. In a noncollinear geometry, the pulse fronts of the pump and signal cannot overlap fully with each other. Noncollinear amplification causes a tilted gain volume in the signal beam (with a noncollinear angle α), resulting in the generation of a signal tilted by the same angle.

The external tilt angle γ is simply given from the relation

$$\tan\alpha = \frac{v_s}{c}\tan\gamma. \tag{31}$$

The group velocity v_s describes the refraction. The pulse-front tilting induces a temporal delay across the beam diameter d by

$$\delta t_{tilt} = \frac{d\tan\gamma}{c}, \tag{32}$$

which gives the maximum pulse broadening via time-space coupling. In a femtosecond NOPA, the tilting is a more serious problem than in a noncollinear OPO because an order-of-magnitude larger spot size is used in OPAs [29]. In the present NOPA for $\alpha = 3.7°$, the tilt angle of the exit signal is calculated to be $6.3°$ at 600 nm. The 0.5 mm diameter of the pump can cause broadening up to 180 fs. This value is too large to explain the present experiments. An interaction within a smaller cross section is taking place in the crystal (see Figure 6-13). The divergence of the amplified signal and the relatively low conversion efficiency support this explanation.

The most evident feature is the spatial chirp of the amplified signal. The pulse-front tilting is accompanied with a dispersion of the exit angle ε [47]

$$\frac{d\varepsilon}{d\lambda} = -\frac{\tan\gamma}{\lambda}. \tag{33}$$

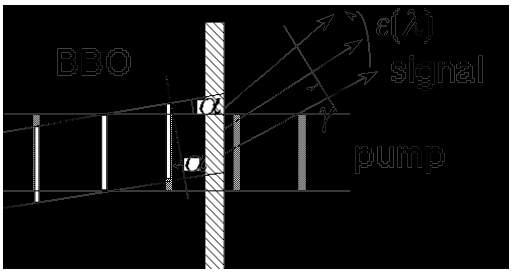

Figure 6-13. Schematic of the noncollinear interaction between the pump pulse and signal pulse. The crystal is on the left side. The volumes occupied by the pump pulse are shown by rectangular shapes elongated perpendicular to the propagation direction. Those for probe pulse are shown by closed gray rectangles. The gain volume introduced by the pump pulse causes the tilting of the wave front of the signal pulse by α in the crystal, resulting in the special and angular dispersions of the exiting signal pulse.

This feature originates from the inhibition of confined beam propagation with pulse-front tilting from the wave front, which is analogous to propagation through a prism [46] or grating [69]. The spatial chirp of the amplified signal is measured by scanning a 100 μm slit on the *xz*-plane over the beam cross section after collimating. The spectrum passing through the slit exhibits a position-dependent feature (Figure 6-14). The spatial chirp is estimated by a weighted average of the spectra. The result shows a characteristic quasi-linear dependence on the exit angle (Figure 6-15). The slope expected from the pulse-front tilting with a tilt angle of $\gamma = 6.3°$ shows an extremely good agreement with the measured spatial chirp.

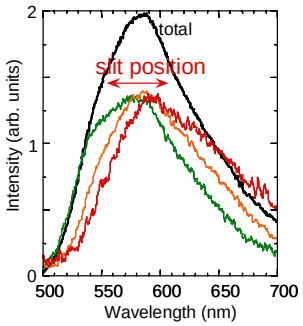

Figure 6-14. Spatial chirp of the signal spectra after passing through the vertical slit. Slits are located at three different positions (thin curves) after the nonlinear crystal of the NOPA. The case of the fully open slit is shown in bold.

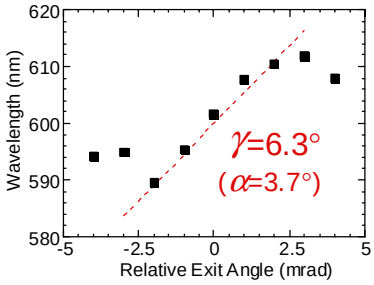

Figure 6-15. Dependence of the center-of-mass wavelength of signal spectra as a function of the relative exit angle. The dashed line indicates the expected spatial chirp of the signal tilted by 6.3°.

7.1 Tilted pump geometry for pulse front matching

The pulse-front matching geometry is schematically shown in Figure 6-16. The pump beam passes through a prism with incident and exit angles c1 and c2, respectively, causing the pulse-front to tilt. The tilt angle γ_{prism} just after the prism is [47]

$$\tan\gamma_{prism} = -\lambda\frac{d\varphi_2}{d\lambda} = -\frac{\sin\alpha_{apex}}{\cos\phi_1'\cos\phi_2}\lambda\frac{dn}{d\lambda'}, \qquad (34)$$

where n is the refractive index of the prism, α_{apex} is the prism apex angle, and ϕ_1' is the internal incident angle. The tilt angle is then decreased and the pulse width broadened during propagation in free space by the spectral lateral walk-off over the beam cross section [69]. The following telescope recollimates the spectral lateral walk-off and images the tilted fronts on the focal plane with a longitudinal magnification factor, $M = f_1 / f_2$, which gives the tilt angle γ_{ext} at the crystal position

$$\tan\gamma_{ext} = \frac{f_1}{f_2}\tan\gamma_{prism}. \tag{35}$$

The internal tilt angle γ_{int} is reduced by refraction with the relation $\tan\gamma_{\text{int}} = \frac{v_g}{c}\tan\gamma_{ext}$. The pulse-front matching condition $\gamma_{\text{int}} = \alpha$ is then

$$\tan\alpha = \frac{v_g}{c}\frac{f_1}{f_2}\tan\gamma_{prism}. \tag{36}$$

Because the spectral lateral walk-off spectrum (lateral dispersion) in the horizontal direction is insignificant in the present experimental conditions, the beam is nearly optimally recollimated in both horizontal and vertical directions. Since the spot size is reduced by the lateral magnification factor $M^{-1} = f_2 / f_1'$, the design of the telescope is essentially determined by the requirement of the efficient amplification and dimensional restriction.

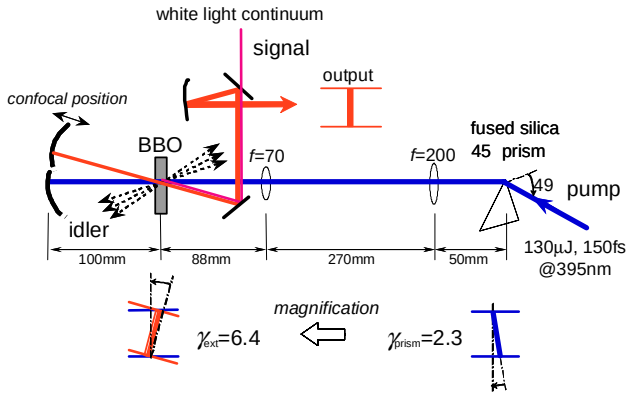

Figure 6-16. Geometry of pulse-front matching optical system. L: lens; M: mirror; CYM: cylindrical mirror; SM: spherical mirror; γ_{int}: internal tilt angle of pulse front of probe pulse in the nonlinear crystal of NOPA; γ_{ext}: external tilt angle of pulse front of probe pulse out of the nonlinear crystal of NOPA; BBO: nonlinear crystal (β-barium borate).

8. CHIRP PROPERTY OF SIGNAL

Because the seeded continuum has a chirp, the OPA is described as chirped-pulse amplification [70], and the amplified signal initially possesses the same chirp. In addition, the signal experiences phase distortion caused by the nonlinear effect in the BBO crystal and by the propagation through dispersive media such as the crystal, air, and the beam splitters in the frequency-resolved auto-correlation (FRAC). To attain a transform limited sub-10 fs pulse, accurate and precise phase correction is required over the whole spectral range.

The dependence of the phase $\phi(\omega)$ (ω: angular frequency) of the pulse on the wavelength is expanded around a central angular frequency ω_0

$$\begin{aligned}\phi(\omega) = \phi(\omega_0) + \left(\frac{d\phi}{d\omega}\right)_{\omega_0}(\omega-\omega_0) + \frac{1}{2}\left(\frac{d^2\phi}{d\omega^2}\right)_{\omega_0}(\omega-\omega_0)^2 \\ + \frac{1}{3!}\left(\frac{d^3\phi}{d\omega^3}\right)_{\omega_0}(\omega-\omega_0)^3 + \frac{1}{4!}\left(\frac{d^4\phi}{d\omega^4}\right)_{\omega_0}(\omega-\omega_0)^4 + \ldots\end{aligned} \tag{37}$$

The central wavelength may not be uniquely defined in the case of an extremely short pulse, which may have an irregular spectral shape with several spikes and a complicated structure.

The distortion of the pulse shape is not caused by the dispersion of the phase velocity but by that of the group velocity. Thus the group delay (GD)

$$\begin{aligned}T(\omega) = \frac{d\phi}{d\omega} = \left(\frac{d^2\phi}{d\omega^2}\right)_{\omega_0}(\omega-\omega_0) + \frac{1}{2}\left(\frac{d^3\phi}{d\omega^3}\right)(\omega-\omega_0)^2 \\ + \frac{1}{6}\left(\frac{d^4\phi}{d\omega^4}\right)(\omega-\omega_0)^3 + \cdots\end{aligned} \tag{38}$$

is used for pulse-propagation characterization. The constant term induces only a temporal shift during the pulse propagation without any shape change and is thus neglected in Equation (38). The coefficients of the expansion $\phi''(\omega), \phi'''(\omega_0), \phi''''(\omega_0), \cdots$ are called GD dispersion (GDD), third-order dispersion (TOD), fourth-order dispersion (FOD), and so on, respectively.

In the propagation through a medium with the path length l and wave vector $\kappa = (\omega) = n(\omega)\omega / c$, the phase shift $\phi(\omega) = \kappa(\omega)l$ yields

$$T(\omega) = \frac{l}{v_g(\omega)}, \tag{39}$$

which gives the intuitive representation of the GD. However, the concept of the GD can be represented in terms of wavelength-dependent optical paths $P(\omega)$ such as a grating pair [46] or prism pair [48].

Because the higher terms, such as a TOD and FOD, become significant in a sub-10 fs regime with a broad spectral range, a more precise phase correction is needed for the compression to the transform-limit.

8.1 Compression to the sub-5 fs regime

The GD compensation of the signal pulses using a pair of ultrabroadband-chirped mirrors (UBCMs) is performed taking into account the higher-order dispersion of the whole system including a $45°$ fused-silica prism pair, air along the optical path, and a beam splitter. By global optimization across the whole spectral range, the best compression is attained in the case of a 1 m slant length and a 6.0 mm internal path length of the prism pair at 650 nm and eight reflections in the four round trips between the two UBCMs in the pair, as shown in Figure 6-17.

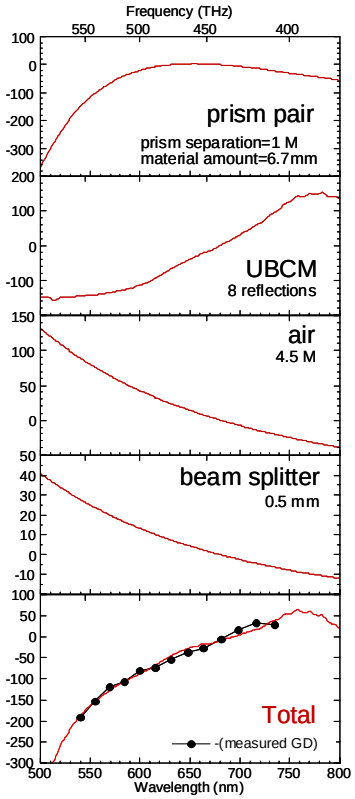

Figure 6-17. Group-delay property of the compressor. The group delays of the prism pair, the UBCM pair with four round trips (thin, solid curve), the prism pair (dashed curve), air with a 4.5 m path length through the air, the beam splitter in the FRAC, and the whole compressor system are shown from top to bottom. Also shown is the measured group delay of the signal (full circles) in the bottom box with the sign reversed.

To obtain the full-bandwidth amplification, the compressor is divided into two portions before and after the BBO crystal. The experimental setup for the sub-5 fs NOPA system is shown in Figure 6-18. The pre-compressor is composed of one UBCM pair in a single round-trip configuration, and the main compressor has another pair in a three round-trip configuration with other elements. The insertion of the UBCM pair before the crystal reduces the seed chirp to about 10 fs GD difference between 530 and 770 nm, and the inequality $\Delta T + \Delta T_{BBO} < \tau_p / 2 + (GMP_{p-s})_{MAX}$ is fulfilled.

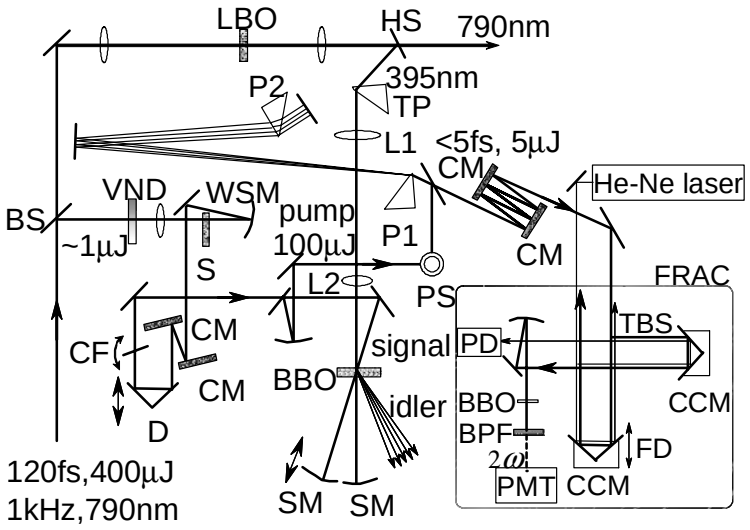

Figure 6-18. Schematic of the visible sub-5-fs pulse generator. L: lens; M: mirror; CYM: cylindrical mirror; SM: spherical mirror; BS: beam splitter; HS: harmonic separator; TP: prism for pulse-front tilting; L1, L2: lenses for the telescope; SMs: spherical mirrors (γ = 100 mm); VND: variable neutral-density filter; WSM: spherical mirrors (γ = 120 mm); CF: cut-off filter; D: optical delay line; PS: periscope; P1,P2: 45° fused silica prisms; and CCMs: corner-cube mirrors.

By tailoring the experimental conditions and parameters as described above, full-bandwidth amplification by the double-path amplifier has been achieved. As evident in the chirp properties of the signal and idler inspected, effects such as a SPM or a cascaded second-order process [71] seem to be weak under our experimental conditions. Therefore the reduction of the initial chirp effect does not significantly change the net pulse parameters, including the overall chirp property.

The pulse energy varies from about 6 to 7 μJ just after the BBO crystal; after the main compressor with about 70% throughput, it becomes about 5 μJ. The highest throughput of about 80% is obtained by using properly selected UBCMs. Then only the reflections on the surfaces of the prisms cause loss.

The spectrum of the signal is shown in Figure 6-19. The spectral shape depends on the positions of the delay lines, which are fixed to maximize the bandwidth. The FWHM is as broad as 240 nm, corresponding to 150 THz, and the transform-limited pulse width is calculated to be 4.4 fs. The bandwidth is slightly narrower than that reported in Reference [37]. The cut-off filter of the seed effectively suppresses the amplification around 790 nm where the chirp exhibits a large nonlinearity. The collimated seed-pump

beam interaction also avoids the spectral broadening of the signal caused by beam divergence [66] that is accompanied by an undesirable spatial chirp. Careful attention to both of these details is essential to obtain a signal compressible to the transform-limit.

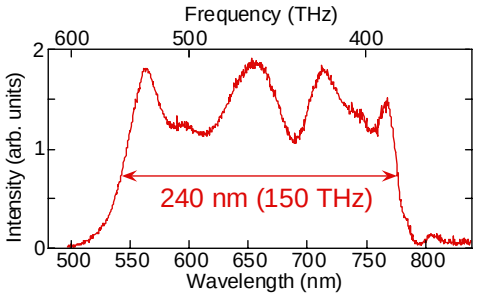

Figure 6-19. Spectrum of the signal pulses under a full-bandwidth operation.

The pulse shape is measured by FRAC. The pulse energy is appropriately reduced by adjusting the radius of open aperture of an iris. Figure 6-20 shows the FRAC trace of the signal after optimization of the parameters and alignment. The sech^2-fit pulse width is as short as 3.5 fs, which is shorter than the transform-limited width. Because of the significant modulation of the spectral intensity, such an assumption cannot give an accurate width [1]. In the present work the pulse width is estimated by Fourier-transformation of the spectrum including the wavelength dependence of the phase in two ways.

First, the phase is calculated from the properties of the measured group delay of the signal $T_{pulse}(\omega)$ and the group delay of the compressor $T_{compresssor}(\omega)$ (see Figure 6-17) yielding

$$\phi(\omega) = \int^{\omega} \left[T_{pulse}(\omega) + T_{compressor}(\omega)\right] d\omega. \tag{40}$$

The scattered values of the measured group delay are caused partly by the poor time resolution and by intensity fluctuation. The measured group delay is smoothed by fitting to a cubic-polynomial function. Using a calculated phase, the FRAC trace of the compressor output is then constructed and depicted by open circles in Figure 6-20.

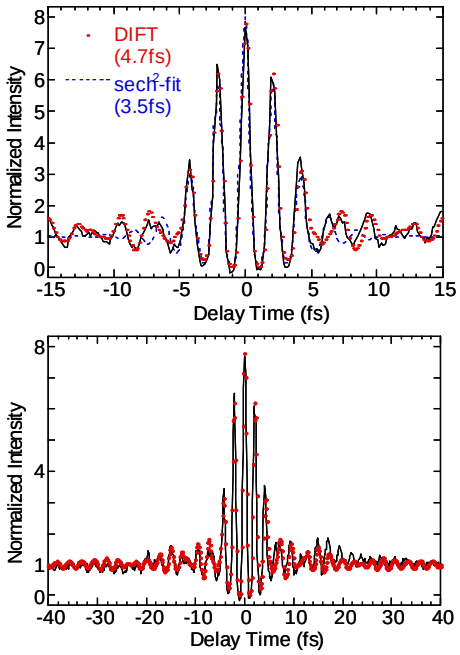

Figure 6-20. Frequency-resolved auto-correlation (FRAC) trace of the compressor output. Traces are (a) for $|\tau|$<15 fs and (b) for $|\tau|$<40 fs (τ: delay time). Measured trace (solid curve), calculated trace with measured group-delay (GD) of signal and of compressor (open circles), calculated trace from the FT of measured spectrum (full circles), and calculated trace using sech^2 with 3.5 fs width (dashed curve) are shown. The calculated pulse width is 4.7 fs, while that obtained by Fourier transformation of measured spectrum is 4.7 ±0.1 fs.

The second approach is to fit the measured FRAC trace with parameters describing the phase. The complicated wavelength dependence of the group delay of the UBCMs is included. The residual phase can be reasonably assumed to have a smooth property and is determined by fitting the trace to a cubic-polynomial function of the frequency [5, 6]. Because an autocorrelation is used, the direction of the time axis is not determined by this process alone. By comparison with the calculated phase mentioned above, the direction can be determined. The fitted FRAC trace is shown in Figure 6-20 with full circles.

Both phase profiles show similar behavior. The deviation is within $\pi/2$ radian over the whole spectral range from 510 to 790 nm. The oscillations are due to the group delay of the UBCMs. The large deviations in the regions of < 500 nm and > 800 nm are due to the limited bandwidth of the UBCMs. However, UBCMs are less effective for pulse-width broadening because the spectral intensity in these regions is weak. The difference between both phases is mainly caused by the uncertainty of the measured group delay

because of a lack of information in the whole spectral range. It is also difficult to determine the precise values of the compressor parameters such as the internal path length.

The calculated and fitted FRAC traces have nearly the same shapes and agree very well with the experimental trace even in the side wing regions. The estimated intensity profiles are shown in Figure 6-21. The calculated profile gives a 4.7 fs pulse duration, whereas the fitted one gives a 4.7 ± 0.1 fs pulse duration. The result indicates that the phase correction with the highest precision is attained using the prism-chirped mirror compressor; almost transform-limited pulses are obtained. It is the first demonstration that the UBCMS can be applied to the visible range over more than 200 THz. And, the electric field oscillates only for 2.2 cycles in the FWHM of the intensity profile.

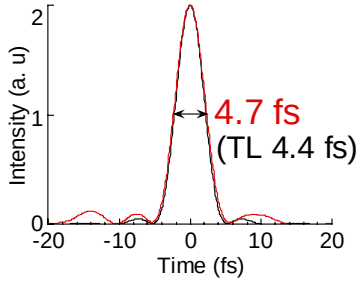

Figure 6-21. Intensity profile of the compressed pulse. The transform-limited pulse width determined by the spectrum is 4.4 fs (thin solid curve), whereas the calculated (thick solid curve) and Fourier-transform-fit to FRAC with phase parametric (dashed curve) pulse widths are 4.7 fs and 4.7 ± 0.1 fs, respectively.

The difference in the intensity profiles clearly indicates the limitation in extracting the pulse shape from a FRAC trace. The phase information is mainly included in the fringes of the side wings, which cannot be measured with high enough signal-to-noise ratios in many cases. Uncertainty results particularly in the shape of the trailing pulses. However, the pulse width, which is defined as the FWHM, is reasonably estimated by this method with a 0.1 fs accuracy. The pulse shape and phase can be precisely determined by other methods such as frequency resolved optical gating (FROG) [3].

9. SECOND-GENERATION NONCOLLINEAR PARAMETRIC AMPLIFIER

The NOPA we developed consists of three parts: The first element is a parametric amplifier with a gain bandwidth sufficient to support sub-4 fs operation. The second component is a grating-chirped-mirror compressor, used for rough group-delay compensation; it has a flexible mirror that allows for fine spectral phase adjustment. The third part comprises a pulse diagnostic set-up based on second-harmonic generation (SHG) FROG with feedback to a personal computer that also controls the actuators of the flexible mirror. An overview of the setup is presented in Figure 6-22. The system is pumped by a 120 fs, 1 kHz repetition rate regenerative amplifier [CPA1000 (Clark MXR)] that is seeded by a fiber laser oscillator (IMRA, Clark). We now address separately the design and functions of each stage of the setup.

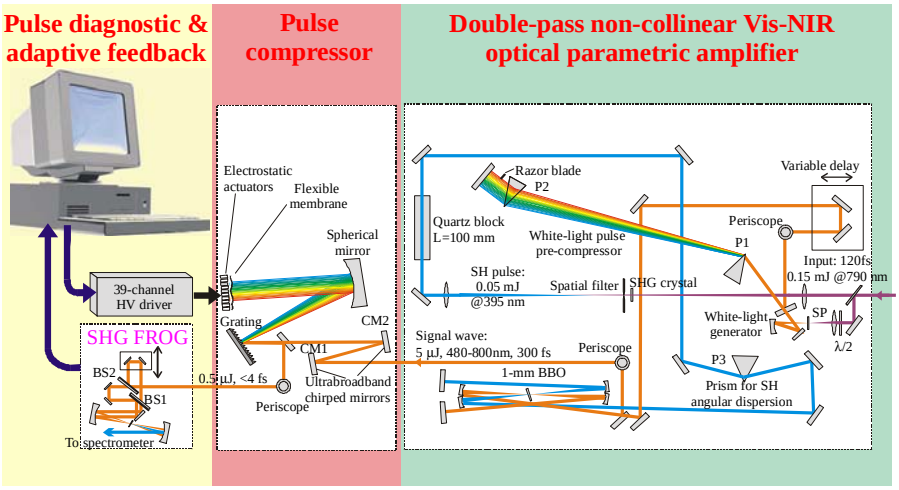

Figure 6-22. Schematic of experimental setup of sub-4 fs NOPA. λ/2: 800 nm wave-plate; SP: 2 mm sapphire plate; P1, P2: 45°quartz prisms; P3: 69° quartz prism (the distance from P3 to the NOPA crystal is 80 cm); CM1,2: ultrabroadband chirped mirrors; GR: 300 lines/mm ruled diffraction grating (Jobin Yvon); SM: spherical mirror, R = -400 mm; BS1,2: chromium-coated d = 0.5 mm quartz beam splitters; SHG crystal: 0.4 mm θ = 29° BBO (EKSMA); NOPA crystal: 1 mm θ = 31.5°BBO (Casix); and SHG FROG crystal: θ = 29° BBO wedge plate d = 5÷20 μm (EKSMA). Spherical mirrors around the NOPA crystal are R = -200 mm. Thick arrows on the left indicate the data flow from the pulse diagnostic setup (SHG FROG) and the feedback to the flexible mirror.

The discovery of "magic" phase-matching conditions in a Type I-BBO crystal pumped by a 400 nm light [26, 72] opened the door to producing

amplified visible pulses with a bandwidth of nearly 200 THz [36, 37, 41]. The uniqueness of this pumping arrangement comes from the fact that the pump inclination to the direction of the seed (~ 3.7°) matches almost perfectly the angle of birefringent walk-off between the *o* and *e* waves inside the crystal. As a result, BBO as long as 1–2 mm can be employed even in 5 fs NOPAs. The implications of noncollinear phase matching are well understood and discussed in numerous papers [26, 29, 31, 32, 34, 36-40, 66, 72].

We paid further attention to the subtleties of parametric amplification in a noncollinear configuration [36, 38], by considering the effect of pulse-front tilting of the signal wave on the ability to compress the signal into a sub-5 fs pulse. To prevent the tilting of the signal pulse in space, an effect that also results in angular dispersion of the amplified pulse, several researchers proposed to use a pump beam with a tilted wave front. This configuration, named pulse-front-matching, was implemented by sending the pump beam through a prism and adjusting the pulse tilt with a telescope consisting of two convex lenses [38, 41, 73].

We took care to find a balanced Mach-Zehnder interferometric autocorrelator [74] to characterize the NOPA pulses [38, 41, 42]. This particular autocorrelator does not have spatial resolution and, therefore, is insensitive to wave-front tilt. This does not necessarily mean the real pulse width does not suffer from broadening of the pulse width due to pulse-front tilting, however. The required spatial sensitivity can also be achieved by using an asymmetric number of reflections in the interferometer.

Together with the effect of pulse-front matching, the angular dispersion of the pump beam in the sub-5 fs NOPA is an important factor in terms of enhancing the phase-matching bandwidth. Even with relatively thick second-harmonic crystals (1–2 mm LBO or BBO) and comparatively long (120–150 fs) pulses from standard regenerative amplifiers employed to pump the NOPAs [37, 38, 41, 42], the resulting second-harmonic radiation has a bandwidth of several nanometers. Wide-bandwidth parametric amplification can subsequently be achieved by pointing the seed beam in a specific direction for each spectral component of the pump, as schematically shown in Figures 6-23 and 6-24. The adjustment of the pump beam dispersion, required for phase-matching optimization, is obtained by selecting the apex angle of a prism in the second-harmonic pathway [Figure 6-23(b)] and the distance from the prism to the focusing optic. The required second-harmonic (SH) dispersion

$$\delta\alpha(\lambda) = atan\left[\tan\left(\gamma(\lambda_0) - \gamma(\lambda)\right)\frac{l}{f}\right],, \tag{41}$$

where λ is the pump (SH) wavelength, λ_0 denotes the central component of the SH spectrum, l and f are the distance from the prism to the focusing optic and the focal distance, respectively. The exit angle of the SH beam behind the prism is

$$\gamma(\lambda) = asin\left[n(\lambda)\sin\left[\theta_{apex} - asin\left(\frac{\sin\gamma_0}{n(\lambda)}\right)\right]\right]. \tag{42}$$

In Equation (42), γ_0 is the angle between the SH beam and the normal to the input face of the prism (incidence angle onto the prism), θ_{apex} stands for the apex angle of the prism, and $n(\lambda)$ is the refractive index of glass.

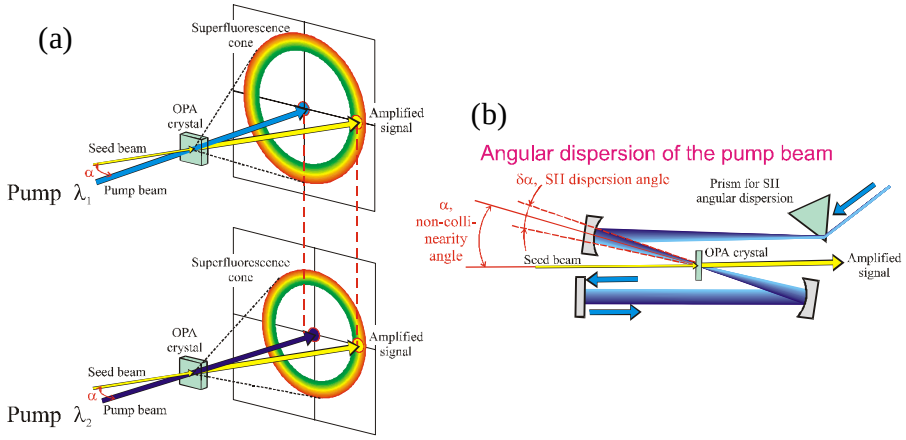

Figure 6-23. Extension of parametric bandwidth by adjusting the incidence angle of individual pump wavelengths onto a NOPA crystal. (a) Schematic representation of noncollinear pump geometry. (b) Second-harmonic dispersion adjustment based on the use of a prism and a focusing optic.

In our second-generation NOPA system, the distance between the Brewster-angled prisms for second-harmonic dispersion and a focusing mirror (Figure 6-22) is 80 cm. The radius of curvature for the concave mirror is R = -200 mm. Standard formalism for type I phase-matching in crystals [17] was used in this calculation to obtain the results depicted in Figure 6-24. We assumed that the efficiency of the parametric frequency conversion is not high. Thus we could disregard any pulse-reshaping effect that can lead to

an effective reduction of the group-velocity mismatch between the pump and signal waves because of a kind of nonlinear pulling effect in the reshaping process. As a result, we believe the data shown in Figure 6-24 represent a low estimate of the signal bandwidth that can be simultaneously phase-matched in the NOPA. The pairs of curves with dark shaded areas in between composing dark stripes in Figure 6-24 represent cases of individual pump wavelengths. The cases of wavelengths of 389, 392, and 395 nm are shown. The thickness of each dark stripe gives the FWHM of the angular phase matching [17] and is determined by the nonlinear interaction length, assumed to be equal to the crystal thickness of 1 mm. The whole shaded area in Figure 6-24 corresponds to the combined bandwidth produced by the entire second-harmonic spectrum, shown as a shaded contour in the inset.

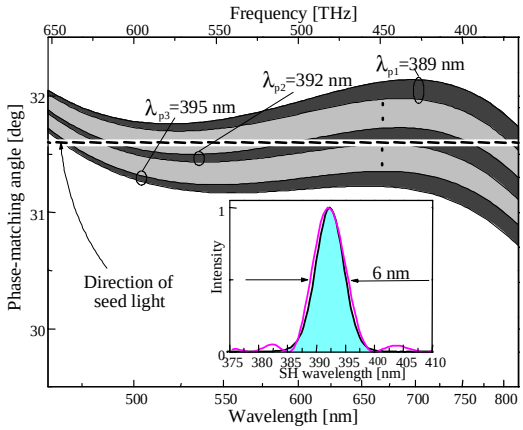

Figure 6-24. Phase matching in a 1 mm Type I BBO crystal, $\theta = 31.5°$. Dark-shaded contours indicate FWHM of the angular phase matching for individual monochromatic pump wavelengths after optimization of their incidence angles. Dashed line denotes the direction of the seed beam. Inset depicts experimentally measured second-harmonic spectrum used to pump the NOPA (shaded contour) and calculated conversion efficiency of a 0.4 mm Type I BBO second-harmonic-generation crystal.

To maximize the effect by employing the widest region of pump frequencies, we used a thinner, 0.4-mm, BBO for the frequency doubling of the fundamental 120 fs pulses. This crystal provides an ~30% conversion efficiency in contrast to the higher value of about 50% in the 1 mm BBO used in our first NOPA; however, it ensures a larger spectral width of the second harmonic. The corresponding frequency conversion efficiency is given in the inset to Figure 6-24 by a solid curve and indicates that this

crystal causes no significant reduction of the resulting second-harmonic bandwidth.

Analogous ideas about bandwidth extension have been applied in other parametric schemes. Angular dispersion of the frequencies in the fundamental beam has been used to obtain achromatic phase matching for second-harmonic generation [62], whereas a multipass OPA using slightly different beam directions in every pass [58] has been shown to dramatically broaden the resultant bandwidth of the amplified pulse. Recently, a single-stage OPA pumped by two noncollinear beams has also been demonstrated as an efficient means of boosting the spectral width [75].

Another method for obtaining extremely broad bandwidth with short pulses is to use a two-stage compressor. This device incorporates a flexible mirror for adaptive pulse shaping plus a simple and trustworthy feedback loop based on a one-dimensional spectral measurement. Our rapid numerical algorithm for adaptive control of the flexible mirror is superior to more complex search routines, which are less resistant to laser intensity fluctuations. The automated optimization results in the generation of two-cycle pulses with a carrier wavelength near 600 nm. The absence of deep modulation on the amplified spectrum in combination with adaptive phase correction lead to a high-quality temporal profile and allow the concentration of more than 90% of the pulse energy within a 7.5 fs time window.

10. CONCLUSIONS AND OUTLOOK

In this work, we report the design of a sub-5 fs visible–near-IR parametric amplifier with adaptive pulse tailoring that permits a 20-fold compression of the pump pulses from a standard Ti:sapphire chirped-pulse-amplification system. Whereas smooth parametric spectra were generated that correspond to 3.5 fs pulses (if ideally compressed), we managed to obtain 3.9 fs pulses after passing the signal beam through a hybrid compressor based on a diffraction-grating telescopic dispersion line, specially designed multilayer-dielectric-chirped mirrors, and a computer-controlled flexible mirror.

As has been shown in this chapter, efficient use of all pump frequencies leads to the broadening of the amplification band. One of the fundamental issues for further progress in the development of a NOPA with even shorter pulse duration is the difficulty with the pulse diagnostics. The type I phase-matching SHG FROG, employed in this work, is stretched to the limit because of the finite phase-matching bandwidth of the SHG crystal. Implementation of a heterodyne third-order FROG technique, based on

automatically phase-matched, frequency-resolved pump-probe in a transparent medium [76] may provide an excellent alternative.

We would like to mention another fascinating use of the NOPA technique. Remarkably, parametric amplifiers provide an alternative approach to the generation of few-cycle optical pulses by using multiple source spectra rather than a single one [77]. This becomes possible as a result of unique phase relations among signal, pump, and idler waves in a white-light-seeded NOPA [78]. Methods for obtaining monocycle pulses include merging the signal and idler spectra [38, 41, 42] or merging the spectra of the signal and the fundamental broadened around 800 nm [79] into a single, coherent bandwidth since the carrier-envelope phase [80] of those waves exhibit identical drift. Moreover, octave-spanning carrier-envelope–phase-locked infrared idler pulses [78] and carrier-envelope-phase–self-referenced visible signal pulses [81] from NOPAs have already been demonstrated. These developments are opening up the possibility of using NOPAs in field-sensitive applications of nonlinear optics [8, 81].

ACKNOWLEDGEMENTS

The author is grateful to Drs. A. Shirakawa, A. Baltuška, and P. Kumbakhar for their essential contributions to the work presented in this chapter. The work presented here was partly sponsored by the “Research for the Future” program of the Japan Society for the Promotion of Science (Grant No. JSPS-RFTF-97P-00101).

REFERENCES

[1] A. Baltuška, Z. Wei, M. S. Pshenichnikov, D. A. Wiersma, and R. Szipocs, Appl. Phys. B **65**, 175-188 (1997).

[2] A. Baltuška, Z. Y. Wei, M. S. Pshenichnikov, and D. A. Wiersma, Opt. Lett. **22**, 102-104 (1997).

[3] A. Baltuška, M. S. Pshenichnikov, and D. A. Wiersma, Opt. Lett. **23**, 1474-1476 (1998).

[4] M. Nisoli, S. DeSilvestri, and O. Svelto, App. Phys. Lett. **68**, 2793-2795 (1996).

[5] M. Nisoli, S. DeSilvestri, O. Svelto, R. Szipocs, K. Ferencz, C. Spielmann, S. Sartania, and F. Krausz, Opt. Lett. **22**, 522-524 (1997).

[6] M. Nisoli, S. Stagira, S. DeSilvestri, O. Svelto, S. Sartania, Z. Cheng, M. Lenzner, C. Spielmann, and F. Krausz, Appl. Phys. B **65**, 189-196 (1997).

[7] R. Szipocs, K. Ferencz, C. Spielmann, and F. Krausz, Opt. Lett. **19**, 201-203 (1994); R. Szipocs and A. Köházi-Kis, Appl. Phys. B **65**, 115-135 (1997); R. Szipocs and F. Krausz, Dispersive dielectric mirror, USA Patent 5734503 (1998).
[8] T. Brabec and F. Krausz, Rev. Mod. Phys. **72**, 545-591 (2000).
[9] G. P. Agrawal, *Nonlinear Optics* (Academic Press, San Diego, 2001).
[10] J. K. Ranka, R. S. Windeler, and A. J. Stentz, Opt. Lett. **25**, 25-27 (2000); J. K. Ranka, R. S. Windeler, and A. J. Stentz, Opt. Lett. **25**, 796-798 (2000).
[11] I. D. Jung, F. X. Kärtner, N. Matuschek, D. H. Sutter, F. Morier-Genoud, G. Zhang, U. Keller, V. Scheuer, M. Tilsch, and T. Tschudi, Opt. Lett. **22**, 1009-1011 (1997); Y. Chen, F. X. Kärtner, U. Morgner, S. H. Cho, H. A. Haus, E. P. Ippen, and J. G. Fujimoto, J. Opt. Soc. Am. B **16**, 1999-2004 (1999); U. Morgner, F. X. Kärtner, S. H. Cho, Y. Chen, H. A. Haus, J. G. Fujimoto, E. P. Ippen, V. Scheuer, G. Angelow, and T. Tschudi, Opt. Lett. **24**, 411-413 (1999); G. Steinmeyer, D. H. Sutter, L. Gallmann, N. Matuschek, and U. Keller, Science **286**, 1507-1512 (1999).
[12] R. K. Shelton, L. S. Ma, H. C. Kapteyn, M. M. Murnane, J. L. Hall, and J. Ye, Science **293**, 1286-1289 (2001); R. K. Shelton, S. M. Foreman, L. S. Ma, J. L. Hall, H. C. Kapteyn, M. M. Murnane, M. Notcutt, and J. Ye, Opt. Lett. **27**, 312-314 (2002).
[13] Z. Y. Wei, Y. Kobayashi, Z. G. Zhang, and K. Torizuka, Opt. Lett. **26**, 1806-1808 (2001).
[14] P. E. Powers, R. J. Ellingson, W. S. Pelouch, and C. L. Tang, J. Opt. Soc. Am. B **10**, 2162-2167 (1993).
[15] V. Petrov, F. Seifert, O. Kittelmann, J. Ringling, and F. Noack, J. Appl. Phys. **76**, 7704-7712 (1994); M. K. Reed and M. K. Steiner-Shepard, IEEE J. Quantum Electron. **32**, 1273-1277 (1996).
[16] K. R. Wilson and V. V. Yakovlev, J. Opt. Soc. Am. B **14**, 444-448 (1997).
[17] V. G. Dmitriev, G. G. Gurzadyan, and D. N. Nikogosyan, *Handbook of Nonlinear Optical Crystals* (Springer-Verlag, Berlin, 1997).
[18] F. Seifert, V. Petrov, and F. Noack, Opt. Lett. **19**, 837-839 (1994); M. Nisoli, S. De Silvestri, V. Magni, O. Svelto, R. Danielius, A. Piskarskas, G. Valiulis, and A. Varanavicius, Opt. Lett. **19**, 1973-1975 (1994).
[19] M. K. Reed, M. K. Steiner-Shepard, and D. K. Negus, Opt. Lett. **19**, 1855-1857 (1994).
[20] M. K. Reed, M. S. Armas, M. K. Steiner-Shepard, and D. K. Negus, Opt. Lett. **20**, 605-607 (1995).
[21] V. V. Yakovlev, B. Kohler, and K. R. Wilson, Opt. Lett. **19**, 2000-2002 (1994).
[22] S. R. Greenfield and M. R. Wasielewski, Opt. Lett. **20**, 1394-1396 (1995).
[23] S. Takeuchi and T. Kobayashi, J. Appl. Phys. **75**, 2757-2760 (1994).
[24] E. S. Wachman, W. S. Pelouch, and C. L. Tang, J. Appl. Phys. **70**, 1893-1895 (1991).
[25] Q. Fu, G. Mak, and H. M. van Driel, Opt. Lett. **17**, 1006-1008 (1992); A. Shirakawa, H. W. Mao, and T. Kobayashi, Opt. Commun. **123**, 121-128

(1996); D. T. Reid, C. McGowan, M. Ebrahimzadeh, and W. Sibbett, IEEE J. Quantum Electron. **33**, 1-9 (1997).

[26] G. M. Gale, M. Cavallari, T. J. Driscoll, and F. Hache, Opt. Lett. **20**, 1562-1564 (1995).

[27] P. Di Trapani, A. Andreoni, G. P. Banfi, C. Solcia, R. Danielius, A. Piskarskas, P. Foggi, M. Monguzzi, and C. Sozzi, Phys. Rev. A **51**, 3164-3168 (1995).

[28] P. Di Trapani, A. Andreoni, P. Foggi, C. Solcia, R. Danielius, and A. Piskarskas, Opt. Commun. **119**, 327-332 (1995).

[29] P. Di Trapani, A. Andreoni, C. Solcia, P. Foggi, R. Danielius, A. Dubietis, and A. Piskarskas, J. Opt. Soc. Am. B **12**, 2237-2244 (1995).

[30] J. Wang, M. H. Dunn, and C. F. Rae, Opt. Lett. **22**, 763-765 (1997).

[31] A. Shirakawa and T. Kobayashi, IEICE Trans. Electron. **E81C**, 246-253 (1998).

[32] A. Shirakawa and T. Kobayashi, App. Phys. Lett. **72**, 147-149 (1998).

[33] F. Hache, M. Cavallari, and G. M. Gale, in *Ultrafast Phenomena X*, edited by P. F. Barbara, J. G. Fujimoto, W. H. Knox and W. Zinth (Springer-Verlag, Berlin, 1996).

[34] T. Wilhelm, J. Piel, and E. Riedle, Opt. Lett. **22**, 1494-1496 (1997).

[35] G. Cerullo, M. Nisoli, and S. De Silvestri, App. Phys. Lett. **71**, 3616-3618 (1997).

[36] A. Shirakawa, I. Sakane, and T. Kobayashi, Opt. Lett. **23**, 1292-1294 (1998).

[37] G. Cerullo, M. Nisoli, S. Stagira, and S. De Silvestri, Opt. Lett. **23**, 1283-1285 (1998).

[38] A. Shirakawa, I. Sakane, M. Takasaka, and T. Kobayashi, App. Phys. Lett. **74**, 2268-2270 (1999).

[39] E. Riedle, M. Beutter, S. Lochbrunner, J. Piel, S. Schenkl, S. Sporlein, and W. Zinth, Appl. Phys. B **71**, 457-465 (2000).

[40] G. Cerullo, M. Nisoli, S. Stagira, S. De Silvestri, G. Tempea, F. Krausz, and K. Ferencz, Opt. Lett. **24**, 1529-1531 (1999); G. Cerullo, M. Nisoli, S. Stagira, S. De Silvestri, G. Tempea, F. Krausz, and K. Ferencz, Appl. Phys. B **70**, S253-S259 (2000).

[41] T. Kobayashi and A. Shirakawa, Appl. Phys. B **70**, S239-S246 (2000).

[42] T. Kobayashi, A. Shirakawa, and T. Fuji, IEEE J. Sel. Top. Quantum Electron. **7**, 525-538 (2001).

[43] M. Zavelani-Rossi, G. Cerullo, S. De Silvestri, L. Gallmann, N. Matuschek, G. Steinmeyer, U. Keller, G. Angelow, V. Scheuer, and T. Tschudi, Opt. Lett. **26**, 1155-1157 (2001).

[44] G. Cerullo, G. Lanzani, M. Muccini, C. Taliani, and S. De Silvestri, Phys. Rev. Lett. **83**, 231-234 (1999); A. Sugita, T. Saito, H. Kano, M. Yamashita, and T. Kobayashi, Phys. Rev. Lett. **86**, 2158-2161 (2001); T. Kobayashi, A. Shirakawa, H. Matsuzawa, and H. Nakanishi, Chem. Phys. Lett. **321**, 385-393 (2000); T. Fuji, T. Saito, and T. Kobayashi, Chem. Phys. Lett. **332**,

324-330 (2000); T. Kobayashi, T. Saito, and H. Ohtani, Nature **414**, 531-534 (2001); H. Kano, T. Saito, A. Ueki, and T. Kobayashi, Int. J. Mod. Phys. B **15**, 3817-3820 (2001); H. Kano and T. Kobayashi, J. Chem. Phys. **116**, 184-195 (2002); A. Sugita, T. Furuhi, M. Yamashita, and T. Kobayashi, J. Phys. Chem. A **106**, 581-588 (2002); T. Saito and T. Kobayashi, Opt. Mater. **21**, 301-305 (2003); S. Adachi, V. M. Kobryanskii, and T. Kobayashi, Phys. Rev. Lett. **89**, - (2002); T. Kobayashi, T. Saito, and S. Adachi, J. Lumin. **102**, 722-726 (2003).

[45] M. Wittmann, A. Nazarkin, and G. Korn, Opt. Lett. **26**, 298-300 (2001).

[46] E. Treacy, IEEE J. Quant. Electr. **5**, 454 (1969).

[47] Z. Bor and B. Racz, Opt. Commun. **54**, 165-170 (1985).

[48] R. L. Fork, O. E. Martinez, and J. P. Gordon, Opt. Lett. **9**, 150-152 (1984).

[49] D. Zeidler, T. Hornung, D. Proch, and M. Motzkus, Appl. Phys. B **70**, S125-S131 (2000).

[50] E. Zeek, K. Maginnis, S. Backus, U. Russek, M. Murnane, G. Mourou, H. Kapteyn, and G. Vdovin, Opt. Lett. **24**, 493-495 (1999); E. Zeek, R. Bartels, M. M. Murnane, H. C. Kapteyn, S. Backus, and G. Vdovin, Opt. Lett. **25**, 587-589 (2000).

[51] R. Bartels, S. Backus, E. Zeek, L. Misoguti, G. Vdovin, I. P. Christov, M. M. Murnane, and H. C. Kapteyn, Nature **406**, 164-166 (2000).

[52] M. R. Armstrong, P. Plachta, E. A. Ponomarev, and R. J. D. Miller, Opt. Lett. **26**, 1152-1154 (2001).

[53] P. Baum, S. Lochbrunner, L. Gallmann, G. Steinmeyer, U. Keller, and E. Riedle, Appl. Phys. B **74**, S219-S224 (2002).

[54] A. Baltuška, T. Fuji, and T. Kobayashi, Opt. Lett. **27**, 306-308 (2002).

[55] R. Trebino and D. J. Kane, J. Opt. Soc. Am. A **10**, 1101-1111 (1993); R. Trebino, K. W. DeLong, D. N. Fittinghoff, J. N. Sweetser, M. A. Krumbugel, B. A. Richman, and D. J. Kane, Rev. Sci. Instrum. **68**, 3277-3295 (1997).

[56] R. Byer and R. L. Herbst, in *Nonlinear Infrared Generation*, edited by Y. R. Shen (Springer-Verlag, Berlin, 1997).

[57] R. Danielius, A. Piskarskas, A. Stabinis, G. P. Banfi, P. Di Trapani, and R. Righini, J. Opt. Soc. Am. B **10**, 2222-2232 (1993).

[58] T. S. Sosnowski, P. B. Stephens, and T. B. Norris, Opt. Lett. **21**, 140-142 (1996).

[59] S. Fournier, R. Lopez-Martens, C. Le Blanc, E. Baubeau, and F. Salin, Opt. Lett. **23**, 627-629 (1998).

[60] M. Nisoli, S. Stagira, S. De Silvestri, O. Svelto, G. Valiulis, and A. Varanavicius, Opt. Lett. **23**, 630-632 (1998).

[61] G. Szabo and Z. Bor, Appl. Phys. B **50**, 51-54 (1990); R. A. Cheville, M. T. Reiten, and N. J. Halas, Opt. Lett. **17**, 1343-1345 (1992); T. Hofmann, K. Mossavi, F. K. Tittel, and G. Szabo, Opt. Lett. **17**, 1691-1693 (1992); S. H. Ashworth, M. Joschko, M. Woerner, E. Riedle, and T. Elsaesser, Opt. Lett. **20**, 2120-2122 (1995).

[62] B. A. Richman, S. E. Bisson, R. Trebino, M. G. Mitchell, E. Sidick, and A. Jacobson, Opt. Lett. **22**, 1223-1225 (1997); B. A. Richman, S. E. Bisson, R. Trebino, E. Sidick, and A. Jacobson, Opt. Lett. **23**, 497-499 (1998).
[63] P. Kumbhakar and T. Kobayashi, J. Appl. Phys. **94**, 1329-1338 (2003).
[64] D. Eimerl, L. Davis, S. Velsko, E. K. Graham, and A. Zalkin, J. Appl. Phys. **62**, 1968-1983 (1987).
[65] M. K. Reed, M. K. Steiner-Shepard, M. S. Armas, and D. K. Negus, J. Opt. Soc. Am. B **12**, 2229-2236 (1995).
[66] G. M. Gale, F. Hache, and M. Cavallari, IEEE J. Sel. Top. Quantum Electr. **4**, 224-229 (1998).
[67] *Handbook of Chemistry and Physics* (CRC Press, Cleveland, 1988-1989).
[68] W. J. Tomlinson, R. H. Stolen, and C. V. Shank, J. Opt. Soc. Am. B **1**, 139-149 (1984); R. L. Fork, C. H. B. Cruz, P. C. Becker, and C. V. Shank, Opt. Lett. **12**, 483-485 (1987).
[69] O. E. Martinez, Opt. Commun. **59**, 229-232 (1986).
[70] A. Dubietis, G. Jonusauskas, and A. Piskarskas, Opt. Commun. **88**, 437-440 (1992).
[71] F. Hache, A. Zeboulon, G. Gallot, and G. M. Gale, Opt. Lett. **20**, 1556-1558 (1995).
[72] T. J. Driscoll, G. M. Gale, and F. Hache, Opt. Commun. **110**, 638-644 (1994).
[73] R. Danielius, A. Piskarskas, P. Di Trapani, A. Andreoni, C. Solcia, and P. Foggi, Opt. Lett. **21**, 973-975 (1996).
[74] C. Spielmann, L. Xu, and F. Krausz, Appl. Optics **36**, 2523-2525 (1997).
[75] E. Zeromskis, A. Dubietis, G. Tamosauskas, and A. Piskarskas, Opt. Commun. **203**, 435-440 (2002).
[76] S. Yeremenko, A. Baltuska, F. de Haan, M. S. Pshenichnikov, and D. A. Wiersma, Opt. Lett. **27**, 1171-1173 (2002).
[77] O. Albert and G. Mourou, Appl. Phys. B **69**, 207-209 (1999); Y. Kobayashi and K. Torizuka, Opt. Lett. **26**, 1295-1297 (2001).
[78] A. Baltuška, T. Fuji, and T. Kobayashi, Phys. Rev. Lett. **88**, art. no.-133901 (2002).
[79] M. S. Pshenichnikov, personal communication 2001.
[80] S. T. Cundiff, J. Phys. D. **35**, R43 (2002).
[81] A. Baltuška, T. Fuji, and T. Kobayashi, Opt. Lett. **27**, 1241-1243 (2002).

Chapter 7

OPTICAL FREQUENCY MEASUREMENT

Thomas Udem, Marcus Zimmermann, Ronald Holzwarth, Marc Fischer, Nikolai Kolachevsky, Theodor W. Hänsch
Max-Planck-Institut für Quantenoptik

Abstract: The new alliance between the time and frequency domains in laser spectroscopy has made it possible to develop ultrafast counting schemes that can keep track of single optical oscillations. With this achievement, counting optical oscillations of more than 10^{15} cycles in one second has become a simple task. High-resolution spectroscopy for basic research and metrology greatly benefit from this technology as it has allowed the highest possible precision. This development has also led to the construction of all-optical atomic clocks that are expected to eventually outperform current state-of-the-art cesium clocks. The possibility to measure almost any frequency ratio with very high precision can be used to search for possible variations of natural constants.

Key words: hydrogen spectroscopy, optical atomic clocks, optical frequency metrology, optical frequency synthesis

1. FREQUENCY COMBS

Frequency can be measured with by far the highest precision of all physical quantities. In the radio frequency (rf) domain (say up to 100 GHz), frequency counters have existed for a long time. Almost any of the most precise measurements in physics have been performed with such a counter that uses an atomic clock as a time base. To extend this accurate technique to higher frequencies, so called harmonic frequency chains have been constructed since the late 1960s [1]. In such a chain, nonlinear elements produce frequency multiples (harmonics) of a given oscillator to which a subsequent oscillator is phase locked. The latter is necessary because

nonlinear devices usually produce weak signals, at least when they are driven with a continuous wave (cw). Electronic phase-locked loops can be used to stabilize any kind of oscillator, even lasers, provided their intrinsic stability is sufficient so that there is no need for very rapid frequency corrections. Repeating the multiplication and phase-lock procedure many times makes it possible to convert a reference radio frequency, say from an atomic clock, to much higher frequencies. Because of the large number of steps necessary to build a long harmonic frequency chain, it was not before 1995 when visible laser light was first referenced phase coherently to a cesium atomic clock using this method [2].

The disadvantage of these harmonic frequency chains was not only that they could easily fill several large laser laboratories at one time, but that they could be used to measure only a single optical frequency. Even though mode-locked lasers for optical frequency measurements were used in rudimentary form in the late 1970s [3], this method did not become practical until the advent of femtosecond (fs) mode-locked lasers. Such a laser necessarily emits a very broad spectrum, comparable in width to the optical carrier frequency. Currently the field's work horse is the Ti:sapphire Kerr-lens mode-locked laser, but fiber-based lasers are expected to take over for frequency metrology applications.

In the frequency domain, a train of short pulses from a femtosecond mode-locked laser is the result of a phase-coherent superposition of many cw longitudinal cavity modes. These modes at ω_n[1] form a series of frequency spikes called a frequency comb. The individual modes can be selected by phase locking other cw lasers to them. As has been shown, the modes are remarkably uniform, i.e., the separation between adjacent modes is constant across the frequency comb [4, 5]. This strictly regular arrangement is the most important feature used for optical frequency measurement and may be expressed as:

$$\omega_n = n\omega_r + \omega_{CE} . \tag{1}$$

Here the mode number n of some 10^5 may be enumerated such that the frequency offset ω_{CE} lies in between 0 and $\omega_r = 2\pi/T$. The mode spacing is thereby identified with pulse repetition rate, i.e., the inverse pulse repetition

[1] The notation used in this chapter corresponds to that of other chapters through the following relationships:

$\omega_n = 2\pi\nu_n$
$\omega_r = 2\pi f_r$
$\omega_{CE} = 2\pi f_0$
$\Delta\varphi = \Delta\phi_{ce}$

time *T*. With the help of Equation (1), two radio frequencies ω_r and ω_{CE} are linked to the optical frequencies ω_n of the laser. For this reason, mode-locked lasers are capable of replacing the harmonic frequency chains of the past.

To derive these frequency comb properties [6, 7], as detailed by Equation (1), it is useful to consider the electric field *E(t)* of the emitted pulse train. If the pulses were exact time-shifted copies, *E(t) = E(t - T)*, a simple Fourier transformation would yield a strictly periodic spectrum with a mode separation of ω_r and a zero comb offset $\omega_{CE} = 0$. However, this is not what occurs in a real laser. Because of intracavity dispersion, the group and phase velocities do not match for the pulse that is stored in the cavity. This causes the carrier wave to continuously shift with respect to the pulse envelope (see Figure 7-1). The pulses that emerge at the output-coupling mirror after each round trip show a discrete pulse-to-pulse carrier-envelope phase shift of $\Delta\varphi$.

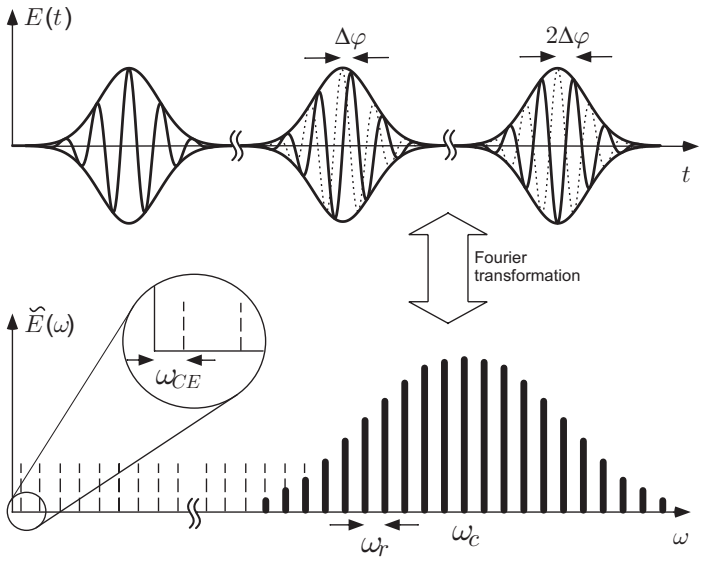

Figure 7-1. Three consecutive pulses of the pulse train emitted by a mode-locked laser and the corresponding spectrum. The pulse-to-pulse phase shift $\Delta\varphi$ results in an offset frequency $\omega_{CE} = \Delta\varphi/T$ because the optical carrier wave at ω_c moves with the phase velocity while the envelope moves with the group velocity.

The difference between phase and group velocity is determined by the dispersion properties of the cavity as a whole. The remarkable property of Kerr-lens mode-locked lasers, such as the Ti:sapphire laser, is that this difference is the only effect of intracavity dispersion on the pulse train. Higher-order dispersive terms that would continuously deform the pulse are

strongly suppressed. For this reason, the properties of the pulse train are most conveniently derived by separating the optical carrier wave that propagates with its phase velocity at ω_c from the pulse-envelope function: $E(t) = A(t)e^{-i\omega_c t}$. The pulse repetition time $T = 2\pi/\omega_r$ is determined from the group velocity by demanding that *A(t) = A(t - T)*. Since it is strictly periodic it may be written in terms of a Fourier series

$$E(t) = A(t)e^{-i\omega_c t} + c.c. = \sum_q A_q e^{-i(\omega_c + q\omega_r)t} + c.c., \qquad (2)$$

where A_q are Fourier components of *A(t)*. This equation represents a comb of laser frequencies with spacing ω_r that is shifted as a whole from the harmonics of ω_r, just as in Equation (1). The only difference is the numbering of modes, which clearly is a matter of convention.

2. THE CESIUM D_1 LINE AND THE FINE STRUCTURE CONSTANT

The first application of a fs mode-locked laser in optical frequency metrology occurred in 1998 with the determination of the transition frequency of the cesium D_1 line at 335 THz (895 nm) [8]. In that experiment, we compared the frequency of the cesium D_1 resonance line with the 4th harmonic of a CH_4-stabilized 3.39 μm He-Ne laser. The frequency of this reference laser was known to within 2.6 parts in 10^{13}. To bridge the large frequency gap of 18.39 THz between the 4th harmonic near 848 nm and the 895 nm Cs D_1 line, we used the frequency comb generated by a Mira 900 system (Coherent Inc.) delivering 70 fs pulses with a repetition frequency of 75 MHz. Even though this was already the largest frequency gap bridged coherently at that time, it was clear that the method could do much better with shorter pulses.

The cesium D_1 line was observed in a 7.5 cm long cell at room temperature. To probe the cesium D_1 transition, we used a saturation spectrometer with two linearly polarized counter-propagating laser beams with equal intensities (10 μW/cm^2). With this Doppler-free method, we observed 4 hyperfine components of the single stable isotope ^{133}Cs for the transitions from the ground states $F_g = 3$ and $F_g = 4$ to the excited states $F_e = 3$ and $F_e = 4$. The observed line width was about 6 MHz (FWHM), somewhat larger than the natural line width. Stray magnetic fields were reduced by a double-cylindrical μ-metal shielding to values below 2 μT along the laser beam axis. We found the line center of the resonances by

fitting a Lorentzian with a linear-frequency-dependent background to it as shown in Figure 7-2.

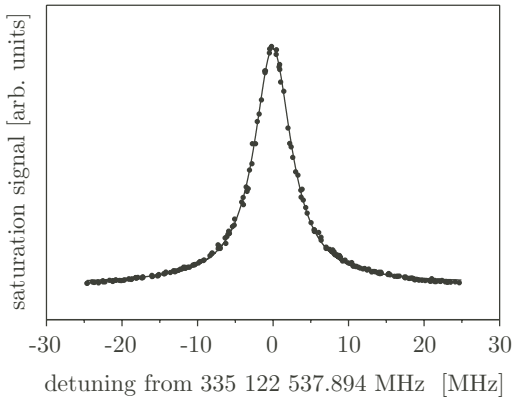

Figure 7-2. The $F_g = 4 \rightarrow F_e = 4$ component of the cesium D_1 transition obtained from a saturation spectrometer and a Lorentzian fit.

The cesium D_1 frequency can be used to derive a value for the fine structure constant α by taking advantage of the extremely well-known Rydberg constant, $R_\infty = \alpha^2 c m_e / 2h$. Steven Chu and collaborators at Stanford University have measured the photon recoil shift of the D_1 line $f_{rec} = f_{D_1}^2 h / 2 m_{Cs} c^2$ with an atom interferometer aiming for an accuracy near the parts-per-billion (ppb) level. Together with the very precise values for the proton–electron mass ratio m_p / m_e [9] and the cesium–proton mass ratio m_{Cs}/m_p [10], the fine structure constant is derived according to

$$\alpha^2 = \frac{2R_\infty}{c}\frac{h}{m_e} = 2R_\infty \frac{2 f_{rec} c}{f_{D_1}^2}\frac{m_{Cs}}{m_p}\frac{m_p}{m_e}. \qquad (3)$$

The atomic mass ratios are measured with high precision in terms of the ratios of their cyclotron frequencies in Penning traps. Please note that all necessary ingredients to Equation (3), including the Rydberg constant that is determined by spectroscopy on atomic hydrogen, are based on intrinsically accurate frequency measurements. Because α scales all electromagnetic interactions, it can be determined by a variety of independent physical methods. Unfortunately, different values measured with comparable accuracy disagree with each other by up to 3.5 standard deviations [11], and the derivation of the currently most accurate value of α from the electron g -

2 experiment relies on extensive QED calculations [12]. The evaluation via Equation (3) provided the first independent confirmation of the g - 2 value at the ppb level of accuracy [11, 13].

3. OPTICAL SYNTHESIZERS

The availability of octave-spanning frequency combs allows the construction of a simple optical synthesizer. This synthesizer is capable of converting a given radio frequency phase coherently into the optical domain by virtue of Equation (1). To do so, one has to measure and/or phase-lock both ω_r and ω_{CE} to a radio frequency reference. While ω_r may be measured with a photo detector anywhere in the output beam of the fs laser, the carrier-envelope offset frequency ω_{CE} is not determined that easily unless one has an octave-spanning frequency comb.

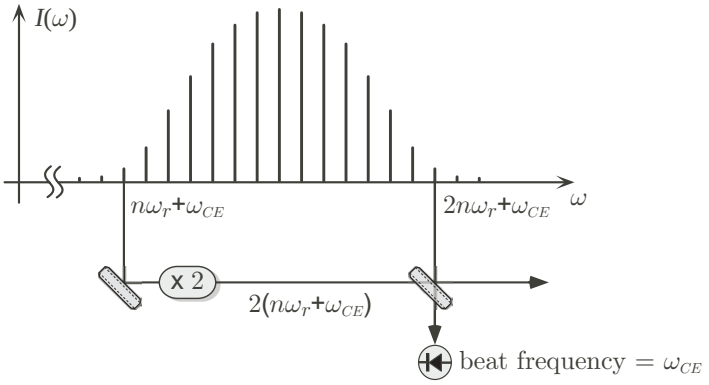

Figure 7-3. The offset frequency ω_{CE} that displaces the modes of an octave-spanning frequency comb from being exact harmonics of the repetition rate ω_r is measured by frequency-doubling some modes at the "red" side of the comb and beating them with modes at the "blue" side.

In that case, a group of modes from the low-frequency end of the comb around $n_L\omega_r + \omega_{CE}$ is frequency doubled in a nonlinear crystal and beat notes with another group of modes around n_H at the high-frequency end of the comb are created. As sketched in Figure 7-3, this technique creates signals at the difference frequency of two optical waves on a photodetector: $2(n_L\omega_r + \omega_{CE}) - (n_H\omega_r + \omega_{CE}) = (2n_L - n_H)\omega_r + \omega_{CE}$. These beat frequencies are created for all possible combinations of n_L and n_H. However, the detected beat notes cannot exceed the bandwidth of the photodetector. One can further restrict the number of signals to precisely one by using an rf-

low-pass filter. If this filter has a cut-off frequency of $\omega_r/2$, only the beat note at ω_{CE}, belonging to all combinations with $2n_L - n_H = 0$, remains. The octave-spanning comb ensures that these combinations exist, i.e., that the modes n_L and n_H with $n_H = 2n_L$ are simultaneously active modes. Knowing both ω_{CE} and ω_r means that frequencies of all modes according to Equation (1) are known and may be used for optical frequency measurements. This is accomplished by creating another beat note ω_b between an unknown laser at ω_l and a nearby mode of the comb. The frequency of that laser can then be determined by $\omega_l = n\omega_r + \omega_{CE} + \omega_b$. The mode number n may be determined by a coarse measurement of ω_l with a wave meter or by repeating the measurement with slight variation in ω_r.

This technique is called self-referencing [5, 14] and requires a frequency comb spanning a full optical octave in its simplest form. Alternatively, any combination of two *different* harmonics from the *same* comb will serve that purpose. Self-referencing has been performed with the beating of the 2nd and 3rd harmonic of comb components [15] and by comparing modes with frequency ratio of 7:8 [16]. The frequency comb, even without the knowledge of ω_{CE}, can be thought of as a ruler in frequency space that allows the precise measurement of large optical frequency differences. The initial utilization of frequency combs was for that purpose [8].

To stabilize the frequency comb to a precise rf reference, it is not sufficient to measure the two comb parameters ω_r and ω_{CE}; they also have to be controlled separately. The repetition frequency is most conveniently controlled via the cavity length through a piezoelectric transducer. For a typical laser, the intrinsic stability of the repetition rate is high enough that the attainable bandwidth of the transducer is sufficient to keep it in phase with a good rf reference. The other comb parameter ω_{CE} is controlled by changing the intensity of the stored pulse. It was shown that for a soliton-like laser such as the Ti:sapphire Kerr-lens mode-locked laser, the group and phase velocity depend in a different way on the peak intensity of the stored pulse [17]. Therefore one can adjust the pulse-to-pulse slippage of the carrier-envelope phase, and thereby ω_{CE}, by controlling the average laser power. For a Ti:sapphire Kerr-lens mode-locked laser, this can be done by controlling the power of the pump laser. In this way the comb offset, just like the repetition frequency, can be adjusted to stay in phase with the rf reference. The two controls are not completely independent, but they affect the round-trip group delay and the round-trip phase delay differently. Keeping the servo bandwidths for ω_r as low as possible and for ω_{CE} as high as possible usually decouples the two servo systems. Having two two-phase servo systems operational that lock ω_r and for ω_{CE} to a radio frequency reference such as an atomic clock ensures that, by virtue of Equation (1) and

the large integer *n*, the radio frequency reference is up-converted phase coherently to the optical region.

4. OCTAVE-WIDE FREQUENCY COMBS

Only now octave-spanning fs Ti:sapphire lasers are becoming possible. Therefore, external spectral broadening has been key to the simple ν-to-2ν self-referencing scheme described in the previous section. That spectral broadening employs self-phase modulation, whose origin is a slight intensity dependence of the refractive index of most materials. After propagating a length *l*, the intensity-dependent refractive index $n(t) = n_0 + n_2 I(t)$ leads to a self-induced phase shift of the field in Equation (2) of

$$\Phi_{NL}(t) = -n_2 I(t)\omega_c l / c, \text{ with } I(t) = |A(t)|^2. \quad (4)$$

This time-dependent phase shift leads to a frequency modulation that is proportional to the time derivative of the self-induced phase shift $\partial_t \Phi_{NL}(t)$. For fused silica with its positive Kerr coefficient $n_2 = 3.2\times10^{-16}\ \mathrm{cm}^2/\mathrm{W}$, the leading edges of the pulses create extra frequencies shifted to the red $(\partial_t \Phi_{NL}(t) < 0)$, while the trailing edges cause blue-shifted frequencies to emerge. Self-phase modulation modifies the envelope function according to

$$A(t) \rightarrow A(t)e^{i\Phi_{NL}(t)}. \quad (5)$$

Because $\Phi_{NL}(t)$ has the same periodicity as *A(t)*, the comb structure of the spectrum, as previously derived, is not affected.

In an optical fiber, this process can be quite efficient as compared to bulk material, even though the nonlinear coefficient in fused silica is comparatively small. This efficiency arises because of the fiber core carrying a high-intensity pulse over an extended length. The details of fiber actions on the pulse train are, in fact, more complicated because other nonlinear effects such as Raman scattering may contribute. Whatever the fiber does to the pulses, however, a periodic input should produce a periodic output of some kind if the fiber action is the same for all the pulses. Therefore the comb structure, as derived from the periodic envelope function, is maintained.

Effective self-phase modulation in a regular single-mode fiber takes place only over a limited fiber length. Dispersion causes the pulse to broaden temporally. This broadening continuously lowers the peak intensity as the pulse travels along the fiber until the nonlinear interaction comes to a halt.

Very efficient spectral broadening can be observed in photonic crystal fibers (PCFs) that can suppress this effect to some extent [18]. A PCF uses an array of submicron-sized air holes that surround the fiber core and run the length of a silica fiber to change its effective dispersion. This can be used to maintain high peak power over an extended propagation length and to significantly increase the spectral broadening. With these fibers, it has become possible to broaden low-power, high-repetition-rate lasers to beyond one optical octave.

Effective spectral broadening of femtosecond light pulses was performed in very much the same way a long time before the invention of PCFs. Formerly, spectral broadening was accomplished with very powerful laser pulses obtained with laser post-amplifiers. However, so far this technique only works by reducing the pulse repetition rate, thereby concentrating the available power into fewer pulses. This reduction is disastrous for frequency metrology because it also reduces the power that is left per mode. It would also be very difficult to separate single modes out of such a dense comb. The PCFs allow spectral broadening of fs pulses to more than an optical octave at repetition rates of 1 GHz.

Meanwhile, some lasers are reaching an octave-spanning spectrum even without using external self-phase modulation. Some designs use intracavity self-phase modulation [19] while others employ specially designed cavities [20] or mirrors [21]. These lasers avoid mechanical stability problems associated with the tiny core of PCFs. However, their power is generally weak at the spectral edges that are used for self-referencing. So far only one laser system had been phase stabilized in this way [20].

5. APPLICATION TO HYDROGEN

In our lab, high-resolution spectroscopy on atomic hydrogen was the incentive to develop wide-span optical frequency combs. Initially, the task was to bridge a gap of about 2 THz in our previous harmonic frequency chain to determine the sharp hydrogen 1*S*–2*S* transition frequency relative to a very precise methane-stabilized He-Ne laser. This laser operates at 3.39 μm, which is close to the 28^{th} subharmonic of the 1*S*–2*S* transition at 121 nm. The accuracy-limiting factor at that time was the frequency mismatch between the 28^{th} harmonic of the He-Ne laser standard and the hydrogen transition. For the first measurement of this kind, 6,372 longitudinal modes from a precisely calibrated cavity were used to determine the frequency gap [22]. This method introduced an uncertainty of 45 kHz.

In the following years, phase-coherent methods were developed to bridge optical frequency gaps in the THz range. The first method applied in our

laboratory was the use of optical-frequency interval dividers [23, 24]. The concept was to phase lock the second harmonic of a laser $2f$ to the sum frequency generated by two additional lasers at $f_1 + f_2$. In doing so, the laser frequency f is set at the precise midpoint between f_1 and f_2: $f = (f_1 + f_2)/2$. In this way, an arbitrary large frequency gap $f_2 - f_1$ can be divided in two. These dividers can be cascaded such that n stages would divide an optical frequency gap by 2^n. With a 5-stage interval-divider chain, we have divided the aforementioned gap to become accessible to radio frequency counting techniques. At the time, the accuracy of the experiment was limited by the reproducibility of our He-Ne laser standard to about 840 Hz [6].

Already then it was clear that, given a way to measure frequency gaps that are comparable in size to the optical frequency itself, absolute optical frequency measurements could be performed using the ν-to-2ν method described above [23]. The first electro-optic frequency comb was brought to our lab by Motonobu Kourogi from the Tokyo Institute of Technology in 1997. This device was capable of measuring frequency gaps of several THz using a single laser. It replaced the much-more-complicated interval divider stages but was itself soon replaced by a femtosecond frequency comb. With the frequency comb, it was possible for the first time to measure frequency gaps comparable to the optical carrier frequency and thereby convert the 1*S*–2*S* transition frequency phase coherently to the radio frequency domain [16]. Given a precise radio frequency reference, the accuracy was limited by the hydrogen spectrometer.

6. THE FIRST OPTICAL SYNTHESIZER

In 1999 [25], the $(1S, F = 1, m_F = \pm 1) \rightarrow (2S, F' = 1, m'_F = \pm 1)$ two-photon transition frequency in atomic hydrogen was compared phase coherently to the frequency of the ground-state hyperfine splitting in ^{133}Cs. For this purpose, one of the most precise Cs atomic fountain clocks (FOM) [26], built in the group of A. Clairon at the Bureau National de Métrologie – Systèmes de Référence Temps Espace (BNM-SYRTE) in Paris, was brought to our laboratory. A photonic crystal fiber that would have allowed us to produce an octave-spanning frequency comb was not at our disposal at that time. Therefore, we set up a self-referencing scheme that compared modes with a frequency ratio of 7:8, as shown in Figure 7-4. The frequency comb was produced by a Mira 900 (Coherent Inc. with about 70 fs pulse duration) with some spectral broadening in a regular single-mode fiber. The total span of the frequency comb was in excess of 1/14 of the dye laser's frequency, or 44 THz.

In 2003 [27] we repeated this measurement with a much simpler ν-to-2ν self-referencing scheme as described above (see Figure 7-3). This modification did not improve the accuracy of the frequency measurement of the dye laser, which was in both cases determined by the Cs fountain clock, but vastly simplified the experimental setup.

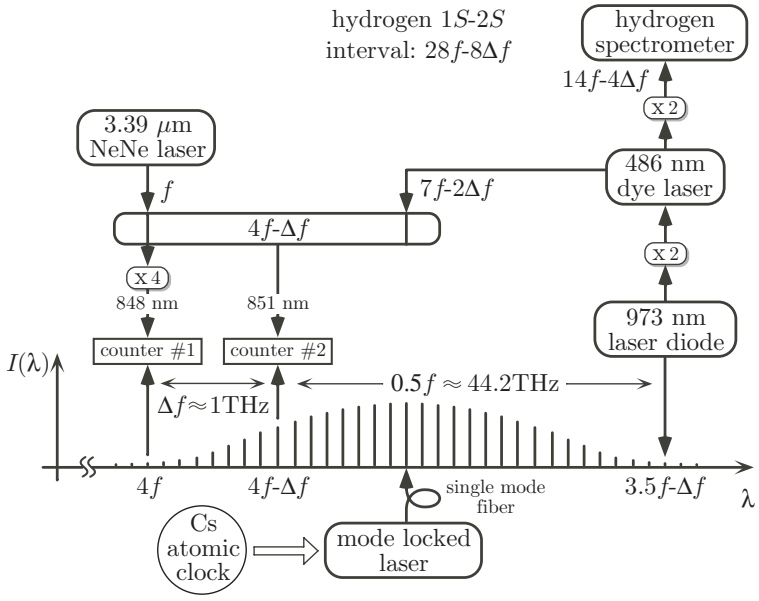

Figure 7-4. Sketch of the first (still somewhat complicated) self-referenced frequency comb. While the second harmonic of the dye laser at 486 nm is used to excite the 1*S*–2*S* transition, its subharmonic 3.5*f*-Δ*f* and the 4th harmonic of the He-Ne laser are compared to the frequency comb. The ratio of these frequencies is 7:8 instead of the 1:2 in a much simpler ν-to-2ν self-referencing scheme. Because the 3.39 μm He-Ne laser could not be tuned precisely to the 28th subharmonic of the dye laser, a second, much smaller frequency gap Δ*f* was present in this setup and was measured simultaneously with the same frequency comb. The oval symbol represents an optical interval divider that fixes the center frequency 4*f* – Δ*f* relative to its inputs 4*f* and 7*f* - 2Δ*f*. All optical connections represent phase-locked lasers except where the rf counters are located. These are used to measure beat notes with the nearest comb modes. Once the two frequency gaps 0.5*f* and Δ*f* have been precisely measured with a Cs clock-referenced frequency comb, the dye laser at 14*f* + 8Δ*f* is readily calculated. In addition, we can calculate the frequency of any other mode in the frequency comb and fix the carrier-envelope phase by locking the comb with $\omega_{CE} = 0$.

7. THE HYDROGEN SPECTROMETER

The cw dye laser near 486 nm that is used to excite the hydrogen atoms can be locked to a high-finesse reference cavity to narrow its line width and fix its frequency. A new cavity made from Ultra-Low-Expansion (ULE) glass was used for the 2003 measurement. Its drift was measured to be less than 1 Hz s^{-1} for the entire time of the measurement. Due to better thermal and acoustic isolation and improvements in the laser-locking electronics, the laser line width was narrower than it had been in 1999. An upper limit for the laser line width was deduced from an investigation of the beat signal between two laser fields locked separately to independent Zerodur and ULE cavities to about 120 Hz at a laser wavelength of 486 nm.

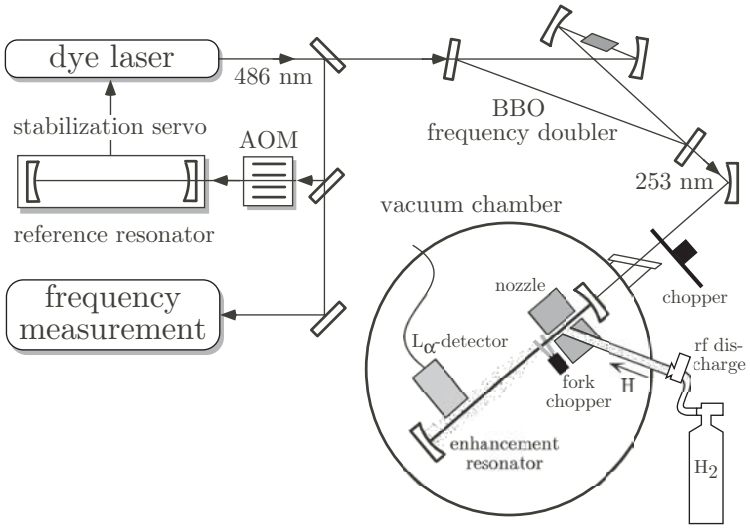

Figure 7-5. Hydrogen spectrometer. The 486 nm light from the dye laser is frequency doubled in a Barium β-Borate (BBO) crystal. The resulting radiation is used to drive the 1*S*–2*S* two-photon transition that is free of the first-order Doppler effect if the two photons are counter-propagating. The latter is ensured by a linear enhancement cavity in the vacuum chamber that is held at a pressure of about 10^{-8}–10^{-7} mbar. The acousto-optic modulator (AOM) allows the dye laser to be tuned away from the resonance of the reference resonator to scan the hydrogen line.

As shown in Figure 7-5, molecular hydrogen is dissociated in a gas discharge and forms a cold atomic beam after contact with a copper nozzle that is kept at 5–7 K. The region of the atomic beam is shielded from stray electric fields by a Faraday cage. Some of the atoms are excited from the ground state to the metastable 2*S* state by the absorption of two counter-propagating photons from the laser field in the enhancement cavity. In this

arrangement, the first-order Doppler effect of the two photons exactly cancels each other. Those atoms that are flying close to the cavity axis can enter the detection region where the 2*S* atoms are quenched in a small electric field and forced to emit a L_α-photon, which is detected with a solar-blind photo multiplier. We have periodically blocked the laser beam and the atomic beam. This procedure eliminates background counts from the exciting laser. The delay Δt between blocking the 243 nm radiation and the start of photon counting sets an upper limit on the velocity of the atoms that contribute to the signal. Therefore, velocity-dependent systematic effects, such as the second-order Doppler shift and the time-of-flight broadening, are smaller for spectra recorded at larger Δt. The hydrogen beam is blocked by a fork chopper in less than 200 μs after the blocking of the excitation light to prevent slow atoms from being blown away by fast atoms that emerge subsequently from the nozzle. With the help of a multi-channel scaler, we count all photons and sort them into 12 equidistant delay-time bins. From each scan of the laser frequency over the hydrogen 1*S*–2*S* resonance, we get 12 distinct spectra, as shown for a sample line in the left panel of Figure 7-6. To correct for the second-order Doppler shift, we use an elaborated theory model [28] to fit all the delayed spectra simultaneously with one set of 7 fit parameters. Besides the second-order Doppler effect, the other dominating systematic effect is the dynamic AC Stark shift that scales linearly with the excitation light intensity. We have compensated for that effect by varying the laser intensity and extrapolating the transition frequency to zero intensity, as shown in the right portion of Figure 7-6. The result of the fitting procedure is the 1*S*–2*S* transition frequency for the hydrogen atom at rest.

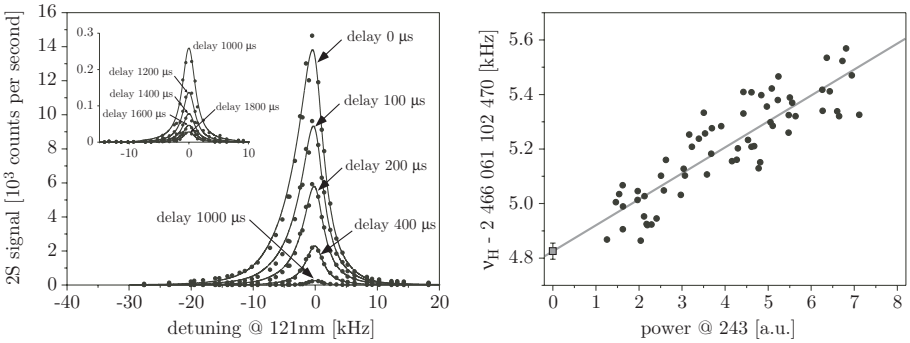

Figure 7-6. Left: simultaneous fit of a 1*S*–2*S* transition spectrum recorded at different detection delays. The nozzle temperature was 7 K. Right: AC Stark shift extrapolation to zero power for all the lines recorded during one day of data taking.

To check for possible cycle slipping, all phase-locked frequencies were counted to verify consistency with the phase-lock systems. Data points were

accepted only where all counter readings were consistent. Additionally, it was verified that the dye laser was continuously locked to the reference resonator during the measurement. To exploit the superior short-term stability of that resonator, we measured the frequency of the standing light field in the resonator first. To compensate for the slow drifts of the resonator, we fit a second-order polynomial to that drift and then, knowing the AOM detuning, we used the polynomial in the subsequent determination of the dye laser frequency. The left part of Figure 7-7 shows the absolute frequency of the standing light field inside our new ULE reference resonator. The right hand side of the figure shows the normalized Allan variance of the dye laser locked to the reference resonator, measured relative to the Cs fountain clock FOM. For longer averaging times, the plot of the Allan variance is generated by juxtaposing 1 s counter readouts. Whereas it is known that such a procedure can alter the functional dependence of the Allan variance [29], white frequency noise, as produced by the Cs fountain, is immune to this form of bias. The observed $\tau^{-1/2}$ dependence coincides with the independently measured fountain clock instability for averaging times shorter than ≈ 10 s. The short-term stability of the laser system is better than the stability of the fountain clock. However, the long-term stability is limited by the drift of the ULE reference resonator. For the given stability of the Cs fountain clock and the cavity, the optimum record length is around 500 s. For longer averaging times, the Cs fountain is more stable than the drift-corrected ULE cavity.

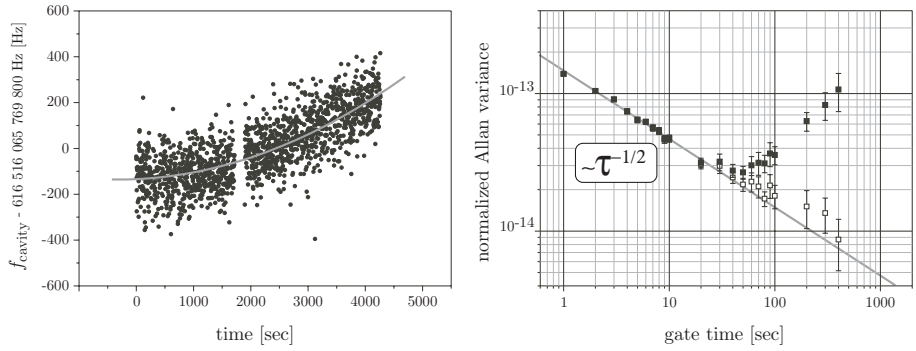

Figure 7-7. Left: Absolute frequency of the standing light field inside the reference resonator (AOM shifted dye laser, see Figure 7-5) as a function of time. The solid line is a parabolic fit to the data. The linear contribution to the drift is less than 0.1 Hz per s in this example and below 1 Hz per s at all times. Right: Normalized Allan variance vs averaging time computed from a time series of 1 s counter readings with considerable dead time. The straight line indicates the $\tau^{-1/2}$ dependence, which is the signature of the Cs fountain clock. The raw data analysis (solid squares) shows that the stability for averaging times longer than 20 s is limited

by the drift of the ULE reference cavity. Open squares represent data corrected for the parabolic cavity drift.

8. THE 1*S*–2*S* TRANSITION FREQUENCY

We have measured the 1*S*–2*S* transition in atomic hydrogen during 10 days in 1999 and during 12 days in 2003. Both data sets have been analyzed using the same theoretical line-shape model and are therefore comparable. In Figure 7-8, the results of the extrapolation to zero-excitation light intensity and the respective statistical error bars for each day are presented. Since 1999, the statistical uncertainty for each day of measurement has been significantly reduced because of the narrower laser line width and better signal-to-noise ratio; however, the scatter of the daily averages did not reduce accordingly. We have tested several possible reasons for this additional scatter, including an intrabeam pressure shift, a background gas-pressure shift, Stark effects due to the rf gas discharge, and the DC Stark shift. We have been able to exclude all of these effects, at least on a conservative level of 10–20 Hz. A possible origin of the observed scatter can be due to a residual first-order Doppler effect arising from a violation of the axial symmetry of the enhancement cavity mode and the hydrogen atomic beam. The scattering of the excitation light on intracavity diaphragms could also cause slight changes of the field distribution and the corresponding first-order Doppler effect. However, such changes should average to zero over multiple adjustments of the hydrogen spectrometer because the shifts can have both signs. As the scatter is the same for both the measurement sets, we believe them to be equivalent. The main statistical and systematic uncertainties of these measurements are collected in Table 7-1. The averaging of the 1999 and 2003 daily data points was performed without weighting them.[2] For both measurements, the dominating uncertainty arises from the day-to-day scatter while the pure statistical uncertainty for each day is significantly smaller. In fact, weighting of the daily data only slightly influences the results (on the level of $\sigma/2$).

Comparing both measurements, we deduce a difference of $\nu_{H,2003} - \nu_{H,1999}$ equal to (-29 ± 57) Hz within 44 months. This difference corresponds to a relative drift of ν_H against the ^{133}Cs ground-state hyperfine splitting of $\partial_t(\ln(\nu_H / \nu_{Cs})) = (-3.2 \pm 6.3) \times 10^{-15}$ per year.

[2] The result of 2 466 061 102 474 870 Hz was inadvertently described in [25] as “the weighted mean value” but was calculated without consideration of the daily statistical uncertainties.

Table 7-1. Results of the (1*S*, $F = 1$, $m_F = \pm 1 \rightarrow 2S$, $F' = 1$, $m'_F = \pm 1$) transition frequency measurement ($\nu_{H,1999}$, $\nu_{H,2003}$) and uncertainty budgets ($\sigma_{H,1999}$, $\sigma_{H,2003}$) for the 1999 and 2003 measurements, respectively.

Contribution	$\nu_{H,1999}$ [Hz]	$\sigma_{H,1999}$ [Hz]	$\nu_{H,2003}$ [Hz]	$\sigma_{H,2003}$ [Hz]
Extrapolated value – 2 466 061 102 474 kHz	870	36	851	25
Background gas-pressure shift	10	10	0	2
Intrabeam pressure shift	0	10	0	10
Line-shape model	0	20	0	20
DC Stark shift	0	5	0	5
Blackbody radiation	0	1	0	1
Standing wave effects	0	10	0	1
Intensity zero uncertainty	0	1	0	0
Fountain clock uncertainty	0	5	0	5
Total – 2 466 061 102 474 kHz	880	45	851	34

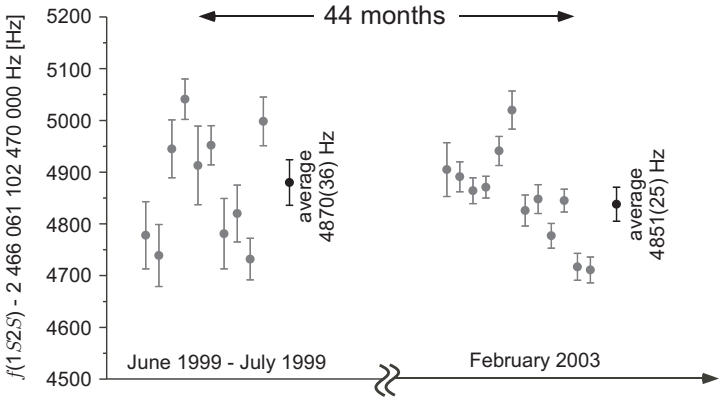

Figure 7-8. Experimental results and averages for the 1999 and 2003 measurements of the (1*S*, $F = 1$, $m_F = \pm 1 \rightarrow 2S$, $F' = 1$, $m'_F = \pm 1$) transition frequency in atomic hydrogen. Each data point represents one day of averaging. The two results are unweighted mean values of the daily averages.

9. CHECKING FOR SLOW DRIFTS OF A NATURAL CONSTANT

In the era of rapid development of precision experimental methods, the stability of fundamental constants becomes a question of basic interest. Any drift of nongravitational constants is forbidden in all metric theories of gravity, including general relativity. The basis of these theories is Einstein's Equivalence Principle (EEP), which states that weight is proportional to mass and that in any local freely falling reference frame, the result of any nongravitational experiment must be independent of time and space. This hypothesis can be proven only experimentally because no theory exists that predicts the values of fundamental constants. In contrast to metric theories, string theory models, which aim to unify quantum mechanics and gravitation, allow for, or even predict, violations of EEP. Limits on the variation of fundamental constants might therefore provide important constraints on these new theoretical models.

A recent analysis of quasar absorption spectra with red-shifted UV transition lines indicates a variation of the fine structure constant on the level of $\Delta\alpha/\alpha = (-0.54 \pm 0.12)\times 10^{-5}$ for a red-shift range ($0.2 < z < 3.7$) [30]. On geological timescales, a limit for the drift of α has been deduced from isotope abundance ratios in the natural fission reactor of Oklo, Gabon, which operated about 2 Gyr ago. Modeling the processes that have changed the isotope ratios of heavy elements gives a limit of $\Delta\alpha/\alpha = (-0.36 \pm 1.44)\times 10^{-8}$ [31]. In these measurements, the high sensitivity to the time variation of α is achieved through very long observation times at moderate resolution for $\Delta\alpha$. Therefore, they are vulnerable to systematic effects. In fact, more recent observation of quasar absorption spectra, performed by different groups, seem to rule out a variation of α on the level observed by Webb et al. [32].

In contrast to astronomical or geological observations, laboratory experiments can reach an accuracy of 10^{-15} with better controlled systematics. For this reason, laboratory measurements can compete, even though the temporal separation of observations is necessarily smaller by many orders of magnitude. In general, frequency measurements must be performed with any form of unit and therefore always yield the ratio of two frequencies. If one compares with the ground-state hyperfine splitting of ^{133}Cs, for example, the measurement would be in units of Hz. However, for the purpose of testing the stability of natural constants, any other frequency ratio may be used. In fact, as will be shown below, measuring the ratio of two optical frequencies could be advantageous. The frequency comb provides a convenient way to measure optical frequency ratios. This

measurement is accomplished by locking one mode of the frequency comb to one optical transition, referencing the carrier envelope offset frequency to the repetition rate and observing a beat note between the comb and the other optical frequency [33].

To map any possible variation of the measured frequency ratio on the variation of natural constants, the following expression for electronic (optical) transitions is commonly used:

$$\nu_{opt} = A\, R_y\, F_{rel}(\alpha)\,, \tag{6}$$

where R_y is the Rydberg frequency expressed in hertz and $F_{rel}(\alpha)$ takes into account relativistic and many-body effects. The constant A is a pure numerical factor and does not depend on any natural constant. For hydrogen, one would use the Schrödinger energies with $A = 1/n^2$ and $F_{rel}(\alpha) = 1$ to describe the first-order scaling in α, which is sufficient here. The corresponding expression for hyperfine transitions reads:

$$\nu_{hf} = A'\, R_y\, \alpha^2\, \frac{\mu_n}{\mu_B} F'_{rel}(\alpha)\,, \tag{7}$$

with a different constant A' and a different relativistic correction $F'_{rel}(\alpha)$. From these two equations, it is clear that the Rydberg constant cancels in any frequency measurement. The last expression depends on the Bohr magneton μ_B and the nuclear magnetic moment μ_n. The size of the latter depends mainly on the strong coupling constant that may also be subject to a slow drift. This is the reason why optical-to-optical comparisons are desirable. However, having more than one optical-to-hyperfine comparison at hand, the drift of the different constants may be separated [27].

Even though the frequency measurements in use for such an evaluation are rather accurate, the derived drift is not. Therefore only low-order numerical values for the derivatives of the relativistic corrections are used in the evaluation. For the cesium ground state splitting, one finds [34]

$$\alpha\partial_\alpha \ln F_{Cs}(\alpha) \approx +0.8\,. \tag{8}$$

Whereas for the hydrogen optical transitions, the Schrödinger approximation with

$$\alpha\partial_\alpha \ln F_H(\alpha) \approx 0 \tag{9}$$

is sufficient. The relative drift of the hydrogen/cesium frequency ratio is therefore approximated by

$$\partial_t \ln(\nu_H / \nu_{Cs}) = -\partial_t \ln(\mu_{Cs} / \mu_B) - 2.8\partial_t \ln(\alpha) . \quad (10)$$

For clarity, we set $x \equiv \partial_t \ln(\alpha)$, and $y \equiv \partial_t \ln(\mu_{Cs} / \mu_B)$ and get for an experimental constraint with the result of the previous section:

$$y + 2.8x = (3.2 \pm 6.3) \times 10^{-15}\ \mathrm{yr}^{-1} \quad \text{for H.} \quad (11)$$

To separate the relative drift rates of *x* and *y*, other transition frequency ratios have to be observed over time. In fact, in similar experiments performed at the National Institute of Standards and Technology (NIST) in Boulder, Colorado (USA) and the Physikalisch-Technische Bundesanstalt (PTB) in Braunschweig, Germany, other optical transition frequencies in a single trapped Hg^+ ion [35] and a single trapped Yb^+ ion [36] have been compared to the cesium ground-state splitting using a self-referenced frequency comb. These measurements lead to the following experimental constraints:

$$y + 6.0x = (0.2 \pm 7.0) \times 10^{-15}\ \mathrm{yr}^{-1} \text{ for } Hg^+ , \quad (12)$$

$$y + 1.9x = (1.2 \pm 4.4) \times 10^{-15}\ \mathrm{yr}^{-1} \text{ for } Yb^+ . \quad (13)$$

Since Equations (11) through (13) represent an over-determined set for the two variables *x* and *y*, a least-square adjustment procedure yields the most likely values and their uncertainties [36]:

$$x = \partial_t \ln(\alpha) = \frac{\dot{\alpha}}{\alpha} = (-0.3 \pm 2.0) \times 10^{-15}\ \mathrm{yr}^{-1}, \text{ and} \quad (14)$$

$$y = \partial_t \ln(\mu_{Cs} / \mu_B) = (+2.4 \pm 6.8) \times 10^{-15}\ \mathrm{yr}^{-1} . \quad (15)$$

Figure 7-9 shows the current limit for the drift rates from laboratory measurements. The uncertainties of these limits reach within a factor of ten to the uncertainties of the relative drift rates derived from astronomical observations [30, 32]. In the near future, one can expect a significant

improvement of the laboratory measurements, even without an increase of experimental accuracy, just because the available time interval increases. One can also expect that additional optical transition frequencies may be measured that will further restrict the extent of the ellipse in Figure 7-9. It should also be pointed out that, since there is no accepted physical model that would describe the drift of natural constants,[3] there is no reason to assume it to be linear in time. In this sense, astronomical and laboratory measurements are somewhat complementary because they observe on different time scales.

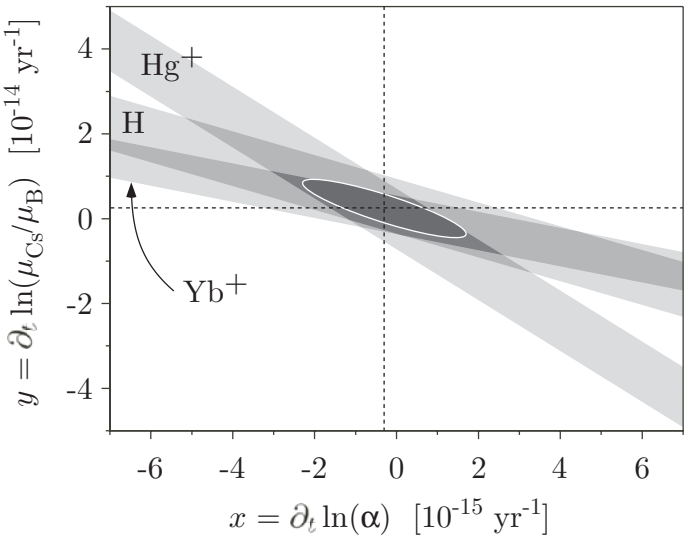

Figure 7-9. Combining the drift rates of optical transitions in hydrogen, Hg^+ and Yb^+. The experimentally allowed region for the drift rates of α and μ_{Cs}/μ_B is shown in the form of an ellipse.

It has also been argued that a possible drift of the coupling constants must be correlated [37], at least if one believes in the existence of a Grand Unified Theory. In such a theory, the fundamental interactions are described within the same framework. The drift rates must therefore be synchronized in some sense. According to Calmet et al. [37], the fractional time variation of hadron masses and along the same line the nuclear magnetic moments, should change about 38 times faster than the fractional time variation of the fine structure constant α. The analysis presented here is independent of such

[3] If there was such a model that describes the drift of natural constants in terms of other constants, it would simply mean that our current constants are not fundamental.

assumptions as it separates the drift rates of different constants. In that sense, the conclusions are model independent.

REFERENCES

[1] L. O. Hocker, A. Javan, D. R. Rao, L.Frenkel, and T. Sullivan, Appl. Phys. Lett. **10**, 147-149 (1967); K. M. Evenson, J. S. Wells, F. R. Petersen, B. L. Danielson, and G. W. Day, Appl. Phys. Lett. **22**, 192 (1973).

[2] H. Schnatz, B. Lipphardt, J. Helmcke, F. Riehle, and G. Zinner, Phys. Rev. Lett. **76**, 18-21 (1996).

[3] J. N. Eckstein, A. I. Ferguson, and T. W. Hänsch, Phys. Rev. Lett. **40**, 847-850 (1978).

[4] T. Udem, J. Reichert, R. Holzwarth, and T. W. Hänsch, Opt. Lett. **24**, 881-883 (1999); S. A. Diddams, L. Hollberg, L. S. Ma, and L. Robertsson, Opt. Lett. **27**, 58-60 (2002); L. S. Ma, Z. Y. Bi, A. Bartels, L. Robertsson, M. Zucco, R. S. Windeler, G. Wilpers, C. Oates, L. Hollberg, and S. A. Diddams, Science **303**, 1843-1845 (2004).

[5] R. Holzwarth, T. Udem, T. W. Hänsch, J. C. Knight, W. J. Wadsworth, and P. S. J. Russell, Phys. Rev. Lett. **85**, 2264-2267 (2000).

[6] T. Udem, A. Huber, B. Gross, J. Reichert, M. Prevedelli, M. Weitz, and T. W. Hänsch, Phys. Rev. Lett. **79**, 2646-2649 (1997).

[7] J. Reichert, R. Holzwarth, T. Udem, and T. W. Hänsch, Opt. Commun. **172**, 59-68 (1999).

[8] T. Udem, J. Reichert, R. Holzwarth, and T. W. Hänsch, Phys. Rev. Lett. **82**, 3568-3571 (1999).

[9] P. J. Mohr, Rev. Modern Phys. **72**, 351-495 (2000).

[10] M. P. Bradley, J. V. Porto, S. Rainville, J. K. Thompson, and D. E. Pritchard, Phys. Rev. Lett. **83**, 4510-4513 (1999).

[11] A. Wicht, J. M. Hensley, E. Sarajlic, and S. Chu, Physica Scripta **T102**, 82-88 (2002).

[12] T. Kinoshita, Reports on Progress in Physics **59**, 1459-1492 (1996); T. Kinoshita, IEEE Trans. Instrum. Meas. **50**, 568-571 (2001).

[13] J. M. Hensley, Ph.D Thesis, Stanford University (2001).

[14] S. A. Diddams, D. J. Jones, J. Ye, S. T. Cundiff, J. L. Hall, J. K. Ranka, R. S. Windeler, R. Holzwarth, T. Udem, and T. W. Hänsch, Phys. Rev. Lett. **84**, 5102-5105 (2000).

[15] T. M. Ramond, S. A. Diddams, L. Hollberg, and A. Bartels, Opt. Lett. **27**, 1842-1844 (2002).

[16] J. Reichert, M. Niering, R. Holzwarth, M. Weitz, T. Udem, and T. W. Hänsch, Phys. Rev. Lett. **84**, 3232-3235 (2000).

[17] H. A. Haus and E. P. Ippen, Opt. Lett. **26**, 1654-1656 (2001).

[18] P. Russell, Science **299**, 358-362 (2003).

[19] R. Ell, U. Morgner, F. X. Kärtner, J. G. Fujimoto, E. P. Ippen, V. Scheuer, G. Angelow, T. Tschudi, M. J. Lederer, A. Boiko, and B. Luther-Davies, Opt. Lett. **26**, 373-375 (2001).

[20] T. M. Fortier, D. J. Jones, and S. T. Cundiff, Opt. Lett. **28**, 2198-2200 (2003).

[21] T. Fuji, A. Unterhuber, V. S. Yakovlev, G. Tempea, A. Stingl, F. Krausz, and W. Drexler, Appl. Phys. B **77**, 125-128 (2003).

[22] T. Andreae, W. Konig, R. Wynands, D. Leibfried, F. Schmidtkaler, C. Zimmermann, D. Meschede, and T. W. Hänsch, Phys. Rev. Lett. **69**, 1923-1926 (1992).

[23] T. W. Hansch, in *The Hydrogen Atom*, edited by M. Inguscio (Springer Verlag, Berlin, 1989), p. 93.

[24] H. R. Telle, D. Meschede, and T. W. Hänsch, Opt. Lett. **15**, 532-534 (1990).

[25] M. Niering, R. Holzwarth, J. Reichert, P. Pokasov, T. Udem, M. Weitz, T. W. Hänsch, P. Lemonde, G. Santarelli, M. Abgrall, P. Laurent, C. Salomon, and A. Clairon, Phys. Rev. Lett. **84**, 5496-5499 (2000).

[26] M. Abgrall, Ph.D Thesis, L'universite Paris (2003).

[27] M. Fischer, N. Kolachevsky, M. Zimmermann, R. Holzwarth, T. Udem, T. W. Hänsch, M. Abgrall, J. Grunert, I. Maksimovic, S. Bize, H. Marion, F. P. Dos Santos, P. Lemonde, G. Santarelli, P. Laurent, A. Clairon, C. Salomon, M. Haas, U. D. Jentschura, and C. H. Keitel, Phys. Rev. Lett. **92**, 230802 (2004).

[28] A. Huber, B. Gross, M. Weitz, and T. W. Hänsch, Phys. Rev. A **59**, 1844-1851 (1999).

[29] P. Lesage, IEEE Trans. Instrum. Meas. **32**, 204-207 (1983).

[30] J. K. Webb, M. T. Murphy, V. V. Flambaum, V. A. Dzuba, J. D. Barrow, C. W. Churchill, J. X. Prochaska, and A. M. Wolfe, Phys. Rev. Lett. **87**, 091301 (2001).

[31] Y. Fujii, A. Iwamoto, T. Fukahori, T. Ohnuki, M. Nakagawa, H. Hidaka, Y. Oura, and P. Moller, Nucl. Phys. B **573**, 377-401 (2000).

[32] H. Chand, Astronomy and Astrophysics **417**, 853-871 (2004); R. Quast, Astron. and Astrophys. **415**, L7-L11 (2004).

[33] S. A. Diddams, T. Udem, J. C. Bergquist, E. A. Curtis, R. E. Drullinger, L. Hollberg, W. M. Itano, W. D. Lee, C. W. Oates, K. R. Vogel, and D. J. Wineland, Science **293**, 825-828 (2001).

[34] V. A. Dzuba, V. V. Flambaum, M. T. Murphy, and J. K. Webb, Phys. Rev. A **63**, art. no.-042509 (2001).

[35] S. Bize, S. A. Diddams, U. Tanaka, C. E. Tanner, W. H. Oskay, R. E. Drullinger, T. E. Parker, T. P. Heavner, S. R. Jefferts, L. Hollberg, W. M. Itano, and J. C. Bergquist, Phys. Rev. Lett. **90**, 150802 (2003).

[36] E. Peik, Phys. Rev. Lett., submitted (2004).

[37] X. Calmet and H. Fritzsch, Euro. Phys. J. C **24**, 639-642 (2002).

Chapter 8

OPTICAL FREQUENCY MEASUREMENT USING FREQUENCY MULTIPLICATION AND FREQUENCY COMBS

Harald Schnatz, Jörn Stenger, Burghard Lipphardt, Nils Haverkamp, and Carl-Otto Weiss
Physikalisch-Technische Bundesanstalt

Abstract: We review the development of phase-coherent optical frequency measurement from its start with the harmonic frequency chain to the present use of optical comb generators. We demonstrate that the frequency fluctuations of a femtosecond comb laser—used in optical frequency measurement—can be eliminated completely from the measurement process, allowing ultimate frequency measurement performance. This principle was applied to the frequency measurements of the Ca cloud standard and the Yb^+ single-ion standard. The latter measurements confirm the suitability of these optical standards as future atomic clocks.

Key words: frequency comb, frequency chains, optical atomic clocks, optical frequency metrology, optical frequency references

1. INTRODUCTION

In the past, the measurement of optical frequencies with reference to standard rf frequencies was done analogously to microwave techniques. Essentially, higher frequencies were measured by harmonic mixing with lower frequencies, progressing from the microwave range through the infrared (IR) to the visible spectral range. The oscillators used were solid state and electron tube microwave sources up to 500 GHz and lasers for higher frequencies. For nonlinear elements, diodes with progressively smaller *RC*-time constants for increasing frequency were used, directly scaled from the microwave range.

Commonly used devices included micron-size semiconductor Schottky diodes (up to about 5 THz) [1] and metal-insulator-metal point contacts that work up to about 200 THz [2]. Above 100 THz, second-harmonic generation in bulk crystals was used. In this way it was possible to phase-coherently relate the 657 nm cold Ca atom optical frequency standard with a standard frequency generated by a cesium clock [3].

It may be worth remembering at this point in time, optical frequency measurements were only a rudiment in a much more ambitious program. The idea of scaling microwave techniques to the optical range arose from the development of the laser out of the maser. Consequently, several groups started to work on a program to develop "optical electronics" in the 1960s (prominent among these groups was Javan's group at MIT). This group envisioned scaling electronic elements in such a way that they would be capable of handling frequencies as high as visible optical radiation frequencies; thus they envisioned the generation of coherent optical radiation with transistor oscillators rather than with atom amplifiers using population inversion. This project would have entailed, of course, guiding light by wires or metal cables, which is possible over distances of small multiples of the wavelength. Techniques of this kind resurfaced in the 1980s and 1990s in near-field microscopy research.

The first steps in this program consisted of scaling diodes to high frequencies because a transistor was basically composed of two diodes. This research led to the successful implementation of optical frequency measurements where diodes served as the necessary, fast harmonic mixers.

Somehow, probably also under the impression of the successes of laser physics and technology, this ambitious program of "optical electronics" was forgotten. No serious efforts were ever made to realize diodes of the necessary small response time and negative resistance (not just a negative differential resistance as is sufficient for harmonic mixing), as necessary for amplification. Only half-hearted efforts were made (using metals with a higher plasma frequency) to increase the frequency response of point contact diodes beyond 200 THz, a limit imposed by the plasma frequency of commonly used metals [4].

Nevertheless, the desirability of a technique of "optical electronics" is still the same as it was in the 1960s; indeed, one might expect this program to be taken up again in the future, reinvigorated by an urgent need for ever-increasing speeds in electronics.

What was accomplished during this epoch, however, was the demonstration that electronic techniques can – if not amplify optical radiation – multiply and mix frequencies of radiation up to the visible spectral range.

2. FREQUENCY MEASUREMENTS BY REPEATED HARMONIC MIXING (FREQUENCY CHAINS)

Most lasers in the IR that can be used for a "frequency multiplication chain" are gas lasers. They are tunable only within approximately a Doppler-gain linewidth, i.e., 10^{-6} of their carrier frequency. For all practical purposes, this means a fixed frequency. Therefore the frequency multiplication chains were essentially designed (and only useful) for measuring one particular optical standard.

A certain flexibility was provided by the fact that, at around 30 THz, CO_2 lasers were used that had more than 100 different gain lines with gaps between 20 and 100 GHz. The chains aimed first at one particular CO_2-laser line. The continuation to higher frequencies was made possible by other CO_2-laser lines (which provided a certain frequency flexibility). The frequency gap between the two CO_2-laser lines used was bridged by using harmonics of millimeter wave sources.

In the Physicalisch-Technische Bundesanstalt (PTB), the frequency multiplication chain (Figure 8-1) was designed for the 657 nm Ca and the 3.39 µm CH_4 transitions. The microwave/far-IR part aimed at the $^{12}CO_2$ R(32) line to reach the CH_4 transition and used the $^{12}CO_2$ P(14) line for the continuation to Ca frequency standard. The gap of ~1 THz between these lines was bridged by the 8th harmonic of a 126 GHz oscillator. For details of this optical frequency measurement chain see [5].

Figure 8-2 shows the stability of frequency measurements for the CH_4 line at 3.39 µm and the Ca line at 657 nm. Both measurements are limited by the available short-term stability of the low-frequency reference (an H maser), which is also given.

The conclusion drawn from these results is that the combined instability of the optical references and the frequency measurement is smaller than that of the low-frequency reference. This effect occurred in spite of the fact that cycle slips in the phase locks, particularly at the 400 GHz step, could not be completely avoided. This result shows that optical atomic clocks are feasible. For the results of repeated measurements of the Ca line, see Section 5.1.

Optical frequency chain measurements as described need essentially one special set-up for an optical frequency range of only a few tens of GHz. The arrangements are thus specialized, complex, occupy a large amount of space, and consist of costly and difficult-to-operate lasers.

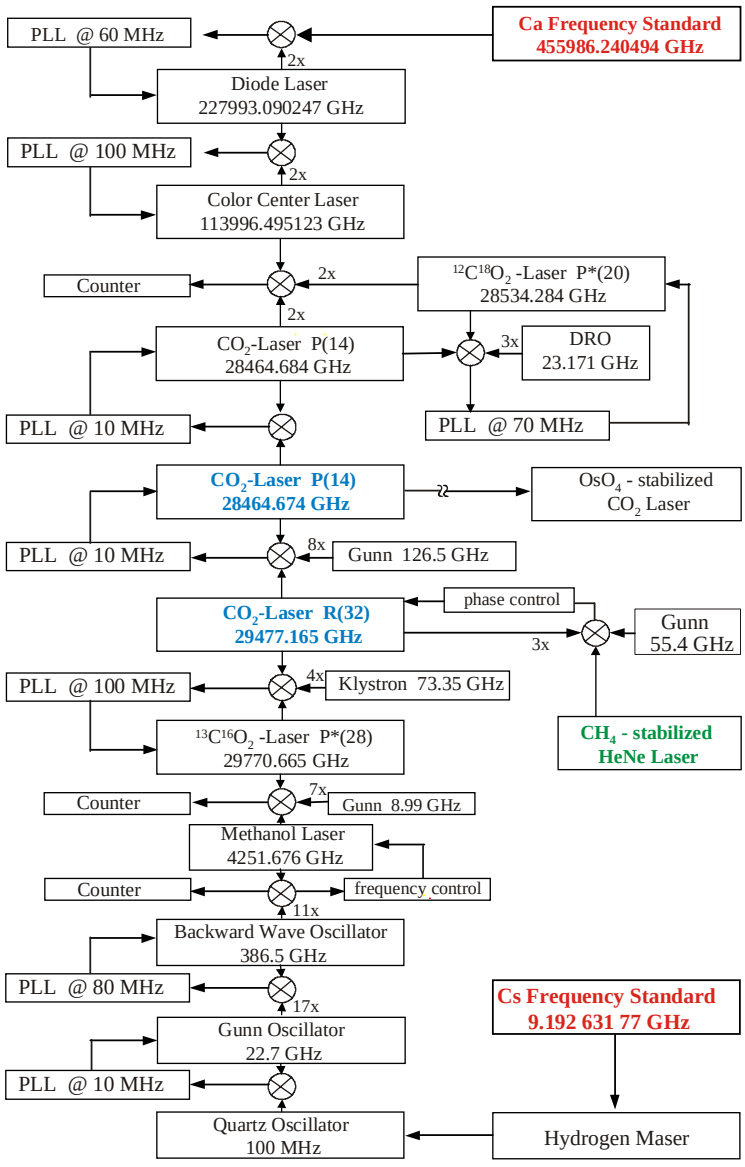

Figure 8-1. Harmonic frequency chain to the Ca frequency standard. (PLL: phase-locked loop; ⊗: harmonic mixers.)

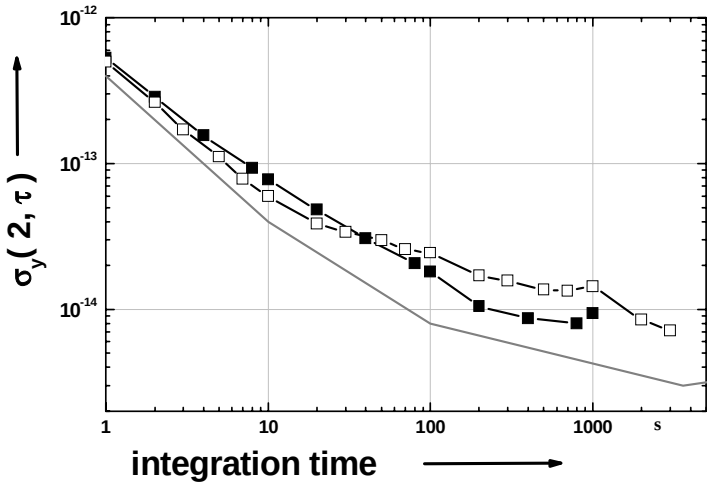

Figure 8-2. Allan standard deviation of Ca (■) and CH_4 (□) frequency standards. For comparison, the typical stability of an H maser is represented by the line without measurement points.

3. FREQUENCY INTERVAL DIVISION APPROACH

Several approaches to overcome the limitations of optical frequency measurement chains have been proposed. Among them are frequency interval bisection [6], optical-parametric oscillators (OPO) [7], optical comb generators [8, 9], sum- and difference-frequency generation in the near IR [10], frequency-division-by-three [11], and four-wave mixing in laser diodes [12]. All of these techniques rely on the principle of difference-frequency synthesis, in contrast to the harmonic-generation method used in the frequency chains.

Two techniques were primarily used: (a) frequency-interval division and (b) passive optical-comb generation. In method (a), the concept is that any optical frequency interval can be measured by successive frequency interval division. An interval is halved in the first step, divided by 4 in the second step, and then by 8, 16, etc. until the interval is small enough to be counted electronically. If the initial interval is the one between ν and 2ν (i.e., created by second-harmonic generation), then this process leads to the determination of the optical frequency ν. This "interval bisection" was first demonstrated by Telle et al. [6]. For the experiment, one uses a third laser (ν_3) at the arithmetic mean of the frequencies ν_1 and ν_2 to determine the interval (Figure 8-3). The frequency ν_3 bisects the interval between ν_1 and ν_2 if $2\nu_3 =$

$\nu_1 + \nu_2$. Complete frequency chains have been planned using this approach [6]. However, difficulties were encountered in obtaining the lasers in certain ranges of the visible spectrum.

To measure the frequency of the 1*S*–2*S* transition in atomic hydrogen, Hänsch's group in Garching built a frequency chain starting from a CH_4-stabilized reference laser at 3.39 µm and reaching the UV at 243 nm. The technique combined conventional harmonic mixing with optical interval bisection [13, 14]. The CH_4-reference frequency itself had to be calibrated using the harmonic-mixing frequency chain at PTB and a transportable CH_4-frequency standard.

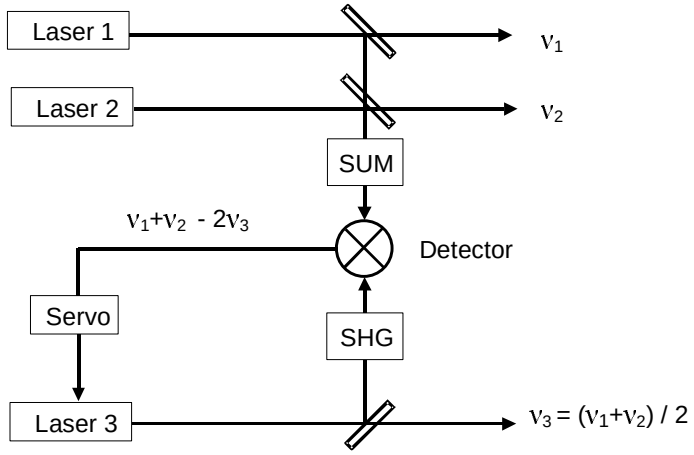

Figure 8-3. Diagram of an optical difference-frequency divider for frequency-interval bisection (adapted from Reference [6]).

An alternative method for frequency-interval division is to inject the two frequencies forming the interval into a laser that emits roughly at the half-interval frequency. Frequency components are generated via four-wave mixing symmetrically around the mid-interval frequency and act as "seeds" for the laser emitting near the mid-interval frequency. The four-wave-mixing products are all of equal frequency when the laser emits the half-interval frequency, and consequently a phase synchronization of the laser emission occurs. Thus the interval is divided by the laser phase-coherently. Due to the degeneracy of the two four-wave mixing processes occurring, there is phase bistability for the laser emission. The phase bistability is the basis for the formation of spatial solitons currently under consideration for optical information processing [15].

The second method (b) was conceived early [8]. Using an electro-optic modulator, driven at a microwave frequency (typically 5–10 GHz) in an optical resonator, a wide spectrum of modulation sidebands is produced. If the round-trip time of the light in the optical resonator is synchronized with the microwave period, the phase modulation of the light adds up over a number of round trips. This means that the phase excursion of the phase modulation is increased by a factor equal to the optical resonator finesse, thereby increasing the number and strength of the modulation sidebands. In this way, Kourogi [16] was able to generate frequency combs of 30 THz widths. Such a frequency comb generator was used by Huber et al. [17] to bridge a gap of ~2 THz in the 800 nm range. The width of the comb was further increased by passing the optical radiation through a nonlinear fiber that effects self-phase modulation.

During the last decade, a number of measurements of the properties of hydrogen, such as the 1*S*–2*S* transition frequency [18], the isotope shift in deuterium [19], the 1*S* Lamb shift [20], and the Rydberg constant [13, 21] were performed via optical frequency measurements. Incorporating novel techniques like Kurogi's optical comb generator [16], the frequency chain in Garching could be modified to measure the frequency of the In^+ clock transition at 236.5 nm [22]. More details of the various frequency measurements performed with different concepts at different laboratories can be found in recent review articles [23]. Although frequency-interval division had proved its usefulness, no complete chain was ever built using this principle.

4. OPTICAL FREQUENCY MEASUREMENT USING FEMTOSECOND LASERS

Apart from sequential-interval bisection, a frequency comb with precisely spaced comb lines may be used to measure the interval ν to 2ν. The requirement for this is that the comb width is $> (2\nu - \nu)$, i.e., larger than an octave. Initially efforts were directed at expanding the comb width of passive comb generators [16], but with the demonstration [24] that mode-locked Ti:sapphire lasers emit excellent spectral combs, the efforts concentrated on "active" comb generators, i.e., on mode-locked lasers. The concept foresaw using the comb spectrum emitted directly by the mode-locked Ti:sapphire laser, which is far less than an octave wide, and to reduce the octave interval by dividing the interval by 2 or 4, as described above. During the course of these efforts, however, evidence appeared of a more-than-an-octave-wide "continua" generated by mode-locked pulses in fibers with narrow cores [25, 26]. The suggestion was that these continua might

actually be coherent frequency combs if driven by mode-locked lasers, which by themselves emit coherent combs. In other words, the suggestion was that the generated octave-wide continua maintain the coherence of the driving field. Experiments quickly showed that these continua can, in fact, be coherent combs, and the first optical frequency measurements using octave-spanning combs were demonstrated [27]. Tests showed pulse-to-pulse coherence across the entire optical spectrum, and by comparing the interval division method with a comb-frequency measurement, the coherent nature of the comb was further ascertained [28].

In most frequency measurement schemes, errors can occur due to "cycle slipping." Considering that mode-locking a laser also involves a "phase-locking" process, 2π phase slips are conceivable that would adversely affect frequency measurement. A test, however, showed no indication of such cycle slips. By measuring an octave interval [29], it was shown that the frequency-measurement errors must be below $\Delta\nu/\nu = 10^{-18}$. In fact, the observed 10^{-18} limit was clearly caused by slow phase changes due to slow changes of optical path lengths because of temperature changes and can thus be improved (see Section 6.2).

The mechanism(s) that generate octave-wide spectra in nonlinear fibers are not entirely understood yet. In [30], it is argued that self-phase modulation (SPM) that is commonly assumed to account for the spectral broadening is by far too weak to generate octave-wide spectra. Model calculations show that wide spectra occur only under a condition where the pump pulse disintegrates into fundamental fiber solitons whose wavelength red-shifts in time (to cover the wide spectrum towards the IR) while the "dispersive waves" (i.e., the radiation "shedded" from the initial pulses in the process of soliton formation) blue-shift in time covering the short wavelength range. In a remotely related paper [31], it was shown that the dispersive waves themselves can subsequently transform to solitons, shedding additional light covering additional spectral ranges. Thus at the end a wide spectrum is generated.

These model calculations seem realistic since they predict several features to be critical that are in agreement with experimental results: (1) a particularly short pulse is not important (indicating that SPM is not the main mechanism for spectral broadening) and (2) wide spectra are only obtained in the case where the center of the input spectrums is close to the zero-dispersion point of the fiber. Therefore, it appears that octave-wide spectra are produced by not just one mechanism. Rather, several effects contribute, including Raman amplification, four-wave mixing, soliton formation, and SPM.

The question arises on how such incoherent processes can produce coherent comb spectra. All observations point to the following explanation: initially, in the interaction of the light with the fiber, SPM (which produces a coherent spectrum) creates a field that, at all comb frequencies (i.e., even at the edges of the width of an octave), exceeds the incoherent noise strongly. Thus incoherent amplification mechanisms must start from a coherent "seed" (instead of incoherent noise), resulting in a coherent octave comb. Because of the complete phase coherence of the entire comb, the phase fluctuations of one comb line are very small. The entire laser field acts as one coherent field; thus the phase fluctuations induced by spontaneously emitted photons (Shawlow-Townes phase diffusion) are exceedingly small given the total laser power of several 100 mW. The comb is extremely "rigid."

We mention that this enormous rigidity, or phase coherence, is not, in general, a property of mode-locked lasers. Mode-locked dye lasers, for example, lock predominantly by slow cascaded four-wave-mixing processes, where in each mixing process, (vacuum-) noise is added, so that in such systems the coherence range in the comb is much smaller than the comb width. It is this particular mode-locking mechanism of the Ti:sapphire laser that utilizes the essentially instantaneous Kerr effect that produces an instantaneous and completely synchronous refractive-index modulation for all modes throughout the spectrum.

Generally, optical oscillators possess extreme spectral purity limited only by spontaneous emission. One wonders if such high spectral purity could be transferred to other spectral regions where applications require it, e.g., to the rf/microwave range. To transfer the spectral purity to lower frequencies, a "noiseless-optical-frequency divider" would evidently be needed; however, such a device does not exist. Fortunately, as discussed above, the optical frequency can be measured in terms of the pulse repetition rate (the comb line spacing), such that the optical frequency is a (in general noninteger) multiple of the pulse repetition frequency. In this sense, the mode-locked laser contains a built-in divider. The latter is very low noise because of the rigidity of the comb spectrum. The laser radiation contains rf frequencies in the difference-frequency domain. However, these frequencies have to be converted to electrical signals. Although this optical-to-electrical conversion presents a limitation (photodiodes can only handle limited amounts of optical power), it can be estimated that microwave signals thus generated will be superior in phase noise to the fields of the best (cryogenic) microwave oscillators.

We now briefly describe the basic properties of a Kerr-lens, mode-locked laser that emits a periodic train of short pulses generating an optical frequency comb of distinct lines with well-defined, equidistant spacing. The

spectral span of this comb reflects the duration of an individual pulse, while the spacing between the lines is determined by the pulse repetition frequency.

We start with a time domain description of the pulses emitted by a mode-locked laser, as shown in the upper part of Figure 8-4. Every time the pulse circulating inside the cavity hits the output coupler, the laser emits a pulse. This process results in a train of pulses separated by time $\tau = l_c / v_g$, where l_c is the round-trip length of the cavity and v_g is the group velocity. Because of unavoidable dispersion in the cavity, the group and phase velocities v_p are, in general, not equal. This inequality results in a shift of the carrier phase with respect to the peak of the envelope for each round trip.

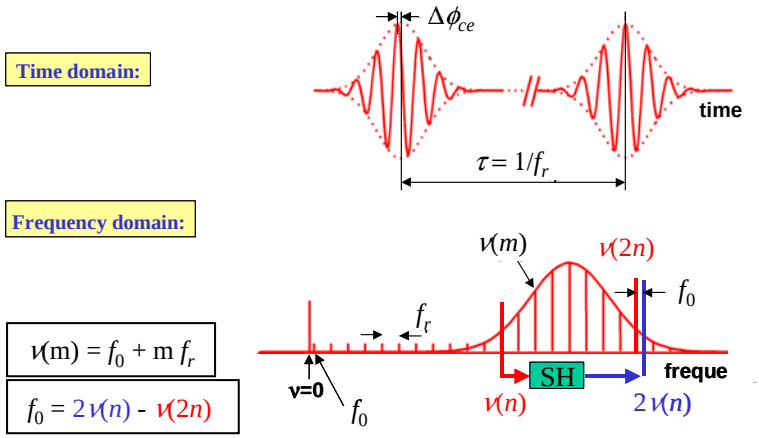

Figure 8-4. Representation of the output field of a mode-locked laser in the time domain or frequency domain, including the definition and measurement of the carrier-envelope-offset frequency f_0.

This shift between successive pulses is described by $\Delta\phi_{ce}$, which is proportional to the difference of the inverse of the group- and phase-velocities. Taking the Fourier transform of a train of pulses, together with the condition that the field reproduces itself after each round trip coherently, yields a comb spectrum with angular frequencies

$$\omega_m \equiv \frac{m \cdot 2\pi}{\tau} + \frac{\Delta\phi_{ce}}{\tau}. \qquad (1)$$

Dividing by 2π yields the frequencies of the m^{th} comb mode,

$$\nu(m) = mf_r + \frac{\Delta\phi}{2\pi} f_r = mf_r + f_0 . \qquad (2)$$

Therefore, the frequency of any line of the spectral comb emitted by such a laser, as shown in the lower part of Figure 8-4, is given by an integer m, the pulse repetition frequency f_r of the laser, and the carrier-envelope offset-frequency, f_0, which accounts for an offset of the entire comb with respect to the frequency zero. The frequency f_0 represents the time derivative of the optical (carrier) phase $\Delta\phi_{ce}$ as measured with respect to the pulse envelope.

The determination of the frequency of the m^{th} comb mode $\nu(m)$ therefore requires precision measurements of f_r, f_0, and m. The determination of m can be performed by a wavelength measurement, for example. The measurement of the pulse repetition rate f_r is straightforward to carry out. However, since f_r enters the optical frequency measurement process with the large factor m, the noise properties of the measurement are demanding.

The measurement of f_0 is also a demanding task. Several more or less complex schemes, depending on the comb span available, have been proposed for the measurement of f_0 [32]. The simplest concept requires an octave span of the frequency comb that is not directly available from the laser used. The available span has to be expanded, e.g., by external spectral broadening. Microstructure air-silica fibers, which allow the tailoring of the group-velocity dispersion (GVD) properties [26], are highly suited for SPM of moderate peak power pulses. They provide both lateral and temporal confinement of the pulses over long interaction lengths. If the octave span is achieved, then the f_0 measurement can be accomplished by second-harmonic generation (SHG) of the spectral lines in the low-frequency wing of the comb, as shown in Figure 8-4. This method has been developed at JILA [33] and MPQ [34].

Whereas the frequencies of the comb lines are shifted by f_0 with respect to the origin, their second harmonics are shifted by $2f_0$ (Figure 8-4). Thus, the beat notes between these harmonics and the corresponding high-frequency-wing lines of the comb shows the desired component at f_0 (n=2m)

$$\delta\nu = 2f_0 + 2mf_r - f_0 - nf_r = f_0 + (2m - n) f_r . \qquad (3)$$

When all three quantities f_r, f_0, and m are known, any unknown external optical frequency ν_{ext} of a laser emitting within the spectral range of the comb can, in turn, be determined by measuring the beat-note frequency $\Delta\nu$ with a suitable comb line. The absolute frequency ν_{ext} is then expressed by $\nu_{ext} = \nu(m) + \Delta\nu$. Furthermore, it is possible to directly reference the comb

spacing (f_r) and position (f_0) to the microwave cesium time standard, thereby determining the absolute optical frequencies of all of the comb lines.

This recent advance in optical frequency measurement technology has facilitated the realization of the ultimate goal of a practical optical frequency synthesizer: it forms a phase-coherent grid linking the entire optical spectrum to a microwave standard, or vice versa.

5. OPTICAL FREQUENCY MEASUREMENTS

We have used such "self-referenced" combs to measure the frequencies of the Ca cold atom cloud standard at 657 nm [35] and the single Yb^+-ion standard at 435 nm [36]. The arrangement in Figure 8-5 was used. The comb generator used a 10 fs Kerr-lens mode-locked Ti:sapphire laser [32] and a microstructure fiber for broadening the comb spectrum [26]. By coupling 30 mW into a 10 cm long fiber, we covered the spectrum from 500 to 1200 nm.

The pulses behind the fiber are frequency doubled and coherently superposed with the fundamental comb radiation. Variable delay adjusts the pulse arrival times so that the pulses of fundamental and frequency-doubled radiation overlap in time. A grating filters out the high frequency end of the spectrum that contains the f_0 beat, which is detected by a photo detector. The f_0 beat frequency is filtered by a tracking oscillator as developed for classical frequency multiplication work. It is an optimum filter strategy, for lasers and oscillators exhibiting only frequency noise with Fourier components in the kHz range [5].

The critical frequency to be measured is f_r since the optical interval ν to 2ν is measured as a very high multiple of this quantity. Instead of f_r itself, a high harmonic of it in the 10 GHz range (~100^{th} harmonic) is detected after spectral filtering of the laser light by a solid etalon of 10 GHz free spectral range. The 10 GHz beat is down-converted with a low noise 10 GHz signal synthesized from the rf-frequency standard (a hydrogen maser referenced to a cesium fountain clock). The difference frequency is again multiplied by 96 and by 3, reducing frequency-counter digitization errors to below the level of the noise of the H maser and thereby, the frequency that is effectively measured is 3 THz.

For the measurement of frequencies of optical standards, the light of these standards is heterodyned with a narrow range of the comb spectrum filtered out by interference filters around the standards' frequencies. The usual tracking oscillator is used for optimal filtering of the heterodyne signal.

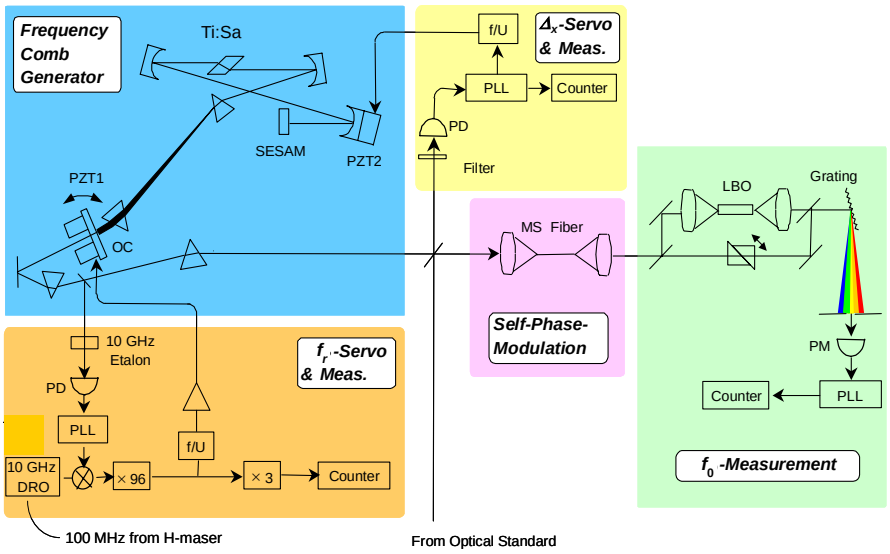

Figure 8-5. Femtosecond laser as frequency comb generator and generated comb spectrum. LBO: Lithium β-Borate crystal and SESAM: Semiconductor Saturable Absorber Mirror.

The optical standards that are used for absolute optical frequency measurement at PTB are located in two different buildings, and the comb generator in a third building. The standards' radiation is brought to the comb generator by ~250 m long single-mode fibers and the rf standard signal by air-dielectric cables. Measurements have shown that the changes in the cable and fiber lengths due to temperature changes, which produce temporal phase changes (corresponding to frequency shifts), remain below $\Delta\nu/\nu = 10^{-15}$. At the present level of precision for absolute frequency measurements, these changes can be neglected.

5.1 Ca frequency measurement

An improved Ca spectrometer uses an ensemble of cold Ca atoms prepared in a magneto-optical trap (MOT) [37]. The contributions to the uncertainty of the improved standard were investigated earlier [38], resulting in an overall uncertainty of 8 Hz ($\delta\nu/\nu = 2 \times 10^{-14}$). A summary of the historical record of frequency measurements of laser-cooled Ca frequency standards is shown in Figure 8-6. Earlier frequency measurements based on the harmonic frequency chain (see 1995–1997 in Figure 8-6) led to a fractional uncertainty of 2.5×10^{-13}. The first measurements of the Ca standard with a femtosecond laser comb agreed within the combined uncertainties (September 2000) [39]. In the meantime further measurements

were performed. These measurements were limited mainly by the uncertainties resulting from the corrections due to magnetic quadrupole fields of the MOT and AC-Stark shifts (June 2001). A frequency measurement with reduced uncertainty was then performed [35] where the spurious phase shifts resulting from misalignment and curvature of wave fronts were reduced and the systematic shifts due to the quadrupole MOT field and the AC-Stark shift were eliminated.

For a weighted mean of all frequency measurements shown in Figure 8-6, the measurements of June 2001 were averaged, and the uncertainty of the single measurements of 23 Hz kept as they were taken on a single day with no changes in the settings, so that the systematic shifts were not independent. The same was true for the two days of measurements in October 2001 that were averaged and their uncertainty determined to 8 Hz. With a new comb system, additional frequency measurements were done in October 2003, and individual data points were treated in the way described above, resulting in a total uncertainty of these measurements of 6 Hz. The weighted mean of all the frequency measurements performed at PTB with the harmonic chain and the femtosecond frequency comb is thus,

$$\nu_{Ca} = (\,455\,986\,240\,494\,149 \pm 6)\ \text{Hz}$$

with a relative standard uncertainty 1.3×10^{-14}.

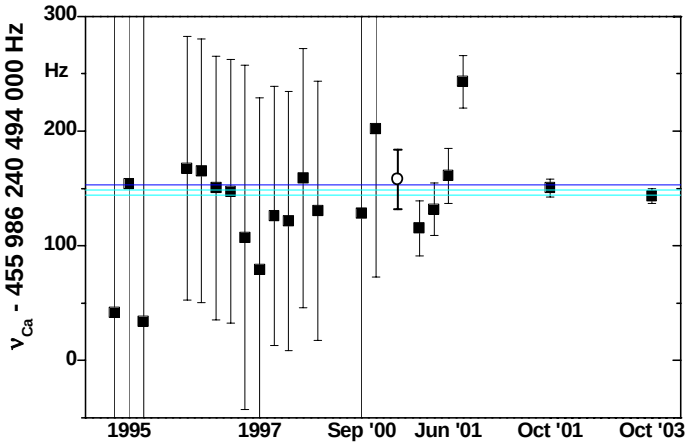

Figure 8-6. Frequency measurements of laser-cooled Ca optical frequency standards over the past eight years. The full-square data points represent data from PTB [38] while the single open-dot data point represents the frequency value reported by the NIST group [40]. Prior to 1999: a harmonic frequency chain; since 2000: femtosecond optical combs.

The Ca frequency measurement is in good agreement with recent measurements made at the National Institute of Standards and Technology (NIST), Boulder, also using a femtosecond comb generator [40]. The consistency of the Ca results between the two laboratories, over time and with different apparatus, demonstrates the good reproducibility of these standards with respect to the cesium primary frequency standards.

5.2 Yb^+ frequency measurement

Several measurements of the absolute frequency of the Yb^+ ion trap frequency standard were performed in 2001 and 2003. The results are shown in Figure 8-7. By averaging the data over the measuring period in 2001, a value for the 6s $^2S_{1/2}$ (F = 0) – 5d $^2D_{3/2}$ (F = 2) electric-quadrupole clock transition of the $^{171}Yb^+$ ion of

$$\nu_{Yb+} = 688\ 358\ 979\ 309\ 312\ \text{Hz} \pm 6\ \text{Hz}$$

was derived [41]. An additional measurement of its frequency was performed in 2003 with a new frequency comb generator. The results of this measurement deviated from the previous one by (–2.3 ± 6.4) Hz.

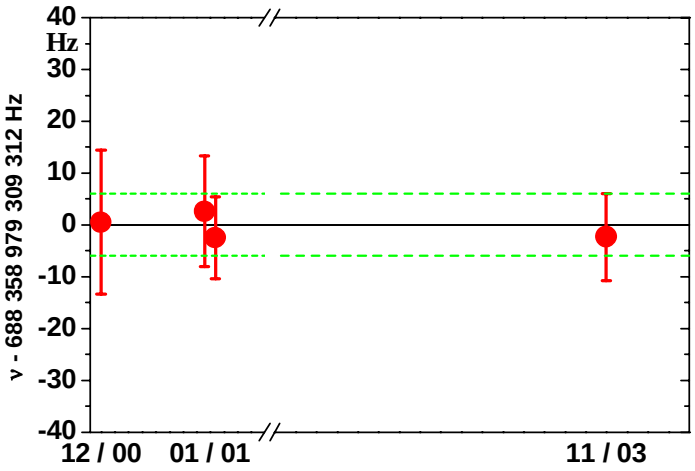

Figure 8-7. Frequency measurements of laser-cooled Yb^+ optical frequency standards over the past three years. The first three data points represent published data from Reference [41].

The combined 1σ-uncertainty of 6.4 Hz of the latest measurement is given by statistical and systematic contributions. Sources of systematic uncertainties are the realization uncertainty of the cesium fountain frequency

standard [42] and the $^{171}Yb^{+}$ frequency standard. The dominant contribution to the total uncertainty of the frequency value is the statistical uncertainty of the frequency measurement of 5 Hz because of the limited time of observation. The most significant systematic contribution to the uncertainty of 3 Hz is due to a quadrupole shift caused by unknown electric field gradients in the trap. This quadrupole Stark effect has recently been measured [43]. The reproducibility of frequency comparisons of two traps over an extended time, which included reloading traps, seems to indicate that this quadrupole Stark shift would, with the traps used presently, be below 1 Hz.

The weighted mean of the frequency of electric-quadrupole clock transition of the $^{171}Yb^{+}$ ion is

$$\nu_{Yb+} = 688\ 358\ 979\ 309\ 311 \pm 6 \text{ Hz}.$$

The measurement of the frequency of the electric-quadrupole clock transition of the $^{171}Yb^{+}$ ion with a relative uncertainty of 1×10^{-14} demonstrates the potential of the $^{171}Yb^{+}$ standard as a precise optical frequency reference.

In accordance with the measurements using the traditional frequency chain on the Ca standard and on the CH_4 IR standards [3, 44], the absolute frequency measurements are dominated by the noise of the low-frequency reference (the hydrogen maser) for short integration times.

6. TEST ON THE PRECISION OF FREQUENCY MEASUREMENT WITH FREQUENCY COMBS

6.1 Transfer technique

Ideally in a frequency measurement, the measurement instrument itself, i.e., the frequency multiplication chain or frequency comb, should not limit the measurement in any way. Obviously any laser setup exhibits frequency/phase-fluctuations. Even if one has the necessary "transducers" for phase locking all desired frequencies, the residual phase excursions $d\phi/dt$ still allow changes of the frequencies.

The faster the transducers (i.e., typically piezo transducers limited in speed by the mirror masses), the smaller the phase excursions can be held. (Evidently, with the increase of control speed, an increased signal-to-noise ratio of the control signals is required.)

In general, to become independent of transducer speed in frequency synthesis, the "transfer technique" is used. As an example, one may consider a frequency multiplication step (Figure 8-8). The frequency f_2 of a laser is measured against a reference near its frequency. (In a frequency multiplication chain this reference would be a harmonic of a lower frequency f_1 that is already known.) The beat signal $b_{1,2}$ between the reference and the laser contains all the frequency fluctuations of the transfer laser.

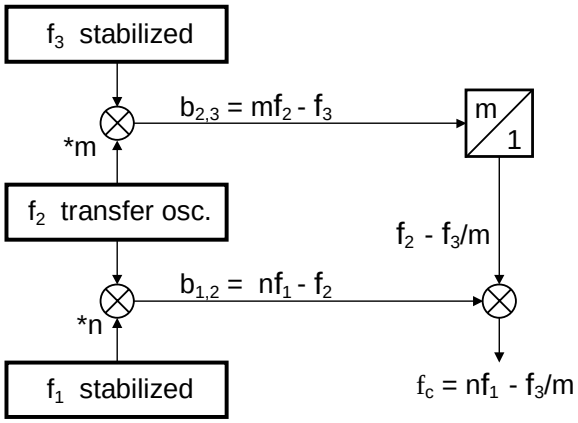

Figure 8-8. Using an intermediate oscillator in the transfer mode. The signal f_c is independent from f_2.

The laser's frequency is then multiplied m-fold and its harmonic compared with the frequency of another stabilized laser f_3 of approximately m-fold higher frequency. The latter beat signal $b_{2,3}$ contains the frequency fluctuations multiplied m times. Thus the frequency fluctuations of the transfer laser can be eliminated completely from the measurement by dividing the beat signal frequency $b_{2,3}$ electronically by m and subtracting it (e.g., by a mixer that produces a difference frequency) from the beat signal frequency $b_{1,2}$. The resulting difference frequency then measures directly the difference of the n^{th} harmonic of the reference and the laser frequency divided by m. All frequency fluctuations of the transfer laser itself are eliminated purely electronically, and no fast transducers are needed. The transfer laser itself does not enter into the measurement. It just "transfers" information from the reference frequency level by a (n x m)-multiple to the laser frequency level. Thus the name: "transfer technique." We have used the scheme of phase-coherent transfer in our conventional frequency multiplication chain [5].

For any phase-coherent frequency measurement, the maintenance of the coherence or "phase-tracking-ability" of the harmonic mixing signals is the essential requirement for a frequency measurement. Simply stated: if a frequency is multiplied by a factor N, its period duration is divided by N. If the low starting frequency shows a certain level of phase noise (i.e., the zero crossings of the field jitter by an amount Δt), then there is a critical factor N_{crit} above which Δt exceeds the period duration of the multiplied frequency. This means that, on average, the period to which a zero crossing belongs is no longer defined. (This phenomenon is called "coherence collapse.") If an oscillator "transfers" information between two other oscillators (relating their frequency in some way), the transfer technique can be generalized. In the way, the femtosecond comb generator can act as a transfer oscillator, and its frequency fluctuations thus do not enter the measurement process.

For the realization of absolute frequency measurement using the transfer technique, the scheme in Figure 8-9 was used. This scheme realizes physically the relation of the frequency ν of an optical frequency standard with the three measured frequencies f_r, f_0, and $\Delta\nu$: $\nu = m f_r + f_0 + \Delta\nu$. To keep the requirements on the phase detector stabilities reasonable, the pulse repetition frequency is measured as a high harmonic ($m_1 \sim 100$). The detector output frequency around 11 GHz is then down-converted to a range of a few MHz using a suitable harmonic of the absolute reference (hydrogen maser referenced to a cesium clock). The resolution of the frequency measurement is further increased by a factor m_3 using an additional tracking generator with a harmonic phase-locked loop. In this kind of harmonic generation, the harmonic number must be limited because of the decrease of the signal-to-noise ratio and of the necessary increase of the tracking bandwidth with the harmonic number that would both ultimately cause cycle slips.

On the other hand, the optical frequencies can be divided by the factor m directly. However, this reduces the resolution and the phase noise of the dividers will provide a serious limitation. Therefore, the two "optical" beats are summed and divided by m_2. This procedure leads to the optimized combination $m = m_1 \cdot m_2 \cdot m_3$. For practical reasons, we choose m_1 and m_3 in the range of 100 and 294, respectively.

In this way, the frequency ν_c represents the beat between the up-converted low-frequency reference (hydrogen maser referenced to cesium clock) and the down-converted optical-frequency standard. All information is contained in the frequency ν_c that is independent of the fluctuations of the comb. Since the input signals ν and f_{LO} are stable, it is possible to filter the signal ν_c by a filter of a few Hz(!) bandwidth, increasing the *SNR* ratio enormously.

This technique differs completely from the conventional approach in its handling of the technical frequency noise contributions. One radio frequency signal containing all necessary information about the external optical signals is synthesized and stabilization of the comb is not necessary. Technically, the complete cancellation of all femtosecond comb fluctuations requires a processing of the optical signals with a sufficiently high bandwidth. Considering the typical Fourier frequency range of the noise of f_0 and the beat signal $\Delta\nu$ of a few MHz, this requirement can be easily fulfilled.

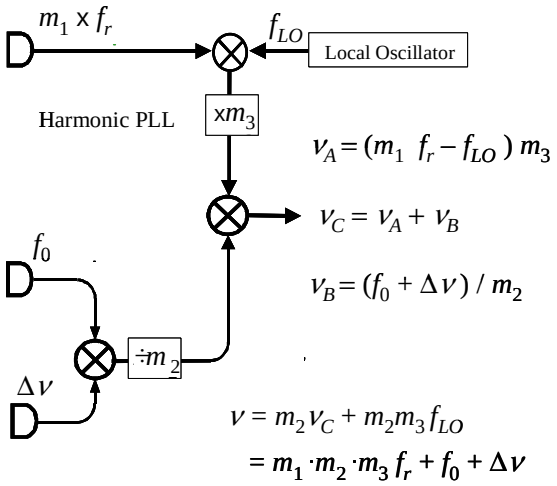

Figure 8-9. Linking microwave and optical frequencies: signal-processing scheme.

6.2 Frequency ratio

Any absolute frequency measurement requires that the frequency ν is measured and expressed in the SI-unit Hertz. The primary unit Hertz is technically realized by a cesium-clock controlled H-maser generating a standard frequency of 100 MHz, for example. Therefore, any absolute frequency measurement is principally limited by the frequency instability of the hydrogen maser. However, optical frequencies are measured (in many cases) with respect to an optical reference frequency by measurement of their frequency difference [45]. Then, only a fraction of the H-maser noise enters the measurement process and is given by the ratio between the frequency difference and the absolute frequency.

Measuring the ratio of two frequencies does not require a frequency reference. Because the ratio is a unitless number, it is not referred to an absolute frequency and its stability is that of the optical frequency standard

with the larger instability. Thus, frequency ratios for oscillators with better stability can be determined with smaller uncertainty if a technique is available to realize the frequency *ratio* without introducing additional noise. Such a technique is the transfer oscillator concept, described above, which has been generalized for signals with rational frequency ratios [29, 46].

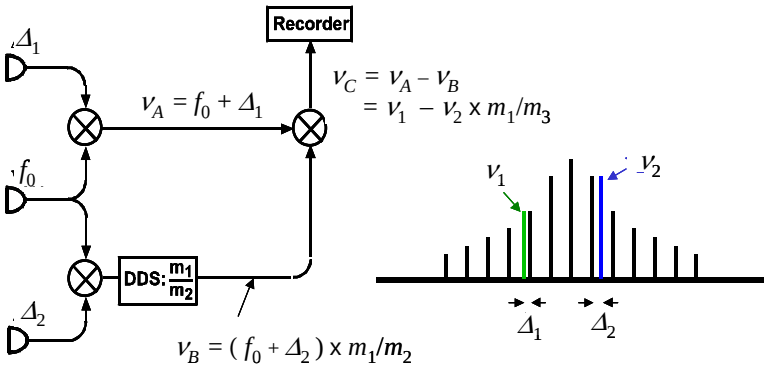

Figure 8-10. Modified transfer concept for the measurement of optical frequency ratios. ν_C represents the beat note between arbitrary optical frequencies ν_1 and ν_2.

If, as with the optical comb generator, two frequencies are related by the comb through a "rational" harmonic $\nu_2/\nu_1 = m_2/m_1$, then the two beats have to be treated accordingly. One of the beat frequencies has to be multiplied by m_2/m_1, and the result has to be subtracted from the other beat frequency. Figure 8-10 shows the scheme for the measurement of the ratio of the frequencies of two optical standards whose frequencies are given by

$$\nu_1 = m_1 \cdot f_r + f_0 + \Delta_1 \text{ and } \nu_2 = m_2 \cdot f_r + f_0 + \Delta_2 .$$

Three signals are detected: f_0 and two beat signals of two external frequency standards with the modes of the femtosecond frequency comb, Δ_1 and Δ_2. The sum frequency of Δ_1 and f_0 is generated by a mixer. The sum frequency of Δ_2 and f_0 is additionally processed with a direct-digital synthesizer (DDS). Such a device generates an output signal from an input signal with a frequency ratio given by a long digital tuning word. It numerically approximates the ratio of the two integers, m_1 and m_2, by $j/2^n$, where j is an integer and n the bit length of the tuning word. The resulting possible error is negligible for commercially available $n = 48$ bit devices.

Generating the difference frequency of the signals ν_A and ν_B with the help of a mixer, results in the ratio

$$\frac{\nu_2}{\nu_1} = \frac{m_2}{m_1} + \frac{1}{\nu_1}\left(\Delta_2 + f_0 - \frac{m_2}{m_1}(\Delta_1 + f_0)\right) = \frac{m_2}{m_1} + \frac{\nu_C}{\nu_1}.$$

The frequency ν_C is a measure of the (small) deviation of the optical signals frequency ratio ν_2/ν_1 from m_2/m_1. Since $\nu_C << \nu_1, \nu_2$, the requirements on the radio frequency reference are, in general, not demanding. The frequency ν_C carries the full information of the fluctuations of the ratio ν_2/ν_1 and can be considered as the frequency of the beat note between ν_1 and ν_2 as *projected* to the vicinity of ν_1. However, the uncertainty of ν_1 enters and limits the precision of the ratio if the term in the brackets is not zero. By proper choice of f_r and f_0, this term can be made equal to zero and the ratio of optical frequency standards can be measured without knowledge of the comb-related frequencies (except for the definite determination of the mode numbers m_1 and m_2). By measuring ν_C, this scheme allows one to realize a relative frequency measurement of an unknown frequency ν_2 with respect to an arbitrary frequency reference ν_1.

As well as measuring the ratio of two optical frequencies, the method allows the measurement of the ratio of an optical and a radio frequency. This rf reference can be related to a primary standard, thereby realizing the absolute frequency measurement described in the previous paragraph.

The measurement of a frequency ratio has been used with a subharmonic of the Yb^+ ion-frequency standards ν_{Yb^+} at 871 nm [47], and an iodine-stabilized Nd:YAG laser ν_0 at 1064 nm [48]. Referring to Figure 8-10, the beat note of ν_{Yb^+} with a comb mode was Δ_2 and that of ν_0 was Δ_1. The output of the last mixer in Figure 8-10 is equivalent to the beat signal between the iodine and Yb^+ signals at a virtual frequency of $\nu_C = 43$ THz.

Figure 8-11 shows the resulting Allan standard deviation of this ratio measurement (open squares) and of an absolute optical frequency measurement of the Yb^+ optical frequency standard (full dots). The accuracy of the absolute frequency measurement is limited by the noise of the hydrogen maser (solid line). In contrast, the frequency noise of the beat note between the Yb^+ and iodine signals is expected to be substantially smaller than that of the H-maser, at least at Fourier frequencies $f > 0.1$ Hz. The direct frequency comparison of two independent I_2-stabilized standards shows frequency instabilities similar to that found for the Yb^+/I_2-ratio measurement, indicating that this ratio measurement was limited by the noise of the I_2-stabilized standard. The dashed line assumes a white noise level of $\approx 3 \times 10^{-14}$ at 1 s.

This experiment demonstrated the capability of phase-coherently linking optical frequencies from very different spectral regions without introducing additional noise from the measurement process. Thus frequency-ratio

measurements between optical frequencies with short-term instabilities superior to that of a microwave reference can be carried out.

Using the setup we just described, it was not possible to investigate any possible noise contribution from the femtosecond comb; the stability of even the high-quality reference-signal pair was not good enough. Therefore, in a second experiment, we used the signal ν_0 and its second harmonic ν_{SH} that was generated in a nonlinear crystal. The frequency-doubling process enabled the generation of a pair of reference frequencies with almost completely correlated fluctuations, leading to a fixed frequency ratio of 2:1 even for the shortest averaging times.

Referring to Figure 8-10, the beat note of ν_{SH} with a comb mode was Δ_2 and that of ν_0 was Δ_1. The DDS was replaced by a frequency divider of 2. Both comb lines generating the beat notes at the fundamental and the second harmonic were themselves generated in the microstructure fiber.

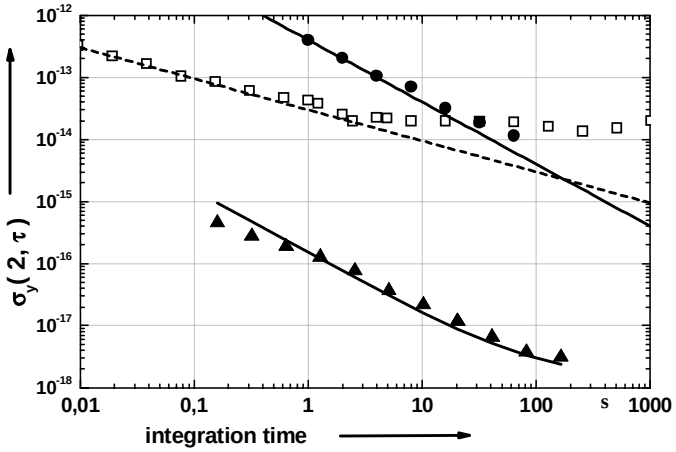

Figure 8-11. Allan standard deviation of the Yb^+ frequency standard (full dots) with respect to an H-maser. The frequency instability of a typical hydrogen maser reference (solid line) is given for comparison. The open squares represent the stability of an I_2-stabilized–frequency-doubled Nd:YAG laser as derived from the frequency ratio with respect to Yb^+ standard. The triangles show the Allan standard deviation for the frequency ratio between the second harmonic and the fundamental of the I_2-stabilized Nd:YAG laser.

The triangles in Figure 8-11 show the Allan standard deviation for this measurement. The instability is more than two orders of magnitude smaller than for the ν_{Yb+}/ν_0 measurement, for which high-quality oscillators were already used. The optical frequency ratio can be measured at averaging times of 100 s to a level of $\sim 10^{-18}$ corresponding to mHz fluctuations. The residual fluctuations at the large averaging times do not indicate a limitation of the

frequency measurement but are the result of the slow optical phase variations caused by the changes in the optical path lengths between the optical elements on the table where the system was set up, in temperature, in the motion of the air, and so forth. These variations could evidently be reduced further so that 10^{-18} does not represent a limit in measurement precision.

In any case, the lower curve shows unambiguously that the transfer method works well and that a frequency comb used in the transfer mode is adequate for forming a part of future atomic clocks based on optical transitions; it would not limit the transfer of optical stability to the rf range, even at the projected precision and stability of 10^{-18}.

Figure 8-12 shows a Fourier transform of the measurements represented by the lowest curve of Figure 8-11. The 9 mHz spectral line representing the frequency measurement uncertainty corresponds to the "virtual measurement frequency" of 43 THz. Converted to the measured optical frequency of 282 THz it would show a spectral line of 60 mHz width (still remarkably narrow) at 282 THz as characterizing the measurement, or the coherence of the measurement process.

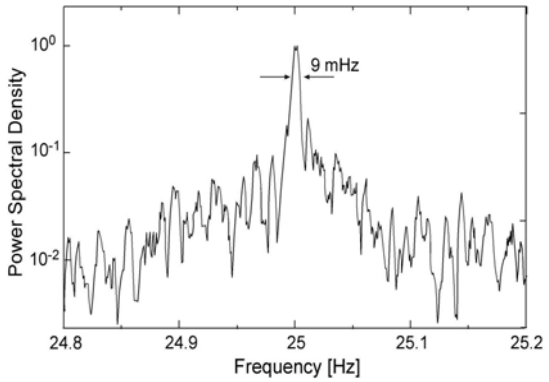

Figure 8-12. Power spectrum of the beat note between sub-harmonics of the outputs of an I_2 and an Yb^+-frequency standard taken at a virtual frequency of 43 THz as calculated from the recorded phase excursions by fast Fourier transform.

7. SUMMARY

Frequency chains have been developed and operated for many years in several laboratories. However, during the last few years, great progress has been achieved in the development of optical frequency standards and optical

frequency synthesis. These advances are based on precision spectroscopy with cold absorbers and improvements of phase-coherent optical frequency measurements. In the past, each laboratory focused on different target frequencies and hence different frequency standards. With the development of optical frequency measurements based on femtosecond lasers, a new era in optical frequency metrology was started. In fact, optical frequency measurements based on femtosecond lasers will soon be available in many laboratories. This concept is well suited for measuring the absolute frequency of essentially *any* optical frequency standard with reproducibility at the level of the present primary atomic frequency standards.

The control of the comb frequencies, especially the carrier offset frequency f_0, which arises from the pulse to pulse phase shift of the carrier envelope phase, allows one to investigate extreme nonlinear processes that are directly sensitive to the electric field of each pulse such as x-ray generation, and it can be used to tightly synchronize independent mode-locked lasers operating in different spectral regions [49].

With the femtosecond comb, it is possible to compare different optical frequency standards by beat frequency measurements, and the reproducibility of stabilized lasers can now be determined over long periods of time by comparisons with the cesium atomic clock. Furthermore, the use of active optical-frequency comb generators allows one to develop accurate clocks operating in the optical frequency range.

It can be envisaged that the uncertainty of the best optical frequency standards will eventually become lower than that of the present realization of the second. This new situation may lead to a replacement of the (cesium-based) definition of the second by an optical reference frequency. With the continuing fast progress in the development of optical frequency standards, the selection of the “best reference” will be a challenging and exciting task.

ACKNOWLEDGEMENTS

The authors gratefully acknowledge the contributions of C. Degenhardt, J. Helmcke, E. Peik, F. Riehle, U. Sterr, H. R. Telle, and C. Tamm.

REFERENCES

[1] C. O. Weiss and A. Godone, IEEE J. Quantum Electron. **20**, 97-99 (1984).
[2] D. J. E. Knight, K. I. Pharaoh, and M. Zucco, in *5th Symposium of Frequency Standards and Metrology*, Woods Hole, MA, 1995), p. 465-467.

[3] H. Schnatz, B. Lipphardt, J. Helmcke, F. Riehle, and G. Zinner, Phys. Rev. Lett. **76**, 18-21 (1996).
[4] H. U. Daniel, M. Steiner, and H. Walther, App. Phys. **25**, 7-12 (1981).
[5] C. O. Weiss, G. Kramer, B. Lipphardt, and H. Schnatz, in *Frequency Measurement and Control Advanced Techniques and Future Trends*, 2000), Vol. 79, p. 215-247.
[6] H. R. Telle, D. Meschede, and T. W. Hänsch, Opt. Lett. **15**, 532-534 (1990).
[7] N. C. Wong, Opt. Lett. **15**, 1129-1131 (1990).
[8] M. Kourogi, K. Nakagawa, and M. Ohtsu, IEEE J. Quantum Electron. **29**, 2693-2701 (1993); M. Kourogi, T. Enami, and M. Ohtsu, IEEE Photonics Technol. Lett. **6**, 214-217 (1994).
[9] L. R. Brothers, D. Lee, and N. C. Wong, Opt. Lett. **19**, 245-247 (1994).
[10] D. A. van Baak and L. Hollberg, Opt. Lett. **19**, 1586-1588 (1994).
[11] O. Pfister, M. Murtz, J. S. Wells, L. Hollberg, and J. T. Murray, Opt. Lett. **21**, 1387-1389 (1996); P. T. Nee and N. C. Wong, Opt. Lett. **23**, 46-48 (1998).
[12] C. Koch and H. R. Telle, J. Opt. Soc. Am. B **13**, 1666-1678 (1996).
[13] T. Andreae, W. Konig, R. Wynands, D. Leibfried, F. Schmidtkaler, C. Zimmermann, D. Meschede, and T. W. Hänsch, Phys. Rev. Lett. **69**, 1923-1926 (1992).
[14] T. Udem, A. Huber, B. Gross, J. Reichert, M. Prevedelli, M. Weitz, and T. W. Hänsch, Phys. Rev. Lett. **79**, 2646-2649 (1997).
[15] V. B. Taranenko, K. Staliunas, and C. O. Weiss, Phys. Rev. Lett. **81**, 2236-2239 (1998).
[16] K. Imai, M. Kourogi, and M. Ohtsu, IEEE J. Quantum Electron. **34**, 54-60 (1998).
[17] A. Huber, T. Udem, B. Gross, J. Reichert, M. Kourogi, K. Pachucki, M. Weitz, and T. W. Hänsch, Phys. Rev. Lett. **80**, 468-471 (1998).
[18] F. Schmidt-Kaler, D. Leibfried, S. Seel, C. Zimmermann, W. Konig, M. Weitz, and T. W. Hänsch, Phys. Rev. A **51**, 2789-2800 (1995).
[19] F. Schmidt-Kaler, D. Leibfried, M. Weitz, and T. W. Hänsch, Phys. Rev. Lett. **70**, 2261-2264 (1993).
[20] M. Weitz, A. Huber, F. Schmidtkaler, D. Leibfried, and T. W. Hänsch, Phys. Rev. Lett. **72**, 328-331 (1994).
[21] F. Nez, M. D. Plimmer, S. Bourzeix, L. Julien, F. Biraben, R. Felder, O. Acef, J. J. Zondy, P. Laurent, A. Clairon, M. Abed, Y. Millerioux, and P. Juncar, Phys. Rev. Lett. **69**, 2326-2329 (1992).
[22] J. von Zanthier, J. Abel, T. Becker, M. Fries, E. Peik, H. Walther, R. Holzwarth, J. Reichert, T. Udem, T. W. Hänsch, A. Y. Nevsky, M. N. Skvortsov, and S. N. Bagayev, Opt. Commun. **166**, 57-63 (1999).
[23] S. T. Cundiff, J. Ye, and J. L. Hall, Rev. Sci. Instrum. **72**, 3746-3771 (2001); J. Ye, H. Schnatz, and L. W. Hollberg, IEEE J. Sel. Top. Quantum Electron. **9**, 1041-1058 (2003).
[24] T. Udem, J. Reichert, R. Holzwarth, and T. W. Hänsch, Phys. Rev. Lett. **82**, 3568-3571 (1999); T. Udem, J. Reichert, R. Holzwarth, and T. W. Hänsch, Opt. Lett. **24**, 881-883 (1999); J. Stenger and H. R. Telle, in *Laser Frequency Stabilization: Standards, Measurement and Applications*, edited by J. L. Hall and J. Ye (SPIE, San Jose, CA, 2001), Vol. 4269, p. 72.

[25] J. C. Knight, T. A. Birks, P. S. Russell, and D. M. Atkin, Opt. Lett. **21**, 1547-1549 (1997); N. G. R. Broderick, T. M. Monro, P. J. Bennett, and D. J. Richardson, Opt. Lett. **24**, 1395-1397 (1999).
[26] J. K. Ranka, R. S. Windeler, and A. J. Stentz, Opt. Lett. **25**, 25-27 (2000).
[27] S. A. Diddams, D. J. Jones, L. S. Ma, S. T. Cundiff, and J. L. Hall, Opt. Lett. **25**, 186-188 (2000); S. A. Diddams, D. J. Jones, J. Ye, S. T. Cundiff, J. L. Hall, J. K. Ranka, R. S. Windeler, R. Holzwarth, T. Udem, and T. W. Hänsch, Phys. Rev. Lett. **84**, 5102-5105 (2000).
[28] R. Holzwarth, M. Zimmermann, T. Udem, and T. W. Hänsch, IEEE J. Quantum Electron. **37**, 1493-1501 (2001).
[29] J. Stenger, H. Schnatz, C. Tamm, and H. R. Telle, Phys. Rev. Lett. **88**, 073601 (2002).
[30] A. V. Husakou and J. Herrmann, Phys. Rev. Lett. **8720**, art. no.-203901 (2001).
[31] W. S. Man, H. Y. Tam, M. S. Demokan, and D. Y. Tang, Opt. Quant. Electron. **33**, 1139-1147 (2001).
[32] H. R. Telle, G. Steinmeyer, A. E. Dunlop, J. Stenger, D. H. Sutter, and U. Keller, Appl. Phys. B **69**, 327-332 (1999).
[33] D. J. Jones, S. A. Diddams, J. K. Ranka, A. Stentz, R. S. Windeler, J. L. Hall, and S. T. Cundiff, Science **288**, 635-639 (2000).
[34] R. Holzwarth, T. Udem, T. W. Hänsch, J. C. Knight, W. J. Wadsworth, and P. S. J. Russell, Phys. Rev. Lett. **85**, 2264-2267 (2000).
[35] J. Helmcke, G. Wilpers, T. Binnewies, C. Degenhardt, U. Sterr, H. Schnatz, and F. Riehle, IEEE Trans. Instrum. Meas. **52**, 250-254 (2003).
[36] C. Tamm, T. Schneider, and E. Peik, in *Frequency Standards and Metrology, Proceedings of the 6th Symposium*, edited by P. Gill (World Scientific Publishing, 2001), p. 369-384.
[37] F. Riehle, G. Wilpers, U. Sterr, T. Binnewies, and J. Helmcke, in *Frequency Standards and Metrology, Proceedings of the 6th Symposium*, edited by P. Gill (World Scientific Publishing, 2001), p. 339-357.
[38] G. Wilpers, T. Binnewies, C. Degenhardt, U. Sterr, J. Helmcke, and F. Riehle, Phys. Rev. Lett. **89** (2002).
[39] J. Stenger, T. Binnewies, G. Wilpers, F. Riehle, H. R. Telle, J. K. Ranka, R. S. Windeler, and A. J. Stentz, Phys. Rev. A **63**, 021802 (2001).
[40] T. Udem, S. A. Diddams, K. R. Vogel, C. W. Oates, E. A. Curtis, W. D. Lee, W. M. Itano, R. E. Drullinger, J. C. Bergquist, and L. Hollberg, Phys. Rev. Lett. **86**, 4996-4999 (2001).
[41] J. Stenger, C. Tamm, N. Haverkamp, S. Weyers, and H. R. Telle, Opt. Lett. **26**, 1589-1591 (2001).
[42] S. Weyers, U. Hubner, R. Schroder, C. Tamm, and A. Bauch, Metrologia **38**, 343-352 (2001); T. Heindorff, A. Bauch, P. Hetzel, G. Petit, and S. Weyers, Metrologia **38**, 497-501 (2001).
[43] C. Tamm, personal communication 2004.
[44] F. Riehle, H. Schnatz, B. Lipphardt, G. Zinner, T. Trebst, and J. Helmcke, IEEE Trans. Instrum. Meas. **48**, 613-617 (1999).
[45] G. Kramer, B. Lipphardt, and U. Hubner, in *Joint Meeting of the EFTF and the IEEE International Frequency Control Symposium* (IEEE, Besancon, 1999), Vol. 99CH36313.

[46] H. R. Telle, B. Lipphardt, and J. Stenger, Appl. Phys. B **74**, 1-6 (2002).
[47] C. Tamm, D. Engelke, and V. Bühner, Phys. Rev. A **61**, 053405 (2000).
[48] P. Cordiale, G. Galzerano, and H. Schnatz, Metrologia **37**, 177-182 (2000).
[49] R. K. Shelton, S. M. Foreman, L. S. Ma, J. L. Hall, H. C. Kapteyn, M. M. Murnane, M. Notcutt, and J. Ye, Opt. Lett. **27**, 312-314 (2002); R. K. Shelton, L. S. Ma, H. C. Kapteyn, M. M. Murnane, J. L. Hall, and J. Ye, Science **293**, 1286-1289 (2001).

Chapter 9

FEMTOSECOND LASERS FOR OPTICAL CLOCKS AND LOW NOISE FREQUENCY SYNTHESIS

Scott A. Diddams[1], Jun Ye[2] and Leo Hollberg[1]
[1]*Time and Frequency Division, National Institute of Standards and Technology*

[2]*JILA, National Institute of Standards and Technology and University of Colorado*

Abstract: In the late 1990's mode-locked femtosecond lasers were introduced as an important new tool for the synthesis and measurement of optical frequencies. The simplicity, robustness and improved precision of femtosecond lasers have now led to their prominence in the field of optical frequency metrology. In addition, their use is developing significant new time-domain applications based on the precise control of the carrier-envelope phase. It is anticipated that narrow linewidth lasers referenced to optical transitions in atoms and ions will soon be the best electromagnetic frequency references of any kind, with projected fractional frequency instability below $1\times10^{-15}\tau^{-1/2}$ and uncertainties approaching 1×10^{-18}. When used in conjunction with such ultraprecise frequency standards, the femtosecond laser serves as a broadband synthesizer that phase coherently converts the input optical frequency to an array of optical frequencies spanning hundreds of terahertz and to countable microwave frequencies. The excess fractional frequency noise introduced in the synthesis process can approach the level of 1×10^{-19}.

Key words: optical atomic clocks, optical frequency metrology, mode-locked lasers, frequency comb, optical frequency synthesis

1. INTRODUCTION

Recent developments in time and frequency metrology have brought us to the point where we can begin to address the possibility of using atomic clocks "ticking" at optical frequencies (~500 THz) to measure time intervals

with uncertainties approaching 1 part in 10^{18}. This represents a dramatic shift from the past fifty years of precision time keeping, where atomic clocks

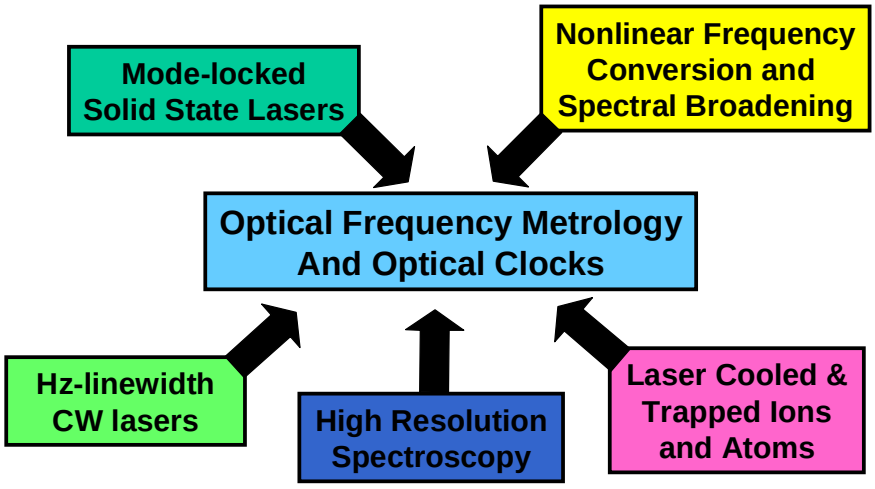

Figure 9-1. The development of optical clocks and optical frequency metrology has arisen out of many different sub-fields of atomic, molecular, and optical physics. While optical clocks have their roots in the precision optical-frequency spectroscopy of cooled and trapped ions and atoms, the emergence of robust mode-locked solid-state femtosecond lasers and nonlinear spectral broadening/conversion techniques has provided new opportunities and invigorated the field as a whole.

have exclusively operated at microwave frequencies, with the 9,192,631,770 Hz ground-state hyperfine transition in cesium-133 being the internationally recognized definition for the SI second. The jump from microwave to optical frequencies has been jointly fueled by advances in several branches of atomic and optical physics, including laser cooling and trapping, precision spectroscopy, frequency stabilized lasers, nonlinear fiber optics, spectral broadening and frequency conversion, and femtosecond mode-locked lasers (see Figure 9-1). Over the past 30–40 years, developments in precision optical frequency spectroscopy with highly stabilized lasers have formed a solid basis for the surge of activity in optical frequency metrology since 1999. Pioneers of this field [1-8] recognized that the spectroscopy of cooled and trapped atoms with narrow linewidth lasers would be valuable for precision measurements in general, and even 20–30 years ago, prototype "optical clocks" were being developed [6, 9]. While it was clear that clocks operating at optical frequencies had much potential for improved stability and accuracy, a longstanding problem in the development of such clocks has been a reliable and straightforward means of counting the extremely rapid

optical oscillations. Solutions to this counting problem involved harmonic frequency chains [10, 11] at several national facilities or an alternative approach based on interval bisection [12]. However, both of these techniques required significant resources and were rather complicated, meaning it was unlikely they could ever become widespread and reliable. In 1998-99, this scenario was rapidly changed after the group of T. Hänsch demonstrated that mode-locked femtosecond lasers could play an important role in optical frequency metrology [13, 14]. With the subsequent introduction of highly nonlinear optical fibers that could broaden the femtosecond laser spectrum to bandwidths greater than one octave, all of the pieces rapidly came together for the implementation of a simple and elegant single-step phase-coherent means of counting optical frequencies [15, 16].

As illustrated by Figure 9-1 and this brief introduction, the science and technology that underlie optical clocks are rich and varied. Several excellent reviews and introductions to this topic already exist [17-22] and others are found in this volume itself. Instead of attempting to provide a comprehensive review, we will focus on the role that femtosecond lasers play in emerging optical clocks and in low noise frequency synthesis. We will begin by presenting the main components that make up an optical clock and highlight some of the most relevant detail of the atomic references. The bulk of this chapter will then describe in detail the role of the femtosecond laser in optical clocks and low-noise optical and microwave frequency synthesis. This description will include various methods by which the femtosecond laser can be controlled as well as some tests that have searched for inaccuracies in such laser systems when they are used in precision frequency measurements. An overview of the array of different femtosecond laser synthesizers that have been developed since 2000 will be presented. And in conclusion, we will discuss recent experiments focused on the distribution of optical clock signals through optical fiber networks using mode-locked lasers.

1.1 Basic components of optical clocks

Most common clocks consist of two major components: an oscillator that produces periodic events or “clock ticks,” and a counter for accumulating and displaying each tick [23]. For example, the swing of a pendulum provides the periodic events that are counted, accumulated, and displayed via a set of gears driving a pair of clock hands. Similarly, in a quartz watch, the mechanical vibrations of a small quartz crystal are electronically detected, accumulated, and displayed to generate time. However, because of the influence of environmental fluctuations, the nature

of an artifact-based standard makes it very difficult for a quartz oscillator to remain reproducible at a level of 1 μs per day. Atomic clocks add a third component that solves this problem: the resonance of a well-isolated atomic transition that is used to control the oscillator frequency. This is where precision spectroscopy becomes vital to ensure that the evolution of a clock signal is ultimately governed by fundamental quantum physics. If the frequency of the oscillator is controlled to match the transition frequency between two unperturbed atomic states (i.e., the oscillator is locked to the atomic transition frequency), then the time generated can have the desired long-term stability and accuracy. For an atomic clock based on a microwave transition, high-speed electronics count and accumulate a defined number of cycles of the reference oscillator to mark a second of time. As sketched in Figure 9-2, the basic concepts are the same for an atomic clock based on an optical transition at a much higher frequency. In this case, the oscillator is a stabilized laser with its frequency locked to an optical transition. However, no electronic device exists that can directly count the extremely rapid optical oscillations. Until very recently, devices that could divide an optical frequency down to a countable microwave (called "frequency chains") were complicated, large-scale devices requiring significant resources for operation [11, 24, 25]. However, as will be described in detail in Section 3, the advent of femtosecond-laser-based clockwork greatly simplifies this problem of directly counting the optical frequency.

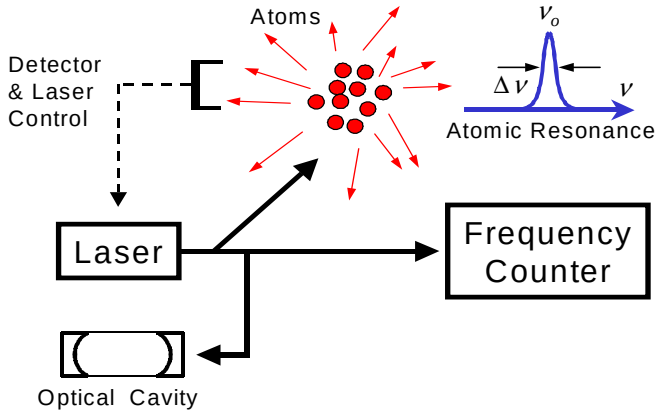

Figure 9-2. Schematic diagram of an optical clock. A laser is first stabilized to a Fabry-Perot optical cavity that provides a means to narrow the laser linewidth leading to good short-term stability. The center of a narrow resonance in an appropriate atomic sample then provides a stable reference to which the frequency of the laser can be steered. Once its frequency is locked to the center of the atomic resonance, a predetermined number of optical cycles are counted to mark a second of time.

1.2 Uses of optical atomic clocks

While timekeeping is an important aspect of our everyday lives, most of us do not really care or need to know the exact time to much better than ~60 seconds at any point in our daily routines. Computer networks that record financial transactions and reservations may require timekeeping that is ~100 times better than this, but still at the modest level of millisecond accuracy. However, many technological applications, such as communication and navigation systems (e.g., the Global Positioning System, GPS [26]), are much more demanding, requiring clocks that are stable and accurate at the level of 10–100 nanoseconds per day. The most accurate clocks are ultimately referenced to natural resonances in atoms, and they provide a unique tool for the scientific exploration of basic atomic structure and the physical interactions between atoms and their environment. It is necessary for timekeeping purposes to have clocks that are accurate at the level of 100 picoseconds per day (1 part in 10^{15}), but it is also arguable that clocks with such performance are equally valuable as basic science research tools. The next generation optical clocks that are currently being developed will move beyond this already astounding level of performance, with projected uncertainties approaching 1 part in 10^{18}. In other words, if such a clock could run indefinitely, it would neither gain nor lose one second in the lifetime of our universe.

It is valid and important to ask why scientists, or society for that matter, might want still better clocks. A brief look back in the history of timekeeping provides some idea of how we might expect emerging optical clocks to benefit society in the coming decades. In the 1950s when microwave atomic clocks based on cesium (and other atoms and molecules) were first developed, the situation was not so different from where we find ourselves today. The first atomic clocks were quickly recognized as being significantly better than the existing mechanical and quartz-based clocks, yet at the same time, they were mainly a tool of scientific interest. At that point, few people would imagine that just 30 years into the future, a constellation of satellites containing cesium and rubidium atomic clocks would circumnavigate the globe providing accurate time and position to all people below. The GPS and its constituent atomic clocks are now an integral part of our lives. While it is difficult to extrapolate to the next 50 years, it is fully expected that optical clocks will find numerous applications in advanced communications and navigation systems. For example, the very stable optical clock ticks may be especially useful for tracking and communication between satellites and spacecraft in the much greater expanses beyond our planet. Indeed, stable and precise lasers are envisioned

to provide both laser distance ranging (length metrology) and time keeping simultaneously for satellites [27].

For the near future, it is already clear that optical clocks and optical frequency metrology will provide interesting and new scientific avenues to study our universe—pushing the limits on tests of the most fundamental physical laws to new levels. Of particular interest is the continued application of optical frequency standards in spectroscopy and the improved determination of the fine structure constant α and the Rydberg constant R_∞ [14, 28]. As measurement accuracy improves, metrologists may find themselves in the unique position of being able to observe physical "constants" evolve in time [29]. Indeed, laboratory tests on the possible divergence of clocks based on different atomic transitions already provide some of the most stringent constraints of the variation of α [30, 31]. Experiments of fundamental importance for which precision clocks/oscillators are of value include searches for variations in the isotropy of space, a preferred reference frame, and Lorentz and Charge-Parity-Time (CPT) symmetry violation [32]. Following the recent trapping of cold antihydrogen at CERN [33], in the coming years it may be possible to compare optical clocks based on the 1S–2S transitions in both hydrogen and anti-hydrogen [34]. Such measurements would provide precisions tests of the fundamental symmetry between matter and antimatter [35].

1.3 A brief history of the development of optical clocks

In the decade following the invention of the laser, it became clear to many researchers that a stable optical oscillator had great potential for precision measurements including time keeping. The reader is referred to the references [24] and the contributions of Chapter 8 in this volume for a more detailed history of the development of optical frequency standards and optical clocks. Here, we present only a brief overview of this topic touching on a few of the most important advances.

Not long after the invention of the laser, efforts were in place to stabilize its frequency to the center of its Doppler-broadened gain profile. From that point forward, an increasingly sophisticated set of tools was used to improve the resolution and fidelity with which a laser's frequency could probe, and be stabilized to, a narrow spectroscopic feature in an atom, ion, or molecule. The proposal to use the divided-down output of a laser-based oscillator suitably locked to a quantum reference as a time and/or frequency standard was put forth by pioneers such as Javan [36] and Dehmelt [1]; however, the difficult task of counting optical cycles was a formidable challenge that could be addressed by only a few research groups and national laboratories with sufficient resources. This effort resulted in the so-called harmonic

frequency chains that employed successive nonlinear steps to multiply the frequency of a cesium-based primary standard up to the IR and then, ultimately, the optical domain. At NIST (then National Bureau of Standards), a cesium-referenced frequency measurement of the 88 THz methane-stabilized helium-neon laser was combined with a krypton-referenced wavelength measurement of the same stabilized laser to provide a hundredfold improvement to the measurement of the speed of light. This was a conclusive demonstration of the value of laser-based frequency standards, and soon thereafter, the speed of light was defined as a fixed value such that an optical frequency standard could also serve as an absolute length standard (e.g., $\lambda = c/f$). The result of this advance cannot be overstated. The ubiquitous 633 nm helium-neon laser, with its *frequency* stabilized to a known transition in iodine, has served for the past 20 years as the *length* standard for wide variety of industrial and scientific applications.

The widespread use of atomically stabilized lasers for time standards has been more difficult to realize. Beyond the serious problem of counting optical cycles, this is due, at least in part, to the continued improvements and excellent performance accessibility of cesium-based microwave frequency standards (the latest developments of cesium standards around the world can be found in Reference [37]). Nonetheless, in the 1980s at least two groups developed operational "optical clocks" based on the 88 THz methane-stabilized helium-neon laser and conventional frequency chains [6, 9]. The fractional short-term stability for these devices was already in the 10^{-12} regime where the limitation arose from the microwave standard against which the optical clock was compared. In the 1990s laser cooling and trapping techniques were introduced and refined frequency chains were developed to connect optical transitions to the microwave domain. Noteworthy in this respect were the efforts surrounding Ca (456 THz) [10] and Sr^+ (445 THz) [11] at the Physikalisch-Technische Bundesanstalt of Germany and the National Research Council of Canada, respectively.

2. THE ATOMIC REFERENCE

Every optical atomic clock needs a quantum reference, which is most commonly an electronic transition in an atom, molecule, or ion. As might be expected, many factors go into the choice of a specific reference, and atoms, molecules, and ions all have advantages and disadvantages relative to one another. In this section, we will first describe the benefit one gains by choosing an optical reference as opposed to a microwave reference. Then we will spend some time describing references based on single trapped ions,

an ensemble of laser-cooled and trapped atoms, and molecular gases. Specific examples from laboratory systems will also be provided.

When the center-of-mass motion of the quantum reference for the clock is well controlled, the coherent interaction time in both optical and microwave domains can be the determining factor of the spectral resolution. However, the optical part of the electromagnetic spectrum provides ~100,000 times higher operating frequencies. Therefore, the resonance quality factor, $Q = \nu/\nu_0$, of an optical clock transition is expected to be significantly higher than that available in the microwave domain. (Here, ν_0 is the atomic transition frequency and $\Delta\nu$ is the transition linewidth.) A superior Q factor provides a more stable frequency standard, and is essential for making a more accurate standard as well. This is seen in the Allan deviation $\sigma_y(\tau)$ which provides a convenient measure of the fractional frequency instability of a clock as a function of the averaging time τ [38]. For an oscillator locked to an atomic transition, the Allan deviation is

$$\sigma_y(\tau) \approx \left\langle \frac{\Delta\nu_{rms}}{\nu_0} \right\rangle_\tau \approx \frac{1}{\pi \cdot Q}\sqrt{\frac{T}{\tau N}}, \qquad (1)$$

where $\Delta\nu_{rms}$ is the measured frequency fluctuation, N is the number of atoms, and T is the cycle time (i.e., the time required to make a determination of the line center) with $\tau > T$. This expression assumes that technical noise is reduced to a sufficiently small level that the quantum-mechanical atomic projection noise is the dominant stability limit [39]. In this limit, $\sigma_y(\tau)$ decreases as the square root of the averaging time for all clocks, so a tenfold decrease in the short-term instability leads to a hundredfold reduction in averaging time τ to reach a given stability and uncertainty. This point is particularly important if one ultimately hopes to reach a fractional frequency uncertainty of 10^{-18}, which is the anticipated level for ion-based optical clocks. In this case, an extremely small short-term instability, i.e., $\sigma_y(\tau) \leq 1\times10^{-15}\,\tau^{-1/2}$, is clearly desirable to avoid inordinately long averaging times (see Figure 9-3).

Since $\sigma_y(\tau)$ scales as $1/Q$, all else being equal, the shift from microwave to optical frequencies should improve the short-term stability by a factor of 10^5. Thus, with a linewidth of about 1 Hz and 10^6 atoms detected every 0.5 seconds, theoretically, these systems could support an instability $\sigma_y(\tau) \approx 5 \times 10^{-19}\tau^{-1/2}$. This simplistic estimate ignores significant complications that will degrade the performance. Nonetheless, it promises that in the years ahead there will be plenty of room for improvement using optical frequency standards. The current status and near-term prospects of the Allan deviation for optical and microwave frequency standards is shown in Figure 9-3

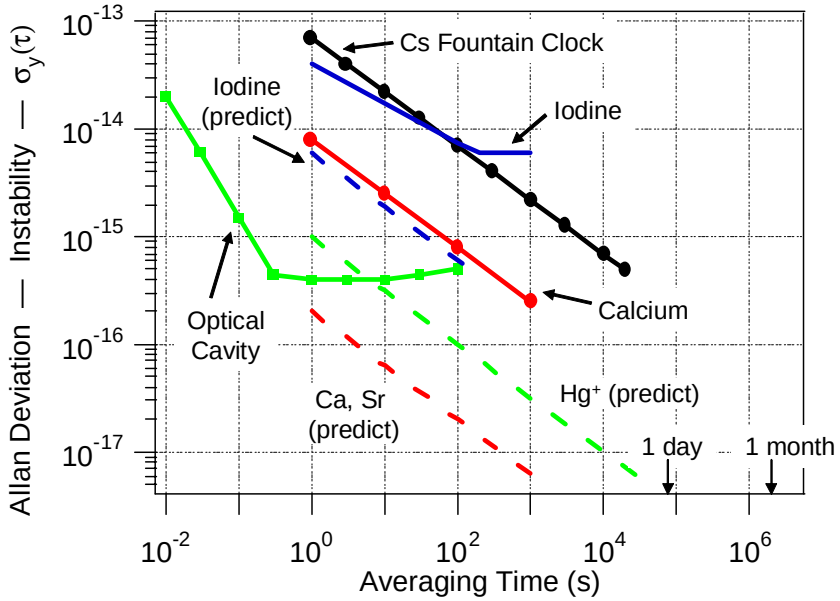

Figure 9-3. Fractional frequency instability as characterized by the Allan deviation of a microwave frequency standard (cesium fountain clock) and several promising optical frequency standards. The plotted curves are based on measured data, except where predicted curves are given as dashed lines.

2.1 Single ion references

Trapped ions, particularly single laser-cooled ions, have numerous advantages as optical frequency standards and clocks [1, 40]. Perhaps one of their most important attributes is the nearly ideal independence between the trapping potential for the center-of-mass motion and the internal atomic level structure that provides the clock reference. Importantly, ions can be confined in an rf trap and laser-cooled so that the amplitude of the residual motion is much less than the optical wavelength of the probe radiation (the Lamb-Dicke limit). This nearly eliminates the velocity-dependent Doppler broadening and shifts associated with motion of the ion relative to the probing radiation. In a cryogenic environment, the ion is nearly unperturbed by atomic collisions, and the effects of blackbody radiation are also very small. The storage time of a single ion in a trap can be months; hence, the probe interaction time is usually constrained by other technical issues such as the laser coherence time or, fundamentally, by the natural lifetime of the transition under study. This permits extremely high-*Q* resonances to be

observed. All of these factors are critically important for the achievement of the highest accuracy.

The technical challenges of making an optical frequency standard based on a single ion are formidable but single-ion standards have now been achieved in a handful of laboratories around the world. At NIST, an optical-frequency standard based on a single trapped $^{199}Hg^{+}$ ion is being developed. The performance of this standard is immediately competitive with the performance of the best microwave standards and has the potential to surpass those standards in terms of stability, frequency reproducibility, and accuracy. For this standard, a single $^{199}Hg^{+}$ ion is trapped in a small rf Paul trap (≈1 mm internal dimensions) and laser cooled to a few milliKelvins using 194 nm radiation. A highly stabilized dye laser at 563 nm with a linewidth of less than 1 Hz is frequency doubled to 282 nm (1,064 THz) to probe the clock transition [41]. Measured linewidths as narrow as 6.7 Hz on the 282 nm transition have been reported [42]. For an averaging time τ in seconds, the projected instability of an optical frequency standard using a single Hg^{+} ion is $1 \times 10^{-15}\tau^{-1/2}$, and fractional frequency uncertainties approaching 1×10^{-18} seem feasible.

One apparent difficulty of modern optical standards is the requirement that suitable transitions for laser cooling, fluorescence detection, and the clock itself be present in the same atom or ion. While some atoms have good clock transitions, their cooling and detection transitions might be less than ideal. Wineland et al. have proposed an efficient solution to this problem in the case of ion-based clocks that involves simultaneously trapping a "clock" ion and a "logic" ion [43]. Using techniques developed for quantum computation applications [44], the logic ion would provide the functions of sympathetic cooling and detection, leaving more flexibility in choosing the best clock ion with a narrow, unperturbed and accessible transition. This approach is currently be implemented at NIST using $^{27}Al^{+}$ as the clock ion and $^{9}Be^{+}$ as the logic ion.

2.2 Neutral atom references

Some neutral atoms also have narrow optical transitions that are relatively insensitive to external perturbations and are thus attractive as optical frequency standards. Neutral atoms have some advantages and disadvantages relative to ions. Using the well-established techniques of laser cooling and trapping, they are fairly easy to confine and cool to low temperatures. However, in contrast to ions, the trapping methods for neutrals perturb the atomic energy levels, which is unacceptable for use in a frequency standard. To avoid the broadening and shifts associated with the trap, neutral atoms are released from the trap before the clock transition is

probed. The atoms fall from the trap under the influence of gravity and expand with low thermal velocities (typically a few cm/s). The resulting atomic motion brings with it limitations in accuracy (and even stability) that are associated with velocity-dependent frequency shifts. Two of the more troublesome effects are the limited observation time and the incomplete cancellation of the first-order Doppler shift associated with wave-front curvature and wave-vector mismatch. Reduced observation times limit the line *Q*, the stability, and the accuracy. However, neutral atoms do have at least one significant advantage: large numbers of atoms can be used, producing a large signal-to-noise ratio (*SNR*) in a short time and the potential for exceptional short-term stability.

The atomic Ca optical frequency standard [45, 46] is one of the most promising and extensively studied cases. It has a 400 Hz wide clock transition at 657 nm ($^1S_0 - {}^3P_1$) that is reasonably immune from external perturbations. It is readily laser cooled and trapped, and it is experimentally convenient because the relevant transitions are accessible with tunable diode lasers. Cooling and trapping of about 10^7 Ca atoms to mK temperatures can be accomplished in a magneto-optic trap (MOT) with frequency doubled diode laser tuned to the 423 nm $^1S_0 - {}^1P_1$ transition. With the cooling radiation turned off, an injection-locked and stabilized diode laser at 657 nm (456 THz) then probes the clock transition with the separated excitation method of optical Ramsey-Bordé spectroscopy. Optical fringes with high signal-to-noise ratio are observed using shelving detection on the cooling transition. With this technique, the present Ca standard can provide short-term fractional frequency instability of about 4×10^{-15} in 1 s of averaging. Second stage cooling on the narrow $^1S_0 - {}^3P_1$ to temperatures ~10 μK has been achieved with the aid of 552 nm light that quenches (i.e., depopulates) the long-lived $^3P_1$ state [47]. The 10-μK temperatures reduce velocity-related systematic shifts, and it appears that uncertainties at or below 10^{-15} will be attainable with such a system.

Ultimate neutral atom-based systems with high accuracy will demand a stringent separation between the external degrees of freedom (controlled by the trapping potential) and internal level structure (clock transitions), similar to that obtained with single trapped ions. A crucial step towards high reproducibility and accuracy is to confine neutral atoms in the Lamb-Dicke regime, while at the same time limiting the effect of the confining potential to only the external degrees of freedom [48]. The fermionic isotope of ^{87}Sr has a nonzero nuclear magnetic moment (I = 9/2) that gives rise to magnetic substructure in both the ground and excited states [49]. Moreover, ^{87}Sr possesses a doubly forbidden J = 0 to J = 0 clock transition, $^1S_0$ (F = 9/2) – $^3P_0$ (F' = 9/2), which has a ~1mHz linewidth (corresponding to an intrinsic

line Q of 4.3×10^{17}) and is expected to be highly insensitive to external electromagnetic fields and collisional shifts [50]. The Sr atoms are first cooled in two stages to temperatures <1 μK [51]. These pre-cooled atoms can then be efficiently transferred into a far-off-resonance optical lattice trap where sideband cooling can bring the atoms to the motional ground state. Using a magic wavelength (~800 nm) for the latter trap ensures that both the ground and excited ($^3P_0$) state experience the same energy shift anywhere inside the trap. The sensitivity to the light polarization is reduced because of the fact that J = 0 for both clock states. The ^{87}Sr $^1S_0$ (F = 9/2) – $^3P_0$ (F' = 9/2) transition can then be interrogated free from broadening and shifts due to Doppler, recoil, and trapping potential related shifts.

2.3 Molecular references

The abundance and relatively convenient gas-cell spectroscopy of molecular resonances make them attractive references for optical clocks as well. Indeed, IR transitions in molecules such as CH_4, CO_2, and OsO_4 were some of the first references explored [25, 52] and continue to be used in several research programs around the world [53]. Their natural linewidths range from a few megahertz to below a kilohertz, limited by molecular fluorescent decay. Useable linewidths are usually ≥10 kHz due to the transit of molecules through the light beam. Transitions to higher levels of these fundamental rovibrational states, usually termed overtone bands, extend these rovibrational spectra well into the visible with similar ~ kHz potential linewidths. Until recently, the rich spectra of the molecular overtone bands have not been adopted as suitable frequency references in the visible due to their small transition strengths. However, with one of the most sensitive absorption techniques, which combines frequency modulation with cavity enhancement, an excellent *SNR* for these weak but narrow overtone lines can be achieved, enabling the use of molecular overtones as standards in the visible [54].

Perhaps the most widespread example of a molecular reference is the iodine molecule. The narrow-linewidth I_2 transitions in the visible wavelength region have provided excellent cell-based optical frequency references for laser stabilization. Frequency-doubled Nd:YAG/$^{127}I_2$ at 532 nm has proved to be one of the best portable optical frequency standards with compact size, reliability, and high stability ($<5 \times 10^{-14}$ at 1 s) [55]. To reach a better frequency stability, it is useful to explore I_2 transitions towards the dissociation limit at wavelengths below 532 nm where the natural linewidths decrease at a faster rate than the line strengths. The systematic variation of the I_2 transition linewidths within the range of 498–532 nm has been measured, with the linewidth decreasing by nearly sixfold when the

wavelength is decreased from 532 nm to near the dissociation limit [56]. The high *SNR* results indicate that I_2 transitions in the wavelength range 501–532 nm hold great promise for future development of optical frequency standards, especially with the advent of all-solid-state Yb:YAG lasers. One exciting candidate is the 514.67 nm standard that has a projected instability $<10^{-14}$ at 1 s [57].

Table 9-1. Some of the promising optical frequency references for emerging and future optical clocks. Presently achieved values of instability and uncertainty are listed, while the projected values are given in parentheses. The research institute is given in the last column.

	Frequency (THz)	1-s Fractional Instability	Fractional Uncertainty	Institute
Ions				
Hg^+	1064	3×10^{-15} (1×10^{-15})	1×10^{-14} ($<1\times10^{-17}$)	NIST
In^+	1267		2×10^{-13}	MPQ
Sr^+	445		5×10^{-15}	NRC, NPL
Al^+	1124			NIST
Yb^+	688		9×10^{-15} ($<1\times10^{-17}$)	PTB
Yb^+	642		2×10^{-12}	NPL
Neutral Atoms				
H	2466		2×10^{-14}	MPQ
Ca	456	4×10^{-15} ($<2\times10^{-16}$)	2×10^{-14} ($<1\times10^{-15}$)	PTB, NIST
Sr				U. Tokyo, JILA, SYRTE, LENS
Yb				KRISS, NIST
Molecules				
OsO_4	29		3×10^{-13}	Paris Nord
CH_4	88			Lebedev, NPL, PTB, Novosibirsk
I_2	563	4×10^{-14}	9×10^{-12}	JILA, PTB, NMIJ, BIPM

2.4 Local oscillator requirements

While it is necessary to start with a suitable atomic transition, whether it be in an ion, atom, or molecule, as diagramed in Figure 9-2, another important element of an optical clock is the local oscillator. For an optical clock, the local oscillator is comprised of a continuous wave (cw) laser that has its emission spectrum narrowed and stabilized to an isolated high-Q Fabry-Perot optical cavity. The optical cavity must have sufficiently good short-term stability to permit interrogation of a narrow spectroscopic feature in the quantum reference (i.e., ion, atom, or molecule) with a good *SNR*. For example, in the case of the single Hg^+ ion, the optical transition linewidth is just a few hertz wide, which requires a local oscillator with a sub-hertz linewidth. Significant effort has been invested for the past few decades in the reduction of the laser linewidth down to this sub-hertz level [41, 58]. A key aspect in this development has been improved techniques for the mechanical and thermal isolation of the Fabry-Perot optical cavity from the surrounding laboratory environment [41]. A more recent advance in this evolution focuses on reducing the acceleration sensitivity of the cavity through geometrical design and by careful choice of how the cavity is supported.

3. FEMTOSECOND LASER-BASED OPTICAL FREQUENCY SYNTHESIZERS

The possibility of using a mode-locked laser as a tool for optical frequency metrology was first demonstrated with picosecond lasers by Hänsch and co-workers in the late 1970s [59]. The essence of this original idea was to use the comb of frequencies emitted from a mode-locked laser as a precise "optical frequency ruler." The spacing of the tick marks of such an optical frequency ruler is given by the repetition rate f_r at which pulses are emitted from the mode-locked laser, while the differential phase shift $\Delta\phi_{ce}$ between the pulse carrier and the pulse envelope each round trip determines the overall offset of the comb elements $f_0 = f_r\ (\Delta\phi_{ce}/2\pi)$. The relationship between these two parameters and the n^{th} element of the optical frequency comb is given by the simple expression

$$\nu_n = nf_r + f_0 . \qquad (2)$$

This technique lay largely dormant until experiments in 1998 demonstrated that the frequency comb associated with a femtosecond mode-locked laser could be readily controlled and provided a more versatile and

precise method for counting optical frequencies than existing technologies [13]. In fact, in just a matter of years, the new femtosecond comb technology has fully replaced laboratory efforts that existed for decades; it is now widely accepted that mode-locked femtosecond lasers will play a critical role in the next generation of atomic clocks based on optical frequencies [46, 60, 61]. Moreover, due to the simplicity and relatively low cost, the techniques and tools described here can be implemented in university and industrial research laboratories, which has resulted in a variety of interesting and exciting new avenues of research [62-64].

The absence of robust solid-state femtosecond lasers likely contributed to the twenty-year delay between the first conceptual experiments and practical implementation of the frequency comb concept. Although the femtosecond dye laser was developed throughout the 1970s and 1980s, it was not until the 1990s that robust and high-power femtosecond lasers based on titanium-doped sapphire (Ti:sapphire) were perfected [65, 66]. (Chapter 2 of this volume presents a detailed account of development of solid-state mode-locked laser technology.) For comb generation, it was natural that femtosecond Ti:sapphire would become the source of choice. When combined with nonlinear microstructure and tapered fibers [67], octave-spanning spectra could be generated. A few representative Ti:sapphire laser configurations and resulting spectra are shown in Figure 9-4. It is important to realize that the array of frequency modes given by Equation (2) reside beneath the broad spectral envelopes shown in this figure (which were recorded with a low resolution grating spectrometer). As will be described in further detail below, such a simple means for generating very broad spectra allows for the straightforward measurement and control of f_0 in addition to providing a network of useful comb lines spanning the visible and near-IR.

In this section, we will not dwell on the actual generation of the frequency comb from a femtosecond laser. The reader is referred to several excellent review articles on this topic [17, 18, 21], in addition to the other chapters in this book. Instead, we will explain the details of how a femtosecond laser is actually used in an optical clock and for low noise frequency synthesis. We first spell out some of the specific metrological considerations that arise in the use and choice of a femtosecond laser for optical clocks and synthesis applications. Next, we discuss the "mechanical" details of actually using and controlling a femtosecond laser. We will then present what is currently known about the achievable noise properties of the laser itself. Finally, while Ti:sapphire femtosecond lasers continue to be the most widely used options for optical clocks and frequency metrology, fiber-based femtosecond laser sources and alternative solid-state lasers that can be

efficiently pumped offer significant advantages in terms of size and cost. We will spend the last part of this section looking at these sources and the benefits they might have for future optical clocks.

3.1 Considerations in designing a femtosecond comb for use in an optical clock

The first experiments [13, 15, 16] verifying the valuable contribution of femtosecond lasers to optical frequency metrology all employed femtosecond lasers that had been developed over the previous decade for experiments in ultrafast science [66]. While such lasers worked very well for the initial proof-of-principle experiments, and continue to be used in many cases, they lacked other desirable qualities for frequency metrology. The ultimate femtosecond laser for optical frequency metrology and optical clocks is likely to be a continuously evolving device, but nonetheless, in this section we attempt to lay out some of the desirable characteristics of these devices as they relate to their use in frequency metrology and optical clocks.

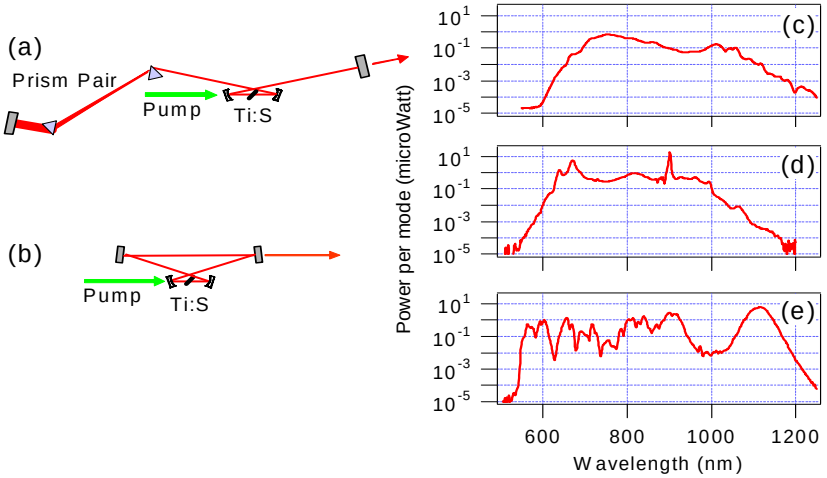

Figure 9-4. Common Ti:sapphire femtosecond lasers used for frequency metrology and their output spectra. (a) Conventional linear cavity design employing a combination of chirped mirrors and prisms produces the broadband spectrum shown in (c). The ring laser shown in (b) uses only chirped mirrors and can produce the spectrum show in (d). The spectrum shown in (e) is produced using either a laser (a) or (b) in combination with nonlinear microstructure optical fiber.

Repetition rate: There are a few factors that drive the consideration of the best repetition rate. The most obvious feature is that for a constant

average output power from the laser, the mode comb of a high repetition rate laser will have a proportionately higher power per mode. This is a clear advantage for frequency domain applications where we rely on a good *SNR* in the heterodyne beats between a cw laser and an individual tooth of the comb itself. However, one cannot take this point to the extreme. For example, if we again assume a constant output power, as the repetition rate increases, the power per pulse decreases. This is an important consideration if one is to rely on nonlinear processes to broaden the optical spectrum to an octave. As a rule of thumb, with the typical microstructure fibers used with Ti:sapphire lasers around 800 nm, one needs roughly a few hundred picojoules of energy in a ~50 fs pulse to obtain an octave of spectral broadening. This can be achieved with a 1 GHz repetition rate laser, but given the same average power, it is not likely to be possible if the laser could operate with a 10 GHz repetition rate.

Photodetectors & electronics: Since many uses of the femtosecond laser comb ultimately involve a connection to the rf/microwave domain, the photodetectors that provide this connection as well as the subsequent electronics that are used must also be a consideration. While photodetectors and microwave electronics with bandwidths up to ~50 GHz are commercially available, devices that operate much above 10 GHz tend to be more costly, more difficult to use, and less sensitive. This last factor can actually result in a loss of *SNR* that one had hoped to achieve precisely by choosing a higher repetition rate in the first place. This can be particularly true with the photodetector that is used to detect the optical clock output at f_r, where extremely high *SNR* is required to generate stable electrical signals [68]. Another important electronics-related consideration surrounding the choice of repetition rate is the frequency one might ultimately choose for connecting the f_r output of the femtosecond laser to existing rf/microwave sources and standards. The best choice of low-noise electronic synthesizers that would divide or multiply f_r up or down to common frequencies of 5, 100 or 9,192.631770 MHz will certainly be a consideration for the most demanding applications.

Size, simplicity & robustness: While size, simplicity, and robustness are not necessarily synonymous, it is often true that a smaller device of simple construction can be more robust. For example, small size lends itself to improved temperature stability, which directly impacts the operation of any femtosecond laser and the required dynamic range for the various servo controls. This is a point in favor of higher repetition rate systems, or at least systems with smaller footprints. When it comes down to the actual design of the laser, this factor would also tend to favor the use of chirped mirrors or fully integrated optics (such as a fiber laser) over the use of prisms for

dispersion control. The reliable generation of octave-spanning spectra directly from the laser is also a significant simplification as it allows one to eliminate sensitive microstructured nonlinear fibers from the apparatus.

Spectral coverage: A study of the different atoms, ions, and molecules used in emerging optical-frequency standards (see Table 9-1) reveals that many of the atomic transitions of interest fall in the 500–1100 nm range (or harmonics thereof). Thus, Ti:sapphire-based femtosecond laser combs centered at 800 nm are a good starting place and direct continuum generation or subsequent broadening in nonlinear microstructure fibers provides overlap with most of the wavelengths that are presently of interest. While nonlinear microstructure fibers have performed amazingly well in all experiments to date, they present challenging technical limitations on the ability to control the femtosecond laser over long periods. Coupling of the light into their ~1.7 μm diameter cores is difficult to maintain for long times at a level where an octave of spectrum is attained. An attractive alternative is recently developed femtosecond lasers that directly emit octave-spanning spectra suitable for self-referencing [69-71]. These lasers have slightly less bandwidth than is typically achieved from nonlinear microstructure fibers; however, initial experiments indicate the broadband lasers can be much more robust [72, 73]. A full understanding and optimization of these extremely broadband lasers is yet to emerge, but we anticipate they will play a very important role in optical clocks, perhaps reducing the need for nonlinear microstructure fibers.

Noise: Perhaps the most important consideration for any synthesizer is its residual or excess noise. More specific details on the presently achieved noise levels will be presented below, but from a general design point of view, there are important considerations that should be pointed out with regards to systems that employ nonlinear microstructure fibers. First, it is important to construct a femtosecond laser with robust and stable mechanical configurations and environmental shielding. Understanding the laser dynamics and noise sources is also fundamental to design and implementation of stabilization feedback loops [74, 75]. Because of its highly nonlinear nature, microstructure fiber can significantly amplify both technical and fundamental shot noise on the input light [76, 77]. With careful attention, the most significant aspects of the technical noise can be reduced; however, the shot noise on the laser output will always be present and potentially represents a more formidable problem. Of particular significance is the finding that longer pulses and chirped pulses generate more noise when launched into nonlinear microstructure fibers [77, 78]. For example, 75 fs pulses containing a few nanojoule of energy can make a stunning continuum stretching from 450 to 1400 nm, but excess broadband noise makes it nearly useless for precision frequency metrology.

3.2 Frequency synthesis with a femtosecond laser

The basic function of the femtosecond laser in an optical clock is to provide a phase-coherent link between the uncountable optical reference frequency and the more accessible microwave domain. Using a mechanical analogy, we can imagine the femtosecond laser to be a one-step reduction, or multiplication, gear. Alternatively, one can discuss the femtosecond laser as being an extremely broadband optical frequency synthesizer, with general properties not so different from commonly used rf and microwave synthesizers. While the mechanical analogy is straightforward conceptually, the synthesizer picture is the more useful one as it allows us to employ rigorous characterization techniques developed in the rf and microwave domains.

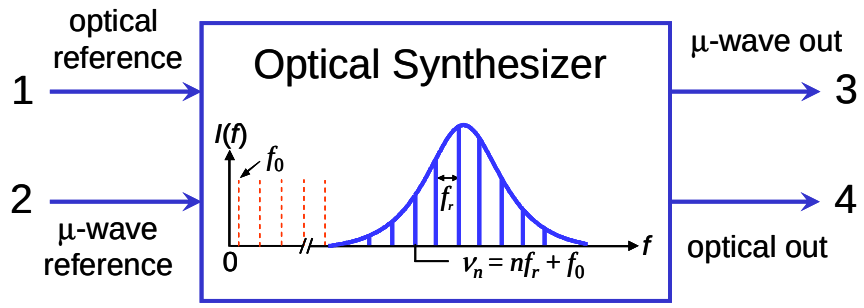

Figure 9-5. The femtosecond laser-based optical frequency synthesizer.

As shown in Figure 9-5, the femtosecond laser-based synthesizer can employ either a microwave (μ-wave) or optical input reference that is phase coherently linked to an optical or microwave frequency at the output. These operations can all be carried out and understood by considering the underlying frequency comb structure associated with the femtosecond laser. The first uses of the femtosecond laser-based synthesizer involved supplying a microwave reference at port 2 and obtaining coherently related optical frequencies in the form of the optical comb of Equation (2) at port 4 [15, 16, 79]. This path relies on the femtosecond laser to effectively multiply f_r by approximately a factor of 10^6 to reach the optical domain. In principle, the multiplicative factor could be a much smaller value, on the order of 10^2 or 10^3, to instead yield microwave frequencies in the hundreds of gigahertz (or even terahertz range). This potentially interesting use of the synthesizer (ports 2 → 3) has so far received less attention. When used to down-convert an optical frequency input to a microwave output (ports 1→ 3), the frequency

of the output is given by the repetition rate f_r or one of its harmonics [46, 60, 61]. The synthesizer can also function to effectively synthesize new optical frequencies that are displaced from the input optical reference by a freely chosen offset plus-or-minus harmonics of f_r (ports $1 \rightarrow 4$) [80].

3.2.1 Methods of control

Control of f_0: To accomplish all of these operations, it is required that at least two of the three variables given in Equation (2), in addition to n, be measured and controlled. For example, one might control f_r and f_0 and use ν_n as an output. Alternatively, Equation (2) can be inverted such that one tooth ($n = N$) of the comb ν_N and f_0 are controlled and f_r is then the output. Whereas it is relatively straightforward to measure the repetition rate f_r by monitoring the pulse train with a sufficiently fast photodetector, it is more challenging to measure the offset frequency f_0 of the comb. In principle, once f_r is measured, it is sufficient to use a cw laser with well-known frequency to measure and stabilize f_0. While this might be practical in some situations, it doubles the number of required frequency standards (one for f_0 and a second for f_r) required for using the synthesizer and potentially limits the performance.

A more elegant means of measuring and controlling f_0 involves using nonlinear frequency generation to compare different regions of the frequency comb [81]. As shown in Figure 9-6(a), if the laser spectrum covers more than one octave, then the comb elements at the low-frequency end of the spectrum can be doubled in a nonlinear crystal and subsequently heterodyned against the high-frequency components of the comb to yield $2(nf_r + f_0) - (mf_r + f_0) = f_0$ when $n = m/2$. Spectral broadening of low power Ti:sapphire lasers to more than an octave is accomplished through self-phase modulation (SPM) in microstructure fibers [67]. Such an approach was first demonstrated by Jones et al. [16] and continues to be the most common manner in which to measure f_0. This so-called "ν-to-2ν" self-referencing scheme has also been demonstrated with low-power Cr:LiSAF [82] and Er-doped fiber lasers [83]. It has also been shown that "ν-to-2ν" self-referencing can be accomplished with Ti:sapphire lasers that directly emit an octave-spanning spectrum [71, 84]. As summarized by Telle et al. [81], it is not necessary to have an octave-spanning spectrum from the femtosecond laser to measure f_0. The price to be paid, however, is that extra steps of nonlinear conversion must be employed. For example, with a spectrum spanning 2/3 of an octave, f_0 can be obtained through the comparison of the second harmonic and third harmonic of separated portions of the optical spectrum, e.g., $3(nf_r + f_0) - 2(mf_r + f_0) = f_0$ when $n = 2m/3$ [72, 84, 85].

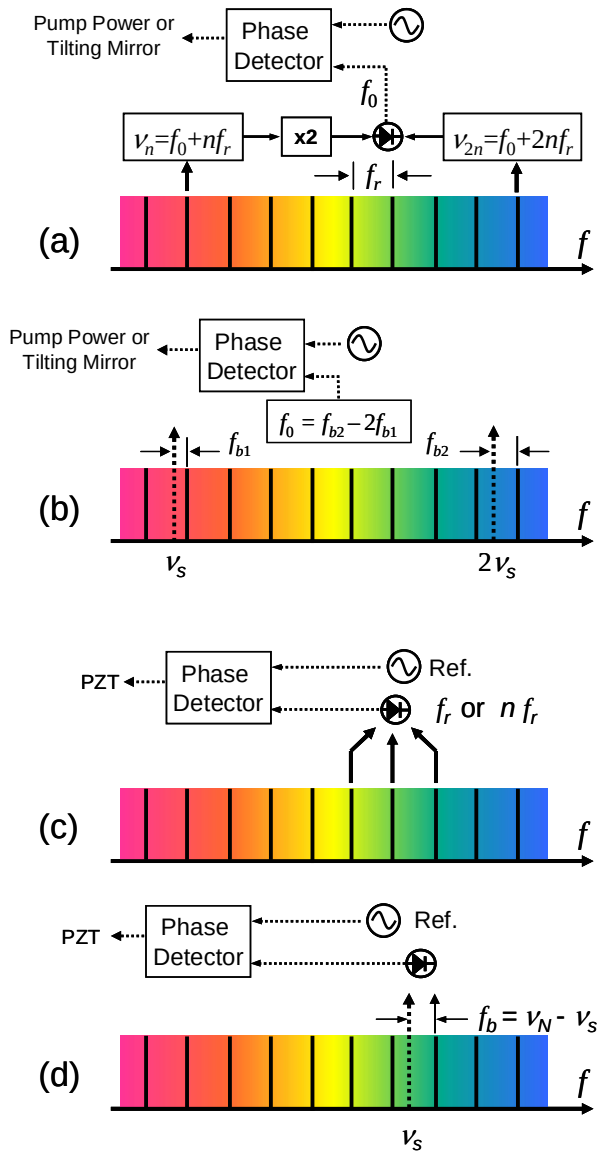

Figure 9-6. Techniques for measuring and controlling f_0 (a, b) and f_r (c,d). See text for details.

Once f_0 has been measured, it is typically phase-locked to a stable rf source or to a rational fraction of f_r itself. Such a phase-lock requires an actuator inside the laser cavity that provides a differential change to the group and phase velocities of the circulating field. Two common modes of

control have so far been used. The first employs modulation of intracavity laser power [79, 86], and the second (which is applicable in linear cavities employing prism pairs) involves the tipping of one of the cavity mirrors [18, 87]. While the merits and physical mechanisms of these differing techniques remain a topic of discussion, both have been successfully implemented to reduce the residual fluctuations of f_0 to the millihertz level relative to a stable reference. When f_0 is phase-locked to D.C. or a harmonic of f_r, precise stabilization has the consequence of maintaining the relative carrier-envelope phase at a fixed value for times approaching one hour [88]. This has enabled the subsequent amplification and use of such lasers for experiments in phase-sensitive extreme nonlinear optics experiments (see, for example, Reference [64] and Chapter 10 of this volume).

Control of f_r: As already mentioned, f_r can be detected with a sufficiently fast photodetector. The rf spectrum of the resulting photocurrent consists of a series of harmonics of f_r, one of which can be filtered and phase-locked to a low-noise rf source (Figure 9-6(c)). In this case, it is common to use a piezo-mounted cavity mirror as an actuator for changing f_r. A more careful consideration of Equation (2) highlights some of the difficulties and disadvantages of controlling f_r in the rf/microwave domain as just described. Because the optical frequency ν_n scales as the multiplicative mode number n, the spectral density of phase noise on the rf reference source to which f_r is phase-locked is multiplied by a factor of n^2. For a mode in the optical domain with $n \approx 500{,}000$ (f_r = 1 GHz), this implies that the phase noise of the rf reference is increased by 115 dB when it is effectively multiplied up to the optical domain using the femtosecond laser comb. A high-quality quartz-based rf reference at 1 GHz might have a typical noise floor of –110 dBc/Hz, but when it serves as the reference for f_r, there will be nothing remaining of the phase-coherent carrier in the optical mode ν_n. This is similar to the well-known problem of "carrier collapse," which places extreme demands on the rf reference (as well as all intermediate electronic components) for f_r.

There are, however, a few ways to minimize this phase-noise multiplication problem. First of all, one can rely on the relatively good short-term stability of the femtosecond laser itself. On time scales less than ~1ms, the noise of a typical Ti:sapphire laser has been measured to fall below that of most high quality microwave sources [20, 68]. This means that if one controls f_r relative to a microwave reference, a control bandwidth of $\leq$1 kHz is all that is required to remove the low-frequency thermal and acoustic noise of the mode-locked laser. Use of higher bandwidth will simply transfer the noise of the microwave reference to f_r, which will subsequently be multiplied up to the optical comb elements. Although the observed optical linewidth may still be on the order of 0.1–1 MHz, one generally finds that the fractional stability of the optical comb elements can

be equal to the fractional stability of the microwave reference. Of course, if a microwave reference for f_r with lower phase noise is available (such as a cryogenic sapphire microwave oscillator), then one can potentially narrow the optical linewidth further.

However, in the near future it is likely that the lowest-noise electromagnetic oscillators of any kind will be based on cw lasers referenced to stable Fabry-Perot optical cavities and/or atomic or molecular resonances. In fact, cw lasers with sub-hertz linewidths have recently been demonstrated [41], allowing the use of such a source to control f_r in the optical domain.

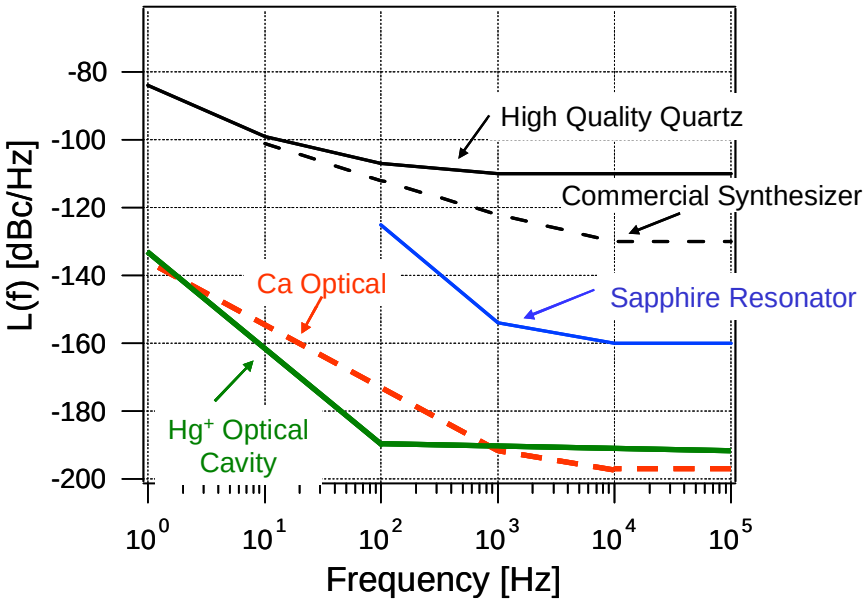

Figure 9-7. Phase noise of various oscillators and synthesizers at 1 GHz. The quartz curve corresponds to a high-quality 5 MHz oscillator and assumes noise-free multiplication to 1 GHz. The commercial synthesizer is residual synthesizer noise that would be added to the reference oscillator (typically quartz). The sapphire resonator curve represents a state-of-the-art commercial product with its frequency divided down from 10 GHz to 1 GHz. The dotted Ca curve is a projection of what should be achievable, and the Hg^+ optical cavity is estimated from experimental data [41].

As seen in Figure 9-6(d), this is typically done by making an optical-offset phase-lock between one tooth (mode N) of the femtosecond comb (ν_N) and the stable cw reference laser ν_S. The resulting expression for f_r is

$$f_r = (\nu_S - f_0 + f_b)/N \,, \qquad (3)$$

where f_b is the arbitrary (yet phase-locked) beat frequency between ν_S and ν_N. This expression illustrates that any frequency fluctuations in ν_S are divided by N before appearing in f_r (spectral density of phase fluctuations are divided by N^2). Since both f_0 and f_b are phase-locked microwave frequencies <1 GHz having fluctuations well below 1 Hz, the fluctuations of ν_S will likely dominate the noise of f_r. Assuming a perfect frequency divider, the anticipated limits to the phase noise spectral density of a sub-hertz laser (Hg^+ optical cavity) and the Ca optical standard are compared to other low-phase-noise sources in Figure 9-7. Clearly, the phase noise of the optical standards offers significant potential in this regard. At present, the noise from the femtosecond laser and the optical detection of f_r (1 GHz) has been measured to be -120 dBc/Hz at 1 Hz offset, decreasing to ~ -155 dBc/Hz at 1 kHz [89]. It has been shown that the phase noise on the optical comb of the femtosecond laser itself can be significantly less than this level [90], leading to the conclusion that the dominant noise sources for optical-to-microwave conversion with the femtosecond laser synthesizer are introduced in photodetection of f_r and subsequent electronic processing and measurement.

Alternative control methods: Instead of frequency-doubling a portion of the octave spanning comb spectrum as described above, one can use a cw laser and its second harmonic to access and control f_0 and f_r. [91]. This is diagramed in Figure 9-6(b). Measurement of the heterodyne beat between the cw laser frequency, ν_s, and the comb line n gives $f_{b1} = \nu_s - (nf_r + f_0)$ and between the second harmonic of the cw laser and comb line $2n$ gives $f_{b2} = 2\nu_s - (2nf_r + f_0)$. Mixing the beats with appropriate weighting factors gives $f_{b2} - 2f_{b1} = 2\nu_s - (2nf_r + f_0) - (2\nu_s - 2(nf_r + f_0)) = f_0$, which represents another detection scheme of f_0. On the other hand, it is now also possible to establish a direct phase coherent link between optical and microwave frequencies without the need of stabilizing f_0. The following expression, $f_{b2} - f_{b1} = 2\nu_s - (2nf_r + f_0) - (\nu_s - (nf_r + f_0)) = \nu_s - nf_r$, illustrates this principle. After appropriate processing, this error signal is used to stabilize the phase of f_r coherently to ν_s, thereby producing an output clock signal in the rf domain derived from ν_s [61].

There are several other methods for removing the dependence of the frequency comb on f_0. For example, by using difference-frequency generation (DFG) between different spectral portions of the same frequency comb, a DFG comb independent of f_0 in the IR spectral region with excellent accuracy and stability can be generated [92, 93]. Furthermore, a DFG comb (again, independent of f_0) tuned to 800 nm might also pave the way to an all-optical carrier-envelope phase-stabilization scheme by re-injecting this DFG comb into the femtosecond laser cavity. Equivalent to the DFG approach, sum-frequency generation (SFG) between an IR optical frequency standard

(e.g., a methane-stabilized He-Ne laser at 3.39 µm) with the long-wavelength portion of a frequency comb yields an SFG comb that can be tuned to spectrally overlap with the short-wavelength portion of the original frequency comb. The resultant heterodyne beat between the two combs of the same origin leads again to a carrier-envelope frequency-independent optical clockwork. We have recently implemented such an optical clockwork based on SFG between a cw optical parametric oscillator (OPO) at 3.39 µm idler wavelength and a custom-tailored mode-locked Ti:sapphire laser with two dominant spectral peaks at 834 and 670 nm. No additional single-frequency lasers phase-locked to the Ti:sapphire comb are necessary.

Finally, it is important to note the clever "transfer oscillator" [94, 95] concept in which a judicious choice of frequency-ratio mixing effectively eliminates the noise properties of the *unstabilized* femtosecond laser when it is used to determine the ratio of widely separated optical frequencies or even optical and microwave frequencies. An advantage of this technique is that it allows one to replace the more difficult and relatively slow (<100 kHz) control of the femtosecond laser with more straightforward and faster (~1 MHz bandwidth) phase-tracking oscillators on the various heterodyne beats.

3.3 Testing the synthesizer

As might be expected, the introduction of mode-locked femtosecond lasers into the field of optical frequency metrology was met with some initial questions about how well such a new technology could perform relative to what existed. Such healthy skepticism has led to some interesting and valuable tests of Equation (2). Table 9-2 provides a summary of some of the relevant experimental tests of the femtosecond laser synthesizer. It is not always straightforward to understand precisely what is being tested in some of these experiments, but in general they can all be viewed as placing simultaneous constraints on f_r and f_0.

The most obvious question one can ask about Equation 2 is whether or not the comb of optical frequencies is indeed uniform or evenly spaced. The time domain perspective of how the mode-locked laser functions leads one to the conclusion that this must be the case. An uneven spacing of the modes would imply that different portions of the spectrum experience different roundtrip delays in the cavity. Were this the case, the pulse would rapidly spread and break apart, which is not consistent with the solitonlike operation of mode-locked lasers. The first frequency-domain verification of this operation was offered by the group of T. Hänsch, by comparing a 44 THz wide comb from a femtosecond laser with an optical interval divider, thus confirming the uniformity at the level of a few parts in 10^{18} [13, 96].

While these impressive experiments can also be viewed as a test of the uniformity of f_0, one apparent weakness is that they employed only a single femtosecond laser and did not verify that the actual frequency position of the modes of the comb could be controlled or reproduced at this level.

Table 9-2. Summary of various tests of the femtosecond laser synthesizers

What was tested	Fractional Uncertainty	Systems Used	Reference
Uniformity of f_r	3×10^{-18}	fs laser broadened to 44 THz in standard fiber	[13] [96]
Microwave to optical frequency synthesis	5.1×10^{-16}	ν-to-2ν fs synthesizer with 3.5ν-4ν frequency chain	[79]
Microwave to optical frequency synthesis	1.6×10^{-12}	ν-to-2ν fs synthesizer and harmonic frequency chain	[97]
Optical-to-optical frequency synthesis	4×10^{-17}	Two ν-to-2ν fs synthesizers	[98]
Optical-to-optical ratio and SHG	7×10^{-19}	Single fs laser and cw laser +SHG	[94]
Microwave to optical frequency synthesis	1×10^{-15}	Two ν-to-2ν fs synthesizers	[99]
Uncertainty of DFG relative to fundamental comb	6.6×10^{-21}	Single fs laser and DFG and SFG	[92]
Optical-to-optical frequency synthesis	1.4×10^{-19}	Two ν-to-2ν and two 2ν-to-3ν fs synthesizers	[100]

To minimize the possibility of unknown systematic effects, a better test of the mode-locked laser frequency comb is the comparison of several independent devices. A few tests have been performed using microwave standards to reference both a femtosecond laser-based synthesizer and a more traditional frequency chain or interval divider, which were subsequently compared in the optical domain [79, 97, 99]. The best result in this case was an uncertainty limit as low as 5×10^{-16} [79]. In general, the limit in these cases was imposed by the short-term instability and associated long averaging times [79, 99] or by the uncertainty of the optical standard that was measured [97]. Significantly improved short-term instability can be obtained when the femtosecond laser-based synthesizer is referenced to an optical standard. In an earlier test, two such devices were compared and agreement was found at the level of 4×10^{-17} [98]. More recently, this same

test was repeated with four systems, two of which employed octave-spanning spectra generated in nonlinear microstructure fiber and two which generated broad spectra directly from the laser [100]. With improved short-term instability and longer averaging times, a fractional frequency uncertainty limit of near 1×10^{-19} was achieved. Using the "transfer oscillator" technique already discussed above [94], Stenger et al. tested a femtosecond laser comb by measuring the ratio of the frequency of a cw laser to its second harmonic with an uncertainty of 7×10^{-19}.

3.4 Alternatives to Ti:sapphire

In the few years since the introduction of femtosecond lasers into field of frequency metrology, the palette of available sources has already begun to broaden beyond that of Ti:sapphire lasers (see Figure 9-7). The reliability of the mature Ti:sapphire laser has made it the natural place to begin this exciting field, and it is likely that femtosecond laser-based synthesizers employing Ti:sapphire will continue to be used in many applications. However, the present size and cost of the pump laser for Ti:sapphire-based systems has motivated the search for alternative systems. In the future, it would not be surprising to find that femtosecond laser-based synthesizers and optical clocks will be widely used in science and technology and will be commercially available in compact packages similar to today's microwave synthesizers and clocks. The availability of robust, low-priced femtosecond-laser synthesizers will be particularly important for applications in air- or space-borne platforms or widespread applications (such as communications systems) for which cost and rugged packaging are of greatest importance.

To date, some of the promising femtosecond lasers that have produced octave-spanning spectra include diode-pumped Cr:LiSAF [82], a fiber-laser-pumped Cr:Forsterite [101], and an Er-doped fiber laser [83, 85, 102]. Each of these has some advantages and disadvantages relative to Ti:sapphire. For example, both Cr:LiSAF and Cr:Forsterite have more convenient and compact pumping schemes either directly with diode lasers or with a Yb-doped fiber laser. One of the trade-offs here is that these laser hosts are not as broadband and efficient as Ti:sapphire and tend to have worse thermal properties. An Er-fiber laser-based comb generator has a number of advantages over Ti:Sapphire. It can be much more compact, robust, lighter, and power-efficient than a bulk optic solid-state laser system, and would require less alignment. Additionally, it can be easily integrated into a telecommunication system in the important 1300–1600 nm regime. However, at this point, the Er-fiber-based systems only operate at repetition

rates of 50–100 MHz and can have excess noise that is not fully understood [85].

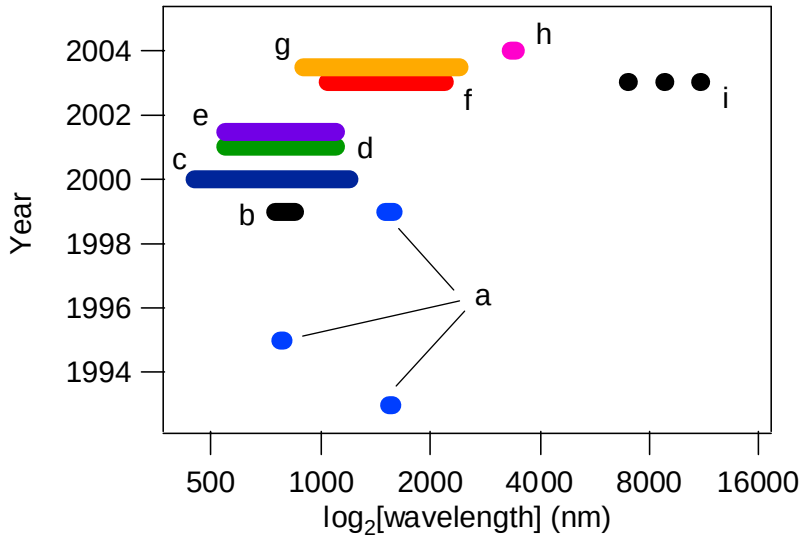

Figure 9-7. Spectral extent of some sources used as combs in frequency metrology. (a) Electro-optic modulator-based comb developed by Kourogi et al. [103]; (b) Ti:sapphire femtosecond laser comb [13, 14]; (c) Octave-spanning femtosecond laser comb generated using microstructure fiber [15, 16]; (d) Broadband spectrum generated directly from a Ti:sapphire laser [69]; (e) Cr:LiSAF femtosecond laser plus microstructure fiber [82]; (f) Octave-spanning comb generated with femtosecond Cr:forsterite and nonlinear optical fiber [104]; (g) Octave-spanning comb generated with Er-fiber laser and nonlinear optical fiber [83]; (h) Offset-frequency-free comb near 3400 nm generated via difference-frequency generation [93]; (i) Tunable frequency comb generated via difference-frequency generation between synchronized Ti:sapphire lasers [105].

If wavelength coverage is a concern, one can take advantage of nonlinear frequency conversion external to the femtosecond laser itself. This has been demonstrated for 2ν-to-3ν with Cr:forsterite and fiber laser sources [85, 106]. Another interesting option is to use DFG between two extremes of a Ti:sapphire laser comb to generate a frequency comb further in the IR [92, 93]. While this provides extra wavelength tunability for the femtosecond source, it also is a means of generating a frequency comb that is independent of the offset frequency f_0. As also shown in Figure 9-7, wide tunability between 7 and 10 microns can also be accomplished with independent Ti:sapphire lasers that are synchronized and potentially phase-locked [105].

4. SIGNAL TRANSMISSION AND CROSS-LINKING

With the advent of optical atomic clocks and the associated superior short-term frequency stability, transfer of signals linked to such clock/frequency standards over an appreciable distance with a minimal loss of stability has become an active subject for research [107, 108]. The stability of the best microwave and optical frequency standards, for times less than ~ one week, can now exceed the capabilities of the traditional transmission systems (i.e., GPS, Two-Way Time transfer [109]) used to distribute these time/frequency reference signals to remote sites. The instabilities in transmission channels can contribute a significant fraction of the overall uncertainty in the comparison of high-performance standards that are not co-located. While improvement in the transfer process over large-scale signal paths remains challenging, researchers have started experimenting with optical fibers as effective means for local networks of dissemination or comparison of time and frequency standards, both in the microwave and optical domains. The attractiveness of this approach lies in the fact that an environmentally isolated fiber can be considerably more stable than open-air paths, especially at short time scales. Furthermore, the same advantages enjoyed by communication systems in optical fiber (e.g., low loss, scalability, etc.) can be realized in a time/frequency distribution system. Active stabilization of fiber-optic channels for the distribution of reference frequencies can also be employed to improve the stability of the transmitted standard. Besides the obvious benefit of more precise time/frequency transfer, an actively stabilized optical fiber network can play a critical role in the implementation of long-baseline coherent interferometry or ultralow timing jitter in particle-accelerator-based novel light sources.

An rf signal can be transferred in an optical fiber network by amplitude modulating a suitable optical carrier (for example at 1.55 μm) used for transmission and then recovering the modulation frequency at the remote end as the transferred reference signal. However, the instability of this rf modulation-based frequency transfer protocol seems to rise to a few parts in 10^{13} at 1-s over a 6.9 km long fiber linking JILA to NIST. Jet Propulsion Laboratory colleagues have demonstrated the rf transfer instability of parts in 10^{14} at 1 s for a 16 km-long fiber under active noise cancellation control [110]. In comparison, direct transfer of a cw laser-based optical frequency standard through the same 6.9 km fiber suffered an instability of a few parts in 10^{14} at 1 s. This instability is further reduced to 3×10^{-15} at 1 s after active optical-phase-noise cancellation is implemented [107]. A femtosecond laser located at the remote end can be phase locked to this incoming cw laser

carrier, essentially redistributing the optical frequency to the microwave domain via the mode-locked laser's repetition frequency.

With the development of precision femtosecond comb technology, it appears natural to use a mode-locked source to transfer both optical and microwave reference signals at the highest level of stability. Of course, the first logical step is to extend the precision optical-comb spectral coverage into the 1.5 μm wavelength region, where compact, reliable, and efficient mode-locked lasers exist for fiber distribution networks. This step has been accomplished by tight synchronization between the repetition rates and coherent phase locking of the optical carriers of the 1.5 μm mode-locked laser sources and a Ti:Sapphire-based femtosecond frequency comb, which is used as the clockwork for an optical atomic clock based on the molecular iodine transition. A phase-coherent link between mode-locked lasers requires two distinct conditions to be met [63, 111]. First, the comb spacing of the 1550 nm source ($f_{r,1550}$) must be stabilized to the optical clock's comb spacing ($f_{r,775}$). Second, the two combs' offset frequencies ($f_{0,775}$ and $f_{0,1550}$) must be phase locked together. This latter step requires spectral overlap between the two combs. The optical comb of the 1550 nm source is frequency doubled and compared against the Ti:sapphire comb at a mutually accessible spectral region to generate a heterodyne beat.

We have investigated a number of different types of passively mode-locked lasers in the 1550 nm region, including an erbium/ytterbium-doped waveguide laser [112], an erbium-doped fiber laser [108, 113], and a mode-locked laser diode (MLLD) [75, 114]. Each laser offers at least two control parameters to obtain simultaneous time synchronization and carrier phase-locking. For example, stabilization through the cavity length is a common feature for all these lasers. The carrier-envelope-offset frequency ($f_{0,1550}$) can be tuned in both waveguide and fiber lasers through control of the intensity of their pump lasers. A MLLD, on the other hand, can be tuned with both the injection current and the reverse bias voltage on the saturable absorber. Among the three mode-locked laser sources, the waveguide laser achieved the lowest residual timing jitter with a record-low, root-mean-square relative timing jitter of 14.4 fs integrated from 10 Hz to 375 MHz (the Nyquist frequency), owing to the laser's high-Q cavity and overall gain dynamics. Although the MLLD has a larger rms timing jitter of ~22 fs within the bandwidth of 1 Hz – 100 MHz, it does offer the advantage of a compact size, robust operation, and completely electrical control, along with the potential in device improvements to lower the jitter at high frequencies.

Transfer of optical frequency standards is then implemented by using the stabilized mode-locked laser sources at 1.5 μm that are transmitted through an optical fiber network. We have explored the dual transfer process for both the optical carrier frequency and the rf signal represented by the laser's

repetition frequency and to compare the transfer of such an rf signal with that of a modulated optical carrier. When the 1.5 μm mode-locked laser is phase coherently connected to a Ti:sapphire mode-locked laser serving as the clockwork for an optical atomic clock, both the optical carrier frequency and the repetition frequency of the 1.5 μm mode-locked laser are connected to a single optical frequency standard. Therefore a single fiber link allows a user at the remote end to either simply use a fast photodiode to recover the rf reference signal or establish a more elaborate, direct connection to the optical carrier. Simultaneous existence of both the optical phase and the pulse-repetition-rate information would also enable novel measurement capabilities on material dispersion and length determination. The experimental results confirm that with the use of a mode-locked laser at 1.5 μm, the instability of the transfer process for the repetition frequency (rf reference) over the 6.9 km long fiber is nearly the same as that of optical carrier transfer of a cw laser discussed earlier, and is almost an order of magnitude better than that of transfer of a rf-modulated cw laser carrier. Furthermore, it is clear that a pulsed transfer process preserves the stability of the optical carrier as in the cw optical transfer process. Preliminary results on pulsed transfer under active noise cancellation indicate rf transfer instability reaching a few parts in 10^{15} at 1 s. We are currently exploring the utility of such ultrastable frequency transfer for time-domain experiments where the goal is to deliver extremely low-jitter timing signals throughout a fiber network, permitting ultrafast lasers located at remote areas be synchronized together at a precision level of a few femtoseconds within a multi-megahertz bandwidth.

ACKNOWLEDGEMENTS

The work presented in this chapter would not have been possible without the valuable contributions of many people. In particular, we would like to thank Albrecht Bartels, Jim Bergquist, Martin Boyd, Sebastien Bize, Lisheng Chen, Steven Cundiff, Anne Curtis, Seth Foreman, Rich Fox, John Hall, Kevin Holman, Darren Hudson, Tetsuya Ido, Erich Ippen, Euguene Ivanov, David Jones, Jason Jones, Franz Kärtner, Thomas Loftus, Andrew Ludlow, Long-Sheng Ma, Adela Marian, Kevin Moll, Oliver Mücke, Nathan Newbury, Chris Oates, Jin-Long Peng, Tanya Ramond, Matthew Stowe, Thomas Udem, Kurt Vogel, Guido Wilpers, Robert Windeler, and Dave Wineland.

REFERENCES

[1] H. Dehmelt, Rev. Mod. Phys. **62**, 525-530 (1990).

[2] H. G. Dehmelt, IEEE Trans. Instrum. Meas. **31**, 83-87 (1982).

[3] J. L. Hall, Science **202**, 147-156 (1978); J. L. Hall, M. Zhu, and P. Buch, J. Opt. Soc. Am. B **6**, 2194-2205 (1989).

[4] T. W. Hänsch, I. S. Shahin, and A. L. Schawlow, Nature-Physical Science **235**, 63 (1972).

[5] S. N. Bagayev, Y. D. Kolomnikov, V. N. Lisitsyn, and V. P. Chebotayev, IEEE J. Quant. Electr. **4**, 868 (1968).

[6] V. P. Chebotayev, V. G. Goldort, V. M. Klementyev, M. V. Nikitin, B. A. Timchenko, and V. F. Zakharyash, Appl. Phys. B **29**, 63-65 (1982).

[7] D. J. Wineland, Science **226**, 395-400 (1984); D. J. Wineland, J. C. Bergquist, W. M. Itano, F. Diedrich, and C. S. Weimer, in *The Hydrogen Atom*, edited by G. F. Bassani, M. Inguscio and T. W. Hänsch (Springer-Verlag, Berlin, 1989), p. 123-133.

[8] A. Clairon, A. Vanlerberghe, C. Salomon, M. Ouhayoun, and C. J. Borde, Opt. Commun. **35**, 368-372 (1980).

[9] C. O. Weiss, G. Kramer, B. Lipphardt, and E. Garcia, IEEE J. Quantum Electron. **24**, 1970-1972 (1988).

[10] H. Schnatz, B. Lipphardt, J. Helmcke, F. Riehle, and G. Zinner, Phys. Rev. Lett. **76**, 18-21 (1996).

[11] J. E. Bernard, A. A. Madej, L. Marmet, B. G. Whitford, K. J. Siemsen, and S. Cundy, Phys. Rev. Lett. **82**, 3228-3231 (1999).

[12] H. R. Telle, D. Meschede, and T. W. Hänsch, Opt. Lett. **15**, 532-534 (1990).

[13] T. Udem, J. Reichert, R. Holzwarth, and T. W. Hänsch, Opt. Lett. **24**, 881-883 (1999).

[14] T. Udem, J. Reichert, R. Holzwarth, and T. W. Hänsch, Phys. Rev. Lett. **82**, 3568-3571 (1999).

[15] S. A. Diddams, D. J. Jones, J. Ye, S. T. Cundiff, J. L. Hall, J. K. Ranka, R. S. Windeler, R. Holzwarth, T. Udem, and T. W. Hänsch, Phys. Rev. Lett. **84**, 5102-5105 (2000).

[16] D. J. Jones, S. A. Diddams, J. K. Ranka, A. Stentz, R. S. Windeler, J. L. Hall, and S. T. Cundiff, Science **288**, 635-639 (2000).

[17] T. Udem, R. Holzwarth, and T. W. Hänsch, Nature **416**, 233-237 (2002).

[18] S. T. Cundiff, J. Ye, and J. L. Hall, Rev. Sci. Instrum. **72**, 3746-3771 (2001).

[19] J. L. Hall, J. Ye, S. A. Diddams, L.-S. Ma, S. T. Cundiff, and D. J. Jones, IEEE J. Quantum Electron. **37**, 1482-1492 (2001).

[20] L. Hollberg, C. W. Oates, E. A. Curtis, E. N. Ivanov, S. A. Diddams, T. Udem, H. G. Robinson, J. C. Bergquist, R. J. Rafac, W. M. Itano, R. E. Drullinger, and D. J. Wineland, IEEE J. Quantum Electron. **37**, 1502-1513 (2001).

[21] S. T. Cundiff and J. Ye, Rev. Mod. Phys. **75**, 325-342 (2003).

[22] J. Ye, H. Schnatz, and L. W. Hollberg, IEEE J. Sel. Top. Quantum Electron. **9**, 1041-1058 (2003).

[23] J. Jespersen and J. Fitz-Randolph, *From Sundials to Atomic Clocks: Understanding Time and Frequency* (NIST, U.S. Department of Commerce, Gaithersburg, 1999).

[24] D. A. Jennings, K. M. Evenson, and D. J. E. Knight, Proc. IEEE **74**, 168-179 (1986); C. O. Weiss, G. Kramer, B. Lipphardt, and H. Schnatz, Frequency Measurement and Control: Advanced Techniques and Future Trends **79**, 215-247 (2000).

[25] O. Acef, J. J. Zondy, M. Abed, D. G. Rovera, A. H. Gerard, A. Clairon, P. Laurent, Y. Millerioux, and P. Juncar, Opt. Commun. **97**, 29-34 (1993).

[26] J. Levine, Rev. Sci. Instrum. **70**, 2567-2596 (1999); J. Levine, Reports on Progress in Physics **65**, 1119-1164 (2002).

[27] J. Ye, Opt. Lett. **29**, 1153-1155 (2004).

[28] M. Niering, R. Holzwarth, J. Reichert, P. Pokasov, T. Udem, M. Weitz, T. W. Hänsch, P. Lemonde, G. Santarelli, M. Abgrall, P. Laurent, C. Salomon, and A. Clairon, Phys. Rev. Lett. **84**, 5496-5499 (2000); C. Schwob, L. Jozefowski, B. de Beauvoir, L. Hilico, F. Nez, L. Julien, F. Biraben, O. Acef, and A. Clairon, Phys. Rev. Lett. **82**, 4960-4963 (1999); B. de Beauvoir, C. Schwob, O. Acef, L. Jozefowski, L. Hilico, F. Nez, L. Julien, A. Clairon, and F. Biraben, Euro. Phys. J. D **12**, 61-93 (2000).

[29] S. G. Karshenboim, Can. J. Phys. **78**, 639-678 (2000).

[30] J. D. Prestage, R. L. Tjoelker, and L. Maleki, Phys. Rev. Lett. **74**, 3511-3514 (1995).

[31] H. Marion, F. P. Dos Santos, M. Abgrall, S. Zhang, Y. Sortais, S. Bize, I. Maksimovic, D. Calonico, J. Grunert, C. Mandache, P. Lemonde, G. Santarelli, P. Laurent, A. Clairon, and C. Salomon, Phys. Rev. Lett. **90** (2003); S. Bize, S. A. Diddams, U. Tanaka, C. E. Tanner, W. H. Oskay, R. E. Drullinger, T. E. Parker, T. P. Heavner, S. R. Jefferts, L. Hollberg, W. M. Itano, and J. C. Bergquist, Phys. Rev. Lett. **90**, 150802 (2003).

[32] A. Brillet and J. L. Hall, Phys. Rev. Lett. **42**, 549-552 (1979); D. Hils and J. L. Hall, Phys. Rev. Lett. **64**, 1697-1700 (1990); V. A. Kostelecky and C. D. Lane, Phys. Rev. D **6011**, art. no.-116010 (1999); D. Bear, R. E. Stoner, R. L. Walsworth, V. A. Kostelecky, and C. D. Lane, Phys. Rev. Lett. **85**, 5038-5041 (2000).

[33] G. Gabrielse, N. S. Bowden, P. Oxley, A. Speck, C. H. Storry, J. N. Tan, M. Wessels, D. Grzonka, W. Oelert, G. Schepers, T. Sefzick, J. Walz, H. Pittner, T. W. Hänsch, and E. A. Hessels, Phys. Rev. Lett. **89**, 233401 (2002); M. Amoretti, C. Amsler, G. Bonomi, A. Bouchta, P. Bowe, C. Carraro, C. L. Cesar, M. Charlton, M. J. T. Collier, M. Doser, V. Filippini, K. S. Fine, A. Fontana, M. C. Fujiwara, R. Funakoshi, P. Genova, J. S. Hangst, R. S. Hayano, M. H. Holzscheiter, L. V. Jorgensen, V. Lagomarsino, R. Landua, D. Lindelof, E. L. Rizzini, M. Macri, N. Madsen, G. Manuzio, M. Marchesotti, P. Montagna, H. Pruys, C. Regenfus, P. Riedler, J. Rochet, A. Rotondi, G. Rouleau, G. Testera, A. Variola, T. L. Watson, and D. P. van der Werf, Nature **419**, 456-459 (2002).

[34] J. Walz, P. Fendel, M. Herrmann, M. Konig, A. Pahl, H. Pittner, B. Schatz, and T. W. Hänsch, J. Phys, B **36**, 649-654 (2003); J. Walz, H. Pittner, M. Herrmann, P. Fendel, B. Henrich, and T. W. Hänsch, Appl. Phys. B **77**, 713-717 (2003).

[35] R. Bluhm, V. A. Kostelecky, and N. Russell, Phys. Rev. Lett. **82**, 2254-2257 (1999).
[36] A. Javan, Annals of the New York Academy of Sciences **168**, 715 (1970).
[37] P. Gill, Proc. 6th Symp. on Freq. Standards and Metrology, World Scientific, Singapore (2002).
[38] D. W. Allan, Proc. IEEE **54**, 221 (1966).
[39] W. M. Itano, J. C. Bergquist, J. J. Bollinger, J. M. Gilligan, D. J. Heinzen, F. L. Moore, M. G. Raizen, and D. J. Wineland, Phys. Rev. A **47**, 3554-3570 (1993); C. Santarelli, P. Laurent, P. Lemonde, A. Clairon, A. G. Mann, S. Chang, A. N. Luiten, and C. Salomon, Phys. Rev. Lett. **82**, 4619-4622 (1999).
[40] J. J. Bollinger, J. D. Prestage, W. M. Itano, and D. J. Wineland, Phys. Rev. Lett. **54**, 1000-1003 (1985); A. A. Madej and J. E. Bernard, Frequency Measurement and Control: Advanced Techniques and Future Trends **79**, 153-194 (2000).
[41] B. C. Young, F. C. Cruz, W. M. Itano, and J. C. Bergquist, Phys. Rev. Lett. **82**, 3799-3802 (1999).
[42] R. J. Rafac, B. C. Young, J. A. Beall, W. M. Itano, D. J. Wineland, and J. C. Bergquist, Phys. Rev. Lett. **85**, 2462-2465 (2000).
[43] D. J. Wineland, M. Barrett, J. Britton, J. Chiaverini, B. DeMarco, W. M. Itano, B. Jelenkovic, C. Langer, D. Leibfried, V. Meyer, T. Rosenband, and T. Schatz, Philos. Trans. R. Soc. Lond. Ser. A **361**, 1349-1361 (2003).
[44] M. D. Barrett, B. DeMarco, T. Schaetz, V. Meyer, D. Leibfried, J. Britton, J. Chiaverini, W. M. Itano, B. Jelenkovic, J. D. Jost, C. Langer, T. Rosenband, and D. J. Wineland, Phys. Rev. A **68** (2003).
[45] C. W. Oates, E. A. Curtis, and L. Hollberg, Opt. Lett. **25**, 1603-1605 (2000); T. Udem, S. A. Diddams, K. R. Vogel, C. W. Oates, E. A. Curtis, W. D. Lee, W. M. Itano, R. E. Drullinger, J. C. Bergquist, and L. Hollberg, Phys. Rev. Lett. **86**, 4996-4999 (2001).
[46] G. Wilpers, T. Binnewies, C. Degenhardt, U. Sterr, J. Helmcke, and F. Riehle, Phys. Rev. Lett. **89** (2002).
[47] E. A. Curtis, C. W. Oates, and L. Hollberg, J. Opt. Soc. Am. B **20**, 977-984 (2003).
[48] M. Takamoto and H. Katori, Phys. Rev. Lett. **91** (2003).
[49] X. Y. Xu, T. H. Loftus, J. W. Dunn, C. H. Greene, J. L. Hall, A. Gallagher, and J. Ye, Phys. Rev. Lett. **90** (2003).
[50] H. Katori, M. Takamoto, V. G. Pal'chikov, and V. D. Ovsiannikov, Phys. Rev. Lett. **91** (2003).
[51] T. Mukaiyama, H. Katori, T. Ido, Y. Li, and M. Kuwata-Gonokami, Phys. Rev. Lett. **90** (2003).
[52] J. L. Hall, C. J. Borde, and K. Uehara, Phys. Rev. Lett. **37**, 1339-1342 (1976); V. P. Chebotayev, Radio Science **14**, 573-584 (1979); A. Clairon, B. Dahmani, A. Filimon, and J. Rutman, IEEE Trans. Instrum. Meas. **34**, 265-268 (1985).
[53] M. A. Gubin, D. A. Tyurikov, A. S. Shelkovnikov, E. V. Kovalchuk, G. Kramer, and B. Lipphardt, IEEE J. Quantum Electron. **31**, 2177-2182 (1995); J. von Zanthier, J. Abel, T. Becker, M. Fries, E. Peik, H. Walther, R. Holzwarth, J. Reichert, T. Udem, T. W. Hänsch, A. Y. Nevsky, M. N. Skvortsov, and S. N. Bagayev, Opt. Commun. **166**, 57-63 (1999); B. Frech, L. F. Constantin, A. Amy-Klein, O. Phavorin, C. Daussy, C. Chardonnet,

and M. Murtz, Appl. Phys. B **67**, 217-221 (1998); A. Shelkovnikov, C. Grain, C. T. Nguyen, R. J. Butcher, A. Amy-Klein, and C. Chardonnet, Appl. Phys. B **73**, 93-98 (2001).

[54] J. Ye, L.-S. Ma, and J. L. Hall, IEEE Trans. Instrum. Meas. **46**, 178-182 (1997); J. Ye, L.-S. Ma, and J. L. Hall, J. Opt. Soc. Am. B **15**, 6-15 (1998).

[55] J. Ye, L. Robertsson, S. Picard, L.-S. Ma, and J. L. Hall, IEEE Trans. Instrum. Meas. **48**, 544-549 (1999); A. Y. Nevsky, R. Holzwarth, J. Reichert, T. Udem, T. W. Hänsch, J. von Zanthier, H. Walther, H. Schnatz, F. Riehle, P. V. Pokasov, M. N. Skvortsov, and S. N. Bagayev, Opt. Commun. **192**, 263-272 (2001); F. L. Hong, J. Ishikawa, K. Sugiyama, A. Onae, H. Matsumoto, J. Ye, and J. L. Hall, IEEE Trans. Instrum. Meas. **52**, 240-244 (2003).

[56] W. Y. Cheng, L. S. Chen, T. H. Yoon, J. L. Hall, and J. Ye, Opt. Lett. **27**, 571-573 (2002).

[57] R. J. Jones, W. Y. Cheng, K. W. Holman, L.-S. Chen, J. L. Hall, and J. Ye, Appl. Phys. B **74**, 597 (2002); A. Goncharov, A. Amy-Klein, O. Lopez, F. du Burck, and C. Chardonnet, Appl. Phys. B **78**, 725-731 (2004).

[58] C. Salomon, D. Hils, and J. L. Hall, J. Opt. Soc. Am. B **5**, 1576-1587 (1988).

[59] J. N. Eckstein, A. I. Ferguson, and T. W. Hänsch, Phys. Rev. Lett. **40**, 847-850 (1978).

[60] S. A. Diddams, T. Udem, J. C. Bergquist, E. A. Curtis, R. E. Drullinger, L. Hollberg, W. M. Itano, W. D. Lee, C. W. Oates, K. R. Vogel, and D. J. Wineland, Science **293**, 825-828 (2001).

[61] J. Ye, L.-S. Ma, and J. L. Hall, Phys. Rev. Lett. **87**, 270801 (2001).

[62] T. H. Yoon, A. Marian, J. L. Hall, and J. Ye, Phys. Rev. A **63**, 011402 (2000); A. Poppe, R. Holzwarth, A. Apolonski, G. Tempea, C. Spielmann, T. W. Hänsch, and F. Krausz, Appl. Phys. B **72**, 977-977 (2001); R. Kienberger, M. Hentschel, M. Uiberacker, C. Spielmann, M. Kitzler, A. Scrinzi, M. Wieland, T. Westerwalbesloh, U. Kleineberg, U. Heinzmann, M. Drescher, and F. Krausz, Science **297**, 1144-1148 (2002).

[63] R. K. Shelton, L.-S. Ma, H. C. Kapteyn, M. M. Murnane, J. L. Hall, and J. Ye, Science **293**, 1286-1289 (2001).

[64] A. Baltuška, T. Udem, M. Uiberacker, M. Hentschel, E. Goulielmakis, C. Gohle, R. Holzwarth, V. S. Yakoviev, A. Scrinzi, T. W. Hänsch, and F. Krausz, Nature **421**, 611-615 (2003).

[65] P. F. Moulton, J. Opt. Soc. Am. B **3**, 125-133 (1986); D. E. Spence, P. N. Kean, and W. Sibbett, Opt. Lett. **16**, 42-44 (1991).

[66] M. T. Asaki, C. P. Huang, D. Garvey, J. P. Zhou, H. C. Kapteyn, and M. M. Murnane, Opt. Lett. **18**, 977-979 (1993); R. Szipocs, K. Ferencz, C. Spielmann, and F. Krausz, Opt. Lett. **19**, 201-203 (1994).

[67] J. K. Ranka, R. S. Windeler, and A. J. Stentz, Opt. Lett. **25**, 25-27 (2000); T. A. Birks, W. J. Wadsworth, and P. S. Russell, Opt. Lett. **25**, 1415-1417 (2000).

[68] E. N. Ivanov, S. A. Diddams, and L. Hollberg, IEEE J. Sel. Top. Quantum Electron. **9**, 1059-1065 (2003).

[69] R. Ell, U. Morgner, F. X. Kärtner, J. G. Fujimoto, E. P. Ippen, V. Scheuer, G. Angelow, T. Tschudi, M. J. Lederer, A. Boiko, and B. Luther-Davies, Opt. Lett. **26**, 373-375 (2001).

[70] A. Bartels and H. Kurz, in *XIII International Conference on Ultrafast Phenomena*, edited by M. M. Murnane, N. F. Scherer, D. J. D. Miller and A. M. Weiner (OSA, Vancouver, BC, 2002), Vol. 72, p. 173-174.

[71] T. M. Fortier, D. J. Jones, and S. T. Cundiff, Opt. Lett. **28**, 2198-2200 (2003).

[72] T. M. Ramond, S. A. Diddams, L. Hollberg, and A. Bartels, Opt. Lett. **27**, 1842-1844 (2002).

[73] S. A. Diddams, A. Bartels, T. M. Ramond, C. W. Oates, S. Bize, E. A. Curtis, J. C. Bergquist, and L. Hollberg, IEEE J. Sel. Top. Quantum Electron. **9**, 1072-1080 (2003).

[74] K. W. Holman, R. J. Jones, A. Marian, S. T. Cundiff, and J. Ye, Opt. Lett. **28**, 851-853 (2003).

[75] K. W. Holman, D. J. Jones, J. Ye, and E. P. Ippen, Opt. Lett. **28**, 2405-2407 (2003).

[76] N. R. Newbury, B. R. Washburn, K. L. Corwin, and R. S. Windeler, Opt. Lett. **28**, 944-946 (2003).

[77] K. L. Corwin, N. R. Newbury, J. M. Dudley, S. Coen, S. A. Diddams, B. R. Washburn, K. Weber, and R. S. Windeler, Appl. Phys. B **77**, 269-277 (2003).

[78] J. M. Dudley and S. Coen, Opt. Lett. **27**, 1180-1182 (2002); R. Holzwarth, M. Zimmermann, T. Udem, and T. W. Hänsch, IEEE J. Quantum Electron. **37**, 1493-1501 (2001).

[79] R. Holzwarth, T. Udem, T. W. Hänsch, J. C. Knight, W. J. Wadsworth, and P. S. J. Russell, Phys. Rev. Lett. **85**, 2264-2267 (2000).

[80] J. D. Jost, J. L. Hall, and J. Ye, Opt. Expr. **10**, 515 (2002); L. S. Chen and J. Ye, Chem. Phys. Lett. **381**, 777-783 (2003).

[81] H. R. Telle, G. Steinmeyer, A. E. Dunlop, J. Stenger, D. H. Sutter, and U. Keller, Appl. Phys. B **69**, 327 (1999).

[82] R. Holzwarth, M. Zimmermann, T. Udem, T. W. Hänsch, P. Russbuldt, K. Gabel, R. Poprawe, J. C. Knight, W. J. Wadsworth, and P. S. J. Russell, Opt. Lett. **26**, 1376-1378 (2001).

[83] F. Tauser, A. Leitenstorfer, and W. Zinth, Optics Expr. **11**, 594-600 (2003); B. R. Washburn, S. A. Diddams, N. R. Newbury, J. W. Nicholson, M. F. Yan, and C. G. Jorgensen, Opt. Lett. **29**, 250-252 (2004).

[84] U. Morgner, R. Ell, G. Metzler, T. R. Schibli, F. X. Kärtner, J. G. Fujimoto, H. A. Haus, and E. P. Ippen, Phys. Rev. Lett. **86**, 5462-5465 (2001).

[85] F. L. Hong, K. Minoshima, A. Onae, H. Inaba, H. Takada, A. Hirai, and H. Matsumoto, Opt. Lett. **28**, 1516-1518 (2003).

[86] K. W. Holman, R. J. Jones, A. Marian, S. T. Cundiff, and J. Ye, IEEE J. Sel. Top. Quantum Electron. **9**, 1018-1024 (2003).

[87] J. Reichert, R. Holzwarth, T. Udem, and T. W. Hänsch, Opt. Commun. **172**, 59-68 (1999).

[88] T. M. Fortier, D. J. Jones, J. Ye, S. T. Cundiff, and R. S. Windeler, Opt. Lett. **27**, 1436-1438 (2002).

[89] A. Bartels, S. A. Diddams, C. W. Oates, G. Wilpers, W. H. Oskay, J. C. Bergquist, and L. Hollberg, in *Conference on Lasers and Electo-optics*, San Francisco, 2004), postdeadline presentation.

[90] A. Bartels, C. W. Oates, L. Hollberg, and S. A. Diddams, Opt. Lett. **29**, 1081-1083 (2004).
[91] J. Ye, J. L. Hall, and S. A. Diddams, Opt. Lett. **25**, 1675 (2000).
[92] M. Zimmermann, C. Gohle, R. Holzwarth, T. Udem, and T. W. Hänsch, Opt. Lett. **29**, 310-312 (2004).
[93] O. D. Mücke, O. Kuzucu, N. C. Wong, E. P. Ippen, F. X. Kaertner, S. M. Foreman, D. J. Jones, L.-S. Ma, J. L. Hall, and J. Ye, CLEO 2004 postdeadline presentation and Opt. Lett., in press (2004).
[94] J. Stenger, H. Schnatz, C. Tamm, and H. R. Telle, Phys. Rev. Lett. **88**, 073601 (2002).
[95] H. R. Telle, B. Lipphardt, and J. Stenger, Appl. Phys. B **74**, 1-6 (2002).
[96] R. Holzwarth, Ph.D Thesis, Ludwig-Maximilians-Universität (2001).
[97] J. Ye, T. H. Yoon, J. L. Hall, A. A. Madej, J. E. Bernard, K. J. Siemsen, L. Marmet, J.-M. Chartier, and A. Chartier, Phys. Rev. Lett. **85**, 3797 (2000).
[98] S. A. Diddams, L. Hollberg, L.-S. Ma, and L. Robertsson, Opt. Lett. **27**, 58-60 (2002).
[99] L.-S. Ma, L. Robertsson, S. Picard, M. Zucco, Z. Y. Bi, S. H. Wu, and R. S. Windeler, Opt. Lett. **29**, 641-643 (2004).
[100] L.-S. Ma, Z. Y. Bi, A. Bartels, L. Robertsson, M. Zucco, R. S. Windeler, G. Wilpers, C. Oates, L. Hollberg, and S. A. Diddams, Science **303**, 1843-1845 (2004).
[101] K. L. Corwin, I. Thomann, T. Dennis, R. W. Fox, W. Swann, E. A. Curtis, C. W. Oates, G. Wilpers, A. Bartels, S. L. Gilbert, L. Hollberg, N. R. Newbury, S. A. Diddams, J. W. Nicholson, and M. F. Yan, Opt. Lett. **29**, 397-399 (2004).
[102] H. Hundertmark, D. Wandt, C. Fallnich, N. Haverkamp, and H. R. Telle, Opt. Expr. **12**, 770-775 (2004).
[103] M. Kourogi, K. Nakagawa, and M. Ohtsu, IEEE J. Quantum Electron. **29**, 2693-2701 (1993); K. Imai, M. Kourogi, and M. Ohtsu, IEEE J. Quantum Electron. **34**, 54-60 (1998); K. Imai, B. Widiyatmoko, M. Kourogi, and M. Ohtsu, IEEE J. Quantum Electron. **35**, 559-564 (1999).
[104] I. Thomann, L. Hollberg, S. A. Diddams, and R. Equall, Appl. Optics **42**, 1661-1666 (2003).
[105] S. M. Foreman, D. J. Jones, and J. Ye, Opt. Lett. **28**, 370-372 (2003).
[106] I. Thomann, A. Bartels, K. L. Corwin, N. R. Newbury, L. Hollberg, S. A. Diddams, J. W. Nicholson, and M. F. Yan, Opt. Lett. **28**, 1368-1370 (2003).
[107] J. Ye, J. L. Peng, R. J. Jones, K. W. Holman, J. L. Hall, D. J. Jones, S. A. Diddams, J. Kitching, S. Bize, J. C. Bergquist, L. W. Hollberg, L. Robertsson, and L.-S. Ma, J. Opt. Soc. Am. B **20**, 1459-1467 (2003).
[108] K. W. Holman, D. J. Jones, D. D. Hudson, and J. Ye, Opt. Lett. **29**, 1554-1556 (2004).
[109] J. Levine, IEEE Trans. Ultrason. Ferroelectr. Freq. Control **46**, 392-398 (1999).
[110] M. Calhoun, R. Sydnor, and W. Diener, (Jet Propulsion Laboratory, Pasadena, CA, 2002), p. 1-11.
[111] R. K. Shelton, S. M. Foreman, L.-S. Ma, J. L. Hall, H. C. Kapteyn, M. M. Murnane, M. Notcutt, and J. Ye, Opt. Lett. **27**, 312-314 (2002).

[112] J. B. Schlager, B. E. Callicoatt, R. P. Mirin, N. A. Sanford, D. J. Jones, and J. Ye, Opt. Lett. **28**, 2411-2413 (2003).
[113] J. Rauschenberger, T. M. Fortier, D. J. Jones, J. Ye, and S. T. Cundiff, Opt. Expr. **10**, 1404-1410 (2002).
[114] D. J. Jones, K. W. Holman, M. Notcutt, J. Ye, J. Chandalia, L. A. Jiang, E. P. Ippen, and H. Yokoyama, Opt. Lett. **28**, 813-815 (2003).

Chapter 10

GENERATION AND MEASUREMENT OF INTENSE PHASE-CONTROLLED FEW-CYCLE LASER PULSES

Andrius Baltuška[1,2], Gerhard G. Paulus[2,3], Fabrizio Lindner[2], Reinhard Kienberger[1,2], and Ferenc Krausz[1,2]

[1] *Institut für Photonik, Technische Universität Wien*

[2] *Max-Planck-Institut für Quantenoptik*

[3] *Department of Physics, Texas A&M University*

Abstract: Intense, ultrashort waveforms of light can be produced with a predetermined electromagnetic field. These waveforms are essential in many applications of extreme nonlinear optics, most prominently in laser-driven sources of high-energy attosecond radiation. Field reproducibility in each laser shot requires a stable carrier-envelope phase. We analyze different schemes of phase-stable amplification and identify constraints limiting the precision. We describe a phase-stabilized system based on a 20 fs multipass Ti:sapphire amplifier supplemented with a fiber compression stage for producing few-cycle pulses. The amplifier introduces only a slow phase drift and, therefore, can be seeded by a standard phase-stabilized oscillator. The phase stability of the 5 fs, 400 μJ pulses is verified by high harmonic generation, in which different carrier-envelope phases produce distinctly different XUV spectra. The carrier-envelope phase (with a $\pm\pi$ ambiguity) is calibrated from a series of spectra. The calibration allows full characterization of the electric field. The estimated precision of the phase control is better than $\pi/5$, which reduces the timing jitter between the driving laser pulse and the XUV bursts to ~250 as and enables the generation of stable, isolated attosecond pulses. We demonstrate a more robust phase measurement based on the detection of electron emission from photoionized atoms in opposite directions. This method determines the carrier-envelope phase with the $\pi/10$ accuracy and without inversion ambiguity. Using the photoionization technique, we demonstrate the Gouy effect for focused few-cycle pulses. This result is of critical importance for any phase-dependent strong-field applications of ultrashort laser pulses.

Key words: carrier-envelope phase, ultrashort pulses, Gouy phase shift, high harmonic generation, above threshold ionization, phase-stabilized amplifiers

1. INTRODUCTION

The applications of ultrafast laser science demand an increasing degree of control over many parameters of intense ultrashort laser pulses. Some forms of control, such as techniques for adjusting spatial and temporal intensity pulse profiles and the sweep of carrier frequency (chirp) across the electric field, are already well established [1]. There are also well-developed methods for pulse diagnostics, which can fully characterize the envelope of the pulse and its chirp, that are an integral part of any control scheme [2, 3]. New demands, such as control over the time-dependent polarization state of the pulse field on the scale of a single optical cycle [4], emerge in the context of strong-field applications sensitive to the strength of individual light-wave cycles within the laser pulse rather than to the intensity envelope.

As broadband laser systems approach the single-cycle regime [5-7], the electric-field strength of the pulses varies substantially from peak to peak of every optical half cycle. Therefore, it becomes necessary to precisely control the evolution of the electric field underneath the pulse envelope for ultrashort wave forms of light used in field-sensitive experiments. The parameter that determines the offset of the most prominent field peak with respect to the pulse envelope is the carrier-envelope phase. Change of the carrier-envelope phase represents the slippage of the carrier wave through the pulse envelope, which takes place in conventional mode-locked laser systems [8] i.e., those without carrier-envelope-phase stabilization.

The development of techniques suitable for carrier-envelope-phase stabilization of mode-locked oscillators [9-11] and demonstration of such laser systems [12, 13] were significant steps toward accomplishing full control over the temporal and spectral properties of femtosecond laser pulses. Maintaining the value of the carrier-envelope phase and fixed repetition frequency manifests itself in the frequency domain as a perfectly defined and steady comb of laser modes across the laser bandwidth and thereby provides an invaluable tool for frequency metrology [9, 10, 14-18]. Driven by the demand for simple, precise, and robust instrumentation for frequency measurements, the technology of carrier-envelope-phase control of mode-locked femtosecond lasers has rapidly matured [17, 18] and is now commercially available [19]. In comparison with laser oscillators operating at megahertz-to-gigahertz repetition rates, phase stabilization of laser amplifiers is significantly complicated by their low, typically 1–10 kHz, repetition rate. Whereas it is possible to trace the carrier-envelope-phase offset in the output of an oscillator and compensate it by active stabilization of the laser cavity [12, 13], the output phase of a standard chirped-pulse-amplifier (CPA) is random [20-22]. Therefore, the information on phase excursions monitored behind the amplifier is insufficient for the phase

stabilization of the output pulse train. Other techniques, possibly in combination with the use of a phase-stabilized seed oscillator, are required. Several different strategies for carrier-envelope stabilization of amplified laser pulses will be discussed.

The significance of the carrier-envelope-phase control of intense ultrashort laser pulses, and the motivation for pursuing it, can be readily grasped from the numerical example presented in Figure 10-1. This simulation compares the XUV/soft x-ray emission from a target of noble gas exposed to three different driving optical fields depicted in Figure 10-1(a)–(c). The generation of the soft x-ray radiation [23, 24] includes the following steps: (1) ionization occurring in the vicinity of the field peaks, (2) acceleration of the detached electrons by the laser electric field, and (3) recombination of the electron into its ground state following a recollision with the parent ion. The sum of the binding and the kinetic energy of the electron is thus released as a high-energy photon. The highest-energy soft x-ray quanta, which are emitted at the cutoff frequency, appear after approximately two-thirds of the optical cycle following the moment of ionization. This release of a photon nearly coincides with the first zero crossing of the electric field behind the strongest field peak.

Figure 10-1(d)–(i) shows the corresponding temporal structure of the soft x-ray radiation emitted around 65 and 130 eV, respectively. The latter photon energy represents the cutoff obtainable for a neon gas target with a length of 2 mm and a pressure of 100 mbar. Pulse intensity was chosen to reach the cutoff frequency of 130 eV. It is obvious from Figures 10-1(d) and (g) that for a 20-femtosecond pulse, typical of many currently available laser amplifiers, the x-ray bursts are emitted repeatedly over many successive optical cycles. For this driving laser pulse, the threshold of field strength [horizontal bars in Figures 10-1(a)–(c)] required to generate cutoff-frequency x-ray photons can be overcome by multiple field peaks because of their comparable magnitude. Consequently, regardless of the carrier-envelope-phase setting, the emitted x-rays consist of a train of attosecond spikes.

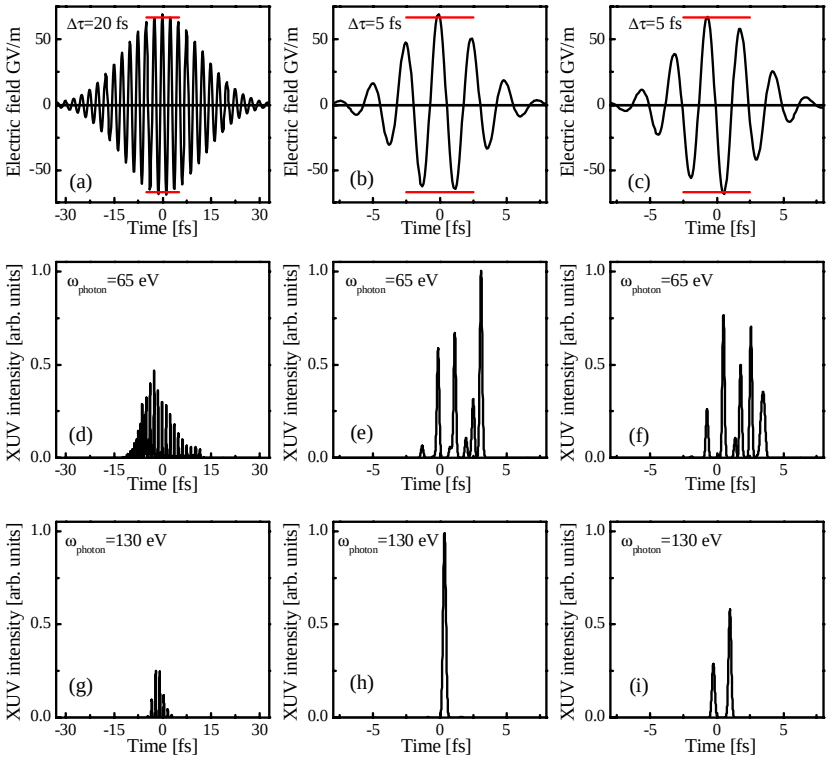

Figure 10-1. Numerical simulation of laser-driven soft x-ray emission from noble gas atoms. (a) Electric field of a 20 fs laser pulse. (b) Electric field of a 5 fs laser pulse optimized for generation of a single subfemtosecond x-ray pulse. (c) Electric field of a 5 fs pulse producing the two highest energy x-ray pulses. (d) – (f) Time-domain structures of x-ray radiation emitted in a 10 eV bandwidth at half the cutoff energy. (g) – (i) Time-domain structures of x-ray radiation emitted in a 10 eV bandwidth at the cutoff energy. The lower x-ray peak yield in (d) and (g) in comparison to (e), (f), (h), and (i) is the consequence of higher ionization by more numerous field peaks of the 20 fs pulse. In total, gas concentration loss due to ionization was 6.7% and 1.7% for the 20 and 5 fs pulses, respectively. Horizontal bars in (a)–(c) show the peak intensity threshold required to yield cutoff-frequency x-ray radiation.

The situation changes dramatically for a 5 fs driving pulse [Figure 10-1(b) and (c)]. Whereas the emission at half the cutoff energy also comprises a train of spikes [Figure 10-1(e)–(f)], the soft x-rays at the cutoff frequency [Figure 10-1(h) and (i)] are extremely sensitive to the arrangement of the optical cycles in the driving laser field. A $\pi/2$ change in the carrier-envelope phase determines whether a single half cycle or two field peaks fulfill the threshold requirement that, in turn, leads to the generation of an isolated subfemtosecond pulse [Figure 10-1(h)] or a pair of bursts [Figure 10-1(i)].

The case study presented in Figure 10-1 underscores several compelling reasons for seeking carrier-envelope-phase control of amplified laser pulses in conjunction with the generation of subfemtosecond pulses [25] and their use in the emerging field of attosecond metrology [26, 27] and spectroscopy [28]. First, pulse-to-pulse fluctuations of the carrier-envelope phase lead to an unstable temporal profile of the soft x-ray pulses, including duration variations and, for some phases, strong prepulses. Second, a variable carrier-envelope phase results in large intensity instability of the soft x-ray bursts, which severely limits their utility. Third, carrier-envelope-phase shifts cause timing jitter between the soft x-ray burst and the envelope peak of the driving laser field. This timing jitter further reduces the temporal resolution of excite-probe experiments that use the laser and the soft x-ray pulses, respectively, as excitation and probe [28] and vice versa. The implications of carrier-envelope-phase variations on the higher-order harmonic generation (extending into the XUV/soft x-ray range) have been studied in a number of papers [6, 23, 24, 29-31]. The lack of carrier-envelope-phase control has been identified as a cause of an excessive spectral noise observed in x-ray spectra [32, 33]. Similar critical dependence on the value of the carrier-envelope phase is expected in other nonlinear optical interactions that exhibit a threshold with respect to the field strength of the incident laser pulse [6]. In particular, the first clear experimental evidence of a carrier-envelope-phase-dependent effect was obtained in an above-threshold ionization measurement in gas [34]. In this scheme, the angular yield of photoelectron emission was found to correlate with the carrier-envelope phase of the circularly polarized driving pulses. Once carrier-envelope-phase-stabilized pulses at the required intensity level become available, it should be possible to steer photoelectrons from gas [34] or solid [35] targets in a predefined way by adjusting the phase of light. In principle, carrier-envelope-phase control of laser pulses would open the way to synthesizing intense wave forms of light (i.e., very brief high-peak-intensity electromagnetic fields exactly reproducible in every laser shot) that could be used to control the motion of charged particles with ultimate precision. Next to phase stabilization, an essential part of carrier-envelope phase control is the measurement of the actual phase value. Standard techniques of pulse characterization [2, 3] are insensitive to carrier-envelope phase since its value has no influence on the shape of the pulse envelope. Information on the relative pulse-to-pulse phase drift can be obtained by various methods involving interference of spectrally overlapping harmonic orders [10-13, 20, 22, 36, 37]. However, such techniques do not permit phase calibration. Instead, the use of high-order nonlinear responses has been suggested for this purpose [6, 30, 38, 39]. In the context of the numerical example presented in Figure 10-1, we have seen that phase

calibration is needed to ascertain the presence of isolated attosecond pulses, especially if such pulses are intended for time-resolved attosecond applications.

This chapter investigates both the problem of carrier-envelope-phase stabilization of amplified ultrashort laser pulses and methods of phase calibration. Several possible schemes of carrier-envelope-phase control capable of operating at kilohertz repetition rates are addressed. We look into the origin of phase distortion added throughout pulse amplification and beam passage through peripheral components, such as dispersive pulse compressors, and stages of nonlinear spectral broadening. We then explain in detail the operation of a carrier-envelope-phase-stabilized multipass Ti:sapphire 5 fs amplifier [40]. Next, we focus on measuring the actual value of the carrier-envelope phase. To perform such phase calibration, we develop a method relying on the spectrum of XUV emission from a noble gas. The robustness of this approach is confirmed both experimentally and by numerical simulations. Whereas phase determination based on the spectral XUV measurement is very practical in conjunction with the generation of isolated subfemtosecond pulses in that spectral range, the information provided by this technique is still insufficient for a complete characterization of the electric field of the driving laser pulse. Therefore, we also present an accurate, unambiguous carrier-envelope measurement based on directional observation of photoelectron emission. We demonstrate that a dual time-of-flight photoelectron detector can be used to calibrate the carrier-envelope phase and visualize the Gouy phase shift of a few-cycle light field in a focused or defocused beam.

2. CARRIER-ENVELOPE PHASE OF A MODE-LOCKED PULSE TRAIN AND A SINGLE ATTOSECOND PULSE

The temporal evolution of a linearly polarized electric field of a single pulse of light can be expressed

$$E_L(t) = A_L(t)\cos\left[\omega_L(t)t + \phi\right]. \quad (1)$$

This description includes three physical quantities: the amplitude $A_L(t)$, the frequency of field oscillations $\omega_L(t) = \omega_0 + \beta(t)$,[4] and the carrier-envelope phase, ϕ. The latter parameter determines the timing of the carrier-wave

[4] The notation used in this chapter corresponds to that of other chapters through the following relationships: $\omega_n = 2\pi\nu_n$; $\omega_r = 2\pi f_r$; $\omega_{CE} = 2\pi f_0$; $\Delta\phi = \Delta\phi_{ce}$

oscillations with respect to the amplitude envelope $A_L(t)$, whereas $\beta(t)$ stands for a possible chirp, i.e., a carrier frequency sweep across the pulse. The relationship between the carrier-wave and the envelope changes as a result of pulse propagation through a dispersive medium. Therefore, Equation (1) is only relevant at a specific location. Also, referring to a carrier-envelope–phase-stabilized pulse train, we mean that at a given point in space every pulse has the same parameters in Equation (1) and imply that the phase evolution with propagation is identical for all these pulses.

For applications of nonlinear optics that are sensitive to the strength of individual field peaks, a change in ϕ makes a physically measurable difference only if the amplitude is subject to significant variation within the light period $T_0 = 2\pi/\omega_0$, i.e., $\left|\frac{\partial A_L(t)}{\partial t}\right| \cong \left|\frac{2\pi}{T_0} A_L(t)\right|$. Evidently, this condition is fulfilled for 5 fs pulses [Figure 10-1(b) and (c)], where the XUV emission depends on ϕ, as opposed to 20 fs pulses [Figure 10-1(a)] where the strength variation between neighboring peaks is substantially smaller. Nevertheless, the carrier-envelope phase preserves a clear meaning regardless of the pulse duration. This can be easily understood by invoking the frequency-domain representation of a mode-locked laser spectrum [9-13, 17, 18, 41]. The frequency of each individual laser mode is

$$\omega_n = n\omega_r + \omega_{CE}, \tag{2}$$

where n is the mode number, ω_r is the repetition rate of the laser, and ω_{CE} is a frequency shift from an exact integer multiple of ω_r. Equation (2) describes the comb of frequencies across the mode-locked bandwidth that is of interest in frequency-domain metrology [17, 42]. The physical origin of the frequency mismatch ω_{CE} lies in the difference between the group delay (the cavity round-trip time of the envelope) and the phase delay (the round trip of the carrier wave). Consequently, the carrier-envelope phase (i.e., the position of the carrier-wave oscillation with respect to the envelope that is advancing at a different velocity) is shifted with each successive laser pulse by

$$\Delta\phi = 2\pi \frac{\omega_{CE}}{\omega_r}. \tag{3}$$

The phase slippage [8] $\Delta\phi$ can be compensated by managing the cavity dispersion [15, 36, 43], thereby forcing all emitted pulses to carry the same

value of ϕ. Reduction of the repetition rate (e.g., by selecting every m^{th} pulse with a pulse picker in front of a chirped-pulse-amplifier) leads to an m-fold increase of the mode density but does not scale the frequency mode mismatch, which remains $\mathrm{mod}_{\omega_r/m}\{\omega_{CE}\}$. In fact, the generation of new frequency modes is the result of applying a modulation that is nonlinear in the time domain (the fast switching of the pulse picker). This nonlinearity does not destroy the properties of the frequency comb as all the modes remain rigorously locked to each other. The same reasoning applies to the case of a single-isolated laser pulse ($\omega_r = 0$) that corresponds to a continuously filled spectrum, $I_L(\omega)$. In this treatment, ϕ can be interpreted as a frequency-independent offset of the spectral phase $\phi_L(\omega)$. This relationship is immediately apparent from the following Fourier-transform link between the time- and frequency-domain electric fields

$$E_L(t) = \frac{1}{2\pi}\int \sqrt{I_L(\omega)}\exp\left[i\left(\phi_L(\omega) - \omega t + \phi\right)\right] d\omega + c.c.. \qquad (4)$$

Here the intensity spectrum $I_L(\omega)$ and the phase $\phi_L(\omega)$ fully determine the quantities $A_L(t)$ and $\omega_L(t)$ [2] but do not specify the carrier-wave offset. The spectral manifestation of ϕ, given by Equation (4), is particularly valuable for describing various single-shot measurements of the carrier-envelope-phase throughout the chapter.

3. MEASUREMENT OF PHASE VARIATIONS

In this section, we address practical methods for characterizing carrier-envelope phase changes that are vital for implementing phase-stabilizing feedback loops.

3.1 Detecting carrier-envelope drift of oscillator pulses

The standard tracking technique is employed in several carrier-envelope–phase-controlled oscillators [12, 13, 16-18] and will be discussed later in this section. It relies on detecting the frequency beat from the laser modes of the frequency comb that are separated by a spectral octave, i.e., they differ in their frequency by a harmonic order. The lower-frequency mode is then frequency doubled and the two modes are brought into interference with each other, producing a beat at the carrier-envelope frequency

$$\omega_{CE} = 2(n\omega_r + \omega_{CE}) - (2n\omega_r + \omega_{CE}). \quad (5)$$

This scheme requires a very broadband, octave-spanning spectrum, which is unavailable from a typical mode-locked oscillator. To gain the necessary bandwidth, the laser spectrum can be broadened in a medium with third-order nonlinearity. Using a photonic crystal fiber (PCF) [44], this task can be accomplished even with nJ pulses. The device incorporating the spectral broadening, frequency doubling, and beat-signal generation is called a nonlinear interferometer or ν-to-2ν setup. In state-of-the-art broadband mode-locked oscillators, it has already become possible to derive the ν and the 2ν, frequency components directly from the laser spectrum, thus obviating the need for extracavity spectral broadening [45]. For further details on ν-to-2ν interferometry, see Chapter 1.

3.2 Detecting carrier-envelope drift of amplified pulses

There are three significant difference in the phase-drift of amplified laser pulses compared with an oscillator. First, the repetition rate of the amplifier must be lowered, typically by 5 orders of magnitude, to 1–10 kHz, which complicates accurate detection of ω_r and ω_{CE}. Second, the availability of high-energy pulses simplifies the problem of producing an octave-spanning continuum. Third, laser amplifiers exhibit a considerably higher peak intensity noise as compared to "quiet" Kerr-lens–mode-locked oscillators [46]. Consequently, the excursions of a quasi-monochromatic ν-to-2ν signal detected behind the amplifier do not necessarily indicate a change in carrier-envelope phase but might reflect pulse energy fluctuations.

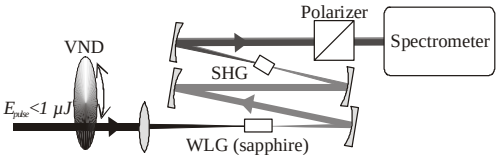

Figure 10-2. Setup for phase characterization of amplified pulses by nonlinear spectral interferometry. VND: variable neutral density filter; SHG: second harmonic generator; WLG: white light generator.

Initial amplifier phase tracking schemes [7, 20, 40] took advantage of abundant pulse energy and used different types of single-shot nonlinear spectral interferometry. The objective was to use broadband detection of the ν-to-2ν beat as opposed to the narrowband scheme acceptable in the case of

an oscillator. The essence of this approach can be described as follows. After generating a sufficiently broadband spectrum, $I_{WL}(\omega)$, the pulse is sent to a second-harmonic-generation (SHG) crystal, resulting in an up-shifted field

$$\begin{aligned} E_{SHG}(\omega) \propto \exp(i2\varphi)\int \chi^{\langle 2\rangle}(\omega:\omega',\omega-\omega')\sqrt{I_{WL}(\omega')I_{WL}(\omega-\omega')} \\ \times\exp\left[i\left(\phi_{WL}(\omega')+\phi_{WL}(\omega-\omega')\right)\right]d\omega' \\ = \sqrt{I_{SHG}(\omega)}\exp\left[i\left(\phi_{SHG}(\omega)+2\varphi\right)\right], \end{aligned} \tag{6}$$

where $\phi_{WL}(\omega)$ is the spectral phase of the white light and $\chi^{\langle 2\rangle}$ is the second-order susceptibility. The interference between the white-light and SHG pulses, separated by the time delay τ_0, yields a spectrum

$$\begin{aligned} S(\omega) = (1-a)I_{WL}(\omega) + aI_{SHG}(\omega) \\ + 2\sqrt{a(1-a)I_{WL}(\omega)I_{SHG}(\omega)}\cos\left(\phi_{SHG}(\omega)-\phi_{WL}(\omega)+\omega\tau_0+\varphi\right), \end{aligned} \tag{7}$$

where the coefficient a stands for the polarizer transmission for the polarization of the SHG light. For a sufficiently large pulse separation τ_0, corresponding to many spectral fringes in the interferogram $S(\omega)$, the argument of the cosine in Equation (7) can be recovered using the standard algorithm of spectral interferometry [47]. The phase of the newly obtained complex spectral function then directly yields the differential phase of the two fields, $\mathrm{mod}_{2\pi}\left\{\phi_{SHG}(\omega)-\phi_{WL}(\omega)+\varphi\right\}$. In principle, such an interference measurement can be used not only to characterize the pulse-to-pulse changes of ϕ, but also to find the actual value of ϕ. In practice, however, this is not feasible because with current methods, $\phi_{SHG}(\omega)$ and $\phi_{WL}(\omega)$ can only be characterized with the precision of an arbitrary constant [2]. Only by fully accounting for the evolution of the spectral phase in the SHG crystal, which includes both linear and nonlinear pulse propagation, would it be possible to retrieve the value of ϕ in this scheme. Therefore, the ν-to-2ν interferometer can only measure the full carrier-envelope phase after calibration by an independent external experiment, as shown in Section 7. Otherwise, this device reflects the phase jump in the j^{th} laser pulse with respect to another (e.g., 0^{th}) pulse arriving earlier from the same pulse train and chosen as reference, i.e., the interferometer measures $\delta\phi_j = \phi_j - \phi_0$. The difference between the method outlined above and Fourier-transform-spectral-interferometry based on the use of parametric waves, as reported in Reference [22], is that, in the latter case, one measures the interference between the frequency-doubled idler and the signal pulses. The advantage is that the white-light continuum injected into the parametric device does not

have to span an octave and the interference is observed close to the spectral peak of the signal rather than in the continuum wing.

In this work, however, we opted for a simpler setup, as shown in [Figure 10-2], which is similar to the scheme published in Reference [20]. For further simplification, we replaced white-light generation in a hollow waveguide with bulk continuum generation in a 2 mm of sapphire. Because of the dispersion of the sapphire and of the 1 mm BBO (β-BaB_2O_4) frequency-doubling crystal, the white-light and SHG are sufficiently separated in time to employ spectral interferometry. The spectral interferogram is measured by a fiber-coupled spectrometer behind a polarizer cube that selects the common polarization of the beams. With a 2 MHz acquisition card, single-shot ν-to-2ν interferograms can be detected for every 3rd laser shot at a 1 kHz repetition rate. In the ν-to-2ν unit shown in Figure 10-2, the timing jitter, $\tau = \tau_0 + \delta\tau$, has an immediate impact on the fringe pattern of the measured interferogram, as will be shown in Section 3.3. However, for the collinear arrangement, depicted in Figure 10-2, the problem of timing jitter is negligible as the interfering beams follow the same path.

3.3 Measuring the phase difference by linear interferometry

We have presented interferometric methods that employ nonlinear frequency conversion and reveal variations in the value of the carrier-envelope phase. Here we discuss the technique of linear spectral interferometry [48, 49], which measures the phase difference between the test and reference arms of an interferometer. It is instructive to compare the relevance of this method to the characterization of carrier-envelope-phase drift with the measurement of pulse envelope and chirp. If the intensity spectrum $I_L(\omega)$ and the phase $\phi_L(\omega)$ are determined in front of an interferometer and the phase accumulated inside the interferometer $\phi(\omega)$ is recovered by spectral interferometry, then the phase of the outgoing pulse is known and equals $\phi_L(\omega) + \phi(\omega)$. Therefore, once $\phi_L(\omega)$ is found with a nonlinear optical technique (e.g., autocorrelation or frequency-resolved optical gating [2]), complete phase characterization can be performed with linear methods provided a reference beam derived after the nonlinear measurement is available. In essence, we have just stated the principle of the pulse measurement by TADPOLE (Temporal Analysis by Dispersing a Pair Of Light E-fields) [2].

Linear spectral interferometry can be used in exactly the same way to study carrier-envelope-phase deviations occurring behind a nonlinear ν-to-

2ν interferometer. To do so, a small fraction of the reference beam can be split behind the point where the changes of ϕ are tracked with the ν-to-2ν unit and sent to propagate through free space (air). For practical purposes, fluctuations of air density are the only cause of carrier-envelope-phase jitter of the reference pulses. Therefore, we consider these pulses carrier-envelope-phase stable. The test beam is directed into an optical arrangement (e.g., an amplifier) and accumulates a phase difference $\phi(\omega)$ with respect to the reference. As a consequence of beam-pointing instability during propagation through elements with angular dispersion and other linear and/or nonlinear dispersion changes [50], the test pulse can pick up a frequency-dependent phase offset

$$\delta(\omega) = \delta(\omega_0) + \frac{1}{2}\delta'(\omega_0)(\omega - \omega_0) + \frac{1}{6}\delta''(\omega_0)(\omega - \omega_0)^2 + \ldots . \qquad (8)$$

We assume that $\delta(\omega)$ corresponds to a very minute dispersion modification that does not involve reshaping of the pulse envelope. Otherwise, in case $A_L(t)$ is modified, carrier-envelope-phase control would become irrelevant. Indeed, a tiny (<1 μm) change in the propagation length within dispersive material already leads to a sizable leap in the carrier-envelope phase [8], which we call $\delta\phi$. Consequently, we can justifiably disregard higher-order terms, starting with the parabolic phase distortion. In fact, $\delta\phi$ represents the sum of frequency-independent terms in Equation (8). The linear shift with frequency term in Equation (8) is next in significance. It simply represents the time shift due to a modified propagation length and, therefore, has no bearing on the carrier-envelope dynamics. Thus we will only pay attention to the phase jump, $\delta\phi$, in the characterization of the phase drift of the test pulse and treat the test-reference timing offset separately.

As was pointed out in Section 3.2, a temporal jitter between the interfering pulses causes fringe rearrangement in the spectrogram $S(\omega)$. This timing variation is inevitable, especially if the reference beam is not interferometrically stabilized. For large laser systems, the path of the reference beam can be several meters long and fluctuate by several wavelengths. Thus, the ability of spectral interferometry (linear or nonlinear) to discriminate between $\delta\phi$ and the timing jitter needs to be scrutinized.

Figure 10-3 gives an overview of the properties of spectral interferometry. Figure 10-3(a) shows a typical interferogram and the power spectrum of its Fourier transform (inset) used in phase retrieval. In Figure 10-3(b), we examine the impact on the interferogram of a pure time shift ($\delta\tau$) and a pure phase jump ($\delta\phi$), depicted by the solid and the dashed curves, respectively. Figure 10-3(c) presents the corresponding phases after subtracting the phase slope $\omega\tau_0$, which is due to the delay between the test

and reference pulses. The shape of the intensity spectrum $I_L(\omega)$ [solid curve in Figure 10-3(a)] and differential phase $\phi(\omega)$ [dotted curve in Figure 10-3(c)] are selected arbitrarily. The values of $\delta\tau$ and $\delta\phi$ are chosen so that the interferograms in Figure 10-3(b) closely resemble each other. Nevertheless, there is a fundamental difference because the timing variation changes the fringe period. This change can be clearly observed in an interferogram consisting of a large number of fringes. Therefore, a charged coupled device (CCD) camera-based spectrograph (which covers the relevant spectral width and has a sufficiently high resolution) makes it possible to separate the contributions of $\delta\phi$ and $\delta\tau$ as long as Fourier-transform–spectral-interferometry noise criteria [49] are met. We implemented the time jitter correction numerically in our Fourier-transform–spectral-interferometry code by extracting a linear phase obtained by back-transformation into the frequency domain.

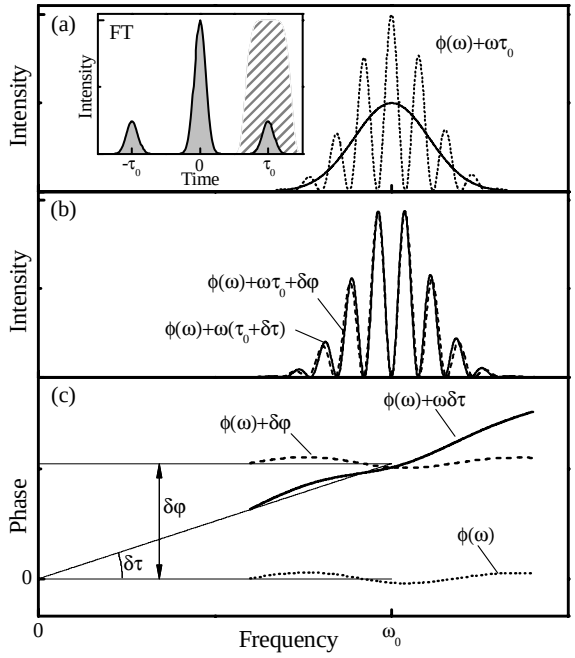

Figure 10-3. Discrimination between phase and timing jitter in Fourier-transform spectral interferometry. (a) Intensity spectrum (solid curve) and spectral interferogram (dotted curve). (b) Spectral interferograms modified by a timing shift (solid curve) and a frequency-independent phase shift (dashed curve). (The fringe period changes in the case of timing shift.) (c) Differential spectral phases after time-delay slope subtraction. Dotted and solid and dashed curves correspond to interferograms in (a) and (b), respectively. Inset shows the power

spectrum of the Fourier transform to the time domain. Dashed contour corresponds to a possible filter required in the phase extraction to isolate the temporal peak at τ_0.

The immediate implication of the timing-problem solution is the ability to trace carrier-envelope-phase jumps with respect to a reference beam propagating in free space. We believe this method can be particularly useful for extending carrier-envelope-phase stabilization in a multistage laser system, in which the earliest stage is phase stabilized and subsequent stages are expected to introduce only slow phase drift.

4. PHASE JITTER OF THE WHITE-LIGHT CONTINUUM

The ν-to-2ν phase characterization methods presented in Section 3 (and all phase-stabilized laser systems reported by 2002 [12, 13, 18]) rely on white-light generation to create a phase-coherent, spectrally broadened replica of the input laser pulse. The phase noise added in the process of white-light generation is an intrinsic problem of carrier-envelope-phase stabilization loops [18]. In this section, we outline the reason for the phase coherence between the white light and the initial pulse and then study the influence of intensity fluctuations on phase noise.

4.1 Phase lock between the input pulse and the white-light continuum

Generally, white-light generation consists of several nonlinear wave-mixing processes that lead to generation of new frequency components. Therefore, it is not immediately clear whether white-light generation can be relied on for producing a frequency-broadened, but phase-offset-repeating, replica of the laser pulse. The complete propagation equation for pulse self-action (assuming the perturbative regime of nonlinear optics [6]) is derived directly from Maxwell's equation [6, 51] to be

$$\left[\nabla^2 + k^2(\omega)\right]E(\mathbf{r},\omega) = \frac{\omega^2}{\varepsilon_0 c^2} P^{nl}(\mathbf{r},\omega), \tag{9}$$

where $E(\mathbf{r},\omega)$ and $P^{nl}(\mathbf{r},\omega)$ denote the electric field and generated nonlinear polarization, respectively. The particular form of $P^{nl}(\mathbf{r},\omega)$ that describes both the delayed Raman response (i.e., slow nonlinearity) and the

parametric four-wave mixing based on fast-electronic Kerr nonlinearity, also known as the process of self-phase-modulation [51] is

$$\begin{aligned} P^{nl}(\mathbf{r},\omega) &= \iint \chi^{\langle 3\rangle}(\omega:\omega_1,\omega_2,\omega_1+\omega_2-\omega) \\ &\quad \times E(\mathbf{r},\omega_1)E(\mathbf{r},\omega_2)E^{*}(\mathbf{r},\omega_1+\omega_2-\omega)d\omega_1 d\omega_2 \\ &= \exp\left[i(\varphi+\varphi-\varphi)\right] \\ &\quad \times \iint \chi^{\langle 3\rangle}(\omega:\omega_1,\omega_2,\omega_1+\omega_2-\omega)\sqrt{I(\mathbf{r},\omega_1)I(\mathbf{r},\omega_2)I(\mathbf{r},\omega_1+\omega_2-\omega)} \\ &\quad \times \exp\left[i\left(\phi(\mathbf{r},\omega_1)+\phi(\mathbf{r},\omega_2)-\phi(\mathbf{r},\omega_1+\omega_2-\omega)\right)\right]d\omega_1 d\omega_2, \end{aligned} \tag{10}$$

where $\chi^{\langle 3\rangle}$ represents the effective third-order susceptibility and the conjugation symbol marks emission [52]. The propagation-dependent change of dispersion is included in $\phi(\mathbf{r},\omega)$. Here we assume that all mixing frequencies are positive [53]. The appearance of the conjugation operator in the convolution integral in Equation (10) accounts for the preservation of the initial phase offset ϕ in the output field. After solving Equation (9) over the interaction length of the white-light-generation medium $\mathbf{r}_0 \to \mathbf{r}_1$, the resultant output pulse will generally carry a different value of the carrier-envelope phase [6, 54] than the input pulse (i.e., $\phi_{WL} \neq \phi$), which is also the case for any type of dispersive linear or nonlinear pulse propagation. Nevertheless, the important criterion for an accurate carrier-phase-phase drift determination is the ability of the white-light continuum to repeat (without distortion) the input phase offset. This ability is the consequence of the rule for phase summation in Equation (10). After plugging Equation (10) into Equation (9), ϕ cancels out, i.e., it has no effect on $\phi(\mathbf{r}_1,\omega)$ of the output field regardless of the microscopic origin of the nonlinearity. The presence of a resonant or nonresonant fifth-order parametric wave mixing ($EE^{*}EE^{*}E$) [55] does not lead to a ϕ-dependent propagation either. However, the solution for pulse propagation does become ϕ-dependent if second-harmonic generation and/or third-harmonic generation cannot be neglected. To account for these contributions, $P^{nl}(\mathbf{r},\omega)$ should also include the terms describing the three-wave mixing of second-harmonic generation and the four-wave mixing of third-harmonic generation, with their phase summation rules given by the field products EE and EEE, respectively.

We would like to underscore two points. First, the phase shift added by both the nonresonant and/or resonant white-light generation does not depend on the carrier-envelope phase of the input pulse. Therefore, the techniques of spectral broadening can be readily applied to schemes for measuring the

carrier-envelope-phase drift. Second, mixing in of undesired mechanisms of frequency conversion, such as second-harmonic generation (or, in a broader sense, sum-frequency generation) and third-harmonic generation, can distort the frequency-independent phase of the white-light pulse even if there are no intensity fluctuations of the input pulse. In typical experimental conditions, however, second- and third-harmonic generation do not play a significant role. For instance, non-phase-matched second-harmonic radiation is often observed in the cladding of conventional single-mode fibers, but it is probably not sufficiently strong to cause a noticeable pulse-to-pulse phase jitter. For bulk-material chirping (typically performed in sapphire or CaF_2), the contributions of second- and third-harmonic generation are negligible.

4.2 Phase noise resulting from intensity fluctuations

In Section 4.1, we dismissed the interplay between different types of nonlinearity as a concern for added phase jitter in white-light generation. In practice, a much more important phase distortion is the variation of the intensity-induced phase shift [56]. As the result of intensity-dependent nonlinear interaction, the phase accumulated throughout the white-light generation can vary from pulse to pulse and compromise the fidelity of carrier-envelope-phase-drift characterization. In the case of ν-to-2ν interferometers suited for oscillators, these problems can arise from mechanical vibrations of the PCF, which affect the amount of light coupled in. In contrast, ν-to-2ν interferometers for amplified pulses can employ bulk white-light generation (cf. Section 3.2), which is almost insensitive to beam-pointing fluctuations. Typical studies of the phase stability of white-light generation consist of interference measurements of independently produced white-light continua [57, 58]. The influence of white-light-generation phase noise on the operation of phase-stabilization loops has also been investigated by measuring the carrier-envelope drift with two independent PCF-based ν-to-2ν interferometers [18, 59].

Here, we check the phase jitter of white-light generation in bulk sapphire against increased intensity noise of amplified pulses [46]. The white-light-generation stage shown in Figure 10-2 was supplemented by the linear interferometer depicted in Figure 10-4. This addition allowed us to measure the phase shift of the white light with respect to the replica of the injected pulse. The intensity of the beam was varied with a neutral density filter while single-shot–white-light interferograms and laser spectra were being recorded by a dual-channel spectrometer. The synchronous registration of the laser spectra is necessary to calibrate the pulse energy in each laser shot.

We used a multipass Ti:sapphire amplifier with an rms intensity noise of 1%. The optimized setting of the neutral density filter corresponds to a pulse

energy of 0.7 μJ in front of the sapphire and a focal-spot diameter of ~ 30 μm. These parameters allowed us to generate a bandwidth adequate for ν-to-2ν measurement. For these conditions, the rms phase jitter retrieved from the laser–white-light interferogram was ~100 mrad.

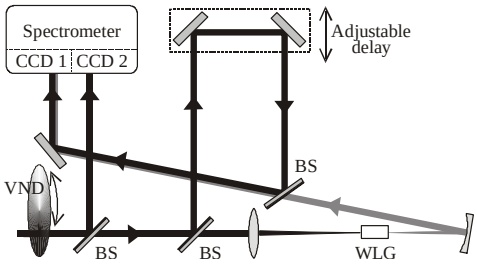

Figure 10-4. Single-shot spectral interferometer for measurement of carrier-envelope-phase jitter arising from white-light generation. VND: variable neutral density filter and BS: dielectric beamsplitter.

Next, we recorded phase statistics for various settings of the neutral density filter. The resultant phase evolution, plotted as a function of incident pulse energy, is presented in Figure 10-5. The data cover several distinct regimes, indicated in Figure 10-5 by vertical sections. First, we notice that there is an abrupt phase change that corresponds to the increasing strength of self-focusing and filament formation. This phase change can be explained by an alteration in the group velocity of light with the increase of the intensity-dependent part of the refractive index of sapphire. After the markedly noisy region of the onset of filamentation, the phase shows a certain "rebound" that probably indicates an increase in the filament length. The rebound is followed by an interval of stable filamentation that is relatively broad in terms of pulse energy — about ±8% around the energy set point of the ν-to-2ν setup. At higher pulse energies, we observe a collapse of the filament and multiple filamentation. The phase noise and the downward phase trend somewhat resemble the situation before the formation of a single stable filament. Measurement at even higher energies could not be performed with a multifilament beam because of the breakdown of the interference pattern into several modes.

In the regime of a stable filament, the phase exhibits a quasi-linear change with energy. The rate of this variation, given by the straight line in Figure 10-5, is 12 mrad/nJ. This rate corresponds to an 84 mrad phase shift for a 1% jump in the pulse energy.

The phase evolution covers only the spectral overlap region between the white light and the input pulse, i.e., approximately a 60 nm bandwidth.

Therefore, the results of our measurement correspond to the best-case scenario since phase excursions in the blue (2ν) spectral region cannot be visualized. Additionally, the second-harmonic generation of the red-shifted part of the continuum also causes an intensity-dependent phase shift and, consequently, is likely to worsen the precision of the ν-to-2ν carrier-envelope-phase-drift characterization.

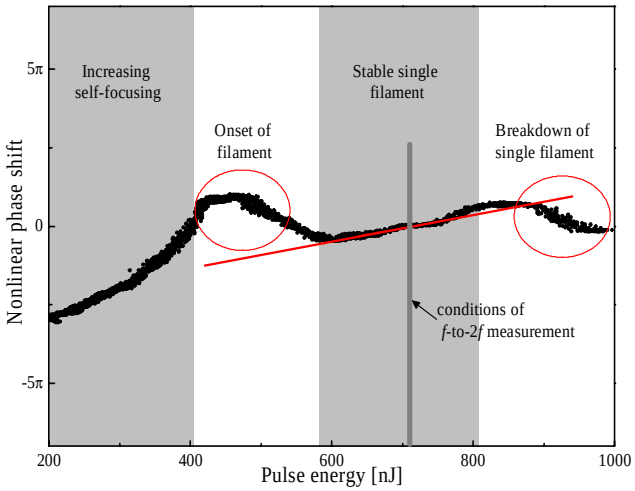

Figure 10-5. Intensity-phase coupling of the white-light generation in bulk sapphire. Solid dots depict phase changes extracted from single-shot interferograms. Straight line shows a linear fit marking the slope of phase intensity-dependent variation in the vicinity of the pulse energy used for ν-to-2ν characterization.

The issues of the phase properties of white-light generation presented in this section are important for identifying the limitations of carrier-envelope-phase-control schemes and for evaluating the applicability of white-light generation as a tool for extending a mode-locked frequency comb [58] and creating phase-coherent frequency-shifted pulse replicas [21].

5. CONCEPTS OF PHASE-CONTROLLED AMPLIFICATION

In this section, we suggest several practical designs of carrier-envelope phase-stabilized amplifiers. The corresponding schematics are sketched in Figure 10-6 and can employ both CPA [60] and optical parametric amplification (OPA) [61, 62]. Two types of carrier-envelope phase noise or

drift in amplifiers must be considered. The first kind of phase noise is associated with the fluctuations of the intensity-dependent nonlinear phase contribution. It can vary randomly from pulse to pulse as the result of pump energy fluctuations and, therefore, cannot be compensated with active phase-stabilization loops. To minimize this problem, the value of the *B*-integral [63] $\psi(t) = k(\omega_0) n_2 \int I(t,z) dz$, i.e., the accumulated nonlinear phase, or self-phase modulation in the amplifier, should be on the order of π. This condition is fulfilled in typical CPA amplifiers. Recent measurements of time-domain interferometric cross-correlation between seed-oscillator pulses and their amplified replicas have shown that the phase jitter at the output of a multipass Ti:sapphire amplifier lies below 0.1 rad [64]. In fact, with pump energy fluctuations being the chief contributor to the jitter of the nonlinear phase, the use of low-noise diode-pumped pump lasers should make it possible to phase stabilize amplifiers operating at higher *B*-integral values.

The second kind of carrier-envelope drift is caused by beam-pointing instability that leads to path-length fluctuations in dispersive elements [50] of the amplifier. Such mechanical perturbations occur on a relatively slow timescale, with characteristic time constants of 1 second or longer. Therefore, the resulting carrier-envelope phase modulation could be easily traced and precompensated.

The schemes of carrier-envelope-phase control amplification, discussed here, can be divided into three categories: (1) all-optical phase self-stabilization [Figure 10-6(a)]; (2) passive triggering on a seed pulse with an appropriate carrier-envelope-phase value [Figure 10-6(b)]; and (3) use of carrier-envelope–phase-stabilized seed with a subloop for phase correction of the amplifier output [Figure 10-6(c)–(e)].

Recently it has been shown that passive carrier-envelope-phase stabilization can be obtained in an appropriately configured OPA [21]. This is achieved by seeding the OPA with a white-light pulse generated by the OPA pump pulse. As discussed in Section 4, both the seed and the pump pulses are phase coherent and, in the process of difference-frequency generation, the phases of these two pulses cancel. Therefore, the amplified idler pulse, which is a result of difference-frequency generation between the pump and the seed, is free of carrier-envelope drift even when the OPA is pumped with random-carrier-envelope-phase pulses. This scheme, shown in Figure 10-6(a), can be used as a phase-stable extension of a conventional, free-running CPA. Subsequent amplification can be carried out by broadband chirped-pulse OPA into a TW–PW regime [62]. The drawback of this approach is that the red-shifted output wavelength of the idler wave does not permit postamplification to be carried out in the laser gain medium used

to generate the pump beam. Consequently, implementation of all-optical phase stabilization in high-energy systems is not straightforward and demands development of dedicated amplification stages.

Other designs presented in Figure 10-6(b)–(e) are intended as upgrades of existing amplified systems. Figure 10-6(b) represents the simplest possible realization of phase control based on the 10^5 difference in the repetition rates of the seed oscillator and a kHz amplifier. The carrier-envelope phase-evolution of the oscillator pulse train is quasi-periodic [8, 13]. The rate of the pulse-to-pulse phase slippage $\Delta\phi$ can be adjusted by manipulating the cavity dispersion. With a ν-to-2ν interferometer, one can monitor the evolution of the ω_{CE} beat and employ this signal to trigger a pulse picker to select an oscillator pulse with a desired phase [13]. To ensure proper amplification, the pulse picker must be triggered shortly after the flash of the kHz pump laser and within the lifetime of population inversion, which leaves room to select an "appropriate" seed pulse from thousands of oscillator shots. The key drawback of this scheme is the relatively poor precision with which such a selection can be performed, since there could be several additional laser shots between the triggering pulse and the one that is actually sent to the amplifier. In this situation, variations of the quasi-periodic phase change would introduce a variable carrier-envelope-phase shift of the selected pulse. Another difficulty in this method is the lack of an obvious mechanism to correct phase fluctuations arising in the amplifier.

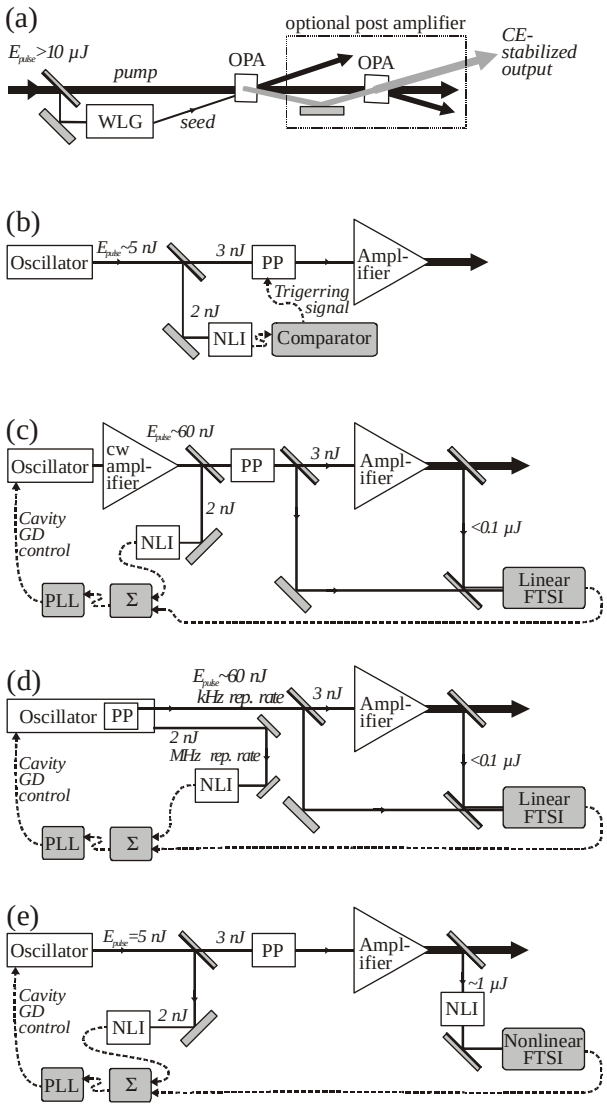

Figure 10-6. Multiple concepts of phase-stable pulse amplification. (a) All-optical (passive) phase stabilization with optical parametric amplification (OPA). (b) Phase-selective seed by a free-running oscillator. (c)–(e) Schemes employing a phase-stabilized seed oscillator with a secondary phase-correction loop behind the amplifier based on linear (c), (d) and nonlinear (e) phase-drift detection. Concepts (c) and (d) require high-energy seed that can be attained with a cw-amplified or a long-cavity oscillator (c) and a cavity-dumped oscillator (d). PP: pulse picker; PLL: phase-locked loop; NLI: nonlinear ν-to-2ν interferometer; and FTSI: Fourier-transform spectral interferometry.

The schemes drawn in Figure 10-6(c) and (d) are based on the use of a carrier-envelope-controlled oscillator [12, 13]. They explore the possibility of sending a reference (pilot) beam for the measurement of the phase offset in the amplifier. Information on the slow phase drift behind the amplifier is obtained with the linear spectral-interferometry described in Section 3.3. It can then be plugged into the phase-stabilization loop of the oscillator. The core of the phase-stabilizing electronics is the phase-lock loop (PLL in Figure 10-6) that forces the beat signal ω_{CE} to oscillate in phase with an external local oscillator via a feedback to the intracavity dispersion. The inverse of the phase offset measured by spectral interferometry at the amplifier output can then be combined with the phase of the local oscillator signal ($1/4\,\omega_r$), thus precompensating this offset already in the oscillator.

The use of the reference beam for (a potentially single-shot) spectral interferometry imposes the demand for high-seed pulse energy. Pulses of tens of nanojoules can be obtained by intermediate cw amplification of the seed pulse train before ν-to-2ν characterization, by employing long-cavity oscillators [13, 65] or using a cavity-dumped oscillator [66]. This type of laser has a dual output. It emits a pulse train through the output coupler at the full repetition rate, which can be conveniently used to drive the ν-to-2ν interferometer. At the same time, the pulses ejected by the intracavity pulse picker are directly synchronized with the amplifier and satisfy the needs for a kHz seed and a spectral interferometry reference.

The remaining concept for phase control of an amplifier [Figure 10-6(e)] offers the most compatibility with existing CPA systems and is well suited for retrofitting them. This scheme requires implementation of a standard phase-lock loop of the seed oscillator, which consists of a ν-to-2ν interferometer for the oscillator, electronics, and an additional secondary feedback loop. The feedback loop consists of a high-energy ν-to-2ν interferometer and computer for the spectral interferometry. Neither the oscillator nor the amplifier requires significant modification. We have followed this blueprint to upgrade a standard multipass Ti:sapphire CPA system [46] for carrier-envelope–phase-stabilized operation.

6. PHASE-STABILIZED 5 fs, 0.1 TW-AMPLIFIED SYSTEM

In our high-power laser setup [Figure 10-6(e)], we have incorporated a commercially available phase-stabilized 10 fs laser system (FS 800, Menlo Systems GmbH). It consists of a dispersive-mirror-controlled Kerr-lens–mode-locked Ti:sapphire oscillator (Femtosource Compact Pro, Femtolasers GmbH), a ν-to-2ν interferometer, and phase-locking electronics that drive an

acousto-optic modulator to control the intensity of the cw pump laser (Verdi V, Coherent). About 50% of the output of the oscillator is diverted into 2 cm of PCF for detection of the carrier-envelope beat frequency. The reference signal (i.e., the local oscillator) for the phase-locked loop is derived by dividing the repetition rate of the oscillator (80 MHz) by a factor of 4. As can be seen from Equation (3), selecting ω_r or its (sub)harmonics as the reference signal is the best choice to control the value of ω_{CE}. Before activating the phase lock loop, we set the intracavity carrier-envelope-phase shift $\Delta\phi$ to approximately $2\pi(m + 1/4)$, where m is an integer. This rough adjustment of $\Delta\phi$ is performed by changing the optical path length through a pair of thin intracavity wedges of fused silica. At this stage, ϕ is approximately reproduced in every fourth round trip in the laser cavity, resulting in a quasi-periodic modulation of the ν-to-2ν beat signal at $\omega_r/4$, i.e., 20 MHz. Next, to enhance the accuracy of the phase reproducibility, ω_{CE} and $\omega_r/4$ are phase locked. Phase locking is achieved by controlling $\Delta\phi$ via nonlinear effects in the Ti:sapphire crystal through the variation of the pump intensity [8]. For this purpose, the cw pump laser is passed through the acousto-optic modulator [13, 50], which varies the power of the transmitted beam according to the phase error [Figure 10-6(c)–(e)]. As a result, every fourth pulse in the 80 MHz pulse train carries the same carrier-envelope phase, giving rise to an accurate optical field reproduction.

In 2004, we employed a multipass Ti:sapphire chirped-pulse amplifier (Femtopower, Femtolasers GmbH). The Q-switched diode-pumped pump laser (Corona, Coherent Inc.) of the amplifier and the pulse picker (Pockels cell) in the amplifier were synchronized with exactly every $80{,}000^{\text{th}}$ pulse from the oscillator to ensure that only pulses with identical ϕ are amplified (at a 1 kHz repetition rate). The nanojoule pulses are temporally stretched by a glass block before their energy is boosted to ≈ 1 millijoule in 9 passes through a 40 mm Ti:sapphire crystal. After amplification, the duration of the pulses is reduced to ≈20 fs in a refractive pulse compressor consisting of two pairs of Brewster-angled prisms. To shorten the pulse even further, the output of the amplifier is injected into a 1 m hollow-core glass fiber filled with neon gas and subsequently passed through a set of ultrabroadband chirped mirrors. To detect carrier-envelope-phase variations, a small fraction (< 1%) of the energy of the 20 fs pulses is split off from the main beam directly behind the amplifier and fed into the second ν-to-2ν interferometer sketched in Figure 10-2 and discussed in Section 3.2. The parameters of the resultant output pulses are summarized in Figure 10-7(a). The insets in Figure 10-7(a) depict the measured spectrum and second-order interferometric autocorrelation of the compressed pulses. An iterative pulse retrieval from these data yields a near-bandwidth-limited pulse with an

amplitude envelope $A_L(t)$, as shown by the thin-dashed line in Figure 10-7(a). It also yields a pulse duration [full width at half maximum of $A_L(t)^2$] of $\tau_L = 5.4 \pm 0.5$ fs.

Experimental results obtained with the second ν-to-2ν interferometer in different phase-stabilization regimes of the amplifier are summarized in Figure 10-7(b). In the case of a phase-unlocked seed oscillator, the interference pattern is completely averaged out within approximately 200 laser shots [black curve, left inset of Figure 10-7(b)]. This finding underscores the importance of a single-shot monitoring capability for the ϕ drift. In contrast, seeding the amplifier system with phase-locked pulses preserves a clear interference pattern for CCD exposure times as long as several seconds. The only additional stabilization required is the tracing of ω_{CE} at the oscillator output. The temporal evolution of the carrier-envelope-phase variation in this mode, which we term simple phase lock, is exemplified in Figure 10-7(b) by the dotted curve. These data reveal that the carrier-envelope phase of the high-energy 20 fs pulses remains virtually stable for periods of up to several seconds. This is remarkable considering the sensitivity of the carrier-envelope phase to path-length change in any solid optical medium [8]. Beam direction instabilities in the microradian range can produce path-length changes of this order of magnitude in the prism compressor and are likely to provide a significant contribution to the phase drifts on a longer time scale. However, compared with other femtosecond amplifiers that employ long-pulse–diffraction-grating-based stretchers, our system presents a clear advantage in terms of its angular beam stability. This stability results from employing bulk-material pulse chirping.

The slow drift of ϕ shown by the dotted curve in Figure 10-7(b) can be readily tracked by computer analysis of the ν-to-2ν fringe pattern [right inset in Figure 10-7(b)]. A voltage proportional to the change of ϕ is generated by a personal computer that performs the ν-to-2ν Fourier-transform spectral interferometry analysis. As shown in Figure 10-6(e), this signal is combined with the fast-changing feedback from the first ν-to-2ν unit that monitors the phase evolution of the seed oscillator. The absence of fast phase changes in the amplifier allows us to accumulate the interferograms measured in the second nonlinear interferometer [Figure 10-2] for about 20–30 ms (i.e., 20–30 laser shots). The implementation of this signal integration smoothens the operation of the feedback loop by preventing accidental overshoots of the carrier-envelope-phase control. Once stabilized at a certain value of ϕ, the phase behind the amplifier can be controlled with the Fourier-transform–spectral-interferometry computer by adding an offset value to the feedback signal. The simultaneous use of both feedback loops allows us to stabilize the phase for extended periods (>> 1 minute). The solid curve in Figure 10-7(b) shows the typical phase drift measured in the second ν-to-2ν device

with both feedbacks active. The device exhibits a rms jitter of ~75 mrad. This figure, however, should not be confused with the actual precision with which the carrier-envelope phase can be maintained behind the amplifier. Since the phase characterization in the nonlinear interferometer is influenced by the device noise (cf. discussion in Section 3), the feedback loop would not be able to discriminate this measurement noise from the real phase jitter in the amplifier. Therefore, an external (out-of-loop) experiment is required to confirm the carrier-envelope phase stability. It will be presented in Section 7.

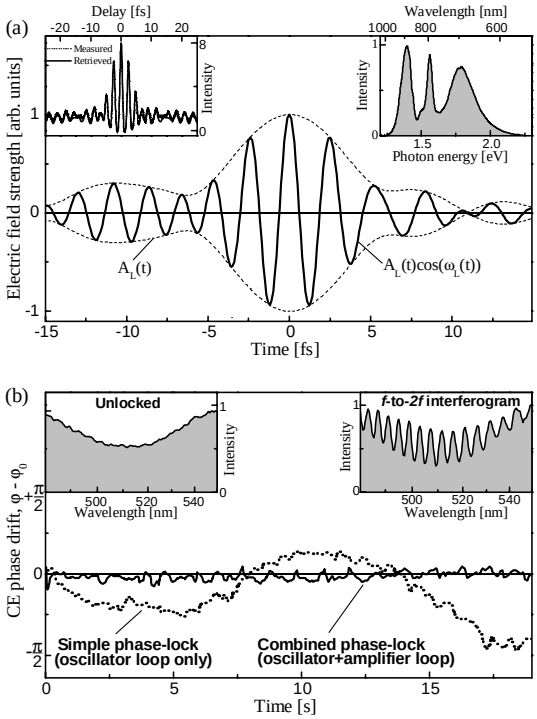

Figure 10-7. Performance overview of the phase-stabilized amplified system. (a) Pulse properties behind the hollow-fiber–chirped-mirror compressor: retrieved pulse envelope (dashed curves) and a possible electric field (solid curve) of the compressed pulse. Insets show measured intensity spectrum (right) and measured and retrieved second-order interferometric autocorrelation (left). (b) Carrier-envelope phase dynamics with oscillator-only phase stabilization (dotted curve) and combined oscillator-amplifier phase stabilization (solid curve). Insets show ν-to-2ν interference spectrograms recorded with the nonlinear interferometer at the amplifier output [Figure 10-6(e)].

We turn now to the carrier-envelope-phase stability of pulses passing through a hollow waveguide used to obtain the spectral broadening, as shown in the right inset of Figure 10-7(a). We placed the second ν-to-2ν interferometer behind the amplifier rather than at the output of the hollow-fiber-chirped-mirror compressor to obtain better intensity stability of the 20 fs pulses (around 1% rms). The intensity noise of the white light emerging from the fiber is higher and varies from 1.6% rms in the spectral region of the input laser pulse to 4% at 650 nm. At the same time, the spectral breadth of this white-light is insufficient to support ν-to-2ν detection under optimal conditions for generating 5 fs pulses. To assess the detrimental effect of hollow-fiber white-light generation on carrier-envelope-phase stability, we repeated the experiments described in Section 4 (Figure 10-4). The resultant pulse-to-pulse rms phase noise was found to range from 80 mrad to 140 mrad depending on the pressure of neon in the capillary. We also conducted intensity-dependence measurements of the phase offset within a ±15% energy range around the mean-energy value (700 μJ) injected into the fiber. This study revealed a 3.4 mrad/μJ slope of the phase within the region of spectral overlap between the laser pulse and the white light. Unfortunately, with spectral-interferometry, it was impossible to assess the phase jitter across the whole spectrum. Nevertheless, one cannot expect dramatic phase excursions in the spectral wings since they would have an immediate impact on the pulse profile. Such envelope fluctuations of the compressed pulse have not been observed in our system. The spectral-interferometry measurements justify the use of ν-to-2ν detection in front of the hollow fiber.

7. CONTROL OF LIGHT FIELD OSCILLATIONS

The reference phase in the combined feedback loop of our high-power phase-controlled laser system can be adjusted within a range of 2π, providing a convenient means of setting ϕ to an arbitrary value. Nevertheless, the techniques we have implemented so far merely enable us to keep ϕ constant and vary it by a known amount, whereas the actual value of ϕ remains unknown. As opposed to the ν-to-2ν technique, strong-field phenomena driven by few-cycle pulses have been predicted to be sensitive to ϕ and potentially could serve for its determination. The processes predicted to be suitable for this purpose include high-order harmonic emission [30, 31, 67] and above-threshold ionization [20, 34, 38, 39, 68]. We chose high-order harmonic generation for our investigations because it has a relatively simple experimental implementation and relies on linearly polarized light, which is readily available in our setup. In addition, a clear intuitive insight into this

process had been developed in several excellent models [23, 24, 69] that have been tested and confirmed by a large number of numerical studies and experiments [29-31, 70].

The relevant aspects of the process can be summarized as follows. The highest-energy XUV or soft x-ray photons are emitted around the zero transition(s) of the laser electric field near the peak of the envelope. This is implicit in semiclassical models [6, 23, 24, 69] and was recently verified in an attosecond experiment [27]. The energy of the emitted photon is essentially determined by the intensity of the laser half-cycle preceding the emission. For a few-cycle pulse with $\phi \approx 0$ or π [the "cosine" wave, shown in Figure 10-1(b)], there is only one most intense half cycle that implies the emission of an isolated x-ray burst at the highest photon energies [Figure 1(h)]. The presence of such an isolated feature in the time domain corresponds to a smooth spectrum. In stark contrast, an identical pulse with a "sine" carrier [$\phi \approx \pm \pi/2$, Figure 10-1(c)] exhibits two most intense half cycles, giving rise to a pair of soft x-ray bursts separated by $T_0/2$ in time [Figure 10-1(i)]. In the frequency domain, this temporal structure implies a modulated (quasi-harmonic) spectrum up to the highest photon energies.

To check the validity of this simple intuitive picture, we developed a computer code simulating propagation of an intense few-cycle laser pulse through an ionizing medium. The program solves Maxwell's equations in three space dimensions and calculates the emergence of high-order harmonics using a refined version [6] of the quantum theory of Lewenstein et al. [24, 71]. Figure 10-8 summarizes the results of the simulations relevant to the experiments described below. In the simulation, the laser pulse duration is τ_L = 5 fs, the pulse energy is 0.2 mJ, the beam diameter is $2w_L$ = 122 μm, the medium is neon, the pressure is 100 mbar, and the length is 2 mm. Figure 10-8(a)–(d) displays the computed spectral distribution of few-cycle-driven coherent soft x-ray emission from neon in the cutoff range for four different values of the carrier-envelope phase of the driving laser pulse. Figure 10-8(e) and (f) shows the temporal intensity profile of cutoff x-rays transmitted through a Gaussian filter [solid contour in Figure 10-8(a)] for ϕ = 0 and $\phi = \pi/2$ (solid curves) along with the instantaneous intensity of the driving laser [i.e., $E_L(t)^2$], depicted by dashed curves. Detailed numerical simulations show that the smoothest and most-modulated spectral-cutoff features actually correspond to the values of ~20° and ~110°, respectively, rather than to the intuitive values of 0° and 90°. However, this discrepancy is insignificant in our experiments, because it lies within the uncertainty with which we can identify different carrier-envelope phase values.

The results of our simulations, together with previous numerical studies [6, 30, 31, 72], support our intuitive analysis and show a strong spectral

dependence between the temporal structure of the x-ray bursts and the spectral shape of the cutoff region. The width of the smooth spectral continuum, $\Delta(\hbar\omega)_{\text{cont}}$, that corresponds to an isolated x-ray burst depends on the ratio of instantaneous intensity $E_L(t)^2$ of the strongest half cycle and its neighboring peak. The corresponding difference of instantaneous intensity is marked by Δ in Figure 10-8(e). Because of the linear dependence between the highest-emitted x-ray photon energy and the peak laser intensity, the continuum bandwidth can be expressed as:

$$\Delta(\hbar\omega)_{cont} = \frac{\hbar\omega_{cutoff} - I_p}{\left(E_L(t)^2\right)_{\max}}\Delta, \tag{11}$$

where I_p is the ionization potential. Table 10-1 lists the instantaneous intensity ratio and the width of the continuum (calculated at 125 eV) for several values of τ_L/T_0, which is the number of oscillation cycles within the laser pulse duration.

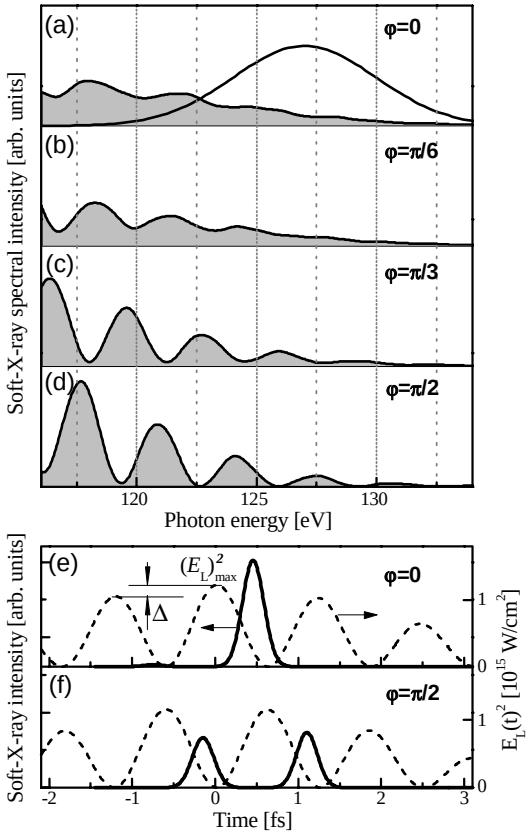

Figure 10-8. Numerical simulations of few-cycle-driven coherent soft x-ray emission from ionizing atoms. (a)–(d) Cutoff-range spectra are shown for different carrier-envelope-phase settings of the driving laser pulse. (e)–(f) The solid curves depict the temporal intensity profile of the cutoff harmonic radiation filtered through a Gaussian bandpass filter with a full width at half maximum of 7 eV [solid contour in (a), whereas the dashed curves plot $E_L(t)^2$]. These results support the intuitive analysis that the field carrying $\phi = 0$ is predicted to produce a single soft x-ray burst [filtered in the cutoff (e)]. Deviation of ϕ from zero gradually suppresses the magnitude of the main burst and gives rise to a satellite spike. The latter becomes most prominent for $|\phi| \rightarrow \pi/2$ (f). In the frequency domain, the isolated pulse emerging for $\phi = 0$ implies a continuous spectrum shown in (a) that becomes increasingly modulated with the appearance of the second burst for $|\phi| \rightarrow \pi/2$ (b)–(d).

Table 10-1. Expected spectral width of the cutoff continuum for a $\phi = 0$ wave as a function of pulse duration.

τ_L/T_0 †	$\Delta/(E_L(t)^2)_{max}$ ‡	$\Delta(\hbar\omega)_{cont}$@125eV *
2	0.16	20 eV
3	0.07	8.8 eV
4	0.04	5.0 eV
5	0.03	3.8 eV

† Number of oscillation cycles within the laser pulse duration

‡ Instantaneous intensity ratio

* width of continuum.

According to Table 10-1, $\tau_L/T_0 \leq 2.5$ is required to produce a continuum with a sizeable (>10 eV) bandwidth in the 100 eV range. For few-cycle pulses that meet with this criterion, the appearance of the predicted continuum [Figure 10-8(a)] is robust over a broad range of parameters as long as the propagation length does not exceed half the coherence length [6]. Experimentally, this condition is readily fulfilled by operating at a gas density equal to or below that resulting in the maximum cutoff yield. We generated high-order harmonics by gently focusing 5 fs, 0.2 mJ laser pulses into a 2 mm neon gas medium. The cycle-averaged peak intensity was estimated to be 7×10^{14} W/cm^2. The neon gas was supplied in a thin-walled metal tube [32] with a backing pressure of 160 mbar. However, the pressure in the interaction region was somewhat lower because of the gas expansion into the surrounding vacuum chamber. Thin zirconium foils were installed in the pathway of the emitted soft x-ray radiation to block the laser light and low-order harmonics. The high-energy part of the spectrum (above 80 eV) was spectrally analyzed with a simple spectrometer consisting of a 10,000-line/mm transmission grating and a backside-illuminated soft x-ray CCD camera (Roper Scientific).

Figure 10-9 shows a series of soft x-ray spectra generated for different values of the carrier-envelope phase of the 5 fs pump pulses. For settings of $\phi = \phi_0$, the harmonics near the cutoff ($\hbar\omega > 120$ eV) completely merge into a continuum. With a gradual change of the phase, the continuous spectral distribution of the cutoff radiation begins to break up into discrete harmonic peaks, with the maximum modulation depth appearing for settings of $\phi = \phi_0 \pm \pi/2$. This behavior is in agreement with the intuitive picture and the computer simulations under the assumption of $\phi_0 = 0 + n\pi$, where n=0.1. The residual ambiguity in the determination of ϕ relates to the inversion symmetry of the interaction with the atomic gas medium. A π-shift in ϕ results in no change of the light wave other than reversing the direction of

the electromagnetic field vectors. In an isotropic medium, such a phase flip cannot lead to any measurable physical consequences.

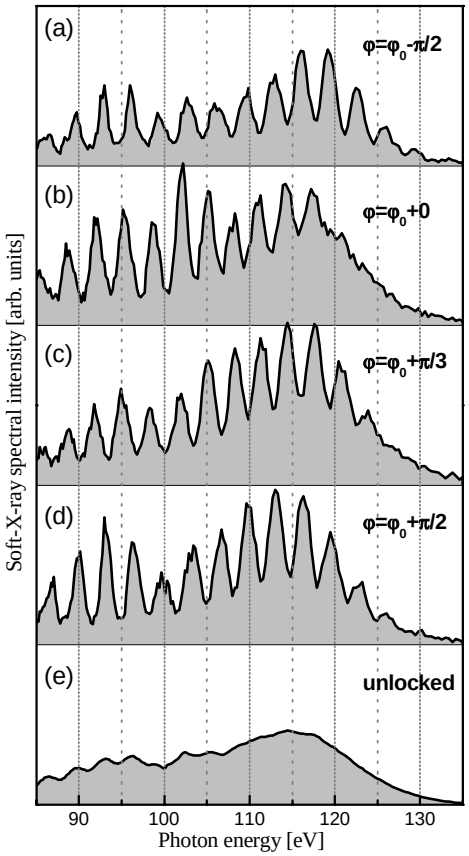

Figure10- 9. Measured spectral intensity of soft x-ray emission from ionizing atoms driven by 5 fs pulses. (a)–(d) Data obtained with phase-stabilized pulses for different carrier-envelope-phase settings are shown. (e) Spectrum measured without carrier-envelope-phase stabilization. X-ray CCD exposure was 0.5 s in all cases.

The presence of distinct spectral behavior in the cutoff region allows us to calibrate the actual value of the carrier-envelope phase. A continuum with a bandwidth of ≈16 eV is clearly visible in Figure 10-9(b) and is in fair agreement with the value of $\Delta(\hbar\omega)_{cont}$ = 20 eV predicted by our simple considerations for 5 fs, 750 nm (τ_L/T_0 = 2) light pulses (Table 10-1). On the contrary, the x-ray spectra corresponding to the phase settings shifted by

$\pm\pi/2$ [Figure 10-9(a) and (d)] display a pronounced modulation surviving into the cutoff. Therefore, the carrier-envelope phase can be evaluated with the highest possible accuracy by recording pairs of soft x-ray harmonic spectra at $\phi_1 = \phi$ and $\phi_2 = \phi + \pi/2$, where ϕ is varied in small steps. In this method, $\phi = 0$ (or, equivalently, π) can be identified from a pair of spectra that exhibit the smallest and the largest modulation depth in the cutoff range, respectively. Applying this procedure to the data in Figure 10-9, we conclude that the phase setting $\phi_0 \approx 0$. The current amplitude and phase stability of our source permits identification of the carrier-envelope-phase value with an accuracy better than $\pi/5$. The obtained value of ϕ is subsequently used to calibrate the interference pattern recorded in the second ν-to-2ν interferometer. After performing this calibration, we can subsequently change ϕ (with accuracy better than $\pi/10$) using the interferometer.

The soft x-ray experiments with phase-stabilized pulses also show that the harmonic peaks shift with ϕ. This effect was predicted by previous [31, 73] and current simulations. It clearly manifests itself in the spectra shown in Figure 10-9. This shift indicates that the peaks visible in the few-cycle-driven harmonic spectra do not, strictly speaking, represent genuine harmonics, because the laser frequency is kept unchanged. Thus its harmonics are expected to remain invariant as well. The shift of these "quasi-harmonics" is a direct consequence of the variation of the field amplitude within T_0 and the confinement of emission within a couple of oscillation cycles. This carrier-envelope-phase-induced shift completely smears the harmonic structure of the near-cutoff soft x-rays generated by our 5 fs pulses in the absence of phase stabilization [Figure 10-9(e)].

To gain further insight into the effect of spectral shift and smearing, we recorded x-ray spectra obtained with longer laser pulses of about 10 fs. The energy of the pulses sent to the target was increased to reach the same cutoff frequency as in the data in Figure 10-9. The spectra we obtained are displayed in Figure 10-10 and exhibit several differences with respect to the 5 fs case. First, there is no pronounced continuum in the cutoff region that would permit identification of the ϕ_0 phase offset, as is expected for this pulse width in accordance with Table 10-1. Second, there are clear spectral peaks at photon energies up to 110 eV that survive into the phase-unlocked regime (Figure 10-10, bottom panel). The blowup in Figure 10-10(b) shows that the frequencies of these peaks do not vary with phase and, consequently, represent true odd-number harmonic orders of the laser field. However, the situation is dramatically changed toward the cutoff, because the spectral peaks seen there [Figure 10-10(c)] shift their frequency by the full laser photon energy. Similar behavior was observed by another group of researchers who detected single-shot x-ray spectra with a carrier-envelope-

phase-unlocked laser [74]. Apparently, a quasi-periodic spectral pattern is the result of complicated interference among x-rays bursts generated by a laser field, the amplitude of which changes significantly within an optical cycle [72]. The "genuine" harmonics at low frequencies are produced by many participating peaks of the laser field, whereas the "spurious" harmonics near the cutoff are formed by very few field peaks. In this regard, the anomaly in the energy interval of 95–105 eV in Figure 10-10 is noteworthy. This "intermediate" region features quasi-harmonic peaks with a period equal to the energy of one laser photon. This is remarkable, since such periodicity corresponds to laser field peaks separated by T_0 rather than by the usual $T_0/2$ (i.e., by the time spacing between the nearest half cycles). We believe the reason for this transient behavior is the involvement of three neighboring half cycles capable of generating x-rays at that frequency, a condition that cannot be fulfilled at both lower- and higher-photon energies.

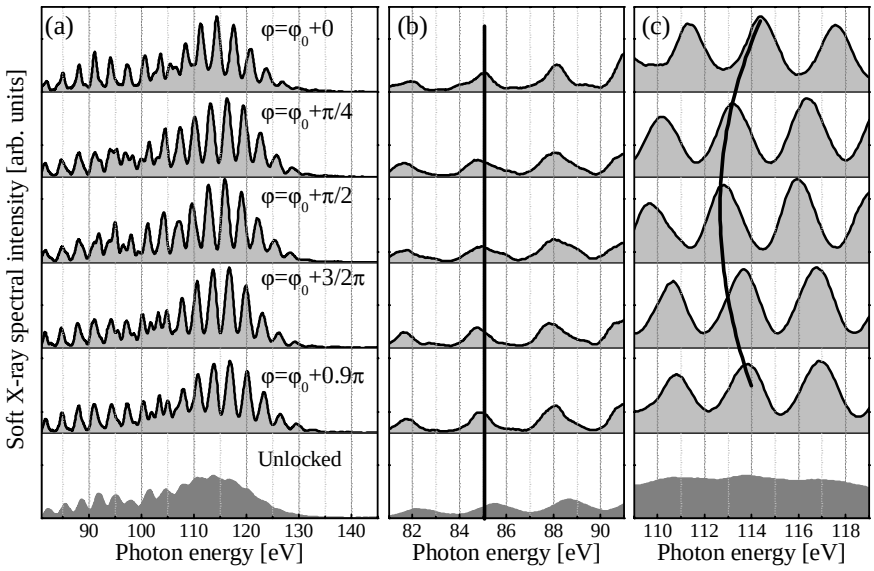

Figure 10-10. Measured spectral intensity of soft x-ray emission from ionizing atoms driven by 10 fs pulses. (a) Full-range spectra. (b) and (c) Close-ups on spectral regions with distinctly different spectral dependencies on the carrier-envelope phase.

Both the experiments with 5 and 10 fs pulses underscore the benefits that carrier-envelope-phase stabilization brings to the study of coherent laser-driven x-ray sources.

8. CARRIER-ENVELOPE-PHASE MEASUREMENT WITHOUT AMBIGUITY

Carrier-envelope-phase effects (discussed above in the context of soft x-ray emission) are also expected to be observed in other strong-field experiments. The ability to measure and precisely stabilize the carrier-envelope phase is crucial for many applications. Clear evidence of phase effects has been seen in photoionization without phase control for few-cycle pulses [34, 75]; in soft x-ray generation with phase-stabilized pulses [40] and in the single-shot regime [74, 76]; and in photoemission from surfaces with nonamplified few-cycle pulses [77]. Phase-dependent effects in semiconductors have been predicted [78]. In fact, carrier-envelope-phase effects due to the field asymmetry of few-cycle pulses can be easily understood when compared with coherent control by an asymmetric two-color light field [79]. Nonlinear photoionization provides a straightforward approach to looking for signatures of the carrier-envelope phase. Particular emphasis is given to noninversion symmetric emission of photoelectrons, i.e., a different count rate for electrons emitted to the right and to the left. A number of theoretical investigations have been devoted to the problem in the past years [38, 68, 80-82]. Most of them concentrate on total yields of photoelectrons. Here we present experimental results of nonlinear photoionization from a gas target [75, 83] with the intense phase-stabilized, few-cycle light source described in Section 6. The spatially asymmetric field of few-cycle laser pulses leads to different photoionization rates for opposite directions. By detecting this difference, it is possible to measure the carrier-envelope phase of intense few-cycle laser pulses without the field-inversion ambiguity present in the x-ray emission experiment on the centro-symmetric system (described in Section 7).

As in the case of x-ray emission where the interaction with most prominent half cycles of a 5 fs laser pulse causes the generation of the most energetic x-ray photons, the highest-peak-strength half cycles are responsible for the release of photoelectrons with the largest drift momenta during nonlinear photoionization. The results of a classical calculation illustrating the difference for cosinelike and sinelike light waves are depicted in Figure 10-11 and give a qualitative explanation of how this effect can be utilized for carrier-envelope-phase calibration.

In our experiments, xenon atoms were ionized with 5 fs laser pulses with peak intensities of nearly 10^{14} W/cm^2. Absorption of eight photons is necessary to overcome the ionization threshold. Higher-order ionization processes, known as above-threshold ionization [84], are also observed at correspondingly high photoelectron energies.

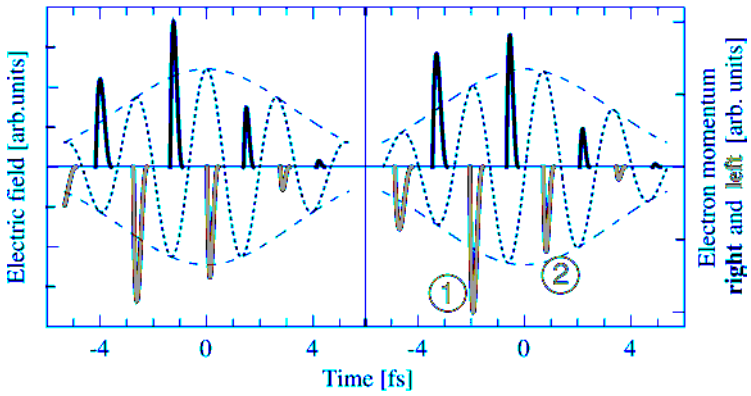

Figure 10-11. Electric field (short-dashed curve) and envelope (long-dashed curve) of a 5 fs laser pulse for CE phase 0 (left panel) and $-\pi/2$ (right panel). The drift momentum of high-energy photoelectrons as a function of the ionization time t_0 is shown in black (emission to the right) and gray (emission to the left). It was calculated with a classical model. Note that highest momentum does not necessarily coincide with highest electron yield: In the right panel the ionization probability at times labeled with 1 is considerably lower than those labeled with 2 because of lower field strength at t_0.

To study the above-threshold-ionization phenomena, we employed the time-of-flight (TOF) spectrometer schematically depicted in Figure 10-12. In this apparatus, two opposing electrically and magnetically shielded TOF detectors are mounted in an ultrahigh vacuum apparatus. Xenon atoms are fed in through a nozzle from the top and are ionized in the focus of a few-cycle laser beam. The lens shown in the sketch is a concave mirror with a focal length of 250 mm. The pulse energy was attenuated to 20 µJ. The laser polarization is linear and parallel to the flight tubes. The laser field changes sign while propagating through the focus. Slits with a width of 250 µm are used to block the electrons emitted outside the focal region. The position of the slits can be adjusted. A photodiode and microchannel plates detect the laser pulses and photoelectrons, respectively. The laser repetition rate is 1 kHz and 50 electrons are typically recorded per pulse at each microchannel plate. A pair of glass wedges (apex angle 2.8°) is used to optimize dispersion and adjust the carrier-envelope phase. Therefore, a Δs translation of one wedge introduces a $\Delta x = \Delta s \cdot \tan(2.8°)$ change in the total glass thickness seen by the laser beam. For our laser pulses centered at the wavelength of 760 nm, an addition of 52 µm of fused silica changed the carrier-envelope-phase value by 2π without affecting the pulse duration.

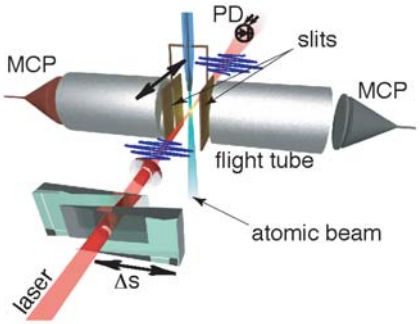

Figure 10-12. The "stereo above-threshold-ionization'' spectrometer. MCP: microchannel plates and PD: photodiode.

Figure 10-13(a) shows a series of above-threshold-ionization spectra corresponding to different carrier-envelope phases. Simply by inspecting the high-energy part (>20 eV) of the spectra, one can verify that a carrier-envelope phase shift by $\Delta\phi = \pi$ corresponds to a change from the electron spectrum emitted into the left detection channel to the spectrum emitted to the right one. Furthermore the above-threshold-ionization spectrum is invariant under a 2π phase shift. For high electron energies, the difference between the left and right electron yield reaches up to an order of magnitude and can be controlled by adjusting the carrier-envelope phase. This phase-determined yield discrimination constitutes a new kind of *coherent control* and exhibits, to our knowledge, the highest contrast observed so far.

Figure 10-13(b) displays the ratio of photoemission to the left and to the right for different spectral regions. The ratio of high- and low-energy electrons oscillates with a periodicity of $\Delta\phi$ in excellent agreement with the periodicity expected from glass dispersion. Besides the much higher contrast for high-energy electrons, a phase shift of both sets of data is also apparent. To determine the carrier-envelope phase, we have to establish the connection between the phase of the field and the above-threshold-ionization signal. We do this by using high-energy (>20 eV) electrons. One reason for choosing this spectral region is its higher sensitivity to the carrier-envelope phase. The sensitivity is similar to that in the spectral cutoff of x-ray radiation discussed in Section 7. More importantly, the dominant overall features in this spectral region of above-threshold ionization are known to be rather independent of specific properties of the atomic species and of laser intensity.

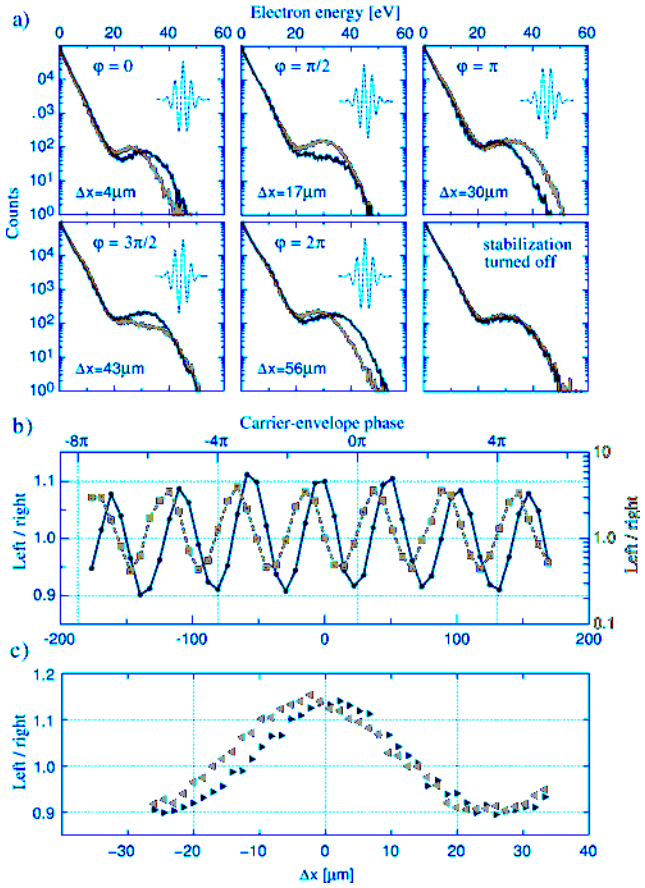

Figure 10-13. (a) Photoelectron spectra for different CE phases controlled by fine movement of one of the wedges. Δx indicates the glass added hereby. The black curves correspond to emission to the right (positive direction), the gray ones to the opposite direction. The insets show the corresponding real time variation of the electric field, as deduced from the phase assignment shown in Figure 10-14. Only without phase stabilization were identical spectra measured to both left and right as expected. (b) Left-right ratio of the total electron yield (solid black curve) and high-energy electrons (dashed gray curve) as a function of glass thickness Δx added or subtracted by moving one of the wedges. $\Delta x = 0$ corresponds to optimal dispersion compensation, i.e., the shortest pulses. Maximal left/right ratio for the total yield does not coincide with that for high-energy electrons. Note the different scales for low- and high-energy electrons. The upper horizontal scale indicates the CE envelope phase of the pulse, as deduced from the comparison with theory shown in Figure 10-14. (c) Fine-increment phase scan indicating long-term CE phase stabilization drift of the laser setup. The measurement was performed over ≥10 min by slowly scanning the wedges forth (triangles pointing to the right) and back (triangles pointing to the left) using a fine increment of the glass thickness. The mismatch at the start and the end indicates a phase drift of ~50 mrad/min.

Figure 10-14 shows a comparison between measurements and classical calculations. The latter take into account only the high-energy electrons. In the experimental and theoretical data, the ratio of emission to the left and right depends in a characteristic way on electron energy and the carrier-envelope phase. These dependences lead to the inclined stripes in the false-color representations. Another common feature is that the asymmetry of left-right emission increases with the strengthening of the electron energy. Unlike the asymmetry contrast, these characteristic features do *not* depend on the pulse shape or duration. The sharp edges in the calculation originate from classical energy conservation. This artifact is removed by energy-time uncertainty in quantum mechanics. Matching the characteristic features of the theoretical and experimental data leads to an unambiguous determination of the carrier-envelope phase with an estimated error of $\pi/10$.

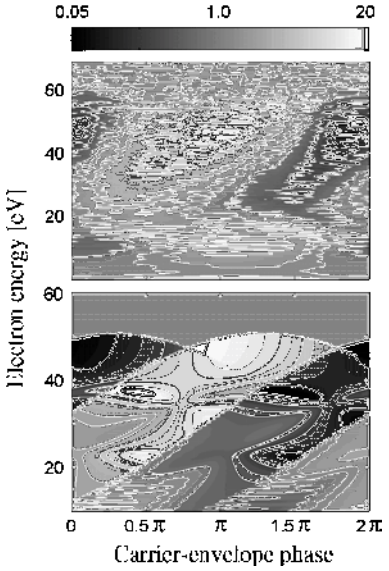

Figure 10-14. Determination of the CE phase. Grayscale representation (logarithmic scale) of the left-right ratio of photoelectrons as a function of the electron energy and the CE phase. Higher values (white) indicate dominant left emission, lower values (black) dominant right emission. For the theoretical part (bottom panel), only rescattered electrons were taken into account. The parameters used are the same as in the experiment. This comparison allows precise carrier-envelope phase determination. Within the convention of Equation (1), the electric field is now uniquely characterized.

The calculation used to determine the carrier-envelope phase is based on the insight that at high intensities above-threshold ionization can be understood in terms of quasi-static field ionization at some time t_0 and subsequent classical evolution of the electron in the laser field [23, 85]. For a

review, see [86]. A considerable fraction of the photoelectrons generated when atoms or molecules are exposed to intense laser pulses do not escape directly. Rather, they return to the ion core within times of typically less than an optical cycle and in precise synchronization with the electric field of the laser pulse. The characteristics of returning electrons can be observed in the kinetic energy spectra of photoelectrons. The underlying mechanism is elastic scattering of the electrons when they return to the ion core at $t = t_1$ and are subsequently accelerated by the laser field. Consequently, photoelectrons with high kinetic energy are observed. In the photoelectron spectra, they manifest themselves in the high-energy plateau on the exponentially decreasing count rate at low electron energies [87].

The kinetic energy spectrum of the plateau electrons is sensitive to the carrier-envelope phase for several reasons. First, high-energy electrons returning to the ion core can be created only in subfemtosecond time intervals close to peaks of the electric field of the laser pulse (see Figure 10-11). However, the probability that they will tunnel through the atomic potential at t_0 depends exponentially on the field strength $E_L(t_0)$ [cf. Equation (1)]. As few-cycle pulses are involved, tunneling is likely only for those very few optical half-cycles close to the pulse maximum. Generally, the highest kinetic energies are reached for electrons returning to the core when the electric field becomes nearly zero, i.e., $E_L(t_1)=0$. For few-cycle pulses, the field amplitude E_L also needs to be as high as possible for $t > t_1$ to allow efficient acceleration after rescattering. Since the start time t_0 and return time t_1 differ by almost one optical cycle, both the highest possible field strength at t_0 and the highest possible amplitude after t_1, are difficult to meet and result in a strong dependence of photoionization on the carrier-envelope phase. Number, strength, and timing of the wave packets lead to distinctive structures in the above-threshold-ionization spectra. Their analysis therefore provides detailed information about the key processes of attosecond science. Quantum mechanical calculations are in very good qualitative agreement with this classical treatment [82].

Having established that above-threshold ionization can be used for precise determination of the carrier-envelope phase, we provide an example of the sensitivity of the instrument. Figure 10-13(c) shows a measurement performed with fine $\Delta\phi$ increments. These results reveal small phase drifts that we attribute to the laser system and its stabilization scheme. The phase drifts are of the order of 50 mrad/min, measured for more than 10 minutes. Since the stereo above-threshold-ionization phase meter is not only able to measure the carrier-envelope phase, but also to detect small phase drifts, it clearly has the potential to be used in a feedback loop. In addition, the target gas pressure is so low ($< 10^{-4}$ mbar) that the above-threshold-ionization

experiment does not affect the laser beam. Thus a stereo above-threshold-ionization phase meter can be placed anywhere along a laser beam line.

9. GOUY PHASE SHIFT FOR FEW-CYCLE LASER PULSES

So far we have considered carrier-envelope stabilization of amplified few-cycle pulses and their applications. We have also addressed the question of determining the carrier-envelope phase value. An important issue for nonlinear processes driven with phase-stabilized few-cycle pulses is that they usually take place in the focus of the laser beam. However, an electromagnetic beam propagating through a focus experiences an additional π phase shift with respect to a plane wave. This can be explained by introducing the phenomenon predicted by Kirchhoff and experimentally observed by Gouy [88], any spherical wave radiating from a source that is small compared with the wavelength advances in phase by $\pi/2$ within a short distance of the source. This phase, also referred to as Gouy phase, is a general property of a focused wave, including sound waves [89]. Intuitive explanations of this phase anomaly have been proposed [90]. Recently, direct observations of the polarity change of focused single-cycle terahertz pulses have been reported [91]. For applications of carrier-envelope-stable few-cycle light fields, phase matching of higher-order harmonic generation (see Section 7) is governed by the atomic response and the Gouy phase shift of the focused fundamental laser beam [92]. Moreover, the Gouy phase strongly affects the spatial variation of the carrier-envelope phase of ultrashort pulses around the beam focus.

In principle, the Gouy phase shift of a TEM_{00} wave can be described by a simple formula depending on the focusing geometry and the wavelength,

$$\phi = -\arctan\left(\frac{z}{z_R(\lambda)}\right), \tag{12}$$

where the beam is traveling in the $+z$ direction and z_R is the Rayleigh distance (dependent on the wavelength λ). Because of the large bandwidth of few-cycle pulses, their different spectral components experience the Gouy phase shift on different spatial scales. In particular, the *blue* colors undergo a steeper phase change than the *red* colors. It has been shown theoretically [38, 93] that this leads to a difference of phase and group velocities in the vicinity of the focus and, therefore, to carrier-envelope-phase slippage. For this reason, the CE phase variation cannot be generally described by

Equation (12). Indeed, the details of the phase change in the focus depend on the spatial profile of the laser beam and on the focusing geometry. In all cases, an overall π phase shift is expected between two symmetric positions far away from a spherical focus. Because of the continuous phase change of the pulse propagating through the focal region, the corresponding electric field of light takes on all possible phase variations. For example, a focused "+cos" *E*-field will be a sinelike wave in the focal region and will reemerge as a "-cos" field beyond the focus. This variation, of course, can affect the outcome of a phase-sensitive light–matter interaction that is not confined to a length much shorter than the Rayleigh range. Thus, precise control of the spatial variation of the carrier-envelope phase within the whole focal region is crucial to any phase-dependent experiment.

We present the experimental determination of the evolution of the carrier-envelope phase in the focus of few-cycle laser pulses. Together with the determination of the carrier-envelope phase presented in Section 8, this result constitutes a full and unambiguous characterization of the electric field of laser pulses in space and time within the paraxial approximation (i.e., neglecting the small longitudinal component of the electric field). We studied the spatial variation of the carrier-envelope phase using the same technique that was presented in Section 8, i.e., by simultaneously detecting above-threshold-ionization photoelectron spectra in opposite directions (Figure 10-12). The pulse energy of carrier-envelope-controlled 5 fs pulses was attenuated to 20 μJ, and the beam focused with a *f*/30 geometry into a low-density xenon gas jet. Under these focusing conditions, the electric field is expected to undergo a π phase shift over a few millimeters. To reveal the the Gouy phase, one has to selectively detect the electrons generated at a well-defined position of the focus. A pair of moveable slits perpendicular to the beam (*z* direction) and to the polarization axes allows the entire focal region to be scanned. The slit width is 250 μm, well below the Rayleigh range (≈1 mm). To achieve optimum spatial resolution in the *z* direction, the slits are placed at a distance of only 1 mm from the beam (Figure 10-12). With this setup, the angular distribution of the emitted photoelectrons does not affect the phase resolution, which is estimated to be ≈0.1 rad.

Figure 10-15 shows the asymmetry of the electron count rate (left/right ratio) as a function of the glass thickness introduced by moving the fused-silica wedges in front of the above-threshold-ionization spectrometer. We made the measurement by moving the pair of slits to a distance of ≈2 mm before (dashed line) and after (solid line) the focus. The phase shift of π between the two curves is a direct measurement of the Gouy phase shift in the focus.

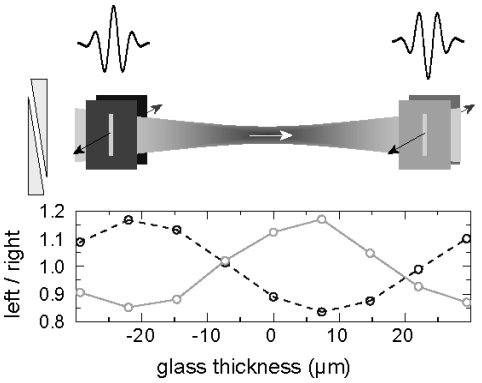

Figure 10-15. Variation of glass thickness in the beam path to change the carrier-envelope phase of the pulses. The left/right ratio of the electron yield exhibits clear oscillations with a periodicity consistent with glass dispersion at the wavelength of the laser. The measurement was performed before (dashed line) and after (solid line) the focus. The π phase shift is due to the Gouy carrier-envelope phase shift resulting from the passage through the focus.

The electric-field polarity reversal observed by measuring the phase value in front of and behind the focus does not describe the details of the phase slippage in the focal region itself. Since many experiments take place over an extended area of the focus (e.g., higher-order harmonic generation in the XUV), it is essential to characterize the phase variation precisely and, in particular, to recognize possible anomalies in the behavior of the carrier-envelope phase evolution. Indeed, the possible presence of an anomalous phase change in the focus has been suggested as an explanation of the observed enhancement of the harmonic-generation efficiency by using truncated Bessel beams [94].

To analyze the phase variation within the focal range, we acquired electron spectra at several positions by moving the pair of slits. Figure 10-16 shows the detected left/right asymmetry as a function of the electron energy and of the carrier-envelope phase for a few *z* positions. Different approaches are possible to retrieve the phase variation. The integrated electron yield provides a clear phase indication and can be used to show the overall phase shift in the focus (Figure 10-15). However, scanning the focal range implies measuring at constantly changing intensities. Since it is predicted that the maximum of the integrated left/right asymmetry should occur at a phase that depends on the intensity [81], it is not easy to decouple the Gouy phase shift from the possible intensity-dependent phase shift. A better approach relies on the spectral information in Figure 10-16. Light and dark shades correspond to spectral regions of strong asymmetry. Since these colors are easily distinguishable, they can be used to follow the phase evolution. The

measurements were made by approaching the focus from the outer part and by moving the slits alternatively before and after the focus. With this procedure, measurements of symmetric positions around the focus are consecutive, thus reducing detrimental effects from possible long-term phase drifts.

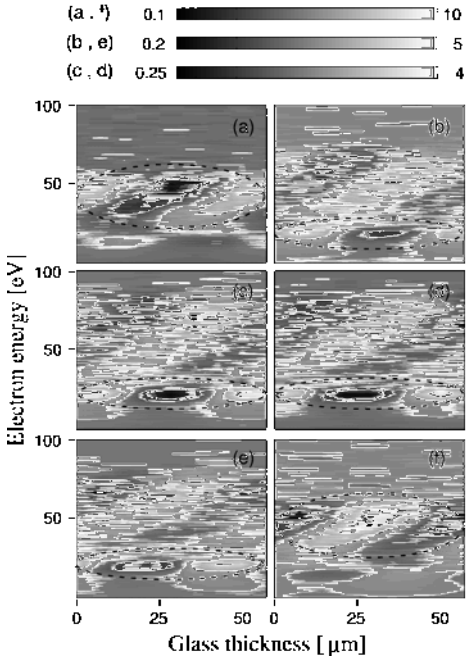

Figure 10-16. Left/right asymmetry maps (logarithmic scale) for different longitudinal positions as a function of the electron energy and glass thickness introduced. Lighter shades indicate dominant left emission; darker shades— dominant right emission. The maps (a) –(f) correspond, respectively, to the positions: z=-1.75 mm, z=-1.0 mm, z=-0.25 mm, z=+0.25 mm, z=+1.0 mm, z=+1.75 mm (positive values represent positions *after* the focus). The phase difference is determined by evaluating the shift of the characteristic structures (indicated by the dashed lines) of the asymmetry pattern. The extension of the electron yield to higher energies in the central part of the focus is due to the higher intensity.

Figure 10-16(a) and (f) corresponds to the outer part of the focal range. The strong asymmetry in the high-energy part of the spectra [*above-threshold-ionization plateau* (dashed area)] changes sign while passing through the focus, confirming the π phase shift already discussed (see Figure 10-15). More interestingly, Figure 10-16(b)–(e) corresponds to positions in the central part of the focus. The asymmetry in the plateau is partly smeared out, but another clear asymmetric area appears in the low-energy part of the

spectra [20–25 eV (dashed area)], just before the above-threshold-ionization plateau. Its nature is not entirely understood, but, because of being definitely a carrier-envelope phase effect, it can be exploited to retrieve the phase variation in the focus. By moving in the direction of beam propagation, i.e., from before to after the focus [Figures 10-16(a)–(f)], the characteristic pattern moves toward the left side of the graphs, i.e., toward decreasing glass thickness. This pattern is in full agreement with the intuitive physical origin of the Gouy carrier-envelope-phase shift. Indeed, in a dispersive medium like glass, the phase velocity exceeds the group velocity. The same situation occurs in the propagation of the ultrashort pulse in the laser focus [93]. Thus, it is not surprising that to observe similar features, less glass is needed after the focus with respect to a symmetric position before the focus. The Gouy carrier-envelope-phase shift determination can be performed simply by numerically evaluating the shift of the asymmetry pattern; converting the glass-thickness shift obtained (μm) into phase difference (rad) is then straightforward.

Figure 10-17 shows the retrieved carrier-envelope phase shift for the positions of Figure 10-16 and for several others not shown there. For comparison, the Gouy phase of a Gaussian beam [Equation (12)] with an *f*/30 focusing geometry is also shown (solid line). Note that the carrier-envelope-phase shift is *not* expected to follow the Gouy phase, the latter being a property of cw lasers. The beam in our experiments is a few-cycle pulse-truncated Bessel beam. The use of a spherical focusing mirror in our setup inevitably introduces a slight astigmatism.

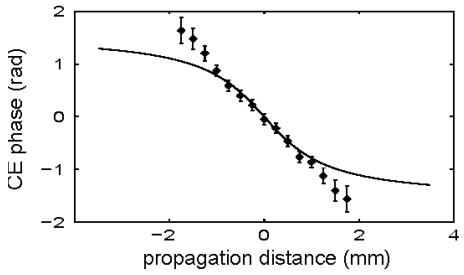

Figure 10-17. Retrieved carrier-envelope Gouy phase shift as a function of the propagation distance in the focus. The solid line is the Gouy phase of a cw Gaussian beam, shown for comparison. In the outer part of the focus, the electron count rate rapidly decreases, making detection of additional experimental points difficult.

The pulses undergo the π phase shift within a few Rayleigh distances. Because of the rapid decrease of electron yield at lower intensities, the measurements were stopped at a distance of ≈2 mm before and after the focus. This prevented observation of the expected area of constant carrier-

envelope phase in the outer part of the focus. However, the region of interest for all experiments is entirely covered, and the estimated error for the experimental data is relatively low (≤0.1 rad). The phase changes smoothly with a constant slope and does not exhibit any wiggles or irregularities, which is particularly important for experiments.

10. CONCLUSIONS AND OUTLOOK

We demonstrated the generation of intense few-cycle light pulses with a reproducible temporal evolution of the electromagnetic field. With these light wave forms, we explored the sensitivity of microscopic atomic currents to the timing of light-field oscillations with respect to the pulse peak. The short-wavelength (XUV, soft x-ray) radiation emitted by the atomic currents allowed determination of this timing with sub-T_0/10, i.e., sub-250 attoseconds, accuracy. The generation of intense few-cycle light with a reproducible and known wave form is expected to benefit the emerging field of attosecond physics in several ways.

The high-frequency atomic currents, employed as a light-waveform detector in the current experiments, are also sources of subfemtosecond XUV/soft x-ray pulses [25, 26]. Therefore, the measurement and stabilization of the carrier-envelope phase presented in this research directly opens the door to generating single, isolated subfemtosecond pulses that are ideally suited for most spectroscopic applications. Ultrashort wave packets with controlled field oscillations will also benefit the techniques that have been introduced for attosecond metrology [26, 27] and spectroscopy [28]. They are indispensable to measuring the shape and chirp of subfemtosecond XUV or x-ray pulses [95] and to observing inner-shell atomic processes on an attosecond timescale [28]. In addition, control over the temporal structure of electron wave packets liberated by optical-field ionization also relies on synthesized light wave forms. Few-cycle light with controlled field oscillations will be able to launch an electron wave packet with well-controlled subfemtosecond temporal structure into the continuum and precisely steer its subsequent motion. One intriguing scenario is to make the electron recollide with its parent ion and use this recollision to excite and/or probe molecular [96], atomic, or possibly even nuclear dynamics. Finally, yet another potential application area of high-intensity wave forms is electron acceleration in the forward direction to ultrarelativistic energies in a highly controlled manner.

ACKNOWLEDGEMENTS

We gratefully acknowledge the contributions of M. Uiberacker, E. Goulielmakis, M. Lezius, Th. Udem, R. Holzwarth, V.S. Yakovlev, and A. Scrinzi to this work. This research has been supported by the Austrian Science Fund (Grants No. F016, No. Z63, and No. P15382), the European ATTO network, and The Welch Foundation (Grant No. A-1562).

REFERENCES

[1] A. M. Weiner, Rev. Sci. Instrum. **71**, 1929-1960 (2000).
[2] R. Trebino, K. W. DeLong, D. N. Fittinghoff, J. N. Sweetser, M. A. Krumbugel, B. A. Richman, and D. J. Kane, Rev. Sci. Instrum. **68**, 3277-3295 (1997).
[3] C. Iaconis and I. A. Walmsley, Opt. Lett. **23**, 792-794 (1998).
[4] E. Constant, Ph.D Thesis, University of Sherbrooke (1997).
[5] G. Steinmeyer, D. H. Sutter, L. Gallmann, N. Matuschek, and U. Keller, Science **286**, 1507-1512 (1999); B. Schenkel, J. Biegert, U. Keller, C. Vozzi, M. Nisoli, G. Sansone, S. Stagira, S. De Silvestri, and O. Svelto, Opt. Lett. **28**, 1987-1989 (2003).
[6] T. Brabec and F. Krausz, Rev. Mod. Phys. **72**, 545-591 (2000).
[7] A. Baltuška, T. Fuji, and T. Kobayashi, Opt. Lett. **27**, 306-308 (2002).
[8] L. Xu, C. Spielmann, A. Poppe, T. Brabec, F. Krausz, and T. W. Hänsch, Opt. Lett. **21**, 2008-2010 (1996).
[9] T. Udem, Ph.D Thesis, Ludwigs-Maximilians Universität (1997).
[10] J. Reichert, R. Holzwarth, T. Udem, and T. W. Hänsch, Opt. Commun. **172**, 59-68 (1999).
[11] H. R. Telle, G. Steinmeyer, A. E. Dunlop, J. Stenger, D. H. Sutter, and U. Keller, Appl. Phys. B **69**, 327 (1999).
[12] D. J. Jones, S. A. Diddams, J. K. Ranka, A. Stentz, R. S. Windeler, J. L. Hall, and S. T. Cundiff, Science **288**, 635-639 (2000).
[13] A. Apolonski, A. Poppe, G. Tempea, C. Spielmann, T. Udem, R. Holzwarth, T. W. Hänsch, and F. Krausz, Phys. Rev. Lett. **85**, 740-743 (2000).
[14] T. Udem, J. Reichert, R. Holzwarth, and T. W. Hänsch, Opt. Lett. **24**, 881-883 (1999); T. Udem, R. Holzwarth, and T. W. Hansch, Nature **416**, 233-237 (2002); M. Zimmermann, C. Gohle, R. Holzwarth, T. Udem, and T. W. Hansch, Opt. Lett. **29**, 310-312 (2004).
[15] R. Holzwarth, T. Udem, T. W. Hänsch, J. C. Knight, W. J. Wadsworth, and P. S. J. Russell, Phys. Rev. Lett. **85**, 2264-2267 (2000).
[16] S. A. Diddams, D. J. Jones, J. Ye, S. T. Cundiff, J. L. Hall, J. K. Ranka, R. S. Windeler, R. Holzwarth, T. Udem, and T. W. Hänsch, Phys. Rev. Lett. **84**, 5102-5105 (2000).

[17] S. T. Cundiff, J. Ye, and J. L. Hall, Rev. Sci. Instrum. **72**, 3746-3771 (2001).
[18] S. T. Cundiff, J. Phys. D. **35**, R43 (2002).
[19] MenloSystem-GmbH (http://www.menlosystem.com)
[20] M. Kakehata, H. Takada, Y. Kobayashi, K. Torizuka, Y. Fujihira, T. Homma, and H. Takahashi, Opt. Lett. **26**, 1436-1438 (2001).
[21] A. Baltuška, T. Fuji, and T. Kobayashi, Phys. Rev. Lett. **88**, art. no.-133901 (2002).
[22] A. Baltuška, T. Fuji, and T. Kobayashi, Opt. Lett. **27**, 1241-1243 (2002).
[23] P. B. Corkum, Phys. Rev. Lett. **71**, 1994-1997 (1993).
[24] M. Lewenstein, P. Balcou, M. Y. Ivanov, A. Lhuillier, and P. B. Corkum, Phys. Rev. A **49**, 2117-2132 (1994).
[25] M. Drescher, M. Hentschel, R. Kienberger, G. Tempea, C. Spielmann, G. A. Reider, P. B. Corkum, and F. Krausz, Science **291**, 1923-1927 (2001); P. M. Paul, E. S. Toma, P. Breger, G. Mullot, F. Auge, P. Balcou, H. G. Muller, and P. Agostini, Science **292**, 1689-1692 (2001).
[26] M. Hentschel, R. Kienberger, C. Spielmann, G. A. Reider, N. Milosevic, T. Brabec, P. Corkum, U. Heinzmann, M. Drescher, and F. Krausz, Nature **414**, 509-513 (2001).
[27] R. Kienberger, M. Hentschel, M. Uiberacker, C. Spielmann, M. Kitzler, A. Scrinzi, M. Wieland, T. Westerwalbesloh, U. Kleineberg, U. Heinzmann, M. Drescher, and F. Krausz, Science **297**, 1144-1148 (2002).
[28] M. Drescher, M. Hentschel, R. Kienberger, M. Uiberacker, V. Yakovlev, A. Scrinizi, T. Westerwalbesloh, U. Kleineberg, U. Heinzmann, and F. Krausz, Nature **419**, 803-807 (2002).
[29] I. P. Christov, M. M. Murnane, and H. C. Kapteyn, Phys. Rev. Lett. **78**, 1251-1254 (1997).
[30] A. de Bohan, P. Antoine, D. B. Milosevic, and B. Piraux, Phys. Rev. Lett. **81**, 1837-1840 (1998).
[31] G. Tempea, M. Geissler, and T. Brabec, J. Opt. Soc. Am. B **16**, 669-673 (1999).
[32] C. Spielmann, N. H. Burnett, S. Sartania, R. Koppitsch, M. Schnurer, C. Kan, M. Lenzner, P. Wobrauschek, and F. Krausz, Science **278**, 661-664 (1997).
[33] C. G. Durfee, A. R. Rundquist, S. Backus, C. Herne, M. M. Murnane, and H. C. Kapteyn, Phys. Rev. Lett. **83**, 2187-2190 (1999).
[34] G. G. Paulus, F. Grasbon, H. Walther, P. Villoresi, M. Nisoli, S. Stagira, E. Priori, and S. De Silvestri, Nature **414**, 182-184 (2001).
[35] C. Lemell, X. M. Tong, F. Krausz, and J. Burgdorfer, Phys. Rev. Lett. **90**, - (2003); V. S. Yakovlev, P. Dombi, G. Tempea, C. Lemell, J. Burgdorfer, T. Udem, and A. Apolonski, Appl. Phys. B **76**, 329-332 (2003).
[36] A. Poppe, R. Holzwarth, A. Apolonski, G. Tempea, C. Spielmann, T. W. Hansch, and F. Krausz, Appl. Phys. B **72**, 977-977 (2001).
[37] Y. Kobayashi and K. Torizuka, Opt. Lett. **25**, 856-858 (2000).

[38] P. Dietrich, F. Krausz, and P. B. Corkum, Opt. Lett. **25**, 16-18 (2000).
[39] I. P. Christov, Opt. Lett. **24**, 1425-1427 (1999).
[40] A. Baltuška, T. Udem, M. Uiberacker, M. Hentschel, E. Goulielmakis, C. Gohle, R. Holzwarth, V. S. Yakoviev, A. Scrinzi, T. W. Hansch, and F. Krausz, Nature **421**, 611-615 (2003).
[41] J. Eckstein, Ph.D Thesis, Stanford University (1978).
[42] S. T. Cundiff and J. Ye, Rev. Mod. Phys. **75**, 325-342 (2003).
[43] U. Morgner, R. Ell, G. Metzler, T. R. Schibli, F. X. Kärtner, J. G. Fujimoto, H. A. Haus, and E. P. Ippen, Phys. Rev. Lett. **86**, 5462-5465 (2001).
[44] J. C. Knight, T. A. Birks, P. S. Russell, and D. M. Atkin, Opt. Lett. **21**, 1547-1549 (1997); J. K. Ranka, R. S. Windeler, and A. J. Stentz, Opt. Lett. **25**, 25-27 (2000); J. K. Ranka, R. S. Windeler, and A. J. Stentz, Opt. Lett. **25**, 796-798 (2000).
[45] R. Ell, U. Morgner, F. X. Kärtner, J. G. Fujimoto, E. P. Ippen, V. Scheuer, G. Angelow, T. Tschudi, M. J. Lederer, A. Boiko, and B. Luther-Davies, Opt. Lett. **26**, 373-375 (2001); A. Bartels and H. Kurz, Opt. Lett. **27**, 1839-1841 (2002); T. M. Fortier, D. J. Jones, and S. T. Cundiff, Opt. Lett. **28**, 2198-2200 (2003).
[46] S. Sartania, Z. Cheng, M. Lenzner, G. Tempea, C. Spielmann, F. Krausz, and K. Ferencz, Opt. Lett. **22**, 1562-1564 (1997).
[47] M. Takeda, H. Ina, and S. Kobayashi, J Opt Soc Am **72**, 156-160 (1982).
[48] C. Dorrer and F. Salin, J. Opt. Soc. Am. B **15**, 2331-2337 (1998).
[49] C. Dorrer, J. Opt. Soc. Am. B **16**, 1160-1168 (1999); C. Dorrer, N. Belabas, J. P. Likforman, and L. Joffre, Appl. Phys. B **70**, S99-S107 (2000).
[50] F. W. Helbing, G. Steinmeyer, U. Keller, R. S. Windeler, J. Stenger, and H. R. Telle, Opt. Lett. **27**, 194-196 (2002).
[51] G. P. Agrawal, *Nonlinear Fiber Optics* (Academic Press, San Diego, 1995); P. V. Mamyshev and S. V. Chernikov, Opt. Lett. **15**, 1076-1078 (1990); J. Botineau and R. H. Stolen, J Opt Soc Am **72**, 1592-1596 (1982).
[52] N. Bloembergen, *Nonlinear Optics* (World Scientific, Singapore, 1996).
[53] S. M. Gallagher, A. W. Albrecht, T. D. Hybl, B. L. Landin, B. Rajaram, and D. M. Jonas, J. Opt. Soc. Am. B **15**, 2338-2345 (1998).
[54] T. Brabec and F. Krausz, Phys. Rev. Lett. **78**, 3282-3285 (1997).
[55] S. Mukamel, *Principles of Nonlinear Optical Spectroscopy* (Oxford University Press, New York, 1995).
[56] H. A. Haus and E. P. Ippen, Opt. Lett. **26**, 1654-1656 (2001).
[57] X. Gu, L. Xu, M. Kimmel, E. Zeek, P. O'Shea, A. P. Shreenath, R. Trebino, and R. S. Windeler, Opt. Lett. **27**, 1174-1176 (2002); P. Baum, S. Lochbrunner, J. Piel, and E. Riedle, Opt. Lett. **28**, 185-187 (2003).
[58] M. Bellini and T. W. Hänsch, Opt. Lett. **25**, 1049-1151 (2000).
[59] T. M. Fortier, J. Ye, S. T. Cundiff, and R. S. Windeler, Opt. Lett. **27**, 445-447 (2002); T. M. Fortier, D. J. Jones, J. Ye, S. T. Cundiff, and R. S. Windeler, Opt. Lett. **27**, 1436-1438 (2002).
[60] D. Strickland and G. Mourou, Opt. Commun. **56**, 219-221 (1985); M. D. Perry and G. Mourou, Science **264**, 917-924 (1994).

[61] A. Dubietis, G. Jonusauskas, and A. Piskarskas, Opt. Commun. **88**, 437-440 (1992); I. N. Ross, P. Matousek, M. Towrie, A. J. Langley, and J. L. Collier, Opt. Commun. **144**, 125-133 (1997).

[62] I. N. Ross, J. L. Collier, P. Matousek, C. N. Danson, D. Neely, R. M. Allot, D. A. Pepler, C. Hernandez-Gomez, and K. Osvay, Appl. Opt. **39**, 2422-2427 (2000).

[63] A. E. Siegman, *Lasers* (University Science Books, Mill Valley, California, 1986).

[64] C. Corsi and M. Bellini, Appl. Phys. B **78**, 31-34 (2004).

[65] S. H. Cho, F. X. Kartner, U. Morgner, E. P. Ippen, J. G. Fujimoto, J. E. Cunningham, and W. H. Knox, Opt. Lett. **26**, 560-562 (2001).

[66] M. S. Pshenichnikov, W. P. Deboeij, and D. A. Wiersma, Opt. Lett. **19**, 572-574 (1994); G. N. Gibson, R. Klank, F. Gibson, and B. E. Bouma, Opt. Lett. **21**, 1055-1057 (1996); A. Baltuska, Z. Wei, M. S. Pshenichnikov, D. A. Wiersma, and R. Szipocs, Appl. Phys. B **65**, 175-188 (1997).

[67] F. Krausz, T. Brabec, M. Schnürer, and C. Spielmann, Opt. Photon. News. **9**, 46-50 (1998).

[68] E. Cormier and P. Lambropoulos, Euro. Phys. J. D **2**, 15-20 (1998).

[69] K. J. Schafer, B. Yang, L. F. Dimauro, and K. C. Kulander, Phys. Rev. Lett. **70**, 1599-1602 (1993).

[70] C. Kan, N. H. Burnett, C. E. Capjack, and R. Rankin, Phys. Rev. Lett. **79**, 2971-2974 (1997).

[71] N. Milosevic, A. Scrinzi, and T. Brabec, Phys. Rev. Lett. **88**, 093905 (2002).

[72] V. S. Yakovlev and A. Scrinzi, Phys. Rev. Lett. **91**, 153901 (2003).

[73] E. Priori, G. Cerullo, M. Nisoli, S. Stagira, S. De Silvestri, P. Villoresi, L. Poletto, and P. Ceccherini, Phys. Rev. A **61**, 063801 (2000).

[74] M. Nisoli, G. Sansone, S. Stagira, S. De Silvestri, C. Vozzi, M. Pascolini, L. Poletto, P. Villoresi, and G. Tondello, Phys. Rev. Lett. **91**, 213905 (2003).

[75] G. G. Paulus, F. Lindner, H. Walther, A. Baltuska, E. Goulielmakis, M. Lezius, and F. Krausz, Phys. Rev. Lett. **91**, 253004 (2003).

[76] G. Sansone, C. Vozzi, S. Stagira, M. Pascolini, L. Poletto, P. Villoresi, G. Tondello, S. De Silvestri, and M. Nisoli, Phys. Rev. Lett. **92**, 113904 (2004).

[77] A. Apolonski, P. Dombi, G. G. Paulus, M. Kakehata, R. Holzwarth, T. Udem, C. Lemell, K. Torizuka, J. Burgdorfer, T. W. Hansch, and F. Krausz, Phys. Rev. Lett. **92**, 073902 (2004).

[78] O. D. Mücke, T. Tritschler, M. Wegener, U. Morgner, and F. X. Kartner, Phys. Rev. Lett. **89**, 127401 (2002).

[79] A. N. Chudinov, Y. E. Kapitzky, A. A. Shulginov, and B. Y. Zel'dovich, Opt Quant Electron **23**, 1055-1060 (1991); D. W. Schumacher, F. Weihe, H. G. Muller, and P. H. Bucksbaum, Phys. Rev. Lett. **73**, 1344-1347 (1994); M. J. J. Vrakking and S. Stolte, Chem. Phys. Lett. **271**, 209-215

(1997); A. Haché, Y. Kostoulas, R. Atanasov, J. L. P. Hughes, J. E. Sipe, and H. M. van Driel, Phys. Rev. Lett. **78**, 306-309 (1997); T. Kanai and H. Sakai, J. Chem. Phys. **115**, 5492-5497 (2001).

[80] I. P. Christov, Appl. Phys. B **70**, 459-462 (2000); R. M. Potvliege, N. J. Kylstra, and C. J. Joachain, J. Phys. B **33**, L743-L748 (2000).

[81] S. Chelkowski and A. D. Bandrauk, Phys. Rev. A **65**, - (2002).

[82] D. B. Miloševic, G. G. Paulus, and W. Becker, Opt. Expr. **11**, 1418-1429 (2003).

[83] F. Lindner, G. G. Paulus, H. Walther, A. Baltuska, E. Goulielmakis, M. Lezius, and F. Krausz, Phys. Rev. Lett. **92**, - (2004).

[84] P. Agostini, F. Fabre, G. Mainfray, G. Petite, and N. K. Rahman, Phys. Rev. Lett. **42**, 1127-1130 (1979).

[85] K. C. Kulander, K. J. Schafer, and J. L. Krause, in *Superintense Laser Atom Physics*, edited by B. Pireaux, A. L'Huillier and J. Rzazewski (Plenum, New York, 1994), Vol. B 316, p. 95.

[86] W. Becker, F. Grasbon, R. Kopold, D. B. Milosevic, G. G. Paulus, and H. Walther, Adv. Atom. Mol. Opt. Phy. **48**, 35-98 (2002).

[87] G. G. Paulus, W. Nicklich, H. L. Xu, P. Lambropoulos, and H. Walther, Phys. Rev. Lett. **72**, 2851-2854 (1994); G. G. Paulus, W. Becker, W. Nicklich, and H. Walther, J. Phys. B **27**, L703-L708 (1994).

[88] L. G. Guoy, Compt. Rendue Acad. Sci. Paris **10**, 1251-1253 (1890).

[89] N. C. R. Holme, B. C. Daly, M. T. Myaing, and T. B. Norris, App. Phys. Lett. **83**, 392-394 (2003).

[90] R. W. Boyd, J. Opt. Soc. Am. **70**, 877-880 (1980); S. M. Feng and H. G. Winful, Opt. Lett. **26**, 485-487 (2001).

[91] A. B. Ruffin, J. V. Rudd, J. F. Whitaker, S. Feng, and H. G. Winful, Phys. Rev. Lett. **83**, 3410-3413 (1999); P. Kuzel, M. A. Khazan, and J. Kroupa, J. Opt. Soc. Am. B **16**, 1795-1800 (1999); R. W. McGowan, R. A. Cheville, and D. Grischkowsky, App. Phys. Lett. **76**, 670-672 (2000).

[92] P. Balcou and A. L'Huillier, Phys. Rev. A **47**, 1447-1459 (1993); M. Lewenstein, P. Salières, and A. L'Huillier, Phys. Rev. A **52**, 4747-4754 (1995); F. Lindner, W. Stremme, M. G. Schätzel, F. Grasbon, G. G. Paulus, H. Walther, R. Hartmann, and L. Struder, Phys. Rev. A **68**, 013814 (2003).

[93] Z. L. Horváth, J. Vinkó, Z. Bor, and D. von der Linde, "Acceleration of femtosecond pulses to superluminal velocities by Gouy phase shift," Appl. Phys. B. **63**, pp. 481-484, 1996.

[94] M. Nisoli, E. Priori, G. Sansone, S. Stagira, G. Cerullo, S. De Silvestri, C. Altucci, R. Bruzzese, C. de Lisio, P. Villoresi, L. Poletto, M. Pascolini, and G. Tondello, Phys. Rev. Lett. **88**, 033902 (2002).

[95] J. Itatani, F. Quere, G. L. Yudin, M. Y. Ivanov, F. Krausz, and P. B. Corkum, Phys. Rev. Lett. **88**, 173903 (2002); M. Kitzler, N. Milosevic, A. Scrinzi, F. Krausz, and T. Brabec, Phys. Rev. Lett. **88**, 173904 (2002); R. Kienberger, E. Goulielmakis, M. Uiberacker, A. Baltuska, V. Yakovlev, F. Bammer, A. Scrinzi, Th.Westerwalbesloh, U. Kleineberg, U. Heinzmann, M. Drescher, and K. F., Nature **427**, 817-821 (2004).

[96] H. Niikura, F. Legare, R. Hasbani, A. D. Bandrauk, M. Y. Ivanov, D. M. Villeneuve, and P. B. Corkum, Nature **417**, 917-922 (2002); H. Niikura, F. Legare, R. Hasbani, M. Y. Ivanov, D. M. Villeneuve, and P. B. Corkum, Nature **421**, 826-829 (2003).

Chapter 11

QUANTUM CONTROL OF HIGH-ORDER HARMONIC GENERATION

Applied Attosecond Science

Emily Gibson, Ivan Christov, Margaret M. Murnane, and Henry C. Kapteyn
JILA, University of Colorado and National Institute of Standards and Technology; Department of Physics, University of Colorado; and NSF Engineering Research Center for Extreme-Ultraviolet Science and Technology

Abstract: We discuss the physical processes involved in the generation and optimization of extreme ultraviolet and soft x-ray light though the process of high-order harmonic generation. We show that by manipulating the sub-optical-cycle attosecond dynamics of this process using optimized waveguide structures and pulse shapes, we can control the energy of the emitted photons, the phase matching of the conversion process, and the spatial and temporal coherence of the light. High-order harmonic generation is a useful source of short wavelength light with ultrashort time duration. Thus, optimization and manipulation of high-order harmonic generation demonstrates control of electron dynamics on attosecond time scales.

Key words: high harmonic generation, phase matching, attosecond

Ultrafast laser technology makes it possible to generate extremely high field intensities above 10^{18} W/cm^2 or, alternatively, to probe extremely short time durations corresponding to only a few femtoseconds [1]. One of the most prominent applications of very high-power, ultrashort-pulse lasers has been to study the regime of "nonperturbative" light-matter interactions [2]. At intensities above ~10^{14} W/cm^2, the magnitude of the electric field of the laser radiation is comparable to the field binding an electron to an atom. In this regime, the strong electric field can easily ionize atoms. Once the atom is ionized, the subsequent motion of the free electron is controlled by the oscillating laser field, and the electron can easily reach kinetic energies many times that of the original electron binding energy.

One of the most significant consequences of this intense laser-matter interaction is the process of high harmonic generation (HHG) [3]. In HHG,

the ionized electron recollides and then recombines with its parent ion, releasing a high energy photon. The energy and phase of the emitted high-harmonic light depend on the detailed electron trajectory in the laser field—dynamics that occur on a fraction of an optical cycle, or attosecond, timescale. Thus, the properties of HHG are sensitive to the *field* evolution of the driving laser [4]; in contrast, traditional nonlinear processes, such as second-harmonic generation, are insensitive to many aspects of the driving field such as the carrier-envelope offset (CEO). Detailed studies of the dependence of high-harmonic generation on the time-history of the driving laser field represent the first results from the field of *attosecond science* [5, 6], an area of research that has received considerable attention in the early 2000s [7]. Consequences of the attosecond dynamics of HHG include the ability to manipulate electron dynamics with attosecond precision [8-10], the phase matching of the conversion process (*attosecond engineering)* [11, 12], and the ability to generate pulses of light with subfemtosecond duration. The strong dependence on the laser field also means that HHG is sensitive to the CEO of the driving laser pulse [13-15]. By combining pulse shaping techniques with recently developed methods to control the CEO of an ultrafast pulse by locking the mode frequencies to a cw reference [16], it becomes possible to control the complete electric field of the pulse in the time domain with attosecond precision. This allows us to access the fastest time scales that are possible with modern laser technology.

1. THE PHYSICS OF HIGH-ORDER-HARMONIC GENERATION

High-order-harmonic generation results when an intense laser field interacts with a gas or material. An intuitive model of the process at the atomic level was developed by Corkum, Kulander, and others [4, 17] and is sometimes referred to as the “three-step” model. In the first step, the strong electric field of the laser suppresses the Coulomb barrier binding an electron to the atom, freeing the valence electron either by tunneling or “over-the-barrier” ionization. The freed electron is then accelerated by the field. Since the laser field is oscillating, the electron can, with some probability, return to its parent ion and recombine, emitting a high-energy photon. This process occurs for many atoms driven coherently over several laser cycles, resulting in emission of higher-order odd harmonics in a coherent, low-divergence beam. The three-step model accurately predicts that the highest photon energy that can result from HHG occurs when an electron is ionized at a

phase of 18 degrees after the peak of the laser cycle. This cutoff photon energy is then predicted to be:

$$E_{\max} = I_p + 3.2U_p, \tag{1}$$

where I_p is the ionization potential of the atom and U_p is the ponderomotive energy given by

$$U_p = e^2E^2 / 4m\omega^2 \propto I\lambda^2, \tag{2}$$

where e, E, m, ω, I, and λ are the electron charge, field amplitude, electron mass, laser frequency, intensity, and wavelength, respectively. The highest photon energy therefore scales linearly with the laser intensity.

The "recollision" energies associated with the intensities required to field-ionize atoms can be as high as several hundred electron volts [18, 19]. Thus, the emitted high-harmonic photons can correspond to the combined energy of several hundred of the incident photons. The linear relationship between the cutoff and the incident intensity also presents very attractive scaling as compared to, for example, EUV (extreme ultraviolet) laser schemes where the power requirements scale as the photon energy to the 3rd–5th power [20]. However, to take advantage of this favorable scaling, several challenges must be overcome. The HHG process necessarily ionizes the gas, generating free-electron plasma. The dispersion of the plasma causes a mismatch in the phase velocities of the fundamental and harmonic light, significantly reducing the amount of harmonic signal produced. Also, the plasma can defocus the laser beam, decreasing the peak intensity, and thereby limiting the maximum harmonic energy [21]. To date, the highest energy HHG emission has been achieved using short-duration laser pulses and noble gases with high ionization potentials that can reduce the amount of ionization for a given peak intensity [18, 19]. This emission can extend from the ultraviolet up to the soft x-ray region of the spectrum (>500 eV), making it an ideal source for pure and applied science such as photoemission spectroscopy [22], plasma interferometry [23], or metrology for optics for EUV lithography.

2. "SINGLE-ATOM" EFFECTS IN HIGH-ORDER-HARMONIC GENERATION: MANIPULATION AND COHERENT CONTROL

A simple classical picture of HHG as given by the three-step model accurately predicts the range of photon energies that can be obtained for a given incident laser intensity. However, electrons are not "classical" objects, and a more accurate picture of the HHG process includes the wave nature of the oscillating electron. A fully quantum, analytical theory of HHG has been derived by Lewenstein et al. [4] and has been extremely successful in describing both the general characteristics of HHG, such as the photon energy cutoff, as well as more specific characteristics such as the divergence properties of the generated beam [24] and the specific spectral characteristics of the emission [5]. Qualitatively, the spectral characteristics of HHG emission are a result of the fact that the ionized electron has an associated deBroglie wavelength corresponding to the kinetic energy acquired in the laser field, $\lambda = h/p$, where h is Planck's constant and p is the electron momentum. The emission also has a phase related to the total phase the electron accumulates during its free trajectory, approximately [24]

$$\varphi \approx q\omega t_f - \tau_s U_p, \tag{3}$$

where q is the harmonic order, ω is the laser frequency, and $\tau_s = t_f - t_i$ is the time difference between when the electron is ionized and when it recombines with the ion. The phase of the emitted x-rays is therefore not simply related to the phase of the driving laser but also includes an "intrinsic phase" component that can vary rapidly with intensity. The intrinsic phase has consequences for both the spatial and spectral emission characteristics. Spatially, this intrinsic phase can result in a complex spatial profile of the harmonic emission when generated using a beam that is converging toward a focus. This is in contrast to the near-Gaussian profile for HHG generated by a beam diverging from a focus [24, 25] or the ~100% spatial coherence of light generated using a waveguide configuration [26]. In the spectral domain, this time-varying intrinsic phase results in large frequency shifts and spectral broadening or narrowing of the harmonic emission [5].

From a nonlinear optics point of view, HHG is unique as a purely electronic nonlinearity with a finite time response. In many ways, HHG is simply an extension of nonlinear optical processes such as second-harmonic generation (SHG). In SHG, an electron driven in an "anharmonic" potential,

which is created by the crystalline configuration of the material, moves in a nonsinusoidal path that results in emission of radiation at the second-harmonic frequency. This is the same for HHG, with the "anharmonic" potential consisting of free space with the very strong perturbation of an ionic core localized in a small area. The fact that the electron takes a fraction of an optical cycle to return to the core means that the atomic emission depends on the *time history* of the driving field over the preceding interval of a few hundred attoseconds. This finite response time makes it possible to manipulate the atomic response through quantum control techniques by manipulating the laser pulse shape in time. The first studies relating to quantum control of high-harmonic generation were simple studies of the effect of the chirp of the driving laser pulse on the spectrum of high-harmonic generation [5]. HHG emission generated near the peak of the driving laser pulse exhibits an intrinsic-phase-induced negative chirp since $\varphi \tilde{\propto} I_{laser}$; i.e., the harmonic emission spectrum varies from blue to red in time. Any chirp imprinted on the laser pulse itself adds to the intrinsic chirp, resulting in an asymmetry in the spectral linewidth of the emission with respect to chirp. These experiments demonstrated a direct spectral-temporal coupling that is a result of the attosecond time response of the HHG nonlinearity.

This phenomenon can be exploited in a dramatic way through a technique called intra-atomic phase matching (IAPM) by temporally shaping the driving laser pulse [8, 10]. A simple picture of IAPM is given in Figure 11-1. In HHG, the radiation is emitted as a series of attosecond-time-scale bursts, twice each cycle of the laser field. However, for a particular spectral component of each burst corresponding to an individual harmonic order, the phase is not fixed to the driving laser but varies on a cycle-by-cycle basis as the light intensity increases and decreases, changing the value of the intrinsic phase. This effect results in a partial destructive interference that reduces the intensity of the emitted harmonics.

In IAPM, the intensity of a selected harmonic is optimized by adjusting the shape of the laser pulse so that a nonlinear chirp is added to the light pulse. This pulse shaping shifts the position of the peaks in the laser field on a suboptical cycle basis; i.e., on timescales $\leq$100 attoseconds. The harmonic bursts from each half-cycle of the laser field can then add constructively, optimizing the harmonic emission intensity. IAPM thus makes it possible to "re-phase" the harmonic emission from an atom for a selected harmonic order. Furthermore, this optimization can in some circumstances be extremely selective, with the pulse shape chosen to optimize one harmonic order while suppressing the neighboring harmonics. IAPM thus represents a useful manipulation of attosecond time-scale electron dynamics and demonstrates the ability to do *attosecond engineering*. Another interesting

aspect of the IAPM process is that although it involves precise manipulation of a laser pulse and an electron wave function, it was not predicted beforehand but instead was discovered by applying learning algorithm techniques to optimize the HHG emission by manipulation of the laser pulse shape [27]. The physics of this process was subsequently explained and reproduced by implementing a learning algorithm in conjunction with the three-step model theory of HHG. This computational model reproduced the experiment and made it possible to deduce the mechanism behind IAPM [10]. Optimization of high-harmonic emission to generate nearly monochromatic radiation (i.e., primarily a *single* harmonic) is desirable for many applications in ultrafast spectroscopy using EUV radiation. Other recent, closely related work has shown that the spectral and temporal characteristics of high-harmonic radiation are sensitive to the carrier-envelope offset of the driving laser pulse [15].

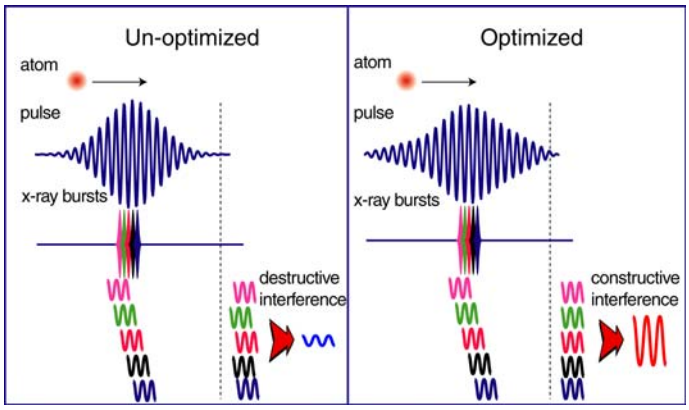

Figure 11-1. Illustration of intra-atomic phase matching. When the optimized pulse shape is used, a particular harmonic constructively adds over each half cycle (from [9]).

3. PHASE MATCHING OF HIGH-HARMONIC GENERATION

Although the single-atom effect of high-order harmonic generation presents intriguing physics, applications of HHG radiation as a “table-top” coherent soft x-ray source depend upon optimizing the total flux generated from an ensemble of atoms. In nonlinear optical processes, the conversion efficiency from the fundamental to the harmonic field is enhanced by *phase*

matching. In its simplest manifestation, phase matching will occur when the driving laser and the harmonic signal travel with the same phase velocity, so that signal generated throughout the conversion region adds constructively. In HHG, since the ionization level is changing throughout the pulse and the increasing density of free electrons has a large effect on the phase velocity of the driving laser, phase matching can only be obtained in limited time windows in the pulse. Enhancement of the flux from HHG is possible by guiding the driving laser with a hollow-core, gas-filled waveguide [28, 29]. The laser light is guided by glancing incidence reflection, allowing propagation over an extended interaction length with a well-defined intensity and phase profile. The fundamental and harmonic light propagate through the waveguide with phase velocities determined by the dispersion of the neutral gas, the plasma, and the waveguide at the two different frequencies. The difference in the wave vectors of the fundamental and harmonic light results in a phase mismatch

$$\Delta k = \frac{q_{11}^2 \lambda}{4\pi a^2} + P\eta N_{atm} r_e \left(q\lambda - \lambda/q\right) - \frac{2\pi(1-\eta)}{\lambda}\Delta\delta\,, \tag{4}$$

where λ, q, a, u_{11}, η, P, N_{atm}, and r_e are the fundamental wavelength, harmonic order, waveguide radius, the first zero of the Bessel function J_0, ionization fraction, gas pressure in atmospheres, number density at 1 atm, and classical electron radius, respectively; $\Delta\delta = \delta(\lambda) - \delta(\lambda/q)$ is the difference in the index of refraction at the fundamental and harmonic frequencies of gas at 1 atm. Here, the small contribution from the nonlinear refractive index is neglected. The waveguide allows control over the experimental parameters, such as gas pressure and radius, to optimize phase matching.

For low levels of ionization, the pressure can be adjusted so that the waveguide and plasma dispersion balance the dispersion due to the neutral atoms, which is of opposite sign, and phase matching can be achieved (Δk = 0). Since phase matching is accomplished by adjusting the phase velocity of the fundamental and the harmonic radiation to travel at a phase velocity ~c, the bandwidth of this phase matching is very broad, encompassing many harmonic orders. However, for higher intensities, the changing ionization during the pulse means that there is a narrow time window for phase matching so that only the harmonics generated in that window are enhanced. When phase matched, the harmonic signal increases quadratically with interaction length until it is limited by background absorption of the gas. This method of phase matching has limitations. When a large enough fraction of the gas is ionized, the plasma dispersion is greater than the

neutral dispersion for any pressure. Thus phase matching is no longer possible, and the phase velocity of the fundamental light exceeds that of the generated harmonic signal. The critical ionization fraction is [30]

$$\eta_{cr} = \left(1 + \frac{N_{atm} r_e \lambda^2}{2\pi\Delta\delta}\right)^{-1}. \quad (5)$$

Figure 11-2 plots the pressure required to achieve phase matching as a function of the ionization fraction.

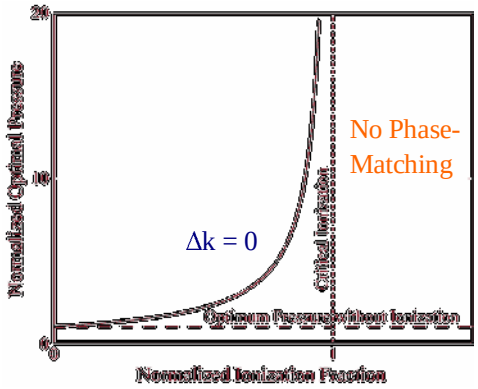

Figure 11-2. Plot of pressure for phase matching as a function of normalized ionization fraction (η/ηcr). Beyond critical ionization, phase matching is no longer possible.

For low intensities, and therefore lower harmonic orders, where the ionization fraction is small, phase matching is primarily achieved by balancing the waveguide dispersion with the neutral gas dispersion. At the higher intensities required to generate higher energy harmonics, however, the plasma term becomes significant and higher neutral gas pressures are needed to compensate. Beyond the critical ionization, phase matching is not possible [13, 31]. The optimum pressure also depends on the diameter of the waveguide; for the case of "plane-wave" propagation without a waveguide in a uniform-density gas, phase matching will occur when the fractional ionization equals the critical ionization [30]. However, this requires either very high pulse energy or high gas pressure and results in spatially varying phase matching that can create a complex spatial mode of the harmonic emission. In contrast, the use of the hollow waveguide allows for better phase matching, resulting in build-up of an EUV beam with a spatial mode

of extremely high coherence [26, 32]. In 2004, stable beams of EUV light with full spatial coherence had only been generated using the hollow waveguide geometry.

Another consequence of the time-varying–phase-matching conditions is sensitivity to the CEO of the pulse, both for few-cycle pulses and also in the case of light pulses with durations of tens of femtoseconds [13, 15, 33]. At the peak of the pulse, the ionization fraction is increasing significantly in a series of steps over each half cycle, so that the phase-matching conditions vary rapidly with time. The ionization as a function of time for a particular driving laser pulse can be calculated using the Ammosov-Delone-Krainov (ADK) tunneling ionization rates [34]. Figure 11-3 shows the fractional ionization of argon gas for two different values of the CEO. The amount of ionization created at each half-cycle is dependent on the CEO; however, the final level of ionization is the same for both pulses.

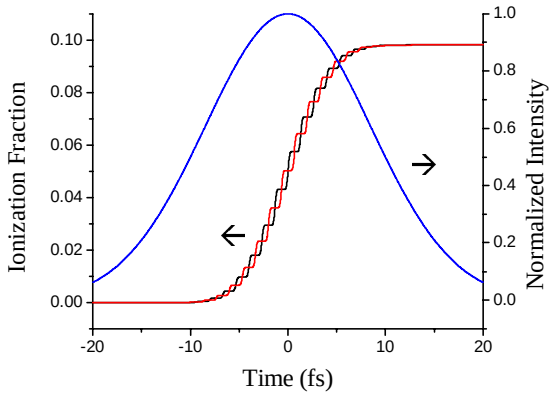

Figure 11-3. Calculation of the fractional ionization of argon using ADK ionization rates for a 20 fs pulse with peak intensity of 2.2 x 10^{14} W/cm^2 for a cosine and sine pulse.

For a given harmonic order, tuning the pressure can allow phase matching at different half cycles of the pulse. Durfee et al. observed evidence of the CEO effect on phase-matching [13]. Figure 11-4(a) shows the calculation of the pressure dependence of the flux of the 29th harmonic for one value of the CEO for a 20 fs pulse. The different peaks correspond to optimal phase matching at different ionization "steps." The exact position of these peaks depends on the intensity, the pressure, *and* the CEO of the pulse. For a fixed gas pressure, the positions of the peaks move around as the phase-matching conditions change with the CEO. Figure 11-4(b) shows the experimentally measured 29th order harmonic signal. In the pressure region corresponding to phase matching at the peak of the pulse, where the amount of ionization is dependent on the CEO, the signal shows a strongly

oscillating behavior, consistent with the effect of a rapidly varying CEO. This fluctuation is only observed at higher pressures because, at lower pressures, exact phase matching between the fundamental and the harmonic is never achieved, and thus the relative ionization and CEO are averaged along the length of the waveguide. Rapidly increasing levels of ionization, together with a stable carrier-envelope offset, may make it possible to phase match only the emission from a particular single half cycle, giving a single, enhanced attosecond-duration pulse.

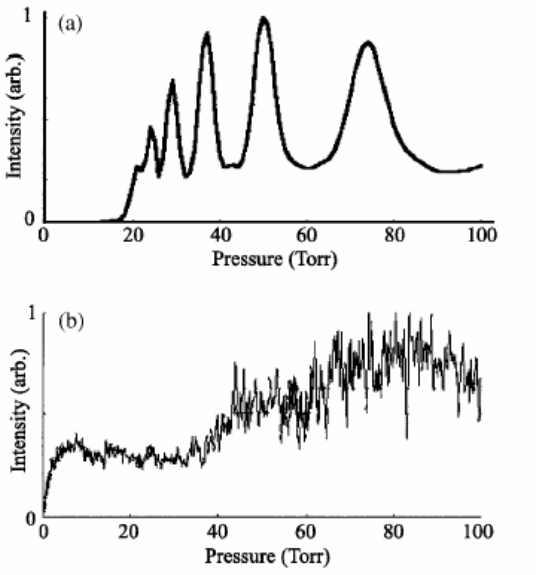

Figure 11-4. (a) Calculation of the flux of the 29th harmonic for a 20 fs laser pulse and peak intensity of 2.2 x 10^{14} W/cm^2 as a function of argon pressure using a 3 cm waveguide. (b) Experimentally measured flux for the same conditions as (a) (from [29]).

4. QUASI-PHASE MATCHING OF HIGH-HARMONIC GENERATION

Implementing high-order-harmonic generation in a waveguide geometry has many advantages. However, normal phase matching in a straight waveguide is limited to relatively low levels of ionization below the critical ionization fraction (typically 0.5%, 1% and 5% in He, Ne and Ar, for example). This restricts the enhancement of HHG emission to photon

energies < 80 eV for a 20 fs pulse. At higher photon energies and ionization levels, the plasma contribution becomes much greater than the neutral gas contribution, making phase matching impossible. In the absence of phase matching, the harmonic emission builds up periodically over a coherence length and then interferes with out-of-phase light generated in the next section of the nonlinear medium, drastically reducing the total flux.

In recent work, we showed that the inability to phase match in high ionization levels can be overcome for the first time by applying quasi-phase -matching (QPM) techniques to the HHG process. The ability to quasi-phase match HHG significantly extends the range of photon energies where it is possible to generate flux efficiently. The process of QPM was first proposed in 1962, shortly after the birth of nonlinear optics. Armstrong et al. [35] proposed a "phase-corrective scheme," whereby the phase mismatch in a nonlinear optical process is periodically corrected by introducing a periodicity in the medium itself of the coherence length. For example, quasi-phase matching of second-harmonic light can be achieved by periodically reversing the crystal orientation, and therefore the polarity of the nonlinear response, so that a 180-degree phase shift is introduced every coherence length. This reverses the destructive interference, allowing continual build-up of the harmonic signal. Practical implementation of this concept awaited the development of crystal-poling techniques in the mid-1990s [36].

Unfortunately, the generation of coherent light at EUV wavelengths must take place in a gas or on a surface, making the use of standard QPM techniques impossible. Fortunately, the extreme nonlinear nature of HHG makes alternate approaches possible. For example, quasi-phase matching of the frequency conversion process can be achieved by restricting HHG to regions where the signal will be in phase and add constructively. Some ideas for quasi-phase matching of HHG include using a modulated density gas or plasma to periodically change the nonlinear susceptibility [37]. Another proposal suggests using counter-propagating light to modulate the intensity of the driving laser [38]. Since both the intrinsic phase and the amplitude of the harmonic emission vary quite dramatically with laser intensity, even modest periodic modulations of the laser intensity can result in a phase modulation of the generated harmonic light. Experimentally, quasi-phase matching of HHG was first implemented using a technique proposed by Christov et al. [11]. In this technique, a hollow-core waveguide is modified to have a periodically changing inner diameter to modulate the driving laser intensity. Figure 11-5(a) shows a calculation of the signal of the 95^{th} harmonic as a function of propagation length in a straight waveguide using a 15 fs pulse with a peak intensity of 7×10^{14} W/cm^2 and 1 Torr of argon. The calculation uses three-dimensional propagation models, and the harmonic generation signal is calculated using a quasi-classical approximation for the

dipole moment. Figure 11-5(b) shows the same calculation using a hollow-core waveguide with a 0.5 mm period sinusoidal corrugation that changes the laser intensity by 5%. The modulated waveguide causes a dramatic enhancement in the final signal (note the different scales of the two plots).

We can understand the basic physics for enhancement of the HHG signal by using classical nonlinear optics theory for quasi-phase-matching. In a simplified model of harmonic generation, the field of harmonic order q, after propagating a distance L in a nonlinear medium, is related to the phase mismatch, Δk, by

$$E_q \propto \int_0^L E_\omega^n(z) d(z) e^{-i\Delta k z} dz, \tag{6}$$

where E_ω is the fundamental field, n is the effective order of the nonlinear process, $d(z)$ is the nonlinear coefficient, and Δk is the phase mismatch calculated in Equation (4). In our case, the nonlinear coefficient can be expressed as a general periodic function of z with period Λ [36]

$$d(z) = \sum_{m=-\infty}^{\infty} D_m e^{iK_m z}, \tag{7}$$

where $K_m = 2\pi m / \Lambda$ is the effective wave vector of QPM, Λ is the modulation period of the quasi-phase matching, and m is the order of the QPM process. Equations (6) and (7) show that the harmonic signal will be enhanced when $K_m \approx \Delta k$. The signal enhancement is greatest for m = 1, but QPM still enhances the generated HHG signal for higher values of m.

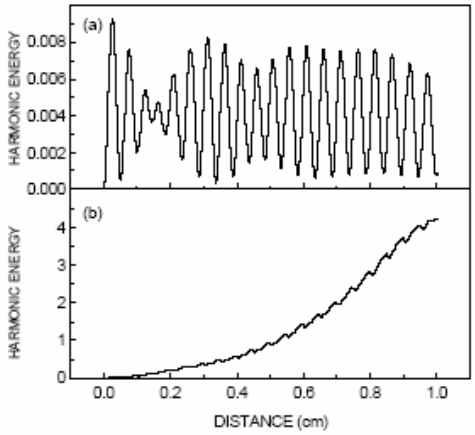

Figure 11-5. (a) Calculation of the signal of the 95th harmonic for a straight waveguide as a function of propagation distance. (b) Calculation for a 0.5 mm period modulated waveguide (from [11]).

The first set of experiments demonstrating quasi-phase matching of HHG showed a dramatic extension of the harmonic spectrum using modulated waveguides [12]. In this experiment, 25 fs duration pulses from a high repetition rate (2–5 kHz, 1 mJ/pulse) Ti:sapphire laser system operating at 760 nm [39] were focused into 150 μm diameter modulated-hollow-core waveguides filled with various gases. The modulated waveguides used in this experiment were produced using precision glass-blowing techniques starting with a straight hollow-core fiber (also 150 μm in diameter). The modulations were approximately sinusoidal, with a radial depth on the order of 10 microns, corresponding to a 13% modulation of the fiber radius. The initial experiments used waveguides with modulation periods varying from 1–0.5 mm. Figure 11-6 shows the experimentally measured HHG spectra from He for three different modulated-waveguide periodicities. As the modulation period is reduced from 1 mm to 0.75 mm to 0.5 mm, the highest observable harmonic energy increases from 112 eV to 175 eV.

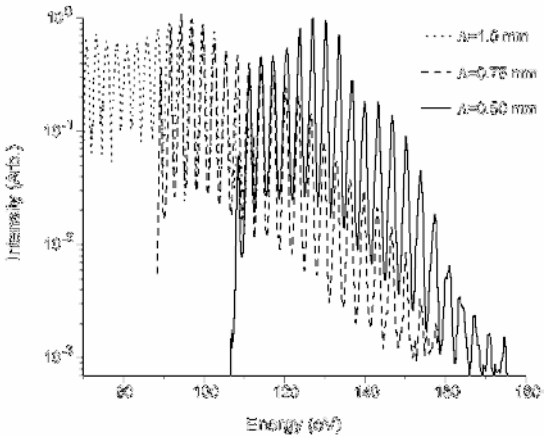

Figure 11-6. Experimental harmonic spectra from 111 Torr He with a driving pulse of 25 fs and peak intensity ~5 x 10^{14} W/cm^2 for different modulated-waveguide periodicities (from [12]).

The significance of QPM is that it permits phase matching of HHG at higher ionization levels and hence higher photon energies than was previously possible. This effect becomes apparent from a calculation of the coherence length that results from the mismatch in the phase velocity of the fundamental and harmonic because of ionization. At high ionization levels, the phase mismatch is predominantly due to the plasma dispersion and is given by

$$\Delta k_{plasma} \approx \frac{q n_e e^2 \lambda}{4\pi m_e \varepsilon_o c^2}, \tag{8}$$

where λ is the laser wavelength and n_e is the electron density. For example, for fully ionized argon at a pressure of 1 Torr, n_e = 3.5 x 10^{16} cm^{-3}, giving Δk ~7550 m^{-1} for the 95th harmonic order (150 eV). Therefore, the coherence length, L_c, given by $L_c = \pi/\Delta k$, is ~0.4 mm. Thus, very substantial levels of ionization can be compensated for by using QPM with modulation periods in the range of 1–0.25 mm that can be readily manufactured with glass-blowing techniques.

In initial experiments, the ionization level in helium was still relatively low (~1%) and only ~4% in argon. However, more recent experiments have demonstrated QPM in fully ionized gas. The results of more recent experiments performed at higher laser intensities of 1.6 x 10^{15} W/cm^2, in 9

Torr of Ne gas, using 0.25 mm-modulated and straight waveguides, are shown in Figure 11-7 [40]. At these intensities, a simple calculation of the cutoff harmonic energy, given in Equation (1), yields an expected cutoff of 330 eV. However, the observable harmonic emission from the straight waveguide [Figure 11-7 (lower curve)] only extends to around 225 eV. In contrast, the harmonic emission from the 0.25 mm-modulated waveguide (upper curve) is brighter and extends to significantly higher energies, where the carbon edge at 284 eV is clearly visible.

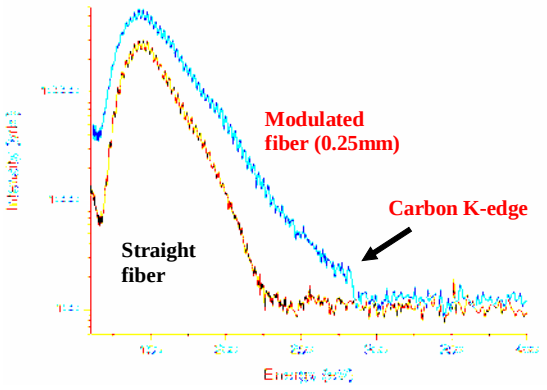

Figure 11-7. Comparison of experimental harmonic spectra for neon for straight and modulated fibers [40].

Using the expression in Equation (8), which is valid at high ionization levels, we calculate Δk ~90,000 m^{-1} for the 183rd harmonic order at the C edge (284 eV) for ~60% ionized Ne. The effective wave vector for first-order QPM for a modulation period of 0.25 mm is K_1 ~25,000 m^{-1}. Again, the harmonic signal will be enhanced when $K_m \approx \Delta k$. For the harmonics in Ne near the C edge, the large phase mismatch of ~90,000 m^{-1} can be compensated for using third or fifth order (m = 3,5) QPM. For these cutoff harmonics, the phase mismatch above 225 eV is large enough that the signal can only be observed using a modulated waveguide and is not seen in a straight waveguide.

Based on conservative estimates of detection efficiency, filter transmission, and measurements of grating efficiency, we determined a minimum flux of between 10^6–10^8 photons/sec in a 10% bandwidth at the C edge. This flux may be sufficient for biological imaging applications, and a number of improvements should further increase it.

The data of Figure 11-7 illustrate that the highest observed harmonic orders are not limited by the I_p + 3.17 U_p relation but by ionization-induced phase mismatch. The modulated waveguide compensates for this phase

mismatch, making it possible to observe higher harmonics. By the peak of the laser pulse, calculations indicate that Ne should be ~70–90% ionized, which is well above the ionization level at which it has been previously possible to demonstrate phase-matching enhancement. Although past work observed HHG from He in the water window, this process was not phase matched and produced significantly lower signal levels [18, 41].

In the future, since the highest HHG photon energy scales linearly with laser intensity, using very reasonable laser parameters (i.e., pulse durations of 10 fs, intensities of $5x10^{15}$ W/cm^2, and waveguides with 0.1 mm periodicity), it will be possible to generate high-order quasi-phase-matched light at photon energies beyond 1 keV.

5. CONCLUSION

Recent advances in laser technology and in our understanding of electron dynamics in strong fields have resulted in enormous progress in the quest to develop practical coherent light sources at wavelengths much shorter than visible light. The use of quantum control techniques makes it possible to generate light with a spectrum that can be engineered for specific applications and to allow for the generation of attosecond-duration pulses. Using quasi-phase-matching techniques, there is a clear path to pursue for generating flux sufficient to implement a table-top soft x-ray microscope and to reach multi-keV energies.

ACKNOWLEDGEMENTS

The authors gratefully acknowledge funding for this work by the National Science Foundation and the Department of Energy.

REFERENCES

[1] S. Backus, C. G. Durfee, M. M. Murnane, and H. C. Kapteyn, Rev. Sci. Instrum. **69**, 1207-1223 (1998).

[2] T. Brabec and F. Krausz, Rev. Mod. Phys. **72**, 545-591 (2000).

[3] A. McPherson, G. Gibson, H. Jara, U. Johann, T. S. Luk, I. A. McIntyre, K. Boyer, and C. K. Rhodes, J. Opt. Soc. Am. B **4**, 595-601 (1987); M. Ferray,

A. Lhuillier, X. F. Li, L. A. Lompre, G. Mainfray, and C. Manus, J. Phys. B. **21**, L31-L35 (1988).

[4] M. Lewenstein, P. Balcou, M. Y. Ivanov, A. L'Huillier, and P. B. Corkum, Phys. Rev. A **49**, 2117-2132 (1994).

[5] Z. Chang, A. Rundquist, H. Wang, I. Christov, H. C. Kapteyn, and M. M. Murnane, Phys. Rev. A **58**, R30-R33 (1998).

[6] M. Bellini, C. Lynga, A. Tozzi, M. B. Gaarde, T. W. Hansch, A. L'Huillier, and C. G. Wahlstrom, Phys. Rev. Lett. **81**, 297-300 (1998); H. J. Shin, D. G. Lee, Y. H. Cha, J. H. Kim, K. H. Hong, and C. H. Nam, Phys. Rev. A **63**, 053407 (2001).

[7] P. B. Corkum, N. H. Burnett, and M. Y. Ivanov, Opt. Lett. **19**, 1870-1872 (1994); P. M. Paul, E. S. Toma, P. Breger, G. Mullot, F. Auge, P. Balcou, H. G. Muller, and P. Agostini, Science **292**, 1689-1692 (2001); M. Hentschel, R. Kienberger, C. Spielmann, G. A. Reider, N. Milosevic, T. Brabec, P. Corkum, U. Heinzmann, M. Drescher, and F. Krausz, Nature **414**, 509-513 (2001); R. Kienberger, E. Goulielmakis, M. Uiberacker, A. Baltuska, V. Yakovlev, F. Bammer, A. Scrinzi, T. Westerwalbesloh, U. Kleineberg, U. Heinzmann, M. Drescher, and F. Krausz, Nature **427**, 817-821 (2004); I. P. Christov, M. M. Murnane, and H. C. Kapteyn, Phys. Rev. Lett. **78**, 1251-1254 (1997).

[8] R. Bartels, S. Backus, E. Zeek, L. Misoguti, G. Vdovin, I. P. Christov, M. M. Murnane, and H. C. Kapteyn, Nature **406**, 164-166 (2000).

[9] R. Bartels, S. Backus, I. Christov, H. Kapteyn, and M. Murnane, Chem. Phys. **267**, 277-289 (2001).

[10] I. P. Christov, R. Bartels, H. C. Kapteyn, and M. M. Murnane, Phys. Rev. Lett. **86**, 5458-5461 (2001).

[11] I. P. Christov, H. C. Kapteyn, and M. M. Murnane, Optics Expr. **7**, 362-367 (2000).

[12] A. Paul, R. A. Bartels, R. Tobey, H. Green, S. Weiman, I. P. Christov, M. M. Murnane, H. C. Kapteyn, and S. Backus, Nature **421**, 51-54 (2003).

[13] C. G. Durfee, A. Rundquist, S. Backus, Z. Chang, C. Herne, H. C. Kapteyn, and M. M. Murnane, J. Nonlinear Opt. Phys. Mater. **8**, 211-234 (1999).

[14] G. G. Paulus, F. Grasbon, H. Walther, P. Villoresi, M. Nisoli, S. Stagira, E. Priori, and S. De Silvestri, Nature **414**, 182-184 (2001).

[15] A. Baltuška, T. Udem, M. Uiberacker, M. Hentschel, E. Goulielmakis, C. Gohle, R. Holzwarth, V. S. Yakoviev, A. Scrinzi, T. W. Hansch, and F. Krausz, Nature **421**, 611-615 (2003).

[16] D. J. Jones, S. A. Diddams, J. K. Ranka, A. Stentz, R. S. Windeler, J. L. Hall, and S. T. Cundiff, Science **288**, 635-639 (2000); S. T. Cundiff and J. Ye, Rev. Mod. Phys. **75**, 325-342 (2003).

[17] P. B. Corkum, Phys. Rev. Lett. **71**, 1994-1997 (1993); K. C. Kulander, K. J. Schafer, and J. L. Krause, in *Superintense Laser Atom Physics*, edited by B. Pireaux, A. L'Huillier and J. Rzazewski (Plenum, New York, 1994), Vol. B 316, p. 95.

[18] Z. H. Chang, A. Rundquist, H. W. Wang, M. M. Murnane, and H. C. Kapteyn, Phys. Rev. Lett. **79**, 2967-2970 (1997).
[19] C. Spielmann, N. H. Burnett, S. Sartania, R. Koppitsch, M. Schnurer, C. Kan, M. Lenzner, P. Wobrauschek, and F. Krausz, Science **278**, 661-664 (1997).
[20] H. C. Kapteyn, L. B. Dasilva, and R. W. Falcone, Proc. IEEE **80**, 342-347 (1992).
[21] A. L'Huillier, M. Lewenstein, P. Salieres, P. Balcou, M. Y. Ivanov, J. Larsson, and C. G. Wahlstrom, Phys. Rev. A **48**, R3433-R3436 (1993).
[22] R. Haight and D. R. Peale, Rev. Sci. Instrum. **65**, 1853-1857 (1994); M. Bauer, C. Lei, K. Read, R. Tobey, J. Gland, M. M. Murnane, and H. C. Kapteyn, Phys. Rev. Lett. **8702**, art. no.-025501 (2001).
[23] D. Descamps, C. Lynga, J. Norin, A. L'Huillier, C. G. Wahlstrom, J. F. Hergott, H. Merdji, P. Salieres, M. Bellini, and T. W. Hansch, Opt. Lett. **25**, 135-137 (2000); J. J. Rocca, C. H. Moreno, M. C. Marconi, and K. Kanizay, Opt. Lett. **24**, 420-422 (1999).
[24] P. Balcou, P. Salieres, A. Lhuillier, and M. Lewenstein, Phys. Rev. A **55**, 3204-3210 (1997).
[25] P. Salieres, T. Ditmire, M. D. Perry, A. Lhuillier, and M. Lewenstein, J. Phys. B. **29**, 4771-4786 (1996); J. Peatross, M. V. Fedorov, and K. C. Kulander, J. Opt. Soc. Am. B **12**, 863-870 (1995).
[26] A. R. Libertun, X. Zhang, A. Paul, E. Gagnon, T. Popmintchev, S. Backus, M. M. Murnane, H. C. Kapteyn, and I. P. Christov, App. Phys. Lett. **84**, 3903-3905 (2004).
[27] R. S. Judson and H. Rabitz, Phys. Rev. Lett. **68**, 1500-1503 (1992).
[28] A. Rundquist, C. G. Durfee, Z. H. Chang, C. Herne, S. Backus, M. M. Murnane, and H. C. Kapteyn, Science **280**, 1412-1415 (1998).
[29] C. G. Durfee, A. R. Rundquist, S. Backus, C. Herne, M. M. Murnane, and H. C. Kapteyn, Phys. Rev. Lett. **83**, 2187-2190 (1999).
[30] A. Rundquist, Ph.D Thesis, Washington State University (1998).
[31] E. Constant, D. Garzella, P. Breger, E. Mevel, C. Dorrer, C. Le Blanc, F. Salin, and P. Agostini, Phys. Rev. Lett. **82**, 1668-1671 (1999).
[32] R. A. Bartels, A. Paul, H. Green, H. C. Kapteyn, M. M. Murnane, S. Backus, I. P. Christov, Y. W. Liu, D. Attwood, and C. Jacobsen, Science **297**, 376-378 (2002).
[33] G. Sansone, C. Vozzi, S. Stagira, M. Pascolini, L. Poletto, P. Villoresi, G. Tondello, S. De Silvestri, and M. Nisoli, Phys. Rev. Lett. **92**, 113904 (2004).
[34] D. N. B. Ammosov M.V., Krainov V.P., Soviet Physics JETP **64**, 1191 (1986).
[35] J. A. Armstrong, N. Bloembergen, J. Ducuing, and P. S. Pershan, Phys. Rev. A **127**, 1918 (1962).

[36] M. M. Fejer, G. A. Magel, D. H. Jundt, and R. L. Byer, IEEE J. Quantum Electron. **28**, 2631-2654 (1992).
[37] P. L. Shkolnikov, A. Lago, and A. E. Kaplan, Phys. Rev. A **50**, R4461-R4464 (1994).
[38] S. L. Voronov, I. Kohl, J. B. Madsen, J. Simmons, N. Terry, J. Titensor, Q. Wang, and J. Peatross, Phys. Rev. Lett. **87**, 133902 (2001).
[39] S. Backus, R. Bartels, S. Thompson, R. Dollinger, H. C. Kapteyn, and M. M. Murnane, Opt. Lett. **26**, 465-467 (2001).
[40] E. A. Gibson, A. Paul, N. Wagner, R. Tobey, D. Gaudiosi, S. Backus, I. P. Christov, A. Aquila, E. M. Gullikson, D. T. Attwood, M. M. Murnane, and H. C. Kapteyn, Science **302**, 95-98 (2003).
[41] C. Spielmann, L. Xu, and F. Krausz, Appl. Optics **36**, 2523-2525 (1997).

Chapter 12

APPLICATIONS OF ULTRAFAST LASERS

Sensors of extreme sensitivity

Jean-Claude Diels[1], R. Jason Jones[2] and Ladan Arissian[1]
[1] *Department of Physics and Astronomy, University of New Mexico*

[2] *JILA, National Institute of Standards and Technology and the University of Colorado*

Abstract: We discuss implementations of mode-locked ring lasers, their stabilization via passive optical cavities, and their applications to the development of ultra-sensitive sensors.

Key words: mode-locked laser, ring laser, sensors, optical parametric oscillator, optical cavity stabilization

The frequency of an electromagnetic wave is a quantity that lends itself to the most precise measurement of all physical observables. Stabilized cw lasers have led to accurate and precise length and time measurements, with an accuracy reaching one part in 10^{15} [1]. By transposing the stability of a single frequency laser to more than 1,000,000 equidistant frequencies, the mode-locked laser opens the way to new metrological applications. Some of these applications (optical frequency measurements, atomic clocks, extended combs leading to attosecond pulses, nonlinear optics, and attosecond metrology) have been covered in the previous chapters. The applications discussed in this chapter relate to the remarkable phase relationship that exists across the million equidistant modes. As a consequence of that phase relationship, it is possible to make phase measurements with an unprecedented accuracy. Unlike standard phase measurements that are made by measuring the *arccos* of an interference fringe (essentially an intensity measurement), the phase measurements presented here always convert the phase into a frequency. We will discuss in Sections 1-4 how mode-locked combs lead to practical sensing applications such as measurements of displacements, fields, indices of refraction, and elongation. The sensitivity limit of these applications can be extended through stabilization. The

stabilization technique outlined in Section 5 can lead to extremely sensitive measurements of dispersion, taking advantage of the phase relation between modes across a very large bandwidth (Section 6). Finally, future prospects of stabilizing a ring laser for all sensing applications are discussed in Section 7.

1. MODE LOCKING

The purpose of this introduction to "mode locking" is to bring the reader back to the real world of the typical mode-locked laser, which is quite different from the highly sophisticated sources discussed in this book. The expression mode locking suggests the concept of equidistant, longitudinal modes of a laser cavity emitting in phase. This was, in fact, the early interpretation given for cw lasers emitting a train of pulses at the cavity repetition rate. As detailed in the previous chapters, this frequency description of mode locking is equivalent to having a continuous single frequency carrier, sampled at equal time intervals by an envelope function, in the time domain. Unless sophisticated stabilization techniques (described in earlier chapters) are used, an ordinary mode-locked laser does not fit the above description.

Each cavity mirror is subject to vibrational motions of its support. A typical mechanical resonance is around 100 Hz and has motion amplitude ranging from 0.1 to 1 μm. Because of this motion, the position of the longitudinal modes of the cavity is not fixed in time. The intracavity laser pulse follows this change in time, because it is Doppler-shifted at each reflection from the vibrating mirror. For this reason, one can no longer talk about an output pulse train made up of identical pulses. The difference between the properties of the radiation from an ultrastable "frequency comb" as opposed to the ordinary "mode-locked laser" can be established in a coherence measurement. Coherence can be measured with a Mach-Zehnder interferometer, as sketched in Figure 12-1. In the case of a single pulse, no coherence can be measured for an optical delay of the interferometer exceeding the pulse duration. In the case of a pulse train, as the delay of the Mach Zehnder is being scanned, interferences may occur for delays equal to an integer multiple m of the pulse spacing. In a standard mode-locked laser, the fringe visibility decays rapidly to zero with increasing m. This is because the carrier frequency is Doppler-shifted at each round trip, and the pulse spacing is not constant because of mirror motion. In the frequency domain, there is no longer a perfect comb of delta-function modes in phase.

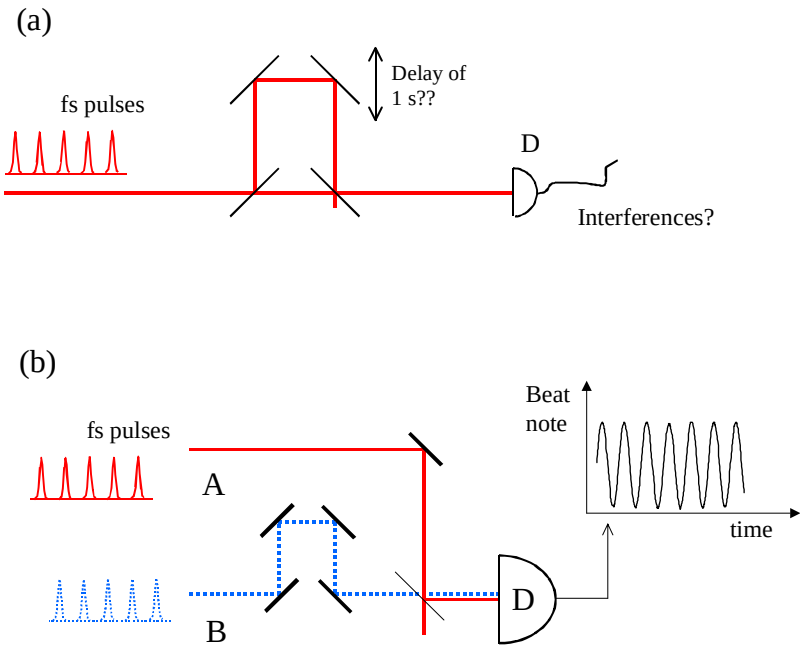

Figure 12-1. Coherence measured by a Mach-Zehnder interferometer. (a) In the case of a regular pulse train, by providing the near perfect frequency comb as discussed in previous chapters, interferences could be observed even in a delay of the interferometer approaching 1 s, or 14 orders of magnitude larger than the pulse duration. (b) The coherence of an unknown source A can be measured by optical beating with a reference source B, provided both sources have the same repetition rate. An optical delay is required to ensure that the pulse of each train interfere at detection.

A Mach-Zehnder interferometer is obviously not a practical instrument for measuring the coherence of a pulse train over many interpulse spacings. As described in the previous chapters, it is possible to have a pulse train coherent over delays 14 orders of magnitude larger than the pulse duration. Another method to measure the coherence of source *A* is to compare it with a perfectly coherent source *B* with the same repetition rate [Figure 12-1(b)]. If two sources of the same repetition rate but different carrier frequencies are made to interfere on a detector, a beat note at the difference between the two carrier frequencies will be observed [2]. The inverse of the bandwidth of this beat note is the coherence time of source *A*. A convolution of the bandwidths of each source is involved if source *B* is not perfectly coherent.

An example of a beat note between two pulse trains of the same repetition rate, but different carrier frequency, is shown in Figure 12-2.

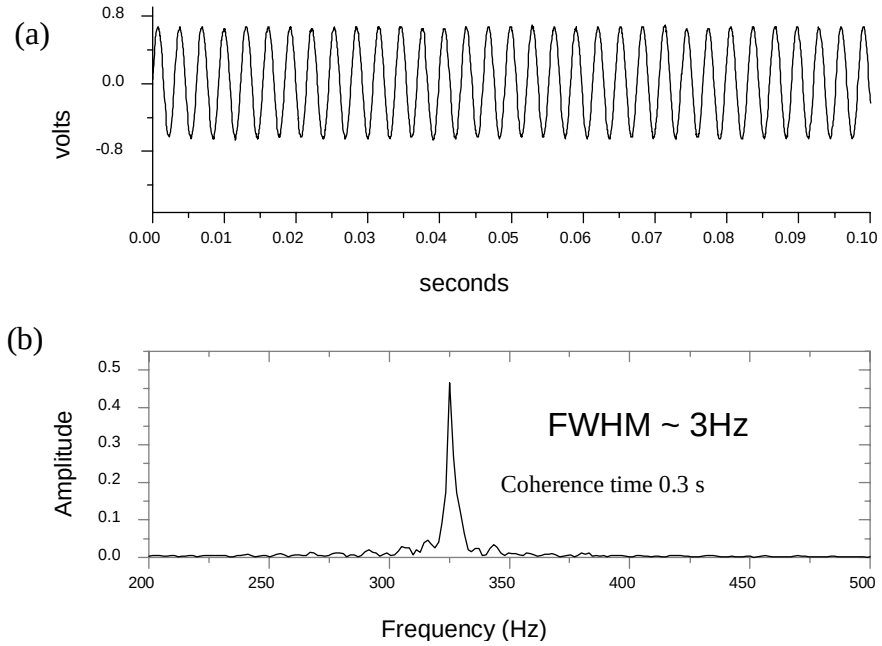

Figure 12-2. (a) Beat note recorded between two femtosecond pulse trains of the same repetition rate. (b) Fourier transform of the same recording, showing a bandwidth of only 3 Hz, or 0.8 Hz broader than the sampling time limit.

It may seem like a "tour de force" to achieve such a degree of stabilization as to record a coherence time of 0.3 s for a comb of fs pulses. Indeed, this bandwidth, obtained for an unstabilized mode-locked laser, is 3 orders of magnitude narrower than that of a single mode of a frequency comb stabilized to a reference cavity [3]. The measurement for Figure 12-2, however, was made with an unstabilized laser. The "trick" in this measurement is that the two beams being interfered have individually low coherence, but the fluctuations in repetition rate and carrier frequency of the two lasers are correlated. The two beams are the outputs corresponding to a clockwise and a counterclockwise circulating pulse in a ring cavity. Therefore, the same fluctuations in the laser apply to the two laser beams since both share the same geometrical mode of the cavity. The properties of such a mode-locked bidirectional ring laser are discussed in Section 2.

2. GROUP AND PHASE VELOCITIES IN RING LASERS

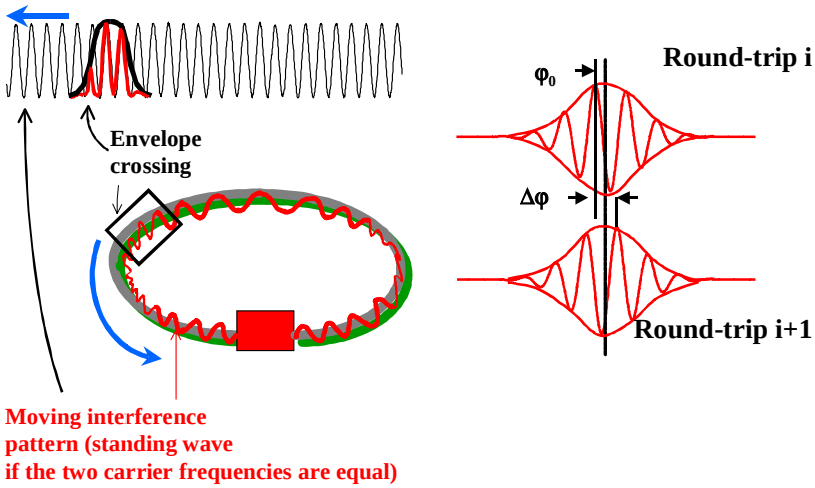

Figure 12-3. Topological representation of a mode-locked ring laser. The pulse envelopes overlap at the same location of the cavity at each round trip.

A topological representation of a mode-locked ring laser is given in Figure 12-3. Two femtosecond pulses circulate in opposite sense in the cavity, crossing at each round trip at the same point in the cavity. In general, a nonlinear element, such as a saturable absorber, forces the pulses to meet at a fixed point. The average group velocity is the same for the counter-circulating beams. The phase velocity, however, may differ for the two directions of circulation. Therefore, the carrier frequency for the two directions may or may not be identical. If the two carrier frequencies are equal, a standing wave is formed in the cavity at the pulse crossing. If the frequency of the clockwise circulating pulse is slightly different from that of the counterclockwise pulse, the interference pattern of the two waves moves under the crossing envelopes (top left, Figure 12-3). Therefore the phase of the interference pattern with respect to the fixed envelope changes at each round trip. It is that change of carrier-to-envelope phase, at each roundtrip, that is being measured by the beat note between the two outputs. At each round-trip, the clockwise and counterclockwise pulses come to the same position (because the group velocity is the same for both directions). Let us assume that at a given round-trip index, *i*, the interference pattern has the

phase ϕ_0 with respect to the envelope. At the next round-trip, $i+1$, the phase of the interference with respect to the envelope is $\phi_0 + \Delta\phi$.

Even though the cavity perimeter fluctuates by as much as a wavelength during the measurement and the comb mode is imperfect, the interference pattern has a bandwidth of only of the order of a few Hz. In fact, in this measurement, the interference pattern is not determined by the total fluctuation of the cavity but by the fluctuation in difference in clockwise vs counterclockwise perimeters *during each single roundtrip*. A difference in perimeter ΔP between the clockwise and counterclockwise circulating beams causes a beat note $\Delta\nu$ given by [4]:

$$\frac{\Delta\nu}{\nu} = \frac{\Delta P}{P}, \tag{1}$$

where P is the perimeter of the ring laser and ν the optical frequency. A beat note $\Delta\nu$ of 3 Hz corresponds to a perimeter difference ΔP of P x 3 Hz/$\nu \approx 10^{-14}$ m. A mirror position fluctuation of 10^{-14} m during a round-trip time of 10 ns corresponds to a motion of 0.01 μm in a mechanical resonance period of 10 ms. To further reduce the bandwidth of the beat note, it is necessary to suppress the fluctuations that cause a difference in time of arrival that, in turn, will cause a difference in perimeter between the two circulating pulses during any round trip. Stabilization of the cavity perimeter may achieve the goal of reducing the beat note bandwidth. The type of stabilization required will be discussed in Section 7, which follows a discussion of the applications of the ring laser.

3. RING LASERS AS SENSORS

The detection of the beat note between the two outputs of a mode-locked ring laser leads to numerous sensing applications of exceptional sensitivity. The "sensor" consists of a mode-locked ring laser operating in a bidirectional mode and a detector located at an equal optical path distance from the intracavity pulse crossing point, as sketched in Figure 12-4. To avoid gain competition and have equal energy for the two counter-circulating intracavity pulses, the amplifying medium should be located 1/4 cavity perimeter away from the pulse crossing point.

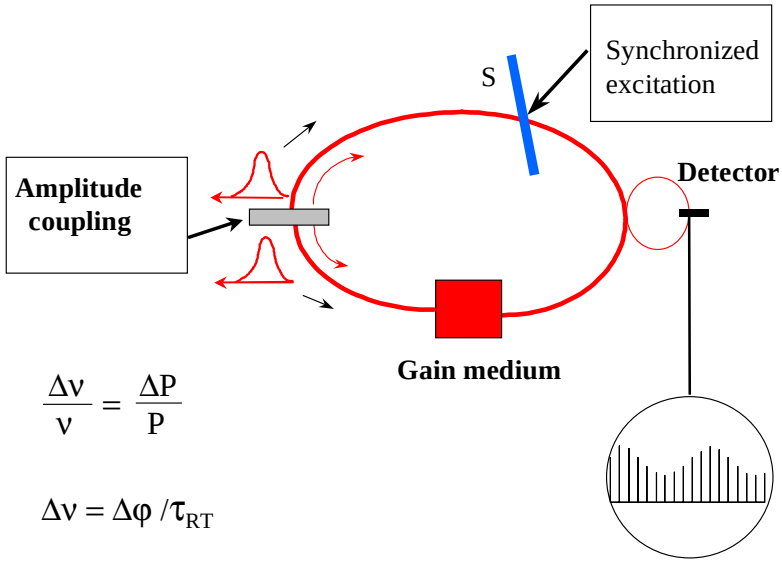

Figure 12-4. The general configuration of the sensor is that of a mode-locked ring laser and a detector located at equal optical path from the pulse crossing point, via the clockwise or counterclockwise direction of circulation. The gain medium is located at 1/4 cavity perimeter from the pulse crossing point. S is the sample of which the characteristics have to be determined. An eventual excitation of the sample is applied exactly at the cavity round-trip time.

There are three types of detection that can be performed: (1) Measurements of nonreciprocal effects, in which the "sample" can be the laser itself (rotation sensing), a flowing fluid (motion measurement by Fresnel drag), a material with a high Verdet constant (magnetic field measurement), or a resonant atomic vapor (intracavity phase spectroscopy); (2) changes of cavity optical length externally synchronized such as electro-optic effect, displacement due to phonons, electric field measurements, or a nonlinear medium (measurement of nonlinear index); and (3) monitoring of continuous small motions

The first type of response exists also with cw lasers, but, with mode-locked ring lasers, the sensitivity is not limited by a dead band. The next two types of response are unique to mode-locked ring lasers, for which the detection is not limited to nonreciprocal effects. While case (2) above requires a signal that can be modulated at the frequency of the cavity repetition rate, a continuous or slow drift can also be detected [case (3)] by sending the two intracavity pulses through separate pathways using electro-optical means [5].

3.1 Case (1): nonreciprocal effects

Without the need for adding any intracavity element, the device of Figure 12-4 can be used for **rotation sensing**. The rotational beat note response $\Delta\nu_R$ is related to the rotation of the laser (angular velocity Ω_R) around its axis by:

$$\Delta\nu_R = \frac{4A}{P\lambda}\Omega_R, \tag{2}$$

where A is the ring area. A large area to perimeter (A/P) ratio is desirable to have an optimum sensitivity to rotation. For applications where rotation sensing is not desired, a figure-of-8 laser with a net-zero area is the preferred geometry. Since the femtosecond ring laser acts as laser gyroscope without a dead band, the sensitivity to rotation is only limited by the bandwidth of the beat note, itself directly related to the stability of the resonator. Without active stabilization of the cavity, the 3 Hz bandwidth of the beat note of the Ti:sapphire ring laser shown in Figure 12-2 corresponds to a sensitivity to rotation of 0.2 degrees/hour, which compares favorably with the best navigational optical gyroscopes. Stabilization of the cavity perimeter would improve this figure by at least three orders of magnitude.

Rotation is not the only effect that causes a differential change in carrier frequency for the counter-circulating pulses. The beat note is extremely sensitive to air flows through the *Fresnel Drag* effect. The first evidence of nonreciprocal response in a ring mode-locked dye laser was a measurement of air flow through the Fresnel drag [6]. Very small air currents (air velocities of the order of 1 mm/s) can also account for the observed beat note bandwidth in Figure 12-2.

Magnetic field detection requires the insertion of a material with a high Verdet constant in the ring cavity, as with sample S sandwiched between two quarter-wave plates in Figure 12-4. The clockwise and counter-clockwise circulating pulses become, respectively, right and left circular polarized in the sample. In presence of a magnetic field, there is a difference in optical path ΔP between the two senses of circulation, resulting in a beat note proportional to the magnetic field. This effect can be particularly large in the presence of resonance. Optimal magnetic field sensitivity requires the use of a material for which the index change due to a magnetic field is maximal. Atomic vapors, such as used in potassium magnetometers [7], have a large resonant Faraday rotation, hence a large magnetic field-induced change in index for circularly polarized light. These vapor magnetometers have been used successfully in aerial mapping of the earth's magnetic field and to locate minerals, in particular magnetic iron deposits and nickel deposits [8]. The beat note response of the ring laser is significantly more sensitive to

magnetic field than the extracavity measurement performed in the potassium magnetometer [7] and should approach the sensitivity of the superconducting weak link detector or SQUID [9]. The latter has the disadvantage that it provides only microscopic information and has a limited dynamic range.

To reach a better sensitivity than the superconducting magnetometer, it is necessary to stabilize the laser to the atomic line selected as magnetic field sensor. Stabilizing a ring laser that produces a continuous train of ultrashort pulses is a very challenging task, which will be discussed in Section 7.

Intracavity spectroscopy is the last example of nonreciprocal measurement that, unlike the previous ones, requires the full mode comb structure of the mode-locked laser. In the case of the atomic vapor used in magnetometers, the level structure is a Λ, of which each branch is near resonance with one of the counter-circulating pulses. The two counter-circulating pulses are thus probing the near resonant dispersion of the sample S. Doppler-resolved near-resonant spectroscopy can be performed by recording the beat note while linearly scanning the carrier frequency of the mode-locked train in one direction. This experiment applied to samarium led to the first observation of the dispersion of the dark resonance [10].

3.2 Case (2): reciprocal effects that can be synchronized to the cavity repetition rate

In Figure 12-4, an arrow at the sample *S* indicates a possibility of changing some property of a cavity element with the same periodicity as the time of arrival of one of the intracavity pulses at that location. The synchronization can be externally applied (through a detector monitoring the pulse rate) or self-induced, as in the measurement of a nonlinear index. If the sample *S* in Figure 12-4 has an intensity dependent index of refraction $n(I)$, there will be a contribution to the beat note given by:

$$\Delta\nu = \frac{\Delta\phi}{\tau_{RT}} \approx \frac{2\pi d}{\lambda}\left(n(I+) - n(I-)\right), \tag{3}$$

where $I+$ and $I-$ are the beam intensities at the sample for the clockwise and counterclockwise circulating pulses, respectively. Equation 3 is valid only in the approximation that the sample thickness d is sufficiently small so that the intensities of each beam can be assumed to be constant in the sample. The difference $n(I+) - n(I-)$ can be varied by translating the sample along the beam axis between two lenses or spherical mirrors [11]. An example of measurement of the nonlinear index of lithium niobate with an optical parametric oscillator ring laser can be found in Reference [12].

The best sensitivity in these measurements can be achieved when all other contributions to the beat note can be eliminated, in particular the nonreciprocal effects listed above. The topology least sensitive to all nonreciprocal effects is the linear limit of an elongated ring. Instead of a clockwise and counterclockwise circulating pulse, in this "linear ring" two pulses circulate simultaneously, meeting exactly in the middle of the resonator. As with the ring laser sensor, a beat note is measured between the output pulse trains corresponding to each of these pulses. Unlike the case of a ring laser, the phase shift is the same for either of the intracavity circulating pulses because they travel through the same optical elements in the same order. There is therefore no bias beat note. To measure the electro-optic coefficient of a sample *S* inserted in this cavity, an electric field is applied at the cavity round-trip rate (1/2 of the pulse rate). To observe a beat note between the two interfering pulse trains requires a voltage only in the milliVolt range to be applied to the sample [13], leading to the most sensitive and accurate method to determine an electro-optic coefficient.

Figure 12-2 indicates that the sensitivity to the position of a reflecting surface is of the order of 0.001 Å. One immediate application is the study of displacements associated with ultrasound phonons, which can be produced in a coating synchronously with the cavity repetition rate. Other applications, such as monitoring the growth rate of a crystal or optical scanning nanoscopy, require a similar sensitivity to slow-moving displacements.

3.3 Case (3): reciprocal effects, slow motions

Either in the ring laser or in its linear limit, an electro-optic device can be inserted in the cavity to split the path of two circulating pulses, sending one through the sample to be analyzed and the other through a reference path [5], which can be stabilized to a reference cavity. Unlike the previous measurement, a stable cavity is not a sufficient attribute to perform accurate measurements. As will be seen in Section 5 on stabilization, the reference cavity may drift; hence there would be an ambiguity in the measurement: is the change in beat note reflecting an elongation of the sample or of the reference cavity? Thus this type of measurement requires accuracy (long-term stability) in addition to short-term stability through the reference cavity. The solution is to use properties of atomic transition to accurately fix a reference repetition rate and carrier frequency [14].

4. INTRACAVITY-PUMPED OPTICAL PARAMETRIC OSCILLATOR AS A MODE-LOCKED RING LASER

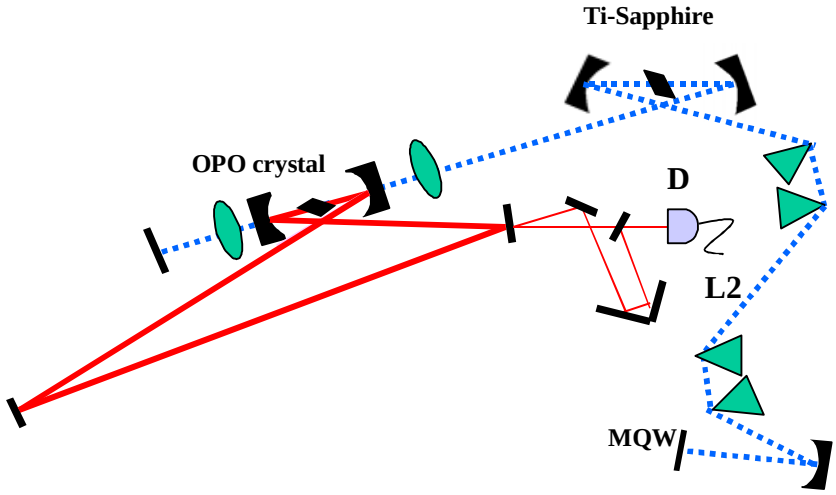

Figure 12-5. Illustration of the intracavity optical parametric oscillator (OPO) pumped by the Ti:sapphire laser. Four LaKL21 prisms are incorporated in the pump cavity to compensate for the group-velocity dispersion (GVD) from the Ti:sapphire crystal, the Periodically Poled Lithium Niobate (PPLN) crystal, and other intracavity elements such as lenses and mirrors. This four-prisms configuration was necessitated by the desire to have large GVD compensation (needed because of the large positive GVD of $LiNbO_3$) and a reasonably short cavity length (1/2 of the perimeter of the OPO cavity). The main control of the GVD compensation is the prism spacing L2. Two quantum wells (MQW) of AlGaAs on top of a mirror structure are used in the cavity as a saturable absorber to mode lock the laser.

Most measurements with ring laser sensors have been performed with either dye lasers [6] or Ti:sapphire lasers [4, 11, 13] mode locked with flowing saturable absorbers. Such systems are appropriate for demonstration purposes, but the future is for all-solid-state compact systems that can be readily stabilized. Some initial results on the most promising system, an intracavity-pumped Optical Parametric Oscillator (OPO) ring, are presented here. A synchronously pumped OPO offers the possibility of decoupling relative phase and repetition rates of the oscillating signals. The repetition rate of the OPO signal is equal to that of the pump laser and can therefore be controlled through stabilization of the mode spacing of the pump laser. The carrier frequency of the OPO is directly determined by the OPO cavity length. The position of the crossing point of the two circulating pulses in the OPO is simply determined by the timing of two successive pump pulses sent

in opposite directions. It is essential that the OPO crystal be part of the pump cavity. Only such an intracavity-pumped configuration can ensure that the OPO gain volumes for either direction are directly superimposed (because they share a common mode of the pump cavity). The operation of such a ring OPO has been demonstrated [15]. The cavity configuration of such an OPO-pumped intracavity by a linear Ti:sapphire laser is sketched in Figure 12-5.

The Ti:sapphire laser radiation consists of 200 fs pulses centered at 785 nm, with a repetition rate of 95MHz. The OPO crystal is a 3 mm Brewster-cut PPLN crystal (HC Photonics, Taiwan) with a period of 19.4 μm (quasi-phase matching for the signal near 1.36 μm) that is temperature stabilized at 408 K to prevent photorefractive damage. The cavity mirrors and crystal are located away from the two crossing points of the ring.

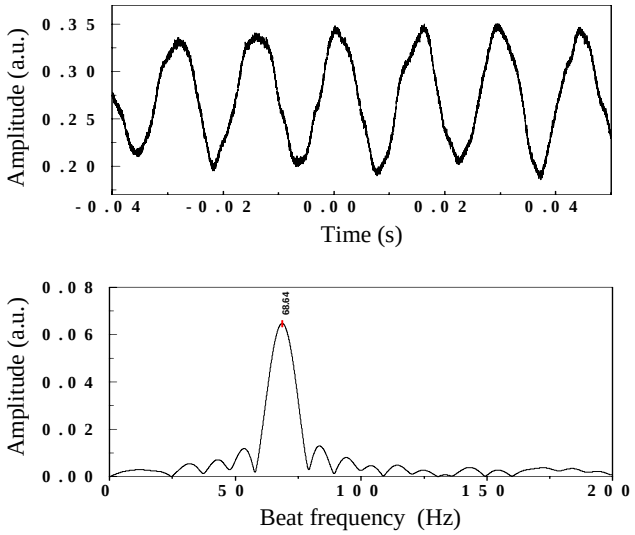

Figure 12-6. Beat frequency (a) taken by a sensitive InGaAs detector (D in Figure12-5) and (b) its Fourier transform.

The observed beat frequency is due to the intensity difference of the intracavity beams. The pump in one direction is attenuated by depletion through the crystal and transmission through four antireflection-coated surfaces and one reflective coating before coming back to pump into the other direction. The intensity difference, combined with the nonlinear refractive index of the lithium niobate crystal, results in a differential phase shift between the counter-circulating OPO beams—hence a beat note. The narrow bandwidth of the beat note in Figure 12-6 demonstrates that indeed, intracavity pumping ensures that the gain for the two directions originates from the same point in the OPO crystal. The absence of any moving part and

the fundamental absence of a dead band make the intracavity-pumped OPO ring the most promising sensor based on nonreciprocal effects in ring cavities. The beat note bandwidth results from cavity length fluctuations and can be eliminated by active stabilization. A reduced beat note bandwidth implies a better sensitivity (resolution) in the response of the ring laser as a sensor for any of the applications listed in Section 3.

5. STABILIZATION OF THE FREQUENCY COMB

The bidirectional ring laser produces a pair of highly correlated pulse trains that allow one to minimize the effects of perturbations on the femtosecond comb and make precision measurements of nonreciprocal effects inside the laser cavity. The absolute noise on each pulse train still has an impact—albeit greatly diminished—on the precision of these measurements. Further reduction of the linewidth of the signal—a beat note in the case of the ring laser—requires active stabilization of the femtosecond laser cavity. This section is devoted to the stabilization technique applied to a linear cavity and its application. In Section 7, this technique is extended to the ring laser.

Stabilization and control of mode-locked lasers has been demanded by novel applications using the femtosecond comb. Like their single frequency counterparts, mode-locked lasers are perturbed by mechanical and acoustic vibrations that shift and broaden the comb structure. However, because of the higher peak intensities of the intracavity pulses and the mode-locking dynamics, these systems are more susceptible to noise induced by pulse energy fluctuations. As discussed in previous chapters, the most common technique for stabilization of the femtosecond laser uses a combination of two phase-locked loops to lock both degrees of freedom (the carrier frequency and the repetition rate) of the femtosecond frequency comb. Some techniques choose to do all measurements in the rf domain, substituting the offset frequency for that of the average frequency. The most straightforward implementation of such techniques requires octave bandwidth spanning.

In the technique described here, optical frequencies are directly used to avoid the multiplication error involved with rf-source measurements. Beat-note detections with a high signal-to-noise ratio and at least one highly stable frequency reference are required. In this method, the average frequency and repetition rate of the femtosecond laser is locked to a stable Fabry-Perot reference cavity. With proper stabilization, the pulse train inherits the stability of the reference cavity and precision measurements of phase shifts are spectrally resolved across a broad bandwidth. In the time domain, one can think of the reference cavity as a "reference pulse" source for time scales

up to the lifetime of the cavity. Although mechanical cavities are susceptible to drifts on long time scales (>10 s), such cavities can provide an extremely high stability reference (σ(1s) ~3 x 10^{-16} [1]) because of a combination of narrow cavity resonances and a linear response to the interrogating laser.

5.1 Locking femtosecond pulses to stable reference cavities

Earlier stabilization experiments with mode-locked lasers often used short Fabry-Perot etalons to stabilize the *average position* of the comb, directly employing the techniques developed for single frequency lasers [16]. More recent experiments have used Fabry-Perot cavities as "mode filters," transmitting every 20^{th} comb component, such that any individual mode of the comb can be unambiguously identified with a wave meter [17, 18].

Constructive interference of the femtosecond pulse with the intra-reference-cavity pulse is achieved when the pulse envelopes and optical phases overlap. Satisfying these two conditions will get to the resonance and energy build-up in the cavity [19], where each pulse in the cavity is a life-time average of the previous pulses. Complete transmission is identical to locking the repetition rate and average frequency of the femtosecond pulses to the reference cavity.

Close-up of such an experiment [20] is shown in Figure 12-7. The reference cavity is a long (62.5 cm) Fabry-Perot resonator made of a solid block of ultralow-expansion quartz (ULE) with high reflectivity mirrors of the same material optically contacted on both ends. The cavity is placed in a vacuum chamber to isolate it from thermal and acoustic noise and, if needed, to control the pressure. The vacuum chamber usually keeps the pressure inside the reference cavity below 15 mTorr. The laser cavity length is twice that of the reference cavity, so that every other mode can be transmitted. Kerr-lens mode locking provides pulses around 40 fs. The two degrees of freedom are controlled with two piezoelectric transducers (PZT). A change in the cavity length (PZT1) results in mode shifting and tilting of the end mirror (PZT2) selects different frequency components and controls the group velocity. These adjustments can be made nearly orthogonal by proper gain adjustment on Servo1 and Servo2. An acousto-optic modulator is used for fast (up to 150 kHz) carrier-frequency corrections without changing the repetition rate of the laser. The error signal is obtained by Pound-Drever-Hall discrimination [21]. The laser beam is phase modulated at 10.7 MHz and detection of the cavity resonance is made at the modulated frequency. Detectors PD1 and PD2 collect marginal reflected light from the reference cavity that is spatially expanded with a grating.

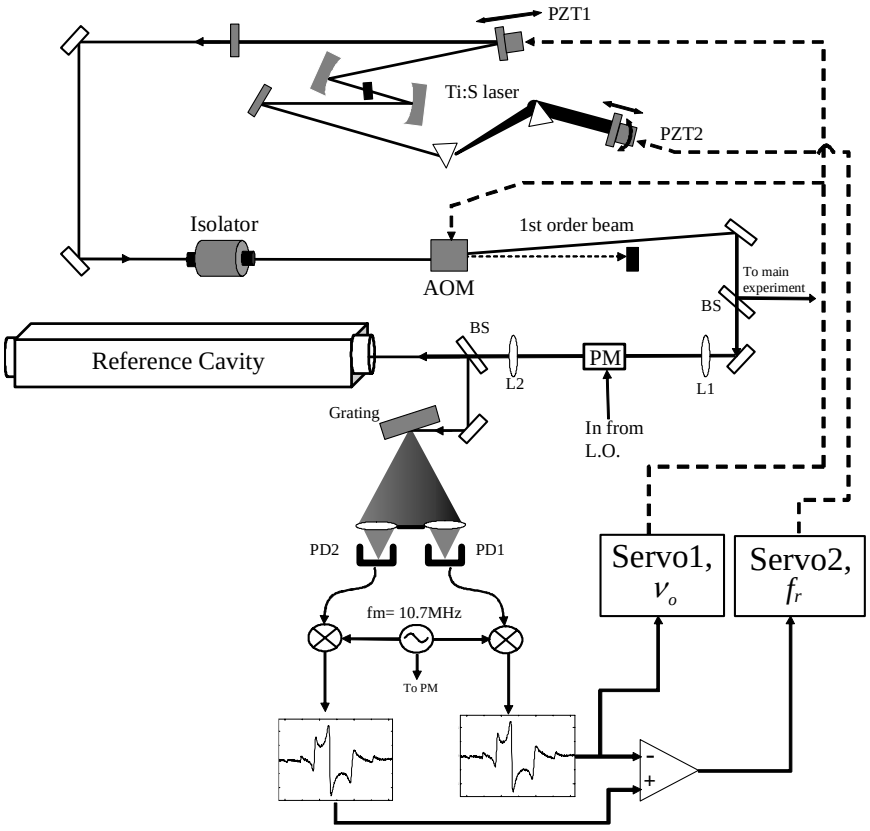

Figure 12-7. Schematic of experimental setup. The laser output, protected from feedback by a Faraday isolator, is sent through an acousto-optic modulator that controls average frequency before being sent through a phase modulator and mode matched to the reference cavity. AOM: acousto-optic modulator; PM: phase modulator; B: beam splitter; PD1 and PD2: photodiodes 1 and 2; and PZT1–3: piezo-electric transducers.

The error signals obtained in this way are the composite signals from *all* longitudinal modes detected within the spectral regions seen at PD1 and PD2. One detector can provide the error signal to lock the *position* of the comb about some average frequency by adjusting AOM and PZT1 (i.e., controlling the cavity length). The difference between the error signals from PD1 and PD2 determines fluctuations in the laser repetition rate that can be stabilized by PZT2, which selects the average group velocity [18]. The sensitivity of this discriminator is equal to the slope of the error signals multiplied by the number of modes between them. This technique provides an extremely sensitive discriminator for the repetition rate by effectively locking a high harmonic of it to the cavity. The reference cavity sees the

stabilized modes of frequency $\nu_m = mf_r + f_0 + f_{VCO}$, where f_r is the laser repetition frequency and f_0 the offset frequency of the comb. The frequency f_{VCO} is provided by the voltage-controlled oscillator (VCO) used to drive the AOM. Note that the sum $f_0 + f_{VCO}$ is stabilized in this technique.

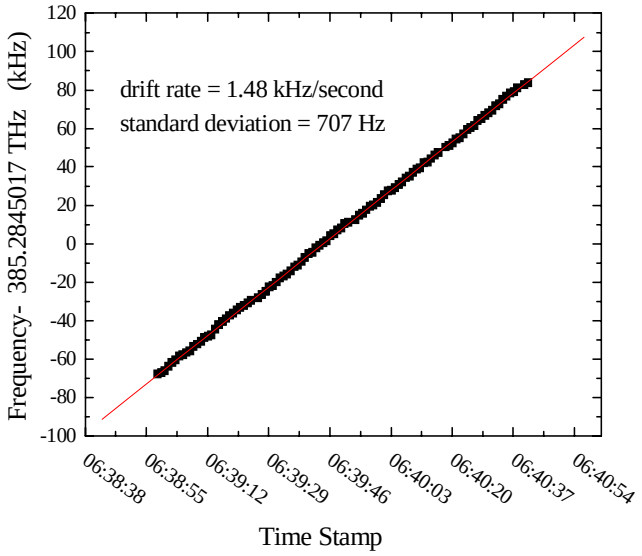

Figure 12-8. Measurement of optical frequencies of the femtosecond comb. One hundred consecutive measurements are made showing the slow, but easily measurable, drift of the reference cavity. Fractional Allan deviation from these counts is $\sigma(1s) \sim 3 \times 10^{-12}$.

5.2 Characterization of femtosecond comb stability

The stability of a femtosecond laser cavity can be confirmed by measuring any single optical frequency of the comb. A frequency mode $\nu_m = mf_r + f_0$ is determined by measuring the repetition rate f_r and the offset frequency f_0. Here the offset frequency of the comb was detected by beat note measurement [22] of a frequency mode with its second harmonic in a "ν–to–2ν interferometer," using microstructure fiber. The nonzero offset frequency of the femtosecond-stabilized comb is because of the finite dispersive phase shifts of the reference cavity mirrors. Figure 12-8 shows the linear drift for mode number 3,212,199 of the femtosecond comb. The value of this drift can be greatly improved through temperature control of the vacuum chamber walls. (Drift rates well below 100 Hz/s are usually obtainable even without temperature stabilization.) The beat note of the 5th harmonic of the repetition rate (120 MHz) with the 6th harmonic of an

accurate 100 MHz frequency reference source provides the repetition rate value. The 1-s Allan deviation for these counts is ~3 x 10^{-12}. This number is limited by the stability of the low-noise frequency reference (100 MHz).

6. DISPERSION MEASUREMENT APPLICATIONS

A reference cavity and a laser have mutual dependency: each one can be a source and reference for the other. As mentioned before, the nonzero offset frequency is due to the phase change upon reflection from the two cavity mirrors. In the frequency domain, this phase shift is usually frequency dependent, i.e., the reference cavity mode spacing changes with frequency. In the time domain, the pulse's frequency component goes through different depths in the mirror coating; thus each frequency component "sees" a different length of the reference cavity, known as an "external cavity."

The stabilized femtosecond laser can act as a frequency comb to characterize the dispersion of the external cavity mirrors. This ruler can measure the dispersion of gases and low-density materials inside the external cavity over a broad bandwidth. Furthermore, the high peak-intensity build-up in the cavity provides a tool to study nonlinear phase shifts. An experimental setup is presented in the following section.

6.1 Cavity characterization

A tunable cw Ti:sapphire laser is added to the setup and locked to a single mode of the reference cavity while femtosecond laser stabilization has been achieved, as shown in Figure 12-9. The equally spaced femtosecond comb provides an absolute frequency grid against which the unequally spaced reference cavity modes can be measured. The beat frequency between the cw laser and the m^{th} mode of the femtosecond comb, $\Delta(m)$, gives a direct measurement of the deviation of the reference cavity frequencies from the equally spaced modes of the femtosecond comb.

Figure 12-10 shows the results of this measurement when the external reference cavity was in a vacuum. Each data point for $\Delta(m)$ corresponds to approximately 100 measured readings. The cavity's free spectra range (FSR) as a function of frequency, $\sigma(f)$, is calculated from the relation $\sigma(f)=\sigma_0(1+\partial\Delta/\partial f)$ and is indicated by the dashed lines and right side ordinate. Notice that the maximum deviation (Δ ~300 kHz) of the FSR is less than the width of the cavity resonance (~1 MHz). This explains why it is possible to align the entire bandwidth of the femtosecond laser to the modes of the external cavity. The mirrors are standard high-reflecting dielectric

mirrors. Higher quality mirrors with lower GVD increase the bandwidth of the transmitted laser and improve locking stability of femtosecond lasers to high-finesse reference cavities.

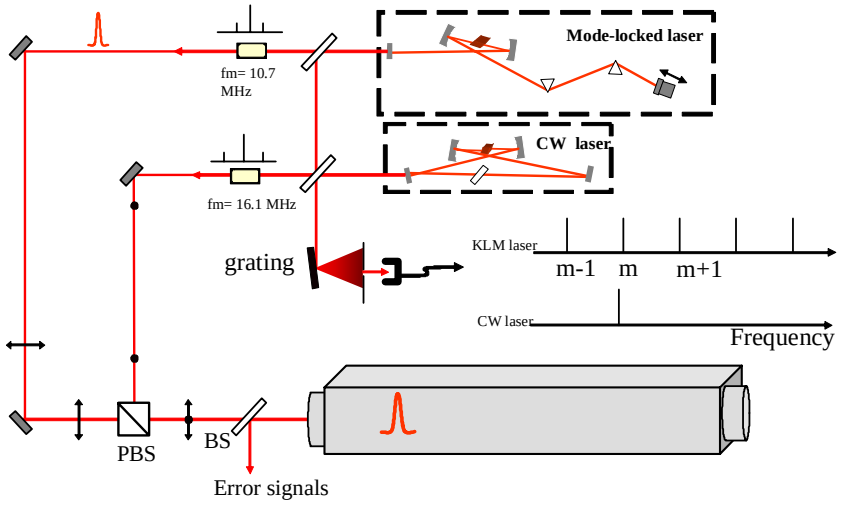

Figure 12-9. Experimental setup to measure longitudinal modes of reference cavity. PBS: polarizing beamsplitter and BS: non-polarizing beamsplitter.

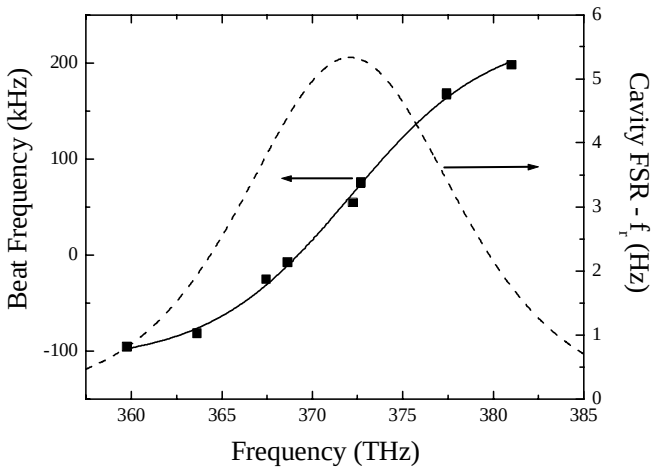

Figure 12-10. Measured deviation (Δ) of the reference cavity longitudinal modes under vacuum from the equidistant positions of the frequency comb (left ordinate; squares) and the calculated mode spacing of the cavity vs frequency (right ordinate; dashed curve).

6.2 Atmospheric dispersion

The same measurement is performed when the external cavity is in atmospheric pressure (Figure 12-11). The dispersion of air may result in a beat note higher than the cavity linewidth (~1 MHz) in some spectral regions, indicating regions of the femtosecond comb that are not coupled into the cavity. From this data, one can calculate the round-trip GVD inside the cavity. The inverse of the pulse round-trip time in the cavity is equal to the FSR and will be frequency dependent in the presence of GVD. The pulse round-trip time is

$$\tau_n = \frac{\partial \Phi_n}{\partial \Omega}, \tag{4}$$

where Φ_n is the total round-trip phase shift inside the cavity. The change in

$$\frac{\partial \sigma}{\partial \Omega} = \frac{\partial}{\partial \Omega}\frac{1}{\tau_n} = -\frac{1}{\tau_n^2}\frac{\partial \tau_n}{\partial \Omega} = -\frac{1}{\tau_n^2}\frac{\partial^2 \Phi_n}{\partial \Omega^2}, \tag{5}$$

and therefore the round-trip GVD can be related to the measured FSR by

$$\Phi_n' = -\frac{1}{\sigma^2}\frac{\partial \sigma}{\partial \Omega}. \tag{6}$$

The calculated round-trip GVD for the cavity at atmospheric pressure is ≈ 20 fs^2. Assuming the calculated GVD is entirely due to the passage of the pulse through the atmosphere in the 62.5-cm long reference cavity, Equation (6) gives $k'' \approx 0.16$ fs^2/cm at 385 THz (780 nm). This value is in good agreement with that calculated for dry air at atmospheric pressure based on the measured index of refraction [23]. The accuracy of this measurement technique and the long interaction length available inside a resonant cavity make this system suitable for pursuing precise measurements of linear and nonlinear dispersion in different media and characterizing phase shifts from dielectric mirrors.

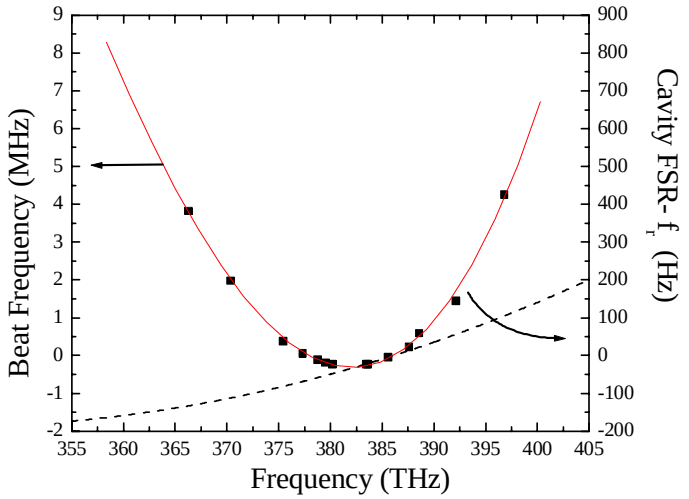

Figure 12-11. Measured deviation of the reference cavity longitudinal modes at atmospheric pressure from the equidistant positions of the frequency comb (left ordinate; data points) and the calculated mode spacing of the cavity vs frequency (right ordinate; dashed curve).

7. RING LASER STABILIZATION

Applying the previous techniques to the stabilization of a bidirectional ring laser is not straightforward. Since the sensor applications involve intracavity measurements, the laser itself, rather than an extracavity beam, is shifted in frequency by an AO modulator. A basic challenge is to find two orthogonal cavity controls to act independently on the pulse repetition rate and the carrier frequency. In the case of the Ti:sapphire ring laser, one can control the carrier frequency through the pump intensity and the repetition rate through the cavity length. These two controls are however not perfectly independent, as opposed to the case of an OPO, where the repetition rate of the OPO is controlled by the pump laser and the OPO signal carrier frequency is determined by the ring perimeter. An example of intracavity-pumped OPO geometry is sketched in Figure 12-12.

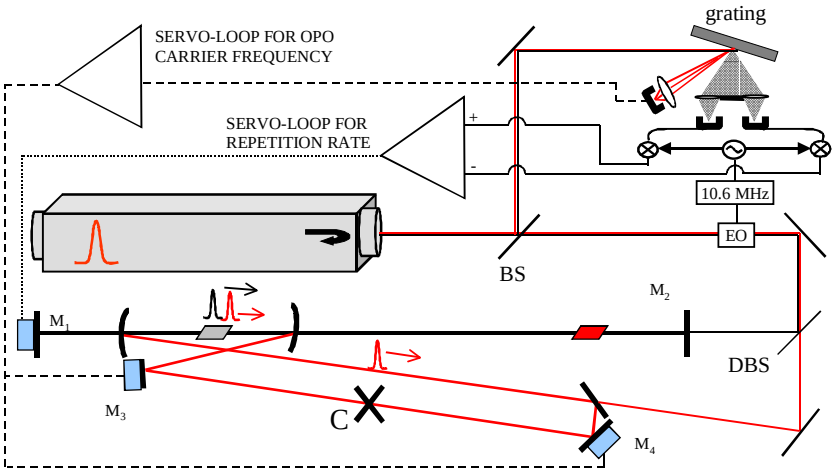

Figure 12-12. Sketch of a possible ring OPO geometry and the stabilization loop.

The beams of the pump laser and the OPO signal are combined by a dichroic beam splitter (DBS). Both beams are given the same phase modulation at 10.5 MHz by an electro-optic crystal. The reflection of the reference cavity (1/2 the cavity length of the pump) is dispersed by a grating. The difference between the two error signals taken at the edges of the pump spectrum are used to control the cavity length (mirror M_1) of the pump laser and hence the repetition rate of the system. The wavelength of the OPO signal is unaffected, since it is solely determined by the OPO cavity perimeter. An error signal is thus derived from the dispersion of the grating at the signal wavelength and mixed with the modulation. The correction signal is sent simultaneously to the piezo drivers of mirrors M_3 and M_4, located symmetrically with respect to the pulse crossing point C. It is essential to symmetrically apply the correction for the signal cavity simultaneously to the two circulating pulses to prevent a broadening of the beat-note bandwidth by the motion of the cavity length-correcting mirrors.

As mentioned earlier, for applications that require long-term stability or accuracy (monitoring or slow drifts in the picometer range), the OPO frequency and the pulse repetition rate have to be locked to some atomic transition. Because of the general tunability of an OPO, there is a large choice of atomic systems available. One approach [14] is to use a Λ level structure that has a two-photon resonance at the carrier frequency of one of the OPO pulses and a ground-level splitting resonant with the pulse repetition rate. The main challenge is to find an error signal (fluorescence, dispersion, absorption) that has a well-defined peak at the proper optical

frequency and repetition rate. This problem has been investigated theoretically for the case of rubidium vapor in Reference [14].

REFERENCES

[1] B. C. Young, F. C. Cruz, W. M. Itano, and J. C. Bergquist, Phys. Rev. Lett. **82**, 3799-3802 (1999).

[2] R. K. Shelton, L. S. Ma, H. C. Kapteyn, M. M. Murnane, J. L. Hall, and J. Ye, Science **293**, 1286-1289 (2001).

[3] R. J. Jones and J. C. Diels, Phys. Rev. Lett. **86**, 3288-3291 (2001).

[4] S. Diddams, B. Atherton, and J. C. Diels, Appl. Phys. B **63**, 473-480 (1996).

[5] J. C. Diels, M. Bohn, J. Jones, and T. T. Dang, (United States Patent, Filed April 27 2000., 2000), Vol. Patent Pending, (UNM Docket No. UNM-490).

[6] M. L. Dennis, J. C. M. Diels, and M. Lai, Opt. Lett. **16**, 529-531 (1991).

[7] P. J. Hood and H. Ward, *Airborne Geophysical Methods* (Academic Press, 1969).

[8] D. J. Teskey, P. J. Hood, L. W. Morley, R. A. Gibb, P. Sawatzky, M. Bower, and E. E. Ready, Can. J. Earth Sci. **30**, 243-260 (1993).

[9] P. J. Hood, Northern Miner, 1-14 (1991).

[10] S. A. Diddams, J. C. Diels, and B. Atherton, Phys. Rev. A **58**, 2252-2264 (1998).

[11] M. Bohn, Ph.D Thesis, University of New Mexico (1998).

[12] X. M. Meng, J. C. Diels, D. Kuehlke, R. Batchko, and R. Byer, Opt. Lett. **26**, 265-267 (2001).

[13] M. J. Bohn, J. C. Diels, and R. K. Jain, Opt. Lett. **22**, 642-644 (1997).

[14] L. Arissian, J. Jones, and J. C. Diels, J. Mod. Opt. **49**, 2517-2533 (2002).

[15] X. M. Meng, Ph.D Thesis, University of New Mexico (2003).

[16] A. I. Ferguson and R. A. Taylor, Opt. Commun. **41**, 271-276 (1982); E. Kruger, Rev. Sci. Instrum. **66**, 4806-4812 (1995).

[17] T. Udem, J. Reichert, R. Holzwarth, and T. W. Hänsch, Phys. Rev. Lett. **82**, 3568-3571 (1999).

[18] J. Reichert, R. Holzwarth, T. Udem, and T. W. Hänsch, Opt. Commun. **172**, 59-68 (1999).

[19] R. J. Jones and J. Ye, Opt. Lett. **27**, 1848-1850 (2002).

[20] R. J. Jones, J. C. Diels, J. Jasapara, and W. Rudolph, Opt. Commun. **175**, 409-418 (2000).

[21] R. W. P. Drever, J. L. Hall, F. V. Kowalski, J. Hough, G. M. Ford, A. J. Munley, and H. Ward, Appl. Phys. B **31**, 97-105 (1983).

[22] D. J. Jones, S. A. Diddams, J. K. Ranka, A. Stentz, R. S. Windeler, J. L. Hall, and S. T. Cundiff, Science **288**, 635-639 (2000).

[23] *Handbook of Chemistry and Physics* (The Chemical Rubber Co., Cleveland, OH, 1985/1986).

Appendix

AUTHOR ADDRESSES

Arissian, Ladan: Department of Physics and Astronomy, 800 Yale Blvd. NE, University of New Mexico, Albuquerque, NM 87131

Baltuška, Andrius: Institut für Photonik, Technische Universität Wien, Gusshausstrasse 27, A-1040 Wien, Austria and Max-Planck-Institut für Quantenoptik, 85748 Garching, Germany

Bartels, Albrecht: Time and Frequency Division, National Institute of Standards and Technology, 325 Broadway M.S. 847, Boulder, CO 80305

Cundiff, Steven T.: JILA, National Institute of Standards and Technology and University of Colorado, University of Colorado, Boulder, CO 80309-0440

Christov, Ivan: JILA and Department of Physics, University of Colorado and NIST, and NSF Engineering Research Center for Extreme-Ultraviolet Science and Technology, Boulder, CO 80309-0440

Diddams, Scott A.: Time and Frequency Division, National Institute of Standards and Technology, 325 Broadway, Boulder, CO 80305

Diels, Jean-Claude: Department of Physics and Astronomy, 800 Yale Blvd. NE, University of New Mexico, Albuquerque, NM 87131

Fischer, Marc: Max-Planck-Institut für Quantenoptik, 85748 Garching, Germany

Gaeta, Alexander L.: School of Applied and Engineering Physics, Cornell University, Ithaca, NY 14853

Gibson Emily: JILA and Department of Physics, University of Colorado and NIST, and NSF Engineering Research Center for Extreme-Ultraviolet Science and Technology, Boulder, CO 80309-0440

Hall, John L.: JILA, National Institute of Standards and Technology and University of Colorado, University of Colorado, Boulder, CO 80309-0440

Hänsch, Theodor W.: Max-Planck-Institut für Quantenoptik, 85748 Garching, Germany

Haverkamp, Nils: Physikalisch-Technische Bundesanstalt, Bundesallee 100, D-38116 Braunschweig, Germany

Hollberg, Leo: Time and Frequency Division, National Institute of Standards and Technology, 325 Broadway, Boulder, CO 80305

Holzwarth, Ronald: Max-Planck-Institut für Quantenoptik, 85748 Garching, Germany

Ippen, Erich: Department of Electrical Engineering and Computer Science, Research Laboratory of Electronics, Massachusetts Institute of Technology, Cambridge, MA, 02139-4307

Jones, R. Jason: JILA, National Institute of Standards and Technology and University of Colorado, University of Colorado, Boulder, CO 80309-0440

Kapteyn Henry C.: JILA and Department of Physics, University of Colorado and NIST, and NSF Engineering Research Center for Extreme-Ultraviolet Science and Technology, Boulder, CO 80309-0440

Kärtner, Franz: Department of Electrical Engineering and Computer Science, Research Laboratory of Electronics, Massachusetts Institute of Technology, Cambridge, MA, 02139-4307

Keller, Ursula: Institut für Quantenelektronik, ETH Zürich Hönggerberg CH-8093 Zürich, Switzerland

Kienberger, Reinhard: Institut für Photonik, Technische Universität Wien, Gusshausstrasse 27, A-1040 Wien, Austria and Max-Planck-Institut für Quantenoptik, 85748 Garching, Germany

Kobayashi, Takayoshi: Department of Physics, Faculty of Science, University of Tokyo, 7-3-1 Hongo, Bunkyo, Tokyo 113-0033, Japan

Kolachevsky, Nikolai: Max-Planck-Institut für Quantenoptik, 85748 Garching, Germany

Krausz, Ferenc: Institut für Photonik, Technische Universität Wien, Gusshausstrasse 27, A-1040 Wien, Austria and Max-Planck-Institut für Quantenoptik, 85748 Garching, Germany

Lindner, Fabrizio: Max-Planck-Institut für Quantenoptik, 85748 Garching, Germany

Lipphardt, Burghard: Physikalisch-Technische Bundesanstalt, Bundesallee 100, D-38116 Braunschweig, Germany

Murnane, Margaret M.: JILA and Department of Physics, University of Colorado and NIST, and NSF Engineering Research Center for Extreme-Ultraviolet Science and Technology, Boulder, CO 80309-0440

Paulus, Gerhard G.: Max-Planck-Institut für Quantenoptik, 85748 Garching, Germany and Department of Physics, Texas A&M University, College Station, Texas 77843-4242, USA

Schnatz, Harald:Physikalisch-Technische Bundesanstalt, Bundesallee 100, D-38116 Braunschweig, Germany

Steinmeyer, Günter: Max-Born-Institut für Nichtlineare Optik und Kurzzeitspektroskopie, Max-Born-Str.2a, D-12489 Berlin, Germany

Stenger, Jörn:Physikalisch-Technische Bundesanstalt, Bundesallee 100, D-38116 Braunschweig, Germany

Udem, Thomas: Max-Planck-Institut für Quantenoptik, 85748 Garching, Germany

Weiss, Carl-Otto: Physikalisch-Technische Bundesanstalt, Bundesallee 100, D-38116 Braunschweig, Germany

Windeler, Robert S.: OFS Laboratories, 600 Mountain Avenue, Murray Hill, NJ 07974

Ye, Jun: JILA, National Institute of Standards and Technology and University of Colorado, University of Colorado, Boulder, CO 80309-0440

Zimmermann, Marcus: Max-Planck-Institut für Quantenoptik, 85748 Garching, Germany

INDEX